Journal of Experimental and Theoretical Physics, Vol. 96, No. 5, 2003, pp. 775–781.
Translated from Zhurnal Éksperimental'noĭ i Teoreticheskoĭ Fiziki, Vol. 123, No. 5, 2003, pp. 883–890.

NUCLEI, PARTICLES, AND THEIR INTERACTION

The Motion of Particle Spin in a Nonuniform Electromagnetic Field

A. Ya. Silenko

Research Institute for Nuclear Problems, Belarussian State University, Minsk, 220050 Belarus
e-mail: silenko@inp.minsk.by

Received September 13, 2002

Abstract—We have applied the Foldy–Wouthuysen transformation to spin-1 particles interacting with a nonuniform electromagnetic field. This allowed us to simultaneously confirm that the Pomeransky–Khriplovich–Sen'kov theory is valid and that the interaction of spin 1-particles with a weak field is properly described by the Corben–Schwinger equation. We analyzed the possibilities for experimentally testing theoretical conclusions by observing spin oscillations for the planar channeling of particles or nuclei in straight crystals. By carrying out such experiments, we can also detect the spin oscillations produced by electromagnetic interaction and measure the quadrupole moments of short-lived nuclei. © *2003 MAIK "Nauka/Interperiodica".*

1. INTRODUCTION

The Good–Nyborg (GN) equation [1, 2] has long been used to describe the spin motion in a nonuniform electromagnetic field. It was derived in terms of classical electrodynamics and is consistent with more recent classical and semiclassical studies (see [3, 4] and references therein). The GN equation and the method used for its derivation served as the basis for deducing the equation of spin motion with radiation [5].

The quantum-mechanical equation of spin motion for spin-1/2 particles in a nonuniform electromagnetic field [6–9] is an exact quantum-mechanical analog of the Bargmann–Michel–Telegdi (BMT) equation [10]. A quantum-mechanical expression for the Lagrangian of particles with arbitrary spin in an electromagnetic field with terms quadratic in spin was derived in [11, 12]. As was shown in [4], the equation of spin motion obtained from this expression significantly differs from the GN equation. This is the strongest argument against the GN equation.

The existence of two mutually exclusive equations of spin motion needs to be independently verified, both theoretically and experimentally. Particles and nuclei with spin 1 are the most convenient objects for such verification. The relativistic wave equations for such particles are slightly simpler than, for example, those for spin-3/2 particles. The Foldy–Wouthuysen (FW) transformation [13] can be used to rigorously derive the equation of spin motion. Using this transformation, we can obtain the Hamiltonian for relativistic particles in an external field. The commutator of the Hamiltonian with the polarization operator, which is simply expressed in terms of the spin operator **S** in FW representation [4], is calculated to obtain the equation of spin motion. In the linear (in spin) approximation, an expression for the Hamiltonian was derived in this way previously [4]. To determine the Hamiltonian with terms quadratic in spin, we use the method suggested in [4].

The possibility of experimentally detecting the polarization evolution due to the quadratic terms in the equation of spin motion is associated with the use of spin oscillations. The latter phenomenon, which exists for particles with a spin of $S \geq 1$, was predicted and described in [14–16]. It consists in periodic polarization variations of a particle beam in a material and, in the case under consideration, is attributable to the dependence of particle energy on the square of one or two projections of the spin operator. Spin oscillations can be used to measure the quadrupole moments, which is particularly relevant to particles (and nuclei) with short lifetimes, e.g., Ω^- hyperons [14–16]. This phenomenon is the result of not only electromagnetic but also strong interaction [17–21]. Because of strong interaction, spin oscillations take place even for a nonpolarized target.

Here, we suggest using the phenomenon of spin oscillations to experimentally detect the polarization evolution due to the quadratic terms in the equation of particle spin motion in an electromagnetic field. This, in turn, allows the equations of spin motion to be experimentally verified.

We use the relativistic system of units with $\hbar = c = 1$.

2. THE HAMILTONIAN FOR SPIN-1 PARTICLES IN A NONUNIFORM ELECTROMAGNETIC FIELD

Here, as in [4], we determined the Hamiltonian for spin-1 relativistic particles in a nonuniform electromagnetic field by using the generalized Sakata–Taketani equation deduced in [22] for particles with an anomalous magnetic moment. The basic equation in its

derivation was the first-order Proca equation with an anomalous magnetic moment (the Corben–Schwinger equation [23]). The extra terms describing the quadrupole moment unrelated to the particle magnetic moment introduced in [22] were disregarded in our calculations. Cumbersome calculations are required to determine the terms of the second order in spin proportional to the derivatives of the field strengths. Therefore, we took into account only the terms linear in field potentials, strengths, and their derivatives. Since electric field plays a more significant role than magnetic field during the motion of particles in crystals, the terms with the derivatives of all orders of the magnetic field strength and with the derivatives of the second or higher orders of the electric field strength were disregarded. We considered a stationary field.

In this approximation, the basic generalized Sakata–Taketani equation for the Hamiltonian is (see [22])

$$\begin{aligned}\mathcal{H} &= e\Phi + \rho_3 m + i\rho_2\frac{1}{m}(\mathbf{S}\cdot\mathbf{D})^2 \\ &-(\rho_3 + i\rho_2)\frac{1}{2m}(\mathbf{D}^2 + e\mathbf{S}\cdot\mathbf{H}) \\ &-(\rho_3 - i\rho_2)\frac{e\kappa}{m}(\mathbf{S}\cdot\mathbf{H}) - \frac{e\kappa}{2m^2}(1+\rho_1) \\ &\times[(\mathbf{S}\cdot\mathbf{E})(\mathbf{S}\cdot\mathbf{D}) - i\mathbf{S}\cdot[\mathbf{E}\times\mathbf{D}] - \mathbf{E}\cdot\mathbf{D}] \\ &+\frac{e\kappa}{2m^2}(1-\rho_1)[(\mathbf{S}\cdot\mathbf{D})(\mathbf{S}\cdot\mathbf{E}) - i\mathbf{S}\cdot[\mathbf{D}\times\mathbf{E}] - \mathbf{D}\cdot\mathbf{E}],\end{aligned} \tag{1}$$

where

$$\rho_1 = \begin{pmatrix} 0 & 1 \\ 1 & 0 \end{pmatrix}, \quad \rho_2 = \begin{pmatrix} 0 & -i \\ i & 0 \end{pmatrix},$$

$$\rho_3 = \begin{pmatrix} 1 & 0 \\ 0 & -1 \end{pmatrix},$$

$$\kappa = \text{const}, \quad \mathbf{D} = \nabla - ie\mathbf{A};$$

Φ, $\mathbf{A}$ and $\mathbf{E}$, $\mathbf{H}$ are the potentials and strengths of the electric and magnetic fields, respectively. The wave eigenfunction of the operator $\mathcal{H}$ is the 6-component bispinor $\Psi = \begin{pmatrix} \phi \\ \chi \end{pmatrix}$, and ρ_i (i = 1, 2, 3) are the Pauli matrices acting on the upper and lower spinors.

As in [4], the operator $\mathcal{H}$ was reduced to a form diagonal in the two spinors using the FW transformation. The diagonalized Hamiltonian (the Hamiltonian in FW representation), which describes the interaction of relativistic particles with an external field, is given by

$$\begin{aligned}\mathcal{H}'' &= \rho_3\epsilon' + e\Phi + \frac{e}{4m} \\ &\times\left[\left\{\left(\frac{\kappa-1}{2} + \frac{m}{\epsilon'+m}\right)\frac{1}{\epsilon'}, (\mathbf{S}\cdot[\boldsymbol{\pi}\times\mathbf{E}] - \mathbf{S}\cdot[\mathbf{E}\times\boldsymbol{\pi}])\right\}_+\right. \\ &-\rho_3\left\{\left(\kappa - 1 + \frac{2m}{\epsilon'}\right), \mathbf{S}\cdot\mathbf{H}\right\}_+ \\ &\left.+\rho_3\left\{\frac{\kappa-1}{2\epsilon'(\epsilon'+m)}, \{\mathbf{S}\cdot\boldsymbol{\pi}, \boldsymbol{\pi}\cdot\mathbf{H}\}_+\right\}_+\right] \\ &+\frac{e\kappa}{4m^2}\left\{\left(\mathbf{S}\cdot\nabla - \frac{1}{\epsilon'(\epsilon'+m)}(\mathbf{S}\cdot\boldsymbol{\pi})(\boldsymbol{\pi}\cdot\nabla)\right),\right. \\ &\left.\left(\mathbf{S}\cdot\mathbf{E} - \frac{1}{\epsilon'(\epsilon'+m)}(\mathbf{S}\cdot\boldsymbol{\pi})(\boldsymbol{\pi}\cdot\mathbf{E})\right)\right\}_+ \\ &+\frac{e}{4\epsilon' m^2(\epsilon'+m)}\left(\kappa + \frac{m}{\epsilon'+m}\right) \\ &\times\{\mathbf{S}\cdot[\boldsymbol{\pi}\times\nabla], \mathbf{S}\cdot[\boldsymbol{\pi}\times\mathbf{E}]\}_+ \\ &-\frac{e\kappa}{2m^2}\nabla\cdot\mathbf{E} + \frac{e}{2\epsilon'^2 m^2}\left(\kappa + \frac{m^2}{4\epsilon'^2}\right)(\boldsymbol{\pi}\cdot\nabla)(\boldsymbol{\pi}\cdot\mathbf{E}),\end{aligned} \tag{2}$$

$$\epsilon' = \sqrt{m^2 + \boldsymbol{\pi}^2},$$

where $\{\ldots, \ldots\}_+$ is the anticommutator and

$$\boldsymbol{\pi} = -i\mathbf{D} = -i\nabla - e\mathbf{A}$$

is the kinetic momentum operator.

We can introduce the g factor to describe the anomalous magnetic moment. In this case, $g = \kappa + 1$ and the Hamiltonian takes the form

$$\begin{aligned}\mathcal{H}'' &= \rho_3\epsilon' + e\Phi + \frac{e}{4m}\left[\left\{\left(\frac{g-2}{2} + \frac{m}{\epsilon'+m}\right)\frac{1}{\epsilon'},\right.\right. \\ &\left.\left.(\mathbf{S}\cdot[\boldsymbol{\pi}\times\mathbf{E}] - \mathbf{S}\cdot[\mathbf{E}\times\boldsymbol{\pi}])\right\}_+ \\ &-\rho_3\left\{\left(g - 2 + \frac{2m}{\epsilon'}\right), \mathbf{S}\cdot\mathbf{H}\right\}_+ \\ &\left.+\rho_3\left\{\frac{g-2}{2\epsilon'(\epsilon'+m)}, \{\mathbf{S}\cdot\boldsymbol{\pi}, \boldsymbol{\pi}\cdot\mathbf{H}\}_+\right\}_+\right]\end{aligned}$$

$$+\frac{e(g-1)}{4m^2}\left\{\left(\mathbf{S}\cdot\nabla-\frac{1}{\epsilon'(\epsilon'+m)}(\mathbf{S}\cdot\boldsymbol{\pi})(\boldsymbol{\pi}\cdot\nabla)\right),\right. \quad (3)$$

$$\left.\left(\mathbf{S}\cdot\mathbf{E}-\frac{1}{\epsilon'(\epsilon'+m)}(\mathbf{S}\cdot\boldsymbol{\pi})(\boldsymbol{\pi}\cdot\mathbf{E})\right)\right\}_+$$

$$+\frac{e}{4\epsilon' m^2(\epsilon'+m)}\left(g-1+\frac{m}{\epsilon'+m}\right)$$
$$\times\{\mathbf{S}\cdot[\boldsymbol{\pi}\times\nabla],\mathbf{S}\cdot[\boldsymbol{\pi}\times\mathbf{E}]\}_+$$

$$-\frac{e(g-1)}{2m^2}\nabla\cdot\mathbf{E}+\frac{e}{2\epsilon'^2m^2}\left(g-1+\frac{m^2}{4\epsilon'^2}\right)(\boldsymbol{\pi}\cdot\nabla)(\boldsymbol{\pi}\cdot\mathbf{E}).$$

It can be shown that in the absence of external field, the lower spinor in the FW representation becomes zero. For particles in an external field, the ratio of the lower and upper spinors, in order of magnitude, does not exceed $|W_{\text{int}}|/E$, where W_{int} is the particle–field interaction energy and E is the total particle energy. Thus,

$$\frac{\chi^\dagger\chi}{\phi^\dagger\phi}\sim\left(\frac{W_{\text{int}}}{E}\right)^2.$$

Therefore, the contribution of the lower spinor is negligible and only the upper spinor is used in the quasiclassical description [4]. It thus follows that the expression for the Hamiltonian $\mathcal{H}''$ closely corresponds to the formula for the Lagrangian of particles with arbitrary spin derived in [11, 12]. Note the presence of terms with the derivatives of **E** that do not contain the operator **S** in expressions (2) and (3). These terms were not calculated in [11, 12]. In the nonrelativistic approximation, formulas (2) and (3) agree with the expression for the Hamiltonian deduced in [22].

Thus, the validity of the results obtained in [11, 12] was confirmed for terms linear and quadratic in spin. It was simultaneously confirmed that the Proca equation and the equivalent equations properly describe, at least, the weak-field effects.

3. PARTICLE SPIN ROTATION AND OSCILLATIONS IN STRAIGHT CRYSTALS

Let us describe the spin motion and the accompanying particle spin oscillations in straight crystals more accurately than in [4]. First, we give the general equation of spin motion [4] derived by using the Lagrangian found in [11, 12]:

$$\frac{d\mathbf{S}}{dt}=\left(\frac{d\mathbf{S}}{dt}\right)_{BMT}+\left(\frac{d\mathbf{S}}{dt}\right)_q, \quad (4)$$

$$\left(\frac{d\mathbf{S}}{dt}\right)_{BMT}=\frac{e}{2m}\left\{\left(g-2+\frac{2}{\gamma}\right)[\mathbf{S}\times\mathbf{B}]\right.$$
$$-(g-2)\frac{\gamma}{\gamma+1}[\mathbf{S}\times\mathbf{v}](\mathbf{v}\cdot\mathbf{B}) \quad (5)$$
$$\left.+\left(g-2+\frac{2}{\gamma+1}\right)[\mathbf{S}\times[\mathbf{E}\times\mathbf{v}]]\right\},$$

$$\left(\frac{d\mathbf{S}}{dt}\right)_q=\frac{Q}{4S(2S-1)}$$
$$\times\left(\left\{\left([\mathbf{S}\times\nabla]-\frac{\gamma}{\gamma+1}[\mathbf{S}\times\mathbf{v}](\mathbf{v}\cdot\nabla)\right),\right.\right.$$
$$\left.\left.\left((\mathbf{S}\cdot\mathbf{E})-\frac{\gamma}{\gamma+1}(\mathbf{S}\cdot\mathbf{v})(\mathbf{v}\cdot\mathbf{E})+(\mathbf{S}\cdot[\mathbf{v}\times\mathbf{B}])\right)\right\}\right.$$
$$+\left\{\left((\mathbf{S}\cdot\nabla)-\frac{\gamma}{\gamma+1}(\mathbf{S}\cdot\mathbf{v})(\mathbf{v}\cdot\nabla)\right),\right.$$
$$\left.\left.\left([\mathbf{S}\times\mathbf{E}]-\frac{\gamma}{\gamma+1}[\mathbf{S}\times\mathbf{v}](\mathbf{v}\cdot\mathbf{E})+[\mathbf{S}\times[\mathbf{v}\times\mathbf{B}]]\right)\right\}\right)$$

$$+\frac{e}{4m^2}\frac{\gamma}{\gamma+1}\left(\left\{[\mathbf{S}\times[\mathbf{v}\times\nabla]],\left[\left(g-1+\frac{1}{\gamma}\right)(\mathbf{S}\cdot\mathbf{B})\right.\right.\right. \quad (6)$$
$$-(g-1)\frac{\gamma}{\gamma+1}(\mathbf{S}\cdot\mathbf{v})(\mathbf{v}\cdot\mathbf{B})$$
$$\left.\left.\left.+\left(g-\frac{\gamma}{\gamma+1}\right)(\mathbf{S}\cdot[\mathbf{E}\times\mathbf{v}])\right]\right\}\right.$$
$$\left.+\left\{(\mathbf{S}\cdot[\mathbf{v}\times\nabla]),\left[\left(g-1+\frac{1}{\gamma}\right)[\mathbf{S}\times\mathbf{B}]\right.\right.\right.$$
$$-(g-1)\frac{\gamma}{\gamma+1}[\mathbf{S}\times\mathbf{v}](\mathbf{v}\cdot\mathbf{B})$$
$$\left.\left.\left.+\left(g-\frac{\gamma}{\gamma+1}\right)[\mathbf{S}\times[\mathbf{E}\times\mathbf{v}]]\right]\right\}\right),$$

where Q is the quadrupole moment and $\gamma=\epsilon'/m$ is the Lorentz factor. The quantities $(d\mathbf{S}/dt)_{BMT}$ and $(d\mathbf{S}/dt)_q$ characterize the spin motion determined by the terms linear [the BMT equation (5)] and quadratic [Eq. (6)] in spin.

This equation does not agree with the GN equation, in which the terms quadratic in spin for the designations used in this study are[1]

$$\left(\frac{d\mathbf{S}}{dt}\right)_G = \frac{Q}{S(2S-1)}\left((\mathbf{S}\cdot\nabla)+\frac{\gamma^2}{\gamma+1}(\mathbf{S}\cdot\mathbf{v})(\mathbf{v}\cdot\nabla)\right)$$
$$\times\left([\mathbf{S}\times\mathbf{E}]-\frac{\gamma}{\gamma+1}[\mathbf{S}\times\mathbf{v}](\mathbf{v}\cdot\mathbf{E})+[\mathbf{S}\times[\mathbf{v}\times\mathbf{B}]]\right)$$
$$+\frac{eg}{2m^2}\frac{\gamma}{\gamma+1}[\mathbf{S}\times[\mathbf{v}\times\nabla]] \quad (7)$$
$$\times\left\{(\mathbf{S}\cdot\mathbf{B})-\frac{\gamma}{\gamma+1}(\mathbf{S}\cdot\mathbf{v})(\mathbf{v}\cdot\mathbf{B})+(\mathbf{S}\cdot[\mathbf{E}\times\mathbf{v}])\right\}.$$

When particles move in straight crystals, $\mathbf{B} = 0$ and the mean magnitude of the vector $\mathbf{E}$ is also zero. Therefore, in this case, the spin motion is determined precisely by the terms quadratic in spin. Of course, the interactions of particles and nuclei with material nuclei also contribute to the spin motion [17–20]. Therefore, it is most convenient to study the effects attributable only to electromagnetic interaction under planar channeling conditions. In this case, positively charged particles (nuclei) move in the gaps between the planes and the strong interaction with material nuclei is less pronounced. The regime of axial channeling of positively charged particles is much less stable.

According to the results obtained in [11, 12] and in this study, the spin-dependent part of the crystal particle–field interaction energy is defined by the operator

$$W = -\frac{Q}{4S(2S-1)}$$
$$\times\left\{\left(\mathbf{S}\cdot\nabla-\frac{1}{\gamma(\gamma+1)}(\mathbf{S}\cdot\boldsymbol{\pi})(\boldsymbol{\pi}\cdot\nabla)\right),\right.$$
$$\left.\left(\mathbf{S}\cdot\mathbf{E}-\frac{1}{\gamma(\gamma+1)}(\mathbf{S}\cdot\boldsymbol{\pi})(\boldsymbol{\pi}\cdot\mathbf{E})\right)\right\}_+ + \frac{e}{4m^4\gamma(\gamma+1)} \quad (8)$$
$$\times\left(g-1+\frac{1}{\gamma+1}\right)\{\mathbf{S}\cdot[\boldsymbol{\pi}\times\nabla],\mathbf{S}\cdot[\boldsymbol{\pi}\times\mathbf{E}]\}_+.$$

In [4], Eqs. (4)–(6) were used to estimate only the spin rotation angle. The results obtained in [14–16] can be used to accurately describe the spin motion and oscillations.

Let the x axis be perpendicular to the system of planes and the z axis be along the beam motion. In this case, the y axis is collinear with the vector $[\boldsymbol{\pi}\times\mathbf{E}]$. For a stationary field, $\mathbf{E} = -\nabla\Phi$. For planar channeling, the following condition is almost always satisfied for the means,

$$\left\langle\frac{\partial^2\Phi}{\partial y^2}\right\rangle = 0, \quad \left\langle\frac{\partial^2\Phi}{\partial z^2}\right\rangle = 0,$$

except for the case where the direction of particle motion simultaneously coincides with the direction of one of the crystal axes. Under these conditions, the expression for the operator W takes the form

$$W = \frac{Q}{2S(2S-1)}S_x^2\frac{\partial^2\Phi}{\partial x^2}$$
$$-\frac{e}{2m^2}\frac{\gamma-1}{\gamma}\left(g-1+\frac{1}{\gamma+1}\right)S_y^2\frac{\partial^2\Phi}{\partial x^2}. \quad (9)$$

The GN equation (7) leads to similar spin oscillation effects, but the form of the second term in (9) slightly changes. The corresponding expression for the operator W can be derived by comparing the equations of spin motions (6) and (7). It differs by the numerical coefficient and is obtained from (9) by the substitution

$$g-1+\frac{1}{\gamma+1}\longrightarrow\frac{g}{2}.$$

In [14, 15], the beam interaction attributable only to the term in operator (9) proportional to Q was considered. However, the problem in [14, 15] was solved in a general form for nonzero $\partial^2\Phi/\partial x^2$ and $\partial^2\Phi/\partial y^2$. Therefore, the evolution of the beam polarization can be described by the formulas in [14, 15] with the substitution

$$\frac{Q}{S(2S-1)}\frac{\partial^2\Phi}{\partial y^2}\longrightarrow-\frac{1}{m^2}\frac{\gamma-1}{\gamma}\left(g-1+\frac{1}{\gamma+1}\right)\frac{\partial^2\Phi}{\partial x^2}.$$

The polarization of particles with $S \geq 1$ is characterized by the mean spin $\langle\mathbf{S}\rangle$ and the quadrupolarization $\langle Q_{ij}\rangle$ [or $\langle S_{ij}\rangle - 2S(S+1)\delta_{ij}/3$], where Q_{ij} is the quadrupole moment operator:

$$Q_{ij} = \frac{3Q}{2S(2S-1)}\left[S_{ij}-\frac{2}{3}S(S+1)\delta_{ij}\right],$$
$$S_{ij} = S_iS_j + S_jS_i.$$

The evolution of the operators S_i and S_{ij} for $S = 1$ particles is described by the equations [14, 15]

$$S_x(t) = S_x(0)\cos\omega_2 t + S_{yz}(0)\sin\omega_2 t,$$
$$S_y(t) = S_y(0)\cos\omega_1 t - S_{zx}(0)\sin\omega_2 t,$$
$$S_z(t) = S_z(0)\cos(\omega_1-\omega_2)t + S_{xy}(0)\sin(\omega_1-\omega_2)t,$$
$$S_{xx}(t) = S_{xx}(0), \quad S_{yy}(t) = S_{yy}(0), \quad S_{zz}(t) = S_{zz}(0), \quad (10)$$
$$S_{xy}(t) = S_{xy}(0)\cos(\omega_1-\omega_2)t - S_z(0)\sin(\omega_1-\omega_2)t,$$

[1] In the equation obtained in [1], the terms dependent on the quadrupole moment do not correspond to Eq. (6) either.

$$S_{yz}(t) = S_{yz}(0)\cos\omega_2 t - S_x(0)\sin\omega_2 t,$$
$$S_{zx}(t) = S_{zx}(0)\cos\omega_1 t + S_y(0)\sin\omega_1 t,$$

where

$$\omega_1 = \frac{Q}{2}\frac{\partial^2\Phi}{\partial x^2},$$
$$\omega_2 = -\frac{e}{2m^2}\frac{\gamma-1}{\gamma}\left(g-1+\frac{1}{\gamma+1}\right)\frac{\partial^2\Phi}{\partial x^2}. \quad (11)$$

The expression for ω_2 that follows from the GN equation can be obtained from (11) by the substitution

$$g-1+\frac{1}{\gamma+1} \longrightarrow \frac{g}{2}.$$

Below, we give the formulas for the mean spin and quadrupolarization derived in [14, 15] for the special case where the incident beam is completely polarized along one of the Cartesian axes. For initial polarization

(i) along the *x* axis,

$$\langle S_x(t)\rangle = \cos\omega_2 t, \quad \langle Q_{yz}\rangle = -\frac{3}{2}Q\sin\omega_2 t; \quad (12)$$

(ii) along the *y* axis,

$$\langle S_y(t)\rangle = \cos\omega_1 t, \quad \langle Q_{zx}\rangle = \frac{3}{2}Q\sin\omega_1 t; \quad (13)$$

(iii) along the *z* axis,

$$\langle S_z(t)\rangle = \cos(\omega_1-\omega_2)t,$$
$$\langle Q_{xy}\rangle = -\frac{3}{2}Q\sin(\omega_1-\omega_2)t. \quad (14)$$

The quantities $\langle S_i\rangle$ and $\langle Q_{ij}\rangle$, which are not given in formulas (12)–(14), are equal to zero. In those cases where the initial beam polarization is not parallel to any of the Cartesian axes, spin rotation takes place [14, 15]. If the initial beam polarization makes an angle $\phi(0)$ with the *x* axis, then the time dependence of the angle between the polarization vector (mean spin) and the *x* axis is defined by the formula[2]

$$\phi(t) = \arctan(\tan\phi(0)\cos\omega_1 t). \quad (15)$$

In this case, the beam polarization vector $\langle\mathbf{S}(t)\rangle$ lies in the plane of the vectors $\mathbf{e}_x$ and $\langle\mathbf{S}(0)\rangle$. Measurement of the spin rotation angle can also be used to verify theoretical conclusions.

Note the nontriviality of the fact that the relativistic formula (9) is almost identical (except for the small second term) to the relativistic expression used previously, including [14–16]. The complete expression for the interaction operator (8) contains extra terms quadratic in spin, which are generally of the same order of magnitude. However, in our case, they may be ignored, because the products $(\boldsymbol{\pi}\cdot\nabla)$ and $(\boldsymbol{\pi}\cdot\mathbf{E})$ are small due to the relative smallness of the energy of transverse particle motion. Consequently, the experimental confirmation of formula (9) would not be a trivial result and would be further evidence for the Pomeransky–Khriplovich–Sen'kov theory.

[2] In this case, ω_2 can be disregarded.

4. DISCUSSION

Let us assess the possibilities for experimentally verifying the results [11, 12] by observing spin oscillations. For the planar channeling of particles (nuclei) in straight crystals, the spin oscillations are determined by the two terms in (9) with different orders of magnitude. The first term is much larger and is attributable to the quadrupole interaction of particles (including relativistic ones) with an electrostatic field.

As follows from formulas (12)–(14), when the beam is polarized along the *y* and *z* axes, the change in mean spin is given by

$$\Delta\langle S_i\rangle = \cos\omega_1 t - 1 = -2\sin^2\frac{\omega_1 t}{2}, \quad i = y, z. \quad (16)$$

For nuclei with a quadrupole moment on the order of $10^{-24}e$ cm^2 or larger at $v/c \sim 10^{-2}$ in a 2-cm-long tungsten crystal, the change in mean spin is on the order of unity. Consequently, the spin oscillations can be observed in this case. As was pointed out in [14–16], the effect under consideration can be used to measure the quadrupole moments of short-lived particles and nuclei. In particular, the quadrupole moment of the Ω^- hyperon can be measured in this way. The difficulties in carrying out this experiment stem from the necessity of producing a hyperon beam of sufficient intensity and from negative particle charge, which hinders stable planar channeling. Therefore, Baryshevsky and Shechtman [16] suggested using the axial channeling of Ω^- hyperons. Nevertheless, the real possibility of observing the spin oscillations of these particles seems to be determined by their strong interaction with material nuclei [18–21].

The fact that the nuclear charge is positive and the nuclear beams can have significant intensity favors the determination of the quadrupole moments for short-lived nuclei. It is also crucially important that the quadrupole moments of short-lived nuclei, particularly those with large spin, are generally large.

If the quadrupole moments of nuclei are much smaller than $10^{-24}e$ cm^2, then $\omega_1 t \ll 1$ and, according to formula (16), the change in mean spin has the second order of smallness in $\omega_1 t$. In this case, a beam with sufficiently large initial quadrupolarization can be used to measure the quadrupole moments [16]. As we see from formulas (10), the change in mean spin in this case has the first order of smallness in $\omega_1 t$. Significant quadrupolarization always takes place for linearly polarized

beams. In particular, a beam linearly polarized at an angle of 45° to the y and z axes is characterized by large quadrupolarization, $\langle S_{yz}\rangle = 0.5$. However, a beam can have large quadrupolarization even at $\langle \mathbf{S}\rangle = 0$ [16]. A beam with initial quadrupolarization can also be used to detect and study spin oscillations in an electromagnetic field and, in particular, to verify the inverse proportionality of $\omega_1 t$ to the beam velocity v ($\omega_1 t = \omega_1 l/v \propto v^{-1}$, l is the crystal length) given by the theory.

For nuclei with a large charge, the probability of electron capture during channeling is high. This circumstance affects the motion of nuclei and the dynamics of their polarization. Therefore, when studying the spin oscillations in an electromagnetic field, a higher accuracy is achieved by using nuclei with a small charge.

Note that for nuclei with spin $S > 1$, the expressions for ω_1 and ω_2 differ from (11) by a constant factor. In addition, the polarization dynamics for such nuclei also depends on the tensor $S_iS_jS_k$.

Under actual conditions, $\partial^2\Phi/\partial x^2$ is not constant and depends on the x coordinate. However, since the particle oscillation frequency along the x axis is much higher than the spin oscillation frequency, the above formulas can be used for a more accurate description by substituting in the quantity $\langle\partial^2\Phi/\partial x^2\rangle$ averaged over the particle trajectory. In this case, $\langle\partial^2\Phi/\partial x^2\rangle$ and ω_1 will slightly differ for different particles. As a result, the oscillation phases for the particles that passed the crystal will also slightly differ. The difference in the particle velocities along the z axis leads to an additional phase shift of the oscillations. The beam depolarization due to multiple scattering should also be taken into account [16, 24]. It causes a gradual damping of the spin oscillations via decrease in their amplitude.

The spin oscillations attributable to the second terms in (8) and (9) take place for the initial beam polarization along the x axis. Since ω_2 is inversely proportional to the square of the mass, only a deuteron beam with significant initial quadrupolarization (tens of percent) can be used to study them. However, the oscillations are very small in this case as well. For deuterons in a 2-cm-long tungsten crystal, the change in mean spin is on the order of 10^{-6} rad. Only the unique capabilities of deuteron polarimeters [25] give hope that such a small change in spin will be detected. In this case, large statistics should be accumulated. However, this problem can hardly be solved at present.

As was noted above, the spin oscillations attributable to strong interaction and existing even when the material is not polarized take place for beams of particles and nuclei in the material [17–19]. In this case, the spin oscillations are associated with the presence of a term proportional to $(\mathbf{S}\cdot\mathbf{n})^2$, where $\mathbf{n}$ is the unit vector along the beam motion, in the zero-angle forward scattering amplitude. The estimates obtained in [19, 20] indicate that such oscillations can be observed experimentally. The spin-dependent part of the forward scattering amplitude, which can be determined using the phenomenon of spin oscillations, contains important information on the nucleon–nucleon interaction at small distances.

The effective particle (nucleus)–material interaction energy corresponds to the zero-angle forward scattering amplitude [20]. If the nuclei that move in the regime of planar channeling have a sufficiently high energy of transverse motion, then they can be scattered by material nuclei in both the subbarrier and suprabarrier interactions. This depends on the relation between the energy of transverse motion of the nuclei and the height of the potential barrier, which is equal to the maximum potential of the planes. In both cases, allowing for the strong interaction modifies formula (9) (the second term proportional to S_y^2 is disregarded here) as follows:

$$W = \frac{Q}{2S(2S-1)}S_x^2\frac{\partial^2\Phi}{\partial x^2} + kS_z^2, \quad k = \text{const}. \qquad (17)$$

It follows from (17) that the spin oscillations are described by formulas similar to (10) when the strong interaction is taken into account. Separating out the contribution given by the first term in (17) to the spin oscillations allows us to experimentally detect the spin oscillations attributable only to electromagnetic interaction and to measure the quadrupole moments of nuclei. For this purpose, the incident beam should either be polarized along the z axis (i.e., along the motion) or have quadrupolarization along the x and y axes. In particular, for spin-1 nuclei, the evolution of the beam polarization in this case is described by the equations

$$S_z(t) = S_z(0)\cos\omega_1 t + S_{xy}(0)\sin\omega_1 t,$$
$$S_{xy}(t) = S_{xy}(0)\cos\omega_1 t - S_z(0)\sin\omega_1 t,$$

where ω_1 is given by formula (11).

The dependence of the interaction energy or the zero-angle particle scattering amplitude on the square of the spin projection leads to a similar dependence for the refractive index of de Broglie waves [18–20]. As a result, the refractive index depends on the magnitude of the spin projection, which determines the birefringence and dichroism of particle beams in material [18–20].

5. CONCLUSIONS

Thus, we have theoretically verified the equations of spin motion for charged particles in a nonuniform electromagnetic field and analyzed the possibilities for experimentally verifying these equations.

The quantum-mechanical equation of spin motion obtained from the Lagrangian derived in [11, 12] does not agree with the earlier universally accepted Good–Nyborg equation [1, 2] deduced in terms of classical electrodynamics. By reducing the Hamiltonian that

describes the interaction of spin-1 particles with an electromagnetic field to the diagonal (in two spinors) form that characterizes the Foldy–Wouthuysen representation, we completely confirmed the formulas derived in [11, 12]. We determined the diagonalized Hamiltonian by taking into account the terms linear in **E**, **H**, and $\partial E_i/\partial x_j$. The derived expressions are cumbersome. Therefore, their correspondence to the results obtained in [11, 12] removes all doubts on the validity of the Pomeransky–Khriplovich–Sen'kov theory, although neither the terms proportional to $\partial H_i/\partial x_j$ nor the additional quadrupole interaction introduced in [22] were taken into account when deducing Hamiltonian (3). Concurrently, we proved the properness of the description of the weak-field effects by the Corben–Schwinger equation [23] (the Proca equation with an anomalous magnetic moment), which had been repeatedly questioned. Note that, in contrast to [11, 12], when calculating the Hamiltonian, we also took into account the spin-independent terms proportional to $\partial E_i/\partial x_j$, which allows the contact interaction to be described.

Our analysis of the possibilities for experimentally verifying theoretical conclusions indicates that such verification can be made for the quadratic (in spin) interaction attributable to the quadrupole moments of nuclei. This interaction produces spin oscillations and rotation for planar channeling in straight crystals. Carrying out such experiments also makes it possible to detect and experimentally study the spin oscillations attributable to electromagnetic interaction. The effects of spin oscillations and rotation for planar channeling in straight crystals can also be used to determine the quadrupole moments of short-lived nuclei.

There are also spin oscillations attributable to the quadratic (in spin) interaction unrelated to the quadrupole moments [the second term in Eq. (9)]. The frequencies of these oscillations differ in the quantum-mechanical Pomeransky–Khriplovich–Sen'kov theory and the classical Good–Nyborg theory. However, the beam polarization variation caused by these oscillations is small and can hardly be observed at present.

ACKNOWLEDGMENTS

I am grateful to Prof. V.G. Baryshevsky for remarks during the writing of this paper and for discussion of the results obtained.

REFERENCES

1. R. H. Good, Phys. Rev. **125**, 2112 (1962).
2. P. Nyborg, Nuovo Cimento **31**, 1209 (1964); **32**, 1131 (1964).
3. I. M. Ternov and V. A. Bordovitsyn, Usp. Fiz. Nauk **132**, 345 (1980) [Sov. Phys. Usp. **23**, 679 (1980)].
4. A. Ya. Silenko, Yad. Fiz. **64**, 1054 (2001) [Phys. At. Nucl. **64**, 983 (2001)].
5. E. G. P. Rowe and G. T. Rowe, Phys. Rep. **149**, 287 (1987).
6. S. L. Cherkas, Izv. Akad. Nauk Belarusi, Ser. Fiz.–Mat. Nauk, No. 2, 70 (1994).
7. A. Ya. Silenko, Poverkhnost, No. 2, 111 (1997).
8. A. Ya. Silenko, Teor. Mat. Fiz. **112**, 161 (1997).
9. A. Ya. Silenko, Poverkhnost, No. 5, 97 (1998).
10. V. Bargmann, L. Michel, and V. L. Telegdi, Phys. Rev. Lett. **2**, 435 (1959).
11. A. A. Pomeransky and I. B. Khriplovich, Zh. Éksp. Teor. Fiz. **113**, 1537 (1998) [JETP **86**, 839 (1998)].
12. A. A. Pomeransky and R. A. Sen'kov, Phys. Lett. B **468**, 251 (1999).
13. L. L. Foldy and S. A. Wouthuysen, Phys. Rev. **78**, 29 (1950).
14. V. G. Baryshevsky and A. A. Sokol'skiĭ, Pis'ma Zh. Tekh. Fiz. **6**, 1419 (1980) [Sov. Tech. Phys. Lett. **6**, 612 (1980)].
15. V. G. Baryshevsky, *Channeling, Emission, and Reaction in Crystals at High Energy* (Belarus. Gos. Univ., Minsk, 1982).
16. V. G. Baryshevsky and A. J. Shechtman, Nucl. Instrum. Methods Phys. Res. B **83**, 250 (1993).
17. V. G. Baryshevsky, Dokl. Akad. Nauk BSSR **35**, 416 (1991).
18. V. G. Baryshevsky, Phys. Lett. A **171**, 431 (1992).
19. V. G. Baryshevsky, J. Phys. G: Nucl. Part. Phys. **19**, 273 (1993).
20. V. G. Baryshevsky, *Nuclear Optics of Polarization Media* (Énergoatomizdat, Moscow, 1995).
21. V. G. Baryshevsky, K. G. Batrakov, and S. Cherkas, J. Phys. G: Nucl. Part. Phys. **24**, 2049 (1998).
22. J. A. Young and S. A. Bludman, Phys. Rev. **131**, 2326 (1963).
23. H. C. Corben and J. Schwinger, Phys. Rev. **58**, 953 (1940).
24. V. L. Lyuboshits, Yad. Fiz. **32**, 702 (1980) [Sov. J. Nucl. Phys. **32**, 362 (1980)].
25. E. J. Stephenson, Preprint No. 99-3, BNL (Brookhaven, 1999); http://www.bnl.gov/muonedm/edm/.

Translated by V. Astakhov

Journal of Experimental and Theoretical Physics, Vol. 96, No. 5, 2003, pp. 782–788.
From Zhurnal Éksperimental'noĭ i Teoreticheskoĭ Fiziki, Vol. 123, No. 5, 2003, pp. 891–898.

NUCLEI, PARTICLES, AND THEIR INTERACTION

Hypernuclei as Chiral Solitons¶

V. B. Kopeliovich

Institute for Nuclear Research, Russian Academy of Sciences, Moscow, 117312 Russia
e-mail: kopelio@cpc.inr.ac.ru, kopelio@al20.inr.troitsk.ru

Received November 13, 2002

Abstract—Identification of flavored multiskyrmions with the ground states of known hypernuclei is successful for several of them, e.g., for the isodoublet ${}^{4}_{\Lambda}\mathrm{H}-{}^{4}_{\Lambda}\mathrm{He}$ and isoscalars ${}^{5}_{\Lambda}\mathrm{He}$ and ${}^{7}_{\Lambda}\mathrm{Li}$. In other cases, agreement is not so good, but as the baryon number increases, the behavior of the binding energy qualitatively agrees with the data. Charmed or beautiful hypernuclei are predicted within this approach to be bound more strongly than strange hypernuclei. This conclusion is stable with respect to a certain variation of poorly known heavy flavor decay constants. *© 2003 MAIK "Nauka/Interperiodica".*

1. INTRODUCTION

One of the actual questions of nuclear and elementary particle physics is the possibility of the existence of nuclear matter fragments with unusual properties, e.g., with flavor being different from that of *u* and *d* quarks. This issue can have interesting consequences in astrophysics and cosmology. The stellar objects RXJ1856 and 3C58, recently observed at Chandra X-ray observatory, can be interpreted precisely as strange quark matter stars. Experimental and theoretical studies of such nuclear fragments were first performed for strangeness (see, e.g., [1, 2] and references therein) and to some extent, also for charm and beauty quantum numbers [3–6]. Theoretical approaches vary from standard nuclear potential models to topological soliton models (the Skyrme model and its extensions). In the latter case, extension of the original $SU(2)$ model to the $SU(3)$ configuration space is necessary. It is known that several different local minima in the configuration space occur in $SU(3)$ extensions of the model [7]. Quantization of configurations near each of these minima is possible, leading to the prediction of the spectrum of quantum states with different flavor quantum numbers. Here, the quantization of $SU(2)$ bound skyrmions embedded in $SU(3)$ is considered following [8–10]. The physical interpretation of such quantum states seems to be simplest in comparison with the others because the lowest energy states can be identified with the usual nuclei. In this way, we previously derived a certain spectrum of "flavored multiskyrmions" regardless of their interpretation [10]. Here, we make an attempt to identify some of these states with the known hypernuclei.

The chiral soliton models provide a picture of baryonic systems outside, at sufficiently large distances, based on several fundamental principles and ingredients incorporated in the model Lagrangian. The details of baryon–baryon interactions do not enter the calculations explicitly, although they certainly affect the results implicitly, via some integral characteristics of baryon systems, such as their masses, moments of inertia (Θ_F and Θ_T below), Σ-term (Γ), etc. The $SU(2)$ rational map ansatz [11], which well approximates the results of numerical calculations [12], was used as the starting point for the evaluation of static properties of bound states of skyrmions necessary for their quantization in the $SU(3)$ configuration space. The knowledge of the "flavor" moment of inertia and the Σ term then allows estimation of the flavor excitation energies [8, 10]. The masses of the lowest states with strangeness, charm, or beauty are calculated within the rigid oscillator version of the bound state approach, and the binding energies of baryonic systems with different flavors, *s*, *c*, or *b*, are estimated.

Within the rational map approximation, at sufficiently large B, the chiral field configuration has the form of a "bubble" with universal properties of the shell where the mass and baryon number of the baryon systems are concentrated. The width of the shell and its average mass density are independent of the baryon number [13]. This picture can be acceptable for not large B (where $B = A$ is the atomic number of the nucleus), e.g., up to $B \sim 16$, and therefore, we discuss here hypernuclei not heavier than hyperoxygen.

2. LAGRANGIAN AND MASS FORMULA

The Lagrangian of the Skyrme model, which in its well-known form depends on the meson decay constants F_π and F_D, the Skyrme constant e, etc., has been presented previously [9, 10], and we give here its density for completeness,

$$\mathcal{L} = \mathcal{L}^{(2)} + \mathcal{L}^{(4)} + \mathcal{L}^{(6)} + \mathcal{L}^{SB}, \qquad (1)$$

¶This article was submitted by the author in English.

which involves the term of the second order in the chiral derivative

$$\mathcal{L}^{(2)} = -\frac{F_\pi^2}{16}\mathrm{Tr}\, l_\mu l_\mu,$$

the antisymmetric fourth-order, or Skyrme, term

$$\mathcal{L}^{(4)} = \frac{1}{32e^2}\mathrm{Tr}[l_\mu l_\nu]^2,$$

the sixth-order term

$$\mathcal{L}^{(6)} = c_6\mathrm{Tr}([l_\mu l_\nu][l_\nu l_\gamma][l_\gamma l_\mu]),$$

and the symmetry (chiral and flavor) breaking terms

$$\begin{aligned}\mathcal{L}^{SB} &= \frac{F_\pi^2 m_\pi^2}{16}\mathrm{Tr}(U + U^\dagger - 2)\\ &+ \frac{F_D^2 m_D^2 - F_\pi^2 m_\pi^2}{24}\mathrm{Tr}(1 - \sqrt{3}\lambda_8)(U + U^\dagger - 2)\\ &+ \frac{F_D^2 - F_\pi^2}{48}\mathrm{Tr}(1 - \sqrt{3}\lambda_8)(U l_\mu l_\mu + l_\mu l_\mu^\dagger U^\dagger).\end{aligned} \quad (2)$$

Here,

$$l_\mu = \partial_\mu U U^\dagger$$

is the left chiral derivative of the unitary matrix $U \in SU(3)$. The sixth-order term $\mathcal{L}^{(6)}$, which can also be presented as the baryon (topological) number density squared, was not included in the original Skyrme model, and we omit it here as well. Recent calculations of flavor excitation energies performed by Shunderyuk provide results that are close to those obtained in [10] and in the present paper. The Wess–Zumino term in the action, which can be written as a five-dimensional differential form, plays a very important role in the quantization procedure, but it does not contribute to most of the static properties of skyrmions (see, e.g., [8, 10]).

The physical values of these constants are as follows: $F_\pi = 186$ MeV; e is close to $e = 4$; and we here take the value $e = 4.12$ [14]. The chiral symmetry breaking part of the Lagrangian depends on meson masses, the pion mass m_π, and the mass of the K, D, or B meson, which we call m_D. The flavor-symmetry-breaking part of the Lagrangian is of the usual form and is sufficient to describe the mass splittings of the octet and decuplet of baryons [14] within the collective-coordinate-quantization approach with configuration mixing. It is important that the flavor decay constant (pseudoscalar decay constant F_K, F_D, or F_B) is different from the pion decay constant F_π. Experimentally, $F_K/F_\pi \approx 1.22$ and $F_D/F_\pi \approx 2.28^{+1.4}_{-1.1}$ [15]. The B-meson decay constant has not been measured yet. In view of this uncertainty, we take two values of $r_c = F_D/F_\pi$ for our estimates, $r_c = 1.5$ and 2, and similarly for $r_b = F_B/F_\pi$, also following theoretical estimates [16].

We begin our calculations with a unitary matrix of chiral fields $U \in SU(2)$, as mentioned above. In the most general case, the classical mass of $SU(2)$ solitons and other static characteristics necessary for our purposes depend on three profile functions, f, α, and β. The general parameterization of U_0 for an $SU(2)$ soliton that we use here is given by

$$U_0 = c_f + s_f \boldsymbol{\tau}\cdot\mathbf{n}$$

with

$$n_z = c_\alpha, \quad n_x = s_\alpha c_\beta,$$

$$n_y = s_\alpha s_\beta, \quad s_f = \sin f, \quad c_f = \cos f, \quad \text{etc.}$$

For the rational map ansatz, $f = f(r)$ and the profile therefore depends on one variable only; the components of vector $\mathbf{n}$ are some rational functions of two angular variables that define the direction of the radius vector $\mathbf{r}$ [11].

The quantization of solitons in the $SU(3)$ configuration space was performed in the spirit of the bound state approach to the description of strangeness, proposed in [17] and used in [18, 19]. We here use a somewhat simplified and very transparent variant, the so-called rigid oscillator version proposed in [8]. The details of the quantization procedure can be found in [8–10], and we do not reproduce them here. We only note that the (u, d, c) and (u, d, b) $SU(3)$ groups are quite similar to the (u, d, s) one; a simple redefinition of hypercharge must be made for the (u, d, c) group.

The following mass formula has been obtained for the masses of states with definite quantum numbers: the baryon (topological) number B, flavor F (strangeness, charm, or beauty), isospin I, and angular momentum J [8, 10],

$$\begin{aligned}E(B, F, I, J) &= M_{B,\mathrm{cl}} + |F|\omega_{F,B}\\ &+ \frac{1}{2\Theta_{T,B}}[c_{F,B}T_r(T_r + 1) + (1 - c_{F,B})I(I + 1)\\ &+ (\bar{c}_{F,B} - c_{F,B})I_F(I_F + 1)] + \frac{J(J + 1)}{2\Theta_{J,B}},\end{aligned} \quad (3)$$

where $\omega_{F,B}$ or $\bar{\omega}_{F,B}$ are the frequencies of flavor (antiflavor) excitations,

$$\omega_{F,B} = \frac{N_c B(\mu_{F,B} - 1)}{8\Theta_{F,B}}, \quad \bar{\omega}_{F,B} = \frac{N_c B(\mu_{F,B} + 1)}{8\Theta_{F,B}}, \quad (4)$$

with

$$\mu_{F,B} = \left[1 + \frac{16\Theta_{F,B}(\bar{m}_D^2\Gamma_B + (F_D^2 - F_\pi^2)\tilde{\Gamma}_B)}{(N_c B)^2}\right]^{1/2},$$

where N_c is the number of colors of the underlying

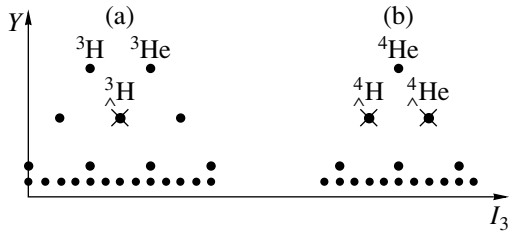

Fig. 1. (a) The location of the isoscalar state with odd B and $|F| = 1$ in the upper part of the (I_3, Y) diagram; (b) the same for isodoublet states with even B. The case of light hypernuclei $_\Lambda$H and $_\Lambda$He is considered as an example.

QCD ($N_c = 3$ in all numerical estimates) and

$$\bar{m}_D^2 = \frac{F_D^2 m_D^2}{F_\pi^2} - m_\pi^2.$$

The terms $\pm N_c B/8\Theta_{F,B}$ in (4) arise from the Wess–Zumino term in the action, which does not contribute to the masses and momenta of inertia of skyrmions [17, 8]. In terms of the quark models, the difference

$$\bar{\omega} - \omega = \frac{N_c B}{4\Theta_{F,B}}$$

is the energy necessary for the production of an additional $q\bar{q}$ pair. The hyperfine structure constants $c_{F,B}$ and $\bar{c}_{F,B}$ are given by [8]

$$c_{F,B} = 1 - \frac{\Theta_{T,B}(\mu_{F,B} - 1)}{2\Theta_{F,B}\mu_{F,B}},$$
$$\bar{c}_{F,B} = 1 - \frac{\Theta_{T,B}(\mu_{F,B} - 1)}{\Theta_{F,B}(\mu_{F,B})^2}. \quad (5)$$

Evidently, $\bar{c} \longrightarrow 1$ as $\mu \longrightarrow \infty$. Contributions on the order of $1/\Theta \sim N_c^{-1}$ that depend originally on angular velocities of rotations in the isospace and the usual space are taken into account in (3). This expression was obtained by quantizing the oscillator-type Hamiltonian describing the motion of the $SU(2)$ skyrmion in the $SU(3)$ collective coordinate space. The classical mass $M_{cl} \sim N_c$ and the energies $\omega_F \sim N_c^0 = 1$. The motion along the flavor direction s, c, or b is described by the amplitude D [8, 10], which is small for the lowest quantum states (lowest $|F|$),

$$D \sim [16\Gamma_B\Theta_{F,B}\bar{m}_D^2 + N_c^2 B^2]^{-1/4}(2|F| + 1)^{1/2}.$$

The amplitude D therefore decreases as $1/\sqrt{m_D}$ with increasing mass m_D and with increasing number of colors N_c, and the method works for any value of m_D, as well as for charm and beauty quantum numbers.

In (3), I is the isospin of the multiplet with a flavor of F, and $T_r = p/2$ is the so-called "right" isospin, the isospin of the nonflavored component of the $SU(3)$ multiplet under consideration, with (p, q) being the numbers of the upper and lower indices in the spinor that describes it. I_F is the isospin carried by flavored mesons that are bound by the $SU(2)$ skyrmion,

$$\mathbf{I} = \mathbf{T}_r + \mathbf{I}_F.$$

Evidently, $I_F \le |F|/2$. The states predicted in the rigid oscillator model do not correspond to definite $SU(3)$ or $SU(4)$ representations. How they can be ascribed to them was shown in [8, 10]. For example, the state with $B = 1$, $|F| = 1$, and $I = 0$ must belong to the octet of the (u, d, s) or (u, d, c) $SU(3)$ group if $N_c = 3$. Here, we consider quantized states of the baryon system that belong to the lowest possible $SU(3)$ irreps (p, q), $p + 2q = 3B$,

$$p = 0, \quad q = 3B/2 \ \text{ for even } \ B$$

and

$$p = 1, \quad q = (3B - 1)/2 \ \text{ for odd } \ B.$$

These are $\overline{35}$, $\overline{80}$, and $1\bar{4}3$-plets for $B = 3$, 5, and 7, $\overline{28}$, $\overline{55}$, and $\overline{91}$ -plets for $B = 4$, 6, and 8, etc. For even B, $T_r = 0$, and for odd B, $T_r = 1/2$ for the lowest $SU(3)$ irreps (see Fig. 1).

The flavor moment of inertia that enters the above formulas [8, 10, 17] for arbitrary $SU(2)$ skyrmions is given by [10]

$$\Theta_F = \frac{1}{8}\int(1 - c_f) \times \left\{F_D^2 + \frac{1}{e^2}[(\partial f)^2 + s_f^2(\partial n_i)^2]\right\} d^3\mathbf{r}, \quad (6)$$

where

$$(\partial n_i)^2 = (\partial\alpha)^2 + s_\alpha^2(\partial\beta)^2.$$

It is simply related to $\Theta_F^{(0)}$ for the flavor symmetric case,

$$\Theta_F = \Theta_F^{(0)} + (F_D^2/F_\pi^2 - 1)\Gamma/4,$$

with Γ defined in (7) below. The flavor inertia increases with B almost proportionally to B. The isotopic moments of inertia are the diagonal components of the corresponding tensor of inertia; in our case, this tensor of inertia is close to the unit matrix multiplied by Θ_T.

The quantities Γ (or the Σ-term), which define the contribution of the mass term to the classical mass of solitons, and $\tilde{\Gamma}$ in $\mu_{F,B}$ are given by

$$\Gamma = \frac{F_\pi^2}{2}\int(1-c_f)d^3\mathbf{r},$$
$$\tilde{\Gamma} = \frac{1}{4}\int c_f[(\partial f)^2 + s_f^2(\partial n_i)^2]d^3\mathbf{r}. \quad (7)$$

For the rational map ansatz, formulas (6) and (7) can be slightly modified [10], but they already look sufficiently simple in such a general form. The masses of solitons were calculated in [12] and [10], the moments of inertia Γ and $\tilde{\Gamma}$ were calculated in [10] for several values of B, and the missing quantities are calculated here.

The contribution to $\mu_{F,B}$ proportional to $\tilde{\Gamma}_B$ is suppressed in comparison with the term on the order of Γ by the small factor on the order of F_D^2/m_D^2, and is more important for strangeness.

3. STRANGE AND BEAUTIFUL HYPERNUCLEI

It is convenient to calculate the energy difference between the state with a flavor F belonging to the (p, q) irrep and the ground state with $F = 0$ and the same B, J, and (p, q) [10],

$$\Delta E_{B,F} = |F|\omega_{F,B} + \frac{\mu_{F,B}-1}{4\mu_{F,B}\Theta_{F,B}}[I(I+1) - T_r(T_r+1)] + \frac{(\mu_{F,B}-1)(\mu_{F,B}-2)}{4\mu_{F,B}^2\Theta_{F,B}}I_F(I_F+1). \quad (8)$$

In deriving (3) and (8), the so-called "interference" moment of inertia was used, whose contribution to the Lagrangian is proportional to the product of angular rotation velocities in the isotopic and ordinary 3D spaces. This moment of inertia is negligible compared with the isotopic and orbital tensors of inertia [20] for all multiskyrmions except those with $B = 1, 2$. We also note that (8) is independent of Θ_T and depends only on Θ_F when the formulas for hyperfine splitting constants are used.

For the state with the isospin $I = 0$ and the unit flavor number $|F| = 1$, the binding energy difference in comparison with the ground state of the nucleus with the same B, (p, q), and $|F| = 0$ is

$$\Delta\epsilon_{B,F} = \omega_{F,1} - \omega_{F,B} - \frac{3(\mu_{F,1}-1)}{8\mu_{F,1}^2\Theta_{F,1}} + \frac{3(\mu_{F,1}-1)}{8\mu_{F,B}^2\Theta_{F,B}}. \quad (9)$$

Such states can exist for odd B, with $I_F = T_r = 1/2$ (see Fig. 1a). For antiflavor excitations, we have similar formulas with the substitution $\mu \longrightarrow -\mu$.

For states with the maximal isospin

$$I = T_r + \frac{|F|}{2},$$

the energy difference can be simplified to [10]

$$\Delta E_{B,F} = |F| \times\left[\omega_{F,B} + T_r\frac{\mu_{F,B}-1}{4\mu_{F,B}\Theta_{F,B}} + \frac{(|F|+2)}{8\Theta_{F,B}}\frac{(\mu_{F,B}-1)^2}{\mu_{F,B}^2}\right]. \quad (10)$$

The case of isodoublets, even B, is described by (8) with $T_r = 0$ (see Table 2 and Fig. 1b). It follows from (10) that when a nucleon is replaced by a flavored hyperon in a baryon system, the binding energy of the system with $|F| = 1$ and $T_r = 0$ changes by

$$\Delta\epsilon_{B,F} = \omega_{F,1} - \omega_{F,B} - \frac{3(\mu_{F,1}-1)}{8\mu_{F,1}^2\Theta_{F,1}} - \frac{3(\mu_{F,B}-1)^2}{8\mu_{F,B}^2\Theta_{F,B}}. \quad (11)$$

For strangeness, Eq. (11) is negative, indicating that stranglets should have binding energies smaller than those of nuclei with the same B.

To obtain the values of the total binding energy of hypernuclei shown in the tables, we add the calculated difference of binding energies given by (9) or (11) to the known binding energy value of the usual (u, d) nucleus. For example, for $B = 3$, it is the average of binding energies of ^{3}H and ^{3}He; for $B = 4$ it is the binding energy of ^{4}He (5.3 MeV = (28.3–23) MeV); etc. (see Fig. 1). Special care should be taken about the spin of the nucleus. For $^3_\Lambda$H and ^{3}H, $^4_\Lambda$He and ^{4}He, $^6_\Lambda$Li and ^{6}Li, $^{13}_\Lambda$C and ^{13}C, and in several other cases, the spins of the ground states of the hypernucleus and the nucleus coincide. For $^5_\Lambda$He ($J = 1/2$) and ^{5}He ($J = 3/2$), $^9_\Lambda$Be ($J = 1/2$) and ^{9}Be ($J = 3/2$), $^{12}_\Lambda$C ($J = 1$) and ^{12}C ($J = 0$), and in some other cases, the difference in the rotation energies,

$$E_J = \frac{J(J+1)}{2\Theta_J},$$

must be taken into account. For example, this difference decreases the theoretical value of the binding energy for $^7_\Lambda$Li by about 7 MeV, and we have 29 MeV instead of 36 MeV. In cases where the spin of the hypernucleus is not known, this correction was not included in Tables 1 and 2. Beginning with $B \sim 10$, the correction to the energy of quantized states due to nonzero angular momentum is small and decreases with increasing B because the corresponding moment of inertia increases proportionally to B^2.

Table 1. Collective motion contributions to the binding energies of isoscalar hypernuclei with the unit flavor, strangeness, or beauty, $S = -1$ or $b = -1$, in MeV

${}_{\Lambda}A$	ω_s	$\Delta\epsilon_s$	ϵ_s^{tot}	$\epsilon_{\text{exp},\,s}^{\text{tot}}$	$\omega_b^{r_b = 1.5}$	$\Delta\epsilon_b$	ϵ_b^{tot}	$\omega_b^{r_b = 2}$	$\Delta\epsilon_b$	ϵ_b^{tot}
1	306	–	–	–	4501	–	–	4805	–	–
${}^{3}_{\Lambda}H$	289	–3	5	2.35	4424	75	83	4751	53	61
${}^{5}_{\Lambda}He$	287	–6	33	31.4	4422	76	103	4749	54	81
${}^{7}_{\Lambda}Li$	282	–3	29	37.6	4429	81	119	4744	59	97
${}^{9}_{\Lambda}Be$	291	–13	40	63.2	4459	40	97	4773	31	88
${}^{11}_{\Lambda}B$	294	–16	59	–	4478	21	96	4786	18	93
${}^{13}_{\Lambda}C$	295	–18	78	104	4488	10	106	4793	11	107
${}^{15}_{\Lambda}N$	300	–23	91	118	4515	–17	97	4810	–7	108

Note: ω_s and ω_b are the strangeness and beauty excitation energies, $\Delta\epsilon_{s,\,b}$ (in MeV) are the changes of binding energies of the lowest baryon system with flavor s or b, $|F| = 1$, in comparison with the usual (u, d) nuclei with the same B. ϵ^{tot} is the total binding energy of the hypernucleus. Experimental values $\epsilon_{\text{exp}}^{\text{tot}}$ are taken from [1, 2]. The energies ω for $B = 1$ are given for comparison. For beauty, the first three columns correspond to $r_b = F_B/F_\pi = 1.5$, and the last three ones, to $r_b = 2$.

Table 2. The binding energies of isodoublets of hypernuclei with the unit flavor, $S = -1$ or $b = -1$, in MeV

${}_{\Lambda}A$	ω_s	$\Delta\epsilon_s$	ϵ_s^{tot}	$\epsilon_{\text{exp}}^{\text{tot}}$	$\omega_b^{r_b = 1.5}$	$\Delta\epsilon_b$	ϵ_b^{tot}	$\omega_b^{r_b = 2}$	$\Delta\epsilon_b$	ϵ_b^{tot}
${}^{4}_{\Lambda}H - {}^{4}_{\Lambda}He$	283	–23	5.3	10.52; 10.11	4402	71	99	4735	52	80
${}^{6}_{\Lambda}He - {}^{6}_{\Lambda}Li$	287	–22	10.3	31.7; 30.8	4430	52	84	4752	40	72
${}^{8}_{\Lambda}Li - {}^{8}_{\Lambda}Be$	288	–20	36.5	46.05; 44.4	4443	43	99	4765	33	89
${}^{10}_{\Lambda}Be - {}^{10}_{\Lambda}B$	292	–23	42	67.3; 65.4	4465	24	89	4778	20	85
${}^{12}_{\Lambda}B - {}^{12}_{\Lambda}C$	294	–24	67	87.6; 84.2	4481	10	102	4788	11	103
${}^{14}_{\Lambda}C - {}^{14}_{\Lambda}N$	299	–28	77	109.3; 106.3	4506	–14	91	4805	–5	100
${}^{16}_{\Lambda}N - {}^{16}_{\Lambda}O$	301	–30	97	–	4521	–28	100	4815	–14	114

Note: The rest of the notation and other details are as in Table 1.

Because $\Theta_{F,\,B}$ increases with increasing B and F_D (m_D), this leads to an increase in binding with increasing B and the mass of the flavor, in agreement with [9, 10]. For beauty (and charm, see below), Eq. (11) is positive for $3 \le B \le 12$. As follows from Tables 1 and 2, our method underestimates the binding energy of strangeness in nuclei beginning with $B = A \sim 9$. This means that other sources of binding should be taken into account, in addition to the collective motion of a baryon system in the $SU(3)$ configuration space.

4. CHARMED HYPERNUCLEI

In this section, binding energies of charmed hypernuclei are presented for two values of the charm decay constant that correspond to the ratio $r_c = F_D/F_\pi = 1.5$

Table 3. The binding energies of the charmed hypernuclei (isoscalars) with unit charm, $c = 1$, in MeV

${}_\Lambda A$	$\omega_c^{r_c = 1.5}$	$\Delta\epsilon_c$	ϵ_c^{tot}	$\omega_c^{r_c = 2}$	$\Delta\epsilon_c$	ϵ_c^{tot}
1	1535	–	–	1673	–	–
${}^{3}_{\Lambda}\text{H}$	1504	27	35	1647	24	32
${}^{5}_{\Lambda}\text{Li}$	1505	25	52	1646	25	52
${}^{7}_{\Lambda}\text{Be}$	1497	32	70	1641	30	68
${}^{9}_{\Lambda}\text{B}$	1518	11	68	1654	17	74
${}^{11}_{\Lambda}\text{C}$	1525	4	79	1658	13	87
${}^{13}_{\Lambda}\text{N}$	1529	0	96	1660	10	106
${}^{15}_{\Lambda}\text{O}$	1540	–11	103	1668	3	117

Note: $\Delta\epsilon_c$ (in MeV) and ϵ^{tot} are the same as in Tables 1 and 2, for the charm quantum number. The results are shown for two values of the charm decay constant corresponding to $r_c = 1.5$ and 2. The chemical symbol is assigned to each nucleus in accordance with its total electric charge.

Table 4. The binding energies of the charmed hypernuclei (isodoublets), with unit charm, $c = 1$, in MeV

${}_\Lambda A$	$\omega_c^{r_c = 1.5}$	$\Delta\epsilon_c$	ϵ_c^{tot}	$\omega_c^{r_c = 2}$	$\Delta\epsilon_c$	ϵ_c^{tot}
${}^{4}_{\Lambda}\text{He} - {}^{4}_{\Lambda}\text{Li}$	1493	12	40	1639	16	44
${}^{6}_{\Lambda}\text{Li} - {}^{6}_{\Lambda}\text{Be}$	1504	9	41	1646	14	46
${}^{8}_{\Lambda}\text{Be} - {}^{8}_{\Lambda}\text{B}$	1510	7	63	1648	15	71
${}^{10}_{\Lambda}\text{B} - {}^{10}_{\Lambda}\text{C}$	1520	0	65	1655	10	75
${}^{12}_{\Lambda}\text{C} - {}^{12}_{\Lambda}\text{N}$	1526	–4	88	1659	7	99
${}^{14}_{\Lambda}\text{N} - {}^{14}_{\Lambda}\text{O}$	1536	–14	91	1666	1	106
${}^{16}_{\Lambda}\text{O} - {}^{16}_{\Lambda}\text{F}$	1543	–19	109	1670	–2	126

Note: The rest of the notation and other details are as in Table 3.

and $r_c = 2$. Although the measurement of this constant has been performed in [15], its variation in some interval seems to be reasonable in view of its big uncertainty. As follows from Tables 3 and 4, the predicted binding energies of charmed hypernuclei do not substantially differ for the values $r_c = 1.5$ and $r_c = 2$. This difference increases with increasing atomic number. For light hypernuclei, this difference is considerably smaller than the difference between binding energies for $r_b = 1.5$ and $r_b = 2$ (see Section 3).

For charmed nuclei, the repulsive Coulomb interaction is greater than for ordinary nuclei with the same atomic number. Moreover, because a charmed nucleus has somewhat smaller dimensions than the ordinary nuclei (an effect that has not been taken into account in the present analysis), this repulsion can decrease the binding energies for charm by several MeV. This does not change our qualitative conclusions, however. For $B = A = 5$ and 13, our results shown in Tables 3 and 4 agree, within 15–20 MeV, with the early result by Dover and Kahana [4], where binding of the charm by several nuclei was studied within the potential approach. In general, we can speak about qualitative agreement with the results of this approach for $B \sim 5$–10 [5, 6] (the results of the potential approach have been reviewed in [6]).

As in the case where $B = 1$, the absolute values of masses of multiskyrmions are controlled by poorly known loop corrections to the classic masses, or the Casimir energy [21]. As was done for the $B = 2$ states, the renormalization procedure is necessary to obtain physically reasonable values of the masses of multibaryons. This generates an uncertainty of about a few tens of MeV; because the binding energy of the deuteron is 30 MeV instead of the measured value 2.225 MeV, approximately 30 MeV characterizes the uncertainty of our approach [10]. This uncertainty is mainly canceled in the differences of binding energies $\Delta\epsilon$ shown in Tables 1–4.

5. CONCLUSIONS

The version of the bound state soliton model proposed in [8] and modified in [9, 10] for the flavor-symmetry-breaking case ($F_D > F_\pi$) allows calculation of the binding energy differences of ground states of flavored and unflavored nuclei. Combined with several phenomenological arguments, this model is very successful in some cases of light hypernuclei, e.g., isoscalars ${}^{5}_{\Lambda}\text{He}$ and ${}^{7}_{\Lambda}\text{Li}$. In other cases, the accuracy of describing the binding-energy is at a level of 10–30 MeV, expected for the entire method, which takes into account only the collective motion of the baryonic systems. There is also a general qualitative agreement with the data in the behavior of binding energy with increasing atomic number. It should be stressed that it is possibly one of the most interesting examples where a field theoretical model provides results that can be directly compared with observation data. This can be considered as an additional argument in favor of the applicability of the chiral soliton approach to the description of realistic

properties of nuclei. For the charm and beauty quantum numbers, the results only slightly depend on the poorly known values of the decay constants F_D or F_B.

The tendency of the binding energies to decrease with increasing B number beginning with $B \sim 10$ is related to the fact that the rational map approximation, leading to the one-shell bubble structure of the classical configuration [11–13], is not good for such values of B. At large values of the flavor symmetry breaking mass, we have approximately

$$\omega_F \approx \frac{m_D\sqrt{\Gamma/\Theta_F}F_D}{2F_\pi}.$$

For rational map configurations at large B, the Σ-term Γ grows faster than the inertia Θ_F because the contribution of the volume occupied by the chiral field configuration is more important for Γ [13]. For larger $B = A$, beginning with several tens, configurations of the skyrmion-type crystals seem to be more realistic than configurations of the rational map type.

Hypernuclei with $|F| \geq 2$ can be studied using similar methods [10]. The analysis of hypernuclei with "mixed" flavors is possible, in principle, but is more involved technically. For example, the isodoublet ${}^{3}_{s,c}\mathrm{H}-{}^{3}_{s,c}\mathrm{He}$ consisting of (n, Λ, Λ_c) and (p, Λ, Λ_c) is expected.

There is a rough agreement between our results and the results in [19, 20], where the flavor excitation frequencies were calculated within another version of the bound state approach and the collective-coordinate-quantization method was used for strangeness. Some details are different, however, and it would be interesting to reproduce our results within other variants of the chiral soliton model. The model that we used overestimates the strangeness excitation energies, but is more reliable for differences of energies entering (9) and (11) and for charm and beauty quantum numbers. Further theoretical studies and experimental search for the baryonic systems with flavors different from u and d could shed more light on the dynamics of heavy flavors in baryonic systems.

ACKNOWLEDGMENTS

I am indebted to A.M. Shunderyuk for checking numerical calculations and to V. Andrianov, A. Gal, and T. Nagae for discussions and remarks. The work was supported by the Russian Foundation for Basic Research (project no. 01-02-16615).

Note added in proof (March 5, 2003). The variation of the only model parameter, Skyrme constant e, has small influence on the results presented here, negligible for charm or beauty quantum numbers. Both quantities Γ and inertia Θ_F scale as $1/(F_\pi e^3)$, and the flavor excitation energies given by (4) at large mass m_D depend on their ratio, and are therefore scale-invariant.

REFERENCES

1. H. Bando, T. Motoba, and J. Zofka, Int. J. Mod. Phys. **21**, 4021 (1990).
2. *Proceedings of International Conference on Hypernuclear and Strange Particle Physics*; Nucl. Phys. A **639** (1998); **691** (2001).
3. A. A. Tyapkin, Yad. Fiz. **22**, 181 (1975) [Sov. J. Nucl. Phys. **22**, 89 (1975)].
4. C. B. Dover and S. H. Kahana, Phys. Rev. Lett. **39**, 1506 (1977).
5. H. Bando and M. Bando, Phys. Lett. B **109**, 164 (1982); H. Bando and S. Nagata, Prog. Theor. Phys. **69**, 557 (1983); B. F. Gibson, C. B. Dover, G. Bhamathi, and D. R. Lehman, Phys. Rev. C **27**, 2085 (1983).
6. N. I. Starkov and V. A. Tsarev, Nucl. Phys. A **450**, 507 (1990); S. A. Bunyatov, V. V. Lyukov, N. I. Starkov, and V. A. Tsarev, Yad. Fiz. **23**, 581 (1992) [Sov. J. Part. Nucl. **23**, 253 (1992)].
7. A. P. Balachandran, A. Barducci, F. Lizzi, *et al.*, Phys. Rev. Lett. **52**, 887 (1984); V. B. Kopeliovich, B. Schwesinger, and B. E. Stern, Pis'ma Zh. Éksp. Teor. Fiz. **62**, 177 (1995) [JETP Lett. **62**, 185 (1995)]; T. A. Ioannidou, B. M. A. G. Piette, and W. J. Zakrzewski, J. Math. Phys. **40**, 6353 (1999); hep-th/9811071; V. B. Kopeliovich, W. J. Zakrzewski, and B. E. Stern, Phys. Lett. B **492**, 39 (2000).
8. K. M. Westerberg and I. R. Klebanov, Phys. Rev. D **50**, 5834 (1994); I. R. Klebanov and K. M. Westerberg, Phys. Rev. D **53**, 2804 (1996).
9. V. B. Kopeliovich, Pis'ma Zh. Éksp. Teor. Fiz. **67**, 854 (1998) [JETP Lett. **67**, 896 (1998)]; hep-ph/9805296.
10. V. B. Kopeliovich and W. J. Zakrzewski, Pis'ma Zh. Éksp. Teor. Fiz. **69**, 675 (1999) [JETP Lett. **69**, 721 (1999)]; Eur. Phys. J. C **18**, 389 (2000); V. B. Kopeliovich, Zh. Éksp. Teor. Fiz. **120**, 499 (2001) [JETP **93**, 435 (2001)].
11. C. Houghton, N. Manton, and P. Suttcliffe, Nucl. Phys. B **510**, 507 (1998).
12. R. A. Battye and P. M. Sutcliffe, Phys. Rev. Lett. **79**, 363 (1997); Rev. Math. Phys. **14**, 29 (2002).
13. V. B. Kopeliovich, Pis'ma Zh. Éksp. Teor. Fiz. **73**, 667 (2001) [JETP Lett. **73**, 587 (2001)]; J. Phys. G **28**, 103 (2002).
14. B. Schwesinger and H. Weigel, Phys. Lett. B **267**, 438 (1991).
15. J. Z. Bai *et al.* (BES Collaboration), Phys. Lett. B **429**, 188 (1998).
16. A. A. Penin and M. Steinhouser, Phys. Rev. D **65**, 054006 (2001); D. Ebert, R. N. Faustov, and V. O. Galkin, hep-ph/0204167.
17. C. G. Callan and I. R. Klebanov, Nucl. Phys. B **262**, 365 (1985).
18. D. O. Riska and N. N. Scoccola, Phys. Lett. B **265**, 188 (1991).
19. M. Schvellinger and N. N. Scoccola, Phys. Lett. B **430**, 32 (1998).
20. C. L. Schat and N. N. Scoccola, Phys. Rev. D **61**, 034008 (2000); Phys. Rev. D **62**, 074010 (2000).
21. B. Moussalam, Ann. Phys. (N.Y.) **225**, 264 (1993); F. Meier and H. Walliser, Phys. Rep. **289**, 383 (1997); H. Walliser, Phys. Lett. B **432**, 15 (1998).

Journal of Experimental and Theoretical Physics, Vol. 96, No. 5, 2003, pp. 789–800.
Translated from Zhurnal Éksperimental'noĭ i Teoreticheskoĭ Fiziki, Vol. 123, No. 5, 2003, pp. 899–911.

NUCLEI, PARTICLES, AND THEIR INTERACTION

Analysis of $e^+e^- \longrightarrow \pi^+\pi^-\pi^+\pi^-$ and $e^+e^- \longrightarrow \pi^+\pi^-\pi^0\pi^0$ Processes in the Energy Range of $\sqrt{s}$ = 0.98–1.38 GeV in Experiments with a Spherical Neutral Detector

M. N. Achasov, K. I. Beloborodov, A. V. Berdyugin, A. G. Bogdanchikov, A. V. Bozhenok, D. A. Bukin, A. A. Valishev, A. V. Vasiljev, V. B. Golubev, T. V. Dimova, V. P. Druzhinin, V. N. Ivanchenko, A. A. Korol, S. V. Koshuba, I. N. Nesterenko, E. V. Pakhtusova, E. A. Perevedentsev, E. A. Pyata, A. A. Salnikov, A. N. Skrinsky, S. I. Serednyakov, Z. K. Silagadze, V. V. Shary*, and Yu. M. Shatunov

Budker Institute of Nuclear Physics, Siberian Division, Russian Academy of Sciences, pr. Akademika Lavrent'eva 11, Novosibirsk, 630090 Russia
Novosibirsk State University, ul. Pirogova 2, Novosibirsk, 630090 Russia
**e-mail: V.V.Shary@inp.nsk.su*

Received January 5, 2003

Abstract—The cross sections of the $e^+e^- \longrightarrow \pi^+\pi^-\pi^+\pi^-$, $e^+e^- \longrightarrow \pi^+\pi^-\pi^0\pi^0$, and $e^+e^- \longrightarrow \omega\pi \longrightarrow \pi^+\pi^-\pi^0\pi^0$ processes, as well as the $e^+e^- \longrightarrow \pi^+\pi^-\pi^0\pi^0$ process with subtracted contribution of the $\omega\pi$ intermediate state, are measured in experiments with a spherical neutral detector on the VEPP-2M collider in the energy range 0.98–1.38 GeV. About 41000 events of the $e^+e^- \longrightarrow \pi^+\pi^-\pi^+\pi^-$ process and more than 54000 events of the $e^+e^- \longrightarrow \pi^+\pi^-\pi^0\pi^0$ process have been selected in experiment. The statistical error in determining the cross section is 2–20%, while the systematic error is 7 and 8%. © *2003 MAIK "Nauka/Interperiodica".*

1. INTRODUCTION

The study of the processes resulting in the production of four π-mesons, viz.,

$$e^+e^- \longrightarrow \pi^+\pi^-\pi^+\pi^-, \quad (1)$$

$$e^+e^- \longrightarrow \pi^+\pi^-\pi^0\pi^0, \quad (2)$$

is one of the important experiments made on the e^+e^- VEPP-2M collider [1] with a spherical neutral detector (SND) [2]. These processes provide vital information for studying excited states of the ρ meson. According to present-day data, there exist two excited states of the ρ meson in the 1–2 GeV region: ρ', or ρ(1450) and ρ'', or ρ(1700) [3]. The parameters of these states were not determined accurately and were obtained from the measured cross sections of the $e^+e^- \longrightarrow \pi^+\pi^-$ and $e^+e^- \longrightarrow \omega\pi$ processes as well as processes (1) and (2) [4–6]. The origin of these states is also not clear. For example, some authors consider the exotic structure of excited states of the ρ meson, i.e., a possible mixing with four-quark mesons [7, 8]. There are indications of the existence of the $\rho_x(1300)$ state [9], which probably is not an ordinary quark–antiquark meson [10]. The measurements of cross sections of processes (1) and (2) made in the present study will make it possible to clarify the situation in this energy range and to improve the accuracy in determining the parameters of ρ' and ρ'' mesons.

The hypothesis concerning the conserved vector current connects the spectral function $v_1(q^2)$ of the $\tau \longrightarrow h^\pm\nu_\tau$ decay with the cross section of the $e^+e^- \longrightarrow h^0$ process, where $h^\pm$, h^0 is a system of several hadrons with quantum numbers $I^GJ^{PC} = 1^+1^{--}$. The cross section of the $e^+e^- \longrightarrow \omega\pi^0$ and $e^+e^- \longrightarrow 4\pi$ processes were compared in [11–13] with the spectral functions of corresponding decays of the τ lepton. It was proved that the hypothesis concerning the conserved vector current for these processes holds to within experimental error. However, the subsequent improvement of the experimental accuracy of measurements on e^+e^- colliders revealed that the measured cross sections of the e^+e^- annihilation differ from values predicted from the decays of τ leptons by approximately 3σ [14]. Here, we compare the obtained cross sections with the predictions based on the hypothesis of vector current conservation from the decays of τ leptons.

In the energy range 1–2 GeV, processes (1) and (2) predominate and make the major contribution to the hadron polarization of vacuum. The anomalous magnetic moment of a muon was measured to a very high degree of accuracy using the g-2 collaboration [15]:

$$a_\mu(\text{exp.}) = (11659203 \pm 8) \times 10^{-10},$$

whose value is comparable to theoretical predictions.

For example, calculations made in [14] lead to the following value:

$$a_\mu = (11659169.1 \pm 7.0 \pm 3.5 \pm 0.3) \times 10^{-10}.$$

According to [14], the contribution of 4π processes in the energy range 1.02–1.8 GeV amounts to $(13.95 \pm 0.90 \pm 0.23) \times 10^{-10}$ for channel (1) and $(16.73 \pm 1.32 \pm 0.20) \times 10^{-10}$ for channel (2). Although the contribution of 4π processes is not decisive, it leads to a considerable contribution to the error in determining the hadron part of the anomalous magnetic moment of a muon.

The first measurements of processes (1) and (2) were made in [16–19]. The most accurate measurements of these processes were made in [20–22]; measurements in [20] were made in an energy range up to 2 GeV. These results are characterized by a large systematic spread (up to 30%) for much smaller statistical errors. It was shown in the CMD-2 experiment [21] that the intermediate state $a_1\pi$ predominates in process (1), while the same state together with the intermediate state $\omega\pi$ predominates in process (2). The most accurate measurements of the cross section of the $e^+e^- \longrightarrow \omega\pi$ process in the $\omega \longrightarrow \pi^0\gamma$ channel were made in [23], which allows an independent verification of the results obtained for process (2).

The present paper aims at measuring the cross sections of processes (1) and (2) using an SND in the energy range 0.98–1.38 GeV.

2. SELECTION OF EXPERIMENTAL EVENTS

Statistical data were gathered in experiments with an SND by scanning the given energy interval. In the energy range 1.06–1.38 GeV (above the ϕ meson resonance), the integrated luminosity of 9.25 pb^{-1} was accumulated. In the region of the ϕ meson resonance peak of $\sqrt{s}$ = 0.98–1.06 GeV, the integrated luminosity was 8.5 pb^{-1}.

Events of process (1) in the energy range 1.06–1.38 GeV were selected using the following rules.

1. The number of charged particles must be greater than or equal to 4, and the number of neutral particles is greater than or equal to 0. Additional charged and neutral particles may appear as a result of superposition of the beam background on experimental events. The sources of charged particle can also be δ electrons, while neutral particles can appear as a result of nuclear interactions of π mesons or splitting of showers in the calorimeter.

2. The total energy deposition in the calorimeter is smaller than $0.75\sqrt{s}$.

3. The shortest distance from a track to the interaction point in the $R\phi$ plane for any charged particle is smaller than 0.2 cm.

4. The Z coordinate of the track point nearest to the beam axis for any charged particle is smaller than 8 cm (the characteristic spread in parameter Z amounts to about 2.5 cm and is associated with the spread in the points of interaction of the e^+e^- beams).

5. Polar angles θ of charged particles satisfy the conditions $-0.9 < \cos\theta < 0.9$.

6. The smallest angle between charged particles is greater than 18°, i.e., equal to the angular size of the cell in the track system.

The main sources of the background are the events of the processes

$$e^+e^- \longrightarrow 3\pi, \quad e^+e^- \longrightarrow 2e^+2e^-, \quad e^+e^- \longrightarrow 2\pi^+2\pi^-\pi^0,$$

and the beam background. Conditions 2–5 suppress both the beam background and the background of the $e^+e^- \longrightarrow 2e^+2e^-$ processes. Condition 6 reduces the systematic error in the efficiency of detection for events with charged particles falling in the same cell of the drift chamber.

Since the magnetic field in the SND is equal to zero, the momenta of particles cannot be measured directly, but are calculated using energy–momentum conservation laws and the angles of escape of charged particles measured in the track system of coordinates. For events involving more than four charged particles, only the first four particles with the largest energy deposition in the calorimeter were considered. Neutral particles were ignored. An additional condition in selecting events of process (1) was the requirement that the system of equations describing the energy–momentum conservation laws has a solution. This condition makes it possible to reduce the beam background to a considerable extent.

In the region of 0.98–1.06 GeV, there exists an additional background from the decay

$$\phi \longrightarrow K_SK_L, \quad K_S \longrightarrow \pi^+\pi^-, \quad K_L \longrightarrow \pi^+\pi^-\pi^0.$$

This decay is characterized by the fact that the point of escape of π mesons lies, as a rule, outside the region of interaction of the e^+e^- beams in view of the departure of K_S (for these energies, the decay lengths for the K_S and K_L mesons are 0.3–1 cm and 2–5.7 m, respectively). Selected events were reconstructed under the assumption that all particles have a common point of escape in the region of interaction of e^+e^- beams. Then the kinematic reconstruction parameter χ^2 was calculated and the events used for the analysis were characterized by a value of χ^2, used for the reconstruction with a common point of escape, smaller than 100. This condition improves the signal-to-noise ratio at the peak of the ϕ meson resonance by a factor of 1.5. After the application of the above-mentioned selection criterion in the energy range of 1.06–1.38 GeV, 36538 events were selected, while the number of events selected in the region of the ϕ meson resonance (0.98–1.06 GeV) was equal to 4297 (see Table 1).

Table 1. Integrated luminosity L, number N of selected events, efficiency ε, radiative correction $1 + \delta$, and cross section σ^{exp} for process (1) as functions of energy E (only the statistical error is indicated for cross sections)

E, MeV	L, nb^{-1}	N	ε	$1 + \delta$	σ^{exp}, nb	E, MeV	L, nb^{-1}	N	ε	$1 + \delta$	σ^{exp}, nb
980.00	129.31	38	0.277	0.908	1.07 ± 0.21	1140.00	288.98	476	0.302	0.898	6.00 ± 0.28
984.10	374.60	107	0.251	0.907	1.20 ± 0.09	1150.00	69.33	139	0.305	0.898	7.33 ± 0.62
1003.80	391.03	121	0.252	0.903	1.25 ± 0.12	1160.00	319.55	647	0.308	0.899	7.33 ± 0.30
1009.68	314.12	106	0.252	0.902	1.43 ± 0.15	1180.00	423.22	1029	0.313	0.899	8.61 ± 0.28
1015.66	369.09	162	0.252	0.901	1.65 ± 0.15	1190.00	172.29	425	0.316	0.900	8.68 ± 0.42
1016.68	637.89	271	0.252	0.901	1.56 ± 0.12	1200.00	438.60	1458	0.319	0.900	11.58 ± 0.32
1017.66	1011.70	527	0.252	0.901	1.72 ± 0.12	1210.00	151.45	464	0.322	0.901	10.58 ± 0.51
1018.64	1063.49	598	0.252	0.901	1.65 ± 0.11	1220.00	342.87	1172	0.324	0.901	11.67 ± 0.36
1019.62	1083.77	719	0.252	0.901	1.87 ± 0.10	1230.00	140.75	450	0.327	0.902	10.85 ± 0.52
1020.58	679.29	389	0.252	0.901	1.69 ± 0.12	1240.00	377.73	1508	0.330	0.903	13.37 ± 0.36
1021.64	347.48	197	0.252	0.901	1.85 ± 0.16	1250.00	209.00	943	0.332	0.904	15.04 ± 0.50
1022.76	380.67	183	0.252	0.900	1.67 ± 0.15	1260.00	162.90	680	0.335	0.905	13.80 ± 0.54
1027.74	386.31	183	0.252	0.900	1.89 ± 0.15	1270.00	241.26	1232	0.337	0.906	16.75 ± 0.49
1033.72	349.90	155	0.252	0.900	1.87 ± 0.17	1280.00	228.98	1173	0.339	0.907	16.67 ± 0.50
1040.00	416.57	206	0.252	0.899	2.08 ± 0.15	1290.00	271.88	1365	0.341	0.908	16.22 ± 0.45
1050.00	280.83	168	0.252	0.898	2.37 ± 0.15	1300.00	259.97	1486	0.343	0.910	18.33 ± 0.50
1060.00	278.80	201	0.284	0.898	2.51 ± 0.13	1310.00	202.04	1102	0.345	0.911	17.39 ± 0.53
1070.00	97.74	78	0.286	0.898	3.11 ± 0.35	1320.00	235.80	1287	0.346	0.913	17.29 ± 0.49
1080.00	578.03	715	0.288	0.897	3.38 ± 0.18	1330.00	292.78	1725	0.347	0.914	18.56 ± 0.45
1090.00	95.15	87	0.290	0.897	3.52 ± 0.38	1340.00	438.69	3102	0.348	0.916	22.20 ± 0.45
1100.00	445.12	459	0.292	0.897	3.92 ± 0.19	1350.00	246.66	1782	0.349	0.918	21.66 ± 0.53
1110.00	90.37	107	0.294	0.897	4.48 ± 0.43	1360.00	624.90	4828	0.350	0.920	23.98 ± 0.36
1120.00	306.38	403	0.297	0.897	4.93 ± 0.25	1370.00	256.16	1974	0.350	0.923	23.86 ± 0.55
1130.00	112.58	165	0.299	0.898	5.46 ± 0.43	1380.00	479.75	3742	0.350	0.925	24.08 ± 0.40

Events of process (2) were selected using the following conditions.

1. The number of charged particles must be equal to 2, the number of neutral particles is greater than or equal to 4 (additional neutral particles appear in the calorimeter as a result of the nuclear interaction of π mesons and the shower splitting in the calorimeter as well as due to superposition of the beam background).

2. The shortest distance between a track and the interaction point on the $R\phi$ plane for any charged particle must be smaller than 0.2 cm.

The background events originate from the processes

$$e^+e^- \longrightarrow \pi^+\pi^-\pi^0, \quad e^+e^- \longrightarrow \pi^+\pi^-3\pi^0,$$
$$e^+e^- \longrightarrow e^+e^-2\gamma,$$

as well as from the beam and cosmic backgrounds. The kinematic reconstruction procedure using the energy–momentum conservation laws makes it possible to suppress the contribution of background processes and to reconstruct the energy of charged π mesons. Since photons are formed as a result of the decay of a π^0 meson, two additional conditions were introduced: the invariant mass of two photons is equal to the mass of the π^0 meson. In the course of reconstruction, the value of χ^2 was calculated. In order to select combinations of photons forming a π^0 meson, the search for possible variants was carried out and a combination with the smallest parameter χ^2 was selected. Figure 1 shows the experimental and simulated distributions of events over parameter χ^2. The final choice was made using the following additional condition.

3. The kinematic reconstruction parameter χ^2 must be smaller than 30.

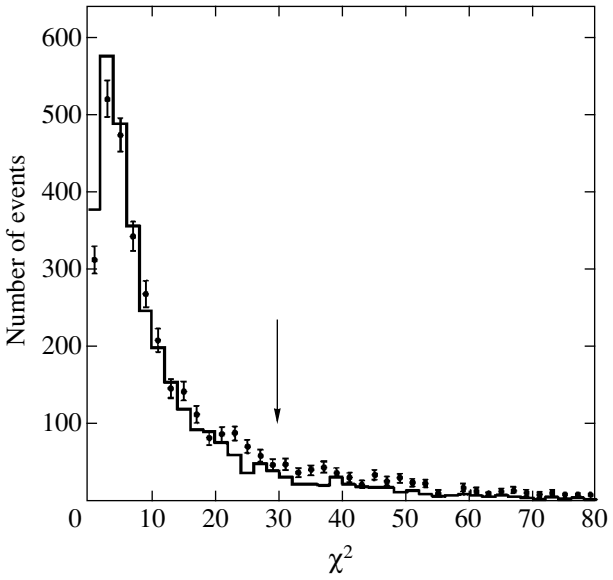

Fig. 1. Distribution of events over the kinematic reconstruction parameter χ^2 in the $e^+e^- \longrightarrow \pi^+\pi^-\pi^0\pi^0$ process. Points with errors correspond to experimental data, while the histogram is obtained as a result of simulation. The arrow indicates the selection criterion (see text). The energy $\sqrt{s}$ = 1380 MeV.

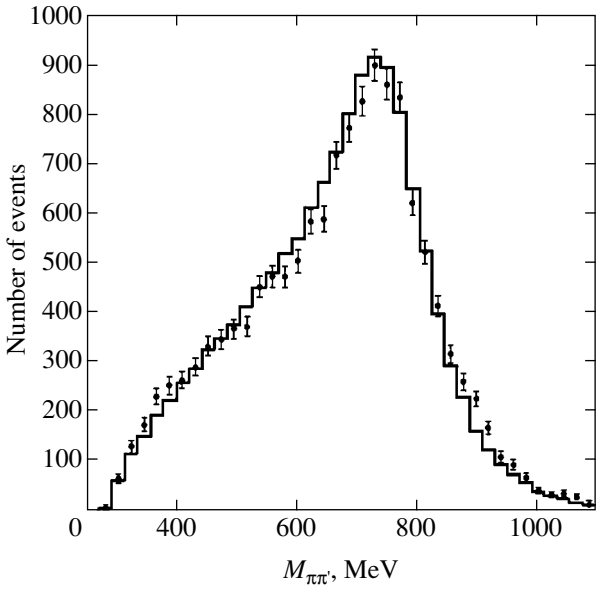

Fig. 2. Distribution of events over the invariant masses of two π mesons in process (1) (the π meson with the minimal energy is discarded). The histogram corresponds to $a_1\pi$ modeling, points with errors represent experimental data, and $\sqrt{s}$ = 1380 MeV.

In the region of the ϕ meson, the above conditions are insufficient for suppressing the background from the $\phi \longrightarrow 3\pi$ decay; for this reason, the kinematic reconstruction was carried out under the assumption that the final state is $\pi^+\pi^-\pi^0$. In order to reduce the number of background events, the following condition was imposed.

4. For energy $\sqrt{s} < 1094$ MeV in the center-of-mass system, the value of the kinematic reconstruction parameter χ^2 for process $e^+e^- \longrightarrow 3\pi$ must be greater than 200.

This condition suppresses the background by a factor of 12, the number of events of process (2) decreasing thereby by 20%. In order to suppress the background from collinear $e^+e^- \longrightarrow K^+K^-$ and $e^+e^- \longrightarrow \mu^+\mu^-$ processes, the following condition was used.

5. For energy $\sqrt{s} < 1094$ MeV in the center-of-mass system, the angle of departure from collinearity for charged particles in the $R\phi$ plane is greater than 10°.

This condition suppresses the background by a factor of 5, the number of events of process (2) being reduced by 10%. As a result, the estimated number of background events for an energy equal to the ϕ meson mass (1020 MeV) amounts to 6%. Away from the region of the ϕ meson, the number of background events decreases several times due to the resonant behavior of the $e^+e^- \longrightarrow 3\pi$ process and in view of an increase in the cross section of process (2) upon an increase in energy. In accordance with these selection criteria, 54470 events were selected in the energy range 0.98–1.38 GeV (see Table 2).

3. MODELS OF INTERMEDIATE STATES OF THE FINAL SYSTEM OF FOUR PIONS

In experiments with CMD-2 [21] and CLEO-2 detectors [12], it was demonstrated that the dynamics of process (1) can be described in the model of the $a_1\pi$ intermediate state,

$$e^+e^- \longrightarrow a_1(1260)\pi \longrightarrow \rho\pi\pi,$$

while the intermediate state must be taken into account in the case of process (2):

$$e^+e^- \longrightarrow \omega\pi \longrightarrow \rho\pi\pi.$$

In order to calculate the efficiency, processes (1) and (2) were simulated by the Monte Carlo method. The matrix elements of the processes were calculated using the formulas given in [21]. The parameters of the a_1 meson were fixed from [3], and the width of the a_1 meson was assumed to be equal to 450 MeV. Figure 2 shows the experimental and simulated distributions for process (1) (the $a_1\pi$ model) over invariant masses of two π mesons. All combinations except those with the π meson possessing the lowest energy were included in the distribution (three such combinations in all). It can be seen that the $a_1\pi$ model correctly describes the experimental situation in the invariant mass spectrum as well as for angular distributions (Figs. 2 and 3). The calculated values of efficiency are given in Table 1.

Table 2. Integrated luminosity L, numbers N_ω and N_{a_1} of selected events, efficiency ε, radiative correction $1 + \delta$, and cross section σ^{exp} for processes (2), (3), and (4) for various values of energy E (only the statistical error is indicated)

E, MeV	L, nb^{-1}	N_ω	N_{a_1}	ε		$1 + \delta$		σ^{exp}, nb		
				(3)	(4)	(3)	(4)	(2)	(3)	(4)
980	129.31	61	27	0.230	0.072	0.860	0.937	5.56 ± 1.58	2.72 ± 0.54	3.14 ± 1.51
1019	54.50	59	5	0.230	0.076	0.887	0.934	8.07 ± 1.65	7.59 ± 1.19	1.33 ± 1.27
1040	68.76	110	7	0.230	0.078	0.898	0.932	9.17 ± 1.47	8.71 ± 0.96	1.43 ± 1.20
1050	83.91	168	6	0.230	0.079	0.902	0.931	10.66 ± 1.35	10.84 ± 0.95	1.03 ± 1.05
1060	278.80	612	21	0.230	0.080	0.906	0.930	11.45 ± 0.75	11.85 ± 0.55	0.92 ± 0.57
1070	97.74	176	12	0.230	0.081	0.910	0.929	10.26 ± 1.25	9.67 ± 0.85	1.67 ± 1.00
1080	578.03	1291	134	0.230	0.082	0.913	0.928	13.67 ± 0.63	11.97 ± 0.39	3.04 ± 0.52
1090	95.15	217	16	0.230	0.083	0.916	0.927	13.01 ± 1.37	12.19 ± 0.94	2.18 ± 1.09
1100	445.12	1586	263	0.312	0.313	0.919	0.927	14.41 ± 0.42	13.99 ± 0.41	1.98 ± 0.21
1110	90.37	257	56	0.312	0.313	0.922	0.926	12.02 ± 0.86	11.15 ± 0.82	2.12 ± 0.45
1120	306.38	1151	238	0.312	0.315	0.925	0.925	15.67 ± 0.54	14.64 ± 0.52	2.67 ± 0.29
1130	112.58	435	68	0.312	0.315	0.928	0.924	15.41 ± 0.88	15.03 ± 0.87	2.07 ± 0.43
1140	288.98	1152	236	0.312	0.316	0.930	0.923	16.50 ± 0.58	15.42 ± 0.56	2.80 ± 0.30
1150	69.33	245	74	0.312	0.317	0.933	0.922	15.78 ± 1.16	13.66 ± 1.07	3.64 ± 0.67
1160	319.55	1293	329	0.313	0.318	0.935	0.921	17.34 ± 0.58	15.59 ± 0.54	3.49 ± 0.33
1180	423.22	1827	553	0.313	0.320	0.939	0.919	19.14 ± 0.54	16.55 ± 0.49	4.44 ± 0.32
1200	438.60	1856	686	0.313	0.322	0.942	0.917	19.54 ± 0.55	16.14 ± 0.49	5.21 ± 0.34
1210	151.45	658	209	0.313	0.323	0.944	0.916	19.36 ± 0.92	16.54 ± 0.83	4.67 ± 0.55
1220	342.87	1429	623	0.314	0.324	0.945	0.915	20.10 ± 0.64	15.79 ± 0.55	6.08 ± 0.41
1230	140.75	581	269	0.314	0.325	0.946	0.915	20.34 ± 1.00	15.65 ± 0.88	6.44 ± 0.63
1240	377.73	1631	851	0.314	0.326	0.947	0.914	22.03 ± 0.63	16.29 ± 0.54	7.57 ± 0.41
1250	209.00	946	446	0.314	0.326	0.949	0.913	22.35 ± 0.85	17.10 ± 0.73	7.17 ± 0.54
1260	162.90	759	327	0.314	0.327	0.950	0.913	22.33 ± 0.94	17.59 ± 0.82	6.71 ± 0.59
1270	241.26	1171	611	0.314	0.328	0.951	0.912	24.69 ± 0.82	18.29 ± 0.70	8.45 ± 0.53
1280	228.98	1052	597	0.315	0.329	0.952	0.912	24.03 ± 0.83	17.28 ± 0.70	8.69 ± 0.54
1290	271.88	1268	729	0.315	0.330	0.953	0.911	24.46 ± 0.76	17.51 ± 0.65	8.91 ± 0.49
1300	259.97	1355	735	0.315	0.331	0.954	0.911	26.57 ± 0.83	19.46 ± 0.72	9.29 ± 0.53
1310	202.04	898	582	0.315	0.332	0.956	0.911	24.29 ± 0.87	16.63 ± 0.74	9.52 ± 0.58
1320	235.80	1104	744	0.315	0.333	0.957	0.911	25.92 ± 0.84	17.49 ± 0.70	10.40 ± 0.56
1330	292.78	1368	967	0.315	0.334	0.959	0.911	26.31 ± 0.75	17.41 ± 0.62	10.85 ± 0.50
1340	438.69	2097	1536	0.315	0.335	0.960	0.912	27.19 ± 0.63	17.77 ± 0.51	11.41 ± 0.44
1350	246.66	1254	1001	0.316	0.336	0.962	0.913	28.81 ± 0.83	18.11 ± 0.69	12.73 ± 0.57
1360	624.90	2919	2185	0.316	0.337	0.965	0.914	28.35 ± 0.54	18.33 ± 0.45	12.07 ± 0.36
1370	256.16	1297	984	0.316	0.338	0.968	0.915	28.99 ± 0.81	18.65 ± 0.67	12.43 ± 0.55
1380	479.75	2416	1847	0.316	0.338	0.972	0.917	28.80 ± 0.58	18.46 ± 0.49	12.41 ± 0.40

The distribution over the invariant masses of two charged π mesons and one neutral meson in channel (2) (Fig. 4) indicates the presence of both the intermediate state $\omega\pi$, corresponding to the reaction

$$e^+e^- \longrightarrow \omega\pi \longrightarrow \pi^+\pi^-\pi^0\pi^0, \qquad (3)$$

and events outside the ω-meson peak, which cannot be described by simulating the process $e^+e^- \longrightarrow \omega\pi$. It will be shown below that these events are correctly described by the model with the intermediate $a_1\pi$ state:

$$e^+e^- \longrightarrow a_1\pi \longrightarrow \pi^+\pi^-\pi^0\pi^0. \qquad (4)$$

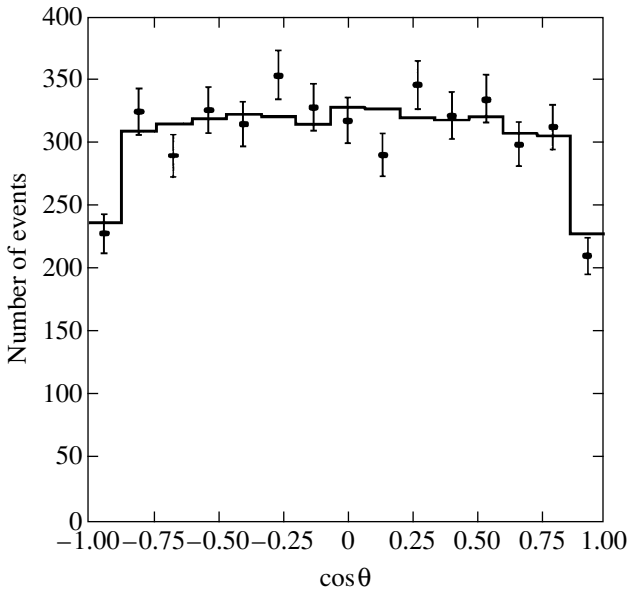

Fig. 3. Distribution of events over the angle of emission of the less energetic π meson in process (1). The histogram corresponds to $a_1\pi$ modeling, points with errors represent experimental data, and $\sqrt{s}$ = 1380 MeV.

In order to separate the events of processes (3) and (4) in process (2), use was made of the distribution over the invariant mass of three π mesons, which is closest to the mass of the ω meson (Fig. 4). If N_1 is the number of events at the ω-meson peak (region 1) and N_2 is the number of events outside it (region 2), the number of events of processes (3) and (4) is defined as

$$N_\omega = \frac{\beta N_1 - (1-\beta)N_2}{\alpha+\beta-1}, \qquad N_{a_1} = \frac{-(1-\alpha)N_1 + \alpha N_2}{\alpha+\beta-1}, \tag{5}$$

where α is the probability that the events of process (3) fall in region 1 and β is the probability that the events of process (4) fall in region 2. Parameters α and β and their energy dependence are determined from simulation. The number of events N_ω and N_{a_1} and the efficiency are given in Table 2. The errors in efficiency associated with the model dependence will be considered in Section 5.

The distributions over invariant masses of the neutral and charged π mesons in the region of invariant masses of 3π outside the ω-meson peak (Fig. 5) contain a peak in the ρ meson resonance region. A similar distribution over invariant masses of charged π mesons (Fig. 5) displays no peak of this kind, which means that events of a non-ωπ process mainly contain a charged ρ meson and do not contain a neutral meson. In other words, the reaction occurs via intermediate states with an isotopic spin $I = 1$ of the resonance. Such a configuration is typical of the intermediate $a_1\pi$ state. It can be seen from Fig. 4 that simulation taking into account the intermediate states $\omega\pi + a_1\pi$ in a ratio determined from experiment correctly describes the invariant mass spectrum and can be used for determining the efficiency of

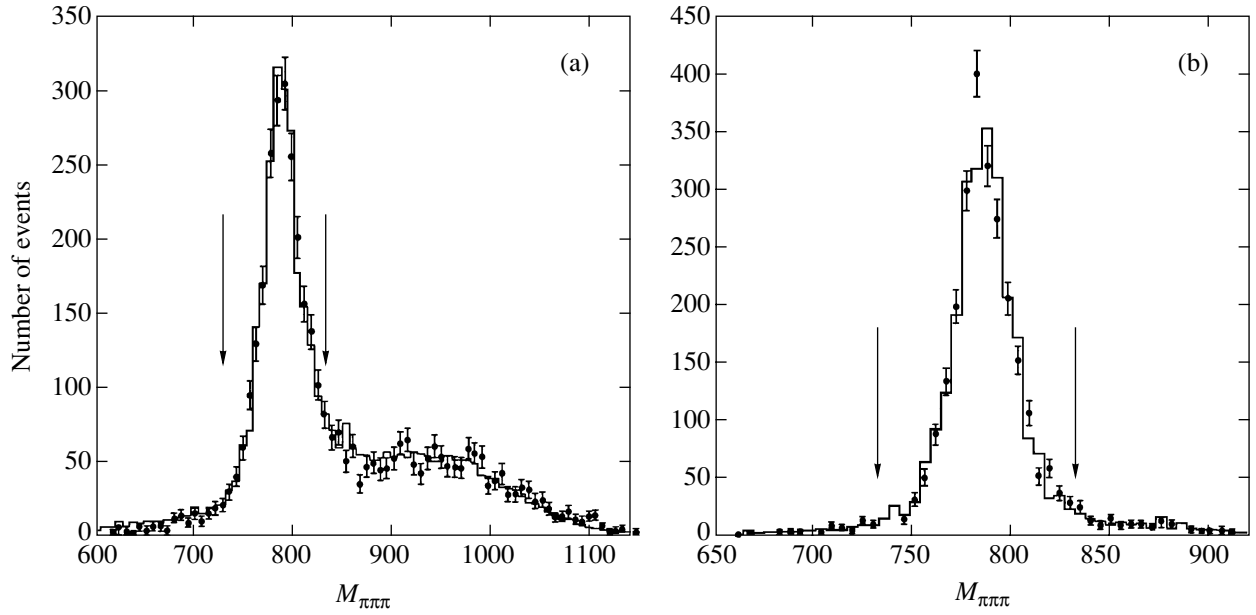

Fig. 4. Distribution of events over the invariant masses for two charged and one neutral π mesons in process (2) (the mass closest to the ω-meson mass is selected). The histogram corresponds to $\omega\pi + a_1\pi$ modeling; points with errors represent experimental data; the arrows indicate the boundaries of regions 1 and 2 described in Section 4. $\sqrt{s}$ = 1380 MeV (a) and $1040 \le \sqrt{s} \le 1080$ MeV (b).

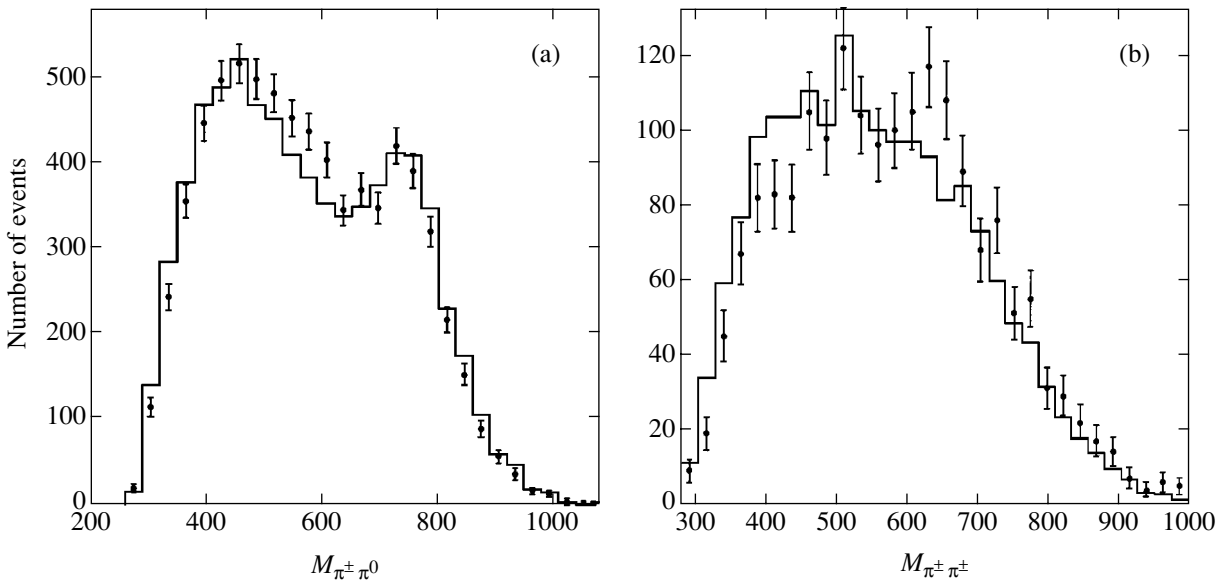

Fig. 5. Distribution of events over the invariant masses of two π mesons in process (2) in the range of invariant masses of 3π outside the ω-meson peak. The $\omega\pi + a_1\pi$ modeling is presented in the experimentally determined relation. The histogram corresponds to the modeling; points with errors represent experimental data. (a) $M_{\pi^\pm\pi^0}$, (b) $M_{\pi^\pm\pi^\pm}$; $\sqrt{s}$ = 1380 MeV.

detecting processes (3) and (4). Possible interference between states (3) and (4) was disregarded since it does not exceed 2%, which is much smaller than the systematic errors of measurements.

The experimental distributions for processes (1) and (2) over the invariant masses of two π mesons and polar angles of particles were compared with the results of simulation for other possible intermediate states (π(1300)π, σρ, and $a_2(1320)\pi$ in processes (1) and (2) and $h_1(1170)\pi$ and $\rho^+\rho^-$ in process (2)). It was found that the results of simulation disagree with experiment.

4. MEASUREMENT OF THE CROSS SECTIONS OF $e^+e^- \longrightarrow 4\pi$ PROCESSES

The cross section of the process at a point with energy E_i was calculated using the formula

$$\sigma^{\exp}(E_i) = \frac{\sigma_{\text{vis}}(E_i)}{\varepsilon_i(1+\delta_{\text{rad}}(E_i))}, \quad \sigma_{\text{vis}}(E_i) = \frac{N_i^{\exp}}{L_i}, \qquad (6)$$

where ε_i, L_i, $\delta_{\text{rad}}(E_i)$, and $\sigma_{\text{vis}}(E_i)$ are the detection efficiency, integrated luminosity, radiative corrections, and visual registration cross section.

In order to calculate the cross section using formula (6), we used the following approximation procedure. We determined the maximum value of the logarithmic likelihood function

$$L = \sum_i \ln P_i(N_i^{\exp}, N_i^{\text{th}}),$$

where P_i is the Gaussian probability of detecting the observed number $N_i^{\exp}$ of events at the ith energy point with the expected number of events N_i^{th},

$$N_i^{\text{th}} = \varepsilon_i L_i \sigma(E_i)(1+\delta_{\text{rad}}(E_i)),$$

and $\sigma(E)$ is the cross section of processes $e^+e^- \longrightarrow 4\pi$. The radiative correction $\delta_{\text{rad}}(E)$ is a functional of the energy dependence $\sigma(E)$ of the cross section [24] and is determined in the course of approximation. It is well known that the cross section of processes (1) and (2) in the energy range under investigation are described by the sum of the contributions from ρ(770), ρ', and ρ'' mesons; consequently, the energy dependence of the cross section was represented as the square of the sum of the corresponding amplitudes in the Breit–Wigner form. Here, the approximation procedure was used only for determining the radiative corrections to the cross section and was not applied for determining the parameters of resonances ρ', ρ'' since the maximal energy of the collider (1380 MeV) makes it possible to carry out measurements only on the left slope of the resonances, and the results of other experiments must be used for determining the parameters of excited states of the ρ meson. Consequently, we can use any function that correctly describes the experimental data in the energy range below 1400 MeV as the approximating function. The registration cross section for process (1), which is measured in the region of a φ meson (Fig. 6), contains a resonance background mainly due to the decay $\phi \longrightarrow K_S K_L$. In order to take this background into account, the approximated function was supplemented with the term

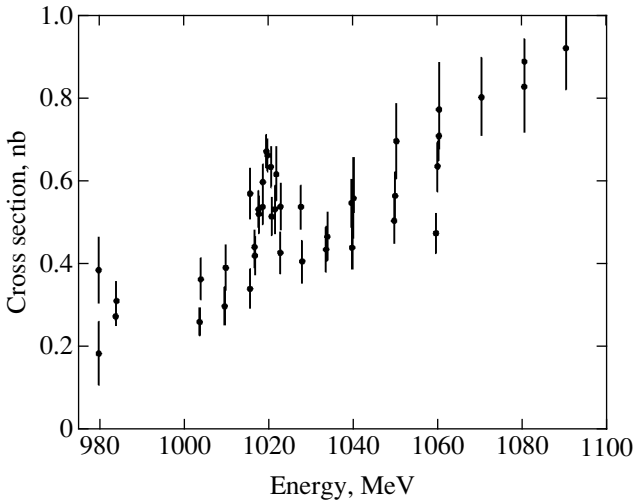

Fig. 6. Visual registration cross section σ_{vis} of process (1).

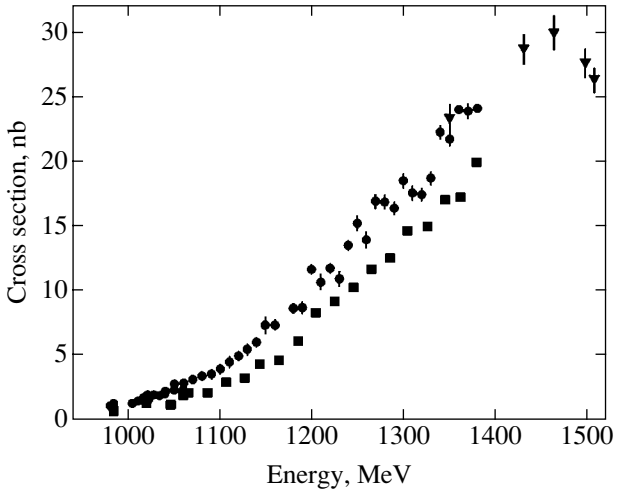

Fig. 7. Cross section of process (1) measured in the present study (●) in comparison with experiments using CMD-2 [21] (■) and DM2 [28] (▼).

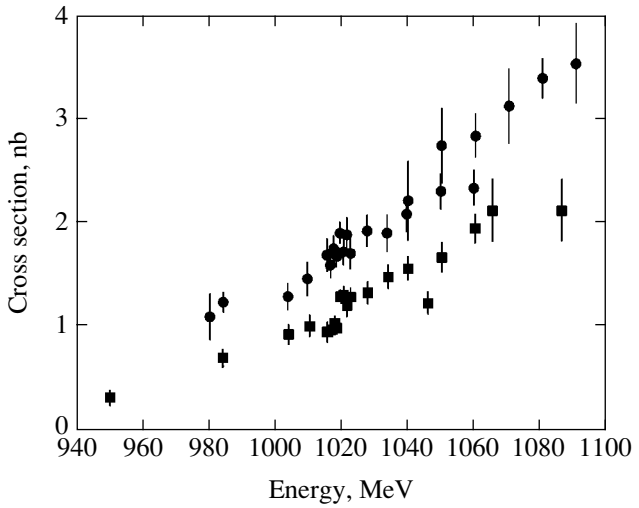

Fig. 8. Cross section of process (1) in the region of the ϕ-meson resonance measured in the present study (●) in comparison with the results of experiments using CMD-2 [21] (■).

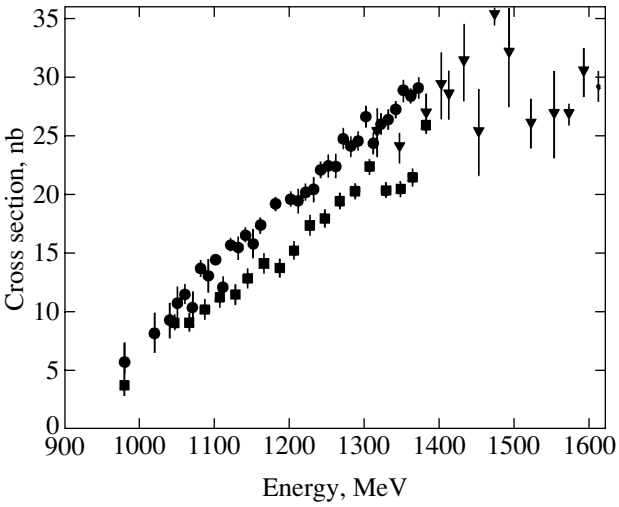

Fig. 9. Cross section of process (2) measured in the present study (●) in comparison with the results of experiments using CMD-2 [21] (■) and DM2 [28] (▼).

describing the resonance dependence of the cross section on energy in the region of the ϕ meson. The energy dependence of the cross section was approximated with the help of a software package developed for approximating cross sections in experiments with an SND [25]. The values of radiative corrections and cross-sections are given in Table 1. The measured cross sections of the process are shown in Figs. 7 and 8.

In order to determine the cross sections of processes (3) and (4), the quantity N_ω or N_{a_1} defined by formulas (5) was substituted into formula (6) for N_i. The radiative corrections were calculated using the approximation procedure described above. The approximation function was in the form of the cross sections given in [23, 26]. The measured cross section of process (3) was divided by the relative probability of the decay $\omega \longrightarrow \pi^+\pi^-\pi^0$ from [3]. The calculated values of radiative corrections and cross sections are given in Table 2. The measured cross sections are shown in Figs. 9–11.

5. SYSTEMATIC ERRORS

In estimating the systematic error in the measured cross sections of processes (1), (2), (3), and (4), we took into account the following sources of errors.

1. The error in computation of integrated luminosity. This error was calculated as the difference in the lumi-

nosity values determined from the processes $e^+e^- \longrightarrow e^+e^-$ and $e^+e^- \longrightarrow \gamma\gamma$ and did not exceed 3%.

2. Errors of simulation of the nuclear interaction between charged pions and the detector. These errors are the sources of the systematic error in determining the detection efficiency. The main contribution to the error comes from inaccurate simulation of pion absorption in the passive substance of the track system (inner shell), leading to the loss of tracks, and from the error in simulation of energy deposition for charged pions in the calorimeter. The error associated with inaccuracy in simulating pion absorption was estimated by varying the limitation imposed on the minimal pulse of π mesons in an event and constituted 2%. The error in efficiency associated with inaccurate modeling of energy deposition was determined by varying the minimal and maximal limitations imposed on the energy deposition in an event and amounted to 3.5%. The total systematic error in estimating the efficiency of processes (1) and (2) was as high as 4%.

3. Model error. In order to determine the model error in the measured cross section, the variation in efficiency upon the addition of the contribution from subsidiary intermediate states ($h_1(1170)\pi$, $\rho^+\rho^-$, $\pi(1300)\pi$, $\sigma\rho$, $a_2(1320)\pi$) was estimated. We assumed that the contribution from these states does not exceed 10% [21]. This value does not contradict the experimental distributions. We also took into account the possible difference between the mass and width of the a_1 meson and the mean values given in [3]. The possible presence of parameter Λ in the a_1-meson form factor

$$F_{a_1}(s) = \frac{1 + M_{a_1}^2/\Lambda}{1 + s/\Lambda}$$

was also taken into consideration (see [21]). We included the possibility of decay of the a_1 meson into the σ meson with a probability of 15% [27], which does not contradict the experimental distribution obtained in this study. The total systematic error of measurement of the cross section of process (1), which is determined by the model dependence, is estimated at 3.5%. The inclusion of the model dependence for process (2) leads to a systematic error of 5%. The possible contribution of subsidiary intermediate states changes the relation between the number of events at the ω-meson peak and outside it in the invariant mass spectrum of three π mesons. This in turn changes the values of coefficients α and β in formula (5) and hence leads to a change in the cross sections of processes (3) and (4), leaving the cross section of process (2) virtually unchanged. The inclusion of this source of systematic errors gives a value of 12% for process (3) and 20% for process (4).

4. The error in calculating the radiative corrections was estimated by using various models for approximating the energy dependence of the cross section. We used models with two (ρ, ρ') or three (ρ, ρ', ρ'') resonances with different energy dependences of the resonance width and with different parameters of their interference. The corresponding error in the measurement of cross section does not exceed 3% in the entire energy range.

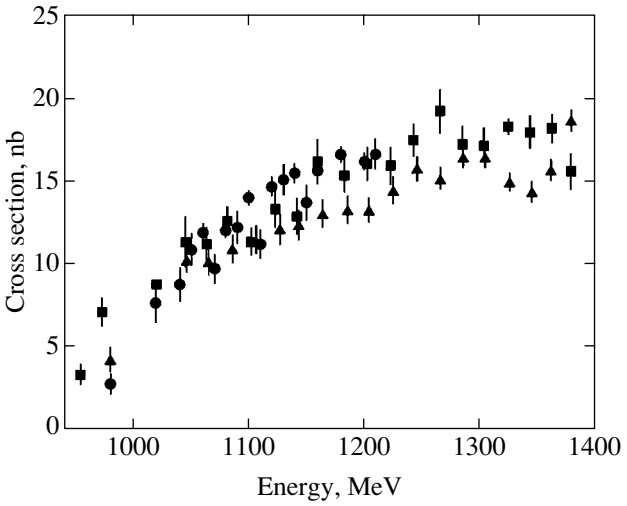

Fig. 10. Cross section of process (3) measured in the present study (●) in comparison with the results of experiments using a SND in the $\omega\pi \longrightarrow \pi\pi\gamma$ channel [23] (■) and CMD-2 [21] (▲).

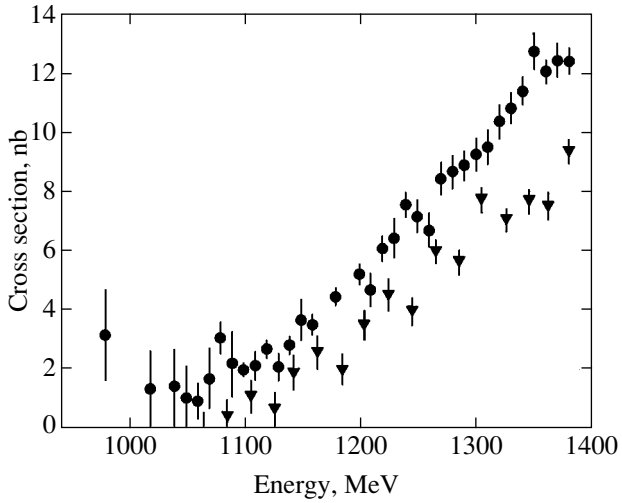

Fig. 11. Cross section of process (4) measured in the present study (●) in comparison with the results of experiments using the CMD-2 detector [21] (▼).

Taking into account the contributions listed above, we find that the systematic errors were 7% for process (1), 8% for process (2), 13% for process (3), and 20% for process (4).

6. DISCUSSION

Figure 7 shows the cross section of process (1) measured in this study in comparison with the results of

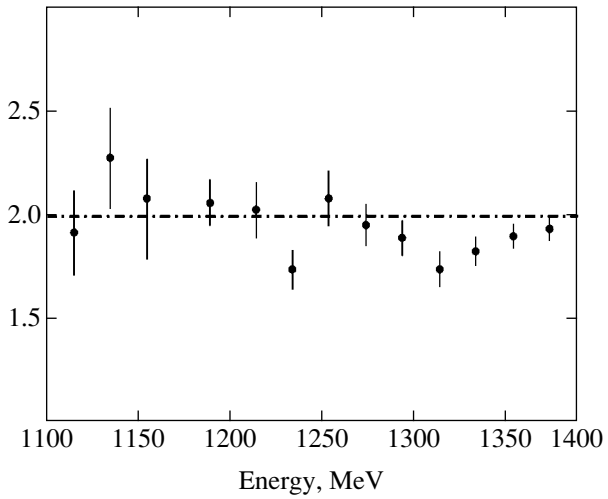

Fig. 12. Ratio of cross sections of processes (1) and (4).

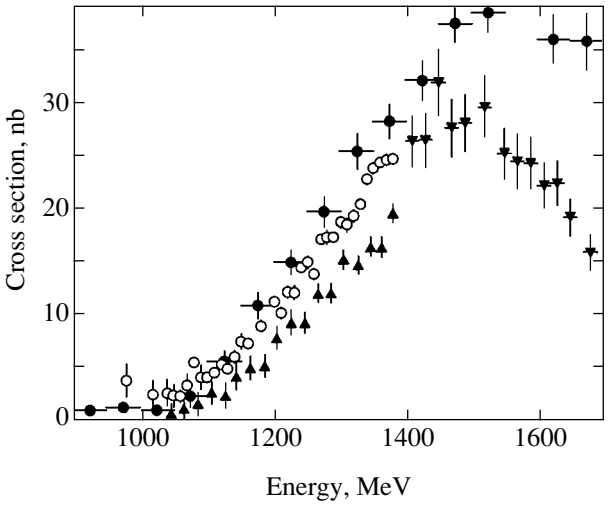

Fig. 13. Comparison of the sum of the cross sections of the $e^+e^- \longrightarrow 4\pi$ process with subtracted contribution of $\omega\pi$ events (see text), measured experimentally with the help of SND (○), CMD-2 (▲), and DM2 (▼) with the structural function of τ-lepton decays in experiments with the CLEO detector [12] (●).

other experiments. It can be seen that the cross section measured by us systematically lies above the cross sections measured by the CMD-2 detector [21], but the observed difference (about 15%) lies within the total systematic error of both experiments. In an energy range of about 1 GeV (Fig. 8), a discrepancy of about 30% is observed, which is considerably larger than the total systematic error. It should be noted that the measured cross section depends only slightly on the model of the intermediate state. For example, for the model with a Lorentz-invariant phase volume, which fails to describe the experimental distributions, the detection efficiency differs from that in the $a_1\pi$ model by less than 10%. This is a consequence of the high detection efficiency due to the large solid angle of the SND.

Figure 9 shows the cross section of process (2) measured in this study. It can be seen that it lies systematically above the cross section obtained with the help of the CMD-2 [21]. However, the observed difference (about 15%) does not exceed the total systematic error either. The measured cross sections of the $e^+e^- \longrightarrow \omega\pi$ process (Fig. 10) are in good agreement with the data obtained with the help of the SND in the $e^+e^- \longrightarrow \omega\pi \longrightarrow \pi^0\pi^0\gamma$ channel [23, 26] using the CMD-2 [21].

If we interpret non-$\omega\pi$ processes as $a_1\pi$ processes, the ratio of the cross sections of processes (1) and (4) will characterize the dynamics of the intermediate states and its value must be close to 2 for high energies and increase with decreasing energy. The experimentally measured ratio of cross sections (Fig. 12) does not differ from 2 to within experimental errors.

In accordance with the hypothesis of vector current conservation, the e^+e^- annihilation cross section in the isovector channel $e^+e^- \longrightarrow V^0 \longrightarrow$ *hadrons* is associated with the decay spectra of corresponding decays of the τ lepton, $\tau^\pm \longrightarrow V^\pm\bar{\nu}_\tau$, via the relation [12]

$$\nu_{\tau\to V\nu_\tau}(q^2) = \frac{q^2}{4\pi^2\alpha^2}\sigma_{e^+e^-\to V^0}(q^2),$$

where $\nu_{\tau\to V\nu_\tau}(q^2)$ is the structural function of τ lepton decay. This makes it possible, on the one hand, to verify the cross section of the $e^+e^- \longrightarrow 4\pi$ processes obtained by us here and, on the other hand, to verify the hypothesis of vector current conservation in the measured cross sections under the assumption that the results obtained are correct.

We compared the structural function measured in the decay process $\tau^\pm \longrightarrow 2\pi^\pm\pi^\mp\pi^0\bar{\nu}_\tau$ [12] with the cross section of the $e^+e^- \longrightarrow 4\pi$ process, written in the form

$$\sigma^{I=1}_{e^+e^-}(q^2) = 0.5\sigma_{e^+e^-\to 2\pi^+2\pi^-} + \sigma_{e^+e^-\to\pi^+\pi^-2\pi^0}; \qquad (7)$$

the contribution of process (3) was subtracted from the cross section $\sigma_{e^+e^-\to\pi^+\pi^-2\pi^0}$. The results of comparison are shown in Fig. 13. For measurements with the help of a DM2 detector, we assumed in relation (7) that

$$\sigma_{e^+e^-\to\pi^+\pi^-2\pi^0} = 0.5\sigma_{e^+e^-\to 2\pi^+2\pi^-}$$

in view of the lack of required data. The cross section of process (3) obtained here was also compared with the results of measurements of the structural function of the CLEO detector for the decay process $\tau^\pm \longrightarrow \omega\pi^\pm\bar{\nu}_\tau$ [12]. The results of comparison are shown in Fig. 14. Here, we disregard the corrections associated with iso-

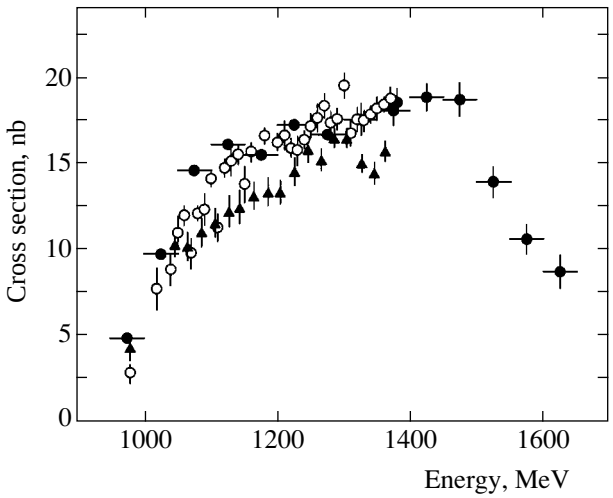

Fig. 14. Comparison of the cross sections of the $e^+e^- \longrightarrow \omega\pi \longrightarrow \pi^+\pi^-\pi^0\pi^0$ process, measured experimentally with the help of SND (○) and CMD-2 (▲), with the structural function of τ-lepton decays in experiments with the CLEO detector [12] (●).

spin symmetry breaking since it was proved [14] that these corrections do not exceed a few percent for the 4π channel, which is much smaller than the overall systematic errors. It can be seen that the data on the e^+e^- annihilation obtained by us here are in accordance with the results obtained with the help of the CLEO detector for decays of the τ lepton to within 10%, which is accounted for by systematic experimental errors. Thus, our measurements do not indicate any deviation from the hypothesis of vector current conservation in the $e^+e^- \longrightarrow 4\pi$ processes. Nevertheless, it should be noted that the slopes of the cross sections being compared are different for energies higher than 1.4 GeV and a discrepancy with the experimental results on the e^+e^- annihilation is observed.

Unfortunately, the cross section measured here is insufficient for determining the parameters of excited states of the ρ meson in view of the limited energy range. A full-fledged approximation requires experimental results obtained at higher energies. However, the measurements in a range above 1.4 GeV are characterized by large statistical and systematic errors. For this reason, new measurements of cross sections in this energy range are required. Such measurements will be made on the VEPP-2000 complex being developed at the Institute of Nuclear Physics, Siberian Division, Russian Academy of Sciences (Novosibirsk) with the help of updated SND [29] and CMD-2M detectors [30].

7. CONCLUSIONS

The cross sections of the processes $e^+e^- \longrightarrow \pi^+\pi^-\pi^+\pi^-$, $e^+e^- \longrightarrow \pi^+\pi^-\pi^0\pi^0$, and $e^+e^- \longrightarrow \omega\pi \longrightarrow \pi^+\pi^-\pi^0\pi^0$, as well as of the process $e^+e^- \longrightarrow \pi^+\pi^-\pi^0\pi^0$ with subtracted contribution of the process $e^+e^- \longrightarrow \omega\pi \longrightarrow \pi^+\pi^-\pi^0\pi^0$, were measured in experiments with a spherical neutral detector on the VEPP-2M collider in the energy range 0.98–1.38 GeV. The statistical error in the measurements of cross sections was 2–20%, while the systematic error was 6%, 7%, 12%, and 20%. The angular and energy distributions, as well as the mass spectra of two and three π mesons, indicate the predominance of intermediate states ωπ and $a_1\pi$. Comparison of the measured cross sections with the structural functions of τ-lepton decays confirms the vector current conservation hypothesis to within 10%.

ACKNOWLEDGMENTS

This study was supported financially by the Russian Foundation for Basic Research (project nos. 99-02-17155 and 01-02-16760a); the Federal Special Program "Integration" (A0100 UNTs "Fundamental Properties of Matter"); and the Sixth Expertise Competition of Scientific Projects Developed by Young Scientists of the Russian Academy of Sciences (1999), Fundamental and Applied Research (grant no. 78).

REFERENCES

1. A. N. Skrinsky, in *Proceedings of Workshop on Physics and Detectors for DAΦNE, Frascati, Italy* (1995), p. 3.
2. M. N. Achasov, V. M. Aulchenko, S. E. Baru, *et al.*, Nucl. Instrum. Methods Phys. Res. A **449**, 125 (2000).
3. *Particle Data Group, Review of Particle Physics*, Eur. Phys. J. C **15** (2000).
4. A. B. Clegg and A. Donnachie, Z. Phys. C **62**, 455 (1994).
5. N. N. Achasov and A. A. Kozhevnikov, Phys. Rev. D **55**, 2663 (1997).
6. N. N. Achasov and A. A. Kozhevnikov, Phys. Rev. D **62**, 117503 (2000).
7. A. Donnachie and Yu. S. Kalashnikova, Z. Phys. C **59**, 621 (1993).
8. A. Donnachie, Yu. S. Kalashnikova, and A. B. Clegg, Z. Phys. C **60**, 187 (1993).
9. D. Aston, N. Awaji, T. Bienz, *et al.*, Nucl. Phys. Proc. Suppl. **21**, 105 (1991).
10. A. Donnachie and A. B. Clegg, Phys. Lett. B **269**, 450 (1991).
11. R. Barate, D. Buskulic, D. Decamp, *et al.* (ALEPH Collaboration), Z. Phys. C **76**, 15 (1997).
12. K. W. Edwards, R. Janicek, P. M. Patel, *et al.* (CLEO Collaboration), Phys. Rev. D **61**, 072003 (2000).
13. S. Eidelman, in *Proceedings of the e^+e^- Physics at Intermediate Energies Conference*, Ed. by D. Bettoni, E-Conf C010430, M07 (2001).
14. M. Davier, S. Eidelman, A. Hocker, and Z. Zhang, hep-ph/0208177.
15. G. W. Bennett, B. Bousquet, H. N. Brown, *et al.* (Muon (g-2) Collaboration), Phys. Rev. Lett. **89**, 101804 (2002).

16. L. M. Kurdadze, M. Yu. Lelchuk, E. V. Pakhtusova, *et al.*, Pis'ma Zh. Éksp. Teor. Fiz. **47**, 432 (1988) [JETP Lett. **47**, 512 (1988)].
17. L. M. Kurdadze, M. Yu. Lelchuk, E. V. Pakhtusova, *et al.*, Pis'ma Zh. Éksp. Teor. Fiz. **43**, 497 (1986) [JETP Lett. **43**, 643 (1986)].
18. C. Bacci, G. De Zorzi, G. Penso, *et al.*, Nucl. Phys. B **184**, 31 (1981).
19. S. I. Dolinsky, V. P. Druzhinin, M. S. Dubrovin, *et al.*, Phys. Rep. **202**, 99 (1991).
20. G. Cosme, B. Dudelzak, B. Grelaud, *et al.*, Nucl. Phys. B **152**, 215 (1979).
21. R. R. Akhmetshin, E. V. Anashkin, M. Arpagaus, *et al.*, Phys. Lett. B **466**, 392 (1999).
22. R. R. Akhmetshin, E. V. Anashkin, M. Arpagaus, *et al.* (CMD-2 Collaboration), Phys. Lett. B **491**, 81 (2000); hep-ex/0008019.
23. M. N. Achasov, K. I. Beloborodov, A. V. Berdyugin, *et al.*, Phys. Lett. B **486**, 29 (2000); hep-ex/0005032.
24. E. A. Kuraev and V. S. Fadin, Yad. Fiz. **41**, 733 (1985) [Sov. J. Nucl. Phys. **41**, 466 (1985)].
25. A. V. Bozhenok, D. A. Bukin, V. N. Ivanchenko, *et al.*, Preprint No. 99-103, IYaF SO RAN (Inst. of Nuclear Physics, Siberian Division, Russian Academy of Sciences, Novosibirsk, 1999).
26. V. M. Aul'chenko, M. N. Achasov, K. I. Beloborodov, *et al.*, Zh. Éksp. Teor. Fiz. **117**, 1067 (2000) [JETP **90**, 927 (2000)].
27. A. E. Bondar, S. I. Eidelman, A. I. Milstein, and N. I. Root, Phys. Lett. B **466**, 403 (1999).
28. D. Bisello, G. Busetto, A. Castro, *et al.*, Preprint No. LAL 90-35 (1990).
29. G. N. Abramov, V. M. Aul'chenko, M. N. Achasov, *et al.*, Preprint No. 2001-29, IYaF SO RAN (Inst. of Nuclear Physics, Siberian Division, Russian Academy of Sciences, Novosibirsk, 2001).
30. V. M. Aul'chenko, R. R. Akhmetshin, V. Sh. Banzarov, *et al.*, Preprint No. 2001-45, IYaF SO RAN (Inst. of Nuclear Physics, Siberian Division, Russian Academy of Sciences, Novosibirsk, 2001).

Translated by N. Wadhwa

Journal of Experimental and Theoretical Physics, Vol. 96, No. 5, 2003, pp. 801–806.
Translated from Zhurnal Éksperimental'noĭ i Teoreticheskoĭ Fiziki, Vol. 123, No. 5, 2003, pp. 912–918.

ATOMS, SPECTRA, RADIATION

Coherent Population Trapping in a Gas of Excited Atoms

P. M. Anisimov, R. A. Akhmedzhanov*, I. V. Zelenskiĭ, R. L. Kolesov, and E. A. Kuznetsova**

Institute of Applied Physics, Russian Academy of Sciences, ul. Ul'yanova 46, Nizhni Novgorod, 603950 Russia

**e-mail: rinat@appl.sci-nnov.ru*

***e-mail: ekuzn@appl.sci-nnov.ru*

Received November 14, 2002

Abstract—Coherent population trapping in a gas discharge was studied for transitions between excited levels of neon atoms. Resonances corresponding to the arising of coherent population trapping in the Λ and *V* schemes for Zeeman sublevels of the lower and upper working states were observed in the presence of a longitudinal magnetic field. The effect of nonlinear polarization plane rotation under coherent population trapping conditions was studied. The possibility of using the results obtained in this work for diagnostics of local magnetic fields and other plasma parameters in gas discharges was considered. *© 2003 MAIK "Nauka/Interperiodica".*

1. Coherent population trapping arising in the excitation of multiple-level quantum systems by coherent fields is one of the physical phenomena that have been extensively studied during recent years. Interest in this phenomenon to a large extent stems from its numerous potential applications in such fields as electromagnetically induced transparency [1], amplification and generation without inversion [2], group velocity decrease and light pulse stopping [3], optical memory and quantum computing [4], optical magnetometry based on the nonlinear Faraday effect [5], superhigh-resolution spectroscopy [6], etc.

Coherent population trapping can in principle be observed in arbitrary multiple-level quantum systems [7]. It is most simply effected in the interaction between two-frequency laser radiation and the so-called Λ scheme (although coherent population trapping was also observed in the cascade [8] and *V* [9] schemes). Usually, this is two Zeeman or hyperfine lower sublevels and an upper, optical level. Transitions from the upper level to both of the lower ones are allowed, whereas the transition between lower levels is forbidden. When the frequency difference between two optical fields coincides with the splitting of the lower sublevels, coherent superposition of the states of the lower sublevels arises, in which atoms are trapped and are not excited to the upper level in spite of the presence of resonant fields. The essence of coherent population trapping is as follows: when certain conditions are satisfied, the medium ceases to interact with exciting fields, which manifests itself by narrow resonances in absorption or fluorescence spectra.

The overwhelming majority of works on coherent population trapping were performed for alkali or rare-earth metal vapors, in which the role of the lower Λ system levels was played by hyperfine (or fine) ground state components. The characteristic decay time of such levels amounted to several seconds, and coherent population trapping resonances were therefore characterized by high quality factors. Note that hyperfine and fine structure levels have low sensitivity to atomic collisions, and the presence of a buffer gas therefore increases the residence time of an atomic system in laser beams without violating the coherence of the lower levels. A different situation arises with excited atoms. Collisions with particles of any kind (atoms, ions, or electrons) cause the decay of the lower working level and thereby considerably increase the rate of coherence relaxation for the low-frequency transition (for instance, the cross sections of quenching collisions between inert gas atoms in a metastable state and second component atoms can attain values on the order of gas kinetic cross sections). As a result, the contrast of coherent population trapping sharply decreases and experimentally observing this process in a system of excited atoms becomes a fairly complex task. On the other hand, a strong influence of external conditions opens up possibilities for developing methods for diagnostics of external factors that act on a "trapped" atom. Such methods are essentially contactless and, if fluorescence is used, local. The development of diagnostic methods based on coherent population trapping in a system of excited atoms is of special importance for plasma media, because transitions from the ground state lie in the region inaccessible to modern lasers.

In this work, we report for the first time experimental data on various schemes for coherent population trapping in atoms excited by a gas discharge and on nonlinear polarization plane rotation under coherent population trapping conditions and consider the feasibility of using this effect for plasma diagnostics.

1063-7761/03/9605-0801$24.00

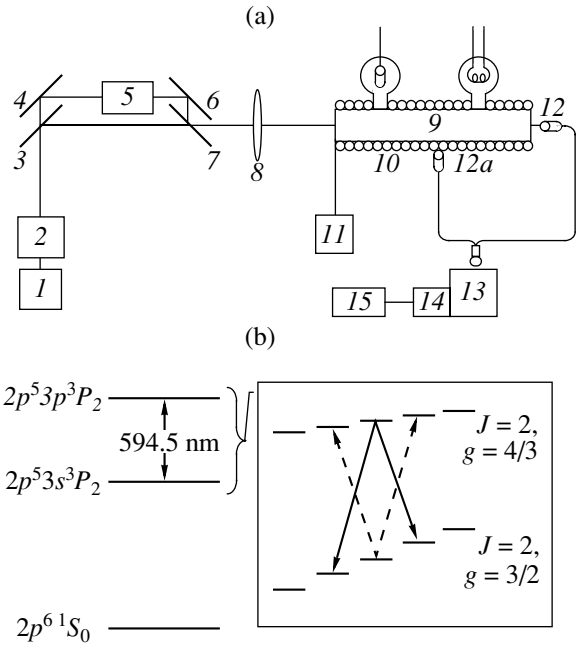

Fig. 1. (a) Scheme of the experimental unit: (*1*) argon laser, (*2*) dye laser, (*3*, *7*) semitransparent mirrors, (*4*, *6*) totally reflecting mirrors, (*5*) acoustooptical modulator, (*8*) focusing lens, (*9*) discharge tube, (*10*) solenoid, (*11*) alternating current generator, (*12*, *12a*) optical fiber, (*13*) monochromator, (*14*) photomultiplier, and (*15*) oscilloscope. (b) Scheme of neon levels used in this study.

2. A scheme of the experiment is shown in Fig. 1a. Atoms were excited in a discharge in a sealed glass tube 8 mm in diameter at a neon pressure of 1.5 Torr. The discharge current was 50 mA. The discharge tube was placed into a solenoid, which created a time-variable (saw-toothed) magnetic field. Radiation from a continuous unimodal dye laser with argon pumping was tuned in resonance with one or another neon transition. The exit laser beam was split in two. One of the beams was shifted in frequency by Δw using an acoustooptical modulator. The two beams were then combined on a semitransparent mirror and directed along the discharge tube axis. The beam intensities at the entrance to the discharge tube were 300 and 900 mW/cm^2, and the beam diameters were 1 mm. The absorption of the laser beams, their polarization rotation, and resonance fluorescence of excited neon atoms were measured experimentally.

The $2p^53s^3P_2 \longrightarrow 2p^53p^3P_2$ transition (see Fig. 1b) was used to demonstrate the feasibility of various coherent population trapping schemes in excited atoms. The lower working level was metastable with a lifetime on the order of 10 μs (under our experimental conditions), and the upper level was radiative with a lifetime of 100 ns. The concentration of atoms in the metastable state estimated from laser radiation absorption (at intensities below the threshold of coherent population trapping) was on the order 10^{11} cm^{-3}, and the temperature determined from the width of the absorption band was around 400 K. The upper and lower working levels are fivefold degenerate with respect to angular momentum projection J_z (see Fig. 1b). They split into Zeeman sublevels in a magnetic field. Because of the difference in *g*-factors, the splitting of the lower level is larger than that of the upper one in equal magnetic fields.

It is easy to see from the scheme of levels what coherent population trapping resonances are possible in experiments. First, a resonance at the degenerate sublevels of the lower working level arises in zero magnetic field. The linearly polarized fields of both beams can be treated as a superposition of σ^+ and σ^- polarized fields with equal amplitudes which form a Λ scheme and transfer the system into a trapped (nonabsorbing) state. Next, a resonance of coherent population trapping in the Λ scheme should arise when the magnetic field reaches a value at which the splitting of the Zeeman sublevels of the lower level with angular momentum projections J_z and $J_z \pm 1$ equals $\Delta w/2$. One of the circularly polarized field components of the first beam and the orthogonally polarized field component of the second beam then become resonant to the corresponding "shoulders" of the Λ scheme formed by two Zeeman sublevels of the lower level and one of the sublevels of the upper level. Lastly, the splitting of the Zeeman sublevels of even the upper level becomes equal to $\Delta w/2$ as the field increases to higher values. This causes the arising of a resonance in the *V* scheme formed by two Zeeman sublevels of the upper level and one of the sublevels of the lower level. The ratio between the magnetic field values at which *V*- and Λ-type resonances appear should coincide with the reciprocal of the ratio between the *g*-factors of the upper and lower states. The experimental magnetic field dependence of the absorption of the total field at a $\Delta w = 50$ MHz frequency detuning is shown in Fig. 2 by the solid line. The suppression of absorption is observed at all three types of coherent population trapping resonances mentioned above. The ratio between the magnetic fields at which Λ- and *V*-type resonances arise is 0.85, which corresponds to the ratio between the *g*-factors of the upper and lower levels

$$g_2/g_1 = 8/9 = 0.89.$$

When one of the fields was switched off, we only observed a resonance at zero magnetic field (Fig. 2, dashed curve). Conversely, if the fields were circularly and orthogonally polarized, only *V*- and Λ-type resonances remained and the resonance at zero magnetic field disappeared (Fig. 2, dot-and-dash line).

Note the following. The minimum coherent population trapping resonance width is determined [10] by the rate of coherent relaxation Γ at the corresponding low-frequency transition, and the threshold intensity necessary for the effect to be observable is proportional to the product of the relaxation rates at the low-frequency, Γ, and optical, γ, transitions. For the *V*-scheme, low-fre-

quency coherence relaxation is determined by population drift from the upper levels, and its rate is therefore comparable with the optical coherence relaxation rate, which as a rule substantially exceeds the rate of low-frequency coherence relaxation in the Λ scheme. For this reason, the contrast of the resonance in the *V* scheme should be much lower and the resonance should be much broader; this conclusion is in agreement with experiment. In addition, we observed polarization plane rotation effects, which arose because of the nonlinear Faraday effect. Measurements were made following the scheme described in [11]. The maximum rotation angle was 10° at a concentration of working atoms around 2×10^{11} cm^{-3} (Fig. 3). This result was hardly inferior to that obtained in special experiments, in which the Faraday effect in Rb vapor was studied at similar concentrations [5, 11].

3. Bearing in mind the results described above, consider the feasibility of using coherent population trapping, for instance, to measure the magnetic field in a plasma. The magnetic field value is one of the most important parameters that determine the dynamics of processes in a plasma. The methods for magnetic field measurements can be divided into three groups, namely, probing methods, spectroscopic methods (based on the Faraday and Zeeman effects), and corpuscular methods. The probing methods, which are used most extensively, are in essence contact methods and are, for this reason, largely applicable to low-temperature plasmas. However, even then the question of the degree of perturbation of medium parameters remains open. Spectroscopic and corpuscular methods give values averaged along the line of observation. In addition, various broadening mechanisms weaken magnetic field effects.

A possible scheme for magnetic field measurements based on coherent population trapping is shown in Fig. 4. Let two laser beams with close frequencies resonant to some optical transition of an atom or ion propagate in the same direction in a plasma with a magnetic field. We also assume that the magnetic field splits the upper and lower levels of the selected transition into Zeeman sublevels. If the difference of the optical field frequencies coincides with twice the Zeeman splitting, the system experiences transition to the coherent population trapping state and ceases to interact with exciting fields. As a result, the population of the upper level decreases, and dips in the fluorescence and absorption spectra appear. Measurements of the fluorescence signal (emitted from the region of intersection between the optical beams and the direction of observation) as a function of the frequency detuning Δw of the exciting fields make it possible to determine the magnetic field value if the Lande factors are known,

$$H = \hbar \Delta w / 2 \mu_B g,$$

where μ_B is the Bohr magneton.

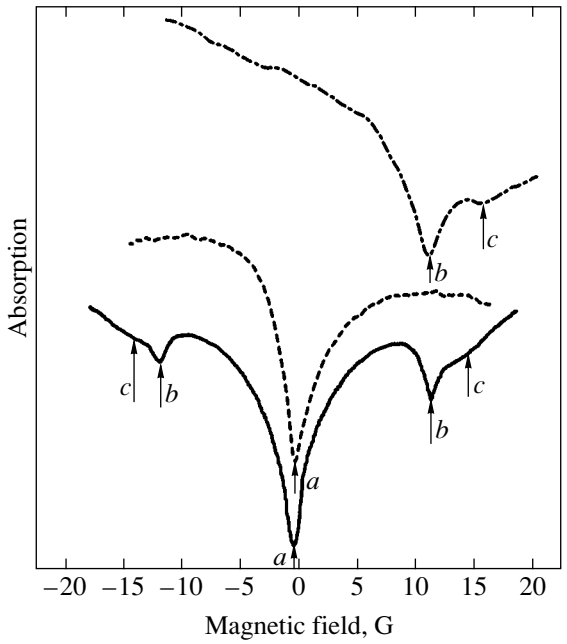

Fig. 2. (a) Coherent population trapping in zero magnetic field and resonances in (b) Λ and (c) *V* schemes.

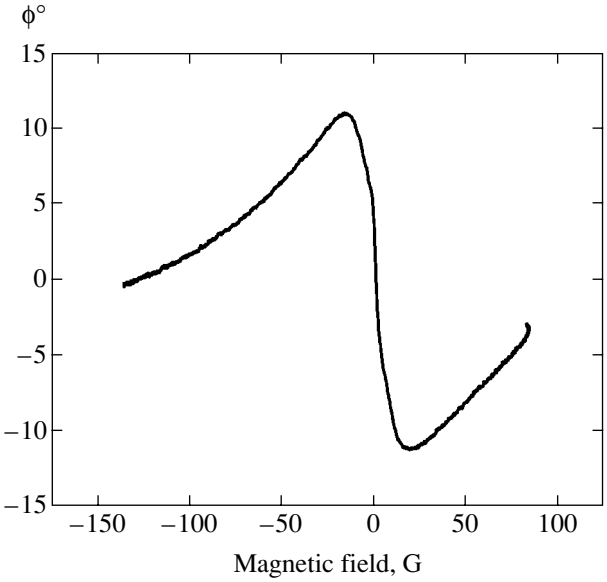

Fig. 3. Magnetic field dependence of the angle of polarization plane rotation.

The advantages of the suggested scheme are obvious. Measurements are contactless and local. When the beams propagate in one direction, the influence of inhomogeneous line broadening decreases substantially. The time resolution is determined by the time that coherent population trapping is established (for allowed transitions, this time ranges from 100 ns to 1 μs). The magnetic field resolution (the smallest measurable magnetic field change) is determined by the width of the coherent population trapping resonance. The range of measurable

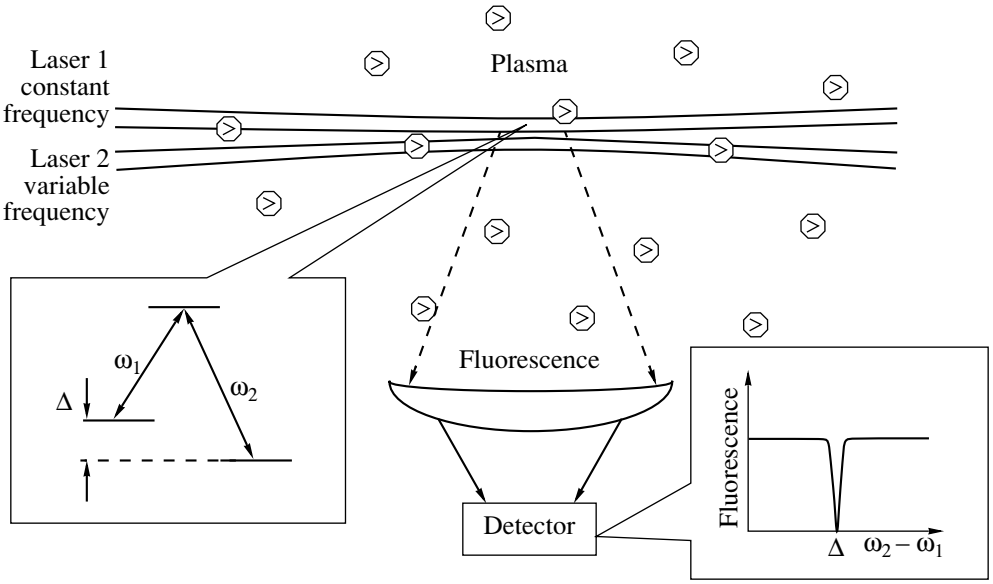

Fig. 4. Scheme of the suggested method for diagnostics of plasma magnetic fields.

magnetic fields is determined by the frequency range of exciting field phase locking. If acoustooptical systems are used, this problem is solved automatically. However, at frequencies higher than several GHz, more complex methods that allow detunings of up to tens of THz to be used should be applied [12].

Measurements are possible if two conditions that determine the range of plasma parameters to be studied are fulfilled. First, flight time τ should be longer than the time of the establishment of coherent population trapping. Next, the resonance fluorescence signal should exceed plasma volume radiation along the observation line. The first condition imposes limitations on the temperature of particles, $\tau < l/v$, where $v = \sqrt{3kT/m}$ is the thermal velocity of particles and l is the diameter of the laser beam. The second condition determines the lower bound for the concentration of absorbing particles $N_{\min}$. To estimate $N_{\min}$, suppose that the main source of noise is fluctuations of photoelectrons from plasma self-radiation at the observed transition frequency. Let scattered radiation knock out N_r photoelectrons from a photocathode. Plasma self-radiation results in the appearance of N_{pl} photoelectrons. As spontaneous radiation effects are independent, the root-mean-square noise value is $\sqrt{N_{pl}}$. The condition for recording can then be written as

$$\sqrt{N_{pl}} \le N_r,$$

$$N_r = \Delta N_2 A_{21} V_r \frac{\Omega}{4\pi} t\eta\Delta\tau,$$

$$N_{pl} = N_2 A_{21} V_{pl} \frac{\Omega}{4\pi} t\eta\Delta\tau,$$

where N_2 and ΔN_2 are the population of the upper resonance level in the absence of laser radiation and the increase in population under the action of laser radiation, respectively; A_{21} is the probability of the transition from the upper to the lower level; V_r and V_{pl} are the plasma probing volume and the plasma volume from which background radiation is emitted, respectively; $\Omega/4\pi$ is the solid angle of the entrance pupil of the system for recording; η is the quantum yield of the photodetector; t is the transmission coefficient of the spectral instrument; and $\Delta\tau$ is the time of observation. It follows that the condition for recording can be written as

$$\sqrt{A_{21} l^4 \Omega\eta\Delta\tau t/4\pi L}\,\frac{\Delta N_2}{\sqrt{N_2}} \ge 1,$$

where l is the necessary spatial resolution and L is the characteristic plasma volume size. At the characteristic dimensions $l \sim 10^{-2}$ m and $L \sim 1$ m and standard recording instrument parameters ($\Omega/4\pi \sim 10^{-2}$, $\eta = 0.3$, and $t = 0.5$), we obtain $T \le 10$ eV and $N_{\min} \ge 10^7$ cm^{-3} for a dipole-allowed transition ($A_{21} \sim 10^7$–10^8 s^{-1}) and a $\Delta\tau \sim 1$ μs time resolution. These values are quite typical of gas-discharge plasmas. The estimates were obtained on the assumption of equal populations of the upper and lower working levels (the least favorable situation) taking into account that a laser only excites part of atoms within the Doppler profile; this part is determined by the Rabi frequency of the controlling field. At the parameters specified above, the magnetic field resolution is not worse than several Gauss.

The method for diagnostics suggested in this work can be used, for instance, in magnetic reconnection

experiments [13]. The parameters typical of these experiments (the temperatures of neutrals, ions, and electrons are on the order of $T_{neut} \approx 1$–2 eV, $T_i \approx 5$–15 eV, and $T_e \approx 10$–15 eV, respectively; their concentrations are $n_{neut} \sim 5 \times 10^{11}$ cm^{-3} and $n_e \approx n_i \sim 5 \times 10^{13}$ cm^{-3}; and the characteristic time and spatial layer scales are about 20–40 μs and 1–2 cm, respectively [14]) are quite acceptable.

The potential of the suggested method for measuring magnetic fields was demonstrated by experiments in which coherent population trapping was studied by measuring fluorescence of excited atoms. Efforts were made to maximally approximate real situations by specially complicating measurement conditions. First, the geometry of experiments was selected in such a way that the ratio between the laser beam diameter and plasma size along the observation line was 2×10^{-2}, and the solid angle of the entrance pupil of the system for recording was 10^{-2}. Next, it is clear that the highest contrast of the effect is attained when transitions involving the metastable level are used. However as mentioned above, strong quenching caused by interaction with surrounding particles in a plasma often equalizes the lifetimes of metastable and radiative levels. To model such a situation, experiments were intentionally performed for the transition

$$2p^5 3s^3P_1(J = 1) \longrightarrow 2p^5 3p^3P_0(J = 0),$$

whose lower and upper levels were radiative, which substantially broadened coherent population trapping peaks. Fluorescence was observed at a right angle to the direction of laser beam propagation at a 607.4 nm wavelength. Linearly polarized fields were used. The experimental magnetic field dependences of the fluorescence signal at different exciting field frequency detunings are shown in Fig. 5. As follows from the figure, the dips in the fluorescence spectra corresponding to coherent population trapping resonances are recorded quite clearly.

Importantly, the potentialities of using coherent population trapping for plasma diagnostics are not limited to magnetic field measurements. The presence of collective plasma [15] or acoustic [16] oscillations allows various schemes for coherent population trapping quite applicable in plasma diagnostics to be constructed. In addition, the lifetime of low-frequency coherence is determined by the population exchange time of Zeeman levels with each other and with the lower levels when the laser beam diameter increases. Depending on discharge parameters, measurements of the width of the coherent population trapping resonance under these conditions, for instance, allow level quenching constants in collisions with heavy particles, electrons, etc., to be determined.

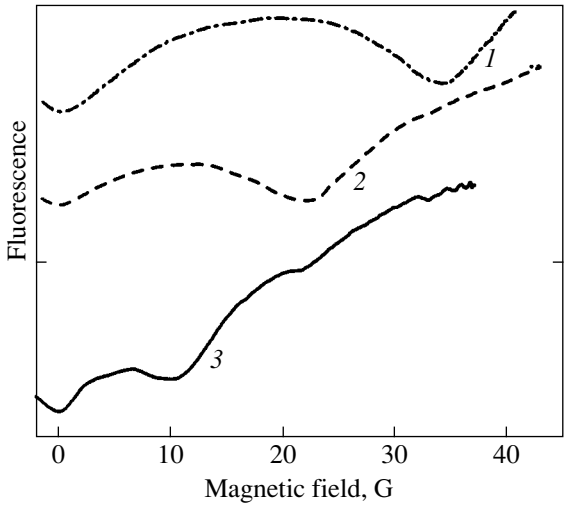

Fig. 5. Coherent population trapping resonances in fluorescence signal; Δw = (*1*) 150, (*2*) 100, and (*3*) 50 MHz.

4. Instead of traditionally used media, we studied coherent population trapping in a gas of excited atoms. Various resonance types corresponding to the arising of coherent population trapping at the Zeeman sublevels of the upper and lower working levels were observed in the absorption and fluorescence spectra. The results of model experiments showed that coherent population trapping in a gas of excited atoms offers promise for measuring local plasma parameters. Importantly, the fluorescence signal could reliably be observed (recorded) even when the lifetime of the metastable state decreased to a radiative state lifetime. Clearly, this considerably broadens the possibilities for practically using the phenomenon of coherent population trapping in diagnostic applications.

ACKNOWLEDGMENTS

The authors thank A.V. Kostrov, O.A. Kocharovskaya, A.G. Litvak, and V.A. Mironov for useful and fruitful discussions. This work was financially supported by the Russian Foundation for Basic Research (project no. 01-02-17779).

REFERENCES

1. S. E. Harris, Phys. Today **50**, 36 (1997).
2. J. Mompart and R. Corbalan, J. Opt. B: Quantum Semiclass. Opt. **2**, R7 (2000).
3. L. V. Hau, S. E. Harris, Z. Dutton, *et al.*, Nature **397**, 594 (1999).
4. O. Kocharovskaya, Y. Rostovtsev, and M. O. Scully, Phys. Rev. Lett. **86**, 628 (2001).
5. I. Novikova and G. R. Welch, J. Mod. Opt. **49**, 349 (2002); D. Budker, V. Yashchuk, and M. Zolotorev, Phys. Rev. Lett. **81**, 5788 (1998).

6. D. Budker, D. F. Kimball, S. M. Rochester, *et al.*, Phys. Rev. Lett. **83**, 1767 (1999).
7. B. D. Agap'ev, M. B. Gornyĭ, B. G. Matisov, and Yu. V. Rozhdestvenskiĭ, Usp. Fiz. Nauk **163** (9), 35 (1993) [Phys. Usp. **36**, 763 (1993)].
8. D. J. Fulton, S. Shepherd, R. M. Moseley, *et al.*, Phys. Rev. A **52**, 2302 (1995).
9. J. Zhao, L. Wang, L. Xiao, *et al.*, Opt. Commun. **206**, 341 (2002).
10. S. E. Harris, J. E. Field, and A. Kasapi, Phys. Rev. A **46**, R29 (1992).
11. R. A. Akhmedzhanov and I. V. Zelenskiĭ, Pis'ma Zh. Éksp. Teor. Fiz. **76**, 493 (2002) [JETP Lett. **76**, 419 (2002)].
12. T. Udem, A. Huber, B. Gross, *et al.*, Phys. Rev. Lett. **79**, 2646 (1997); J. Reichert, M. Niering, R. Hozwarth, *et al.*, Phys. Rev. Lett. **84**, 3232 (2000).
13. M. Yamada, Y. Ono, A. Hayakawa, *et al.*, Phys. Rev. Lett. **65**, 721 (1990).
14. S. C. Hsu, T. A. Carter, G. Fiskel, *et al.*, *Princeton Plasma Physics Laboratory Publications and Reports* (2002).
15. A. G. Litvak and M. D. Tokman, Phys. Rev. Lett. **88**, 095003 (2002).
16. Y. V. Radeonychev, A. G. Litvak, M. D. Tokman, and O. Kocharovskaya, Phys. Rev. Lett. (in press).

Translated by V. Sipachev

Journal of Experimental and Theoretical Physics, Vol. 96, No. 5, 2003, pp. 807–815.
Translated from Zhurnal Éksperimental'noĭ i Teoreticheskoĭ Fiziki, Vol. 123, No. 5, 2003, pp. 919–928.

ATOMS, SPECTRA, RADIATION

Raman Echo under Medium Excitation by Extremely Short Pulses

S. V. Sazonov and A. F. Sobolevskiĭ*
Kaliningrad State University, Kaliningrad, 236041 Russia
**e-mail: nst@alg.kaliningrad.ru*
Received October 4, 2002

Abstract—A generalization of the Bloembergen–Shen model to Raman active molecules with an arbitrary number of normal modes was suggested. The generalized model was used to study Raman echo signal characteristics when a system of molecules was excited by pulses of widths up to one period of optical oscillations. It was shown that a large number of echo responses on Stokes and anti-Stokes components could arise even under a two-pulse action in a continuous monochromatic pumping field. The number of echo responses depended on the number of molecular normal modes and the geometry of measurements. At small exciting pulse "areas," the echo responses whose Stokes and anti-Stokes components corresponded to normal vibrational modes of a molecule had the highest intensity, whereas the components formed by normal mode combinations were strongly suppressed. © *2003 MAIK "Nauka/Interperiodica".*

1. INTRODUCTION

The generation of laser pulses with widths up to one optical oscillation period (extremely short pulses) in laboratory conditions [1–4] stimulated theoretical studies of the interaction of such pulses with matter. The greatest progress was made in studying soliton and quasi-soliton propagation modes of extremely short pulses. In particular, the special features of self-induced transparency for extremely short pulses in multiple-level quantum systems were studied in detail [5]. Another example of nonstationary coherent optics effects is photon echo. The use of extremely short pulses in photon echo measurements also entails peculiarities of its own compared with medium excitations by quasi-monochromatic resonant pulses [6, 7]. The main peculiarity arises because of a large spectral width of extremely short pulses, which have virtually no carrier frequency. As a consequence, the spectrum of such a pulse can simultaneously overlap several quantum transitions, and photon echo signals therefore acquire a multifrequency character [6, 7]. Note however that spectral overlapping of several transitions in the visible range initiates ionization processes, which, on the one hand, mask echo responses and, on the other, considerably complicate theoretical calculations. The condition of spectral overlapping is best satisfied with a system of Raman active transitions forbidden in the electric dipole approximation [8, 9]. These transitions are capable of participating in the formation of Stokes and anti-Stokes Raman echo signals [10–16], which is a powerful tool of vibrational spectroscopy. Experimentally, the use of resonant pulses for exciting a Raman echo is a fairly complex procedure. Because of the two-photon character of Raman active transitions, we often have to use two samples of the medium to be irradiated [10]. The first sample generates the Stokes (anti-Stokes) field component as a result of stimulated Raman scattering (SRS). This component is then directed to the second sample with simultaneously supplying of the initial frequency pulse. Two such paired pulses, the frequency difference between which coincides with the frequency of the most active vibrational mode of the molecule, form the first excitation of the medium. After the second such excitation, we can observe Raman echo signals under nonresonant monochromatic background radiation [10–14].

The use of extremely short pulses for generating a Raman echo can simplify the experimental scheme of medium excitation. As the extremely short pulse spectrum, because of its large width, initially contains Fourier components resonant to the vibrational modes of a molecule, it is sufficient to use a single irradiated medium sample.

Note one more advantage of using extremely short pulses in Raman echo experiments. The generation of a Stokes (anti-Stokes) component under irradiation of a sample active in SRS by a quasi-monochromatic nonresonant field is characterized by the following development of instability: in spite of the presence of several normal molecular modes, the contribution to SRS is, as a rule, made by only one of them, namely, the mode that generates the most intense Stokes component [17]. If a medium active in SRS is irradiated by extremely short pulses, all normal molecular modes are excited because of the resonant capture of all transitions in the system of vibrational sublevels by the spectrum of the pulse. As a result, a Raman echo can become multifrequency in character, which allows the spectrum of echo responses to be used for determining the characteristics of virtu-

ally all normal molecular modes. It follows that the use of extremely short pulses can substantially broaden the potentialities of coherent molecular spectroscopy.

This work is a theoretical study of a Raman echo generated by two or several extremely short pulses under nonresonant monochromatic pumping.

The paper is organized as follows. A generalization of the Bloembergen–Shen model [18] to SRS of a system of molecules with an arbitrary number of vibrational modes is given in Section 2. The generalized model is used in Section 3 to describe medium excitation under the action of extremely short pulses. In addition, Section 3 contains a description of a general procedure for calculating Raman echo parameters when a medium is excited by an arbitrary number of extremely short pulses. In Section 4, we give a thorough analysis and classification of primary (two-pulse) Raman echo signals. The section contains equations for the times of generation, the direction of emission, and the number of echo responses under multiple extremely short pulse actions. In the Conclusions, the main results of this work are shortly summarized.

2. GENERALIZED BLOEMBERGEN–SHEN MODEL FOR DESCRIBING AN SRS ACTIVE MEDIUM

An SRS active medium that experiences an extremely short pulse action will be described quantum-mechanically. Let the medium molecules each have N ($N \geq 1$) normal modes, that is, N vibrational sublevels near the ground electronic state (see figure). The electric dipole transitions between these sublevels are forbidden. However, two-photon transitions via excited electronic states are possible. As the electron optical transitions are not covered by the spectrum of an extremely short pulse and are not resonant to a monochromatic pumping field, it suffices to represent excited electronic states by one remote $(N + 1)$th quantum level (figure).

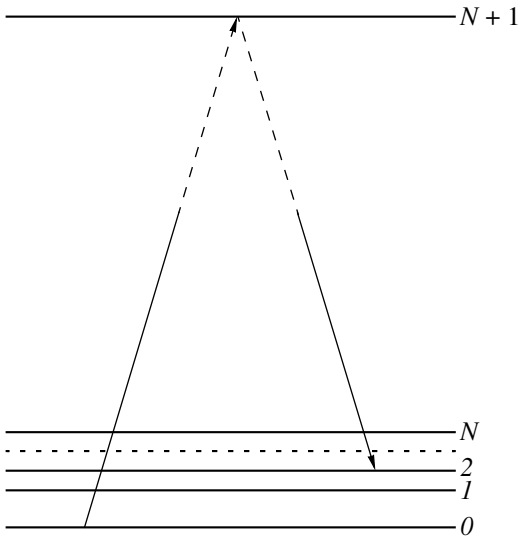

Quantum levels of a molecule with N normal vibrational modes; 0 is the ground electronic level of the molecule; 1, 2, …, N are the vibrational sublevels; and $N + 1$ corresponds to excited electronic states. Shown by arrows is one of the possible two-photon transitions, and dashed lines indicate the absence of the Fourier components resonant to electron optical transitions in the spectrum of exciting extremely short pulses.

The condition of spectral overlapping of all SRS sublevels will be written as

$$\omega_{\mu\nu}\tau_p \ll 1, \quad \mu, \nu = 0, 1, \ldots, N, \tag{1}$$

where $\omega_{\mu\nu}$ is the distance between the μth and νth SRS sublevels on the frequency scale and τ_p is the characteristic time scale of extremely short pulses.

The material balance equations for the matrix elements of the density operator $\hat{\rho}$ of the medium that experiences excitation can be written in the form [19]

$$\dot{\rho}_{\lambda\nu} = -i\omega_{\lambda\nu}\rho_{\lambda\nu} - i[\hat{\rho}, \hat{A}]_{\lambda\nu} - \frac{\rho_{\lambda\nu}}{T_{\lambda\nu}}, \quad \lambda \neq \nu, \tag{2}$$

$$\dot{\rho}_{\lambda\lambda} = -i[\hat{\rho}, \hat{A}]_{\lambda\lambda} + \sum_{\nu=0}^{N+1}\left(\frac{W_\lambda}{T_1^{(\lambda\nu)}}\rho_{\nu\nu} - \frac{W_\nu}{T_1^{(\lambda\nu)}}\rho_{\lambda\lambda}\right). \tag{3}$$

Here, $\hat{A}$ is the matrix of electric dipole transitions with nonzero elements $A_{\lambda, N+1} = A_{N+1, \lambda} = d_\lambda E/\hbar$; $d_\lambda \equiv d_{N+1, \lambda}$ are the matrix elements of the dipole moments of allowed transitions, which are here considered real; E is the extremely short pulse or nonresonant pumping field; $\hbar$ is the Planck constant; W_λ is the equilibrium population of the λth level ($0 \leq W_\lambda \leq 1$); and $T_{\lambda\nu}$ and $T_1^{(\lambda\nu)}$ are the phase and energy relaxation times, respectively, for the $\lambda \longleftrightarrow \nu$ transition. The indices of $\hat{\rho}$ elements run over the values from 0 to $N + 1$ (here and throughout, the sums are not taken over repeating indices in the absence of the corresponding summation sign).

The characteristic electron optical transition frequencies are $\omega_0 \approx \omega_{N+1, \lambda} \sim 10^{16}$ s^{-1} ($\lambda = 0, \ldots, N$), the pumping frequency is $\omega \sim 10^{15}$ s^{-1}, the extremely short pulse width is $\tau_p \sim 10^{-14}$ s, and the frequency of Raman active transitions is $\omega_{\lambda\nu} \sim 10^{13}$ s^{-1} ($\lambda, \nu = 0, \ldots, N$). In addition to condition (1), we then have the inequalities

$$\omega_0\tau_p \gg 1, \quad \frac{\omega_0}{\omega} \gg 1, \tag{4}$$

which allow us to ignore the left-hand sides of (2) in the equations for $\rho_{N+1, \nu} = \rho^*_{\nu, N+1}$. As a result, we obtain algebraic equations for these elements, which corresponds to the situation when the electron dipole moment adiabatically follows electric field alterations.

It follows from this, the condition $(dE/\hbar\omega_0)^2 \ll 1$, and (3) that $\dot{\rho}_{N+1,N+1} \approx 0$. It can be assumed with a high degree of accuracy that the excited electronic states are not populated at the initial time, and therefore $\rho_{N+1,N+1} = 0$ throughout. Using this circumstance and adiabatic approximation (4), we find from (2) that

$$\rho_{N+1,\nu} = \frac{E}{\hbar\omega_{N+1,\nu}}\sum_{\lambda=0}^{N} d_\lambda \rho_{\lambda\nu}. \tag{5}$$

Here, the well-satisfied inequality $\omega_{N+1,\nu} \gg 1/T_{N+1,\nu}$ is also used. Equation (5) relates the $\hat{\rho}$ elements that correspond to electron optical transitions (the left-hand side) to those corresponding to Raman-active transitions (the right-hand side).

Next, we ignore the frequency differences between the electron optical transitions that activate SRS sublevels and the differences of the corresponding dipole moments; that is, we assume that $\omega_{N+1,\mu} \approx \omega_0$ and $d_\mu \approx d$ for $\mu = 0, \ldots, N$, because the vibrational sublevels are closely spaced. This approximation is within the avenue of approach inherent in the Bloembergen–Shen approximation [8, 18] developed for a system with a single vibrational sublevel.

Let us substitute (5) into (2) and (3). For simplicity, we use the approximation of a single energy relaxation time T_1 ($T_1^{(\lambda\nu)} = T_1$ for all λ and ν) [19]. As a result, we obtain a system of equations for the $\hat{\rho}$ elements that only correspond to the SRS sublevels and the ground electronic state. These equations have the form

$$\dot{\rho}_{\mu\nu} = -i\omega_{\mu\nu}\rho_{\mu\nu} + i[\hat{B}, \hat{\rho}]_{\mu\nu} - \frac{\rho_{\mu\nu} - \delta_{\mu\nu}W_\mu}{T_{\mu\nu}}, \quad \nu, \mu = 0, 1, \ldots, N, \tag{6}$$

where the elements of $\hat{B}$ are

$$B_{\mu\nu} = \frac{d^2}{\hbar^2\omega_0}(1 - \delta_{\mu\nu})E^2, \tag{7}$$

$\delta_{\mu\nu}$ is the Kronecker symbol, and $T_{\mu\mu} = T_1$. System (6) includes equations for both off-diagonal ($\mu \neq \nu$) and diagonal ($\mu = \nu$) $\hat{\rho}$ elements.

According to (5), the dipole moment of a molecule equals

$$D = \mathrm{Sp}(\hat{\rho}\hat{d}) = \sum_{\mu=0}^{N} D_\mu \rho_{N+1,\mu} + \text{c.c.} \approx \frac{2E}{\hbar\omega_0}\left(d^2 + \sum_{\lambda=0}^{N}{\sum_{\mu=0}^{N}}' d_\lambda d_\mu u_{\mu\lambda}\right), \tag{8}$$

where $u_{\mu\lambda} = (\rho_{\mu\lambda} + \rho_{\lambda\mu})/2$ and the primed summation symbol indicates the exclusion of the term with $\mu = \lambda$.

The first term in parentheses in (8) corresponds to oscillations of D at the initial field frequency, and the terms under the summation symbol, to oscillations at Raman frequencies. In these terms, we retained the differences between the $\hat{d}$ matrix elements corresponding to transitions at different Raman frequencies; these differences accentuate the intensity differences between the corresponding reemission spectral lines. At the same time, in the $\hat{B}$ matrix, all nonzero $\hat{d}$ matrix elements are considered equal [see (7)], because the difference between them is of no significance when a molecule is excited by an extremely short pulse (see below).

If $N = 1$, system (6)–(8) transforms into the system of the well-known Bloembergen–Shen model [8, 18],

$$\ddot{u} + \frac{2}{T_2}\dot{u} + \omega_\nu^2 u = -2\omega_\nu \frac{d^2E^2}{\hbar^2\omega_0}w, \tag{9}$$

$$\dot{w} = \frac{2d^2E^2}{\hbar^2\omega_\nu\omega_0}\dot{u} - \frac{w - w_\infty}{T_1},$$

$$D = \frac{2d^2}{\hbar\omega_0}(1 + 2u)E, \tag{10}$$

where

$$u = \frac{\rho_{10} + \rho_{01}}{2}, \quad w = \frac{\rho_{11} - \rho_{00}}{2},$$

$$\omega_\nu \equiv \omega_{21} \gg \frac{1}{T_2} \equiv \frac{1}{T_{21}}.$$

Let us find out how the parameters of the quantum-mechanical and empirical (classical) Raman scattering models are related to each other. The empirical model is known to be based on the expansion of the polarizability α of a molecule in normal coordinates q_μ ($\mu = 1, \ldots, N$) of nuclear displacements,

$$\alpha = \alpha_0 + \sum_{\mu=1}^{N}\left(\frac{\partial\alpha}{\partial q_\mu}\right)_0 q_\mu. \tag{11}$$

Subscript "0" in (11) corresponds to $q_\mu = 0$. The dipole moment of the molecule can therefore be written as

$$D = \alpha E = \alpha_0 E + D_R, \tag{12}$$

where

$$D_R = \sum_{\mu=1}^{N}\left(\frac{\partial\alpha}{\partial q_\mu}\right)_0 q_\mu E.$$

Let us write the Raman part of the electric dipole

interaction energy in the form

$$V_R = -D_R E = -E^2 \sum_{\mu=1}^{N} \left(\frac{\partial \alpha}{\partial q_\mu}\right)_0 q_\mu. \quad (13)$$

The equations of motion for q_μ ($\mu = 1, \ldots, N$) then become

$$\ddot{q}_\mu + \frac{2}{T_\mu}\dot{q}_\mu + \omega_\mu^2 q_\mu = -\frac{1}{M_\mu}\frac{\partial V_R}{\partial q_\mu} = \frac{1}{M_\mu}\left(\frac{\partial \alpha}{\partial q_\mu}\right)_0 E^2. \quad (14)$$

Here, T_μ and ω_μ are the damping time and the natural frequency, respectively, of the μth vibrational mode and M_μ is the mass parameter that characterizes the μth mode.

The classical equation (12) corresponds to the quantum-mechanical equation (8). To find a quantum-mechanical analog of (14), let us return to system (6), a particular case of which is (9). First note that (9) transforms into (14) at $u \sim q_1$ and fixed w. The reason for this is the absence of a concept of quantum levels in classical physics.

Expansion (11) implies smallness of q_μ. In quantum-mechanical language, this is equivalent to the assumption of weak excitation of vibrational states. Therefore, in order to determine in what way (14) and (6) are related to each other, we assume that $\rho_{00} = W_0 = 1$ and $\rho_{\mu\mu} = 0$ for $\mu = 1, \ldots, N$ in system (6). Linearizing (6) with respect to the off-diagonal $\hat{\rho}$ and E^2 elements, which means that the terms proportional to $\rho_{\mu\mu}E^2$ are ignored, and taking into account (7), we obtain

$$\ddot{u}_{\mu 0} + \frac{2}{T_{\mu 0}}\dot{u}_{\mu 0} + \omega_{\mu 0}^2 u_{\mu 0} = \omega_{\mu 0}\frac{d^2 E^2}{\hbar^2 \omega_0}, \quad \mu = 1, \ldots, N. \quad (15)$$

Accordingly, (8) can be rewritten in the form

$$D = \frac{2E}{\hbar\omega_0}\left(d^2 + 2\sum_{\mu=1}^{N} d_\mu d_0 u_{\mu 0}\right). \quad (16)$$

A comparison of (12) with (16) and of (14) with (15) yields

$$\omega_\mu = \omega_{\mu 0}, \quad \alpha_0 = \frac{2d^2}{\hbar\omega_0}, \quad \left(\frac{\partial \alpha}{\partial q_\mu}\right)_0 = \pm\frac{\alpha_0}{q_{m\mu}}, \quad q_{m\mu} = \sqrt{\frac{\hbar}{M_\mu \omega_{\mu 0}}}, \quad q_\mu = 2q_{m\mu}u_{\mu 0}. \quad (17)$$

It follows that the role of normal mode frequencies is played by the $\omega_{\mu 0}$ frequencies of the corresponding Raman active transitions. According to (17), the q_μ coordinates of normal modes are directly related to coherence at the $\mu \longleftrightarrow 0$ forbidden transitions.

With $\omega_{\mu 0} \sim 10^{13}$ s^{-1} and $M_\mu \sim 10^{-22}$ g, we obtain $q_{m\mu} \sim 10^{-7}$ cm. As $|u_{\mu 0}|_{\max} = 1/2$, $q_{m\mu}$ has the meaning of a maximum value of the coordinate of the μth normal mode [see the last equation in (17)]. This quantum-mechanical limitation imposed on $q_{m\mu}$ imparts nonlinearity, absent in classical system (14), to vibrational dynamics. It will be shown that this nonlinearity is of fundamental importance for the formation of Raman echo responses.

Equations (17), which correlate the parameters of the classical and quantum models, were obtained by imposing substantial restrictions on the latter. For this reason, the quantum-mechanical theory of SRS processes, which takes into account changes in the populations of all vibrational levels and retains terms that explicitly include nonlinearity, is more complete. We will therefore proceed using (6)–(8) as basic equations and taking into account (17).

3. THE DYNAMICS OF RAMAN-ACTIVE TRANSITIONS UNDER THE ACTION OF EXTREMELY SHORT PULSES AND DURING FREE EVOLUTION

In echo experiments, medium excitations alternate with medium free evolution periods. Condition (1) and the inequality $\tau_p \ll T_{\mu\nu}$ allow us to ignore the first and third terms in (6). System (6) can therefore be rewritten in the operator form

$$\dot{\hat{\rho}} = i[\hat{B}, \hat{\rho}]. \quad (18)$$

Note that $\hat{\rho}$ in (18) only consists of the elements that describe the ground electronic state and vibrational sublevels situated close to it.

It follows from (7) that the $\hat{B}$ operator commutes with itself at different instants of time. Therefore, a solution to (18) can be symbolically written as

$$\hat{\rho}(\tau_l) = \hat{U}^{(l)}\hat{\rho}(\tau_l - t_l)\hat{U}^{(l)+}, \quad (19)$$

where τ_l and t_l are the time of lth pulse action termination and the width of the lth extremely short pulse, respectively. The evolution operator has the form

$$\hat{U}^{(l)} = \exp\left(i\frac{\hat{\theta}_l}{N+1}\right), \quad \hat{\theta}_l = \hat{G}\theta_l, \quad \theta_l = \frac{d^2(N+1)}{\hbar^2\omega_0}\int_{\tau_l - t_l}^{\tau_l} E^2 dt. \quad (20)$$

The elements of the density matrix $\hat{G}$ are $G_{\mu\nu} = 1 - \delta_{\mu\nu}$. The θ_l value will henceforth be called the "area" of the lth extremely short pulse.

In the problem under consideration, the evolution operator can be written in an explicit form. Indeed, set $\hat{G} = \hat{\Sigma} - \hat{I}$, where $\hat{I}$ is the unit operator and $\hat{\Sigma}$ is the

$(N + 1) \times (N + 1)$ matrix all of which elements equal one. As $\hat{\Sigma}$ and $\hat{I}$ commute with each other, we have

$$\hat{U}^{(l)} = \exp\left(-i\frac{\theta_l}{N+1}\right)\exp\left(i\frac{\hat{\Sigma}\theta_l}{N+1}\right).$$

Clearly,

$$\hat{\Sigma}^2 = (N+1)\hat{\Sigma},$$

$$\hat{\Sigma}^3 = (N+1)^2\hat{\Sigma}, \ldots, \quad \hat{\Sigma}^k = (N+1)^{k-1}\hat{\Sigma}, \ldots$$

The series corresponding to the exponential function in the equation for $\hat{U}^{(l)}$ is then easy to sum. Excluding the C numerical phase factor, which is unimportant, we obtain

$$\hat{U}^{(l)} = \hat{I} - \frac{\hat{\Sigma}}{N+1}\left(2\sin^2\frac{\theta_l}{2} - i\sin\theta_l\right). \tag{21}$$

Substituting (21) into (19) allows us to find the change in the states within the system of vibrational sublevels caused by the action of an extremely short pulse.

We were able to sum the series corresponding to the exponential function in the evolution operator thanks to the suggestion that the dipole moments of different quantum transitions were equal. As follows from (21), the action of an extremely short pulse is determined by area θ_l containing these dipole moments in the form of some averaged parameter d [see (20)]. The degree of excitation of molecules can therefore be characterized solely by the area of an extremely short pulse without specifying the equality or difference of $\hat{d}$ matrix elements. At the same time, this difference may be of significance in (8), because it determines the difference of spectral line intensities for the corresponding Raman components in reemission.

Next, consider the dynamics of the state of a system of vibrational sublevels during free evolution. Assuming that $\hat{B} = 0$ in (6) and integrating, we find expressions for the off-diagonal and diagonal $\hat{\rho}$ elements. These expressions have the form

$$\rho_{\mu\nu}(t > \tau_l) = \rho_{\mu\nu}(\tau_l)\exp\left(-i\omega_{\mu\nu}(t-\tau_l) - \frac{t-\tau_l}{T_{\mu\nu}}\right), \quad \mu \neq \nu, \tag{22}$$

$$\rho_{\mu\mu}(t > \tau_l) = \rho_{\mu\mu}(\tau_l)\exp\left(-\frac{t-\tau_l}{T_1}\right) + W_\mu\left[1 - \exp\left(-\frac{t-\tau_l}{T_1}\right)\right]. \tag{23}$$

Equations (19)–(23) determine the temporal dynamics of a system of vibrational sublevels under the action of an extremely short pulse and during free evolution.

As follows from (8), reemission in the optical range can only be recorded in the presence of a background radiation (pumping) field E with input frequency ω. The D_R dipole moment [Eq. (12)] together with the pumping field then causes reemission at Raman frequencies.

For an extended medium whose characteristic size is $L \gg c/\omega$ (c is the velocity of light), of importance is knowledge of the spatial characteristics of echo responses. Following [20], we take into account propagation effects by changing the imaginary exponents in the expressions for the elements of $\hat{\rho}$ and by including spatial phase incursion in the pumping field,

$$t_1 \longrightarrow t_1 + \frac{\mathbf{n}_1 \cdot \mathbf{r}_j}{c},$$

$$\tau_2 - t_2 \longrightarrow \tau_2 - t_2 + \frac{\mathbf{n}_2 \cdot \mathbf{r}_j}{c}, \quad \tau_2 \longrightarrow \tau_2 + \frac{\mathbf{n}_2 \cdot \mathbf{r}_j}{c},$$

$$\ldots\ldots\ldots\ldots\ldots\ldots\ldots\ldots\ldots\ldots\ldots\ldots\ldots\ldots\ldots\ldots$$

$$\tau_r - t_r \longrightarrow \tau_r - t_r + \frac{\mathbf{n}_r \cdot \mathbf{r}_j}{c}, \quad \tau_r \longrightarrow \tau_r + \frac{\mathbf{n}_r \cdot \mathbf{r}_j}{c}, \tag{24}$$

$$t \longrightarrow t + \frac{\mathbf{n} \cdot \mathbf{r}_j}{c}, \quad t > \tau_r,$$

$$\omega t \longrightarrow \omega t - \mathbf{k}_p \cdot \mathbf{r}_j = \omega\left(t - \frac{\mathbf{n}_p \cdot \mathbf{r}_j}{c}\right),$$

where $\mathbf{r}_j$ is the radius vector of the jth molecule in an irradiated sample; $\mathbf{n}_i$ ($i = 1, \ldots, r$) and $\mathbf{n}_p$ are the unit vectors in the directions of extremely short pulse and pumping field propagation, respectively; $\mathbf{n}$ is the unit vector in the echo signal direction; and $\mathbf{k}_p = \omega\mathbf{n}_p/c$ is the pumping field wave vector.

Sequentially applying (19)–(21), (22), (23), and (8) allows us to find the dipole moment of the ith molecule after multiple action of extremely short pulses. Subsequent integration along inhomogeneous broadening contours $g_{\mu\nu} \equiv g_{\mu\nu}(T^*_{\mu\nu}, \Delta_{\mu\nu})$ [here, $T^*_{\mu\nu}$ is the misphasing time of the off-diagonal $\rho_{\mu\nu}$ elements ($\mu, \nu = 0, 1, \ldots, N$) at the $\mu \longleftrightarrow \nu$ forbidden transition and $\Delta_{\mu\nu}$ is the detuning of this transition frequency for some molecule from the central frequency of the contour] for each Raman active transition and the summation over all sample molecules give Raman polarization P_R at Raman frequencies,

$$P_R = \frac{2nE_m}{\hbar\omega_0}\sum_{\lambda=0}^{N}{\sum_{\mu=0}^{N}}' d_\lambda d_\mu \int d\mathbf{r} \times \int_{-\infty}^{\infty} u_{\mu\lambda}(t > \tau_r, \mathbf{r})\cos(\omega t - \mathbf{k}_p \cdot \mathbf{r}) g_{\mu\lambda} d\Delta_{\mu\lambda}. \tag{25}$$

Here, n is the concentration of Raman active molecules

and E_m is the amplitude of the pumping field represented in the form $E = E_m\cos(\omega t - \mathbf{k}_p \cdot \mathbf{r})$.

Because of the smallness of intermolecular distances compared with the radiation wavelength, we replace the summation over molecules by the integration over the sample volume in (25) according to the rule $\sum_j \longrightarrow n\int d\mathbf{r}$.

Generally, a pumping field influences the dynamics of states in the system of vibrational sublevels, because the $u_{\mu\lambda}$ variables in (25) experience pumping effects according to system (6) [E in (7) then denotes the pumping field]. It follows from (6), however, that this influence can be ignored if $B \ll \omega_v$, where B is the characteristic value of $\hat{B}$ matrix elements and ω_v is the lowest natural frequency of all SRS active vibrational modes. This circumstance and (7) and (17) give a condition that allows pumping field influence on free evolution of a system of vibrational sublevels to be ignored, namely,

$$I_p \ll \frac{c}{2\pi}\frac{n\hbar\omega_v}{\chi}, \tag{26}$$

where $I_p = cE^2/4\pi$ is the intensity of pumping and $\chi = n\alpha$ is the electronic susceptibility of the medium.

Setting $\omega_v \sim 10^{13}$ s^{-1}, $n \sim 10^{21}$ cm^{-3}, and $\chi \sim 0.1$, we obtain $I_p \ll 10^{11}$ W/cm^2. Clearly, a pumping field that satisfies condition (26) can act continuously from the very beginning of measurements rather than immediately after the last extremely short pulse ceases to act.

4. RAMAN ECHO PARAMETERS

Let a medium be excited by two extremely short pulses of widths t_1 and t_2 separated by a time interval of $\tau \gg t_1, t_2$. Prior to excitation, the medium is in a state of thermodynamic equilibrium. Then $\rho_{\mu\nu}(0) = W_\mu\delta_{\mu\nu}$, where the initial populations W_μ are distributed according to the Boltzmann statistics. From the outset, the system is under the action of low-intensity [see (26)] monochromatic pumping. Using (19)–(24), we find an expression for $u_{\alpha\lambda}$ after the action of two extremely short pulses, which has the form

$$u_{\alpha\lambda} = \sum_\mu \sum_\nu{}' u_{\alpha\lambda}^{(\mu\nu)}, \tag{27}$$

where $u_{\alpha\lambda}^{(\mu\nu)}$ determines the amplitude of the echo response at the $\omega_{\alpha\lambda}$ frequency if the formation of the response involves the $\mu \longleftrightarrow \nu$ transition ($\alpha\lambda(\mu\nu)$ echo). Below, it is assumed that echo signals are resolved with respect to each other in both frequency and the time of their arising. The last condition is satisfied if the characteristic time interval Δt between sequential signals of the same frequency exceeds the characteristic time determined by inhomogeneous broadening.

The equations for the $u_{\alpha\lambda}^{(\mu\nu)}$ parts that contribute to the echo are as follows:

$$u_{\alpha\lambda}^{(\mu\nu)} = \frac{\sqrt{\Gamma_{\alpha\lambda}^{(\mu\nu)}}}{(N+1)^2}(R_{\alpha\lambda}^{(\mu\nu)}\cos\varphi_{\alpha\lambda}^{(\mu\nu)} + Q_{\alpha\lambda}^{(\mu\nu)}\sin\varphi_{\alpha\lambda}^{(\mu\nu)}), \tag{28}$$

where

$$R_{\alpha\lambda}^{(\mu\nu)} = 4\left(W_\alpha + W_\lambda - \frac{2}{N+1}\right)\left(\delta_{\alpha\mu} + \delta_{\lambda\nu} - \frac{2}{N+1}\right) \times \sin^2\frac{\theta_1}{2}\sin^2\frac{\theta_2}{2} - (W_\alpha - W_\lambda)(\delta_{\alpha\mu} - \delta_{\lambda\mu})\sin\theta_1\sin\theta_2, \tag{29}$$

$$Q_{\alpha\lambda}^{(\mu\nu)} = 2\left(W_\alpha + W_\lambda - \frac{2}{N+1}\right)(\delta_{\alpha\mu} + \delta_{\lambda\nu})\sin^2\frac{\theta_1}{2}\sin\theta_2 + 2\left(\delta_{\alpha\mu} + \delta_{\lambda\nu} - \frac{2}{N+1}\right)(W_\alpha - W_\lambda)\sin\theta_1\sin^2\frac{\theta_2}{2}, \tag{30}$$

$$\varphi_{\alpha\lambda}^{(\mu\nu)} = (\omega \mp \omega_{\alpha\lambda})\left[t - t_{\alpha\lambda}^{(\mu\nu)} - \frac{(\mathbf{n} - \mathbf{n}_{\alpha\lambda}^{(\mu\nu)})\cdot\mathbf{r}}{c}\right], \tag{31}$$

$$t_{\alpha\lambda}^{(\mu\nu)} = \left(1 - \frac{\omega_{\mu\nu}}{\omega_{\alpha\lambda}}\right)\tau, \tag{32}$$

$$\mathbf{n}_{\alpha\lambda}^{(\mu\nu)} = \left(1 - \frac{\omega_{\mu\nu}}{\omega_{\alpha\lambda}}\right)\mathbf{n}_2 + \frac{\omega_{\mu\nu}}{\omega_{\alpha\lambda}}\mathbf{n}_1 + \frac{\omega}{\omega \mp \omega_{\alpha\lambda}}\mathbf{n}_p, \tag{33}$$

$$\Gamma_{\alpha\lambda}^{(\mu\nu)} = \exp\left(-\frac{2t_{\alpha\lambda}^{(\mu\nu)}}{T_{\alpha\lambda}^{(\mu\nu)}}\right), \tag{34}$$

$$\frac{1}{T_{\alpha\lambda}^{(\mu\nu)}} = \frac{1}{T_{\alpha\lambda}} + \left(\frac{1}{T_{\mu\nu}} - \frac{1}{T_{\alpha\lambda}}\right)\frac{1}{1 + |\omega_{\mu\nu}/\omega_{\alpha\lambda}|}. \tag{35}$$

The "–" and "+" signs in (31) and (33) correspond to the Stokes, $\omega - \omega_{\alpha\lambda}$, and anti-Stokes, $\omega + \omega_{\alpha\lambda}$, components.

The $\omega_{\alpha\lambda}$ value in (31) is the transition frequency in the system of vibrational sublevels of a separate molecule. Performing the shift $\omega_{\alpha\lambda} \longrightarrow \omega_{\alpha\lambda} + \Delta_{\alpha\lambda}$ (here, $\omega_{\alpha\lambda}$ is the central frequency of the inhomogeneous broadening contour for the corresponding transition) and substituting (28) into (25), we obtain an equation for P_R.

The total intensity is given by

$$I = \frac{2\omega^4 V^2 \overline{P_R^2}}{3c^3},$$

where V is the sample volume and the bar over P_R^2 denotes averaging over a large number of optical vibrations. Here, we ignore the small frequency difference between Raman components and the pumping field. If

the above conditions of a high relative resolution of echo responses is satisfied, we can write

$$I = \sum_{\alpha=0}^{N}\sum_{\lambda=0}^{N}{\sum_{\mu=0}^{N}}'\sum_{\nu=0}^{N}{}' I_{\alpha\lambda}^{(\mu\nu)},$$

where the intensity of the $\alpha\lambda(\mu\nu)$ echo is given by

$$I_{\alpha\lambda}^{(\mu\nu)} = \frac{8\omega^4 N_a^2}{3c^3}\eta d_\mu^2 d_\nu^2 \frac{E_m^2}{(\hbar\omega_0)^2}\langle\overline{u_{\alpha\lambda}^{(\mu\nu)2}}\rangle, \quad (36)$$

$$\langle\overline{u_{\alpha\lambda}^{(\mu\nu)2}}\rangle = \frac{\Gamma_{\alpha\lambda}^{(\mu\nu)}}{2(N+1)^4}(R_{\alpha\lambda}^{(\mu\nu)2} + Q_{\alpha\lambda}^{(\mu\nu)2}) f(t - t_{\alpha\lambda}^{(\mu\nu)}). \quad (37)$$

Here, angle brackets denote averaging over the inhomogeneous broadening contour, $N_a = nV$ is the number of Raman active molecules in the sample, and η is the dimensionless form factor of the sample. This form factor arises because of the spatial integration in (25); it is expressed via the characteristic cross section area S and pumping wavelength λ ($\eta \sim \lambda^2/S$ [21]). The f function is

$$f(t - t_{\alpha\lambda}^{(\mu\nu)}) = \int_{-\infty}^{\infty} g(\Delta_{\alpha\lambda})\cos[\Delta_{\alpha\lambda}(t - t_{\alpha\lambda}^{(\mu\nu)})]d\Delta_{\alpha\lambda}.$$

Clearly, $f = 1$ at $t = t_{\alpha\lambda}^{(\mu\nu)}$, which is the maximum value of this function. The f value becomes vanishingly small if $t - t_{\alpha\lambda}^{(\mu\nu)} \gg T_{\alpha\lambda}^*$.

Equations (32) and (33) determine the times of the arising and the directions of "luminescence" of the corresponding Raman echo responses. The subscripts in the left-hand sides of (32) and (33) correspond to echo signal frequency shifts with respect to the pumping frequency, $\alpha\lambda \longrightarrow \omega \mp \omega_{\alpha\lambda}$ ($\alpha, \lambda = 0, \ldots, N$). The upper double indices run over the values from 0 to N and indicate the involvement of the corresponding transitions in the formation of the $\alpha\lambda(\mu\nu)$ echo. Enumerating all upper index combinations leads us to conclude that $N(N+1)/2$ echo responses can exist at each Stokes and anti-Stokes component. The total number of potentially possible echo responses equals $N^2(N+1)^2/2$. It is, however, clear that the conditions of spatial synchronism generally cannot be satisfied simultaneously for all these responses. For this reason, the number of Raman echo signals that can be recorded is smaller and determined, apart from other factors, by the geometry of measurements (by extremely short pulse and pumping propagation directions). Note that, among the echo responses at each Stokes and anti-Stokes component, echo signals (one Stokes and one anti-Stokes) should be formed at time 2τ, whose luminescence directions are determined by the equation

$$\mathbf{n}_{\alpha\lambda} = 2\mathbf{n}_2 - \mathbf{n}_1 + \frac{\mathbf{n}_p}{1 \mp \omega_{\alpha\lambda}/\omega}$$

[see (32) and (33) at $\mu = \lambda$ and $\nu = \alpha$]. This result is in agreement with the conclusion drawn in [13], where the Raman echo phenomenon in the presence of one vibrational sublevel was considered. In our problem, the number of Raman echo signals that appear at time 2τ equals $N(N+1)$ (both Stokes and anti-Stokes echo responses are included). As $\omega_{\alpha\lambda}/\omega \sim 10^{-2}$, we can with a high degree of accuracy assume that the spatial synchronism condition is satisfied for all such signals, and these signals propagate in nearly the same direction.

It follows from (29) and (30) that, at $N = 1$,

$$R_{10}^{(01)} = 0, \quad Q_{10}^{(01)} = 2(W_0 - W_1)\sin\theta_1 \sin^2\frac{\theta_2}{2}.$$

This conforms to the well-known result according to which the echo signal is maximum at $\theta_1 = \pi/2$ and $\theta_2 = \pi$. However, if the number of normal vibrational modes is larger, other variants that optimize Raman echo intensities are possible.

It follows from (34) and (35) that relaxation damping of the $\alpha\lambda(\mu\nu)$ echo is determined by phase relaxation times at both the $\alpha \longleftrightarrow \lambda$ and $\mu \longleftrightarrow \nu$ transitions and by their natural frequencies.

Consider the case of small extremely short pulse areas, $\theta_1, \theta_2 \ll 1$. Let, in addition, the temperature of the sample be $T \ll \hbar\omega_{10}/k_B$, where k_B is the Boltzmann constant. In these conditions, the ground electronic level is only populated initially, whereas vibrational levels are not. It then follows from (29) and (30) that $Q_{\alpha\lambda}^{(\mu\nu)} \ll R_{\alpha 0}^{(\alpha\nu)} \approx \theta_1\theta_2$. The intensity of Raman echo signals at the $\omega \mp \omega_{\alpha 0}$ frequencies that correspond to normal modes is therefore $I_{\alpha 0}^{(\alpha\nu)} \approx \theta_1^2\theta_2^2$. All other echo responses (including those corresponding to nonlinear vibrational modes with frequencies equal to the differences of normal mode frequencies) are strongly suppressed in these conditions. Clearly, at small areas, extremely short pulse-induced excitations are weak, and the contribution of nonlinear vibrational components that form difference frequencies is insignificant. A quantum-mechanical explanation is also quite transparent. Indeed, small-area pulses weakly populate vibrational sublevels, and the Stokes and anti-Stokes Raman echo components are largely formed by two-photon transitions from the ground electronic state to these sublevels, which corresponds to the excitation of normal modes only. The use of small-area extremely short pulses therefore singles out normal mode frequencies. For this reason, echo responses from this series will be referred to as "normal" Raman echo signals. Note that the time of the arising of normal Raman echo signals is

$$t_{\alpha 0}^{(\alpha\nu)} = \left(1 - \frac{\omega_{\alpha\nu}}{\omega_{\alpha 0}}\right)\tau \neq 2\tau,$$

because $\nu > \alpha$. The largest possible number of such echo responses at the frequency corresponding to the αth vibrational mode is $2(N - \alpha)$. This, in particular, shows that the Raman echo signal corresponding to the vibrational mode with the highest frequency is absent in this series. This signal is, however, easy to observe at arbitrary areas of exciting extremely short pulses, because the frequencies of the corresponding Stokes and anti-Stokes Raman echo components are farthest from the input continuous pumping frequency. It follows that the total possible number of normal Raman echo signals is

$$2\sum_{\alpha=1}^{N-1}(N-\alpha) = N(N-1).$$

In particular, it follows from this equation that such echo responses do not exist at $N = 1$. Indeed, it has been mentioned above that $R_{10}^{(01)} = 0$ at $N = 1$, and, in the situation under consideration, the contribution to the intensity is determined by the $R_{\alpha 0}^{(\alpha\nu)}$ value. Nevertheless, one echo signal at the Stokes component and one signal at the anti-Stokes component with the $\omega \mp \omega_{10}$ frequencies appear at time 2τ at $N = 1$, which automatically singles out the normal mode.

Taking into account that $\omega_{\alpha\lambda}/\omega \sim 10^{-2}$, the spatial synchronism condition can be satisfied for all Raman echo signals simultaneously when both extremely short pulses are collinearly directed onto the sample. We have

$$\mathbf{n}_{\alpha\lambda}^{(\mu\nu)} = \mathbf{n}_1 + \frac{\mathbf{n}_p}{1 \mp \omega_{\alpha\lambda}/\omega}.$$

True, the Raman echo signals are then virtually unresolved spatially, which impedes recording them. The angle between the propagation directions of the extremely short pulse and pumping should be 120°; Raman echo signals are then emitted along the bisector of this angle.

Several variants that satisfy condition (33) are possible. Consider some particular cases. Suppose that $\mathbf{n}_2 = -\mathbf{n}_1$ (the first pulse reflected from a mirror placed behind the sample can then be used as the second extremely short pulse). Ignoring the $\omega_{\alpha\lambda}/\omega$ ratio, we then find that condition (33) can be satisfied if $|\omega_{\mu\nu}/\omega_{\alpha\lambda}| \leq 1/2$. It follows that this group of echo responses does not contain signals that appear at time 2τ. We are led to conclude that, at opposite propagation directions of two extremely short pulses, Raman echo signals can only be recorded if Raman-active molecules have more than one normal vibrational mode (because the Stokes and anti-Stokes Raman echo signals are formed at time 2τ if $N = 1$).

If $\mathbf{n}_2 = -\mathbf{n}_p$, we obtain the opposite condition, namely, $|\omega_{\mu\nu}/\omega_{\alpha\lambda}| \geq 1/2$. This group of echo-responses includes 2τ signals.

If $\mathbf{n}_1 = -\mathbf{n}_p$, condition (33) can be satisfied at arbitrary $|\omega_{\mu\nu}/\omega_{\alpha\lambda}|$ values. We can then record all echo responses in turn by changing the direction of the second extremely short pulse.

The procedure described in Section 3 allows us to easily generalize (32) and (33) to an r-pulse action,

$$t_{\alpha\lambda}^{\begin{pmatrix}\mu_r\nu_r\\ \cdots\\ \mu_2\nu_2\end{pmatrix}} = \tau_r + \sum_{l=1}^{r-1}\kappa_{\alpha\lambda}^{(l)}\tau_{l+1,l}, \tag{38}$$

$$\mathbf{n}_{\alpha\lambda}^{\begin{pmatrix}\mu_r\nu_r\\ \cdots\\ \mu_2\nu_2\end{pmatrix}} = \mathbf{n}_r + \sum_{l=1}^{r-1}\kappa_{\alpha\lambda}^{(l)}(\mathbf{n}_{l+1} - \mathbf{n}_l) + \frac{\mathbf{n}_p}{1 \mp \omega_{\alpha\lambda}/\omega}, \tag{39}$$

where $\kappa_{\alpha\lambda}^{(l)} = -\omega_{\mu_{l+1}\nu_{l+1}}/\omega_{\alpha\lambda}$. As previously, subscripts $\alpha\lambda$ of t and $\mathbf{n}$ correspond to the $\omega \mp \omega_{\alpha\lambda}$ echo response frequencies, and the upper pairs of indices indicate transitions in the system of vibrational sublevels that are involved in Raman echo formation.

The condition for the appearance of echo responses, which follows from (38), is

$$\sum_{l=1}^{r-1}\kappa_{\alpha\lambda}^{(l)}\tau_{l+1,l} > 0.$$

Equations (38) and (39) coincide with similar equations for two-level quantum systems [22] at $\kappa_{\alpha\lambda}^{(l)} = -1$, 0, 1. The maximum possible number of spin echo signals at each frequency is determined by the equation [7]

$$S_\omega(r, N) = \sum_{l=1}^{r-1}\frac{(r-1)!}{l!(r-1-l)!}[N(N+1)]^l + \frac{(r-1)!}{2}[N(N+1)]^{r-1}. \tag{40}$$

The total number of possible echo responses including signals at the Stokes and anti-Stokes components is $N(N + 1)S_\omega$.

The amplitudes of multiple-pulse Raman echo can be calculated by (19)–(25), which allows the equations for their intensities to be obtained. These equations are very cumbersome and, for this reason, are not given here.

5. CONCLUSIONS

In our view, the study performed in this work reveals the advantages of recording a Raman echo with the use of extremely short pulses compared with quasi-mono-

chromatic exciting signals. We showed the possibility, in principle, of formation of Stokes and anti-Stokes Raman echo signals from normal vibrational modes and also from nonlinear modes containing normal mode frequency differences. With small-area extremely short pulses, we can single out normal vibration frequencies of molecules based on echo response frequencies.

The generalization of the Bloembergen–Shen model to an arbitrary number of vibrational sublevels of a molecule situated close to the ground electronic state allowed us to develop a procedure based on certain simplifying assumptions for calculating Raman echo intensities under arbitrary multiple-pulse actions.

Generally, the spectra of Raman echo signals can contain Stokes and anti-Stokes components formed not only by the differences but also by the sums of normal molecular modes. This effect is, however, of a higher order of smallness compared with those described in the present work. It can be taken into account by solving the self-consistent problem of the formation of Stokes or anti-Stokes components from Raman pumping field components already formed in the medium rather than from the input pumping field.

ACKNOWLEDGMENTS

This work was financially supported by the Russian Foundation for Basic Research (project no. 02-02-17710a).

REFERENCES

1. D. H. Auston, K. P. Cheung, J. A. Valdmanis, and D. A. Kleinman, Phys. Rev. Lett. **53**, 1555 (1984).
2. K. Tamura and M. Nakazava, Opt. Lett. **21**, 68 (1996).
3. T. Brabec and F. Krausz, Rev. Mod. Phys. **72**, 545 (2000).
4. A. M. Zheltikov, Usp. Fiz. Nauk **172**, 743 (2002).
5. A. Yu. Parkhomenko and S. V. Sazonov, Zh. Éksp. Teor. Fiz. **114**, 1595 (1998) [JETP **87**, 864 (1998)].
6. A. Yu. Parkhomenko and S. V. Sazonov, Pis'ma Zh. Éksp. Teor. Fiz. **67**, 887 (1998) [JETP Lett. **67**, 934 (1998)].
7. A. Yu. Parkhomenko and S. V. Sazonov, Opt. Spektrosk. **90**, 788 (2001) [Opt. Spectrosc. **90**, 707 (2001)].
8. É. M. Belenov, P. G. Kryukov, A. V. Nazarkin, and I. P. Prokopovich, Zh. Éksp. Teor. Fiz. **105**, 28 (1994) [JETP **78**, 15 (1994)].
9. A. Nazarkin and G. Korn, Phys. Rev. A **58**, R61 (1998).
10. S. R. Hartmann, IEEE J. Quantum Electron. **4**, 802 (1968).
11. S. Aoki, Phys. Rev. A **14**, 2258 (1976).
12. P. Hu, S. Geschwind, and T. M. Jedju, Phys. Rev. Lett. **37**, 1357 (1976).
13. T. M. Makhviladze and M. E. Sarychev, Zh. Éksp. Teor. Fiz. **69**, 1594 (1975) [Sov. Phys. JETP **42**, 812 (1975)].
14. A. Flusberg, T. Mossberg, and R. Kachru, Phys. Rev. **41**, 305 (1978).
15. A. M. Basharov, Opt. Spektrosk. **57**, 961 (1984) [Opt. Spectrosc. **57**, 587 (1984)].
16. É. A. Manykin and V. V. Samartsev, *Optical Echo-Spectroscopy* (Nauka, Moscow, 1984).
17. D. N. Klyshko, *Physical Fundamentals of Quantum Electronics* (Nauka, Moscow, 1986).
18. Y. R. Shen and N. Bloembergen, Phys. Rev. A **137**, 1738 (1965).
19. R. H. Pantell and H. E. Puthoff, *Fundamentals of Quantum Electronics* (Wiley, New York, 1969; Mir, Moscow, 1972).
20. L. Allen and J. H. Eberly, *Optical Resonance and Two-Level Atoms* (Wiley, New York, 1975; Mir, Moscow, 1978).
21. V. V. Samartsev, Zh. Prikl. Spektrosk. **30**, 581 (1979).
22. G. M. Ershov and U. H. Kopvillem, Zh. Éksp. Teor. Fiz. **63**, 279 (1972) [Sov. Phys. JETP **36**, 147 (1973)].

Translated by V. Sipachev

Journal of Experimental and Theoretical Physics, Vol. 96, No. 5, 2003, pp. 816–831.
Translated from Zhurnal Éksperimental'noĭ i Teoreticheskoĭ Fiziki, Vol. 123, No. 5, 2003, pp. 929–945.

ATOMS, SPECTRA, RADIATION

A Generalized Milne Solution for the Correlation Effects of Multiple Light Scattering with Polarization

V. L. Kuzmin[a,*] and E. V. Aksenova[b]

[a] *St. Petersburg Institute of Commerce and Economics, ul. Novorossiiskaya 50, St. Petersburg, 194021 Russia*
[b] *Institute of High-Performance Computing and Databases, St. Petersburg, 198005 Russia*
**e-mail: vladimir.kuzmin@paloma.spbu.ru*

Received October 25, 2002

Abstract—The Wiener–Hopf method is used to obtain a generalized Milne solution for scalar and electromagnetic fields with single-scattering anisotropy. For the scalar field, the solution found for the time correlation function and the interference component of backscattering is in good agreement with available experimental data. A solution of the Milne problem is constructed for the electromagnetic field. Given anisotropy, the generalized Milne equation is solved in the P_1 approximation for the quantity that describes the degree of depolarization of the scattered light. It is shown that the depolarization of the scattered light can change sign at large anisotropies. *© 2003 MAIK "Nauka/Interperiodica".*

1. INTRODUCTION

Of great importance in studying the coherent and correlation effects in highly inhomogeneous media are, first, the boundedness of the medium, because the scattered light is mainly formed in the near-boundary layer, and, second, the spatial inhomogeneity size, because for multiple scattering to arise in a bounded dielectric, the size of the scattering inhomogeneities must be comparable to the wavelength (see the review [1]). The concept of the diffusive mechanism of radiative transfer in a medium with a random dielectric constant [2] forms a theoretical basis for describing the effects of multiple scattering. The diffusion approximation qualitatively reproduces the picture: it gives a triangular angular function of the coherent backscattering peak [3, 4], a decrease in the peak width with increasing single-scattering anisotropy [5, 6], and a linear dependence of the time correlation function on the square root of time [7, 8]. However, it is not justifiable to use the diffusion approximation, which is valid far from the boundary, at least at the boundary itself, where it is supplemented with boundary conditions like the Dirichlet mixed conditions [2] (see [1]).

For an anisotropic phase function, a spherical function expansion is made to allow for the finite sizes of the scatterers. In this respect, the diffusion approximation is the P_1 approximation, because it corresponds to allowance for the first-order Legendre polynomials. As a result of this allowance for anisotropy, the transport mean free path, $l^* = l_{sc}(1 - \overline{\cos\theta})^{-1}$, becomes the characteristic spatial scale instead of the photon mean free path or the scattering length l_{sc}. Here, $\overline{\cos\theta}$ is the mean cosine of the scattering angle, which is the main parameter that describes single-scattering anisotropy.

In [9–12], the Milne solution was generalized to describe coherent backscattering for an isotropic phase function. In [13], the problem of multiple scattering from a half-space was solved in the limit of a highly forward elongated shape of the phase function, $1 - \overline{\cos\theta} \ll 1$. Note that, apart from $\overline{\cos\theta}$, the result contains no other anisotropy parameters of the form $\overline{\cos^n\theta}$, irrespective of the shape of the phase function. In [14, 15], the Wiener–Hopf method was used to obtain a solution for anisotropic single scattering for the time correlation function in the P_2 approximation and for coherent backscattering in the P_1 approximation. Comparison of the results obtained with the measured time correlation function suggests good agreement with experimental data.

The above authors considered a scalar field by assuming that multiple scattering completely depolarized the incident light and the polarization effects may be disregarded. Experimentally, however, the polarization dependence is preserved [3, 4]; thus, the backscattering peak for the depolarized component is several times smaller than the peak for the polarized component and its shape is not triangular. The coherent effects in liquid crystals [16] also strongly depend on the polarization of the incident and scattered light.

The coherent backscattering effect for an electromagnetic field was first considered in [17] for isotropic scatterers, with the boundary being taken into account by the mirror image method. In [18–22], exact solutions of the boundary-value problem were obtained for the multiple Rayleigh scattering of an electromagnetic field. In [18, 19], the vector transfer equation was solved for backscattering with the interference compo-

nent. In [20, 21], the angular functions of the backscattering peak were calculated by taking into account polarization. In [22], the problem for the time correlation function was also solved for Rayleigh scatterers.

Here, we use the Wiener–Hopf method to solve the problem of multiple scattering from a half-space for an electromagnetic field. We obtain a solution for the polarized and depolarized components of the time correlation function for an isotropic phase function. In the case of nonpolarized incident light, the result for the electromagnetic field, as suggested, differs only slightly from the result obtained in the scalar theory. In the case of polarized light, however, the behavior of the polarized component significantly differs from the behavior of the depolarized component. We find an exact solution for the difference between the polarized and depolarized components, which describes the degree of depolarization with single-scattering anisotropy. The time dependence proves to be strong, although its pattern is linear. Based on our exact solution, we have managed to describe the dependence of the scattered light components on the angle of incidence.

The paper has the following structure. In Section 2, we give the Bethe–Salpeter equation for pair field correlations for the scattering by a medium that occupies a half-space as well as the ladder and interference contributions to the correlation function. In Section 3, we obtain a solution in the P_1 approximation for the scalar field and use it to analyze the time dependence of the correlation function. In Section 4, this solution is used to analyze the angular function of coherent backscattering. In Section 5, we obtain a solution for the polarized and depolarized components of the time correlation function for an isotropic phase function. In Section 6, a solution is found for the difference between the polarized and depolarized components for an anisotropic phase function.

2. BASIC EQUATIONS

The transfer of electromagnetic radiation in a random medium is described by the Bethe–Salpeter integral equation

$$\hat{\Gamma}(\mathbf{R}_2, \mathbf{R}_1, t|\mathbf{k}_f, \mathbf{k}_i) = k_0^2\tilde{G}(\mathbf{k}_f - \mathbf{k}_i, t)\delta(\mathbf{R}_2 - \mathbf{R}_1)\hat{I} + k_0^4\int d\mathbf{R}_3\tilde{G}(-\mathbf{k}_f + \mathbf{k}_{23}, t)\hat{\Lambda}(R_{23})\hat{\Gamma}(\mathbf{R}_3, \mathbf{R}_1, t|\mathbf{k}_{23}, \mathbf{k}_i). \quad (2.1)$$

Here, the tensor function $\hat{\Gamma}(\mathbf{R}_2, \mathbf{R}_1, t|\mathbf{k}_f, \mathbf{k}_i)$, or the propagator of the Bethe–Salpeter equation, describes the transfer of a pair of plane complex-conjugate fields with a wave vector $\mathbf{k}_i$ shifted in time by t from point $\mathbf{R}_1$ to point $\mathbf{R}_2$; $\mathbf{k}_{23} = k_0\mathbf{R}_{23}/R_{23}$, $\mathbf{R}_{23} = \mathbf{R}_2 - \mathbf{R}_3$. Multiple scattering at point $\mathbf{R}_2$ gives rise to a pair of complex-conjugate fields with a wave vector $\mathbf{k}_f$. The wave number is $k_0 = 2\pi/\lambda$, λ is the wavelength, $k_f = k_i = k = nk_0$ is the wave number in the medium, n is the refractive index of the medium: $n = n_1 + in_2$, n_1 and n_2 are the real and imaginary parts of n, respectively, $(2n_2k_0)^{-1} = l$, where l is the total extinction length. The quantity $\tilde{G}(\mathbf{q}, t)$ is the Fourier transform of the pair correlator for the scattering dielectric-constant fluctuations $\delta\varepsilon(\mathbf{r}, t) = \varepsilon(\mathbf{r}, t) = \langle\varepsilon(\mathbf{r}, t)\rangle$,

$$\tilde{G}(\mathbf{q}, t) = \frac{1}{(4\pi)^2} \times \int d\mathbf{r}\langle\delta\varepsilon(0, 0)\delta\varepsilon(\mathbf{r}, t)\rangle\exp(-i\mathbf{q}\cdot\mathbf{r}). \quad (2.2)$$

At $t = 0$, $\tilde{G}(\mathbf{q}, 0) = G_0(\mathbf{q})$ describes the single-scattering cross section, or the phase function, with the momentum transfer $q = 2k\sin(\theta/2)$, where θ is the scattering angle. We will consider an exponential decay of the dielectric-constant fluctuations,

$$\tilde{G}(\mathbf{q}, t) = \tilde{G}_0(\mathbf{q})\exp(-\gamma_q t).$$

In the case of Brownian diffusion,

$$\gamma_q = Dq^2 = \frac{2(1 - \cos\theta)}{\tau},$$

$\tau = (Dk^2)^{-1}$ is the diffusion time scale of a Brownian particle at a distance on the order of λ.

The fourth-rank tensor $\hat{\Lambda}(\mathbf{R})$,

$$\Lambda_{\alpha\beta\mu\nu} = \left(\hat{I} - \frac{\mathbf{R}\otimes\mathbf{R}}{R^2}\right)_{\alpha\mu}\otimes\left(\hat{I} - \frac{\mathbf{R}\otimes\mathbf{R}}{R^2}\right)_{\beta\nu}\frac{\exp(-R/l)}{R^2} \quad (2.3)$$

is the direct product of the complex-conjugate pair of Green functions for the Maxwell wave equation in a far zone. It describes the transformation of a pair of fields with polarizations μ and ν into a pair with polarizations α and β after single scattering. The optical theorem relates the scattering cross section and the scattering length, or the photon mean free path between two elastic scatterings,

$$\frac{2}{3}k_0^4\int d\Omega_f\tilde{G}_0(\mathbf{k}_i - \mathbf{k}_f) = \frac{1}{l_{sc}}. \quad (2.4)$$

The total extinction length l and the scattering length l_{sc} are related by $l^{-1} = l_{sc}^{-1} + l_a^{-1}$, where l_a is the absorption scale length due to inelastic scattering. For the media under consideration, $l_a \gg l$ and the l/l_{sc} ratio is close to unity.

Equation (2.1) is written in the weak-scattering approximation, $\lambda \ll l$. The weak-scattering approximation is also called the ladder approximation, because it formally arises from the summation of the

series over scattering multiplicities in the form of a sum of ladder Feynman diagrams. Therefore, the function $\hat{\Gamma}(\mathbf{R}_2, \mathbf{R}_1, t|\mathbf{k}_f, \mathbf{k}_i)$ is called the ladder propagator.

The observed quantities are the correlators, or the moments of the field $\mathbf{E}(\mathbf{r}, t)$ and its fluctuations $\delta\mathbf{E}(\mathbf{r}, t) = \mathbf{E}(\mathbf{r}, t) - \langle\mathbf{E}(\mathbf{r}, t)\rangle$. The first moment is the mean macroscopic field $\langle\mathbf{E}(\mathbf{r}, t)\rangle$; the second moment, or the coherence function, defines the field correlation function $\langle\delta\mathbf{E}(\mathbf{r}_1, t_1) \cdot \delta\mathbf{E}^*(\mathbf{r}_2, t_2)\rangle$; the fourth moment defines the correlation function of the scattered light intensity

$$\langle\delta\mathbf{E}(\mathbf{r}_1, t_1) \cdot \delta\mathbf{E}^*(\mathbf{r}_1, t_1)\delta\mathbf{E}(\mathbf{r}_2, t_2) \cdot \delta\mathbf{E}^*(\mathbf{r}_2, t_2)\rangle.$$

The main contribution to the intensity correlation function is described by the Gaussian approximation [23], in which the fourth-order correlator is represented as the product of pair correlators:

$$\begin{aligned}&\langle\delta\mathbf{E}(\mathbf{r}_1, t_1) \cdot \delta\mathbf{E}^*(\mathbf{r}_1, t_1)\delta\mathbf{E}(\mathbf{r}_2, t_2) \cdot \delta\mathbf{E}^*(\mathbf{r}_2, t_2)\rangle\\ &= \langle\delta\mathbf{E}(\mathbf{r}_1, t_1) \cdot \delta\mathbf{E}^*(\mathbf{r}_1, t_1)\rangle\langle\delta\mathbf{E}(\mathbf{r}_2, t_2) \cdot \delta\mathbf{E}^*(\mathbf{r}_2, t_2)\rangle\\ &\quad + \left|\langle\delta\mathbf{E}(\mathbf{r}_1, t_1) \cdot \delta\mathbf{E}^*(\mathbf{r}_2, t_2)\rangle\right|^2.\end{aligned} \tag{2.5}$$

In an ordinary geometry of the experiment, where a plane wave of the form

$$\mathbf{E}_{\text{in}}(\mathbf{r}, t) = \mathbf{E}^0\exp(i\mathbf{k}_i \cdot \mathbf{r} - i\omega t)$$

is incident on the system and the scattered light is observed at a large distance r from the scattering system, each pair of fields gives the factor $r^{-2}E^0_{\alpha 1}E^0_{\alpha 2}$, where E^0_α is the amplitude of the incident wave with polarization α.

Let us define the time correlation function of the field observed at a large distance r from the scattering medium as

$$\begin{aligned}&\langle\delta E_\phi(\mathbf{r}, t)\delta E^*_\phi(\mathbf{r}, 0)\rangle\\ &= (1/r^2)T_{\phi\beta_1}T_{\phi\beta_2}C^{(E)}_{\beta_1\beta_2\alpha_1\alpha_2}(t|\mathbf{k}_f, \mathbf{k}_i)E^0_{\alpha_1}E^0_{\alpha_2},\end{aligned} \tag{2.6}$$

where ϕ and α are the polarizations of the scattered and incident light, respectively, with wave vectors $\mathbf{k}_f$ and $\mathbf{k}_i$; the operator $\hat{T} = \hat{I} - \mathbf{k}_f \otimes k_f k^{-2}$ ensures that the scattered wave is transverse.

At $t = 0$, this function describes the intensity of the scattered light. In general, at $t \neq 0$, the quadratic form of this function describes the intensity correlation function. Note that the factor $\exp(-i\omega t)$, where ω is the frequency of the incident monochromatic wave, which vanishes when composing the quadratic form (2.5), is omitted in the function $\hat{C}^{(E)}(t|\mathbf{k}_f, \mathbf{k}_i)$.

As was pointed out above, the ladder diagrams make a major contribution to the scattered light. Physically, they describe two sequential chains of scattering processes, which are identical for the two fields $\mathbf{E}(\mathbf{r}, 0)$ and $\mathbf{E}^*(\mathbf{r}, t)$. Since these two scattering sequences are identical, the phase relations between the fields do not change and, thus, the ladder diagrams describe the incoherent component. At scattering angles close to 180°, the interference component attributable to the cyclic, or fan-shaped [24, 25], diagrams becomes comparable to the main, ladder component. Denoting their contributions by the superscripts L and V, respectively, we have

$$\begin{aligned}&\hat{C}^{(E)}(t|\mathbf{k}_f, \mathbf{k}_i)\\ &= \hat{C}^{(L)}(t|\mathbf{k}_f, \mathbf{k}_i) + \hat{C}^{(V)}(t|\mathbf{k}_f, \mathbf{k}_i).\end{aligned} \tag{2.7}$$

Let the scattering medium occupy the half-space $z > 0$, where z is the Cartesian coordinate normal to the boundary of the medium. In this case, the ladder and interference components of the coherence function are, respectively, [5, 6, 26]

$$\begin{aligned}&C^{(L)}_{\beta_1\beta_2\alpha_1\alpha_2}(t|\mathbf{k}_f, \mathbf{k}_i)\\ &= \int d\mathbf{R}_1 d\mathbf{R}_2\Gamma_{\beta_1\beta_2\alpha_1\alpha_2}(\mathbf{R}_2, \mathbf{R}_1, t|\mathbf{k}_f, \mathbf{k}_i)\\ &\quad\times\exp\left(-\frac{z_1}{l\cos\theta_i} - \frac{z_2}{l\cos\theta_f}\right).\end{aligned} \tag{2.8}$$

$$\begin{aligned}&C^{(V)}_{\beta_1\beta_2\alpha_1\alpha_2}(t|\mathbf{k}_f, \mathbf{k}_i)\\ &= \int d\mathbf{R}_1 d\mathbf{R}_2\left[\Gamma_{\beta_1\alpha_2\alpha_1\beta_2}\left(\mathbf{R}_2, \mathbf{R}_1, t\left|\frac{\mathbf{k}_f - \mathbf{k}_i}{2}, \frac{\mathbf{k}_i - \mathbf{k}_f}{2}\right.\right)\right.\\ &\quad\left. - k_0^4\tilde{G}(\mathbf{k}_f - \mathbf{k}_i, t)\delta(\mathbf{R}_2 - \mathbf{R}_1)\delta_{\alpha_1\beta_1}\delta_{\alpha_2\beta_2}\right]\\ &\quad\times\exp\left[-\frac{z_1 + z_2}{2l}\left(\frac{1}{\cos\theta_i} + \frac{1}{\cos\theta_f}\right)\right.\\ &\quad + in_1k_0(z_1 - z_2)(\cos\theta_i - \cos\theta_f)\\ &\quad\left. + in_1k_0(x_1 - x_2)(\sin\theta_i - \sin\theta_f)\right],\end{aligned} \tag{2.9}$$

where θ_i is the angle of incidence and θ_f is the scattering angle reckoned from the reverse direction of the z axis. The incident and scattered rays lie in the xz plane.

Since single scattering does not contribute to the interference backscattering component, the corresponding term in the integrand of (2.9) is subtracted. It is easy to see that in the case of backscattering, at $\mathbf{k}_f = -\mathbf{k}_i$, the polarized component of the interference contri-

bution $\hat{C}^{(V)}(t|\mathbf{k}_f, \mathbf{k}_i)$ closely matches the polarized component of the ladder contribution $\hat{C}^{(L)}(t|\mathbf{k}_f, \mathbf{k}_i)$ before the subtraction of the single-scattering contribution; in contrast, the depolarized components do not match.

3. A SCALAR FIELD: THE TIME CORRELATION FUNCTION IN THE P_1 APPROXIMATION

Assuming that the light is completely depolarized after multiple scattering, the problem of a vector electromagnetic field reduces to the simpler problem of a scalar field. In this case, the tensor quantities in Eq. (2.1) are replaced with scalars, the tensor dyads in (2.3) are replaced with unity, and the optical theorem takes the form

$$k_0^4 \int d\Omega_f \tilde{G}(\mathbf{k}_f - \mathbf{k}_i, 0) = l_{sc}^{-1}. \tag{3.1}$$

Taking into account the cylindrical symmetry of our problem, we define the two-dimensional Fourier transform in transverse variables $\mathbf{R}_\perp = (x, y)$ and the Laplace transform in variables z_1 and z_2 as

$$\begin{aligned}&\tilde{\Gamma}_{\mathbf{q}}(s_f, s_i, t|\mathbf{k}_f, \mathbf{k}_i)\\ &= \int d\mathbf{R}_{2\perp} \int_0^\infty dz_2 \int_0^\infty dz_1 \Gamma(\mathbf{R}_2, \mathbf{R}_1, t|\mathbf{k}_f, \mathbf{k}_i)\\ &\times \exp\left[-i\mathbf{q}\cdot(\mathbf{R}_2 - \mathbf{R}_1)_\perp - \frac{s_f z_2 + s_i z_1}{l}\right].\end{aligned} \tag{3.2}$$

Since the incoming wave vector $\mathbf{k}_i$ is retained on the right- and left-hand sides of Eq. (2.1), it will suffice to explicitly take into account the dependence only on the outgoing wave vector $\mathbf{k}_f$ on the left-hand side and $\mathbf{k}_{23}$ on the right-hand side of the scalar analog of the Bethe–Salpeter equation. Restricting ourselves to the first-order Legendre polynomials in the spherical function expansion, i.e., to the P_1 approximation, we represent function (3.2) as

$$\begin{aligned}&\tilde{\Gamma}_{\mathbf{q}}(s_f, s_i, t|\mathbf{k}_f, \mathbf{k}_i)\\ &\approx \frac{1}{4\pi}[\gamma_{\mathbf{q}}^{(0)}(s_f, s_i, t) + \gamma_{\mathbf{q}}^{(1)}(s_f, s_i, t)\cos\theta\\ &+ \tilde{q}\gamma_{\mathbf{q}}^{(11)}(s_f, s_i, t)\cos\theta_t],\end{aligned} \tag{3.3}$$

where $\cos\theta = (\mathbf{k}_f \cdot \mathbf{e}_3)k^{-1} = -\cos\theta_f$, $\mathbf{e}_3$ is the unit vector along the z axis, $\cos\theta_t = (\mathbf{k}_f \cdot \mathbf{q})(kq)^{-1}$, and $\tilde{q} = ql$.

Here, $\cos\theta$ and $\cos\theta_t$ are, respectively, the first-order Legendre and associated Legendre polynomials. Making transformation (3.2), substituting expansion (3.3) into the scalar analog of the Bethe–Salpeter equation, and using the orthogonality condition for Legendre polynomials, we obtain a system of equations at low values of the transverse wave vector component $\tilde{q}$:

$$\begin{aligned}&\left[1 - g_0\frac{l}{l_{sc}}m_0(w)\right]\gamma_{\mathbf{q}}^{(0)}(s, s_i, t)\\ &+ g_0 s m_1(w)\gamma_{\mathbf{q}}^{(1)}(s, s_i, t)\\ &- g_0\tilde{q}^2 m_1(w)\gamma_{\mathbf{q}}^{(11)}(s, s_i, t) = g_0 a_0(\mathbf{q}, s, s_i, t),\end{aligned} \tag{3.4}$$

$$\begin{aligned}&3g_1 s m_1(w)\gamma_{\mathbf{q}}^{(0)}(s, s_i, t)\\ &+ \left\{1 - 3g_1\left[m_1(w) - \frac{\tilde{q}^2}{2}(m_1(w) - 3m_2(w))\right]\right\}\gamma_{\mathbf{q}}^{(1)}(s, s_i, t)\\ &- 3g_1 s\tilde{q}^2[m_1(w) - 3m_2(w)]\gamma_{\mathbf{q}}^{(11)}(s, s_i, t)\\ &= 3g_1 a_1(\mathbf{q}, s, s_i, t),\end{aligned} \tag{3.5}$$

$$\begin{aligned}&3g_1 m_1(w)\gamma_{\mathbf{q}}^{(0)}(s, s_i, t)\\ &+ 3g_1 s[m_1(w) - 3m_2(w)]\gamma_{\mathbf{q}}^{(1)}(s, s_i, t)\\ &+ \left\{1 - 3g_1 m_1(w) - \frac{3}{2}g_1 s^2[m_1(w) - 3m_2(w)]\right\}\\ &\times \gamma_{\mathbf{q}}^{(11)}(s, s_i, t) = 3g_1 a_{11}(\mathbf{q}, s, s_i, t),\end{aligned} \tag{3.6}$$

where

$$m_0(w) = \frac{1}{2w}\ln\frac{1+w}{1-w}, \quad m_1(w) = \frac{1}{w^2}(m_0(w) - 1),$$

$$m_2(w) = \frac{1}{w^2}\left(m_1(w) - \frac{1}{3}\right), \quad w^2 = s^2 - \tilde{q}^2.$$

The parameters g_0 and g_1 describe the time evolution of the dielectric-constant fluctuations. In the case of diffusive damping of random inhomogeneities in the medium for time scales t much shorter than the diffusion time scale, $t \ll \tau$, we have

$$g_0 = g_0(t) \approx 1 - 2\frac{t}{\tau}(1 - \overline{\cos\theta}), \tag{3.7}$$

$$g_1 = g_1(t) \approx \overline{\cos\theta} - 2\frac{t}{\tau}(\overline{\cos\theta} - \overline{\cos^2\theta}), \tag{3.8}$$

where $\overline{\cos^n\theta}$ is the nth moment of the cosine of the scattering angle averaged over the phase function,

$$\overline{\cos^n\theta} = \frac{\int \tilde{G}(\mathbf{k} - \mathbf{k}_i, 0)\cos^n\theta\, d\Omega_{\mathbf{k}}}{\int \tilde{G}(\mathbf{k} - \mathbf{k}_i, 0)\, d\Omega_{\mathbf{k}}}. \tag{3.9}$$

These quantities characterize the degree of single-scattering anisotropy. We see from expressions (3.7) and (3.8) that $(t/\tau)(1 - \overline{\cos\theta})$ is a small parameter

instead of t/τ, which allows us to use our results in an extended time interval. In the P_1 approximation, only $\overline{\cos\theta}$, the mean cosine of the scattering angle, is taken into account. The right-hand sides of Eqs. (3.4)–(3.6) are the integrals of the sought-for functions. Discarding the terms of the order of $\tilde{q}^2$, we have

$$a_0(\mathbf{q}, s, s_i, t) = \frac{1}{s + s_i} - \frac{1}{2}\int_1^\infty \frac{ds'}{s'(s' - s)}\gamma_{\mathbf{q}}(s', s_i, t), \tag{3.10}$$

$$a_1(\mathbf{q}, s, s_i, t) = \frac{1}{s_i(s + s_i)} + \frac{1}{2}\int_1^\infty \frac{ds'}{s'^2(s' - s)}\gamma_{\mathbf{q}}(s', s_i, t), \tag{3.11}$$

$$a_{11}(\mathbf{q}, s, s_i, t) = \frac{1}{2}\int_1^\infty \frac{ds'}{s'^3(s' - s)}\Big[\gamma_{\mathbf{q}}(s', s_i, t) + \frac{1}{2}(s'^2 - 1)(\gamma_{\mathbf{q}}^{(1)}(s', s_i, t) - \gamma_{\mathbf{q}}^{(11)}(s', s_i, t))\Big], \tag{3.12}$$

where

$$\gamma_{\mathbf{q}}(s, s_i, t) = \gamma_{\mathbf{q}}^{(0)}(s, s_i, t) - \frac{1}{s}\gamma_{\mathbf{q}}^{(1)}(s, s_i, t). \tag{3.13}$$

In writing the system of equations (3.4)–(3.6), we ignored the intrinsic absorption by assuming that $l/l_{sc} \approx 1$, except for the first term in (3.5), where the entire coefficient of $\gamma_{\mathbf{q}}^{(0)}(s, s_i, t)$ is small when $w \longrightarrow 0$.

Let us now consider the case $\mathbf{q} = 0$, $t \neq 0$, which gives a solution for the time correlation function. The time correlation function is analyzed outside the narrow (several milliradians) coherent backscattering cone where the interference component $C^{(V)}(t|\mathbf{k}_f, \mathbf{k}_i)$ may be disregarded. In this case, function (3.13) at $\mathbf{q} = 0$ defines the time correlation function

$$C^{(E)}(t|\mathbf{k}_f, \mathbf{k}_i) = \frac{S}{4\pi}\gamma_{\mathbf{q}=0}(s_f, s_i, t),$$

where S is the area of the illuminated surface. Setting up a linear combination of Eqs. (3.10) and (3.11), we obtain a closed equation for the function $\gamma_0(s, s_i, t) = \gamma_{\mathbf{q}=0}(s, s_i, t)$:

$$\psi(t, 0, s)\gamma_0(s, s_i, t) = g_0 a_0(0, s, s_i, t) - \frac{3}{s}g_1(1 - g_0)a_1(0, s, s_i, t). \tag{3.14}$$

The following determinant plays a crucial role in solving the system of equations (3.4)–(3.6):

$$\tau(t, \mathbf{q}, s) = (1 - 3g_1 m_1(w))\left(1 - g_0 + \frac{l}{l_a}\right) - g_0 s^2 m_1(w). \tag{3.15}$$

The zero of the determinant s^* in the complex plane s can be determined from a transcendental equation. On short time scales, at $\tilde{q} = 0$, the zero of the determinant is

$$s^* \approx \sqrt{(1 - \overline{\cos\theta})\left[6\frac{t}{\tau}(1 - \overline{\cos\theta}) + \frac{3l}{l_a}\right]}. \tag{3.16}$$

This value of the quantity in question determines the properties of the time correlation function attributable to the diffusive nature of radiative transfer in a highly inhomogeneous medium.

Since the integrals in the expressions for $a_0(0, s, s_i, t)$ and $a_1(0, s, s_i, t)$ contain only the function $\gamma_0(s', s_i, t)$, Eq. (3.14) is a closed integral equation. This equation is similar to the Milne equation for an isotropic phase function and can be solved by the Wiener–Hopf method. Indeed, the function $\psi(t, 0, s)$ can be represented as the ratio of the function

$$s(s + s_i)\left[g_0 a_0(0, s, s_i, t) - \frac{3}{s}g_1(1 - g_0)a_1(0, s, s_i, t)\right],$$

regular in the left half-plane, $\mathrm{Re}\, s < s_i$, to the function $s(s + s_i)\gamma_0(s, s_i, t)$ regular in the right half-plane, $\mathrm{Re}\, s > 0$, of the complex plane s. Since $\psi(t, 0, s)$ is even in s, it can also be represented as the ratio of the functions regular on the right and on the left:

$$\psi(t, 0, s) = \frac{h_+(s)}{h_-(s)}.$$

The products of these functions,

$$h_+(s)s(s + s_i)\gamma_0(s, s_i, t) = h_-(s)s(s + s_i) \times \left[g_0 a_0(0, s, s_i, t) - \frac{3}{s}g_1(1 - g_0)a_1(0, s, s_i, t)\right],$$

must then be regular everywhere and, according to the generalized Liouville theorem, they are the first-order polynomials in s. Our solution differs from the classical Milne solution for an isotropic phase function precisely in the substitution of the constant with a first-order polynomial; this difference arises from the necessity of additionally multiplying Eq. (3.14) by s to remove the singularities on the right- and left-hand sides at $s = 0$.

As a result, the solution of Eq. (3.14) can be represented as

$$\gamma_0(s, s_i, t) = \frac{(C_1 + C_2 s)\sqrt{3}}{s(s + s^*)(s + s_i)} \exp[-J_0(t, s)], \quad (3.17)$$

where $J_0(t, s) = J_{\mathbf{q}=0}(t, s)$ may be called a generalized Chandrasekhar function and has the form

$$J_{\mathbf{q}}(t, s) = \frac{s}{2\pi} \int_{-\infty}^{\infty} \frac{ds'}{s^2 + s'^2} \ln\left[\frac{3\psi(t, \mathbf{q}, is')}{s^{*2} + s'^2}\right]. \quad (3.18)$$

At $t = 0$, the terms of Eq. (3.14) containing $\overline{\cos\theta}$, which describes the anisotropy of the phase function, vanish and solution (3.17) transforms into the standard Milne solution

$$\gamma_0(s, s_i, 0) \equiv \gamma_M(s, s_i) = \frac{3\exp[-J_0(0, s) - J_0(0, s_i)]}{s_i(s_i + s)s}; \quad (3.19)$$

i.e., the intensity of the backscattered light does not depend on single-scattering anisotropy.

The coefficients C_1 and C_2 are constant relative to s. Substituting solution (3.17) into the integral equation (3.14) in the general case, at $t \neq 0$, and expanding the latter into a power series of s, we obtain a sequence of equations sufficient to determine these coefficients. The redundant equations are satisfied automatically, as can be easily verified numerically.

The form of the right-hand side of (3.14) for $s \longrightarrow -s_i$ allows us to derive the identity

$$C_2 - \frac{C_1}{s_i} = \frac{\sqrt{3}}{s_i + s^*} \exp[-J_0(t, s_i)] \times \left[g_0 + \frac{3g_1}{s_i^2}(1 - g_0)\right]. \quad (3.20)$$

We find another equation to determine the parameters C_1 and C_2 by substituting solution (3.17) into Eq. (3.14) and by setting $s = 0$:

$$C_1 = -\frac{\sqrt{3}g_1}{1 - g_1} s_i s^* a_1(0, 0, s_i, t). \quad (3.21)$$

Thus, (3.20) and (3.21) form a closed system of equations that allow C_1 and C_2 to be determined. The parameter C_1 is a small quantity that vanishes in the limit $t = 0$. Therefore, when calculating the parameter $a_1(0, 0, s_i, t)$, we can use the Milne solution by setting $t = 0$ in the integrand.

On short time scales, the main feature of the behavior of the time correlation function is determined by the parameter s^*, because the latter is a linear function of $\sqrt{t/\tau}$, while the Chandrasekhar function is linear in t/τ. For this reason, the solution in the first order in $\sqrt{t/\tau}$ will not change if we discard the terms on the order of $(t/\tau)s^n$, $n \geq 2$, in the original equation (3.14).

Multiple radiative transfer in a random inhomogeneous medium gives rise to a nonanalytic time dependence of the form

$$C^{(E)}(t|\mathbf{k}_f, \mathbf{k}_i) \propto 1 - \kappa\sqrt{\frac{6t}{\tau}}, \quad (3.22)$$

where the initial slope κ determines the rate of decrease of the time correlations and is an important experimentally determined parameter.

In the first order in s^*, we derive

$$C_1 = -\frac{\sqrt{3}g_1 s^*}{s_i(1 - g_1)} \exp[-J_0(0, s_i)] + O\left(\frac{t}{\tau}\right). \quad (3.23)$$

Expression (3.20) then gives $C_2 = C_2^{(1)} + O(t/\tau)$, where

$$C_2^{(1)} = \frac{\sqrt{3}}{s_i} \exp[-J_0(0, s_i)]\left[1 - \frac{s^* g_1}{s_i(1 - g_1)}\right]. \quad (3.24)$$

As a result, on a short time scale, we obtain the time correlation function of the field

$$C^{(E)}(t|\mathbf{k}_f, \mathbf{k}_i) \approx \frac{3}{s_i s_f (s_f + s_i)} \times \exp[-J_0(0, s_i) - J_0(0, s_f)]\left(1 - \kappa\sqrt{\frac{6t}{\tau}}\right), \quad (3.25)$$

where

$$\kappa = \frac{1}{s_i} + \frac{1}{s_f} = \cos\theta_i + \cos\theta_f$$

is the theoretical slope that depends on the angle of incidence and the scattering angle.

For normal incidence, $\cos\theta_i = 1$, the slope is $\kappa = 2$, irrespective of the anisotropy of the phase function, in agreement with available experimental data [8]. This implies that the initial time dependence in the P_1 approximation is universal and the specifics of the scattering system is contained only in the parameter $\tau = 1/Dk^2$.

We calculated the time dependence of the correlation function for various backscattering angles. The dependence on $\overline{\cos\theta}$, in units of $\sqrt{t/\tau}$, is weak. The calculated results are in satisfactory agreement with experimental data [8].

As we see from (3.4), the damping due to inelastic scattering and leading to a finite length l_a reduces to the substitution

$$1 - g_0 \longrightarrow (1 - \overline{\cos\theta})\left(\frac{2t}{\tau} + \frac{l^*}{l_a}\right).$$

This substitution results in a dependence of the small

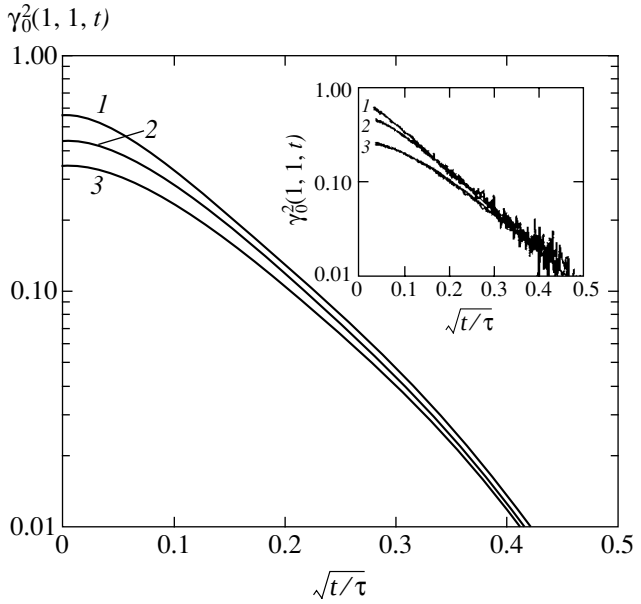

Fig. 1. The normalized intensity correlation function $\gamma_0^2(1, 1, t)$ versus time for three values of the effective layer thickness: L = 2 (*1*), 1 (*2*), and 0.6 (*3*) mm. The experimental curves from [8] are shown in the inset.

parameter s^* on the l^*/l_a ratio:

$$s^* \approx (1 - \overline{\cos\theta})\sqrt{6\frac{t}{\tau} + \frac{3l^*}{l_a}}, \qquad (3.26)$$

where $l^* = l/(1 - \overline{\cos\theta})$ is the transport mean free path. Thus, a linear decrease in the time correlations under the condition $(1 - \overline{\cos\theta})t\tau^{-1} \ll 1$ mentioned above can be observed in the interval $l^*/l_a \ll t/\tau \ll l^*/l$. Taking $\tau \approx$ 3.7 ms, λ = 0.488 μm, the particle diameter d = 0.497 μm, the suspension concentration c = 0.01, and $l^* \approx$ 140 μm from [8] and using the estimate $l_a \approx$ 1 m calculated from these data in the Rayleigh–Hans approximation, we obtain $t \gg$ 0.26 ms, or $\sqrt{t/\tau} \gg 10^{-2}$. However, the deviations in the above paper begin from much higher values of t/τ. These deviations can be explained by the finite sample thickness; they increase with decreasing thickness L (see the inset in Fig. 1). We assume that for a bounded layer of thickness L, the parameter l_a in the above formulas should be substituted with a quantity on the order of L_{eff}. In Fig. 1, the intensity correlation function is plotted against time for three values of the effective layer thickness: we assumed that $L_{\text{eff}} = \alpha L$ and chose α = 10. The values of the thickness were chosen to be the same as in [8]. Note that the calculated and experimental curves are close.

So far, we have considered the situation where the incident and scattered radiations are plane waves with specified wave vectors. When carrying out measurements with optical fibers and wide-angle objectives, we have a situation where the light source or detector or both should be considered as pointlike. The results obtained here can also be used to describe this geometry of the experiment. In the main order in s^*, we derive for the time correlation function of the field:

(i) a normally incident plane wave and a pointlike detector at the plane boundary of the medium,

$$C^{(E)}(t|s_i = 1, s_f > 1) \propto \int_1^\infty \frac{ds}{s}\gamma_0(s, 1, t), \qquad (3.27)$$

(ii) a pointlike source and the pointlike detector, both at the boundary of the medium separated by distance ρ,

$$C^{(E)}(t|s_i > 1, s_f > 1) \propto \rho^{-2}\int_1^\infty \frac{ds}{s}\int_1^\infty \frac{ds'}{s'}\gamma_0(s, s', t).$$

Our numerical calculations yield the slope κ = 1.53 for case (i), a plane incident wave–pointlike detector, and κ = 0.95 for case (ii), a pointlike source–pointlike detector.

In [8], the scattered light was collected by a wide-angle lens. In this case, the integral in (3.27) should be calculated in the finite range $1 < s < s_{\max}$, where $s_{\max} = 1/\cos\theta_{\max}$; $\theta_{\max}$ is the lens opening angle. At $\theta_{\max} = 45°$, our calculations give

$$C^{(E)}(t|s_i = 1, 1 < s_f < \sqrt{2}) \propto 1 - \kappa\sqrt{\frac{6t}{\tau}},$$

where κ = 1.85.

Thus, being insensitive to the anisotropy parameter, the slope proves to be very sensitive to the geometry of the experiment and, in particular, to the lens opening angle.

In [14], the problem on the time correlation function was solved for purely elastic scattering and normal incidence in the P_2 approximation using the Henyey–Greenstein phase function [2]. As a result, in the time interval where the error of the experimental data is small, the theoretical curves for various values of $\overline{\cos\theta}$ almost coincide with the measured ones [8].

4. A SCALAR FIELD: COHERENT BACKSCATTERING

The solution found allows the backscattering enhancement effect to be described. The coherent backscattering intensity $I(\Delta\theta)$ is specified by the interference component of the coherence function at t = 0,

$$I(\Delta\theta) = C^{(V)}(0|\mathbf{k}_f, \mathbf{k}_i),$$

where $\Delta\theta = \theta_f - \theta_i$. Using formulas (2.9) and (33), we

obtain, to within terms of the first order in $\tilde{q} = kl\cos\theta_i\Delta\theta$,

$$I(\Delta\theta) = C^{(V)}(0|\mathbf{k}_f, \mathbf{k}_i) = \frac{S}{4\pi} \times\left[\gamma_{\mathbf{q}}(s_f, s_i, 0) - \frac{4\pi G(\mathbf{k}_f - \mathbf{k}_i, 0)}{\int d\Omega_f G(\mathbf{k}_f - \mathbf{k}_i, 0)}\frac{1}{s_i + s_f}\right]. \quad (4.1)$$

This formula is valid only if $\Delta\theta \ll 1$. When this condition is violated, at $\Delta\theta \sim 1$, the parameter $\tilde{q}$ becomes large, $\tilde{q} \gg 1$. In this case, the interference contribution $C^{(V)}$ is too small to be observable against the background of the contribution from arbitrary Feynman diagrams.

Thus, to determine $\gamma_{\mathbf{q}}(s_f, s_i, 0)$, we must solve Eqs. (3.4)–(3.6) at $t = 0$ and $q \neq 0$. Consider the last equation of this system in the vicinity of $q = s = 0$. We obtain

$$\gamma_{\mathbf{q}}^{(11)}(s, s_i, 0) = -\frac{g_1}{1 - g_1}\gamma_{\mathbf{q}}^{(0)}(s, s_i, 0)[1 + O(\tilde{q})]. \quad (4.2)$$

The nonanalytic dependence on the variables t/τ and $\tilde{q}$ arises because of the determinant zero, i.e., the position of the diffusion pole, near $s = 0$. This implies that we can set $q^2 m_1(w) \approx q^2/3$ in the first equation (3.4) and discard the terms with the factor q^2 in the second equation. Substituting (4.2) into the first two equations then yields

$$\left[\frac{l}{l_a} + \frac{\tilde{q}^2}{3(1 - \overline{\cos\theta})}\right]\gamma_{\mathbf{q}}^{(0)}(s, s_i, 0) - s^2 m_1(w)\gamma_{\mathbf{q}}(s, s_i, 0) = a_0(\mathbf{q}, s, s_i, 0), \quad (4.3)$$

$$3\overline{\cos\theta}\, m_1(w)\gamma_{\mathbf{q}}(s, s_i, 0) + \frac{1}{s}\gamma_{\mathbf{q}}^{(1)}(s, s_i, 0) = \frac{3}{s}\overline{\cos\theta}\, a_1(\mathbf{q}, s, s_i, 0). \quad (4.4)$$

Assuming that $m_1(w) \approx m_1(s)$, we can write these equations as

$$\left[\frac{1}{3}s_q^* - s^2 m_1(s)\right]\gamma_{\mathbf{q}}(s, s_i, 0) = a_0(\mathbf{q}, s, s_i, 0) - \frac{\overline{\cos\theta}}{1 - \overline{\cos\theta}}\frac{s_q^{*2}}{s}a_1(\mathbf{q}, s, s_i, 0), \quad (4.5)$$

where

$$s_q^* = \sqrt{\tilde{q}^2 + \frac{3l(1 - \overline{\cos\theta})}{l_a}}.$$

Equation (4.5) was derived in a similar way as Eq. (3.14) and gives the solution

$$I(\Delta\theta) \sim \gamma_{\mathbf{q}}(s, s_i, 0) = \frac{3}{2}\cos^3\theta_i \exp\left[-2J\left(\frac{1}{\cos\theta_i}\right)\right] \times\left[1 - \kappa\sqrt{\left(\frac{\tilde{q}}{1 - \overline{\cos\theta}}\right)^2 + \frac{3l^*}{l_a}}\right] - \frac{\cos\theta_i}{2}\frac{4\pi G(\mathbf{k}_f - \mathbf{k}_i, 0)}{\int G(\mathbf{k}_f - \mathbf{k}_i, 0)d\Omega_f}. \quad (4.6)$$

The last term in this formula, which describes the single-scattering contribution, for systems with highly anisotropic scattering, i.e., with a small backscattering cross section, may be discarded.

When the single scattering is neglected, Eq. (4.6), which was obtained as a generalization of the exact Milne solution, for normal incidence at $\kappa = 2$ gives

$$I(\Delta\theta) \propto 1 - 2kl^*\Delta\theta. \quad (4.7)$$

At the same time, the initial angular function of the backscattering cone in the diffusion approximation, when the single scattering is also neglected, is described by a linear formula of the form [5, 27]

$$I^{(\mathrm{dif})}(\Delta\theta) \sim 1 - 2\frac{(1 + z^*)^2}{1 + 2z^*}kl\Delta\theta, \qquad z^* = \frac{0.71}{1 - \overline{\cos\theta}}. \quad (4.8)$$

These two equations predict distinctly different dependences on the anisotropy parameter $\overline{\cos\theta}$.

In the diffusion approximation, the time correlation function and the coherent backscattering intensity are symmetric relative to the substitution [27] $\sqrt{6t/\tau} \longleftrightarrow kl^*\Delta\theta$. Formulas (3.25) and (4.6), obtained in terms of the exact solution of the boundary-value problem, confirm this symmetry. However, whereas (3.25) is in good agreement with experimental data, formula (4.6) predicts a narrower backscattering cone than the experimentally determined one [3, 4]. Note that these cone width estimates for strong anisotropy are very sensitive to $\overline{\cos\theta}$: a change in $\overline{\cos\theta}$ by 3% near $\overline{\cos\theta} \sim 0.9$ causes the peak width to change by a factor of 1.5.

5. THE TIME CORRELATION FUNCTION FOR AN ELECTROMAGNETIC FIELD IN THE P_0 APPROXIMATION

In general, the solution of the boundary-value problem for the fourth-rank tensor $\hat{\Gamma}(\mathbf{R}_2, \mathbf{R}_1, t|\mathbf{k}_f, \mathbf{k}_i)$ is very cumbersome. The tensor structure of Eq. (2.1) is significantly simplified for incident plane-polarized light with polarization α. In this case, the indices α_1 and α_2 are the same. Since the problem is symmetric, the indices are then, $\beta_1 = \beta_2 = \beta$ and $\mu = \nu$. Thus, we can consider the fourth-rank tensors with the pairwise coincident indices as second-rank tensors—$\Lambda_{\beta\beta\mu\mu} = \Lambda_{\beta\mu}$ and $\Gamma_{\beta\beta\alpha\alpha} = \Gamma_{\beta\alpha}$—and significantly simplify the problem. The Bethe–Salpeter equation (2.1) for the pairwise coincident polarization indices is

$$\begin{aligned}\Gamma_{\beta\alpha}(\mathbf{R}_2, \mathbf{R}_1, t|\mathbf{k}_f, \mathbf{k}_i) &= k_0^4\tilde{G}(\mathbf{k}_f - \mathbf{k}_i, t)\delta(\mathbf{R}_2 - \mathbf{R}_1)\delta_{\beta\alpha} \\ &+ k_0^4\int d\mathbf{R}_3\tilde{G}(\mathbf{k}_f - \mathbf{k}_{23}, t)\Lambda_{\beta\mu}(R_{23})\Gamma_{\mu\alpha}(\mathbf{R}_3, \mathbf{R}_1, t|\mathbf{k}_{23}, \mathbf{k}_i).\end{aligned} \quad (5.1)$$

We assume that the wave vector of the incident wave lies in the *yz* plane and its field is polarized along the *x* axis, $\alpha = 1$. Then, since the initial polarization was specified, $\alpha = 1$, the column vector $\gamma = (\Gamma_{11}, \Gamma_{21}, \Gamma_{31})/4\pi$ is to be sought for.

We consider an isotropic phase function where the function $\tilde{G}_0(\mathbf{q})$ does not depend on the transferred wave vector $\mathbf{q}$, $\tilde{G}_0(\mathbf{q}) = G_0$. Denoting, for brevity, in the case of an isotropic phase function

$$\tilde{\Gamma}_{\beta 1}(q_\perp = 0, s_f, s_i, t|\mathbf{k}_f, \mathbf{k}_i) \equiv 4\pi\gamma_\beta(s_f, s_i, t), \quad (5.2)$$

we represent the time correlation function as

$$C_{\beta 1}(t|\mathbf{k}_f, \mathbf{k}_i) = \frac{S}{4\pi}\gamma_\beta(s_f, s_i, t). \quad (5.3)$$

In the case of normal incidence, the polarized and depolarized components of the intensity correlation function can be written, using factorization (2.5), as

$$C^I_{\mathrm{pol}}(\theta_f, t) = \gamma_1^2(s_f, 1, t), \quad (5.4)$$

$$\begin{aligned}C^I_{\mathrm{depol}}(\theta_f, t) &= \gamma_2^2(s_f, 1, t)\cos^2\theta_f \\ &+ \gamma_3^2(s_f, 1, t)\sin^2\theta_f,\end{aligned} \quad (5.5)$$

if the field of the incident wave is perpendicular to the scattering plane, and

$$\begin{aligned}C^I_{\mathrm{pol}}(\theta_f, t) &= \gamma_1^2(s_f, 1, t)\cos^2\theta_f \\ &+ \gamma_3^2(s_f, 1, t)\sin^2\theta_f,\end{aligned} \quad (5.6)$$

$$C^I_{\mathrm{depol}}(\theta_f, t) = \gamma_2^2(s_f, 1, t), \quad (5.7)$$

if the field of the incident wave lies in the scattering plane. The plane formed by the wave vectors of the incident and scattered waves is called the scattering plane. We average Eq. (5.1) over the $\mathbf{k}_f$ orientations; i.e., we perform the integration $\int d\Omega_f$. Performing, as in (3.2), the two-dimensional Fourier and twice the Laplace transforms, we obtain

$$\left[\hat{I} - \frac{3}{2}\exp\left(-\frac{2t}{\tau}\right)\hat{\tilde{\Lambda}}(s)\right]\gamma(s, s_i, t) = \mathbf{b}(s, s_i, t). \quad (5.8)$$

Here,

$$\hat{\tilde{\Lambda}}(s) = \frac{1}{8}\begin{pmatrix} 3m_0 + 2m_1 + 3m_2 & m_0 - 2m_1 + m_2 & 4(m_1 - m_2) \\ m_0 - 2m_1 + m_2 & 3m_0 + 2m_1 + 3m_2 & 4(m_1 - m_2) \\ 4(m_1 - m_2) & 4(m_1 - m_2) & 8(m_0 - 2m_1 + m_2) \end{pmatrix}. \quad (5.9)$$

The column vector $\mathbf{b}(s, s_i, t)$ on the right-hand side of (5.8) is

$$\begin{aligned}b_\beta(s, s_i, t) &= \frac{3}{2}\exp\left(-\frac{2t}{\tau}\right)\frac{1}{s_i + s}\delta_{\beta 1} - \frac{3}{4}\exp\left(-\frac{2t}{\tau}\right) \\ &\times\int_1^\infty \frac{ds'}{s'(s' - s)}a_{\beta\mu}(s')\gamma_\mu(s', s_i, t),\end{aligned} \quad (5.10)$$

where

$$\hat{a}(s) = \frac{1}{8s^4}\begin{pmatrix} 3s^4 + 2s^2 + 3 & (s^2 - 1)^2 & 4(s^2 - 1) \\ (s^2 - 1)^2 & 3s^4 + 2s^2 + 3 & 4(s^2 - 1) \\ 4(s^2 - 1) & 4(s^2 - 1) & 8(s^2 - 1)^2 \end{pmatrix}. \quad (5.11)$$

The matrices $\hat{\hat{\Lambda}}$ and $\hat{a}$ have such a structure that the system of equations (5.8) breaks up into two independent subsystems. Indeed, defining the functions

$$\gamma_{\pm}(s, s_i, t) = \frac{1}{2}[\gamma_1(s, s_i, t) \pm \gamma_2(s, s_i, t)] \quad (5.12)$$

and adding and subtracting the first two equations from the three equations of system (5.8), we obtain a closed equation for the component $\gamma_-(s, s_i, t)$ that describes the degree of depolarization,

$$\psi_-(s, t)\gamma_-(s, s_i, t) = \frac{3}{4}\exp\left(-\frac{2t}{\tau}\right)\frac{1}{s_i + s} - \frac{3}{4}\exp\left(-\frac{2t}{\tau}\right)\int_1^\infty \frac{ds'}{s'(s' - s)}[a_{11}(s') - a_{12}(s')]\gamma_-(s', s_i, t), \quad (5.13)$$

where

$$\psi_-(s, t) = 1 - \frac{3}{8}\exp\left(-\frac{2t}{\tau}\right)(m_0 + 2m_1 + m_2), \quad (5.14)$$

and a system of equations for the two remaining components,

$$\begin{pmatrix} 1 - \frac{3}{4}e^{-2t/\tau}(m_0 + m_2) & -\frac{3}{4}e^{-2t/\tau}(m_1 - m_2) \\ -\frac{3}{2}e^{-2t/\tau}(m_1 - m_2) & 1 - \frac{3}{2}e^{-2t/\tau}(m_0 - 2m_1 + m_2) \end{pmatrix}\begin{pmatrix} \gamma_+ \\ \gamma_3 \end{pmatrix} = \begin{pmatrix} \frac{b_1 + b_2}{2} \\ b_3 \end{pmatrix}. \quad (5.15)$$

Equation (5.13) for the function $\gamma_-(s, s_i, t)$, which, by definition, is the difference between the polarized and depolarized scattered components in the case of normal incidence, has the form of the Milne equation and can be solved by the Wiener–Hopf method in the standard way. As a result, we obtain

$$\gamma_-(s, s_i, t) = \frac{3\exp(2t/\tau)}{4(s_i + s)(1 - 0.7\exp(-2t/\tau))} \times \exp[-J_d(s, t) - J_d(s_i, t)], \quad (5.16)$$

where the quantity

$$J_d(s, t) = \frac{s}{2\pi}\int_{-\infty}^{\infty}\frac{ds'}{s'^2 + s^2}\ln\left[\frac{\psi_-(is', t)}{1 - 0.7\exp(-2t/\tau)}\right] \quad (5.17)$$

acts as the Chandrasekhar function [28]. Since the function $\psi_-(s, t)$ is finite at $s = 0$:

$$\psi_-(0, t) = 1 - 0.7\exp\left(-\frac{2t}{\tau}\right), \quad (5.18)$$

the function $\gamma_-(s, s_i, t)$ has no singularity for $s \longrightarrow 0$ and, as a consequence, it is regular in t on short time scales. Thus, the difference between the polarized and depolarized components of the time correlation function varies linearly with t/τ, while these components themselves linearly depend on $\sqrt{t/\tau}$ on short time scales.

We calculated the time dependence of $\gamma_-(1, 1, t)$. According to (5.4) and (5.5), in the case of incident field polarization perpendicular to the scattering plane,

$$\gamma_-(1, 1, t) = \frac{1}{2}(\sqrt{C^I_{\text{pol}}(0, t)} - \sqrt{C^I_{\text{depol}}(0, t)}).$$

The merit of this result is that it is valid for any time scales and the calculated function is an experimentally determined quantity.

Let us now turn to system (5.15) and find its solution in the main order in time parameter t/τ. Using the definition of the functions $m_j(s)$ and taking into account the smallness of t/τ, we transform it to

$$\begin{pmatrix} \frac{2t}{\tau} - \frac{3s^2(m_1 + m_2)}{4} & \frac{t}{\tau} - \frac{3s^2(m_1 - m_2)}{4} \\ \frac{2t}{5\tau} - \frac{3(m_1 - m_2)}{2} & \frac{8t}{5\tau} + \frac{3(m_1 - m_2)(1 - s^2)}{2} \end{pmatrix} \times \begin{pmatrix} \gamma_+ \\ \gamma_3 \end{pmatrix} = \begin{pmatrix} \frac{b_1 + b_2 + b_3}{2} \\ b_3 \end{pmatrix}. \quad (5.19)$$

In writing (5.19), we neglected the quantities on the order of $(t/\tau)s^2$ or higher. As was shown in the scalar case, this neglect does not affect the solution of the Milne problem for $t/\tau \ll 1$. The principal feature in the behavior of the time correlation function, namely, the linear dependence on $\sqrt{t/\tau}$ on short time scales, arises because the determinant of the matrix in Eq. (5.19) becomes zero at $s = 0$ and $t = 0$. We see that the elements of the first row become zero at $s = 0$ and $t = 0$, implying

that we can put $t = 0$ in the elements of the second row in the asymptotic range $t \ll \tau$. As a result, we obtain

$$\left[\frac{2t}{\tau} - s^2 m_1\right]\gamma_+ + \left[\frac{2t}{3\tau} - \frac{s^2(m_1 - m_2)}{2}\right]\gamma_e = \frac{b_1 + b_2 + b_3}{3}, \quad (5.20)$$

$$-\frac{m_1 - m_2}{2}[s^2\gamma_+ - (1 - s^2)\gamma_e] = \frac{b_3}{3},$$

where

$$\gamma_e = \gamma_e(s, s_i, t) = \gamma_3(s, s_i, t) - \gamma_+(s, s_i, t).$$

We see from Eqs. (5.20) that the function $\gamma_e(s, s_i, t)$ is finite for $s \longrightarrow 0$ and $t \longrightarrow 0$, while $\gamma_+(s, s_i, t)$ indefinitely increases in this limit. The finiteness of $\gamma_e(0, s_i, 0)$ in the main order allows us to set $t = 0$ everywhere except for the coefficient of γ_+ in the first equation. This system can then be rewritten as two equations, with the Wiener–Hopf method being applicable to each of them:

$$\psi_+(s, t)\gamma_+(s, s_i, t) = \frac{(b_1 + b_2)(1 - s^2) + b_3}{3}, \quad (5.21)$$

$$\frac{m_1 - m_2}{2}\gamma_c(s, s_i, t) = \frac{b_3}{3}, \quad (5.22)$$

where we defined the new sought-for function

$$\gamma_c(s, s_i, t) = (1 - s^2)\gamma_e(s, s_i, t) - s^2\gamma_+(s, s_i, t),$$

and the quantity $\psi_+(s, t)$ is

$$\psi_+(s, t) = \left[\frac{2t}{\tau} - s^2 m_1(s)\right](1 - s^2) - \frac{1}{2}[m_1(s) - m_2(s)]s^4. \quad (5.23)$$

Given the asymptotic behavior of the functions $m_1(s)$ and $m_2(s)$, for the operator on the right-hand side of (5.23), we have

$$\psi_+(s, t) \approx \frac{s_0^{*2} - s^2}{3} \text{ at } s \longrightarrow 0, \quad t \longrightarrow 0, \quad (5.24)$$

where $s_0^{*2} = 6t/\tau$. Thus, the function $\psi_+(s, t)$ has a zero in the complex plane s, which approaches the coordinate origin when $t \longrightarrow 0$. This behavior reproduces the well-known singularity of the propagator of the Bethe–Salpeter equation and leads to the diffusive propagation of light in the regime of multiple scattering. As a result, using the standard Wiener–Hopf procedure and taking into account the above zero of $\psi_+(s, t)$ in the complex plane, we can represent the solution of Eq. (5.21) as

$$\gamma_+(s, s_i, t) = \frac{d_1}{s + s_0^*}\frac{1 + s}{1 + \sqrt{3}s}\exp[-J_+(s, t)], \quad (5.25)$$

where

$$J_+(s, t) = \frac{s}{2\pi}\int_{-\infty}^{\infty}\frac{ds'}{s'^2 + s^2}\ln\left[\frac{3\psi_+(is', t)}{s'^2 + s_0^{*2}}\frac{1 + s'^2}{1 + 3s'^2}\right]. \quad (5.26)$$

Similarly, solving Eq. (5.22) yields

$$\gamma_c(s, s_i, t) = d_2\left(1 + \sqrt{\frac{2}{15}}s\right)\exp[-J_c(s)], \quad (5.27)$$

where

$$J_c(s) = \frac{s}{2\pi}\int_{-\infty}^{\infty}\frac{ds'}{s'^2 + s^2} \times \ln\left[\frac{15}{2}(m_1(is') - m_2(is'))\left(1 + \frac{2s'^2}{15}\right)\right]. \quad (5.28)$$

The parameters d_1 and d_2 are constants relative to the variable s and will be determined from additional considerations. Here, we used the identity

$$\exp\left\{\frac{-s}{2\pi}\int_{-\infty}^{\infty}\frac{ds'}{s'^2 + s^2}\ln(A^2 + s'^2)\right\} = \frac{1}{A + s}, \quad \text{Re}\, s > 0, \quad A > 0, \quad (5.29)$$

to derive expressions convenient in numerical calculations, because the functions under the logarithm sign in (5.26) and (5.28) become unity when $s' \longrightarrow \infty$ and the integrals rapidly converge. The quantity $J_+(s, t)$, which is a version of the Chandrasekhar function, linearly depends on time at low values of t. Therefore, below, we assume that $J_+(s, t) \approx J_+(s, 0)$.

We determine the constants d_1 and d_2 just as we did for the scalar case. The relation between d_1 and d_2 can be easily obtained from the definition of $\gamma_c(s, s_i, t)$. Indeed, $\gamma_+(s, s_i, t)$ and $\gamma_e(s, s_i, t)$ at $s = 1$ must be finite, because these are the observed components of the time correlation function for backscattering. Therefore, we derive $\gamma_c(1, s_i, t) = -\gamma_+(1, s_i, t)$ at $s = 1$. Using solutions (5.25) and (5.27), we obtain

$$d_2\left(1 + \sqrt{\frac{2}{15}}\right)\exp[-J_c(1)] = -\frac{2d_1}{(1 + s_0^*)(1 + \sqrt{3})}\exp[-J_+(1)]. \quad (5.30)$$

Direct calculation yields

$$d_2 = -0.582\frac{d_1}{1 + s_0^*}.$$

Denote

$$\alpha_n = \int_1^\infty \frac{ds'}{s'^n} \frac{1+s'}{s'(1+\sqrt{3}s')} \exp[-J_+(s')], \quad (5.31)$$

$$\beta_n = \int_1^\infty \frac{ds'}{s'^n} \left(1+\sqrt{\frac{2}{15}}s'\right) \exp[-J_c(s')]. \quad (5.32)$$

The parameters α_n and β_n can be easily calculated numerically.

Substituting the solution found into Eq. (5.21), setting $s = 0$ on the right- and left-hand sides, and using the numerical values of α_n and β_n, we obtain

$$d_1 = 2\left\{\alpha_2 + 0.582\beta_4 + s_0^*\left[\frac{4}{3} - (\alpha_3 + 0.582\beta_4)\right]\right\}^{-1} \approx \frac{2.57}{1+0.894s_0^*}. \quad (5.33)$$

Substituting this quantity into (5.25) yields, in the case of normal incidence and backscattering,

$$\gamma_+(1,1,t) \approx \frac{2.319}{(1+s_0^*)(1+0.895s_0^*)}. \quad (5.34)$$

To within a numerical factor, this expression agrees closely with the Milne solution [29] for the time correlation function in the model of a scalar field:

$$\gamma_{\text{scal}}(1,1,t) \approx \frac{4.22}{(1+s_0^*)^2}. \quad (5.35)$$

To within a numerical factor, it is also identical to the solution in the diffusion approximation for an isotropic phase function if the mirror boundary in the mirror image method is chosen to be at the physical boundary, $z = 0$ [7].

In the case of nonpolarized incident light, $\gamma_- = 0$. Thus, the fact that the time dependences described by (5.34) and (5.35) are similar confirms that the scalar-field approximation can actually be used with an accuracy up to 10% to describe the effects of multiple scattering for nonpolarized light.

In the case of normal incidence and backscattering, the polarized component of the time correlation function is given by

$$\gamma_{\text{pol}}(1,1,t) = \gamma_+(1,1,t) + \gamma_-(1,1,t) \quad (5.36)$$

and the depolarized component is given by

$$\gamma_{\text{depol}}(1,1,t) = \gamma_+(1,1,t) - \gamma_-(1,1,t). \quad (5.37)$$

In the first order in the time variable, retaining only the linear dependence on $\sqrt{t/\tau}$, we may set $t = 0$ in the function $\gamma_-(1,1,t)$. In the main order in $s_0^* = \sqrt{6t/\tau}$, we then obtain

$$\gamma_{\text{pol}}(1,1,t) \approx 3.05(1-1.44s_0^*), \quad (5.38)$$

$$\gamma_{\text{depol}}(1,1,t) \approx 1.59(1-2.75s_0^*). \quad (5.39)$$

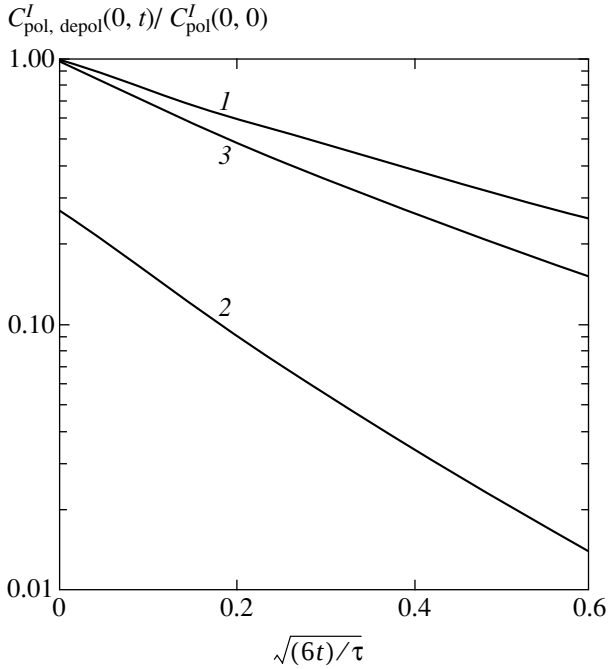

Fig. 2. Time dependences of the polarized (*1*), $C^I_{\text{pol}}(0,t)$, and depolarized (*2*), $C^I_{\text{depol}}(0,t)$, components of the correlation function for the backscattered light intensity calculated using (5.16) and (5.34) and normalized to the square of the intensity of the polarized component. The normalized time correlation function of nonpolarized light (*3*) calculated using (5.35) is also shown for comparison.

The intensity time correlation function is defined as the square of the field correlation function. Figure 2 schematically shows the time correlation functions of the polarized and depolarized intensity components. We see that in the case of polarized light, the description in terms of the scalar theory proves to be inadequate.

The scalar field theory predicts a slope $\gamma_{\text{scal}}(1,1,t) \propto 1 - \gamma s_0^*$, which determines the rate of initial decrease of the field time correlations, exactly equal to two, $\gamma = 2$. The slopes for the polarized and depolarized components differ markedly from this value: $\gamma_{\text{pol}} = 1.44$ and $\gamma_{\text{depol}} = 2.75$. Calculations in the diffusion approximation yield similar values [27], 1.6 and 2.7, respectively. They are in good agreement with the experimental values [27] of 1.6 ± 0.1 and 2.8 ± 0.2 for the scattering of light with $\lambda = 0.488$ μm in a latex solution with a particle diameter of 0.091 μm, which is much smaller than the wavelength.

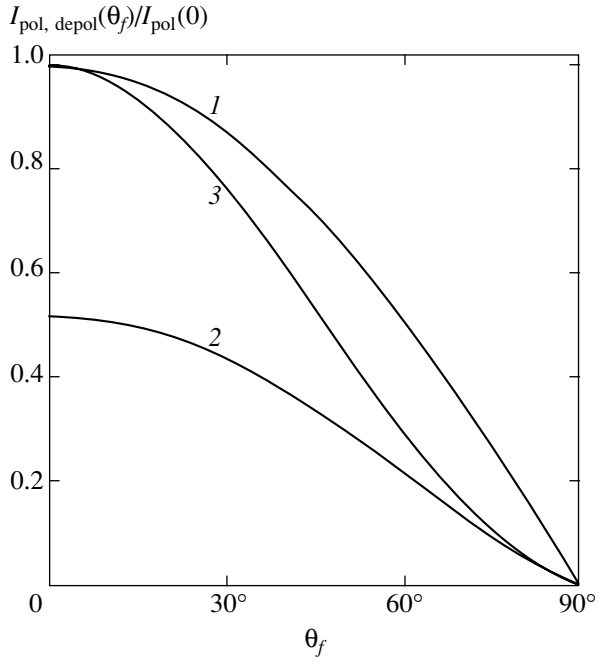

Fig. 3. Polarized, $I_{\text{pol}}(\theta_f)$, and depolarized, $I_{\text{depol}}(\theta_f)$, scattering intensities versus backscattering angle: *1*—the polarized component; *2*—the depolarized component when the incident wave field is normal to the scattering plane; and *3*—the polarized component when the incident wave field lies in the scattering plane. The depolarized component for this geometry almost coincides with curve *2*. The quantities were normalized to the intensity of the polarized scattering component at $\cos\theta_f = 1$.

In the case of nonpolarized incident light or when observing polarization-averaged light, γ_{pol} and γ_{depol}, there is no contribution from γ_- and the slope $\gamma = 1.89$, which determines the rate of decrease of the component γ_+, is close to $\gamma = 2$ in the scalar theory. However, when the two orthogonal polarizations are equally present in the incident light, we cannot get by with the approximation of pairwise equal indices.

At $t = 0$, the derived solution describes the intensity of the scattered light (without the interference component). We calculated the polarized, $I_{\text{pol}}(\theta_f)$, and depolarized, $I_{\text{depol}}(\theta_f)$, scattering intensities as a function of the backscattering angle θ_f for normal incidence. When the scattered ray lies in the *yz* plane, i.e., in the plane perpendicular to the polarization of the incident field, these components are

$$\begin{aligned} I_{\text{pol}}(\theta_f) &= \gamma_+(s_f, 1, 0) + \gamma_-(s_f, 1, 0), \\ I_{\text{depol}}(\theta_f) &= -s_f^{-2}[\gamma_e(s_f, 1, 0) + \gamma_-(s_f, 1, 0)]. \end{aligned} \tag{5.40}$$

When the scattered ray lies in the *xz* plane, i.e., the incident field is oriented in the scattering plane,

$$\begin{aligned} I_{\text{pol}}(\theta_f) &= -s_f^{-2}[\gamma_e(s_f, 1, 0) - \gamma_-(s_f, 1, 0)], \\ I_{\text{depol}}(\theta_f) &= \gamma_+(s_f, 1, 0) - \gamma_-(s_f, 1, 0). \end{aligned} \tag{5.41}$$

In Fig. 3, the polarized and depolarized backscattering intensities are plotted against the scattering angle for the two orientations of the scattering plane and the incident wave polarization under consideration. The angular function of the polarized component is different for different orientations of the incident wave polarization vector relative to the scattering plane. When the field of the incident wave is located in the scattering plane, the intensity of the scattered polarized component decreases with increasing scattering angle appreciably faster, starting from scattering angles on the order of 10°. The angular function of the depolarized component is the same for any initial polarization.

6. AN ELECTROMAGNETIC FIELD: THE DEGREE OF DEPOLARIZATION WITH ANISOTROPY IN THE P_1 APPROXIMATION

We restrict ourselves to calculating the difference between the polarized and depolarized components [see (5.1)] for normal incidence and scattering:

$$\begin{aligned} &\Gamma_-(\mathbf{R}_2, \mathbf{R}_1|t) \\ &= \frac{1}{2}[\Gamma_{11}(\mathbf{R}_2, \mathbf{R}_1|t) - \Gamma_{21}(\mathbf{R}_2, \mathbf{R}_1|t)]. \end{aligned} \tag{6.1}$$

We make the two-dimensional Fourier transform of this quantity and twice the Laplace transform and represent it in the P_1 approximation at $q = 0$ as

$$\begin{aligned} &\tilde{\Gamma}_-(s, s_i, t|\mathbf{k}_f, \mathbf{k}_i) \\ &\approx \frac{1}{4\pi}[\gamma_-^{(0)}(s, s_i t) - \cos\theta_f \gamma_-^{(1)}(s, s_i, t)]. \end{aligned} \tag{6.2}$$

Substituting Eq. (6.2) into the Bethe–Salpeter equation yields a system of equations for the components $\gamma_-^{(0)}(s, s_i, t)$ and $\gamma_-^{(1)}(s, s_i, t)$:

$$\begin{aligned} &(1 - 0.7g_0)\gamma_-^{(0)}(s, s_i, t) \\ &-\frac{3}{8}g_0 s^2(m_1(s) + 2m_2(s) + m_3(s))\gamma_-(s, s_i, t) \\ &= \frac{3g_0}{4(s_i + s)} - \frac{3g_0}{16}\int_1^\infty \frac{ds'}{s'}\left(1 + \frac{1}{s'^2}\right)^2 \frac{\gamma_-(s', s_i, t)}{s' - s}, \\ &\frac{3}{8}g_1 s(m_1(s) + 2m_2(s) + m_3(s))\gamma_-(s, s_i, t) \\ &+\frac{1}{3}\gamma_-^{(1)}(s, s_i, t) = \frac{3g_1}{4(s_i + s)} \\ &+\frac{3g_1}{16}\int_1^\infty \frac{ds'}{s'^2}\left(1 + \frac{1}{s'^2}\right)^2 \frac{\gamma_-(s', s_i, t)}{s' - s}, \end{aligned} \tag{6.3}$$

where we define the quantity

$$\gamma_-(s, s_i, t) = \gamma_-^{(0)}(s, s_i, t) - \frac{1}{s}\gamma_-^{(1)}(s, s_i, t), \qquad (6.4)$$

$m_3(s) = [m_2(s) - 1/5]/s^2$. At $s = s_f$, this combination determines the difference between the polarized and depolarized components of the time correlation function for the field.

Setting up a linear combination of Eqs. (6.3), we obtain a closed integral equation for function (6.4):

$$\psi_-(s, t)\gamma_-(s, s_i, t) = \frac{3g_0}{4(s_i + s)}\left[1 - \frac{3g_1}{sg_0}(1 - 0.7g_0)\right] - \frac{3g_0}{16}\int_1^\infty \frac{ds'}{s'}\left(1 + \frac{1}{s'^2}\right)^2\left[1 + \frac{3g_1}{ss'g_0}(1 - 0.7g_0)\right]\frac{\gamma_-(s', s_i, t)}{s' - s}, \qquad (6.5)$$

where

$$\psi_-(s, t) = (1 - 0.7g_0)\left[1 - \frac{9g_1}{8}(m_1 + 2m_2 + m_3)\right] - \frac{3g_0}{8}s_0(m_1 + 2m_2 + m_3). \qquad (6.6)$$

At low values of s and $t = 0$, we have

$$\psi_-(s, 0) \approx 0.3\left(1 - \frac{69}{70}\overline{\cos\theta}\right) - s^2\frac{23 + 14.1\overline{\cos\theta}}{70}. \qquad (6.7)$$

Since $\psi_-(s, 0)$ is finite at $s = 0$, the solution $\gamma_-(s, s_i, t)$ is formally regular near $t = 0$; i.e., no dependence of the form $\sqrt{t/\tau}$ arises. However, because the zero of the function $\psi_-(s, 0)$ approaches the coordinate origin when $\overline{\cos\theta} \longrightarrow 1$, i.e., in the case of strong single-scattering anisotropy, an almost nonanalytic dependence on t/τ arises in the range of short time scales (given $69/70 \approx 1$).

Given definition (6.6), Eq. (6.5) satisfies all of the conditions under which the Wiener–Hopf method can be used. Based on the method used to solve a similar equation for the scalar field, we obtain

$$\gamma_-(s, s_i, t) = \frac{D_1 + D_2 s}{\psi_-(0, t)s(s + s_i)}\exp[-J_-(s, t)], \qquad (6.8)$$

where

$$J_-(s, t) = \frac{s}{2\pi}\int_{-\infty}^{\infty}\frac{ds'}{s'^2 + s^2}\ln\frac{\psi_-(is', t)}{\psi_-(0, t)}. \qquad (6.9)$$

A condition similar to (3.20) can be imposed on the parameters D_1 and D_2 constant in s:

$$D_1 - \frac{D_1}{s_i} = \frac{3g_0}{4} \times \left[1 + \frac{3g_1}{s_i g_0}(1 - 0.7g_0)\right]\exp[-J_-(s_i, t)]. \qquad (6.10)$$

Substituting solution (6.8) into (6.5) and setting $s = 0$, we obtain

$$D_1 = -\frac{9}{4}g_1(1 - 0.7g_0)\left\{1 + \frac{s_i}{4}\int_1^\infty\frac{ds'}{s'^3} \times\left(1 + \frac{1}{s'^2}\right)^2\frac{(D_1 + D_2 s')\exp[-J_-(s', t)]}{s'(s' + s_i)\psi_-(0, t)}\right\}. \qquad (6.11)$$

The fundamental difference between the derived solution and the solution for the scalar field is the following. The parameter D_1 does not vanish at $t = 0$, implying that, in contrast to the scalar field, the intensity of the backscattered light for the electromagnetic field depends on the anisotropy parameter.

We calculated $\gamma_-(1, 1, t)$, which describes the difference between the polarized and depolarized components of the time correlation function, for various values of $\overline{\cos\theta}$ for normal incidence and scattering. The results are shown in Fig. 4. In the case of weak aniso-

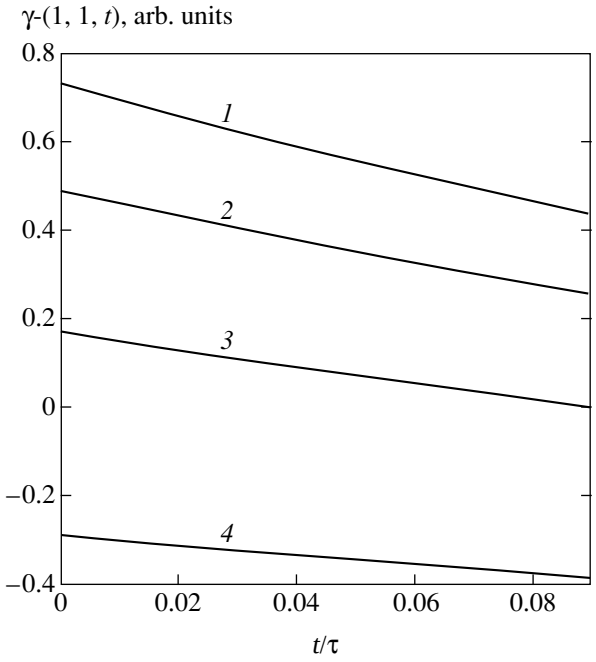

Fig. 4. The difference between the polarized and depolarized components of the time correlation function $\gamma_-(1, 1, t)$ versus time for normal incidence and scattering; $\overline{\cos\theta} = 0$ (*1*), 0.2 (*2*), 0.4 (*3*), and 0.6 (*4*).

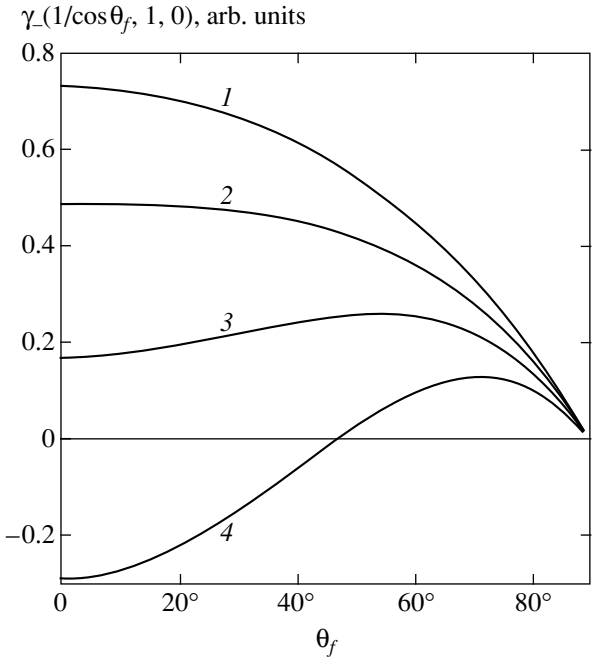

Fig. 5. The difference between the polarized and depolarized backscattering intensities $\gamma_-(s_f, 1, 0)$ versus the scattering angle; the values of $\overline{\cos\theta}$ are the same as those in Fig. 4.

tropy, at low values of $\overline{\cos\theta}$ the degree of polarization decreases linearly with increasing t/τ; it decreases much more slowly than do the polarized and depolarized components themselves, which decrease linearly with increasing $\sqrt{t/\tau}$. However, an unusual situation arises for systems with high values of $\overline{\cos\theta}$: the fraction of the depolarized component in the time correlation function increases with time compared to the polarized component.

Note that the aforesaid refers to the range $t/\tau \ll 1$; since, as was noted above, $\psi_-(0, 0)$ is small for $1 - \overline{\cos\theta} \ll 1$, t/τ rather than $(1 - \overline{\cos\theta})t/\tau$ is the expansion parameter.

We also calculated $\gamma_-(s_f, 1, t = 0)$, which describes the difference between the polarized and depolarized backscattering intensities as a function of the scattering angle. The results are shown in Fig. 5 for various values of $\overline{\cos\theta}$. The difference between the intensities of the polarized and depolarized backscattering components is seen to strongly depend on the anisotropy parameter. For weakly anisotropic systems, the degree of polarization monotonically decreases with increasing scattering angle. For moderate anisotropy parameters, $\overline{\cos\theta} \sim 0.4$, the relative fraction of the depolarized component increases with scattering angle compared to the corresponding value for backscattering. Finally, at large anisotropies, $\overline{\cos\theta} \geq 0.6$, a situation where the polarization changes sign with increasing scattering angle arises: the depolarized component of the scattered light becomes larger than its polarized component.

7. CONCLUSION

We have managed to use the Wiener–Hopf method, which underlies the classical Milne solution for the intensity of the scattering of a scalar field by point scatterers, to solve several more substantive problems of multiple scattering. In the case of a scalar field, we obtained a solution for the time correlation function by taking into account anisotropy in the P_1 and P_2 approximations, which is in satisfactory agreement with experimental data. We found a solution that described the initial angular function of coherent backscattering in the P_1 approximation, which can be used as the initial approximation in numerical calculations for highly anisotropic systems.

We generalized the Milne solution to an electromagnetic field. In the case of isotropic scattering, we found a solution for the time correlation function for the polarized and depolarized components. In the case of anisotropic scattering, a solution was found for the difference between these components. In the case of strong anisotropy, $\overline{\cos\theta} \sim 0.4$–$0.6$, we detected unusual polarization effects. The polarization effects for coherent backscattering by Rayleigh particles were predicted in [20] even for nonpolarized incident light. We described the effects associated with single-scattering anisotropy: the change in the relative rate of decrease of the polarized and depolarized components when passing to highly anisotropic systems and the change of depolarization sign with increasing scattering angle. These effects need to be experimentally tested.

We considered the single-scattering anisotropy in the P_1 approximation. Strictly speaking, it is applicable to weakly anisotropic systems, $\overline{\cos\theta} \ll 1$. Its application to significantly anisotropic scattering is based on the physical assumption that the light becomes almost isotropic after multiple scattering, although the single scattering is highly anisotropic. This assumption needs to be additionally tested.

In the problems under consideration, the scattering must be mainly elastic. The regime of multiple scattering must be realized, $l \ll L$. In addition, the scattering must be weak, $\lambda \ll l$. Such a situation takes place in complex colloidal, often artificial systems: suspensions, gels, foams, and biological tissues. We ignored the near-field effects and disregarded the internal reflection at the boundary [11] due to the difference between the refractive indices.

ACKNOWLEDGMENTS

We wish to thank V.P. Romanov for discussions. This study was supported in part by the Russian Foun-

dation for Basic Research (project no. 02-02-16577) and the Competitive Center for Fundamental Science (project no. PD02-1.2-297).

REFERENCES

1. M. C. W. van Rossum and Th. N. Nieuwenhuizen, Rev. Mod. Phys. **71**, 313 (1999).
2. A. Ishimaru, *Wave Propagation and Scattering in Random Media* (Academic, New York, 1978; Mir, Moscow, 1981), Vols. 1 and 2.
3. M. P. van Albada and A. Lagendijk, Phys. Rev. Lett. **55**, 2692 (1985).
4. P. E. Wolf and G. Maret, Phys. Rev. Lett. **55**, 2696 (1985).
5. E. Akkermans, P. E. Wolf, R. Maynard, and G. Maret, J. Phys. (Paris) **49**, 77 (1988).
6. Yu. N. Barabanenkov and V. D. Ozrin, Zh. Éksp. Teor. Fiz. **94**, 56 (1988) [Sov. Phys. JETP **67**, 1117 (1988)].
7. M. J. Stephen, Phys. Rev. B **37**, 1 (1988).
8. D. J. Pine, D. A. Weitz, P. M. Chaikin, and E. Herbolzheimer, Phys. Rev. Lett. **60**, 1134 (1988).
9. E. E. Gorodnichev, S. L. Dudarev, and D. B. Rogozkin, Zh. Éksp. Teor. Fiz. **96**, 847 (1989) [Sov. Phys. JETP **69**, 481 (1989)].
10. E. E. Gorodnichev, S. L. Dudarev, and D. B. Rogozkin, Phys. Lett. A **144**, 48 (1990).
11. T. M. Nieuwenhuizen and J. M. Luck, Phys. Rev. E **48**, 569 (1993).
12. V. L. Kuz'min and V. P. Romanov, Zh. Éksp. Teor. Fiz. **116**, 1912 (1999) [JETP **89**, 1035 (1999)].
13. E. Amic, J. M. Luck, and T. M. Nieuwenhuizen, J. Phys. A **29**, 4915 (1996).
14. V. L. Kuzmin, V. P. Romanov, and E. V. Aksenova, Phys. Rev. E **65**, 016601 (2002).
15. V. L. Kuzmin and V. P. Romanov, Europhys. Lett. **59**, 206 (2002).
16. D. S. Wiersma, A. Muzzi, M. Colocci, and R. Righini, Phys. Rev. E **62**, 6681 (2000).
17. M. J. Stephen and G. Cwilich, Phys. Rev. B **34**, 7564 (1986).
18. M. I. Mishchenko, Phys. Rev. B **44**, 12597 (1991).
19. M. I. Mishchenko, J. Quant. Spectrosc. Radiat. Transf. **56**, 673 (1996).
20. E. Amic, J. M. Luck, and T. M. Nieuwenhuizen, J. Phys. I **7**, 445 (1997).
21. M. I. Mishchenko, J. M. Luck, and T. M. Nieuwenhuizen, J. Opt. Soc. Am. A **17**, 888 (2000).
22. V. L. Kuz'min, Opt. Spektrosk. **93**, 482 (2002) [Opt. Spectrosc. **93**, 439 (2002)].
23. B. Shapiro, Phys. Rev. Lett. **57**, 2168 (1986).
24. Yu. N. Barabanenkov, Izv. Vyssh. Uchebn. Zaved. Radiofiz. **16**, 88 (1973).
25. A. Golubentsev, Zh. Éksp. Teor. Fiz. **86**, 47 (1984) [Sov. Phys. JETP **59**, 26 (1984)].
26. M. B. van der Mark, M. P. van Albada, and A. Lagendijk, Phys. Rev. B **37**, 3575 (1988).
27. F. C. MacKintosh and S. John, Phys. Rev. B **40**, 2383 (1989).
28. S. Chandrasekhar, *Radiative Transfer*, 2nd ed. (Dover, New York, 1960; Inostrannaya Literatura, Moscow, 1953).
29. V. L. Kuz'min and V. P. Romanov, Opt. Spektrosk. **82**, 642 (1997) [Opt. Spectrosc. **82**, 593 (1997)].

Translated by V. Astakhov

Journal of Experimental and Theoretical Physics, Vol. 96, No. 5, 2003, pp. 832–845.
Translated from Zhurnal Éksperimental'noĭ i Teoreticheskoĭ Fiziki, Vol. 123, No. 5, 2003, pp. 946–961.

ATOMS, SPECTRA, RADIATION

Fractals and Chaotic Scattering of Atoms in the Field of a Standing Light Wave

V. Yu. Argonov and S. V. Prants*

Il'ichev Pacific Oceanological Institute, Far East Division, Russian Academy of Sciences, ul. Baltiiskaya 43, Vladivostok, 690041 Russia

**e-mail: prants@poi.dvo.ru*

Received November 25, 2002

Abstract—The motion of a two-level atom with an internal degree of freedom that interacts with the field of a single-mode standing light wave in a high-Q cavity is treated as a scattering problem. At detunings between atomic and field resonances δ, atomic recoil frequencies α, initial atomic momenta ρ_0, and numbers of excitations N at which the semiclassical equations have chaotic solutions (in the sense of their exponential sensitivity to small changes in the initial conditions), atomic scattering is fractal with strongly pronounced self-similarity of the dependence of time T at which the atom leaves the cavity at its initial momentum; the fractal dimension of this curve is 1.84. In the chaotic regime, there are two infinite sets of atomic initial momenta for which $T = \infty$ (in the idealized case of the absence of any loss). They correspond to separatrix-like trajectories along which the atom asymptotically approaches certain configuration space points and to the trajectories of infinitely long chaotic wandering of atoms in the cavity. These trajectories make up countable and uncountable fractals, respectively. Correlations between Rabi atomic oscillations and atomic motion can lead to Doppler–Rabi resonances, that is, deep oscillations of the internal energy of the atom, for large detunings δ that satisfy the condition $|\alpha\rho_0| \approx |\delta|$. © *2003 MAIK "Nauka/Interperiodica".*

1. INTRODUCTION

As is known, dynamical chaos in classical systems is characterized by exponentially fast divergence of initially close trajectories in a limited phase space region. Such a behavior is possible because of the continuity of the classical phase space, whose points (therefore, classical system states) can be arbitrarily close to each other. The trajectory concept is absent in quantum mechanics, and the phase space is not continuous by virtue of the Heisenberg uncertainty relation. The evolution of an isolated quantum system is unitary, and there can be no chaos in the sense of exponential instability, for instance, of its states. What is usually understood under "quantum chaos" is, in essence, the special features of the unitary evolution of a quantum system (no matter what it is) in the region of its parameter values and initial conditions at which its classical analog is chaotic [1]. However, actual quantum systems are not isolated; they interact with their environment and, if attempts are made to measure their state, with a classical instrument, which should, by virtue of its purpose, be in an unstable state. Coherence loss caused by irremovable interaction with the environment (decoherence) breaks quantum unitarity, suppresses the quantum properties of motion, and reveals its classical properties. A classic example is a periodically kicked quantum rotor. Taking into account the heat bath in quantum equations of motion of such a rotor leads to linear energy diffusion characteristic of the classical analog of this system [2]. The unitary evolution of a quantum rotor without the bath is known to suppress energy diffusion and cause dynamical localization [3]. Such a situation can be modeled with the use of a quantum–classical hybrid, by a system with quantum and classical degrees of freedom interacting with each other. Such hybrids, for instance, arise if the internal degree of freedom of a particle is described by a quantum equation of motion (a Schrödinger or Heisenberg equation), and the degree of freedom dynamically coupled to it, by the Hamilton equation in mechanics or the Maxwell equation in electrodynamics. Semiclassical and semiquantum equations of motion also appear as a consequence of the reduction of Heisenberg equations, which partially conserves quantum correlations and fluctuations (for instance, see the $1/N$ decomposition method [4]). Quantum–classical hybrids are of interest not only by themselves, but also as prototypes of the interaction of quantum objects with a macroscopic environment.

This work was inspired by the impressive advances in cavity quantum electrodynamics and atomic optics, in manipulating separate atoms and photons in high-Q cavities (e.g., see [5–8]), which would, in turn, be impossible without studies on the mechanical action of light on atoms, laser cooling of atoms, etc. (e.g., see [9, 10]). During excitation exchange between an atom and a selected field mode, not only the electronic state of the atom and the state of the field in the cavity, but

also the velocity and the position of the center of mass of the atom change. Under strong coupling conditions [$\Omega_0\sqrt{N} \gg \max(T_a^{-1}, T_f^{-1})$, where $T_{a,f}$ are the relaxation times of the atom and mode, respectively, Ω_0 is the amplitude of the atom–field coupling coefficient, and N is the number of excitations], the corresponding Hamiltonian (1) includes three degrees of freedom (translational, electronic, and field) and their interactions. We showed in [11, 12] that the semiclassical equations of motion that (1) generates may lead to Hamiltonian chaos. Chaos arises because of interactions between nonlinear resonances [13]. It generally manifests itself as atomic motions in the cavity characterized by random wanderings interrupted by regular oscillations close to the optical potential bottom and long flights at a virtually constant velocity (Lévy flights) [14]. The strong-coupling mode was experimentally implemented for Rydberg atoms in microwave cavities [5] and for usual atoms in optical microcavities [6, 7].

In this work, the same atom–field system is considered in the context of chaotic scattering of atoms in the field of a standing light wave. The problem is to give a dynamical and statistical description of scattering of particles that enter a bounded region of some nonlinear determinate "potential" from the outside. Such problems arise with billiards [15], advection of passive impurities in simple hydrodynamic flows [16], ionization of atoms [17], etc. We show that chaotic motion of atoms has fractal properties, namely, the dependence of the exit time of atoms from the cavity at their initial momentum is fractal with strongly pronounced self-similarity. Another object of this paper, not touched upon in [11–14], is to study correlations between Rabi oscillations (atomic internal energy oscillations) and the motion of the atom. For this purpose, we consider the Doppler–Rabi resonance, that is, deep low-frequency Rabi oscillations caused by the Doppler effect, which are observed at a nearly arbitrary ratio between the atomic transition and cavity mode frequencies provided that $|\alpha\rho_0| \approx |\delta|$. We prove in the Appendix that the equations of motion for the electron–field subsystem obtained by the factorization of Heisenberg operator equations are fully equivalent to the quantum equations for the corresponding probability amplitudes describing the internal state of the atom and a Fock state of the field mode. It follows that we indeed deal with a quantum–classical hybrid, at least when the field is in a Fock state.

2. EQUATIONS OF MOTION

A two-level atom with mass m_a and working transition frequency ω_a is situated in a high-Q single-mode cavity. The field within the cavity has the form of a standing wave along axis x with frequency ω_f and wave vector k_f. When the atom moves along this axis, the atom–field coupling coefficient varies and photon absorption and emission change not only the internal state of the atom and the state of the field, but also the velocity of the atom. In the strong-coupling limit, the dynamics of interaction of all three degrees of freedom (translational, electronic, and field) is Hamiltonian with the operator

$$\hat{H} = \frac{\hat{p}^2}{2m_a} + \frac{1}{2}\hbar\omega_a\hat{\sigma}_z + \hbar\omega_f\left(\hat{a}^\dagger\hat{a} + \frac{1}{2}\right) - \hbar\Omega_0(\hat{a}^\dagger\hat{\sigma}_- + \hat{a}\hat{\sigma}_+)\cos(k_f\hat{x}), \quad (1)$$

whose terms describe the kinetic, intraatomic, and field energies and the interaction energy between the atom and the standing wave field. The coordinates and momentum operators of the atom ($\hat{x}$ and $\hat{p}$), the operators of creation and annihilation of photons ($\hat{a}^\dagger$ and $\hat{a}$), and the Pauli spin operators ($\hat{\sigma}$) satisfy the standard commutation relations

$$[\hat{x}, \hat{p}] = i\hbar, \quad [\hat{a}, \hat{a}^\dagger] = 1,$$

$$[\hat{\sigma}_\pm, \hat{\sigma}_z] = \mp 2\hat{\sigma}_\pm, \quad [\hat{\sigma}_+, \hat{\sigma}_-] = \hat{\sigma}_z.$$

In deriving the equations of motion of the strongly coupled atom–field system, we partially simplify the problem by assuming that the atom is a point mass (which is admissible for the atom, whose momentum is much larger than the momentum of the photon). Because the number of excitations is conserved during operator evolution,

$$\hat{N} = \hat{a}^\dagger\hat{a} + \frac{\hat{\sigma}_z + 1}{2}.$$

Hamiltonian (1) gives a closed system of Heisenberg equations for the operators $\hat{x}$, $\hat{p}$, $\hat{\sigma}_z$, $\hat{u} = \hat{a}^\dagger\hat{\sigma}_- + \hat{a}\hat{\sigma}_+$, and $\hat{v} = i(\hat{a}^\dagger\hat{\sigma}_- - \hat{a}\hat{\sigma}_+)$. The transition to the expectation values

$$\xi = k_f\langle\hat{x}\rangle, \quad \rho = \frac{p}{\hbar k_f}\langle\hat{p}\rangle, \quad u = \langle\hat{u}\rangle, \quad v = \langle\hat{v}\rangle, \quad z = \langle\hat{\sigma}_z\rangle \quad (2)$$

in these equations and the factorization of the product of operators, $\langle\hat{N}\hat{\sigma}_z\rangle = \langle\hat{N}\rangle\langle\hat{\sigma}_z\rangle = Nz$, yields the sought semiclassical equations of motion [12],

$$\dot{\xi} = \alpha\rho, \quad \dot{\rho} = -u\sin\xi, \quad \dot{u} = \delta v, \quad \dot{v} = -\delta u + 2Nz\cos\xi, \quad \dot{z} = -2v\cos\xi, \quad (3)$$

where dots denote the differentiation with respect to the normalized time $\tau = \Omega_0 t$. The number of excitations $N = n + (1 + z)/2$ (where n is the mean number of mode photons), the normalized detuning $\delta = (\omega_f - \omega_a)/\Omega_0$, and the normalized optical recoil frequency, $\alpha = \hbar k_f^2/m_a\Omega_0$

(which characterizes changes in the kinetic energy of the atom caused by photon emission and absorption) are the control parameters of the nonlinear dynamical system (3), which has two integrals of motion, namely,

$$W = \frac{\alpha}{2}\rho^2 + U, \tag{4}$$

$$R = u^2 + v^2 + Nz^2. \tag{5}$$

In the expression for the total energy of the system W, the

$$U = -u\cos\xi - \frac{\delta}{2}z \tag{6}$$

term is separated. This term has the meaning of the effective potential energy, because the $-\partial U/\partial\xi = -u\sin\xi$ value is the force that acts on the atom. By virtue of the equality $u^2 + v^2 = n(x^2 + y^2)$ [18], the R/N value is the conserved Bloch vector length $x^2 + y^2 + z^2 = 1$ ($x = \langle\hat{\sigma}_x\rangle$ and $y = \langle\hat{\sigma}_y\rangle$) in the limit of a large number of quanta $n \gg 1$.

As is known, the semiclassical approximation used to derive equations of motion (3) ignores quantum correlation and fluctuation effects. Depending on the operators for which the initial Heisenberg equations are written and on the operator products that are factorized, different equations of motion for identical quantum means can be obtained in the semiclassical approximation. These equations naturally transform into each other in the limit of a large number of quanta. In [13, 14], the operator products of the $\hat{\sigma}_{x,y,z}$ and $(\hat{a}^\dagger \pm \hat{a})$ operators were factorized for Hamiltonian (1) in the Heisenberg representation. The resulting semiclassical equations for the means defined by (2) differed from (3) by the presence of the $(2N-1)z - 3z^2/2 + 1/2$ square trinomial in the equation for $\dot{v}$ (in addition, a different normalization was used in [14]). The attractive property of equations (3) is their closeness in form to the quantum equations of motion for electron–field interaction, as is proved in the Appendix. Moreover, they coincide with the quantum equations for a field in a cavity prepared in a Fock state with a given number of quanta and an atom in one of its energy states. All results were obtained in this work with the use of system (3).

3. CHAOTIC MOTION OF THE ATOM AND ITS STATISTICAL ANOMALIES

If the ω_f mode and ω_a atomic transition frequencies coincide exactly, that is, at $\delta = 0$, system (3) is integrable in quadratures because of the arising of the additional conservation law $u = u_0$ (u_0 is the initial u value). The effective potential energy (6) becomes a single-valued function of the coordinate, $U = -u_0\cos\xi$, and completely reproduces the standing wave structure. Motion in a stationary potential field is described by the physical pendulum equation

$$\ddot{\xi} + \alpha u_0 \sin\xi = 0, \tag{7}$$

which obviously follows from the first two equations of the system and has the well-known solutions in terms of the Jacobi elliptic functions [12]. Equation (4) for the energy determines the analytic dependence of the momentum on the coordinate,

$$\rho = \pm\sqrt{\frac{2}{\alpha}(W + u_0\cos\xi)}. \tag{8}$$

Depending on the initial momentum ρ_0 value, two types of motion are possible, namely, infinite flight of the atom through the cavity at $\rho_0 > \rho_{cr}$ and finite oscillations in the potential well at $\rho_0 < \rho_{cr}$. The intermediate case with $\rho_0 = \rho_{cr}$ corresponds to asymptotic approach of the atom to the point corresponding to the potential energy maximum [motion along the separatrix over the phase portrait, which can be constructed directly from (8)]. Here, ρ_{cr} is the critical momentum determined by the condition $\xi = (2k+1)\pi$, $\rho = 0$, where k is an arbitrary integer. It is easy to show that $\rho_{cr} = 2\sqrt{u_0/\alpha}$. In dimensional units, this corresponds to the $v_{cr} = 2\sqrt{\hbar\Omega_0 u_0/m_a}$ velocity of the atom. It follows that, under the conditions of the exact atom–field resonance, the translational motion of the atom is independent of the dynamics of the electronic and field subsystems and only depends on the initial electron–field interaction energy u_0, which determines the depth of the optical potential U. The population inversion z is a regular Rabi oscillation signal modulated by the standing wave, see Section 5.1 for details.

Equations (3) with two integrals of motion (5) are a Hamiltonian autonomous system with two degrees of freedom and motion over a three-dimensional hypersurface with a given energy W value. Generally, such a system has a positive Lyapunov exponent λ, a negative exponent equal in magnitude to the positive exponent, and two zero exponents. The sum of all Lyapunov exponents of a Hamiltonian system is zero [19]. The largest Lyapunov exponent characterizes the mean rate of the exponential divergence of initially close trajectories,

$$\lambda = \lim_{\tau\to\infty}\lambda(\tau), \quad \lambda = \lim_{\Delta(0)\to 0}\frac{1}{\tau}\ln\frac{\Delta(\tau)}{\Delta(0)}, \tag{9}$$

and serves as a quantitative measure of dynamical chaos in the system. Here, $\Delta(\tau)$ is the distance (in the Euclidean sense) at time τ between two trajectories close to each other at initial time $\tau = 0$. The dependence of λ on control parameters and initial conditions was calculated in [11, 12]; it was shown that dynamical chaos in a strongly coupled atom–field system existed

in a wide range of N, α, and initial atomic momentum ρ_0 values. The $\lambda(\delta)$ dependence is a function which equals zero at $\delta = 0$ and has two maxima almost symmetrical with respect to zero detuning; this function fairly rapidly tends to zero as $|\delta|$ increases [11]. For instance, for a reasonable recoil frequency $\alpha = 10^{-3}$, the number of excitations $N = 10$, and the initial momentum $50 \lesssim \rho_0 \lesssim 100$, λ values were zero (to within the accuracy of calculations) at $|\delta| \gtrsim 1.7$.

It follows from (3) that the translational motion of the atom at $\delta \neq 0$ is described by the equation of a nonlinear physical pendulum with frequency modulation,

$$\ddot{\xi} + \alpha u(\tau)\sin\xi = 0, \qquad (10)$$

in which u is a function of both time and all the other dynamical variables. The normalized Rabi oscillation frequency is a value on the order of $\Omega = \sqrt{\delta^2 + 4N} > 1$, which substantially exceeds the frequency of small-amplitude translational motion $\sqrt{\alpha u_0} \ll 1$. Taking this into consideration, the author of [13] revealed the mechanism of the arising of chaos in an atom–field system. The stochastic layer width was estimated as[1]

$$\Delta \approx 8\pi\left(\frac{\Omega}{\omega}\right)^3 \exp\left(-\frac{\pi\Omega}{2\omega}\right), \qquad (11)$$

where $\omega = \sqrt{2\alpha N|\delta|}/\Omega$ and $\Omega/\omega \gg 1$. The Δ value is the change in energy in the neighborhood of the unperturbed separatrix normalized with respect to the pendulum separatrix energy ω^2. Small changes in the energy cause comparatively small changes in the frequency of oscillations. For energies of motion that are strongly different from the separatrix energy, that is, close to potential well bottoms and high above optical potential U hills, small frequency changes cause small phase changes during the translation motion period. However, close to the unperturbed separatrix, where the period of oscillations tends to infinity, even small frequency changes can cause substantial phase changes. This is the reason for the exponential instability of motions of the parametric nonlinear oscillator (10) and chaotic atomic motions in the field of a periodic standing wave.

A clear idea of the character of chaotic wandering can be developed using the model of "two potentials." In this model, the optical potential U reproduces the structure of the standing wave in the cavity with a 2π period and its amplitude is u_0 (see Fig. 1a). Far from the resonance, at $|\delta| \gtrsim 1.7$, the potential has period π and is approximately described by (25) at $|\delta| \gg 1$ (see Fig. 1e). These potentials will be called resonant and nonresonant, respectively. All numerical calculations were performed in this work for the number of excitations $N = 10$, recoil frequency $\alpha = 10^{-3}$, and initial conditions $\xi_0 = 0$, $z_0 = 0$, and $u_0 = v_0 = \sqrt{4.5}$ (unless otherwise specified, see Section 5). By calculating dynamical variables u, ξ, and z at each instant of time τ, the dependence of U on $\xi(\tau)$ can be constructed according to (6) for an arbitrary detuning value. However, the resulting $U[\xi(\tau)]$ function is aperiodic for the δ values at which the maximum Lyapunov exponent is larger than zero (Figs. 1b, 1c, 1d). This function is generally ambiguous at certain ρ_0 values, because it depends not only on the position of the atom, but also on all dynamical variables of the system. We can say that, when motion in the cavity is chaotic, the resonant and nonresonant potentials shown in Figs. 1a and 1e "virtually" coexist at each instant of time. The well depths in both structures change as time passes, and the atom randomly gets into one or another structure every time it crosses a standing light wave node. The probability of getting into the resonant or nonresonant potential regions depends on the detuning. In particular, in Figs. 1b and 1d, the atom is in the same potential region almost the whole time and only rarely gets into another for a short time. However, note that this model is only a simplification introduced for illustration purposes. The real dynamics is described by system (3), which strictly corresponds to some sensible image only in particular cases.

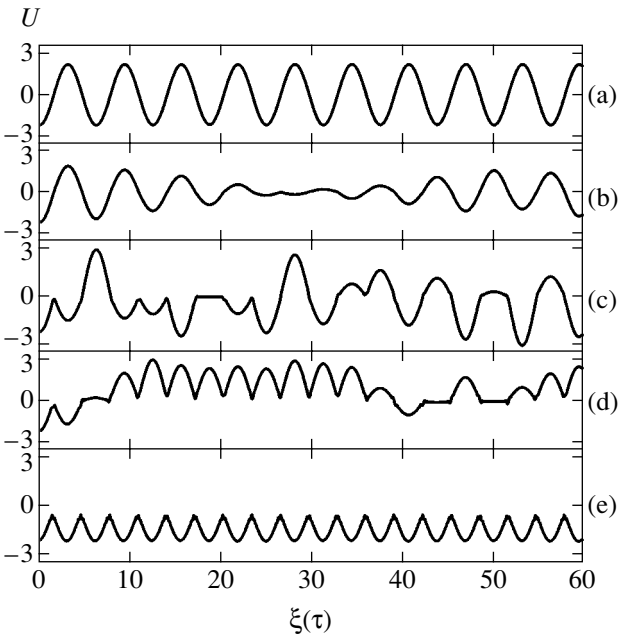

Fig. 1. Dependence of the potential energy of the atom on the coordinate for detunings δ = (a) 0.002, (b) 0.04, (c) 0.4, (d) 0.9, and (e) 2; $\rho_0 = 110$.

[1] The equation for $\dot{v}$ in [13] was written in the form specified in the end of the preceding section. The whole analysis was, however, based on the linearization of the trinomial mentioned above.

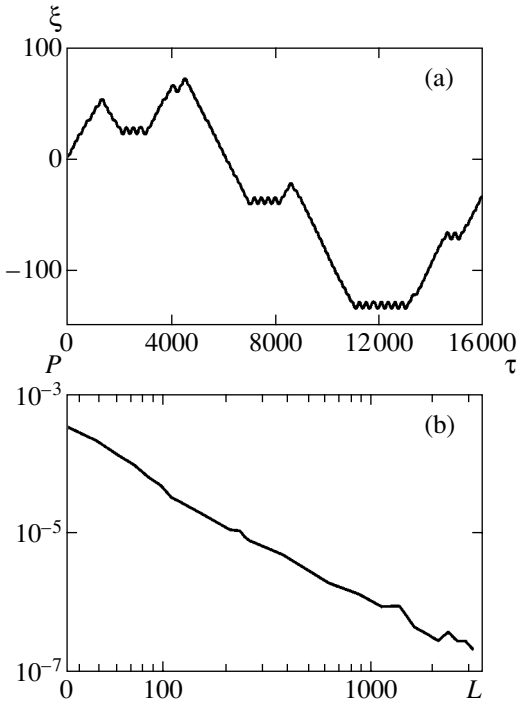

Fig. 2. (a) Chaotic atomic trajectory with Lévy flights and (b) distribution function P in flight lengths L on the log–log scale for $\delta = 0.01$.

An example of a typical chaotic trajectory of the atom in the cavity is shown in Fig. 2a. The atom changes the direction of its motion, alternatively oscillating in small space regions and performing long flights at a virtually constant velocity. These so-called Lévy flights are typical of Hamiltonian systems with a nonuniform phase space, in which regular motion regions (KAM-tori) with a complex hierarchical structure, stochastic layers, semidestroyed tori (cantori), etc., coexist [15, 19, 20]. When a chaotic trajectory approaches the boundary of an external KAM-torus, where cantori are situated, the figurative point can stick there for a long time with mimicking of regular motion. The times of so-called "sticking" to the boundaries of KAM-tori can be arbitrary, because cantori prevent trajectories from escaping into the stochastic "sea." In our case, the sticking effect manifests itself by long atom ballistic flights in the cavity. The existence of such flights results in an anomalous Hamiltonian kinetics, that is, intermittence of normal diffusion and Lévy flights. We define the flight length as the distance covered by the atom between two points of velocity sign reversal. The log–log plot of the flight length distribution function $P(L)$ constructed from the results of calculations with 21 trajectories in the range $93 \le \rho_0 \le 94$ with the integration time equal to 3.2×10^6 dimensionless units for each trajectory is shown in Fig. 2b. An exponential decrease in the initial distribution function region (up to $L \approx 100$) is the contribution of normal diffusion of the atom. The well-defined power law $P(L) \propto L^{-1.5 \pm 0.1}$ in the remaining function region corresponds to Lévy ballistic flights; the recorded length of these flights amounts to 2×10^4 dimensionless length units. A power distribution function is expected to correspond to a power time dependence of the mean square displacement of the atom $\langle \xi^2 \rangle \propto \tau^\gamma$ with the exponent $\gamma > 1$ characteristic of superdiffusion. Note that this result was obtained for comparatively weak chaos observed at $\delta = 0.01$. Similar calculations performed for $\delta = 0.4$ (strong chaos) give a virtually normal distribution of flight lengths.

Lévy flights for motions of an atom in a standing light wave field were observed in [14]. The statistical properties of atom–field interaction were studied in detail. In particular, the distributions of Poincaré recurrence times and the evolution of the moments of atomic positions were calculated. Various regimes of motion were revealed, from virtually normal (Gauss) diffusion of the atom to superdiffusion corresponding to atomic ballistic motion with acceleration. In [14], numerical experiments were performed with a version of semiclassical equations of motion nonlinear in z for a fairly large number of excitations $N = 10$; that is, the $2Nz$ term was predominant in the equation for $\dot{v}$. It follows that, other conditions being equal, the distribution of Poincaré recurrence times and the evolution of the moments of atomic positions for our equations (3) should be similar to the statistical characteristics calculated in [14].

4. THE FRACTAL PROPERTIES OF ATOMIC MOTION

4.1. Chaotic Scattering of Atoms

Consider a Gedanken experiment with a unit consisting of a single-mode Fabry–Perot cavity and two detectors capable of recording atomic collisions with each of the cavity mirrors (Fig. 3a). The cavity length is such that the optical standing wave has two antinodes. Let the origin be at the center of the left antinode and let atoms with different initial momenta ρ_0 directed along the cavity axis be sequentially placed at the point $\xi = 0$ The exit time T of atoms is measured by recording their collisions with the cavity mirrors. Let us study the dependence of the exit time on the initial momentum ρ_0, all other conditions being equal.

If the atom–field resonance is exact, three scenarios are possible. An atom with the initial momentum $\rho_0 < \rho_{cr}/\sqrt{2}$ is incapable of reaching even the node of the standing wave and is captured by the field. If $\rho_{cr}/\sqrt{2} \le \rho_0 < \rho_{cr}$, the atom crosses the node but is incapable of reaching the top of the barrier, changes the direction of its motion, and is recorded by the left detector. Lastly, if $\rho_0 > \rho_{cr}$, the atom overcomes the potential barrier and is recorded by the right detector. Using the analytic

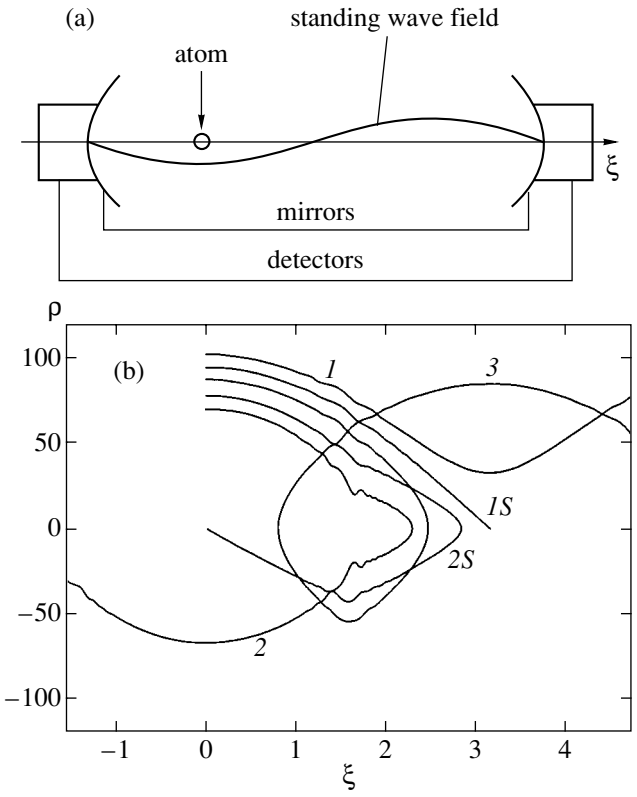

Fig. 3. (a) Scheme of gedanken experiment including a microcavity with a standing light wave and detectors and (b) examples of phase trajectories of chaotic atoms with different initial momenta ρ_0.

expression for the $\xi(\tau)$ dependence obtained in [12] and taking into account the dimensionless mirror coordinates $-\pi/2$ and $3\pi/2$, we obtain the sought dependence in the form

$$T(\rho_0) = \begin{cases} \infty, & \rho_0 < \dfrac{\rho_{cr}}{\sqrt{2}}, \\ \dfrac{1}{\sqrt{\alpha u_0}} F\left[\arcsin\left(-\dfrac{1}{K\sqrt{2}}\right), K\right], & \dfrac{\rho_{cr}}{\sqrt{2}} \le \rho_0 < \rho_{cr}, \\ \infty, & \rho_0 = \rho_{cr}, \\ \dfrac{2}{\alpha\rho_0} F\left[\dfrac{3\pi}{4}, K\right], & \rho_0 > \rho_{cr}, \end{cases} \tag{12}$$

where F is the incomplete elliptic integral of the first kind with the modulus $K = \rho_0\sqrt{\alpha/u_0}/2$.

At small detunings $|\delta| \gtrsim 1.7$, slow atoms are captured by the field, while fast atoms fly through without experiencing noticeable field effects. However, there also exists a fairly wide range of initial momenta ρ_0 such that, because of the chaotic wandering effect, the atom makes a certain number of oscillations within the cavity before being detected. Some possible atomic phase trajectories in the (ξ, ρ) plane are shown in Fig. 3b. In spite of the stochastic properties of atomic motions, the particular shape of each trajectory is unambiguously determined by the initial conditions and system parameters. In particular, the result (specifically, the exit time T) is only determined by the initial momentum ρ_0 value, all other conditions being equal. A numerical study of the $T(\rho_0)$ dependence shows that it has a hierarchical structure typical of chaotic scattering. The dependence of the exit time on the initial momentum is shown in Fig. 4a for a wide range of ρ_0 values.

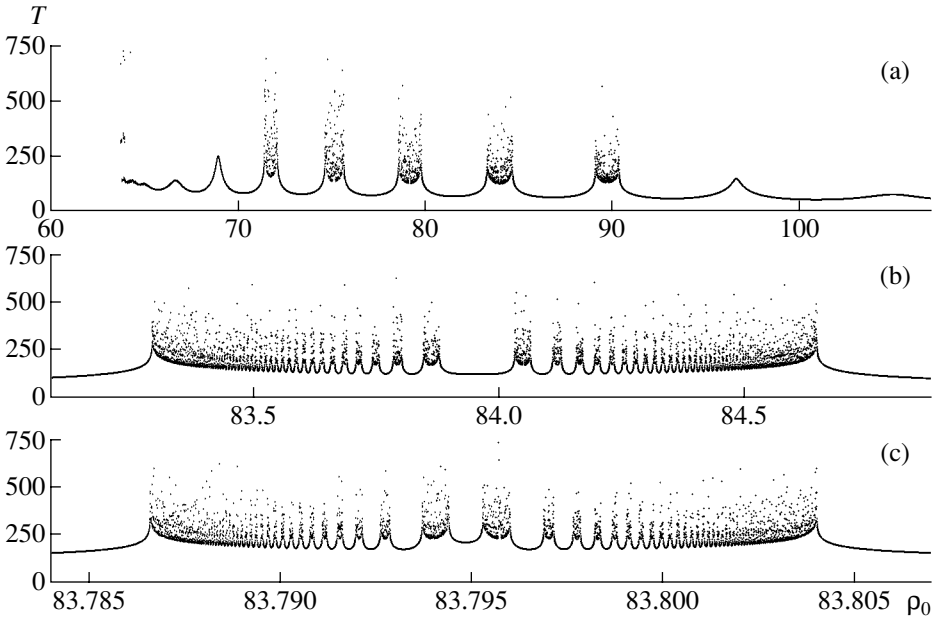

Fig. 4. Fractal dependence of time T at which the atom leaves the cavity on the initial momentum of the atom ρ_0 for $\delta = 0.4$.

According to this figure, the atom does not reach mirrors at low initial momenta $\rho_0 \lesssim 63$, because it is then captured by the standing wave field. At larger ρ_0 values, alternation of smooth and badly resolvable function regions is observed. Magnifying one of such regions shows that the region itself has a similar structure (Fig. 4b). Irresolvable function regions will therefore be called function substructures. A still more impressive picture emerges when we compare Figs. 4b and 4c. Here, multiple magnification exhibits complete self-similarity of the structures. Self-similarity is conserved if magnification is repeated, apparently, no matter what the number of repetitions. The structure shown in Fig. 4a will be called the first-order structure, its substructure (Fig. 4b), the second-order structure, etc. The regular portions of higher order structures correspond to longer exit times *T;* the characteristic increase in *T* remains almost unchanged as the order of the structure increases. Exit times for irregular regions also continuously increase with increasing resolution (structure order). This means that there exist atoms that indefinitely oscillate inside the cavity until they are detected. The set of initial momentum ρ_0 values corresponding to $T = \infty$ is a one-dimensional fractal; that is, a subset of the fractal shown in Fig. 4. It is proved below that the fractal with $T = \infty$ is the sum of two physically different sets, one of which is countable and the other uncountable.

The fractal under consideration is a set of points with the coordinates

$$\left(\rho_0^{(j)} = \rho_0^{(\min)} + \frac{j}{j_{\max}}(\rho_0^{(\max)} - \rho_0^{(\min)}),\ T^{(j)}\right),$$

$$0 \le j \le j_{\max},$$

where $j_{\max}$ will be called the partitioning number of the segment of initial momenta $\rho_0^{(\min)} \le \rho_0 \le \rho_0^{(\max)}$. Let us introduce the value

$$l = \sum_{j=1}^{j_{\max}} \left|T^{(j)} - T^{(j-1)}\right|, \tag{13}$$

which is a peculiar "vertical projection" of the curve length (in this sense, the "horizontal projection" always equals $\rho_0^{(\max)} - \rho_0^{(\min)}$). This value is always finite for smooth curves; for fractal curves, $j_{\max}$ tends to infinity as the partitioning number increases. The Hausdorff–Bezikovich fractal dimension D_F is [21]

$$D_F = \lim_{j_{\max} \to \infty} \frac{\ln l}{\ln j_{\max}} + 1. \tag{14}$$

The fractal dimension calculated in this way for the problem under consideration is $D_F = 1.84 \pm 0.02$.

4.2. The Physical Mechanism of Fractal Structure Formation

The motion of the atom is essentially unstable close to standing wave nodes, where the atom–field coupling coefficient vanishes. Far from the nodes, the atom moves almost regularly. When crossing a node, the atom can choose one of two scenarios. It can either continue to move up to the next node (therefore, to a detector) or change the direction of its motion after a short flight. This allows us to classify all possible atomic trajectories using a single parameter *m*, which is the number of standing wave node crossings until the atom is detected. This is equivalent to the number of half-turns about the $(\pi, 0)$ point on the (ξ, ρ) phase plane. Precisely this principle underlies the numbering of trajectories in Fig. 3b. The trajectories that intersect a node once will be called trajectories of the first type, second-type trajectories have two intersections each, etc. Such a simple classification of trajectories is possible because of the uniqueness of the "free" (unrelated to mirrors) node in the cavity. Note the special-type trajectories similar to *1S* in Fig. 3b. If the resonance is exact, such trajectories are separatrices separating the regions of finite and infinite motion on the phase plane. Outside the resonance, the description of the dynamics of the atom in terms of a two-dimensional phase plane becomes essentially incomplete, and, strictly, these trajectories cannot then be called separatrices. Nevertheless, motion along them is, as with the resonance, an asymptotic approximation to some configuration space point. An important characteristic of chaotic motion is the possibility that the atom can go into an asymptotic trajectory after first making a certain number of oscillations (which is absolutely impossible for regular motion). Let us classify such trajectories as follows: the trajectories that enter the asymptotic mode after one intersection of a standing wave node will be denoted by *1S*, after two intersections, by *2S*, etc. Although the choice of the further scenario after the intersection of a node seems fortuitous, this choice is unambiguously determined by the initial conditions. Calculations show that smooth regions of the large-scale structure shown in Fig. 4a correspond to trajectories of the first type. Visually irresolvable regions are generated by all the other trajectories. The singular points at the boundaries between the regular and irregular regions (which correspond to $T = \infty$) are generated by trajectories of the *1S* type. Quite similarly, regular regions of the second-order structure (Fig. 4b) correspond to trajectories of the second type, and irregular regions, to trajectories of all other types except the first type (trajectories of the first type are absent in the second-order structure), and singular region boundaries, to trajectories of the *2S* type. The principle of formation of higher order structures is the same. Note that the comparative simplicity of the fractal structure is related to the simplest field configuration selected by us. The fractal would become considerably more complex if the cavity were longer.

There are two essentially different mechanisms of the appearance of infinite exit times, namely, infinitely long oscillations of the atom in the cavity ($m = \infty$) and its entry into the asymptotic trajectory ($m \neq \infty$). The set of initial momenta ρ_0 corresponding to asymptotic trajectories is a countable fractal; each of its points is given by a vector in the Hilbert space. Each vector has m integer components, other components being zero. Let us establish this correspondence as follows. In the first-order structure (Fig. 4a), let us number substructures starting from the rightmost one. Each such substructure contains infinitely many substructures of the next order. Let us introduce independent numbering of the latter starting with the center of the second-order structure (Fig. 4b). As distinguished from the first-order structure, substructure numbers are now both positive and negative. Positive numbers are assigned to the substructures situated to the left of the central regular region, and negative numbers, to the substructures on the right of the regular region. None of the substructures is numbered "0." The structures of the other orders are handled similarly. This algorithm allows each substructure of a structure of order m to be correlated with a sequence of m integers, of which the first is the number of the second-order structure that the substructure of interest belongs to or coincides with at $m = 1$, the second integer is the corresponding number of the third-order structure in the second-order one, etc. This sequence of integers is similar to the electronic address of a subcatalog constructed by the principle ⟨subcatalog of the root catalog⟩/⟨subcatalog of the second level⟩/⟨subcatalog of the third level⟩…. Note that the first number in the sequence is always positive, and all the others can take on arbitrary values. Two asymptotic trajectories of the mS type correspond to each substructure of the mth-order structure; they are the boundaries of this substructure. Set a sequence of numbers determining the substructure itself in correspondence to the right boundary of each substructure and a sequence of the same numbers, but with the opposite sign of the first member, to the left boundary. In this way, we define a sequence of m integers determining in the Hilbert space some vector with m nonzero integers for each ρ_0 value that corresponds to the asymptotic motion of the atom after m node crossings.

Unlike asymptotic trajectories, the set of trajectories with $m = \infty$ (and the corresponding initial ρ_0 values) is likely to be uncountable. To each such trajectory corresponds an infinite-order substructure, which can only be described by an infinite sequence of numbers. In spite of different cardinalities, both these fractal sets have the same dimension, which is smaller by one than the dimension of the fractal on the plane considered above; that is, it equals 0.84 ± 0.02.

Like Lévy flights, fractals generate anomalous statistical properties of atom–field coupling. The probability distribution of exit times $P(T)$ shown in Fig. 5 for two different detunings exhibits deviations from the Poisson statistics. Several local distribution function maxima corresponding to different numbers of node crossings m are observed for the stronger chaos with $\delta = 0.4$. For instance, $m = 1$ corresponds to the first maximum with $T \approx 60$; $m \approx 2$, to the second maximum with $T \approx 130$; and $m = 3$, to the third maximum. The corresponding T values can be roughly estimated from the initial velocity of atoms $\alpha\rho_0 \approx 0.08$ used in the calculations. Atoms with $m = 1$ fly a distance of $3\pi/2$ and are recorded by the right detector at time $T = 3\pi/0.16 \approx 60$. For atoms with $m = 2$, which cross the node two times and are detected by the left detector, estimation from the mean velocity equal to the initial velocity undervalues T ($T \approx 100$), because in reality an atom is decelerated near the top of the potential hill (see the trajectory of the second type in Fig. 3b). The distribution function decreases almost exponentially at its tail. The middle part of the distribution function for the weaker chaos with $\delta = 0.2$ also exhibits an exponential decrease. Noticeable deviations from the exponential law are observed for the tail of this function, which, however, includes too few events to approximate it by some simple dependence. The first local maxima at $\delta = 0.2$ were observed at times shorter than the corresponding times for the strong chaos, because a lower initial velocity of atoms was used in the calculations. The probability of the appearance of events with $m \geq 3$ is exceedingly low for the weaker chaos, and almost all atoms move along first- and second-type trajectories.

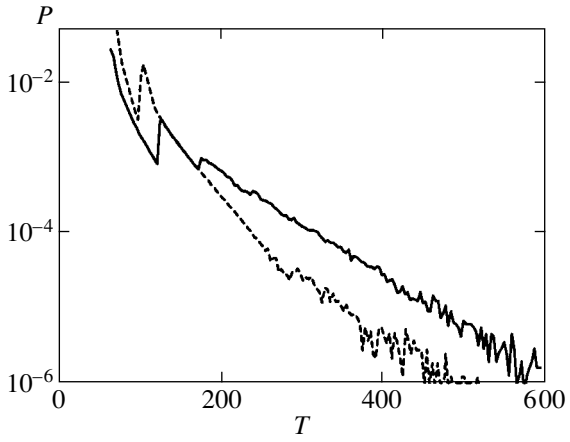

Fig. 5. Probability distribution for exit times $P(T)$ on the logarithmic scale; $\delta = 0.4$ (solid line) and 0.2 (dashed line).

To conclude this section, we would like to stress that atomic fractals of the types considered above are also characteristic of other atom–field interaction models with dynamical chaos. Imagine an atom prepared in the ground state and placed into a cavity with a standing wave whose frequency substantially differs from the atomic transition frequency, that is, $|\delta| \gg 1$. Spontaneous emission then plays hardly any role. Standing wave amplitude (or phase) modulation can cause chaotic motion of the atom [22]. The quantum properties of

such a motion have been studied in several experiments (e.g., see [23]). Adiabatically excluding the probability amplitude of upper level population, we obtain the effective Hamiltonian of atomic translational motion in the field of the amplitude-modulated standing wave in the form

$$H_{\text{eff}} = \frac{\alpha\rho^2}{2} - \epsilon[1 - \sin(\beta\tau)]\sin^2\xi, \quad (15)$$

where ϵ and β are the normalized modulation depth and frequency, respectively. We observed a fractal [24] similar to that shown in Fig. 4 in this Hamiltonian system with one and a half degrees of freedom.

Experimentally, the scheme of standard experiments with the diffraction of atoms on a stationary standing wave [10, 25] appears to be more convenient than the scheme shown in Fig. 3a. In these experiments, a monokinetic atomic beam propagates at almost a right angle to the standing wave axis ξ. We calculated the ξ_{out} position and the transverse momentum ρ_{out} for atoms at some fixed instant of time after the beam passed the region of interaction with the field. The $\xi_{\text{out}}(\xi_0)$ and $\rho_{\text{out}}(\xi_0)$ scattering functions were self-similar for systems (3) and (15) with three and one and a half degrees of freedom, respectively, although, strictly, these functions could not have singularities for obvious reasons.

5. RABI OSCILLATION CORRELATIONS WITH ATOMIC MOTION

5.1. Resonant Rabi Oscillations

Changes in the internal energy of the atom with time (Rabi oscillations) depend not only on the state of the mode in the cavity, but also on the coordinate and momentum of the atom in the standing light wave field. Using the master equation (3) and taking into account the integral of motion R, we can easily obtain the equation for the population inversion under exact resonance conditions ($\delta = 0$),

$$\dot{z} = \mp 2\sqrt{R - Nz^2 - u_0^2}\cos[\xi(\tau)], \quad (16)$$

where $\xi(\tau)$ is the well-known solution for physical pendulum (7) given in our work [12] for the problem under consideration. We assume that $\cos[\xi(\tau)]$ is a known function of time. The solution to (16) can then be written as

$$z(\tau) = \mp\sqrt{\frac{R - u_0^2}{N}}\sin\left[\int_0^\tau \Omega_r[\xi(\tau)]d\tau + \psi_0\right], \quad (17)$$

where

$$\psi_0 = \mp\arcsin\left[\sqrt{\frac{N}{R - u_0^2}}z_0\right]$$

is the initial phase. The magnitude of the variable

$$\Omega_r(\xi) = 2\sqrt{N}\cos\xi \quad (18)$$

has the meaning of the instantaneous Rabi frequency. It follows from solution (17) that, at $\delta = 0$, Rabi oscillations are generally a frequency-modulated signal with a constant amplitude and a variable modulation frequency equal to $\alpha\rho(\tau)$. Oscillations differ in character depending on the ratio between the modulation frequency and the amplitude of the instantaneous Rabi frequency $2\sqrt{N}$. For slow atoms with $|\alpha\rho_0| \ll 2\sqrt{N}$, Rabi oscillations are a signal with a well-defined frequency modulation (Fig. 6a, the top part). If the velocity of the atom is so high ($\rho_0 \gg \rho_{\text{cr}}$) that its variations can be ignored (the Raman–Nath approximation), that is, if $\xi \approx \alpha\rho_0\tau$, Rabi oscillations have a constant modulation frequency $\alpha\rho_0$,

$$z(\tau) \approx \mp\sqrt{\frac{R - u_0^2}{N}}\sin\left[\frac{2\sqrt{N}}{\alpha\rho_0}\sin(\alpha\rho_0\tau) + \psi_0\right]. \quad (19)$$

As the modulation frequency $\alpha\rho \approx \alpha\rho_0$ approaches the amplitude Rabi frequency value $2\sqrt{N}$, the signal gradually loses the form characteristic of slow atoms, and, when these values coincide (at $\alpha = 0.001$, this occurs if $\rho_0 = 2000\sqrt{10}$), the signal does not contain any modulation (Fig. 6a, the middle part). A further increase in ρ_0 causes an increase in the frequency of oscillations and a decrease in their amplitude. In this region, modulation is also absent. In the $|\alpha\rho_0| \gg 2\sqrt{N}$ limit, (19) can be simplified taking into account the smallness of the $2\sqrt{N}/\alpha\rho_0$ value to obtain

$$z(\tau) \approx z_0 - \frac{2v_0}{\alpha\rho_0}\sin(\alpha\rho_0\tau) - \frac{4Nz_0}{\alpha^2\rho_0^2}\sin^2(\alpha\rho_0\tau). \quad (20)$$

It follows that, under resonance conditions, Rabi oscillations of superfast atoms are a signal comprising two harmonic components with frequencies $\alpha\rho_0$ and $2\alpha\rho_0$. Their amplitudes decrease as ρ_0 increases by the laws $1/\rho_0$ and $1/\rho_0^2$, respectively. In the simplest cases of $z_0 = 0$ (Fig. 6a, the bottom part) and $z_0 = \pm 1$, the signal contains a single harmonic.

5.2. Nonresonant Rabi Oscillations

At moderate detunings, chaos can arise in the atom–field system (3). A typical chaotic signal of Rabi oscillations is shown in Fig. 6b (top). The character of frequency modulation of the chaotic signal is similar to that of the resonant signal (Fig. 6a), but the amplitude is approximately constant only for motion between neighboring nodes. When the atom crosses the node, the amplitude changes stochastically. This is a manifes-

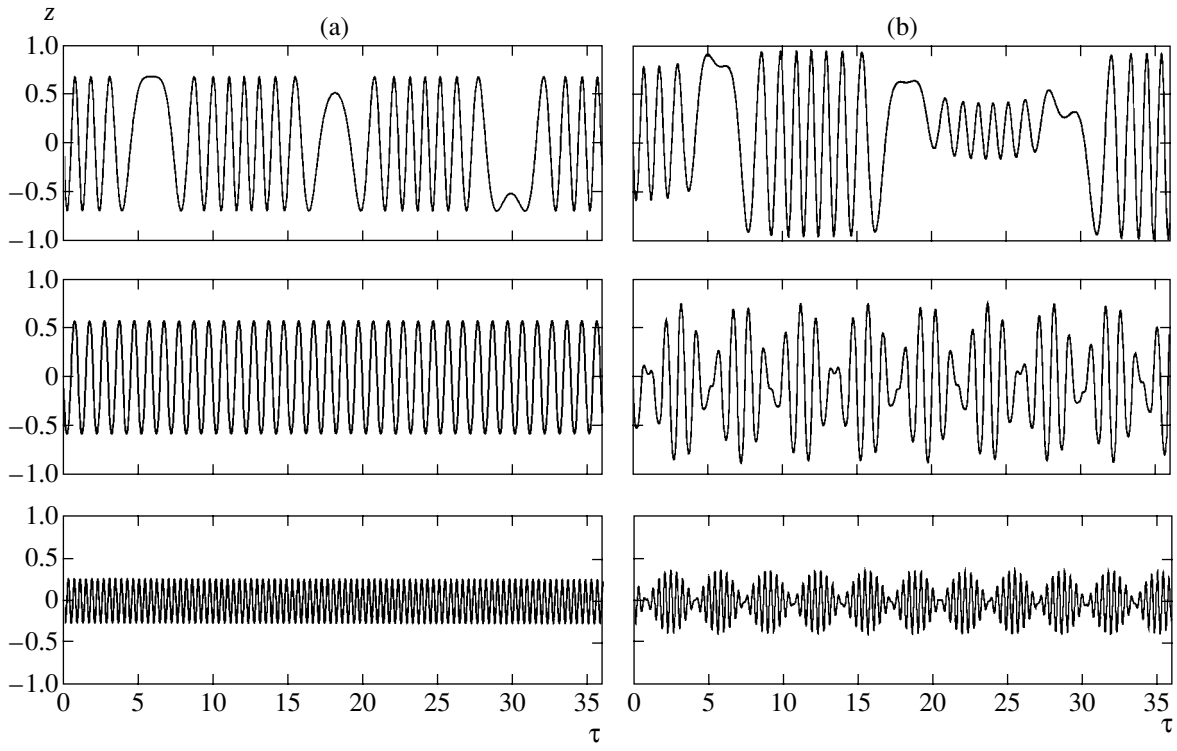

Fig. 6. Resonant and nonresonant Rabi oscillations for different initial momentum values, $\rho_0 = 270$, 6300, and 16000 (from the top down), and different detunings δ = (a) 0 and (b) 1.

tation of the instability of the solution to system (3) for the internal degree of freedom of the atom. For slow atoms [$|\alpha\rho| \ll \max(|\delta|, 2\sqrt{N})$], Rabi oscillations contain both frequency and amplitude modulation, which distinguish the nonresonant from the resonant signal (Figs. 6b and 7, top plots). Like the frequency, the amplitude of oscillations correlates with the standing wave and periodic potential structure. The maximum amplitude of oscillations decreases and the mean frequency increases as the detuning increases (Fig. 7). Frequency modulation gradually disappears and amplitude modulation tends to the law $\cos\xi$. For fast atoms (Fig. 6b, middle and bottom), Rabi oscillations are almost regular, but signals at $\delta = 1$ are substantially different from the corresponding resonant Rabi oscillations shown in Fig. 6a. In the context of the experiment with detection of fractals suggested in the preceding section, such a relation between the internal energy of the atom and the structure of the standing wave allows the number of node crossings m to be easily determined from the shape of the Rabi oscillation signal.

The internal energy of the atom z can approximately be estimated in two important limiting cases. At large detunings $|\delta| \gg \max\{|\alpha\rho|, 2N\}$, the second term in the fourth equation of system (3) can be ignored. For fast atoms with $|\alpha\rho| \gg \max(|\delta|, 2N)$, we can ignore the integral of this term. In both cases, the u and v variables are approximated by harmonic solutions with frequency δ and the internal energy is given by

$$z \approx \begin{cases} z_0 - \dfrac{2\sqrt{u_0^2 + v_0^2}}{\delta}\cos\xi\sin(\delta\tau + \varphi_0), \\ \qquad |\delta| \gg \max(|\alpha\rho|, 2N), \\ z_0 + \dfrac{2\sqrt{u_0^2 + v_0^2}}{\alpha\rho_0}\cos(\delta\tau + \varphi_0)\sin\xi, \\ \qquad |\alpha\rho_0| \gg \max(|\delta|, 2N), \quad \alpha\rho_0^2 \gg 2\sqrt{N}, \end{cases} \tag{21}$$

where $\varphi_0 = \arcsin(u_0/\sqrt{u_0^2 + v_0^2})$. Both Rabi oscillations are amplitude-modulated signals. The higher of the two characteristic frequencies ($|\alpha\rho|$ and $|\delta|$) plays the role of the Rabi frequency, and the lower one is the modulation frequency. The solution for a fast atom was obtained using the Raman–Nath approximation in addition to the $|\alpha\rho| \gg |\delta|$ condition. Generally, this approximation is valid if the initial kinetic energy $\alpha\rho_0^2/2$ is much higher than twice the amplitude of potential energy oscillations. Outside the resonance, this amplitude is determined by the maximum variable u value, which is attained at $z = v = 0$ and equals $u_{\max} = \sqrt{R} \approx \sqrt{N}$. At $\delta = 0$, the solution for a fast atom transforms

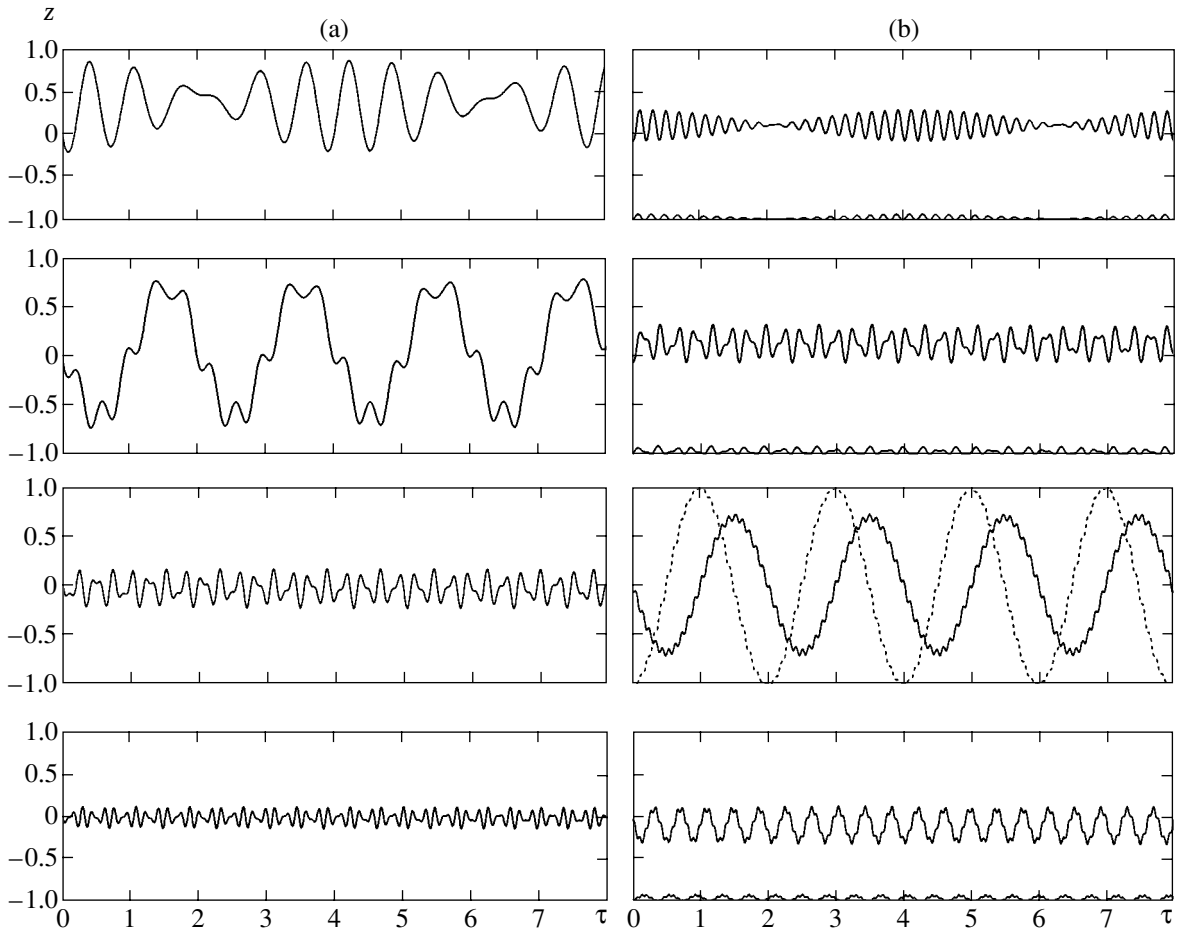

Fig. 7. Doppler–Rabi resonance for different initial momentum values, ρ_0 = 750, 8000, 32000, and 48000 (from the top down), and different detunings, δ = (a) 8 and (b) 32.

into (20). Approximate solutions (21) agree with the results of numerical experiments (Figs. 6, 7a).

Note that the approximations made to derive (21) are fairly crude, because they give trivial harmonic solutions for u and v. A more exact solution for u can be obtained in the approximation $z_{max} - z_{min} \ll |z_0|$, which is valid for both fairly large detunings $|\delta| \gg |\alpha\rho|$ and superfast atoms $|\alpha\rho| \gg |\delta|$ except for the case when $z_0 = 0$. The approximate equation obtained from the third and fourth equations of system (3),

$$\ddot{u} + \delta^2 u \approx 2Nz_0\delta\cos\xi, \tag{22}$$

is then valid. This equation describes a linear oscillator with a given driving force. The solution to it is

$$\begin{aligned} u(\tau) \approx {} & 2Nz_0\sin(\delta\tau)\int d\tau\cos(\delta\tau)\cos\xi \\ & - 2Nz_0\cos(\delta\tau)\int d\tau\sin(\delta\tau)\cos\xi \\ & + u_0\cos(\delta\tau) + v_0\sin(\delta\tau). \end{aligned} \tag{23}$$

For a slow atom with $|\alpha\rho| \ll |\delta|$, solution (23) is approximately written in the form

$$u \approx \frac{2Nz_0}{\delta}\cos\xi + \sqrt{u_0^2 + v_0^2}\sin(\delta\tau + \varphi_0), \tag{24}$$

which allows us to analytically substantiate the effect of a discrete change in the spatial periodicity of the effective potential energy mentioned in Section 3 (Fig. 1e),

$$U \approx \frac{2Nz_0}{\delta}\cos^2\xi. \tag{25}$$

5.3. The Doppler–Rabi Resonance

This interesting effect, almost unnoticeable at small detunings, is observed far from the atom–field resonance if atomic momenta satisfy the condition $|\alpha\rho| \approx |\delta|$. The physical background of the effect is as follows. Let us represent the standing wave as the sum of two counterpropagation waves. In the frame of reference of the moving atom, their frequencies ω_1 and ω_2 do not

coincide because of the Doppler effect,

$$\omega_1 = \omega_f - \frac{v_a}{c}\omega_f, \quad \omega_2 = \omega_f + \frac{v_a}{c}\omega_f, \tag{26}$$

where v_a is the velocity of the atom and c is the velocity of light. Because the velocity of the atom is small compared with the velocity of light, we ignore relativistic effects. We assume that the initial momentum of the atom is sufficiently large for the Raman–Nath approximation $\rho \approx \rho_0$ to hold. Let us renormalize all frequencies with respect to Ω_0 and determine dimensionless detunings between the frequency of the interlevel transition in the atom and the two running wave frequencies as

$$\begin{aligned}\delta_1 &= \frac{\omega_1 - \omega_a}{\Omega_0} = \delta - \alpha\rho_0,\\ \delta_2 &= \frac{\omega_2 - \omega_a}{\Omega_0} = \delta + \alpha\rho_0.\end{aligned} \tag{27}$$

It is easy to see that the $|\delta| = |\alpha\rho_0|$ condition then leads to the resonance of the atom with one of the running waves. If, in addition, $|\delta| \gg 1$, the interaction with the second wave can be ignored, and the atom can be considered as if it were in the field of one wave with an ω_1 or ω_2 frequency. For definiteness, we assume that the signs of δ and $\alpha\rho_0$ coincide and the resonance is observed with the wave running in the direction of atomic motion; the frequency of this wave is ω_1. In the field of one running wave, the electron–field dynamics of the atom is described by the Bloch-type equations [13]

$$\dot{u} = \delta_1 v, \quad \dot{v} = -\delta_1 u + Nz, \quad \dot{z} = -v, \tag{28}$$

which differ from the corresponding equations in (3) by the fact that the running wave amplitude is two times smaller than the standing wave amplitude and the interaction energy with the running wave is independent of the coordinate. Solutions to (28) for the population inversion have the form

$$\begin{aligned}z = \frac{u_0\delta}{\Omega_N^2}(1 - \cos(\Omega_N\tau)) - \frac{v_0}{\Omega_N}\sin(\Omega_N\tau)\\ + z_0\left(\frac{\delta_1^2}{\Omega_N^2} + \frac{N}{\Omega_N^2}\cos(\Omega_N\tau)\right),\end{aligned} \tag{29}$$

where

$$\Omega_N = \sqrt{\delta_1^2 + N} = \sqrt{(\delta - \alpha\rho_0)^2 + N}.$$

In particular, the exact Doppler–Rabi resonance causes the arising of atomic internal energy oscillations with frequency $\sqrt{N}$ and the amplitude, which attains its maximum possible value. Numerical calculations according to complete equations (3) closely agree with approximate solution (29). Rabi oscillations with frequency $\sqrt{N}$ at $\alpha\rho_0 = \delta$, $N = 10$, and two detuning values are shown in Figs. 7a and 7b (the second and third plots from the top down). As expected, moving away from the resonance increases the frequency of oscillations. Against a background of comparatively slow oscillations with the Rabi frequency corresponding to the interaction of the atom with one running wave, we observe fast small-amplitude oscillations, which decrease as δ increases. Their presence is caused by the interaction of the atom with the second wave, with respect to which detuning δ_2 is large. It follows from (29) that, the initial values being $z_0 = \pm 1$ and $u_0 = v_0 = 0$, the internal energy oscillates between its extremal values ± 1 under the Doppler–Rabi resonance conditions. This is substantiated by numerical experiments based on (3). Along with $z_0 = 0$, the case of $z_0 = -1$ is shown in Fig. 7b. For $z_0 = -1$, resonant Rabi oscillations (the third plot from the top down) are shown by a dashed line. It follows that deep Rabi oscillations are possible for a moving atom at an arbitrarily large detuning δ and corresponding atomic velocity.

6. DISCUSSION AND CONCLUSIONS

We have studied the Hamiltonian nonlinear dynamics of the interaction between a two-level atom and a selected mode of a high-Q cavity under strong atom–field coupling conditions. Upon detunings, atom recoil frequencies, atom initial velocities, and numbers of excitations at which semiclassical equations of motion have chaotic solutions with positive maximum Lyapunov exponents, scattering of atoms in the field of a standing light wave is fractal. Numerical experiments reveal strongly pronounced self-similarity of the dependence of the time at which atoms exit from the cavity on their initial momenta. The corresponding curve has a fractal dimension of 1.8. Even in a minimum-size cavity (one significant standing wave node in our numerical experiments), there are infinitely many atomic motion trajectories with an infinite time of escape from the cavity. These trajectories are of two types, namely, separatrix-like trajectories, the motion along which is an asymptotic approach to some configuration space points, and trajectories of indefinitely long atomic wandering (in our simplest case, vibrations) in the cavity. The appearance of the latter is caused by chaotic energy exchange between different degrees of freedom in the atom–field system rather than by the obvious energy limitations that prevent the atom from overcoming optical potential barriers. The sets of initial atomic momenta generating asymptotic and wandering trajectories comprise countable and uncountable fractals, respectively.

Rabi oscillations of the atom correlate with its motion. If the atom–field resonance is exact, the optical potential is constant and reproduces the form of the standing wave. Atomic motions and internal energy

oscillations are regular. For slow atoms, Rabi oscillations are a frequency-modulated signal with a constant amplitude and a noticeable decrease in the rate of population inversion changes close to standing wave nodes. Conversely, for superfast atoms [$|\alpha\rho_0| \gg \max(|\delta|, 2\sqrt{N})$] and slow atoms far from the resonance [$|\delta| \gg (|\alpha\rho_0|, 2\sqrt{N})$], Rabi oscillations contain amplitude modulation at an approximately constant frequency. The Doppler–Rabi resonance, that is, deep oscillations of the internal energy of the moving atom caused by the Doppler effect, arises far from the resonance when $|\alpha\rho_0| = |\delta|$.

In conclusion, consider shortly the prospects for future studies of a strongly coupled atom–field system with Hamiltonian (1). The Appendix contains the Hamilton–Schrödinger equations of motion (A.3) for the probability amplitudes of the electronic atomic and field degrees of freedom related to the classical translational degree of freedom of the atom. Generally speaking, this is an infinite-dimensional nonlinear system of dynamical equations with an infinite number of integrals of motion. Infinite system (A.3) reduces to eight equations for a Fock state of the quantized field mode at $\tau = 0$ and the atom prepared in an arbitrary superposition of its energy states. For the atom prepared in one of its energy states at $\tau = 0$, system (A.3) reduces to semiclassical equations (3). For such an initial state of a fully quantized electron–field subsystem, all results obtained in this work are valid.

ACKNOWLEDGMENTS

This work was supported by the Russian Foundation for Basic Research (project nos. 02-02-17796, 03-02-06895), by the program "Mathematical Methods in Nonlinear Dynamics" of the Russian Academy of Sciences, and by the Program for Basic Research of Far East Division of the Russian Academy of Sciences.

APPENDIX

HAMILTON–SCHRÖDINGER EQUATIONS

Let us represent our atom–field system as a hybrid comprising the classical subsystem of translational motions of the atom and the completely quantum electron–field subsystem. In the Schrödinger representation, the latter is described by the pure state vector

$$|\psi(\tau)\rangle = \sum_{n=0}^{\infty} x_n(\tau)|2, n\rangle + y_n(\tau)|1, n\rangle, \qquad \text{(A.1)}$$

decomposed in the Fock basis of the field $|n\rangle$ ($n = 0, 1, \ldots$) and the basis of the electronic states of the atom, the upper $|2\rangle$ and the lower $|1\rangle$ states. The nonstationary Schrödinger equation with Hamiltonian (1), in which $\hat{x}$ and $\hat{p}$ are replaced by their classical normalized means ξ and ρ, can easily be used to obtain quantum equations for the following combinations of complex-valued probability amplitudes for observing the atom at the higher level and n quanta in the field x_n, or the atom at the lower level and $n + 1$ quanta in the field:

$$u_n = 2\mathrm{Re}(x_n y_{n+1}^*), \quad v_n = 2\mathrm{Im}(x_n y_{n+1}^*), \quad z_n = |x_n|^2 - |y_{n+1}|^2. \qquad \text{(A.2)}$$

After the addition of the classical Hamilton equations for the coordinate and momentum of the atom,

$$\dot{\xi} = \frac{\partial\langle\hat{H}\rangle}{\partial\rho}, \quad \dot{\rho} = -\frac{\partial\langle\hat{H}\rangle}{\partial\xi},$$

we obtain a system of Hamilton–Schrödinger equations that describes the dynamics of the atom–field hybrid,

$$\dot{\xi} = \alpha\rho, \quad \dot{\rho} = -\sum_{n=0}^{\infty}\sqrt{n+1}\,u_n\sin\xi,$$
$$\dot{u}_n = \delta v_n, \quad \dot{v}_n = -\delta u_n + 2\sqrt{n+1}\,z_n\cos\xi, \qquad \text{(A.3)}$$
$$\dot{z}_n = -2\sqrt{n+1}\,v_n\cos\xi.$$

Generally speaking, this is an infinite-dimensional system with an infinite number of integrals of motion $R_n = u_n^2 + v_n^2 + z_n^2$. The expected mean values of the operators of interest to us are expressed via the amplitudes as follows:

$$u(\tau) = \langle\psi(\tau)|\hat{u}(0)|\psi(\tau)\rangle = \sum_{n=0}^{\infty}\sqrt{n+1}\,u_n,$$
$$v = \sum_{n=0}^{\infty}\sqrt{n+1}\,v_n, \quad z = \sum_{n=0}^{\infty} z_n. \qquad \text{(A.4)}$$

If, at $\tau = 0$, the field in the cavity is prepared in a Fock state with a given number of quanta n and the atom is in one of its energy states, infinite-dimensional system (A.3) reduces to five equations. After renormalizing u_n and v_n with respect to $\sqrt{n+1}$, these equations have the form of system (3) formally obtained for the classical field. It follows that the results obtained in this work by solving (3) are also valid for the fully quantized electronic and Fock field degrees of freedom.

REFERENCES

1. B. V. Chirikov, Phys. Rep. **52**, 263 (1979); G. M. Zaslavsky, Phys. Rep. **80**, 157 (1981).
2. F. Haake, *Quantum Signatures of Chaos* (Springer, Berlin, 1991).
3. G. Casati, B. V. Chirikov, J. Ford, *et al.*, Lect. Notes Phys. **93**, 334 (1979).
4. A. Heidmann, J. M. Raimond, S. Rewnaud, *et al.*, Opt. Commun. **54**, 189 (1985).

5. J. M. Raimond, M. Brune, and S. Haroche, Rev. Mod. Phys. **73**, 565 (2001).
6. C. J. Hood, T. W. Lynn, A. C. Doherty, *et al.*, Science **287**, 1447 (2000).
7. P. Münstermann, T. Fischer, P. Maunz, *et al.*, Phys. Rev. Lett. **82**, 3791 (1999).
8. *Cavity Quantum Electrodynamics*, Ed. by P. R. Bermann (Academic, New York, 1994).
9. V. G. Minogin and V. S. Letokhov, *Laser Light Pressure on Atoms* (Nauka, Moscow, 1986; Gordon and Breach, New York, 1987).
10. A. P. Kazantsev, G. I. Surdutovich, and V. P. Yakovlev, *Mechanical Action of Light on Atoms* (World Sci., Singapore, 1990; Nauka, Moscow, 1991).
11. S. V. Prants and L. E. Kon'kov, Pis'ma Zh. Éksp. Teor. Fiz. **73**, 200 (2001) [JETP Lett. **73**, 180 (2001)].
12. S. V. Prants and V. Yu. Sirotkin, Phys. Rev. A **64**, 033412 (2001).
13. S. V. Prants, Pis'ma Zh. Éksp. Teor. Fiz. **75**, 71 (2002) [JETP Lett. **75**, 63 (2002)].
14. S. V. Prants, M. Edelman, and G. M. Zaslavsky, Phys. Rev. E **66**, 046222 (2002).
15. E. Ott, *Chaos in Dynamical Systems* (Cambridge Univ. Press, Cambridge, 1993).
16. M. V. Budyansky, M. Yu. Uleysky, and S. V. Prants, Dokl. Akad. Nauk **386**, 686 (2002).
17. R. Blümel and W. P. Reinhardt, *Chaos in Atomic Physics* (Cambridge Univ. Press, Cambridge, 1997).
18. V. Yu. Sirotkin and S. V. Prants, J. Russ. Laser Res. **21**, 585 (2000).
19. A. J. Lichtenberg and M. A. Lieberman, *Regular and Stochastic Motion* (Springer, New York, 1983; Mir, Moscow, 1984).
20. G. M. Zaslavsky, *Physics of Chaos in Hamiltonian Systems* (Imperial Colledge Press, London, 1998).
21. M. Schroeder, *Fractals, Chaos, Power Laws* (Freeman, New York, 1990).
22. R. Graham, M. Schlautmann, and P. Zoller, Phys. Rev. A **45**, 19 (1992).
23. F. L. Moore, J. C. Robinson, C. Bharucha, *et al.*, Phys. Rev. Lett. **73**, 2974 (1994); H. Ammann, R. Gray, I. Shvarchuck, *et al.*, Phys. Rev. Lett. **80**, 4111 (1998).
24. S. V. Prants and V. Yu. Argonov, E-print archives, physics/0206005.
25. P. L. Gould, G. A. Ruff, and D. E. Pritchard, Phys. Rev. Lett. **56**, 827 (1986); T. Sleator, T. Pfau, V. Balykin, *et al.*, Phys. Rev. Lett. **68**, 1996 (1992).

Translated by V. Sipachev

Journal of Experimental and Theoretical Physics, Vol. 96, No. 5, 2003, pp. 846–856.
Translated from Zhurnal Éksperimental'noĭ i Teoreticheskoĭ Fiziki, Vol. 123, No. 5, 2003, pp. 962–974.

ATOMS, SPECTRA, RADIATION

Electronic Excitation of the Matrix during Drift of Excess Electrons through Solid Xenon

E. B. Gordon[a,*], G. Frossati[b], and A. Usenko[b]

[a]*Institute of Problems of Chemical Physics, Russian Academy of Sciences, Chernogolovka, Moscow oblast, 142432 Russia*
[b]*Kamerlingh Onnes Laboratory, Leiden University, P.O. Box 9504, 2300 RA Leiden, the Netherlands*
**e-mail: gordon@binep.ac.ru*

Received October 31, 2002

Abstract—It is shown experimentally that the exciton luminescence (λ = 172 nm) quantum yield excited by excess electrons drifting through solid xenon at 77 K in fields of 10 kV/cm amounts to 20 ± 5 per electron and that luminescence takes place during the entire drift process. A CW bulky discharge through solid xenon (with a current up to 20 A/cm^2) is realized, and intense visible luminescence due to excitation of impurities by electron impacts is observed. The prospects for using solid rare gases as matrices for studying processes in low-temperature plasmas and for creating effective electric energy converters in the vacuum ultraviolet range are discussed. © *2003 MAIK "Nauka/Interperiodica".*

1. INTRODUCTION

The ability of solid heavy rare gases (HRG) (xenon, krypton, and argon) to serve as conductors of excess electrons is well known: their mobility in HRGs is even higher than in metals and their mean free paths attain several meters. On the other hand, it is well known that the exposure of HRG to fast (>10 eV) electrons leads to a high probability of formation of electron excitations of the matrix (excitons) and, accordingly, to the emission of light in the vacuum ultraviolet (VUV) range. These properties render liquid HRGs promising active media for scintillation detectors of high-energy particles [1].

In 1994, one of the authors (E.B.G) and coworkers proposed a model of excess electron drift through condensed HRG in moderately strong electric fields, which explained the main characteristics of the drift by excitation of excitons by drifting electrons [2, 3]. In view of the smallness of the energy loss of electrons moving through an atomic crystal (or liquid), it has been accepted for a long time that the energy acquired by the electrons is much higher than the thermal energy; it is assumed, however, that it cannot exceed the energy of electron elastic scattering cross section restoration beyond the Ramsauer minimum in the corresponding gas (i.e., 0.3–0.7 eV) [4]. The statement that electrons in a solid can be accelerated to energies of 8–11 eV required for exciting the matrix, which are higher than the mean energies even in gas discharges, appeared bold. Nevertheless, the first attempt at experimental verification of the predictions made in [2, 3], which was made by the Wyder group [5], proved that the drift of electrons emitted by a cold cathode through liquid xenon under a voltage of 70 V indeed leads to intense luminescence in the vicinity of 172 nm, which coincides with the emission spectrum of two-centered excitons in Xe_2^*. Unfortunately, it is impossible to estimate (even approximately) the quantum yield of radiation, i.e., the number of VUV quanta per drifting electron, from the data obtained in [5] or from the more detailed description of these experiments [6]. Consequently, it could not be stated definitely whether the observed electroluminescence is a unique event or, as assumed in [2, 3], a drifting electron attains the energy required for excitation many times, losing the same amount of energy in this process. Naturally, we can speak of practical application of this effect only in the latter case, for example, for designing the effective converters of electrostatic field energy into VUV light.

It should be emphasized that, in accordance with the results of recent analysis [7], the effect discussed here must be inherent only in the condensed state: luminescence has never been observed during electron drift in gaseous xenon under pressures exceeding 10 bar. Moreover, the substitution of densities characteristic of solids and liquids into the formulas of the gas model [8] leads to values of electric fields, for which "excimer" luminescence must be observed, corresponding to an experimentally unattainable range of fields. A transition to the condensed phase radically changes the motion of an electron through the medium. This follows directly from an interesting effect observed for the first time in [4]: the excess electron mobility (measured from the current pulse delay time in weak fields) in gaseous xenon decreases, as expected, in inverse proportion to its pressure, but increases jumpwise by four (!)

orders of magnitude at the critical point, remaining high both in liquids and in solids. This means that the effective elastic scattering cross section in these media is the same as in the gas under a pressure of 0.1 bar. Qualitatively, this can be treated as a geometrical compensation of deviation during the interaction of an electron with many atoms simultaneously (the electron de Broglie wavelength is larger than the atomic spacing). However, there must be no such compensation in the case of "chemical"-type interaction being saturable, viz., electronic excitation, ion formation, or chemical reactions in which an electron interacts with a single center. Consequently, the cross section of such processes must remain close to that of gas-phase processes (the transformation of such a size effect as the Ramsauer effect upon a transition to the condensed phase is of special interest). In particular, this concerns elastic scattering of electrons from the state of a metastable negative excited rare gas ion, which lies 0.4 eV below the atomic (one-center) excitation level, albeit higher than the two-centered (molecular) exciton level for all HRGs. For this reason, the scattering from the structure of a negative ion, which, however, is observable, but does not affect the main drift characteristics in the gas, may turn out to be an important mechanism of an electron elastic losses hampering the accumulation of energy, sufficient for exciting a one-centered exciton (which is a predecessor of a two-centered exciton), in the condensed state [9]. As a result, the electron moves for a long time in the direction of the field at a constant energy and, hence, the electroluminescence quantum yield may be much lower than its limiting value, defined as the ratio of the applied voltage U to energy W_a of excitation of a one-center exciton. The analysis carried out in [7] shows that this is the reason for the constancy of electron drift velocity in strong electric fields.

The difficulties involved in a consistent analysis of specific features of electron drift in condensed media were the impetus for experiments aimed at detecting the predicted effect and determining the electroluminescence quantum yield.

2. EXPERIMENTAL METHOD

This study is devoted to measuring the quantum yield η of VUV radiation during the drift of excess electrons through solid xenon. Its reliable determination is a complex problem since it is necessary in general to find the number of drifting electrons and reconstruct the total number of emitted photons taking into account the observation geometry, the efficiencies of the optical tract and of the photodetector, and so on. The fact that the measurements should be carried out with quite low electron currents complicates the situation additionally. This is due to the difficulties encountered in purifying xenon to such an extent that the concentration of oxygen impurity in it is below 0.3*ppb*, which corresponds to a density of 10^{13} cm^{-3} in solid xenon. At the same time, even a concentration of 10^{11} cm^{-3} of negative ions (emerging as a result of electron capture by O_2 molecules, which are motionless in solid xenon) is sufficient for completely compensating an electric field of 1 kV/cm by the space charge. As a result, the value of the total charge passing through the sample becomes limited from above, and the smaller the current, the longer the solid sample lifetime without recrystallization.

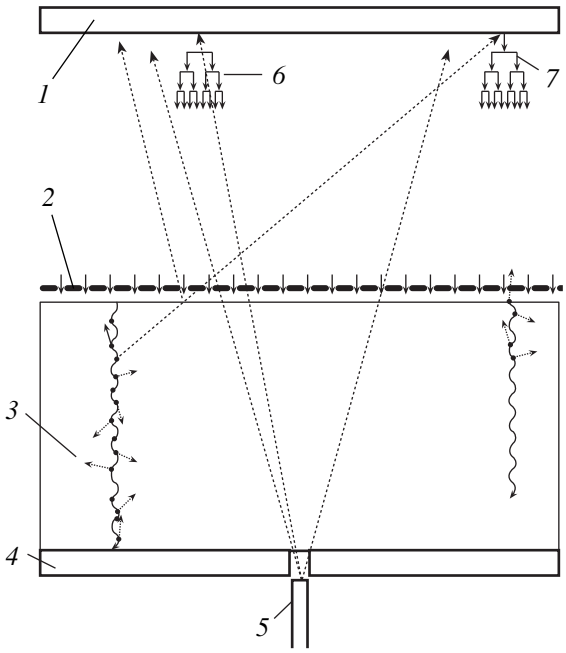

Fig. 1. Schematic of an electrolytic cell: photocathode (*1*), grid (*2*), xenon crystal (*3*), anode (*4*), optical fiber (*5*), and avalanches of primary and secondary electrons (*6* and *7*, respectively). Solid arrows correspond to electrons, and dashed arrows, to photons.

This problem was solved using the method proposed in [10] and illustrated in Fig. 1. We used a three-electrode cell whose zinc cathode possessed a considerable photoelectron emission yield in the ultraviolet spectral range. A xenon crystal was grown at the bottom of the cell between the anode and the grid. The upper part of the cell was filled either with argon to a pressure of a few millibars (if experiments were made at 77 K) or with saturated xenon vapor under the same pressure (in this case, the temperature was maintained at 125 K). The metallic grid was grounded, and voltages (a negative voltage to the cathode and a positive to the anode) were supplied to the electrodes from two independent power supplies. The cathode was irradiated through a window in the stainless steel anode by fourth-harmonic pulses of radiation emitted by a pulsed-periodic Nd:YAG laser (wavelength 266 nm, pulse duration 1 ns, and pulse repetition frequency 10^4 Hz) and fed through a quartz optical fiber. The number of photoelectrons emitted by the cathode per pulse was 10^4–10^5. VUV

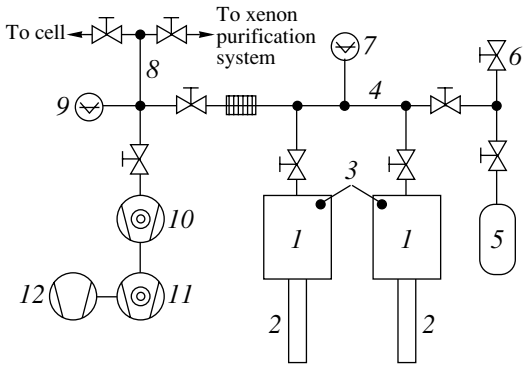

Fig. 2. Vacuum system: tanks (*1*) for storing xenon with fingers (*2*) and nonevaporating getters (*3*); comb (*4*), argon tank (*5*), high-vacuum valve (*6*), IKR-251 vacuum gauge (*7*), vacuum line (*8*), CMR-261 manometer (*9*), high-vacuum turbomolecular pump (*10*), turbomolecular pump (*11*), and membrane pump (*12*).

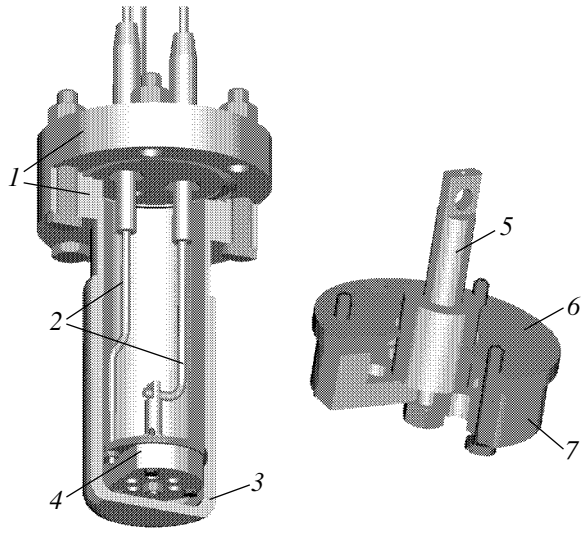

Fig. 3. Xenon purification chamber using electric spark method: vacuum flanges (*1*), copper leads (*2*), glass (Pyrex) cell (*3*), electrode unit (shown separately on the right) (*4*), anode (*5*), titanium ring (*6*), macor insulator (*7*).

light quanta that form during the electron drift through solid xenon and hitting the photocathode must in turn form new photoelectrons.

Such a scheme is advantageous from several points of view. First, the gap between the crystal and the cathode filled with a low-pressure gaps makes it possible to suppress the well-known back diffusion effect that lowers the probability of emergence of electrons from the cathode to the condensed medium under their direct contact by several orders of magnitude even if the free energy of an electron in a substance is lower than in vacuum (as in the case of HRGs) [11]. Second, the electrons accelerated by the electric field ionize the rare gas multiply in the cathode–grid gap, leading to the formation of an electron avalanche. The main thing, however, is that such a photoelectronic multiplier "built-in" the measuring cell also increases the number of secondary electrons formed under the action of exciton radiation. For this reason, positive feedback (during their drift in solid xenon, electrons induce VUV radiation generating new electrons, which are multiplied in the gas, embed in solid xenon, and so on) becomes so strong that it permits overcoming natural losses (limited solid angle of light collection, incomplete transparency of the grid, etc.) up to the attainment of the threshold for the development of a self-sustained discharge.

3. EXPERIMENTAL TECHNIQUE

In the vacuum system shown schematically in Fig. 2, use was made exclusively of materials and facilities intended for operation in ultrahigh vacuum. All pipelines were made of stainless steel, while flanges and copper gaskets were manufactured at Varian. The measuring cell and the xenon purification system were designed without using plastics, glues, or soldering since flux could not be removed completely from the latter. The entire vacuum system could be heated to 200°C for degassing. Evacuation was carried out using a TPU-170 high-vacuum turbomolecular pump supported in tandem by a turbomolecular and TPH-065 membrane pumps (all the pumps were manufactured at Pfeiffer) at the output. The tanks for xenon storage were supplied with special fingers, in which xenon was frozen (when required) by liquid nitrogen, and with commercial nonevaporating getters for maintaining gas purity.

The xenon purification system shown in Fig. 3 was combined with the vacuum system. It was based on the simple and reliable spark discharge method, proposed for the first time by Obodovski *et al.* [12]. The principle of its operation is close to that of a getter-ion pump, but this system operates in a liquid. The cathode of the purification chamber was in the form of a titanium ring sharpened to a razor edge, while the anode was a cylindrical metallic rod; the spacing between the electrodes was 0.2 mm. Before purification, the entire chamber was immersed in a vessel with ethyl alcohol cooled by liquid nitrogen added continuously to it to a pasty consistency. Xenon condensed in the chamber to an extent sufficient for maintaining the level of liquid 1 cm above the cathode plane. When the voltage between the cathode and the anode was high enough, one or two sparks flashed in the liquid xenon and moved in a circle upon sputtering of the cathode material. The spark current was limited by a high-voltage 1-MΩ resistor. Sputtered titanium deposited on the anode absorbed impurities from liquid xenon, while cavitation arising during the breakdown caused intense stirring of the liquid and supplied fresh portions to the purification region. In accordance with recommendations formulated in [12], the degree of purity was determined from the sound, color, and duration of the spark breakdown. The spark

in xenon preliminarily purified by multiple refreezing with evacuation of the remaining vapor at $T = 77$ K was bright and short and was accompanied by a loud bang, while the spark after several hours of electric-spark purification was dull, long, and was accompanied by a quiet hissing. The voltage in this case had to be elevated to 10 kV. According to [12], the degree of purification using this method was higher than 10^{-9}. Its effectiveness could be judged from the following observation: additional condensation of a small amount of xenon purified by refreezing from the comb of the vacuum system immediately led to a noticeable change in the spark characteristics. Purified xenon was stored in a tank with a preliminarily activated getter.

The design of the electrolytic measuring cell is shown in Fig. 4. Its base was a glass cylinder connected to two steel flanges through kovar junctions. The lower flange was connected electrically to the steel anode fixed to it and having a central hole 2 mm in diameter, which was covered from the outside by a sapphire window. The polished end of the quartz optical fiber intended for irradiating the cathode by laser pulses was fixed in the immediate vicinity of the window. The design of the anode part was determined by the necessity both to reduce the parasitic volume below the anode surface to the maximum possible extent and to compensate the mechanical stresses arising during the cell cooling. A massive copper rod of diameter 14 mm, which served as a cold link from liquid nitrogen to the cell, was attached to the lower part of the anode unit. A zinc cathode with a working diameter of 10 mm and a grid were fixed at the upper flange supplied with two high-voltage feedthroughs. The distance between the cathode and the grid was about 2 mm; they were electrically insulated by a ceramic gasket made of macor. Several types of copper and stainless steel grids with a geometrical transparency from 40 to 60% were used. The distance between the grid and the anode could be changed from 1 to 2 mm by varying the length of the cathode holders; the sample thickness changed accordingly. The cell was supplied with two electrical heaters wound on the upper and lower flanges and with a platinum thermometer.

The cell was placed in a transparent glass Dewar filled with liquid nitrogen so that the copper rod was immersed in the liquid. Voltage was supplied to the lower heater to increase the cell temperature to $T =$ 165 K, which corresponds to the coexistence of liquid and gas near the xenon triple point. Xenon was then condensed slowly from the tank to the cell. The amount of gas in the tank was chosen so that the surface of liquid xenon was at the grid level after the completion of the procedure (the upper edge of the sample was noticeably lower after crystallization followed by further cooling). After this, the cell was separated by a vacuum valve from the remaining part of the setup and the sample was solidified slowly by a drop in the voltage supplied to the heater and then cooled further either to 125 K, when the xenon saturated vapor pressure was

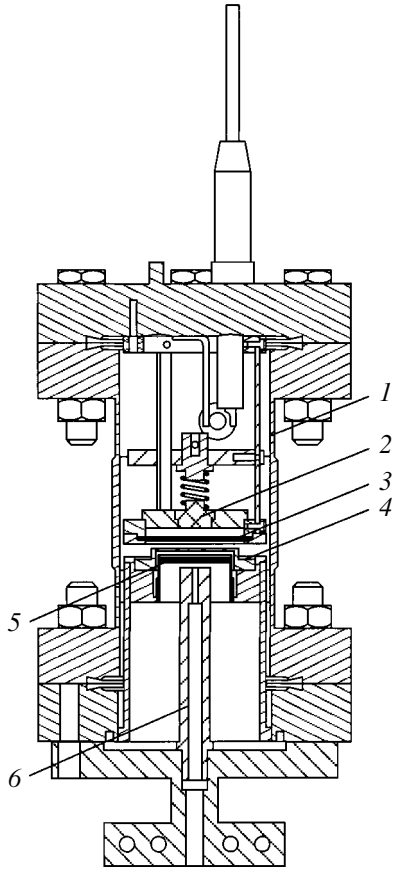

Fig. 4. Electrolytic cell: cell body (*1*), zinc cathode (*2*), grid (*3*), anode (*4*), sapphire window (*5*), fiber shell (*6*).

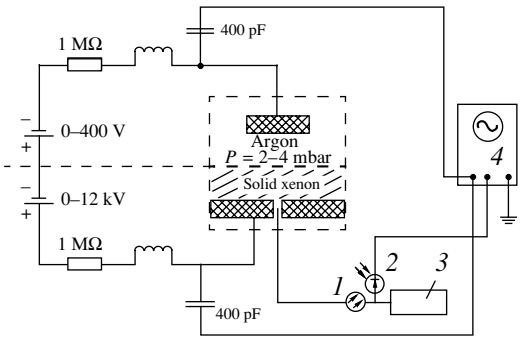

Fig. 5. Electric circuit: radiation input system of the fiber (*1*), photodiode of synchronization system (*2*), Nd:YAG laser ($\lambda = 266$ nm) (*3*), oscilloscope (*4*).

1.2 mbar, or to 77 K. In the latter case, after cooling to 100 K, liquid nitrogen was added to the Dewar flask to the level of the upper flange of the cell and preliminarily purified argon was fed to the cell up to a pressure of 1.2 mbar. The sample remained transparent during the entire procedure.

The electric measuring circuit is shown in Fig. 5. The electron current induced by a laser pulse in the

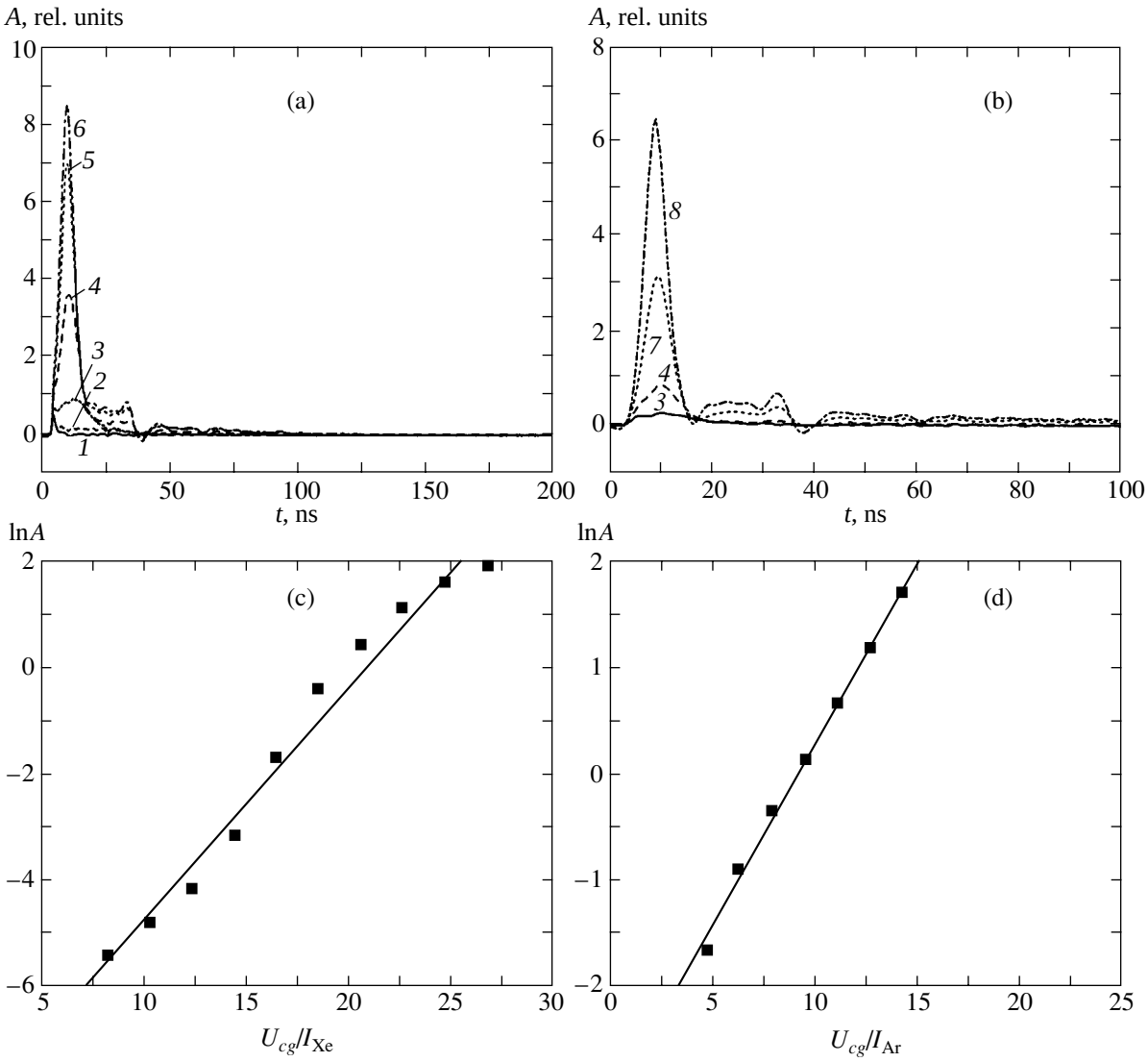

Fig. 6. Electron current pulses in the cathode–grid gap under a gas pressure of 1.2 mbar for different voltages U_{cg} = 0 (*1*), 50 (*2*), 100 (*3*), 150 (*4*), 165 (*5*), 175 (*6*), 200 (*7*), and 245 V (*8*) for xenon (a) and argon (b) and the logarithm of the peak pulse intensity as a function of the dimensionless voltage $U_{cg}/I_{Xe, Ar}$ ($I_{Xe, Ar}$ is the ionization potential of the corresponding atom) (c) Xe: P = 2.4 mbar, T = 300 K, α = 1.55; (d) Ar: P = 3.6 mbar, T = 77 K, α = 1.40. The highest voltage is 5–10 V lower than the charge ignition threshold.

cathode–grid and grid–anode gaps was detected by measuring the varying component of the voltage at the corresponding power supply with the help of a storage oscilloscope (f = 500 MHz, input resistance 50 Ω). Such a circuit allowed us to avoid high voltage across the oscilloscope input and to detect signals with a time resolution not worse than 2 ns. All signals were synchronized by a laser pulse detected by the photodiode.

4. EXPERIMENTAL RESULTS

In order to determine the effectiveness of the method, we had to determine the characteristics of the gaseous "photoelectric multiplier," i.e., its time resolution and the values of the electron multiplication factor attained, which are limited from above by the emergence of a self-sustained discharge between the cathode and the grid. In the evacuated empty cell, the signal from primary electrons emitted from the cathode by a laser pulse, which was measured in the upper (cathode–grid) gap, had a duration of 2 ns (which is close to the laser pulse duration) and was saturated at a voltage of $U_{cg} \approx 100$ V. When rare gas is fed to the cell, the electron current amplitude becomes an exponential function of U_{cg}, the characteristics of the current signal being insensitive to changes in temperature in the range T = 77–300 K, as well as to the presence of a voltage between the grid and the anode. Typical dependences are shown in Figs. 6a and 6b; the maximal voltages shown in the figures are quite close to the discharge

ignition threshold. An increase in the gas pressure broadened the current pulse; for this reason, pressures under which the pulse duration does not exceed 10 ns were used. For convenience of comparing the characteristics of avalanche multiplication of electrons in different rare gases, the dependences of current amplitude J on the applied voltage are shown in Figs. 6c and 6d in the form

$$k \equiv \frac{J}{J_0} = \alpha^{U/I_0} = \exp\left(\frac{U}{I_0}\ln\alpha\right), \quad (1)$$

where k is the multiplication factor, I_0 is the ionization potential of the corresponding gas, and α is the multiplication factor for an electron undergoing inelastic scattering with an atom ($1 < \alpha < 2$). It is interesting to note that the multiplication factor is practically the same for all rare gases used (He, Ar, and Xe) and is quite high (approximately half the energy acquired by an electron from the field is spent on ionization).

On the whole, the characteristics of the photomultiplier satisfy the formulated problem completely: (1) the multiplication factor is reproducible and large enough (k = 300–1000) to significantly compensate the comparatively low probability γ (determined by the cell geometry and the grid transparency) that a VUV quantum from the xenon crystal hits the cathode and the low photoemission yield from zinc $\varepsilon(\lambda = 172\ \text{nm}) \approx 10^{-3}$; (2) the characteristic time of the photomultiplier response to a short signal, which is equal to 10 ns, is shorter than other characteristic times in the system.

Special experiments also confirmed that the presence of solid xenon on the lower (grid–anode) gap did not affect in any way the current characteristics of the photomultiplier provided that the cutoff voltage $U_{ga} < 0$ is supplied across this gap.

The threshold condition for the emergence of a self-sustained discharge in an electrostatic cell with a photocathode is the relation

$$\varepsilon k \eta \gamma = 1, \quad (2)$$

indicating that every primary electron leads to the formation of another electron due to the positive feedback via VUV radiation. Since the quantum yield $\eta = 10$ of electroluminescence in our conditions is quite sufficient for attaining the threshold of a self-sustained discharge, the dependence of the threshold value of voltage on the voltage U_{ga} applied to the crystal could in principle be determined and then the quantum yield η and its dependence on U_{ga} could be determined on the basis of relation (2).

However, this could not be done easily, and the reliability of such a determination could not be sufficiently enough. First, it is impossible to operate under conditions when the grid is frozen in solid xenon. In view of the drift nature of motion of electrons in a solid, the "transparency" of the grid for them is much lower than the geometrical transparency: since the grid thickness is comparable to the mesh size, an electron has a very high probability of appearing at the "channel" walls even if it falls in the transparency region. However, it was impossible to increase the mesh size by more than 0.1 mm due to field "sagging" at a gap width of 1–2 mm. For this reason, we always left a gap of 0.1–0.2 mm between the lower edge of the grid and the upper surface of the sample. This, in turn, led to a simultaneous change in the electron multiplication factor k upon a change in the voltage U_{ga} across the lower gap. This change was significant, the more so because the field strength in the region occupied by the gas was almost twice as high as in the sample because of the high dielectric constant of solid xenon. Moreover, xenon was partly deposited on the grid during sample preparation and cooling, thus changing its transparency for light and especially for electrons. Along with the contamination of the cathode by impurity gases (whose absolute amount was quite large in spite of the very high relative purity of xenon), this led to considerable variations in the magnitudes of current signals from experiment to experiment.

Consequently, the quantum yield of VUV radiation was determined as follows. In the absence of positive feedback, the current in the gap between the cathode and the grid should have the form of a short pulse similar to that shown in Figs. 6a and 6b, since the current associated with electron drift through solid xenon makes zero contribution because it passes through another electrical circuit. In the cell with solid xenon, positive feedback exists in any case. As a matter of fact, our experiments with an electron avalanche in a gas proved that the electron energy in the avalanche is sufficient for effectively ionizing the gas and is obviously sufficient (especially when argon is used) for generating excitons in solid xenon. It is well known that bombardment of the solid xenon surface leads to effective exciton luminescence, the radiative exciton luminescence time in solid xenon being $\tau_R = 30$ ns [9]. This means that a slower (exponentially decreasing) signal having a characteristic time of 30 ns and corresponding to secondary electrons emitted from the cathode under the action of surface exciton emission must be observed at the trailing edge of the electron current pulse in the upper gap corresponding to electron avalanche in the gas. There are no grounds to assume that the yield of this luminescence differs significantly from unity [9]. If, in addition, electrons form excitons in the entire course of their drift through solid xenon, an exponentially decaying signal must be accompanied by a much longer tail from secondary electrons emerging under the action of emission of these excitons. Away from the discharge ignition threshold, where the contribution from ternary, quaternary, etc., electrons can be disregarded, this signal must have the shape of a plateau extending to the time of arrival of primary electrons drifting through the sample at the anode. Naturally, the areas bounded by the current signals generated by bulk and surface excitons are proportional to the number of

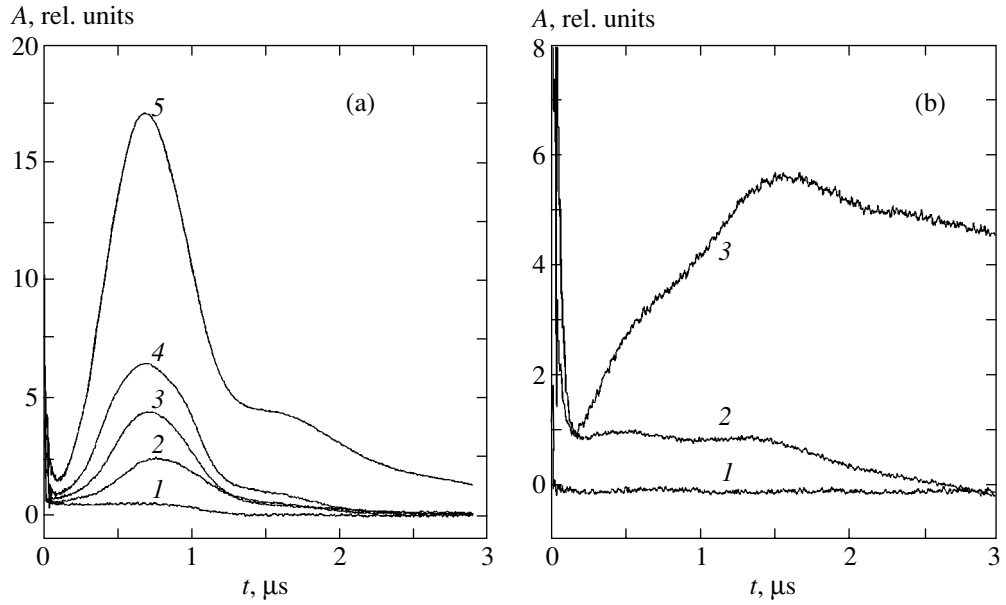

Fig. 7. Electron current in the gas-filled cathode–grid gap for various voltages applied to a xenon crystal: (a) crystal thickness is 1 mm, T = 125 K, xenon gas; U_{cg} = 380 V, U_{ga} = 270 (*1*), 310 (*2*), 330 (*3*), 350 (*4*), and 370 V (*5*); (b) crystal thickness is 2 mm, T = 77 K, argon gas: U_{cg} = 280 V, U_{ga} = 0 V (*1*), U_{cg} = 280 V, U_{ga} = 1000 (*2*), U_{cg} = 400 V, U_{ga} = 700 V (*3*).

corresponding secondary electrons; for this reason, their ratio must be equal to the quantum yield of VUV photons per drifting electron. In this case, practically none of the effects deteriorating the reproducibility of the results (cathode contamination, blocking of the grid by xenon deposited on it, and the effect of and uncontrollable gap between the grid and the crystal surface) affects the value of this ratio since their action is the same at both stages of the signal.

It can be seen from Fig. 7 that experimental results are in good agreement with the above concepts. For low voltages, the current signal in the upper gap contains, apart from the tail decaying with a characteristic time of 30 ns, a plateau whose duration is not only proportional to the thickness d of the solid xenon sample but which also coincides numerically with the drift time of an excess electron through xenon, $\tau = d/v_d$, where v_d is the electron drift velocity (it is well known [13] that velocity v_d is independent of the electric field strength E in the range of E used here). In principle, the value of v_d slightly depends on the degree of xenon purification and on the temperature at which the measurements are made. Consequently, the value of $v_d = 1.3 \times 10^5$ cm/s following from our experimental data appears to match the available results obtained for high-purity xenon [14].

However, the most convincing proof for the validity of the above interpretation is associated with the mechanism of transition to the self-sustained discharge. In the case of the generation of primary electrons by a pulse, the current pulse becomes of the so-called regeneration type associated with the overall contribution to the electron current from secondary, ternary, and all subsequent generations of electrons as the system approaches the threshold. The discharge ignition threshold corresponds to the conditions under which the area bounded by the regeneration peak (i.e., the number of electrons generated by positive feedback) becomes equal to the area bounded by the initial current pulse, which is equal to the number of primary electrons. It can easily be seen that, in view of its integrated nature, the regeneration signal attains is maximal value for times corresponding to the cessation of the positive feedback responsible for the discharge evolution (this statement is mathematically rigorous for rectangular feedback).

In a cell with a photosensitive cathode, the positive feedback ensuring the transition to the discharge is executed by photoelectron emission due to the cathode exposure to ultraviolet radiation induced by electrons [8]. However, while radiation at optically allowed transitions of atoms and molecules, which are excited by electron impacts ($\tau_R \approx 10$ ns) responsible for photoemission of electrons in a low-pressure gas, optical radiation in the presence of a xenon crystal is induced by electrons during the entire time of their drift through solid xenon. Indeed, it can be seen from Fig. 6 that approaching the discharge threshold in a gas-filled cell only broadens the current pulse ($\Delta\tau \approx 10$ ns). On the contrary, the regeneration in a cell with solid xenon (see Fig. 7) evolves more slowly (by two orders of magnitude), and the maximum of the peak is rigidly connected to the instant of time when primary electrons drifting through xenon leave the cell and fall on the anode.[1] In particular, doubling of the solid sample

[1] This is a convenient method (since the magnitude of the signal is large and there is no need to substantiate the disregard of regeneration effects) for determining the electron drift velocity.

thickness leads to a doubling of the time during which the maximum is attained; this is an additional confirmation of the fact that the feedback delay is not associated with electron emission under cathode bombardment by slow and heavy ions from the gas (such a bombardment may be responsible in principle for the discharge evolution [8]).

Thus, it can be stated with confidence that the drift of electrons through solid xenon in an electric field leads to multiple generation of excitons by these electrons and it is the emission of these excitons that is responsible for positive feedback inducing a transition to a self-sustained discharge. The ratio of the areas bounded by the slow (responsible for excitation of the crystal volume) and fast (associated with the surface excitation) components of the secondary electron current for the parameters corresponding to Fig. 7a (T = 77 K, d = 2 mm, and U_{ga} = 1000 V) gives a value of the quantum yield of electroluminescence $\eta = 20 \pm 5$. Naturally, this value depends on the voltage applied to the crystal. Consequently, a more universal characteristic is the efficiency of transformation of the electric field energy into the energy of VUV radiation, which is defined as

$$\kappa = \eta h\nu/eU, \tag{3}$$

where $h\nu$ is the energy of a VUV quantum and U is the applied voltage. For the above parameters, we have κ = 18%. Thus, in spite of high absolute values of quantum yield, the major part of energy acquired by a drifting electron from the electric field is spent on exciting the crystal lattice. This conclusion is in accordance with the constancy of the electron drift velocity in high electric fields E, which was observed in all experimental studies. According to the model developed in [7], v_d may be independent of E only in the case when an electron moving in the direction of the field with velocity v_T most of the time has a linear velocity v_d^∞ corresponding to the threshold energy E_{th} = 8.0 eV of formation of a metastable ion $(Xe^*)^-$. A two-centered exciton Xe_2^* can be formed either as a result of the process

$$(Xe^*)^- + Xe \longrightarrow Xe_2^* + e + 0.8\ \text{eV}, \tag{4}$$

characterized by a low probability due to a large difference in atomic spacings in the xenon crystal and in a two-centered exciton, or as a result of overcoming a narrow ($\Delta E \approx 0.01$ eV $\approx$ 100 K) peak of electron scattering from the structure of a negative ion by the tail of the energy distribution of drifting electrons, after which the electron acquires an energy up to E^* = 8.4 eV, sufficient for the formation of a one-center exciton Xe*, followed by the process

$$Xe^* + Xe \longrightarrow Xe_2^* + 1.2\ \text{eV}. \tag{5}$$

In the latter case, the rate at which the electron acquires energy E^* must strongly depend on temperature, especially for T < 100 K. Unfortunately, the signal from the crystal surface at T = 125 K (see Fig. 7b) is too weak for the quantum yield to be determined reliably; nevertheless, we can state that the quantum yield, as well as the efficiency of transformation at 125 K, is higher than at 77 K.

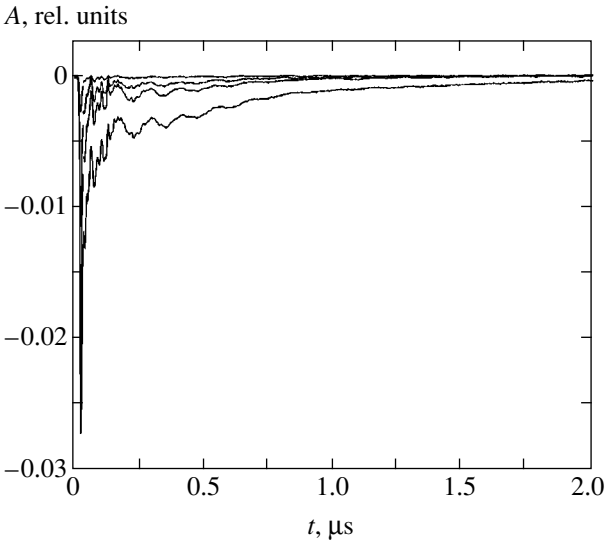

Fig. 8. Electron current in the grid–cathode gap. The crystal thickness is 1 mm, U_{cg} = 300 V, U_{ga} = 250, 290, 310, and 330 V.

The results of measurements of the electron current in the grid–anode gap are much more difficult to interpret (a typical shape of such a signal is shown in Fig. 8). In particular, even in the absence of a positive feedback through UV radiation, the signal must contain a plateau corresponding to the current of primary electrons drifting through solid xenon. Among other things, an uncontrollable contribution to the signal comes from the gas-filled gap between the grid and the upper surface of solid xenon, which is included in the electric circuit. A typical feature of the signals observed is the presence of reproducible quasiperiodic oscillations with a period of 50 ns in the leading front of the signal and about 150 ns in its trailing edge. The origin of these oscillations is not quite clear; at any rate, they are not associated with radioengineering processes in the registration system.

Naturally, after the attainment of the self-sustained discharge threshold, there is no need for creating primary electrons with the help of a laser since a continuous-wave (CW) discharge is formed spontaneously when the required voltages U_{cg} and U_{ga} are applied. The discharge is accompanied by an extremely bright glow characterized by a continuous spectrum in the entire visible range. The intensity of this glow was many orders of magnitude higher than the glow intensity of the gas discharge above solid xenon and in the empty cell filled with xenon. Naturally, the CW discharge ultimately led to xenon melting and sometimes to grid

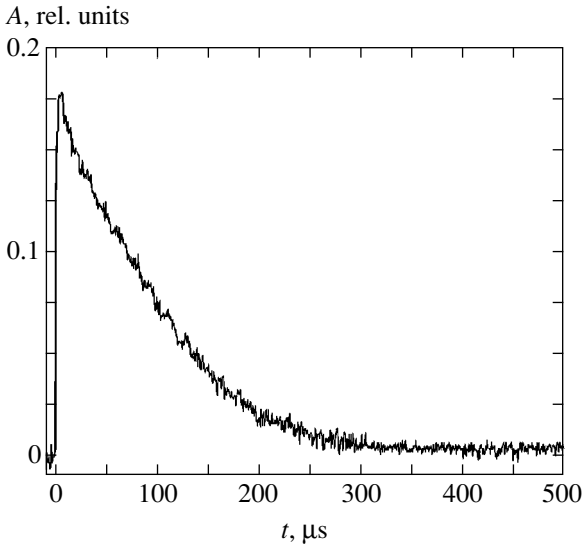

Fig. 9. Visible luminescence pulse during the discharge of a 10-μF capacitor charged to 300 V through solid xenon (of 1 mm thickness).

burning even in the presence of a 1-MΩ resistance limiting the discharge current. For this reason, we used the following approach for determining the attainable discharge current and the intensity of the luminescence accompanying it. We replaced the cathode–grid voltage source by a capacitor with a capacitance of $C = 10$ μF, which was charged to a voltage exceeding the threshold voltage for the discharge ignition (the resistor limiting the current was also removed). The pulse of discharge glow detected with the help of a photodiode is shown in Fig. 9. The intensity of a light pulse from a flash directed to the photodiode of a Minolta digital photographic camera detected for comparison at the same distance (about 2 m) was only three times higher. Knowing the voltage, $U_{cg} = 300$ V, and the characteristic duration, $\tau_p = 70$ μs, of the glow, we could estimate the discharge current, $J \approx CU_{cg}/2\tau_p = 20$ A.

5. EFFECT OF IMPURITIES

Visual observation of the visible luminescence region shows that it emerges from the bulk of the crystal and cannot be identified as luminescence of structural materials excited by exciton VUV radiation. Xenon itself cannot be excited either since it is transparent in the spectral range of its own emission [15]; in addition, the spectrum in this case would contain narrow bands [9]. Consequently, the observed intense luminescence is a result of excitation of trace impurities dissolved in solid xenon either by VUV radiation or by electron impacts.

Surprisingly, the current of discharge or its luminescence did not decrease with time in our experiments in the regime of the self-sustained discharge despite the strong current, although the current signals decrease below the threshold in our experiments (due to the formation of motionless negative oxygen ions compensating by their charge the voltage applied to the crystal) for values of the total charge passing through the sample that are smaller by orders of magnitude. The "bleaching"[2] of negative ions can be due to UV light or high-energy electrons.

In order to analyze the problem quantitatively, we must know the rate of formation of negative ions. Its calculation is a difficult problem since the electron capture cross section decreases strongly upon an increase in the electron energy; for this reason, this rate is very sensitive to the form of the electron energy distribution function for low energies (dissociative attachment of an electron to O_2, whose cross section increases with energy, can hardly take place in a solid) [16]. It is more expedient to use the experimentally measured current decay length Λ for excess electrons drifting through liquid xenon (such an estimate appears quite reliable since the values of the entire electron drift parameters for liquid and solid xenon are close). In liquid xenon purified in accordance with our method, $\Lambda \approx 2$ m [17] for close values of the electric field strength. Since the actual electron mean free path is longer than its drift path by a factor of v_T/v_d (here, v_T is the electron velocity determined by its kinetic energy; $v_T = 10^8$ cm/s for electrons with an energy of a few electronvolts), the electron mean free path prior to its capture by an impurity is given by

$$\lambda = \frac{1}{\sigma_a n} = \frac{v_T}{v_d}\Lambda, \qquad (6)$$

where σ_a is the effective capture cross section and n is the concentration of an electronegative impurity. If we assume the estimate $n \approx 10^{13}$ cm^{-3} for the residual oxygen concentration in xenon obtained in [17], it follows from relation (6) that the effective cross section of electron capture is $\sigma_a = 5 \times 10^{-19}$ cm^2. Such a small value of the cross section indicates, on the one hand, a high mean energy of electrons drifting in liquid xenon (the electron capture cross section in the gas with an electron energy of $T = 0.1$ eV is still as high as 10^{-15} cm^2 [16]) and, on the other hand, the absence of dissociative electron attachment to oxygen in the condensed phase (its cross section in the gas for $T_e \approx 8$ eV is 5×10^{-17} cm^2 [16]).

For typical conditions of our experiments, the concentration of negative ions sufficient for complete compensation of the applied voltage amounts to 10^{11} cm^{-3} [3]. In the analysis of processes that may be responsible for the bleaching of negative ions in solid xenon, the value of this quantity should be compared to the steady-state concentration n^- of O_2^- ions, which can be estimated

[2] The process of electron detachment from traps under the action of light.

from the equality of the rates of their formation and decomposition. Accordingly, we obtain

$$n^- = \left(\sigma_{ed}\Lambda\frac{v_T}{v_d}\right)^{-1}, \quad (7)$$

for the mechanisms of dissociation of negative ions by electron impacts, and

$$n^- = (\sigma_{pd}\Lambda\eta)^{-1}, \quad (8)$$

for photodissociation, where σ_{ed} and σ_{pd} are the cross sections of the corresponding processes. In a gas, $\sigma_{ed} \approx 5\times10^{-15}$ cm^2 for T_e = 5–20 eV, while $\sigma_{pd} = 1\times10^{-17}$ cm^2 for λ = 150–180 nm [16]. Using these values, we find that, for bleaching with electrons, the steady-state concentration of O_2^- is equal only to 10^9 cm^{-3}, and this process can indeed sustain continuously the electric current through xenon. In the case of photodissociation, $n_- \approx 3\times10^{13}$ cm^{-3}, and the process is insufficient for maintaining the concentration of O_2^- at the required low level. Relations (7) and (8) have clear physical meaning: the path traversed by an electron in the medium is longer than the photon path by a factor of $v_T/v_d \approx 10^3$, and the electron impact ionization cross section is much larger than the photoionization cross section. Consequently, in spite of the high quantum yield of electroluminescence, the electron component of the "plasma" is more active than the photon component as regards the dissociation of negative ions.

Similar considerations lead to the conclusion that the strong visible luminescence of solid xenon observed by us during the passage of electron current is induced by the excitation of impurities by electron impacts rather than by photoexcitation.

Analysis of relation (7) leads to one more important conclusion. If the relative concentration of electronegative impurities in xenon is high enough (say, larger than 3×10^{-8}, which corresponds to a high-purity substance for most applications), electroluminescence of solid xenon for high currents must be observed only for a very short time prior to filling the "traps." In other words, there exists an electronegative impurity concentration threshold for the initiation of a steady-state discharge through solid xenon.

6. CONCLUSIONS

It has been proved experimentally that excess electrons drifting through solid xenon in moderately strong electric fields multiply produce excitons, thus leading to intense luminescence in the VUV spectral range. The fact that the luminescence efficiency, which is quite high and attains 18%, is nevertheless much lower than the limiting efficiency confirms the prediction made in [7] and concerning the difficulty of overcoming the electron energy threshold T_e = 8.0 eV corresponding to the formation of a negative ion $(Xe^*)^-$. This means that the energy distribution function for electrons participating in steady-state drift must have a sharp peak at 8.0 eV; the small value of the effective cross section σ_a of electron capture by oxygen, which follows from the results of experiments [11], indicates the absence of a low-energy tail in the distribution.

Undoubtedly, such a behavior of an excess electron must also take place in liquid xenon as well as in liquid and solid krypton and argon. In other words, it can be expected that the drift of excess electrons through condensed HRGs will lead to the formation of ensembles of quasimonochromatic electrons with energies of 8.0, 9.6, and 11.2 eV and to effective electroluminescence at wavelengths of 172, 148, and 127 nm for Xe, Kr, and Ar, respectively. Being monochromatic in energy, drifting electrons move chaotically in contrast to electron (and, by the way, light) beams, and their path length in the medium is three orders of magnitude larger than the sample thickness. The probability of electron action on impurities (including those intentionally introduced into the solid matrix) increases in the same proportion. Realization of the latter idea will make it possible to develop a new method for studying plasmochemical reactions (electron energy, which is even higher than in the low-temperature gas plasma, is sufficient for many electron excitation, dissociation, dissociative attachment, and other processes) at low and ultralow temperatures under the conditions of matrix isolation of reagents and products. In "pure" matrices, this can be used for creating effective direct converters of the electrostatic field energy into VUV (including coherent) radiation.

The three-electrode cell designed for the above experiments may serve as a prototype for a solid-state plasma reactor (a dose of 10^{17} electrons per cm^3 per pulse attained by using a capacitor in the self-sustained discharge mode is quite sufficient for most applications) as well as for an exciton VUV lamp. The ease of realizing a volume discharge through xenon in the three-electrode scheme with a gas gap and a photocathode is especially impressive in comparison with the two-electrode scheme. In the latter case, a razor-type cathode and a voltage of 10 kV is required for a breakdown of a pure liquid xenon layer 0.2 mm thick (as is the case in the xenon purification system), while in the former case, a discharge through a solid xenon sample 1 mm thick can easily be ignited in the planar geometry for a total voltage of only 600–700 V.

ACKNOWLEDGMENTS

The authors are grateful to I.M. Obodovski for valuable advice, to A. Klochkov for assistance in carrying out experiments, and to B.M. Smirnov for fruitful discussions and for submitting the manuscript of his review [18].

This study was supported by the Russian Foundation for Basic Research (project no. 01-03-32247), the program Leading Scientific Schools of the Russian Federation (grant no. 00-15-97400), and a joint grant of the Russian Foundation for Basic Research and the Netherlands Organization for Scientific Research (RFBR-NWO grant no. 047-008-015).

REFERENCES

1. E. Aprile and M. Suzuki, IEEE Trans. Nucl. Sci. **36**, 311 (1989).
2. E. B. Gordon, V. V. Khmelenko, and O. S. Rzhevsky, Chem. Phys. Lett. **217**, 605 (1994).
3. E. B. Gordon, O. S. Rzhevskiĭ, and V. V. Khmelenko, Kvantovaya Élektron. (Moscow) **21** (3), 207 (1994).
4. S. S.-S. Huang and G. R. Freeman, Phys. Rev. A **24**, 714 (1981).
5. A. S. Schussler, J. Burghoorn, P. Wyder, *et al.*, Appl. Phys. Lett. **77**, 2786 (2000).
6. A. S. Schussler, PhD Thesis (High Magnetic Field Lab., Grenoble, France, 1998).
7. E. B. Gordon and A. F. Shestakov, Fiz. Nizk. Temp. **27**, 1192 (2001) [Low Temp. Phys. **27**, 883 (2001)].
8. Yu. P. Raĭzer, *The Physics of Gas Discharge*, 2nd ed. (Nauka, Moscow, 1992).
9. E. V. Savchenko and I. Ya. Fugol', in *Cryocrystals*, Ed. by B. I. Verkin and A. F. Prikhod'ko (Naukova Dumka, Kiev, 1983), Chap. 4.
10. A. Usenko, G. Frossati, and E. B. Gordon, Phys. Rev. Lett. **90**, 153201 (2003).
11. E. Aprile, A. Bolotnikov, D. Chen, *et al.*, Nucl. Instrum. Methods Phys. Res. A **343**, 129 (1994).
12. S. G. Pokachalov, M. A. Kirsanov, A. A. Kruglov, and I. M. Obodovski, Nucl. Instrum. Methods Phys. Res. A **327**, 159 (1993).
13. G. Ascarelli, J. Phys. Chem. **84**, 1193 (1980).
14. E. M. Gushchin, A. A. Kruglov, and I. M. Obodovskiĭ, Zh. Éksp. Teor. Fiz. **82**, 1114 (1982) [Sov. Phys. JETP **55**, 650 (1982)].
15. H. Nahme and N. Schwentner, Appl. Phys. B **51**, 273 (1990).
16. B. M. Smirnov, *Negative Ions* (Atomizdat, Moscow, 1978; McGraw-Hill, New York, 1982).
17. M. Ichige, E. Aprile, T. Doke, *et al.*, Nucl. Instrum. Methods Phys. Res. A **333**, 355 (1993).
18. B. M. Smirnov, Usp. Fiz. Nauk **172**, 1411 (2002) [Phys. Usp. **45**, 1251 (2002)].

Translated by N. Wadhwa

Journal of Experimental and Theoretical Physics, Vol. 96, No. 5, 2003, pp. 857–869.
Translated from Zhurnal Éksperimental'noĭ i Teoreticheskoĭ Fiziki, Vol. 123, No. 5, 2003, pp. 975–990.

ATOMS, SPECTRA, RADIATION

Waveguide Modes of Electromagnetic Radiation in Hollow-Core Microstructure and Photonic-Crystal Fibers

S. O. Konorov[a], O. A. Kolevatova[a], A. B. Fedotov[a,b], E. E. Serebryannikov[a], D. A. Sidorov-Biryukov[b], J. M. Mikhailova[a], A. N. Naumov[b], V. I. Beloglazov[c], N. B. Skibina[c], L. A. Mel'nikov[c], A. V. Shcherbakov[c], and A. M. Zheltikov [a,b,*]

[a] *Physics Department, Moscow State University, Vorob'evy gory, Moscow, 119899 Russia*

**e-mail: zheltikov@top.phys.msu.su*

[b] *International Laser Center, Moscow State University, Vorob'evy gory, Moscow, 119899 Russia*

[c] *Technology and Equipment for Glass Structures Institute, pr. Stroiteleĭ 1, Saratov, 410044 Russia*

Received October 31, 2002

Abstract—The properties of waveguide modes in hollow-core microstructure fibers with two-dimensionally periodic and aperiodic claddings are studied. Hollow fibers with a two-dimensionally periodic cladding support air-guided modes of electromagnetic radiation due to the high reflectivity of the cladding within photonic band gaps. Transmission spectra measured for such modes display isolated maxima, visualizing photonic band gaps of the cladding. The spectrum of modes guided by the fibers of this type can be tuned by changing cladding parameters. The possibility of designing hollow photonic-crystal fibers providing maximum transmission for radiation with a desirable wavelength is demonstrated. Fibers designed to transmit 532-, 633-, and 800-nm radiation have been fabricated and tested. The effect of cladding aperiodicity on the properties of modes guided in the hollow core of a microstructure fiber is examined. Hollow fibers with disordered photonic-crystal claddings are shown to guide localized modes of electromagnetic radiation. Hollow-core photonic-crystal fibers created and investigated in this paper offer new solutions for the transmission of ultrashort pulses of high-power laser radiation, improving the efficiency of nonlinear-optical processes, and fiber-optic delivery of high-fluence laser pulses in technological laser systems. *© 2003 MAIK "Nauka/Interperiodica".*

1. INTRODUCTION

Microstructure fibers [1–9] open new horizons in nonlinear optics and spectroscopy, ultrafast optics, optical metrology, and biomedical optics, providing, at the same time, new insights into the basic physical properties of localized modes of electromagnetic radiation in micro- and nanostructured matter. Unique properties of these fibers provide much flexibility for dispersion tailoring [10, 11] and achieving a high degree of confinement of the light field in the fiber core due to a high refractive-index step between the core and the cladding [12, 13]. A combination of these remarkable possibilities allows many intriguing physical phenomena to be observed and a whole catalogue of nonlinear-optical processes to be enhanced, including the generation of optical harmonics [14, 15] and supercontinuum emission with spectra often spanning more than an octave [16–18], as well as effective parametric interactions [19], four-wave mixing, and stimulated Raman scattering [19, 20] in the field of low-energy laser pulses. Supercontinuum generation is one of the most prominent examples of enhanced nonlinear-optical processes in microstructure and tapered fibers [16–18, 21, 22]. This phenomenon is now changing the paradigm of optical metrology and high-precision measurements [23–25], gaining, at the same time, acceptance in optical coherence tomography [26] and opening new ways for the generation of ultrashort pulses [25] and creation of new sources for spectroscopic applications [18].

Along with conventional waveguiding, supported by total internal reflection, microstructure fibers may, under certain conditions, guide electromagnetic radiation due to the high reflectivity of a periodic fiber cladding within photonic band gaps. Such guided modes can be supported in a hollow core of fibers with a cladding in the form of a two-dimensionally periodic microstructure (two-dimensional photonic crystal). Such fibers, demonstrated for the first time by Cregan *et al.* [26], represent one of the most interesting and promising types of microstructure fibers. Photonic band gaps in the transmission of a two-dimensional periodic cladding in these fibers provide high reflection coefficients for electromagnetic radiation propagating along the hollow core of the fiber, allowing a specific regime of waveguiding to be implemented [26, 27]. This mechanism of waveguiding is of special interest

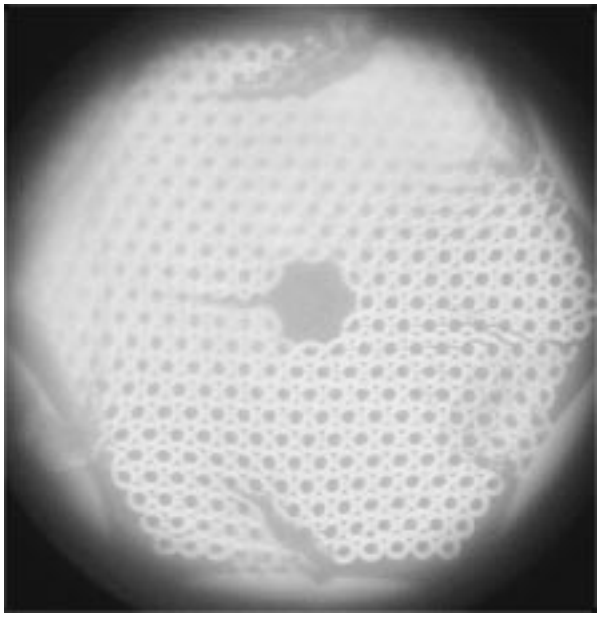

Fig. 1. Cross-sectional image of a microstructure fiber with a two-dimensionally periodic cladding consisting of an array of identical capillaries. This periodic cladding supports guided modes in the hollow core of the fiber due to the high reflectivity of a periodic structure within photonic band gaps. The hollow core of the fiber is formed by removing seven capillaries from the central part of the structure. The period of the structure in the cladding is about 5 μm and the core diameter is about 13 μm.

for telecommunication applications, opening, at the same time, the ways to enhance nonlinear-optical processes, including high-order harmonic generation, in a gas medium filling the fiber core [28]. The possibility of using such fibers for laser manipulation of small-size particles was recently demonstrated by Benabid *et al.* [29].

In this paper, we present the results of our experimental and theoretical investigations of glass fibers with a hollow core and microstructure claddings of different types. We will study hollow fibers with a two-dimensionally periodic cladding, which guide electromagnetic radiation in the hollow core due to the high reflectivity of the cladding within photonic band gaps. The spectrum of air-guided modes localized in the hollow core of our photonic-crystal fibers displays isolated maxima corresponding to photonic band gaps of the cladding. The spectrum of these modes can be tuned by changing cladding parameters. We will explore the effect of cladding aperiodicity on the properties of modes guided in the hollow core of a microstructure fiber and demonstrate that hollow fibers with disordered photonic-crystal claddings can guide localized modes of electromagnetic radiation. The spectrum of such modes still features isolated transmission maxima, but their optical losses are much higher than the optical losses attainable with hollow-core fibers having a photonic-crystal cladding. Hollow-core photonic-crystal fibers created and investigated in this paper offer much promise for telecommunication applications, delivery of high-power laser radiation, laser guiding of atoms and charged particles, as well as high-order harmonic generation and transmission of ultrashort laser pulses.

2. MODELING WAVEGUIDE MODES OF HOLLOW PHOTONIC-CRYSTAL FIBERS: A MODEL OF A PERIODIC COAXIAL WAVEGUIDE AND A FULLY VECTORIAL ANALYSIS

2.1. Model of a Periodic Coaxial Waveguide

For a qualitative analysis of guided modes in hollow-core photonic-crystal fibers (Fig. 1), we employed a model of a coaxial waveguide. Physically, the mechanism behind guided-mode formation in waveguides of this type is similar to the mechanism of waveguiding in hollow-core photonic-crystal fibers, as electromagnetic radiation is confined to the hollow core in both cases due to photonic band gaps of the fiber cladding. The modes of coaxial waveguides have been studied in earlier work [30–34]. In recent years, this effort was, at least partially, motivated by the fabrication and successful demonstration of dielectric coaxial Bragg waveguides [35]. The model of a coaxial waveguide, of course, cannot provide an accurate quantitative description of guided modes in hollow photonic-crystal fibers. However, this model allows the basic features of dispersion properties and transmission spectra of such fibers to be understood in a simple and illustrative way, providing also a general insight into the spatial distribution of electromagnetic radiation in waveguide modes localized in a hollow core of a photonic-crystal fiber.

A two-dimensional periodic structure of the fiber cladding is replaced within the framework of this model by a system of coaxial glass cylinders (see the inset in Fig. 2a) with thickness b and inner radius of the ith cylinder equal to

$$r_i = r_0 + i(b + c),$$

where r_0 is the radius of the hollow core and c is the thickness of the gap between the cylinders. Our calculations were performed for coaxial waveguides with an air- or argon-filled hollow core and a cladding consisting of alternating fused silica and air or argon coaxial layers. The data from [36, 37] were used in our calculations to include material dispersion of gases and fused silica.

In a cylindrical system of coordinates $\{r, \varphi, z\}$ with the z axis directed along the axis of the coaxial waveguide, the longitudinal components of the electric

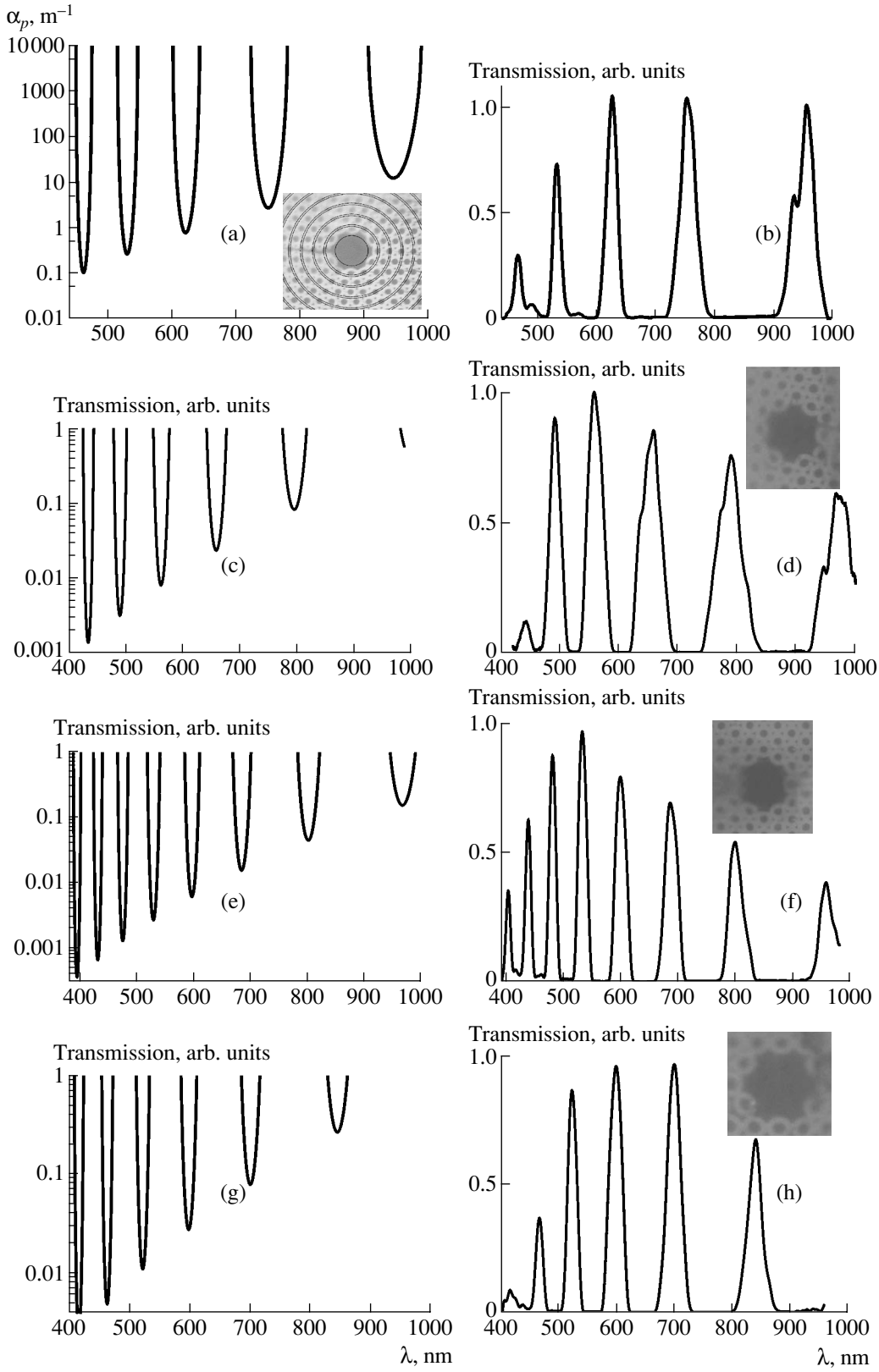

Fig. 2. (a, c, e, g) The attenuation coefficient of the TE_{01} waveguide mode calculated as a function of the wavelength for a periodic coaxial waveguide (see the inset in Fig. 2a) with different parameters: (a) $r_0 = 6.5$ μm, $b = 4.3$ μm, and $c = 0.7$ μm; (c) $r_0 = 7.28$ μm, $b = 4.55$ μm, and $c = 0.95$ μm; (e) $r_0 = 8.6$ μm, $b = 5.55$ μm, and $c = 0.95$ μm; and (g) $r_0 = 7.41$ μm, $b = 4.85$ μm, and $c = 0.75$ μm. (b, d, f, h) Transmission spectra measured for hollow-core photonic-crystal fibers with different cross-sectional geometries (shown in the insets).

and magnetic fields $E_z(r)$ and $H_z(r)$ in the ith layer of the waveguide are written as [31, 33]

$$E_z(r) = \{A_i J_m(q_i^{(n)} r) + B_i Y_m(q_i^{(n)} r)\}\sin(m\phi + \theta_m), \quad (1)$$

$$H_z(r) = \{C_i J_m(q_i^{(n)} r) + D_i Y_m(q_i^{(n)} r)\}\cos(m\phi + \theta_m), \quad (2)$$

where J_m and Y_m are the Bessel functions of the first and second kind; A_i, B_i, C_i, and D_i are the coefficients determined by boundary conditions; $q_i^{(n)}$ is the transverse part of the propagation constant for the nth waveguide mode; ω is the central frequency of laser radiation; $\beta^{(n)}$ is the propagation constant of the nth mode; m is a nonnegative integer; and θ_m is a real quantity. Transverse components of the electric and magnetic fields can be then calculated in a standard way by substituting Eqs. (1) and (2) into the Maxwell equations (see [33]). Approximate analytical expressions for the electric and magnetic fields in the modes of a coaxial Bragg waveguide have been derived in [31].

We analyzed dispersion properties of modes in a coaxial Bragg waveguide by solving, similar to [33], the characteristic equation derived from the relevant boundary conditions for the tangential components of the electric and magnetic fields at $r = r_i$,

$$T(r_i, \varepsilon_i)u_i = T(r_i, \varepsilon_{i+1})u_{i+1}, \quad (3)$$

where ε_i is the dielectric function of the ith layer,

$$T(r, \varepsilon_i) \equiv \begin{bmatrix} J_m(q_i^{(n)} r) & Y_m(q_i^{(n)} r) & 0 & 0 \\ 0 & 0 & J_m(q_i^{(n)} r) & Y_m(q_i^{(n)} r) \\ \dfrac{jm\beta^{(n)} J_m(q_i^{(n)} r)}{q_i^{(n)^2} r} & \dfrac{jm\beta^{(n)} Y_m(q_i^{(n)} r)}{q_i^{(n)^2} r} & -\dfrac{j\mu_0 \omega J_m'(q_i^{(n)} r)}{q_i^{(n)}} & -\dfrac{j\mu_0 \omega Y_m'(q_i^{(n)} r)}{q_i^{(n)}} \\ \dfrac{j\varepsilon_i \varepsilon_0 \omega J_m'(q_i^{(n)} r)}{q_i^{(n)}} & \dfrac{j\varepsilon_i \varepsilon_0 \omega Y_m'(q_i^{(n)} r)}{q_i^{(n)}} & -\dfrac{jm\beta^{(n)} J_m(q_i^{(n)} r)}{q_i^{(n)^2} r} & -\dfrac{jm\beta^{(n)} Y_m(q_i^{(n)} r)}{q_i^{(n)^2} r} \end{bmatrix}, \quad (4)$$

and

$$u_i = [A_i B_i C_i D_i]^t. \quad (5)$$

Geometric parameters of the layers forming the coaxial waveguide were chosen in such a way as to achieve the air-filling fraction of the fiber cladding measured in our experiments. In particular, for the photonic-crystal fiber with the cross section shown in Fig. 1, the period of the photonic-crystal cladding is $\Lambda \approx 5$ μm and the diameter of holes in the cladding is $a \approx 2.1$ μm. The air-filling fraction of the fiber cladding can then be estimated as

$$\eta = \frac{\pi a^2}{4\Lambda^2} \approx 14\%.$$

This estimate on the air-filling fraction of the fiber cladding dictates the following parameters of the coaxial waveguide: $b \approx 4.3$ μm and $c \approx 0.7$ μm. Figures 2a, 2c, and 2e present the results of calculations performed for hollow photonic-crystal fibers with different sizes of air holes and different air-filling fractions of the cladding. As far as the central frequencies and bandwidths of transmission peaks are concerned, predictions of this simple model agree qualitatively well with the experimental transmission spectra measured for these fibers presented in Figs. 2b, 2d, and 2f.

To estimate the magnitude of optical losses for the modes of a coaxial periodic waveguide, we will employ the following simple arguments. Let us write the coefficient of reflection R of the electric field from the periodic structure of the fiber cladding in terms of the notations introduced above:

$$R = 1 - \frac{(A_N)^2 + (B_N)^2}{(A_0)^2 + (B_0)^2}. \quad (6)$$

Introducing the angle φ between the direction of the ray trajectory representing the waveguide mode in the fiber core and the z axis, we can express the distance between the points of two successive beam reflections (the half-period of the ray trajectory) as

$$L_p = \frac{2a}{\tan\varphi}. \quad (7)$$

The number of reflections within a fiber section with a length equal to the attenuation length $L_\alpha = 1/\alpha$ (where α is the magnitude of optical losses) is given by

$$N_r = \frac{L_\alpha}{2L_p}. \quad (8)$$

The magnitude of optical losses then meets the relation

$$R^{N_r} = \exp(-\alpha L_\alpha). \quad (9)$$

Keeping in mind that

$$\tan\varphi = \frac{(u^{(n)}/\alpha)}{\beta^{(n)}} = \frac{q_0^{(n)}}{\beta^{(n)}} = \frac{(k^2\varepsilon_1 - (\beta^{(n)})^2)^{1/2}}{\beta^{(n)}}$$

and using Eqs. (6)–(9), we finally arrive at the following expression for the magnitude of losses of the electric field in a hollow-core periodic coaxial waveguide:

$$\alpha = -\frac{\ln R}{2L_p} = -\frac{\ln\left(1 - \frac{(A_N)^2 + (B_N)^2}{(A_0)^2 + (B_0)^2}\right)(k^2\varepsilon_1 - (\beta^{(n)})^2)^{1/2}}{4\alpha\beta^{(n)}}. \quad (10)$$

Figure 2c displays the results of calculations performed for a hollow periodic coaxial waveguide whose cladding parameters are chosen in such a way as to achieve maximum transmission at the wavelength of 0.8 μm. The period of the cladding in such a waveguide is $b + c = 5.5$ μm, the thickness of the fused silica layer is $b = 4.55$ μm, and the core radius is 7.28 μm. Figure 2d presents the results of experimental measurements carried out on a fiber with the cross-section structure shown in the inset to this figure. Comparison of these plots shows a satisfactory qualitative agreement between the results of calculations and the experimental data. Transmission spectra of photonic-crystal fibers display isolated peaks, which have also been observed earlier in experiments [26, 27]. No localized guided modes can exist outside these frequency ranges. The finite widths of transmission peaks limit the bandwidths and, consequently, the duration of laser pulses that can be transmitted with minimal losses through hollow photonic-crystal waveguides. As shown in [38], laser pulses with durations on the order of tens of femtoseconds can still be transmitted through hollow-core photonic-crystal fibers as localized air-guided modes.

2.2. Fully Vectorial Analysis

Predictions of the model of a periodic coaxial waveguide qualitatively agree with the results of more accurate, but much more complicated, fully vectorial analyses of modes in a hollow photonic-crystal fiber. We performed such an analysis using the approach proposed by Monro *et al.* [39] and based on the numerical solution of the eigenfunction and eigenvalue problem corresponding to the vectorial Maxwell equation for an electric field $\mathbf{E}(z, t) = \mathbf{E}\exp(i(\beta z - ckt))$, $\mathbf{E} = (E_x, E_y, E_z)$:

$$\left[\frac{\nabla^2}{k^2} + n^2\right]E_x + \frac{1}{k^2}\frac{\partial}{\partial y} \times \left(E_x\frac{\partial \ln(n^2)}{\partial x} + E_y\frac{\partial \ln(n^2)}{\partial y}\right) = \frac{\beta^2}{k^2}E_x, \quad (11)$$

$$\left[\frac{\nabla^2}{k^2} + n^2\right]E_y + \frac{1}{k^2}\frac{\partial}{\partial y} \times \left(E_x\frac{\partial \ln(n^2)}{\partial x} + E_y\frac{\partial \ln(n^2)}{\partial y}\right) = \frac{\beta^2}{k^2}E_y, \quad (12)$$

where β is the propagation constant, k is the wave number, ∇ is the gradient operator, and $n^2(x, y)$ is the two-dimensional profile of the refractive index.

Transverse distribution of the electric field in the cross section of the fiber is represented as an expansion in orthonormalized Hermite–Gauss functions:

$$E_x = \sum_{n,m=0}^{F-1} \xi^x_{n,m}\psi_n\left(\frac{x}{\Lambda}\right)\psi_m\left(\frac{y}{\Lambda}\right),$$
$$E_y = \sum_{n,m=0}^{F-1} \xi^y_{n,m}\psi_n\left(\frac{x}{\Lambda}\right)\psi_m\left(\frac{y}{\Lambda}\right). \quad (13)$$

The profile of the refractive index squared, $n^2(x, y)$, is also represented as an expansion in Hermite–Gauss functions and a set of orthogonal periodic functions (cosine functions in our case). Substituting these functional series into the wave equations reduces our vectorial problem to an eigenfunction and eigenvalue problem for the relevant matrix equation. Solving this problem, we can find the propagation constants and spatial field distributions in waveguide modes.

Figures 3a and 3b present transverse field intensity distributions calculated with the use of the above-described approach for a hollow-core photonic-crystal fiber with a cross-sectional structure similar to that shown in Fig. 1 around the maximum-transmission frequency in the visible spectral range. Transverse field intensity distributions shown in Figs. 3a and 3b correspond to the fundamental and higher order modes guided in the hollow photonic-crystal fiber, respectively. Thus, our vectorial numerical analysis also indicates the existence of higher order air-guided modes localized under the above-specified conditions in the hollow core of a photonic-crystal fiber.

We have demonstrated that the predictions of the model of a coaxial periodic waveguide provide satisfactory qualitative agreement with the results of the vectorial analysis of guided modes in a hollow photonic-

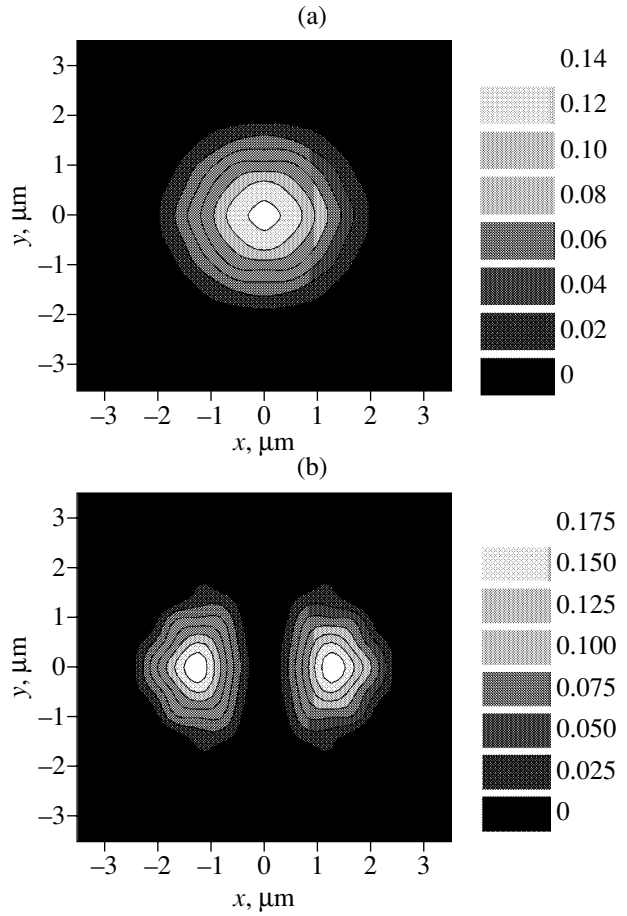

Fig. 3. Transverse radiation intensity distribution in (a) the fundamental and (b) higher order air-guided modes calculated by means of vectorial analysis of electromagnetic field in a photonic-crystal fiber with the cross-sectional structure similar to that shown in Fig. 1.

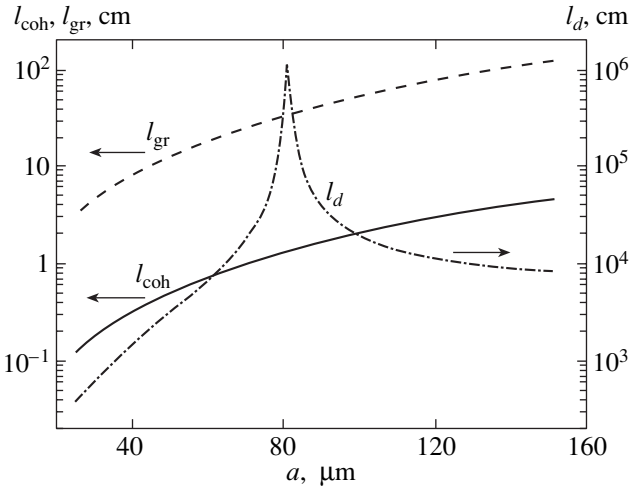

Fig. 4. Dispersion spreading length l_d for 35-fs pulses of 800-nm radiation calculated as a function of the inner radius of a hollow fiber a for the fundamental EH_{11} mode. Coherence length for mode cross-talk l_{coh} and the walk-off length l_{gr} are also shown. The hollow core of the fiber is filled with argon at a pressure of 1 atm.

crystal fiber, as well as with the results of experimental studies (see Section 4). This finding allows us to suggest the model of a hollow coaxial waveguide as a simple framework for elementary estimates of dispersion parameters and qualitative understanding of the spatial distribution of electromagnetic radiation in the guided modes of hollow-core photonic-crystal fibers.

2.3. Group-Velocity Dispersion and Transmission of Ultrashort Pulses

Guided modes of hollow photonic-crystal fibers are ideally suited for the transmission and control of ultrashort light pulses. Due to the fact that the group-velocity dispersion of gases filling a hollow core of photonic-crystal fibers is much lower than the group-velocity dispersion typical of dielectric materials used in standard fibers, temporal spreading of short light pulses transmitted by air-guided modes of hollow-core photonic-crystal fibers is much less critical than in the case of guided modes of standard fibers. This important circumstance, however, by no means exhausts the benefits offered by hollow-core photonic-crystal fibers for the transmission and control of ultrashort pulses of electromagnetic radiation. Aside from the material of the fiber, dispersion properties of guided modes in hollow photonic-crystal fibers are sensitive to the core–cladding geometry. This circumstance allows dispersion tailoring by changing the fiber structure. In the case of microstructure fibers with a dielectric core, which guide electromagnetic radiation by total internal reflection, flat group-velocity dispersion profiles can be shaped, with the sign and the absolute value of group-velocity dispersion controlled by varying the period of the structure and the air-filling fraction of the cladding, and by filling the air holes in the cladding with different materials [12, 13]. Similar efficient solutions for hollow-core photonic-crystal fibers are still to be found. The results of our experimental studies presented in Section 4 demonstrate that the transmission spectrum and, consequently, the dispersion of hollow photonic-crystal fibers can be tuned by changing the structure of the fiber cladding. Numerical simulations [38] reveal regions of low group-velocity dispersion within transmission peaks of these fibers.

Away from the edges of photonic band gaps of a periodic fiber cladding, the frequency dependence of group-velocity dispersion of modes guided in the hollow core of a photonic-crystal fiber is similar to the spectral dependence of group-velocity dispersion for a metal hollow fiber [34]. We can, therefore, employ several useful relations known from the theory of solid-cladding hollow fibers to assess the dependence of the group-velocity dispersion of guided modes in hollow photonic-crystal fibers on parameters of such fibers far from the edges of photonic band gaps. In particular, the

group-velocity dispersion D scales as approximately the inverse square of the inner fiber diameter a [34],

$$D \sim -a^{-2}.$$

The increase in the inner fiber radius thus allows the effects related to the dispersion spreading of ultrashort pulses to be reduced. Figure 4 shows the dispersion length for 35-fs pulses of 800-nm radiation propagating in an argon-filled hollow fiber as a function of the inner radius of this fiber. As can be seen from this dependence, zero group-velocity dispersion is achieved with an inner fiber radius equal to 80 μm.

Figure 5 displays the dependences of the group index and group-velocity dispersion on the wavelength for a hollow fiber with an inner radius of 68 μm filled with molecular hydrogen at a pressure of 0.5 atm. Group-velocity dispersion under these conditions is low within the entire spectral range under study, vanishing at a wavelength of 560 nm (see also [40]). Importantly, for long wavelengths, dispersion properties of guided modes are mainly determined by the waveguide dispersion component, while for short wavelengths, the material dispersion of the gas filling the fiber plays the dominant role. The group velocity and group-velocity dispersion as functions of the wavelength asymptotically tend in these limiting cases (Fig. 5) to dependences characteristic of the waveguide (dotted lines) and material (dashed lines) dispersion components.

Hollow coaxial Bragg waveguides with a small inner radius, on the other hand, allow high absolute values of group-velocity dispersion to be achieved, providing an opportunity to compensate for strong material dispersion of gases filling the fiber core [41]. Reflection from the periodic structure of a fiber cladding is accompanied by an additional phase shift [42], modifying the frequency dependence of group-velocity dispersion and making the spectral dependences of dispersion parameters of hollow coaxial Bragg waveguides and photonic-crystal fibers deviate from the approximate dependences characteristic of guided modes in metal hollow waveguides.

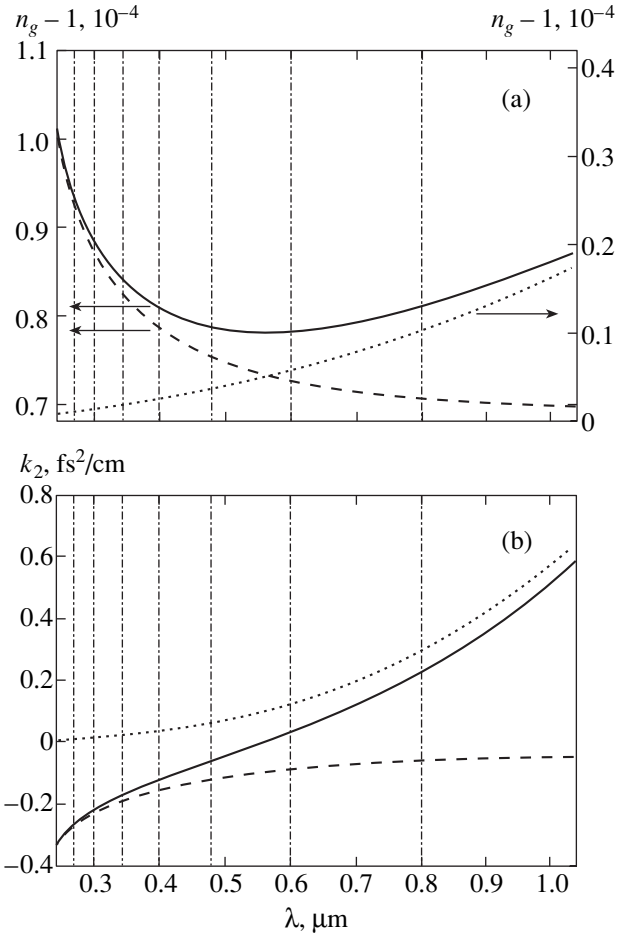

Fig. 5. (a) The group index $n_g = c/v_g$ and (b) group-velocity dispersion calculated as functions of the wavelength (dashed lines) for molecular hydrogen [25], (dotted lines) the EH_{11} waveguide mode, and (solid lines) the EH_{11} mode of a hollow fiber filled with molecular hydrogen. The gas pressure is 0.5 atm. The inner radius of the fiber is 68 μm. The vertical lines show Raman sidebands produced through the stimulated Raman scattering of the second harmonic of a Ti: sapphire laser.

3. EXPERIMENTAL

Hollow microstructure fibers with a two-dimensionally periodic (photonic-crystal) cladding were fabricated with the use of a preform consisting of a set of identical glass capillaries. Seven capillaries were removed from the central part of the preform for the hollow core of photonic-crystal fibers. A cross-sectional image of a fiber fabricated by drawing such a preform is presented in Fig. 1. The typical period of the structure in the cladding of the fiber shown in Fig. 1 is about 5 μm. The diameter of the hollow core of the fiber is then approximately equal to 13 μm. Varying the period of the photonic-crystal structure in the fiber cladding and changing its air-filling fraction, we were able to tune the transmission spectrum of air-guided modes, providing optimal conditions for a waveguide transmission of radiation with different wavelengths (see Section 4). The length of fiber samples employed in our experiments ranged from several centimeters up to 1 m.

Special microstructure fibers have been designed and fabricated to investigate the effect of fiber-cladding aperiodicity on the properties of guided modes. These fibers had an aperiodic cladding, characterized by the presence of short-range order (Fig. 6). A preform with a larger central capillary surrounded by smaller capillaries was employed to fabricate such fibers. The cobweb structure of the cladding in such a fiber, as can be seen from Fig. 6, features, in a certain approximation, a short-range order in the arrangement of glass channels linked by narrow bridges. The fiber cross-section image shown in Fig. 6 also visualizes a set of roughly concen-

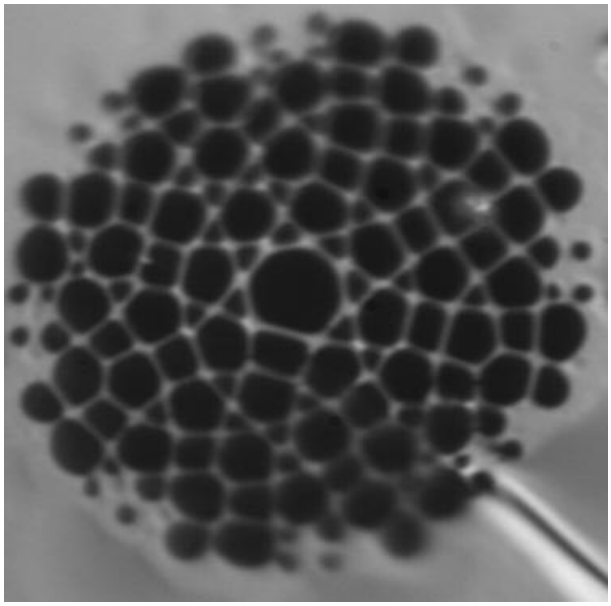

Fig. 6. A cross-sectional microscopic image of a cobweb fiber with a disordered microstructure cladding. The ring system of glass channels at the center of this fiber forms a two-dimensional photonic molecule. The distance between the neighboring channels is 7.4 μm.

tric glass rings, surrounding the fiber core, with a fuzzily defined characteristic spacing between them. Air-filled holes, arranged aperiodically in the fiber cladding, and the larger hole at the center of the fiber form an array of small-diameter glass waveguides linked by thin bridges around the central hole (Fig. 6). Such a microstructure-integrated bundle of fibers provides a high degree of light confinement due to the total internal reflection from the high-refractive-index-step glass–air interface. Dispersion aspects of pulse propagation and nonlinear-optical interactions in such fiber structures can be controlled by exciting different combinations of collective waveguide modes.

The central ring array of waveguides in the considered cobweb fiber is reminiscent in its structure of a cyclic polyatomic molecule consisting of identical atoms (Fig. 6). As shown earlier [43, 44], the properties of guided modes in such a ring array of coupled waveguides are similar to the properties of electron wave functions in a two-dimensional polyatomic cyclic molecule. The basic dispersion properties of guided modes in this coupled-waveguide array can be described in a convenient and illustrative way in terms of the photonic-molecule model. The high degree of light localization in these photonic-molecule modes of a cobweb microstructure fiber provides high efficiency of nonlinear-optical interactions, allowing octave spectral broadening to be achieved with low-energy femtosecond pulses. The results of experimental studies presented in Section 4.2 of this paper demonstrate that this microstructure fiber not only guides electromagnetic radiation through the central array of microstructure-integrated waveguides, but also supports air-guided modes in its hollow core. Our studies of hollow microstructure fibers with periodic and aperiodic claddings performed in this paper allow the influence of cladding aperiodicity and disorder on the properties of air-guided modes in microstructure fibers to be assessed, providing a deeper insight into the physics of such modes, as well as the fundamental aspects of light propagation and scattering in photonic band-gap structures.

4. RESULTS AND DISCUSSION

4.1. Hollow Photonic-Crystal Fibers

The idea of lowering the magnitude of optical losses in a hollow fiber with a periodically microstructured cladding relative to the magnitude of optical losses in a hollow fiber with a solid cladding is based on the high reflectivity of a periodic structure within photonic band gaps [45]. In hollow fibers, the refractive index of the core is lower than the refractive index of the cladding. Therefore, the propagation constants of hollow-fiber modes have nonzero imaginary parts, and the propagation of light in such fibers is accompanied by radiation losses. The magnitude of optical losses in hollow fibers scales [46] is λ^2/a^3, where λ is the radiation wavelength and a is the inner radius of the fiber. Such a behavior of the magnitude of optical losses prevents one from using hollow fibers with very small inner diameters in nonlinear-optical experiments [42, 47]. Our estimates show that the magnitude of radiation losses for the fundamental mode of a hollow fiber with a fused silica cladding and an inner radius of 6.5 μm may reach 20 cm^{-1} for 0.8-μm radiation, which, of course, imposes serious limitations on applications of such fibers. Radiation losses can be radically reduced in the case of hollow fibers with a periodic cladding.

Our experimental studies confirm the possibility of using hollow photonic-crystal fibers with a core diameter of about 13 μm to guide coherent and incoherent radiation. Figure 7 displays the spatial distributions of intensity of incoherent (Fig. 7a) and coherent (Fig. 7b) radiation obtained by imaging the output end of a hollow photonic-crystal fiber with the above-specified parameters. Optimizing the geometry of coupling of laser radiation into the fiber, we were able to achieve a high degree of light-field confinement in the hollow core of the fiber without losing too much energy through mode excitation in the photonic-crystal cladding (Fig. 7a). The spatial distribution of radiation intensity at the output end of the fiber under these conditions corresponded to the fundamental waveguide mode.

To investigate the spectrum of modes guided in the hollow core of photonic-crystal fibers, we used a diaphragm to separate radiation transmitted through the hollow core from radiation guided by the cladding. The spectra of modes supported by the hollow core of pho-

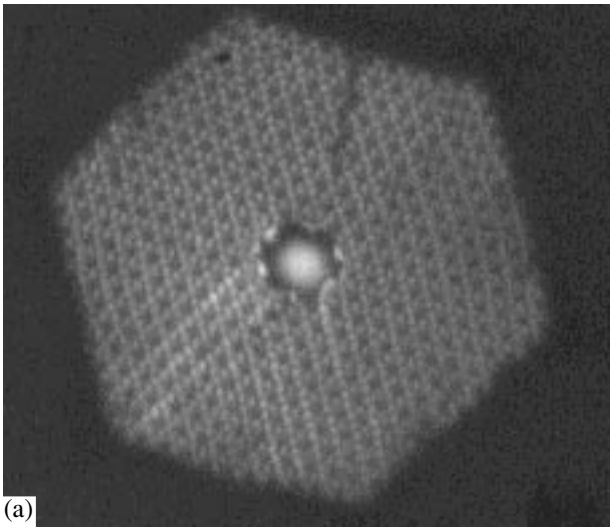

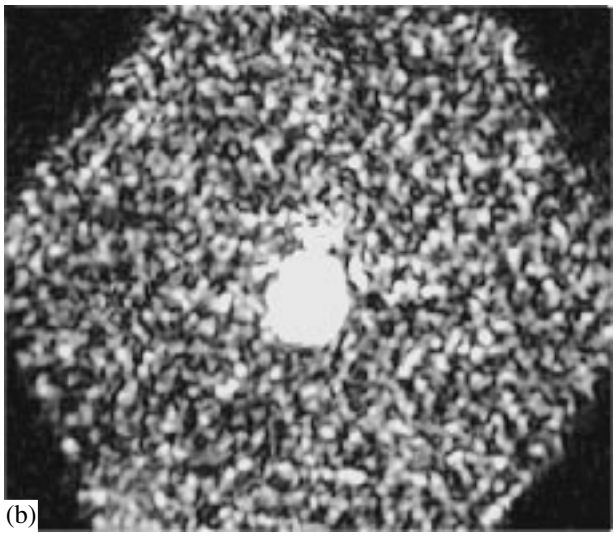

Fig. 7. Radiation intensity distribution in the cross section of a hollow photonic-crystal fiber with a period of the structure in the cladding of about 5 μm and a core diameter of approximately 13 μm. (a) A waveguide mode is excited in the hollow core with a broad beam of incoherent light. (b) The fundamental waveguide mode of the hollow core is excited with 633-nm diode-laser radiation.

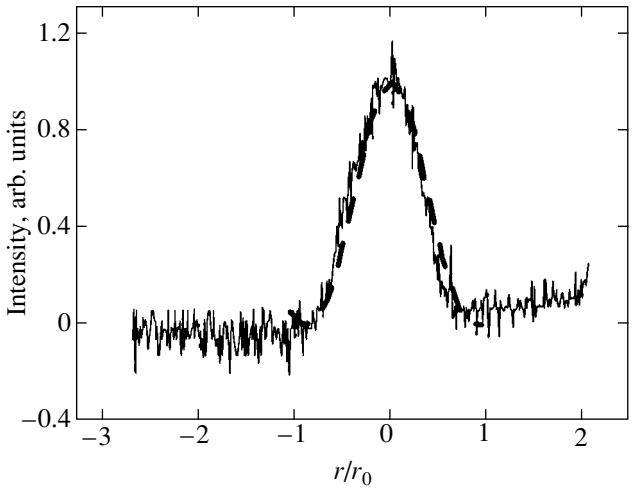

Fig. 8. Transverse intensity distribution of electromagnetic radiation (solid line) measured at the output of a hollow-core photonic-crystal fiber and (dashed line) calculated with the use of the model of a periodic coaxial waveguide.

tonic-crystal fibers were measured within the range of wavelengths from 450 up to 1000 nm. These spectra displayed characteristic well-pronounced isolated peaks (Figs. 2b, 2d, 2f, 2h). Similar peaks in transmission spectra of hollow photonic-crystal fibers have also been observed in earlier work [26, 27]. The origin of these peaks is associated with the high reflectivity of a periodically structured fiber cladding within photonic band gaps, which substantially reduces radiation losses in guided modes within narrow spectral ranges. Radiation with wavelengths lying away from photonic band gaps of the cladding leaks from the hollow core. Such leaky radiation modes are characterized by high losses, giving virtually no contribution to the signal at the output of the fiber. The spectra of air-guided modes in hollow photonic-crystal fibers were tuned by changing the fiber cladding structure. In Figs. 2a–2h, this tunability option is illustrated by transmission spectra measured for hollow photonic-crystal fibers with different cross-sectional structures (shown in the insets to Figs. 2a, 2d, 2f, 2h).

As can be seen from the comparison of the results of calculations (Figs. 2a, 2c, 2e, 2g), carried out with the use of the approach described in Section 2.1, with the experimental data shown in Figs. 2b, 2d, 2f, 2h, the model of a periodic coaxial waveguide provides qualitatively adequate predictions for the positions and the widths of spectral bands where the hollow core of a photonic-crystal fiber can guide electromagnetic radiation with minimum losses. Variations in the structure of the photonic-crystal cladding were modeled with our approach by accommodating the thicknesses of coaxial layers constituting the Bragg waveguide in such a way as to achieve the required air-filling fraction of the photonic-crystal fiber. This approach allowed us to design hollow photonic-crystal fibers providing maximum transmission for a given wavelength. In particular, fibers with the cross-sectional structure shown in the insets to Figs. 2d and 2f feature transmission peaks at a wavelength of 800 nm and can be employed to transmit Ti:sapphire laser radiation. Fibers with the cross-sectional structure presented in the insets to Figs. 2f and 2h display transmission peaks at 532 nm, offering a way to transport second-harmonic radiation of a neodymium garnet laser.

The model of a periodic coaxial waveguide, as can be seen from Figs. 8 and 9, also gives satisfactory qualitative description of radiation intensity distributions in the fundamental (Fig. 8) and higher order (Fig. 9) waveguide modes of a photonic-crystal fiber. Compari-

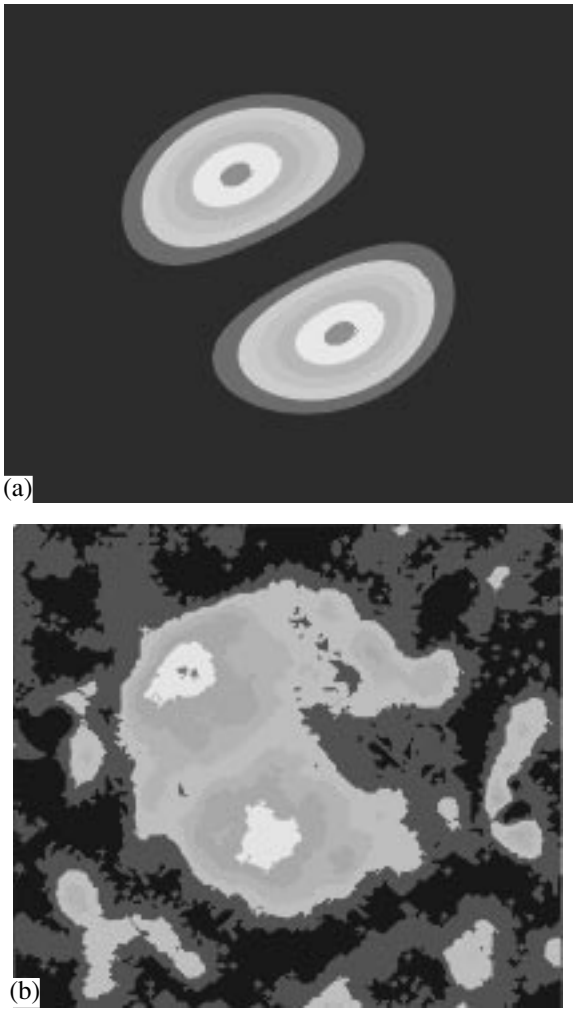

Fig. 9. (a) Transverse distribution of the electric field squared in a higher order mode of a hollow-core photonic-crystal fiber calculated with the use of the model of a periodic coaxial waveguide. (b) Transverse intensity distribution of electromagnetic radiation measured at the output of a hollow-core photonic-crystal fiber with a higher order waveguide mode of the fiber excited with 633-nm radiation of a diode laser.

son of Figs. 7–9 allows a judgement on the qualitative agreement between the experimental data, theoretical predictions obtained with the model of a periodic coaxial waveguide, and the results of a more accurate, but more complicated vectorial analysis of guided modes in a hollow photonic-crystal fiber (see Section 2.2).

The spatial distribution (Fig. 9b) of 633-nm diode-laser radiation (this wavelength falls within one of the transmission peaks in Figs. 2a, 2b, corresponding to the guided modes of the photonic-crystal fiber) at the output of an 8-cm hollow photonic-crystal fiber indicates the existence of multimode regimes of waveguiding around this wavelength. As shown in [28], multimode waveguiding regimes in hollow photonic-crystal fibers can be employed to enhance high-order harmonic

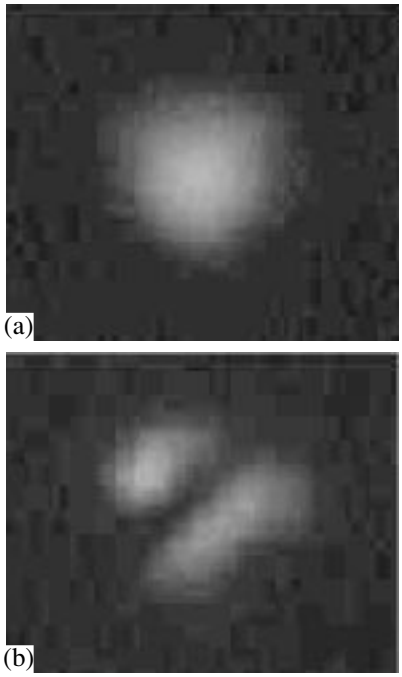

Fig. 10. Transverse intensity distributions of 1.06-μm laser radiation at the output of a hollow-core photonic-crystal fiber (a) in the fundamental and (b) in the higher order waveguide modes.

generation in nonlinear gases filling the hollow cores of these fibers. The waveguide contribution to the mismatch of propagation constants related to the guided modes of the pump and harmonic radiation increases with a decrease in the core diameter of a hollow fiber [48]. Our photonic-crystal fiber with a small core diameter is, therefore, characterized by a strong dispersion of guided modes, allowing considerable phase mismatches related to the material dispersion of nonlinear gases to be compensated. This efficient phase-mismatch compensation becomes possible due to the unique properties of hollow photonic-crystal fibers, as the leaky modes guided in hollow fibers with a solid cladding and a diameter of the hollow core of about 13 μm would have, as mentioned above, unacceptably high losses.

The possibility of transporting high-power laser pulses through hollow-core photonic-crystal fibers was demonstrated by our experiments with 40-ps neodymium garnet laser pulse trains with a total energy of 1 mJ transmitted through a hollow photonic-crystal fiber with an inner diameter of 13 μm. The energy fluence of laser energy in these experiments reached 100 J/cm^2, which was an order of magnitude higher than the optical breakdown threshold for fused silica. A hollow photonic-crystal fiber allowed sequences of picosecond laser pulses to be transmitted in both single-mode (Fig. 10a) and multimode (Fig. 10b) regimes, providing laser fluences and spatial beam quality at the

output of the fiber sufficient to initiate optical breakdown on different targets.

4.2. Hollow Fibers with an Aperiodic Microstructure Cladding

To examine the effect of disorder and aperiodicity of the cladding structure on the properties of guided modes and waveguiding regimes in hollow-core photonic-crystal fibers, we investigated the spectrum of modes supported in the hollow core of microstructure fibers with an aperiodic cladding featuring a short-range order of the cladding structure (Fig. 6). As shown in earlier work [43, 44], a structure consisting of seven linked glass channels in the central part of the cross section of such fibers and surrounding the hollow fiber core guides localized modes of electromagnetic radiation, which are classified as photonic-molecule modes. Our experiments have shown that fibers of this type may also transmit light through guided modes localized in their hollow core. Figure 11a presents the spectrum of radiation transmitted through the hollow core of such fibers. To measure this spectrum, we selected radiation guided through the hollow core from radiation transmitted through the thin ring glass (photonic-molecule) structure surrounding the hollow core with the use of a diaphragm. In spite of the aperiodicity of the fiber cladding, clearly pronounced transmission peaks are observed in the spectra of radiation transmitted through the hollow core of the fiber. The spectra of radiation transmitted through the thin ring glass structure surrounding the hollow core are continuous, indicating different physics of waveguiding and giving rise to a pedestal in the spectra, measured with a diaphragm adjusted to select radiation transmitted through the central part of the fiber, including the hollow core and the photonic-molecule part of the cladding (Fig. 11b).

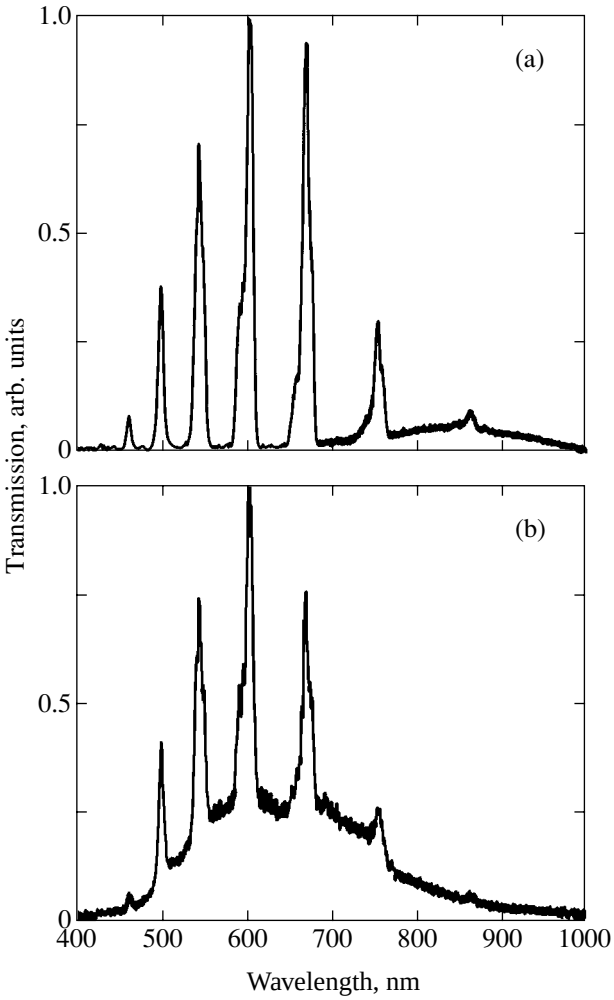

Fig. 11. Transmission spectra of a hollow fiber with a disordered microstructure cladding measured (a) with a diaphragm set to select radiation transmitted through the hollow core of the fiber and (b) with a diaphragm selecting radiation transmitted through the hollow core and the ring glass photonic-molecule structure in the central part of the fiber (see Fig. 6).

One practical aspect revealed by these studies is that waveguiding in a hollow core of photonic-crystal fibers involves some tolerance of deviations from the ideal periodicity of the cladding. The results of these experiments also provide deeper insights into the basic physical issues related to the origin of photonic band gaps and waveguide modes in hollow photonic-crystal and microstructure fibers, as well as regimes of light scattering and interference in disordered and amorphous photonic crystals [49–54]. Our experiments demonstrate, in particular, that air-guided modes in hollow microstructure fibers can be supported, in particular, due to reflection from a cladding with a short-range order. The cladding of microstructure fibers employed in these experiments features, in some approximation, two types of spatial regularity—a short-range order, similar to that typical of amorphous photonic crystals, and the existence of some fuzzily defined characteristic separation between concentric rings in the cladding structure (see Fig. 10).

Localized air-guided modes in hollow photonic-crystal fibers with an ideally periodic cladding are associated with the existence of photonic band gaps in the transmission of the cladding. Within these frequency ranges, electromagnetic radiation cannot leak from the core into the cladding of a fiber. Evanescent fields existing in the photonic-crystal fiber cladding within the photonic band gaps rapidly decay with the growth in the distance from the fiber core. As some disorder is introduced into the fiber cladding, allowed states arise within the photonic band gap. The density of such states increases as the degree of structure disorder grows [54]. Allowed states in the photonic band gap may substantially modify transmission spectra of hollow microstructure fibers. The modes guided along the hollow core of such fibers become more and more lossy, leaking into the cladding as the density of allowed states grows within the photonic band gap of the fiber cladding. The spectrum presented in Fig. 11a

corresponds to an intermediate regime when the density of allowed states arising within the photonic band gaps due to the aperiodicity and disorder of the microstructure cladding is still low, permitting the existence of localized air-guided modes in the hollow core of the fiber.

5. CONCLUSION

Experimental and theoretical studies presented in this paper reveal several important properties of modes guided by hollow-core microstructure fibers with two-dimensionally periodic and aperiodic claddings. We have also demonstrated that such fibers offer new solutions for the transmission of ultrashort pulses of high-power laser radiation, improving the efficiency of nonlinear-optical processes, and fiber-optic delivery of high-fluence laser pulses in technological laser systems. Hollow photonic-crystal fibers support air-guided modes of electromagnetic radiation localized in the hollow core due to the high reflectivity of the fiber cladding within photonic band gaps. Experimentally measured spectra of such modes display isolated maxima corresponding to photonic band gaps of the photonic-crystal cladding. The manifolds of such transmission peaks can be tuned by changing cladding parameters. The effect of cladding aperiodicity on the properties of modes guided in the hollow core of a microstructure fiber was analyzed. We have shown the possibility of designing hollow photonic-crystal fibers providing maximum transmission for radiation with a desirable wavelength. Hollow photonic-crystal fibers designed to transmit 532-, 633-, and 800-nm radiation have been fabricated and tested.

Our experiments also demonstrate the existence of localized air-guided modes of electromagnetic radiation in hollow fibers with disordered and aperiodic microstructure claddings. The spectra of such modes still feature isolated transmission maxima, but their optical losses are much higher than the optical losses attainable with hollow-core fibers having a photonic-crystal cladding. From the technological viewpoint, this implies that requirements on the periodicity of the photonic-crystal fiber cladding can be loosened under certain conditions. Fundamental aspects of these studies involve using isolated transmission peaks observed for hollow microstructure fibers with an aperiodic cladding as a clue to gaining deeper insight into the formation of photonic band gaps and regions of low photonic densities of states and, more generally, understanding regimes of light scattering and interference in random and amorphous photonic crystals.

Hollow-core photonic-crystal fibers created and investigated in this paper offer new solutions to many problems in basic physics and applied optics. Such fibers hold much promise, in particular, for telecommunication applications and delivery of high-power laser radiation. Due to their remarkable properties, these fibers offer a unique opportunity for implementing nonlinear-optical interactions of waveguide modes with transverse sizes of several microns in a gas medium, opening the ways to improve the efficiency of optical frequency conversion for ultrashort pulses and enhance high-order harmonic generation. The spectra of air-guided modes in hollow-core photonic-crystal fibers, featuring isolated transmission peaks, are ideally suited for wave-mixing spectroscopic applications and frequency conversion through stimulated Raman scattering. Further exciting applications of these fibers include generation and guiding of ultrashort pulses, extendable to subfemtosecond X-ray field waveforms, manipulation of atoms and charged particles, and creation of highly sensitive gas sensors.

ACKNOWLEDGMENTS

This study was supported in part by the President of Russian Federation Grant no. 00-15-99304, the Russian Foundation for Basic Research (project nos. 00-02-17567 and 02-02-17098), the Volkswagen Foundation (project I/76 869), and the European Research Office of the US Army (contract no. N62558-02-M-6023).

REFERENCES

1. J. C. Knight, T. A. Birks, P. St. J. Russell, and D. M. Atkin, Opt. Lett. **21**, 1547 (1996).
2. J. C. Knight, J. Broeng, T. A. Birks, and P. St. J. Russell, Science **282**, 1476 (1998).
3. Opt. Express **9** (13) (2001), Focus Issue, Ed. by K. W. Koch.
4. J. Opt. Soc. Am. B **19** (2002), Special Issue, Ed. by C. M. Bowden and A. M. Zheltikov.
5. T. M. Monro, P. J. Bennett, N. G. R. Broderick, and D. J. Richardson, Opt. Lett. **25**, 206 (2000).
6. A. B. Fedotov, A. M. Zheltikov, L. A. Mel'nikov, *et al.*, Pis'ma Zh. Éksp. Teor. Fiz. **71**, 407 (2000) [JETP Lett. **71**, 281 (2000)]; M. V. Alfimov, A. M. Zheltikov, A. A. Ivanov, *et al.*, Pis'ma Zh. Éksp. Teor. Fiz. **71**, 714 (2000) [JETP Lett. **71**, 489 (2000)].
7. A. M. Zheltikov, Usp. Fiz. Nauk **170**, 1203 (2000) [Phys. Usp. **43**, 1125 (2000)].
8. A. M. Zheltikov, M. V. Alfimov, A. B. Fedotov, *et al.*, Zh. Éksp. Teor. Fiz. **120**, 570 (2001) [JETP **93**, 499 (2001)].
9. B. J. Eggleton, C. Kerbage, P. S. Westbrook, *et al.*, Opt. Express **9**, 698 (2001).
10. N. G. R. Broderick, T. M. Monro, P. J. Bennett, and D. J. Richardson, Opt. Lett. **24**, 1395 (1999).
11. A. B. Fedotov, A. M. Zheltikov, A. P. Tarasevitch, and D. von der Linde, Appl. Phys. B **73**, 181 (2001).
12. J. C. Knight, J. Arriaga, T. A. Birks, *et al.*, IEEE Photonics Technol. Lett. **12**, 807 (2000).
13. W. H. Reeves, J. C. Knight, P. St. J. Russell, and P. J. Roberts, Opt. Express **10**, 609 (2002).
14. J. K. Ranka, R. S. Windeler, and A. J. Stentz, Opt. Lett. **25**, 796 (2000).
15. A. N. Naumov, A. B. Fedotov, A. M. Zheltikov, *et al.*, J. Opt. Soc. Am. B **19**, 2183 (2002).

16. J. K. Ranka, R. S. Windeler, and A. J. Stentz, Opt. Lett. **25**, 25 (2000).
17. W. J. Wadsworth, A. Ortigosa-Blanch, J. C. Knight, *et al.*, J. Opt. Soc. Am. B **19**, 2148 (2002).
18. A. B. Fedotov, Ping Zhou, A. P. Tarasevitch, *et al.*, J. Raman Spectrosc. **33** (11/12) (2002).
19. St. Coen, A. H. L. Chau, R. Leonhardt, *et al.*, Opt. Lett. **26**, 1356 (2001).
20. S. Coen, A. Hing Lun Chau, R. Leonhardt, *et al.*, J. Opt. Soc. Am. B **19**, 753 (2002).
21. A. B. Fedotov, A. N. Naumov, A. M. Zheltikov, *et al.*, J. Opt. Soc. Am. B **19**, 2156 (2002).
22. J. M. Dudley, Xun Gu, Lin Xu, *et al.*, Opt. Express **10**, 1215 (2002).
23. S. A. Diddams, D. J. Jones, Jun Ye, *et al.*, Phys. Rev. Lett. **84**, 5102 (2000).
24. D. J. Jones, S. A. Diddams, J. K. Ranka, *et al.*, Science **288**, 635 (2000).
25. R. Holzwarth, T. Udem, T. W. Hansch, *et al.*, Phys. Rev. Lett. **85**, 2264 (2000).
26. S. N. Bagayev, A. K. Dmitriyev, S. V. Chepurov, *et al.*, Laser Phys. **11**, 1270 (2001).
27. I. Hartl, X. D. Li, C. Chudoba, *et al.*, Opt. Lett. **26**, 608 (2001).
28. J. Herrmann, U. Griebner, N. Zhavoronkov, *et al.*, Phys. Rev. Lett. **88**, 173901 (2002).
29. R. F. Cregan, B. J. Mangan, J. C. Knight, *et al.*, Science **285**, 1537 (1999).
30. S. O. Konorov, A. B. Fedotov, O. A. Kolevatova, *et al.*, Pis'ma Zh. Éksp. Teor. Fiz. **76**, 401 (2002) [JETP Lett. **76**, 341 (2002)].
31. A. N. Naumov and A. M. Zheltikov, Kvantovaya Élektron. (Moscow) **32**, 129 (2002).
32. F. Benabid, J. C. Knight, and P. St. J. Russell, Opt. Express **10**, 1195 (2002).
33. P. Yeh, A. Yariv, and E. Marom, J. Opt. Soc. Am. **68**, 1196 (1978).
34. Yong Xu, R. K. Lee, and A. Yariv, Opt. Lett. **25**, 1756 (2000).
35. G. Ouyang, Yong Xu, and A. Yariv, Opt. Express **9**, 733 (2001).
36. T. Kawanishi and M. Izutsu, Opt. Express **7**, 10 (2000).
37. S. G. Johnson, M. Ibanescu, M. Skorobogatiy, *et al.*, Opt. Express **9**, 748 (2001).
38. M. Ibanescu, Y. Fink, S. Fan, *et al.*, Science **289**, 415 (2000).
39. *Landolt–Börnshtein Physikalisch–Chemische Tabellen*, Ed. by W. A. Roth and K. Scheel (Springer, Berlin, 1931 and 1935), Vols. 2 and 3.
40. G. P. Agrawal, *Nonlinear Fiber Optics* (Academic, Boston, 1989; Mir, Moscow, 1996).
41. O. A. Kolevatova and A. M. Zheltikov, Laser Phys. (in press).
42. T. M. Monro, D. J. Richardson, N. G. R. Broderick, and P. J. Bennet, J. Lightwave Technol. **18**, 50 (2000).
43. A. M. Zheltikov and A. N. Naumov, Kvantovaya Élektron. (Moscow) **31**, 471 (2001).
44. G. Ouyang, Yong Xu, and A. Yariv, Opt. Express **10**, 899 (2002).
45. A. M. Zheltikov, Usp. Fiz. Nauk **172**, 743 (2002).
46. A. B. Fedotov, A. N. Naumov, I. Bugar, *et al.*, IEEE J. Sel. Top. Quantum Electron. **8**, 665 (2002).
47. A. B. Fedorov, I. Bugar, A. N. Naumov, *et al.*, Pis'ma Zh. Éksp. Teor. Fiz. **75**, 374 (2002) [JETP Lett. **75**, 304 (2002)].
48. A. Yariv and P. Yeh, *Optical Waves in Crystals: Propagation and Control of Laser Radiation* (Wiley, New York, 1984; Mir, Moscow, 1987).
49. E. A. J. Marcatili and R. A. Schmeltzer, Bell Syst. Tech. J. **43**, 1783 (1964).
50. A. B. Fedotov, F. Giammanco, A. N. Naumov, *et al.*, Appl. Phys. B **72**, 575 (2001).
51. O. A. Kolevatova, A. N. Naumov, and A. M. Zheltikov, Kvantovaya Élektron. (Moscow) **31**, 173 (2001).
52. A. R. McGurn, K. T. Christensen, F. M. Mueller, and A. A. Maradudin, Phys. Rev. B **47**, 13120 (1993).
53. A. Kirchner, K. Busch, and C. M. Soukoulis, Phys. Rev. B **57**, 277 (1998).
54. A. A. Asatryan, P. A. Robinson, L. C. Botten, *et al.*, Phys. Rev. E **60**, 6118 (1999).
55. R. C. McPhedran, L. C. Botten, A. A. Asatryan, *et al.*, Phys. Rev. E **60**, 7614 (1999).
56. Chongjun Jin, Xiaodong Meng, Bingying Cheng, *et al.*, Phys. Rev. B **63**, 195107 (2001).
57. Xiangdong Zhang and Zhao-Qing Zhang, Phys. Rev. B **65**, 245115 (2002).

Translated by A. Zheltikov

Journal of Experimental and Theoretical Physics, Vol. 96, No. 5, 2003, pp. 870–875.
Translated from Zhurnal Éksperimental'noĭ i Teoreticheskoĭ Fiziki, Vol. 123, No. 5, 2003, pp. 991–996.

ATOMS, SPECTRA, RADIATION

Electron in the Coulomb and Strong Low-Frequency Laser Fields

B. A. Zon* and A. S. Kornev**
Voronezh State University, Voronezh, 394006 Russia
**e-mail: zon@niif.vsu.ru*
***e-mail: kornev@tooth.vsu.ru*
Received December 9, 2002

Abstract—Adiabatic approximation is proposed for the electron wave functions in a strong low-frequency electromagnetic field. The functions are tested with the help of the Siegert nonstationary theorem. © *2003 MAIK "Nauka/Interperiodica".*

1. INTRODUCTION

It is well known that the Schrödinger equation

$$-\frac{1}{2}\nabla^2\Psi(\mathbf{r}, t) - \frac{1}{r}\Psi(\mathbf{r}, t) + \mathbf{r}\mathbf{F}(t)\Psi(\mathbf{r}, t) = i\frac{\partial}{\partial t}\Psi(\mathbf{r}, t), \quad (1)$$

describing the motion of an electron in a Coulomb field in the presence of a strong laser field $\mathbf{F}(t)$ (in the dipole approximation) has no closed analytic solution. In Eq. (1) and everywhere below, the atomic system of units is used ($\hbar = m = e = 1$).

In order to estimate the accuracy of approximate solutions to Eq (1), we can borrow the approach used in atomic physics for testing the Hartree–Fock solutions for a multielectron atom [1]. The equality

$$\langle f|\hat{\mathbf{p}}|i\rangle = i\omega_{fi}\langle f|\hat{\mathbf{r}}|i\rangle, \quad (2)$$

which is sometimes called the Siegert theorem [2], holds for the exact solutions $|i\rangle$ and $|f\rangle$ of the time-independent Schrödinger equation. Here, $\hat{\mathbf{p}}$ is the momentum operator and $\omega_{fi} = E_f - E_i$, where E_f and E_i are the energies of states $|f\rangle$ and $|i\rangle$, respectively. The validity of the approximate wave functions is estimated from the extent to which this equality is violated.

The Siegert theorem (2) can also be generalized to the time-dependent case [3, 4]:

$$\langle f|\hat{\mathbf{p}} - c^{-1}\mathbf{A}(t)|i\rangle = \partial_t\langle f|\hat{\mathbf{r}}|i\rangle, \quad (3)$$

where $\mathbf{A}(t)$ is the vector potential of the electromagnetic field and c is the velocity of light.

In our earlier publication [4], it was proposed that the ratio

$$\chi = \frac{|\partial_t\langle f|\hat{\mathbf{r}}|i\rangle|^2}{|\langle f|\hat{\mathbf{p}} - c^{-1}\mathbf{A}(t)|i\rangle|^2}$$

be used as a test parameter. It can easily be verified that this ratio is equal to unity for exact solutions of the Schrödinger equation (1). Naturally, condition (3) is not a sufficient criterion for estimating the accuracy of approximate wave functions. Nevertheless, it provides the required physically substantiated estimate of the accuracy of solutions.

The nonstationary Siegert theorem was used by us earlier [3, 4] for testing the Coulomb–Volkov functions (CVFs) [5, 6], which represent one of the model solutions of the Schrödinger equation (1) with the field

$$\mathbf{F}(t) = \mathbf{e}_z F\sin\omega t. \quad (4)$$

These functions are widely used for studying the interaction of atomic electrons with a high-intensity electromagnetic field (see, for example, [7–11] and the references cited therein). It was shown in our recent publications [3, 4] that application of the CVFs is substantiated, from the standpoint of criterion (3), for the case when the frequency of the laser field is much larger than its amplitude (in atomic units),

$$\omega \gg F. \quad (5)$$

Violation of condition (5) does not imply that the CVFs are absolutely invalid in the present case. It is quite possible that there also exist other arguments substantiating the possibility of their application for calculating some specific physical effects. It is clear, however, that such substantiations should be found when condition (5) is violated.

This study is aimed at construction and analysis of adiabatic wave functions describing infinite motion of an electron in the opposite case of low frequencies,

$$\omega \ll F. \quad (6)$$

2. STATIONARY PROBLEM

Let us first recall the stationary problem of motion of an electron with energy $E > 0$ in the Coulomb poten-

tial created by charge Z in a uniform electric dc field of strength F (see, for example, Section 76 in [12]). In the parabolic coordinates

$$\xi = r + z, \quad \eta = r - z, \quad \varphi = \arctan(y/x), \quad \xi, \eta \geq 0$$

in the Schrödinger equation

$$\left[-\frac{1}{2}\nabla^2 - \frac{Z}{r} + Fz\right]\Psi^{(0)}(F, \mathbf{r}) = E\Psi^{(0)}(F, \mathbf{r}), \qquad (7)$$

the variables can be separated:

$$\Psi^{(0)}(F, \mathbf{r}) = \frac{1}{\sqrt{2\pi\xi\eta}} f_1(\xi) f_2(\eta) e^{im\varphi}; \qquad (8)$$

the corresponding ordinary differential equations have the form

$$\frac{d^2 f_1}{d\xi^2} + \left(\frac{E}{2} + \frac{Z_1}{\xi} - \frac{m^2 - 1}{4\xi^2} - \frac{F}{4}\xi\right) f_1 = 0,$$

$$\frac{d^2 f_2}{d\eta^2} + \left(\frac{E}{2} + \frac{Z_2}{\eta} - \frac{m^2 - 1}{4\eta^2} + \frac{F}{4}\xi\right) f_2 = 0,$$

$$Z_1 + Z_2 = Z.$$

The motion in coordinate ξ is finite; in the WKB approximation ($m^2 - 1 \longrightarrow m^2$), we have

$$f_1(\xi) = \frac{A_1}{\sqrt{p_1(\xi)}} \cos\left(\left|\int_{\xi^*}^{\xi} p_1(\xi')d\xi'\right| - \frac{\pi}{4}\right), \qquad (9)$$

$$p_1(\xi) = \sqrt{\frac{E}{2} + \frac{Z_1}{\xi} - \frac{m^2}{4\xi^2} - \frac{F}{4}\xi}, \qquad (10)$$

where ξ^* is one of the positive roots of the equation $p_1(\xi) = 0$. In order to simplify the subsequent analysis, we confine it to the case of nonzero values of m.

Since we consider the motion with energy $E > 0$, it can easily be verified, using the well-known trigonometrical formulas for the roots of a cubic equation [13], that the smaller positive root (left turning point) corresponds to

$$\xi^* = \xi_1 = \frac{2E}{3F} - \frac{4a}{3}\cos\left(\frac{\alpha}{3} - \frac{\pi}{3}\right), \qquad (11)$$

while the larger root (right turning point) corresponds to

$$\xi^* = \xi_2 = \frac{2E}{3F} + \frac{4a}{3}\cos\frac{\alpha}{3}. \qquad (12)$$

Here, we have

$$a = \sqrt{\left(\frac{E}{F}\right)^2 + \frac{3Z_1}{F}},$$

$$\alpha = \arccos\left\{\frac{1}{a^3}\left[\left(\frac{E}{F}\right)^3 + \frac{9EZ_1}{2F^2} - \frac{27m^2}{16F}\right]\right\}.$$

In this case, it is assumed that the following inequalities hold:

$$\left(\frac{E}{F}\right)^2 \geq \frac{3Z_1}{F}, \qquad (13)$$

$$\left[\left(\frac{E}{F}\right)^3 + \frac{9EZ_1}{2F^2} - \frac{27m^2}{16F}\right]^2 \leq \left|\left(\frac{E}{F}\right)^2 + \frac{3Z_1}{F}\right|^3. \qquad (14)$$

Formula (9) defines function $f_1(\xi)$ in the interval $\xi_1 < \xi < \xi_2$. Outside this interval, function $f_1(\xi)$ decays exponentially. The third (negative) root of the cubic equation corresponds to

$$\xi_0 = \frac{2E}{3F} - \frac{4a}{3}\cos\left(\frac{\alpha}{3} + \frac{\pi}{3}\right). \qquad (15)$$

Constant Z_1 can be determined from the Bohr–Sommerfeld quantization condition. Writing

$$p_1(\xi) = \frac{\sqrt{F}}{2\xi}\sqrt{(\xi - \xi_0)(\xi - \xi_1)(\xi_2 - \xi)},$$

we obtain

$$(n_\xi + 1/2)\pi = \int_{\xi_1}^{\xi_2} p_1(\xi)d\xi$$

$$= -\frac{\sqrt{F}}{3\sqrt{\xi_2 - \xi_0}}\left[(\xi_0 - \xi_2)(\xi_0 + \xi_1 + \xi_2)E\left(\frac{\xi_2 - \xi_1}{\xi_2 - \xi_0}\right)\right. \qquad (16)$$

$$+ [\xi_0^2 + 2\xi_1\xi_2 + \xi_0(\xi_1 + \xi_2)]K\left(\frac{\xi_2 - \xi_1}{\xi_2 - \xi_0}\right)$$

$$\left. - 3\xi_0\xi_1\Pi\left(\frac{\xi_2 - \xi_1}{\xi_2 - \xi_0}\right)\right],$$

where E, K, and Π are elliptic functions [14] and $n_\xi = 0, 1, \ldots$ is the parabolic quantum number.

The motion in coordinate η is infinite, and the wave function in the WKB approximation has the following form (accurate to within normalization):

$$f_2(\eta) = \frac{A_2}{\sqrt{p_2(\eta)}} \cos\left(\left|\int_{\eta_0}^{\eta} p_2(\eta')d\eta'\right| - \frac{\pi}{4}\right), \qquad (17)$$

$$p_2(\eta) = \sqrt{\frac{E}{2} + \frac{Z_2}{\eta} - \frac{m^2}{4\eta^2} + \frac{F}{4}\eta}. \qquad (18)$$

Here, η_0 is the only real root of the equation $p_2(\eta) = 0$, which is defined as

$$\eta_0 = -\frac{2E}{3F} + \frac{4b}{3}\sinh\frac{\beta}{3},$$

where

$$b = \sqrt{\left(\frac{E}{F}\right)^2 - \frac{3Z_2}{F}},$$

$$\beta = \operatorname{arsinh}\left\{b^{-3}\left[\left(\frac{E}{F}\right)^3 - \frac{9EZ_2}{2F^2} - \frac{27m^2}{16F}\right]\right\}.$$

In this case, we assume that the following inequality holds:

$$\left[\left(\frac{E}{F}\right)^3 - \frac{9EZ_2}{2F^2} - \frac{27m^2}{16F}\right]^2 \geq \left[\left(\frac{E}{F}\right)^2 - \frac{3Z_2}{F}\right]^3. \quad (19)$$

It should be noted that inequalities (13), (14), and (19), which correspond to physically obvious conditions of the presence of two turning points on the ξ axis and one turning point on the η axis, can be regarded as inequalities which must be satisfied by the separation constants $Z_{1,2}$.

The integral appearing in Eq. (17) can be expressed in terms of elementary functions if we neglect in Eq. (18) quantities on the order of Z_2/η and m^2/η^2 attenuating with increasing η. A similar approximation was used, for example, for calculating the effect of an external dc field on the probability of the photoelectric effect in atoms [15]. The results obtained in this case are in good agreement with the experiment. It is difficult to substantiate this approximation for weak fields F, but this case is of no interest for the given problem. Thus, we have

$$f_2(\eta) \approx \frac{2A_2}{\sqrt{2E + F\eta}}\cos\left[\frac{\sqrt{(2E + F\eta)^3}}{3F} + \phi(F)\right]. \quad (20)$$

The field dependent phase $\phi(F)$ can be calculated in the WKB approximation by comparing the arguments of the cosine in Eqs. (17) and (20):

$$\phi(F) = -\frac{\pi}{4} + \lim_{\eta\to\infty}\left[\int_{\eta_0}^{\eta} p_2(x)dx - \frac{\sqrt{(2E + F\eta)^3}}{3F}\right]. \quad (21)$$

The integral in this expression can be transformed using integration by parts:

$$\int_{\eta_0}^{\eta} p_2(x)dx = \frac{1}{2}\int_{\eta_0}^{\eta}\left\{1 + \frac{4Z_2x - m^2}{x^2(2E + Fx)}\right\}^{1/2}\sqrt{2E + Fx}\,dx$$
$$= \frac{\sqrt{(2E + Fx)^3}}{3F}\left\{1 + \frac{4Z_2x - m^2}{x^2(2E + Fx)}\right\}^{1/2}\Bigg|_{\eta_0}^{\eta} + \frac{1}{6F} \quad (22)$$
$$\times\int_{\eta_0}^{\eta}\frac{8FZ_2x^2 + (8EZ_2 - 3m^2F)x - 4Em^2}{\sqrt{x^5}\sqrt{(2E + Fx)\eta^2 + 4Z_2x - m^2}}dx.$$

At the lower limit, the expression in the braces in relation (22) vanishes in accordance with the definition of η_0. Performing the limit transition in Eq. (21), we arrive at the final expression for $\phi(F)$:

$$\phi(F) = -\frac{\pi}{4} + \frac{1}{6F}$$
$$\times\int_{\eta_0}^{\infty}\frac{8FZ_2\eta^2 + (8EZ_2 - 3m^2F)\eta - 4Em^2}{\sqrt{\eta^5}\sqrt{(2E + F\eta)\eta^2 + 4Z_2\eta - m^2}}d\eta.$$

Upon normalization to the δ function of energy, the normalization constants A_1 and A_2 appearing in formulas (9) and (17) are given by the condition

$$\frac{1}{4}\int_{\eta_0}^{\infty}d\eta\int_{\xi_1}^{\xi_2}d\xi\left(\frac{1}{\xi} + \frac{1}{\eta}\right)f_1^2(\xi)\,f_2(E;\eta)\,f_2(E';\eta) = \delta(E - E'). \quad (23)$$

Since the value of integral (23) is determined by asymptotically large values of η, the term η^{-1} can be omitted here. Evaluation of the integral with respect to ξ gives

$$\frac{1}{A_1^2} = \int_{\xi_1}^{\xi_2}\frac{d\xi}{2\xi p_1(\xi)}\cos^2\left(\int_{\xi_1}^{\xi} p_1(\xi')d\xi' - \frac{\pi}{4}\right)$$
$$\approx \frac{1}{2\sqrt{F}}\int_{\xi_1}^{\xi_2}\frac{d\xi}{\sqrt{(\xi - \xi_0)(\xi - \xi_1)(\xi_2 - \xi)}} \quad (24)$$
$$= \frac{1}{\sqrt{F(\xi_2 - \xi_0)}}K\left(\frac{\xi_2 - \xi_1}{\xi_2 - \xi_0}\right).$$

The normalization constant A_2 is determined from a comparison of relation (20) with the asymptotic form of the wave function in the one-dimensional problem in a uniform field (see Section 24 in [12]):

$$A_2 = \frac{1}{2^{1/3}\sqrt{\pi}}.$$

3. SOLUTION OF THE NONSTATIONARY PROBLEM

Let us now consider the time-dependent Schrödinger equation (1) in field (4) in the case of an infinite motion of an electron. We will seek the solution to Eq. (1) in the form

$$\Psi(\mathbf{r}, t) = \Phi(\mathbf{r}, t)e^{-iEt}, \tag{25}$$

imposing the requirement that the unknown function $\Phi(\mathbf{r}, t)$ must become independent of time for field "freezing" ($\omega \longrightarrow 0$) and that the quantity $E > 0$ must be transformed into the total energy. We will refer to quantity E as quasi-energy, although it is traditionally determined by the passage to the limit for switched-off field ($F \longrightarrow 0$).

We can neglect the derivative $\partial_t\Phi(\mathbf{r}, t)$ while differentiating solution (25) with respect to time by formally requiring the fulfillment of the condition

$$\omega \ll E. \tag{26}$$

However, this approximation turns out to be good enough in actual practice when the electron energy is only twice as high as the photon energy (see, for example, [16]).

Substituting relation (25) into Eq. (1) and taking into account condition (26), we arrive at an equation coinciding in its structure with the time-independent Schrödinger equation, but exhibiting a parametric dependence on time:

$$-\frac{1}{2}\nabla^2\Phi(\mathbf{r}, t) - \frac{1}{r}\Phi(\mathbf{r}, t) + zF\sin(\omega t)\Phi(\mathbf{r}, t) = E\Phi(\mathbf{r}, t).$$

The solution to this equation is obtained automatically from Eq. (8) using the substitution

$$F \longrightarrow F\sin\omega t. \tag{27}$$

Such a substitution was used for the first time in [17] to take into account the effect of the Coulomb potential on the probability of the tunnel effect in atoms placed in a strong laser field. The successful application of this theory for describing a large body of experimental data [18] suggests that the wave functions constructed using the same physical approximation will be quite accurate.

Thus, the model wave function describing the motion of an electron in a strong low-frequency laser field in the continuous spectrum has the form

$$\Psi_{En_\xi m}(F; \mathbf{r}, t) = \Psi^{(0)}_{En_\xi m}(F\sin\omega t, \mathbf{r})e^{-iEt}. \tag{28}$$

It should be recalled that function $\Psi^{(0)}_{En_\xi m}(F, \mathbf{r})$ is defined by formula (8). Parameters E, n_ξ, and m are assumed to be given.

4. RESULTS OF TESTING

For testing functions (28), we use the nonstationary Siegert theorem (3). For the sake of definiteness, we analyze the z component of the coordinate for free–free transitions in the problem of electron scattering from the Coulomb potential ($Z = 1$) in the presence of a laser field.

While constructing the wave functions for the initial and final states, we will use the model expression (28). We confine our analysis to the case $m = 1$ and $n_\xi = 0$, assuming that the quantum number n_ξ remains unchanged in transitions.

We evaluate the test parameter using the following formula:

$$\chi_z = |\partial_t\langle f|z|i\rangle|^2/|\langle f|\hat{p}_z|i\rangle|^2. \tag{29}$$

It should be noted that, in contrast to the general formula (3), the matrix element of the vector potential vanishes here in view of the orthogonality of functions (8).

In order to eliminate singularities in Eq. (29), we express the matrix element $\langle f|z|i\rangle$ in terms of $\langle f|\hat{p}_z|i\rangle$ in accordance with the nonstationary Siegert theorem (2):

$$\left\langle \Psi^{(0)}_{E_f n_\xi 1}|z|\Psi^{(0)}_{E_i n_\xi 1}\right\rangle = \frac{i}{E_i - E_f}\left\langle \Psi^{(0)}_{E_f n_\xi 1}|\hat{p}_z|\Psi^{(0)}_{E_i n_\xi 1}\right\rangle. \tag{30}$$

Substituting relation (30) into (29) and taking into account expression (28), we obtain

$$\chi_z = 1 + \frac{F^2\omega^2\cos^2\omega t}{(E_f - E_i)^2} \times \left.\frac{\left|\partial_F\langle\Psi^{(0)}_{E_f n_\xi 1}|\hat{p}_z|\Psi^{(0)}_{E_i n_\xi 1}\rangle\right|^2}{\left|\langle\Psi^{(0)}_{E_f n_\xi 1}|\hat{p}_z|\Psi^{(0)}_{E_i n_\xi 1}\rangle\right|^2}\right|_{F \to F\sin\omega t}. \tag{31}$$

Here, we have

$$\langle\Psi^{(0)}_{E_f n_\xi 1}|\hat{p}_z|\Psi^{(0)}_{E_i n_\xi 1}\rangle = -\frac{i}{2}[I_{11}I_{21} - I_{12}I_{22}],$$

$$I_{kk} = \int_{x_{k1}}^{x_{k2}} f^*_{kf}(x_k)\frac{df_{ki}(x_k)}{dx_k}dx_k,$$

$$I_{kl} = \int_{x_{k1}}^{x_{k2}} f^*_{kf}(x_k)f_{ki}(x_k)\frac{dx_k}{x_k},$$

$$k, l = 1, 2, \quad k \neq l,$$

$$x_1 = \xi, \quad x_{11} = \xi_1, \quad x_{12} = \xi_2,$$

$$x_2 = \eta, \quad x_{21} = \eta_0, \quad x_{22} = \eta_{\max}.$$

The quantity $\eta_{\max}$ is not bounded from above in view of the infinite form of motion; however, the value of χ_z

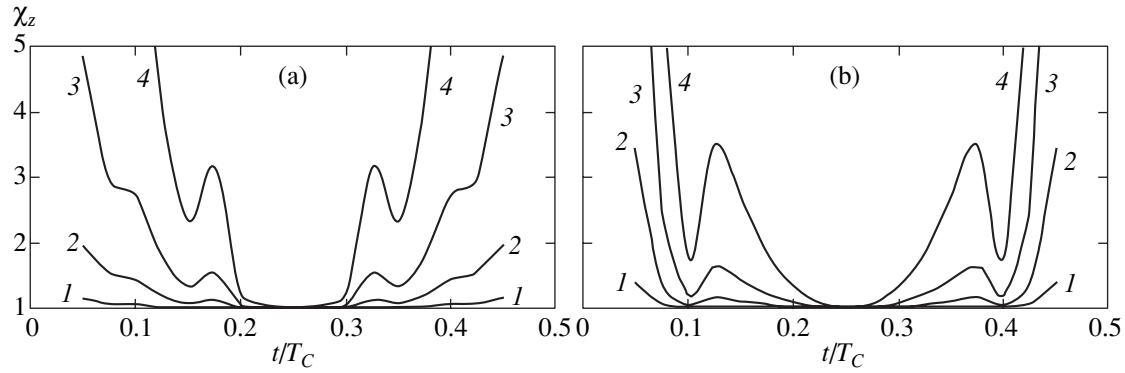

Test parameter χ_z as a function of time ($T_C = 2\pi/\omega$). The values of electron energy $E_{i,f}$ and laser field frequencies ω are given in atomic units: (a) $E_i = 0.002$, $E_f = 0.001$, $\omega = 0.001$ (*1*), 0.0025 (*2*), 0.005 (*3*), and 0.01 (*4*); (b) $E_i = 0.2$, $E_f = 0.1$, $\omega = 0.01$ (*1*), 0.025 (*2*), 0.05 (*3*), and 0.1 (*4*).

becomes independent of η_{max} for large values of η_{max}. Here, we used values of $\eta_{max} = 20$–40.

In the differentiation of WKB functions (9) and (17), the preexponential factors should be treated as constants; i.e., they should not be differentiated:

$$\frac{df_k}{dx_k} = -A_k\sqrt{p_k(x_k)}\sin\left(\int_{x_{k1}}^{x} p_k(x')dx' - \frac{\pi}{4}\right).$$

Thus, we can write

$$I_{kk} = -\frac{1}{2}A_{kf}^* A_{ki}\int_{x_{k1}}^{x_{k2}}\sqrt{\frac{p_{2i}(x_k)}{p_{2f}(x_k)}}$$

$$\times\{\cos[P_k^{(+)}(x_k)] + \sin[P_k^{(-)}(x_k)]\}dx_k,$$

$$I_{kl} = -\frac{1}{2}A_{kf}^* A_{ki}\int_{x_{k1}}^{x_{k2}}\sqrt{p_{2i}(x_k)p_{2f}(x_k)}$$

$$\times\{\sin[P_k^{(+)}(x_k)] + \cos[P_k^{(-)}(x_k)]\}\frac{dx_k}{x_k},$$

where

$$P_k^{(\pm)}(x_k) = \int_{x_{k1}}^{x_k}[p_{kf}(x') \pm p_{ki}(x')]dx'.$$

Integration with respect to coordinates and differentiation with respect to field strength F were carried out numerically. It should also be noted that terms of the type

$$\int_{\eta_0}^{\eta_{max}} g(\eta)\left\{\begin{matrix}\sin\\ \cos\end{matrix}\right\}\left\{\int_{\eta_0}^{\eta}[p_{2f}(\eta') + p_{2i}(\eta')]d\eta'\right\}d\eta,$$

where $g(\eta)$ is a slowly varying function, can be neglected in view of a rapid oscillation of the sine (cosine) and an increase in $p_2(\eta)$.

The results of calculation of parameter χ_z for various frequencies from the infrared range, electron momentum, and for a given field strength of $F = 0.5$ atomic units are shown in the figure as functions of time. It can be seen that a decrease in frequency leads to a higher accuracy of function (28). Accuracy is also improved upon an increase in the momentum of the electron being scattered in accordance with condition (26). Thus, in the range of field strengths, energies, and frequencies under investigation, the criterion for applicability of functions (28) can be formulated as follows:

$$\chi_z = 1\text{–}1.2, \text{ for } \omega/F < 0.01.$$

If this condition is satisfied, the Siegert theorem is violated in the time intervals of duration not exceeding 10% of the laser cycle. The violation of the Siegert theorem at the beginning and end of the half-cycle is due to inapplicability of the computational methods described above for weak fields, but the field strength is low precisely on these time intervals.

Thus, good agreement of theory [17, 18] and experiment, together with the positive results based on the nonstationary Siegert theorem, suggests that functions (28) are valid for an adequate description of the motion of an electron in the Coulomb field as well as in a strong low-frequency laser field. In the static limit, these formulas coincide with the solution of stationary problem (7).

ACKNOWLEDGMENTS

The authors are grateful to F. Ehlotzky and G. Ferrante for fruitful discussions of the results.

This study was supported financially by the Russian Foundation for Basic Research (project nos. 02-02-17466 and 02-02-06131), US Civilian Research and Develop-

ment Foundation, and the Ministry of Education of the Russian Federation (grant no. VZ-010-0).

REFERENCES

1. M. Ya. Amusya, *Atomic Photoeffect* (Nauka, Moscow, 1987; Plenum, New York, 1990).
2. Å. Bohr and B. R. Mottelson, *Nuclear Structure* (Benjamin, New York, 1969; Mir, Moscow, 1971), Vol. 1.
3. A. S. Kornev and B. A. Zon, Laser Phys. **12**, 795 (2002).
4. A. S. Kornev and B. A. Zon, J. Phys. B: At. Mol. Opt. Phys. **35**, 2451 (2002).
5. M. Jain and N. Tsoar, Phys. Rev. A **18**, 538 (1978).
6. P. Cavalieri and G. Ferrante, J. Phys. B: At. Mol. Opt. Phys. **13**, 4495 (1980).
7. G. Duchateau, C. Illescas, B. Pons, *et al.*, J. Phys. B: At. Mol. Opt. Phys. **33**, L571 (2000).
8. G. Duchateau, E. Cormier, and R. Gayet, Eur. Phys. J. D **11**, 191 (2000).
9. A. Jaroń, J. Z. Kamiński, and F. Ehlotzky, Phys. Rev. A **61**, 023404 (2000).
10. S. M. Li, Y. G. Miao, Z. F. Zhou, *et al.*, Phys. Rev. A **58**, 2615 (1998).
11. D. B. Milošević and F. Ehlotzky, Phys. Rev. A **57**, 2859 (1998).
12. L. D. Landau and E. M. Lifshitz, *Course of Theoretical Physics*, Vol. 3: *Quantum Mechanics: Non-Relativistic Theory*, 4th ed. (Nauka, Moscow, 1989; Pergamon, New York, 1977).
13. G. A. Korn and Th. M. Korn, *Mathematical Handbook for Scientists and Engineers*, 2nd ed. (McGraw-Hill, New York, 1968; Nauka, Moscow, 1973).
14. I. S. Gradstein and I. M. Ryzhik, *Tables of Integrals, Summae, Series, and Products*, 4th ed. (Fizmatgiz, Moscow, 1962; Academic, New York, 1980).
15. V. D. Kondratovich and V. N. Ostrovsky, Zh. Éksp. Teor. Fiz. **79**, 395 (1980) [Sov. Phys. JETP **52**, 198 (1980)].
16. G. F. Gribakin and M. Yu. Kuchiev, Phys. Rev. A **55**, 3760 (1997).
17. A. M. Perelomov, V. S. Popov, and M. V. Terent'ev, Zh. Éksp. Teor. Fiz. **50**, 1393 (1966) [Sov. Phys. JETP **23**, 924 (1966)].
18. M. V. Ammosov, N. B. Delone, and V. P. Kraĭnov, Zh. Éksp. Teor. Fiz. **91**, 2008 (1986) [Sov. Phys. JETP **64**, 1191 (1986)].

Translated by N. Wadhwa

Journal of Experimental and Theoretical Physics, Vol. 96, No. 5, 2003, pp. 876–884.
From Zhurnal Éksperimental'noĭ i Teoreticheskoĭ Fiziki, Vol. 123, No. 5, 2003, pp. 997–1005.

ATOMS, SPECTRA, RADIATION

Polariton Effect in Nonlinear Pulse Propagation¶

S. A. Darmanyan[a,*], A. M. Kamchatnov[a,], and M. Nevière[b]**

[a]*Institute of Spectroscopy, Russian Academy of Sciences, Troitsk, Moscow oblast, 142190 Russia*
**e-mail: sdarmanyan@yahoo.com*
***e-mail: kamch@isan.troitsk.ru*
[b]*Institut Fresnel, Faculté des Sciences et Techniques de Saint Jérome 13397, Marseille, Cedex 20, France*

Received July 15, 2002

Abstract—The joint influence of the polariton effect and Kerr-like nonlinearity on the propagation of optical pulses is studied. The existence of different families of envelope solitary wave solutions in the vicinity of the polariton gap is shown. The properties of solutions depend strongly on the carrier wave frequency. In particular, solitary waves inside and outside the polariton gap exhibit different velocity and amplitude dependences on their duration. *© 2003 MAIK "Nauka/Interperiodica".*

1. INTRODUCTION

In recent years, rapid progress in the fabrication of microcavities, organic and inorganic quantum wells, etc., has resulted in great interest in the investigation of electromagnetic properties of these new objects, including propagation of nonlinear pulses in such structures (see, e.g., [1–4]). For example, the propagation of nonlinear pulses along a quantum well imbedded in a microcavity was studied in [4] for two types of nonlinearities: a Kerr-like nonlinearity applied to envelopes of sufficiently long pulses, and a self-induced transparency nonlinearity applied to short and intense pulses with the frequency close to the two-level resonance. In this study, the authors have chosen propagation conditions such that the polariton effect of the formation of the gap can be neglected in the dispersion law of an electromagnetic wave coupled to the polarization wave in the medium. The problem of the pulse propagation can then be reduced to either the nonlinear Schrödinger (NLS) equation or the sine-Gordon equation with the well-known soliton solutions. However, the region of frequencies in the vicinity of the polariton gap is very important because some properties of the structures under consideration manifest themselves in this region only.

We note that related problems have already been studied a long time ago in the theory of nonlinear pulse propagation through a medium in the vicinity of exciton resonances. In [5], the polariton self-induced transparency pulses were found, but it was claimed later [6, 7] that the polariton effect prevents the existence of self-induced transparency pulses. This contradiction was resolved in [8], where it was shown that polariton solitons exist due to a subtle balance of small effects, and these solutions can therefore easily be overlooked if a too rude approximation is made in the evolution equations. The authors of [9, 10] later confirmed this result in general and described some additional remarkable properties of polariton self-induced transparency pulses in the vicinity of the polariton gap beyond perturbation theory. Similar problems have also been studied for the Kerr nonlinearity (see, e.g., [11] and references therein). However, the approximations used were not justified sufficiently well, and some properties of polariton solitons remained unclear. In [12], the governing equations for long pulses and a carrier wave frequency sufficiently far from the polariton gap were reduced to the perturbed NLS equation for the envelope and the corresponding soliton solutions were described. A closely related problem, pulse propagation in a Kerr-nonlinear medium with a singular dispersion relation, was studied in [13], where bright and dark solitary wave solutions were found in the vicinity of the linear resonance.

In this paper, we thoroughly investigate polariton solitons in the case of the Kerr nonlinearity following the method developed by Akimoto and Ikeda [8] and show the existence of localized solutions both inside and outside the polariton gap.

2. MAIN EQUATIONS

We start with the standard equations of the classical theory of electromagnetic waves propagating through an isotropic medium (see, e.g., [14]),

$$\frac{\partial^2 \mathbf{E}}{\partial x^2} - \frac{\epsilon_0}{c^2}\frac{\partial^2 \mathbf{E}}{\partial t^2} = \frac{4\pi}{c^2}\frac{\partial^2 \mathbf{P}}{\partial t^2}, \tag{1}$$

$$\frac{\partial^2 \mathbf{P}}{\partial t^2} + \omega_T^2 \mathbf{P} + \chi|\mathbf{P}|^2\mathbf{P} = \alpha\mathbf{E}, \tag{2}$$

¶This article was submitted by the authors in English.

where ϵ_0 is the background dielectric constant and

$$\alpha = \frac{\epsilon_0(\omega_L^2 - \omega_T^2)}{4\pi}. \tag{3}$$

These equations describe interaction of the electromagnetic field **E** and the polarization wave **P** due to the Kerr-like nonlinearity (measured by the parameter χ). We here ignore the effect of damping. The parameters ω_T^2 and ω_L^2 characterize the dispersion law $\omega = \omega(k)$ of linear waves, which is given by the equation

$$F(k, \omega) \equiv \omega_T^2 - \omega^2 - \frac{4\pi}{c^2}\frac{\alpha\omega^2}{k^2 - \epsilon_0\omega^2/c^2} = 0. \tag{4}$$

As follows from (4), the dispersion law has a gap in the frequency interval

$$\omega_T < \omega < \omega_L, \tag{5}$$

where linear waves cannot propagate. As mentioned above, the envelope function can be introduced for frequencies sufficiently far from polariton gap (5), and system (1), (2) can be reduced to the NLS equation possessing well-known soliton solutions. Here, we are interested in solutions of system (1), (2) for frequencies near and inside polariton gap (5).

We seek the solutions in the form of stationary linearly polarized waves, such that **E** and **P** can be considered as the scalar functions

$$\begin{aligned} E(x, t) &= \mathscr{E}(t - x/V)e^{i\theta}, \\ P(x, t) &= [u(t - x/V) - iv(t - x/V)]e^{i\theta}, \end{aligned} \tag{6}$$

where V is the velocity of the pulse and the phase $\theta(x, t)$ is

$$\theta(x, t) = kx - \omega t - \phi(t - x/V). \tag{7}$$

Substitution of Eqs. (6) and (7) into Eqs. (1) and (2) leads to the system of equations for the variables u, v, $\mathscr{E}$, ϕ,

$$\begin{aligned} &\ddot{u} - (\omega^2 - \omega_T^2 + 2\omega\dot{\phi} + \dot{\phi}^2)u - 2(\omega + \dot{\phi})\dot{v} \\ &\quad - \ddot{\phi}v + \chi(u^2 + v^2)u = \alpha\mathscr{E}, \end{aligned} \tag{8}$$

$$\begin{aligned} &\ddot{v} - (\omega^2 - \omega_T^2 + 2\omega\dot{\phi} + \dot{\phi}^2)v + 2(\omega + \dot{\phi})\dot{u} \\ &\quad + \ddot{\phi}u + \chi(u^2 + v^2)v = 0, \end{aligned} \tag{9}$$

$$\begin{aligned} &\left(\frac{1}{V^2} - \frac{\epsilon_0}{c^2}\right)\ddot{\mathscr{E}} - \left[\left(k^2 - \frac{\epsilon_0}{c^2}\omega^2\right) + 2\left(\frac{k}{V} - \frac{\epsilon_0\omega}{c^2}\right)\dot{\phi}\right. \\ &\quad \left. + \left(\frac{1}{V^2} - \frac{\epsilon_0}{c^2}\right)\dot{\phi}^2\right]\mathscr{E} \\ &= \frac{4\pi}{c^2}[\ddot{u} - u(\omega + \dot{\phi})^2 - \ddot{\phi}u - 2(\omega + \dot{\phi})\dot{v}], \end{aligned} \tag{10}$$

$$\begin{aligned} &\left(\frac{1}{V^2} - \frac{\epsilon_0}{c^2}\right)\ddot{\phi}\mathscr{E} + 2\left[\frac{k}{V} - \frac{\epsilon_0\omega}{c^2} + \left(\frac{1}{V^2} - \frac{\epsilon_0}{c^2}\right)\dot{\phi}\right]\dot{\mathscr{E}} \\ &= \frac{4\pi}{c^2}[\ddot{v} - v(\omega + \dot{\phi})^2 + \ddot{\phi}u + 2(\omega + \dot{\phi})\dot{u}], \end{aligned} \tag{11}$$

where the overdot denotes the derivative with respect to $\xi = t - x/V$.

3. LINEAR APPROXIMATION

We suppose that the variables u, v, $\mathscr{E}$, and ϕ tend to zero at the tails of the pulse (i.e., at infinite $|\xi|$), and system (8)–(11) can therefore be linearized in these regions as

$$\ddot{u} - (\omega^2 - \omega_T^2)u - 2\omega\dot{v} = \alpha\mathscr{E}, \tag{12}$$

$$\ddot{v} - (\omega^2 - \omega_T^2)v + 2\omega\dot{u} = 0, \tag{13}$$

$$\begin{aligned} &\left(\frac{1}{V^2} - \frac{\epsilon_0}{c^2}\right)\ddot{\mathscr{E}} - \left(k^2 - \frac{\epsilon_0}{c^2}\omega^2\right)\mathscr{E} \\ &\quad = \frac{4\pi}{c^2}(\ddot{u} - \omega^2 u - 2\omega\dot{v}), \end{aligned} \tag{14}$$

$$2\left(\frac{k}{V} - \frac{\epsilon_0\omega}{c^2}\right)\dot{\mathscr{E}} = \frac{4\pi}{c^2}(\ddot{v} - \omega^2 v + 2\omega\dot{u}). \tag{15}$$

For the exponential dependence

$$\begin{aligned} (\mathscr{E}, u, v) &= (\mathscr{E}_0, u_0, v_0)\exp(-|\xi|/\tau) \\ &\text{at } |\xi| \longrightarrow \infty, \end{aligned} \tag{16}$$

where τ is the duration of the pulse, system (12)–(15) reduces to algebraic equations that define the *dispersion law* and the velocity of the pulse as functions of τ. It is convenient to introduce the variables

$$X = \frac{ck}{\omega}, \quad Y = \frac{c}{V}, \tag{17}$$

and define the characteristic parameters

$$s = \frac{1}{\omega\tau}, \quad \Lambda^2 = \frac{1}{(\omega_L^2 - \omega_T^2)\tau^2}, \tag{18}$$

such that the ratio

$$\frac{\Lambda^2}{s^2} = \frac{\omega^2}{\omega_L^2 - \omega_T^2} \equiv \Omega^2 \tag{19}$$

is independent of τ. The variable

$$\Delta^2 = \frac{\omega^2 - \omega_T^2}{\omega_L^2 - \omega_T^2} \tag{20}$$

measures the frequency in the vicinity of the polariton gap. The cases where $\Delta^2 > 1$ and $\Delta^2 < 0$ correspond to the upper and lower polariton branches respectively.

Substituting Eq. (16) in Eqs. (12)–(15), we arrive at the system

$$\begin{aligned}(\Lambda^2-\Delta^2)u_0-2s\Omega^2 v_0 &= \frac{\epsilon_0}{4\pi}\mathscr{E}_0,\\ (\Lambda^2-\Delta^2)v_0+2s\Omega^2 u_0 &= 0,\\ (X^2-s^2Y^2)\mathscr{E}_0 &= \epsilon_0(1-s^2)\mathscr{E}_0\\ &+4\pi[(1-s^2)u_0+2sv_0],\\ 2s(XY-\epsilon_0)\mathscr{E}_0 &= 4\pi[(1-s^2)v_0-2su_0].\end{aligned} \tag{21}$$

Eliminating u_0 and v_0 from Eqs. (21) gives the system

$$\begin{aligned}X^2-s^2Y^2 &= \epsilon_0\left[1-s^2+\frac{(1-s^2)(\Lambda^2-\Delta^2)-4s^2\Omega^2}{(\Lambda^2-\Delta^2)^2+4s^2\Omega^4}\right],\\ XY &= \epsilon_0\left[1+\frac{\Lambda^2-\Delta^2+(1-s^2)\Omega^2}{(\Lambda^2-\Delta^2)^2+4s^2\Omega^4}\right],\end{aligned} \tag{22}$$

the solving of which, with Eq. (19) taken into account, yields

$$\begin{aligned}X^2 &= \left(\frac{ck}{\omega}\right)^2\\ &= \frac{\epsilon_0}{2}\left[(1-s^2)-\frac{(1-s^2)(\Delta^2-\Lambda^2)+4\Lambda^2}{(\Delta^2-\Lambda^2)^2+4\Lambda^2\Omega^2}\right.\\ &\left.+(1+s^2)\sqrt{\frac{(\Delta^2-\Lambda^2-1)^2+4\Lambda^2\Omega^2}{(\Delta^2-\Lambda^2)^2+4\Lambda^2\Omega^2}}\right],\end{aligned} \tag{23}$$

$$\begin{aligned}Y^2 &= \left(\frac{c}{V}\right)^2\\ &= \frac{\epsilon_0}{2s^2}\left[-(1-s^2)+\frac{(1-s^2)(\Delta^2-\Lambda^2)+4\Lambda^2}{(\Delta^2-\Lambda^2)^2+4\Lambda^2\Omega^2}\right.\\ &\left.+(1+s^2)\sqrt{\frac{(\Delta^2-\Lambda^2-1)^2+4\Lambda^2\Omega^2}{(\Delta^2-\Lambda^2)^2+4\Lambda^2\Omega^2}}\right].\end{aligned} \tag{24}$$

In the limit of a uniform wave ($\tau \longrightarrow \infty$), when $\Lambda^2 \longrightarrow 0$ and $s^2 \longrightarrow 0$, Eq. (23) reproduces the dispersion law of linear plane waves,

$$\left(\frac{ck}{\omega}\right)^2 = \epsilon_0\left(1-\frac{1}{\Delta^2}\right) \geq 0, \tag{25}$$

which can be transformed into the standard form after substitution of Eq. (20). To find the velocity of the envelope of a linear wave, we must take the limit as $s^2 \longrightarrow 0$ in Eq. (24), which gives

$$\left(\frac{c}{V}\right)^2 = \frac{\epsilon_0}{\Delta^6(\Delta^2-1)}[\Delta^2(\Delta^2-1)+\Omega^2]^2. \tag{26}$$

As could be expected, this velocity V coincides with the group velocity of propagating linear plane waves with dispersion law (4).

In Eqs. (23) and (24), the three parameters Δ^2, s^2, and Ω^2 depend on the frequency ω. For further investigation, it is convenient to express s^2 and Ω^2 in terms of Δ^2,

$$\begin{aligned}\Omega^2 &= \Delta^2+\kappa^2, \quad s^2 = \frac{\Lambda^2}{\Delta^2+\kappa^2},\\ \kappa^2 &= \frac{\omega_T^2}{\omega_L^2-\omega_T^2}.\end{aligned} \tag{27}$$

Equations (23) and (24) then become

$$\begin{aligned}\left(\frac{ck}{\omega}\right)^2 &= \frac{1}{2}\left[1-\frac{\Lambda^2}{\Delta^2+\kappa^2}\right.\\ &-\frac{(1-\Lambda^2/(\Delta^2+\kappa^2))(\Delta^2-\Lambda^2)+4\Lambda^2}{(\Delta^2-\Lambda^2)^2+4\Lambda^2(\Delta^2+\kappa^2)}\\ &\left.+\left(1+\frac{\Lambda^2}{\Delta^2+\kappa^2}\right)\sqrt{\frac{(\Delta^2-\Lambda^2-1)^2+4\Lambda^2(\Delta^2+\kappa^2)}{(\Delta^2-\Lambda^2)^2+4\Lambda^2(\Delta^2+\kappa^2)}}\right],\end{aligned} \tag{28}$$

$$\begin{aligned}\left(\frac{c}{V}\right)^2 &= \frac{\Delta^2+\kappa^2}{2\Lambda^2}\left[-1+\frac{\Lambda^2}{\Delta^2+\kappa^2}\right.\\ &+\frac{(1-\Lambda^2/(\Delta^2+\kappa^2))(\Delta^2-\Lambda^2)+4\Lambda^2}{(\Delta^2-\Lambda^2)^2+4\Lambda^2(\Delta^2+\kappa^2)}\\ &\left.+\left(1+\frac{\Lambda^2}{\Delta^2+\kappa^2}\right)\sqrt{\frac{(\Delta^2-\Lambda^2-1)^2+4\Lambda^2(\Delta^2+\kappa^2)}{(\Delta^2-\Lambda^2)^2+4\Lambda^2(\Delta^2+\kappa^2)}}\right],\end{aligned} \tag{29}$$

where we have also set $\epsilon_0 = 1$, which is equivalent to the replacement $c \longrightarrow c/\sqrt{\epsilon_0}$. We recall that in Eqs. (28) and (29), κ^2 is a constant determined by the system under consideration, the parameter Δ^2 measures the wave frequency, and the parameter Λ^2 measures the pulse duration.

Linear uniform waves cannot propagate with frequencies within polariton gap (5) or

$$0 < \Delta^2 < 1. \tag{30}$$

However, at finite values of τ, two branches of the dispersion curve join into one curve. Plots of Δ^2 against $(ck/\omega)^2$ at several values of Λ^2 are shown in Fig. 1. As

we can see, these curves depend essentially on the values of Λ^2, and the usual approach involving the transition to the NLS equation for the envelope function can only be applied at $\Lambda \ll 1$ and sufficiently far from the polariton gap. The velocity parameter $(c/V)^2$ of the pulse as a function of Δ^2 is shown in Fig. 2 at several values of Λ^2. It has real values even at frequencies inside polariton gap (30). It is important to note that if general nonlinear equations have a pulse solution of form (6)–(7), then its velocity must coincide with its *linear approximation* (29) calculated for the tails of the pulse.

4. SOLITON SOLUTIONS

To find soliton solutions, we return to exact equations (8)–(11) and replace differentiation with respect to $\xi = t - x/V$ by differentiation with respect to $\zeta = \xi/\tau$. Taking Eqs. (17)–(20) into account, we arrive at the system

$$\begin{aligned}\Lambda^2\ddot{u} - (\Delta^2 + 2\Lambda\sqrt{\Delta^2+\kappa^2}\dot{\phi} + \Lambda^2\dot{\phi}^2)u \\ - 2(\Lambda\sqrt{\Delta^2+\kappa^2} + \Lambda^2\dot{\phi})\dot{v} \\ - \Lambda^2\ddot{\phi}v + \tilde{\chi}(u^2+v^2)u = \frac{1}{4\pi}\mathscr{E},\end{aligned} \tag{31}$$

$$\begin{aligned}\Lambda^2\ddot{v} - (\Delta^2 + 2\Lambda\sqrt{\Delta^2+\kappa^2}\dot{\phi} + \Lambda^2\dot{\phi}^2)v \\ + 2(\Lambda\sqrt{\Delta^2+\kappa^2} + \Lambda^2\dot{\phi})\dot{u} \\ + \Lambda^2\ddot{\phi}u + \tilde{\chi}(u^2+v^2)v = 0,\end{aligned} \tag{32}$$

$$\begin{aligned}\Lambda^2\left[\left(\frac{c}{V}\right)^2 - 1\right]\ddot{\mathscr{E}} - \left\{(\Delta^2+\kappa^2)\left[\left(\frac{ck}{\omega}\right)^2 - 1\right]\right. \\ \left. + 2\Lambda\sqrt{\Delta^2+\kappa^2}\left[\frac{c^2k}{V\omega} - 1\right]\dot{\phi} + \Lambda^2\left[\left(\frac{c}{V}\right)^2 - 1\right]\dot{\phi}^2\right\}\mathscr{E} \\ = 4\pi[\Lambda^2\ddot{u} - u(\sqrt{\Delta^2+\kappa^2} + \Lambda\dot{\phi})^2 \\ - \Lambda^2 v\ddot{\phi} - 2(\Lambda\sqrt{\Delta^2+\kappa^2} + \Lambda^2\dot{\phi})\dot{v}],\end{aligned} \tag{33}$$

$$\begin{aligned}\Lambda^2\left[\left(\frac{c}{V}\right)^2 - 1\right]\ddot{\phi}\mathscr{E} + 2\left\{\Lambda\sqrt{\Delta^2+\kappa^2}\left(\frac{c^2k}{V\omega} - 1\right)\right. \\ \left. + \Lambda^2\left[\left(\frac{c}{V}\right)^2 - 1\right]\dot{\phi}\right\}\dot{\mathscr{E}} \\ = 4\pi[\Lambda^2\ddot{v} - v(\sqrt{\Delta^2+\kappa^2} + \Lambda\dot{\phi})^2 \\ + \Lambda^2 u\ddot{\phi} + 2(\Lambda\sqrt{\Delta^2+\kappa^2} + \Lambda^2\dot{\phi})\dot{u}],\end{aligned} \tag{34}$$

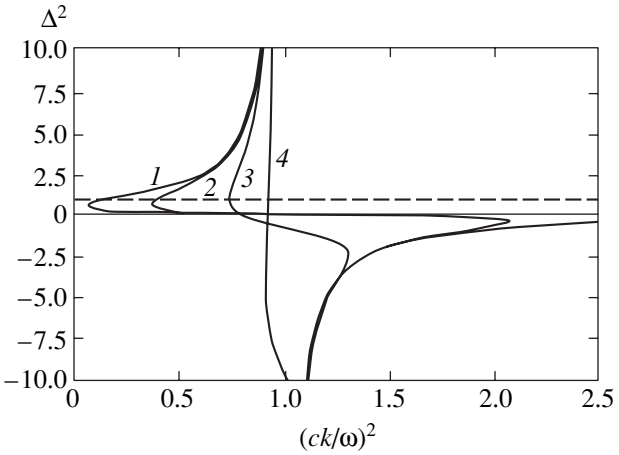

Fig. 1. Dispersion relation of the carrier wave for different values of the pulse duration τ measured by the parameter Λ (see Eq. (23)); $\Lambda^2 = 0.01$ (*1*), 0.1 (*2*), 1 (*3*), 10 (*4*).

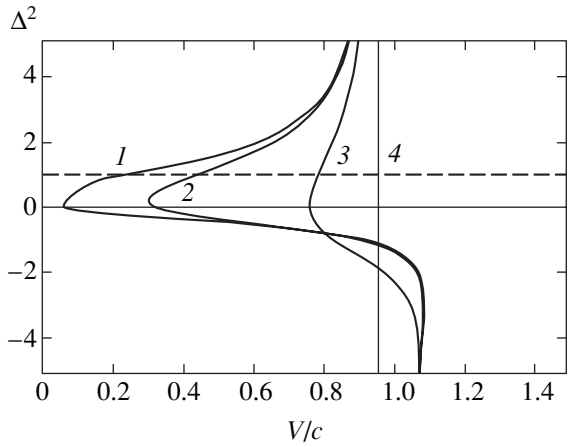

Fig. 2. Pulse velocity as a function of the carrier wave frequency for various values of the pulse duration τ measured by the parameter Λ (see Eq. (24)): $\Delta = 0.2$; $\Lambda^2 = 0.01$ (*1*), 0.1 (*2*), 1 (*3*), 10 (*4*).

where

$$\tilde{\chi} = \frac{\chi}{\omega_L^2 - \omega_T^2}, \tag{35}$$

and the overdot now denotes the derivative with respect to $\zeta = \xi/\tau$.

We consider long pulses with $\Lambda^2 \ll \Delta^2$. For this, we introduce a small parameter ε by

$$\Lambda^2 = \varepsilon^2\Delta^2, \quad \varepsilon \ll 1, \tag{36}$$

such that Eqs. (31)–(34) can be expanded in powers of ε. Because Eqs. (28) and (29) lead to different series expansions in different intervals of Δ^2, we must consider all these cases separately.

4.1. Long pulse above the polariton gap

We begin with the case of waves with

$$\Delta^2 > 1, \tag{37}$$

for which a nonlinear pulse can be represented as the envelope of propagating linear waves with dispersion law (25). For long pulses with

$$\varepsilon^2 \ll 1, \quad \varepsilon^2 \ll \Delta^2 - 1, \tag{38}$$

the coefficients in Eqs. (33) and (34) can be represented as power series expansions in ε,

$$\left(\frac{ck}{\omega}\right)^2 - 1 = -\frac{1}{\Delta^2} + \frac{\Delta^4 - 3\kappa^2 + 4\Delta^2\kappa^2}{\Delta^4(\Delta^2 - 1)}\varepsilon^2 + \ldots = -\frac{1}{\Delta^2} + \alpha_2\varepsilon^2 + \ldots, \tag{39}$$

$$\Lambda^2\left[\left(\frac{c}{V}\right)^2 - 1\right] = \frac{\Delta^6 + 2\Delta^4\kappa^2 + \kappa^4}{\Delta^4(\Delta^2 - 1)}\varepsilon^2 + \ldots = \gamma_2\varepsilon^2 + \ldots, \tag{40}$$

$$2\Lambda\left(\frac{c^2k}{V\omega} - 1\right) = \frac{2\kappa^2}{\Delta^3}\varepsilon - \frac{4\kappa^2(\Delta^2 + 2\kappa^2)}{\Delta^7}\varepsilon^3 + \ldots = \beta_1\varepsilon - \beta_3\varepsilon^3 + \ldots \tag{41}$$

We suppose that the functions $\mathscr{E}$, $\dot{\phi}$, u, and v can also be represented in the form of series expansions,

$$\mathscr{E} = \varepsilon^\nu \sum_{n=0}^{\infty} \varepsilon^n \mathscr{E}_n,$$

and similarly for $\dot{\phi}$, u, and v. Analysis of equations (31)–(34) and (39)–(41) shows that for self-consistency of the procedure, the series expansions of the fields must be as follows:

$$\begin{aligned} \mathscr{E} &= \varepsilon(\mathscr{E}_0 + \varepsilon^2\mathscr{E}_2 + \ldots), \\ \dot{\phi} &= \varepsilon(\theta_0 + \varepsilon^2\theta_2 + \ldots), \\ u &= \varepsilon(u_0 + \varepsilon^2 u_2 + \ldots), \\ v &= \varepsilon(\varepsilon v_1 + \varepsilon^3 v_3 + \ldots). \end{aligned} \tag{42}$$

Substitution of these expansions in Eqs. (31)–(34) then yields a sequence of equations for the coefficients $\mathscr{E}_0$, $\mathscr{E}_2$, θ_0, … In the first approximation, we obtain the relations

$$u_0 = -\frac{1}{4\pi\Delta^2}\mathscr{E}_0, \quad v_1 = \frac{2\sqrt{\Delta^2 + \kappa^2}}{\Delta}\dot{u}_0, \tag{43}$$

which correspond to the plane wave solution with a constant amplitude. In the next approximation, it follows from Eqs. (31) and (33) that

$$\begin{aligned} &-\ddot{\mathscr{E}}_0 + 4\frac{\sqrt{\Delta^2 + \kappa^2}}{\Delta^2}\ddot{\mathscr{E}}_0 - \frac{\tilde{\chi}}{16\pi^2\Delta^6}\mathscr{E}_0^3 \\ &= \mathscr{E}_2 + 4\pi\Delta^2 u_2 - \frac{2\sqrt{\Delta^2 + \kappa}}{\Delta}\theta_0\mathscr{E}_0, \\ &\left(\gamma_2 + 1 - 4\frac{\sqrt{\Delta^2 + \kappa^2}}{\Delta^2}\right)\ddot{\mathscr{E}}_0 - (\Delta^2 + \kappa^2)\alpha_2\mathscr{E}_0 \\ &= -\frac{\Delta^2 + \kappa^2}{\Delta^2}\left(\mathscr{E}_2 + 4\pi\Delta^2 u_2 - \frac{2\sqrt{\Delta^2 + \kappa^2}}{\Delta}\theta_0\mathscr{E}_0\right). \end{aligned} \tag{44}$$

Combination of these two equations yields the equation for $\mathscr{E}_0$ after simple transformations,

$$\ddot{\mathscr{E}}_0 = \mathscr{E}_0 + \frac{\tilde{\chi}}{16\pi^2\Delta^8\alpha_2}\mathscr{E}_0^3. \tag{45}$$

If $\tilde{\chi} < 0$, this equation has the soliton solution

$$\mathscr{E}_0 = \frac{a}{\cosh\zeta}, \tag{46}$$

where

$$a = \sqrt{\frac{32\pi^2\Delta^8\alpha_2}{|\tilde{\chi}|}}, \quad \alpha_2 = \frac{\Delta^4 - 3\kappa^2 + 4\Delta^2\kappa^2}{\Delta^4(\Delta^2 - 1)}, \tag{47}$$

and

$$\zeta = \frac{1}{\tau}\left(t - \frac{x}{V}\right), \quad \left(\frac{c}{V}\right)^2 = \frac{(\Delta^4 + \kappa^2)^2}{\Delta^6(\Delta^2 - 1)}. \tag{48}$$

This shows that V is equal to the group velocity given by Eq. (26) and is independent of the duration of the pulse. Because

$$\varepsilon = \frac{\Lambda}{\Delta} = \frac{1}{\sqrt{\omega^2 - \omega_T^2}\tau}, \quad \tilde{\chi} = \frac{\chi}{\omega_L^2 - \omega_T^2},$$

we obtain

$$\mathscr{E} = \sqrt{\frac{32\pi^2\Delta^6\alpha_2}{|\chi|}}\frac{1}{\tau}\frac{1}{\cosh\left[\frac{1}{\tau}\left(t - \frac{x}{V}\right)\right]}. \tag{49}$$

This is the NLS-type soliton solution.

We note that the above calculations were performed for arbitrary values of κ. However, in a majority of applications, we have

$$(\omega_L - \omega_T) \ll \omega_T,$$

that is,

$$\kappa^2 = \frac{\omega_T^2}{\omega_L^2 - \omega_T^2} \approx \frac{\omega_T}{2(\omega_L - \omega_T)} \gg 1. \quad (50)$$

Expansions (39)–(41) are then valid only under the condition that

$$\kappa^2\varepsilon^2 \approx \frac{1}{4(\omega_L - \omega_T)^2 t^2} \ll 1, \quad (51)$$

which implies that the spectral width of the pulse of the order of $1/\tau$ is much less than the width of the gap $(\omega_L - \omega_T)$. In fact, condition (51) is already satisfied sufficiently well for

$$\frac{1}{\tau} \approx \frac{\omega_L - \omega_T}{2}.$$

4.2. Long pulse at $\Delta^2 = 1$

In this case, the pulse cannot be described by the NLS equation for the wave packet of waves with wave vectors around some nonzero value. From Eqs. (28) and (29), we have the expansions

$$\left(\frac{ck}{\omega}\right)^2 - 1 = -1 + \sqrt{1+\kappa^2}\varepsilon + \ldots = -1 + \bar{\alpha}_1\varepsilon + \ldots, \quad (52)$$

$$\Lambda^2\left[\left(\frac{c}{V}\right)^2 - 1\right] = (1+\kappa^2)^{3/2}\varepsilon$$
$$-\left(2\kappa^4 + \frac{3}{2}\kappa^2 + \frac{1}{2}\right)\varepsilon^2 + \ldots = \bar{\gamma}_1\varepsilon - \bar{\gamma}_2\varepsilon^2 + \ldots, \quad (53)$$

$$2\Lambda\left(\frac{c^2k}{V\omega} - 1\right) = 2\kappa^2\varepsilon - 4(1+2\kappa^2)\kappa^2\varepsilon^3 + \ldots$$
$$= \bar{\beta}_1\varepsilon - \bar{\beta}_3\varepsilon^3 + \ldots \quad (54)$$

We again seek solution of Eqs. (31)–(34) in the form of series expansions, which in this case are

$$\mathscr{E} = \varepsilon^{1/2}(\mathscr{E}_0 + \varepsilon\mathscr{E}_1 + \ldots),$$
$$\dot{\phi} = \varepsilon^{1/2}\theta_0 + \ldots,$$
$$u = \varepsilon^{1/2}(u_0 + \varepsilon u_1 + \ldots), \quad (55)$$
$$v = \varepsilon^{3/2}v_1 + \ldots.$$

In the first approximation, we have

$$u_0 = -\frac{\mathscr{E}_0}{4\pi}, \quad v_1 = 2\sqrt{1+\kappa^2}\dot{u}_0. \quad (56)$$

In the next approximation, Eqs. (31) and (34) give

$$-u_1 + \tilde{\chi}u_0^3 = \frac{\mathscr{E}_1}{4\pi},$$
$$\sqrt{1+\kappa^2}\ddot{\mathscr{E}}_0 + \mathscr{E}_1 - \bar{\alpha}_1\mathscr{E}_0 = -4\pi u_1. \quad (57)$$

Hence,

$$\mathscr{E}_1 + 4\pi u_1 = -\frac{\tilde{\chi}}{16\pi^2}\mathscr{E}_0^3,$$
$$\sqrt{1+\kappa^2}(\ddot{\mathscr{E}}_0 - \mathscr{E}_0) = -(\mathscr{E}_1 + 4\pi u_1), \quad (58)$$

and we arrive at the equation for $\mathscr{E}_0$,

$$\ddot{\mathscr{E}}_0 = \mathscr{E}_0 + \frac{\tilde{\chi}}{16\pi^2\sqrt{1+\kappa^2}}\mathscr{E}_0^3. \quad (59)$$

Thus, we obtain the soliton solution

$$\mathscr{E} = \frac{\varepsilon^{1/2}a}{\cosh\left[\frac{1}{\tau}\left(t - \frac{x}{V}\right)\right]}, \quad a = \sqrt{\frac{32\pi^2(1+\kappa^2)^{1/2}}{|\tilde{\chi}|}}, \quad (60)$$

where V is given by

$$\left(\frac{c}{V}\right)^2 = 1 + \frac{(1+\kappa^2)^{3/2}}{\varepsilon}. \quad (61)$$

Taking into account that

$$\varepsilon = \Lambda = \frac{1}{\sqrt{\omega_L^2 - \omega_T^2}\tau},$$

we can rewrite Eqs. (60) and (61) in terms of the physical parameters

$$\mathscr{E} = \sqrt{\frac{32\pi^2\omega_L}{|\chi|\tau}}\frac{1}{\cosh\left[\frac{1}{\tau}\left(t - \frac{x}{V}\right)\right]},$$
$$\left(\frac{c}{V}\right)^2 = 1 + \frac{\omega_L^3\tau}{\omega_L^2 - \omega_T^2}. \quad (62)$$

The velocity of the pulse therefore depends on τ (curves in Fig. 2 intersect the straight line $\Delta^2 = 1$ at different points depending on τ). Although the parameter κ has disappeared from Eq. (62), expansions (52)–(54) are valid for $\kappa \gg 1$ provided the inequality $(\kappa\varepsilon)^2 \ll 1$ is satisfied. The ratio of the amplitude of solution (62) to that of solution (49) is in magnitude on the order of

$$\frac{1}{\sqrt{\kappa\varepsilon}} \sim \sqrt{(\omega_L - \omega_T)\tau} \gg 1,$$

that is, the amplitude at the boundary of the gap is much greater than the amplitude of the soliton solution sufficiently far from the gap. This implies that the pulse must be sufficiently intense to deform the gap to such an extent that the wave propagation with the frequency $\Delta^2 = 1$ becomes possible. Beyond the gap, there are linear waves that can propagate with arbitrarily small amplitudes and nonlinear effects must only compensate dispersive spreading of the wave packet built from linear waves.

4.3. Long pulse inside the polariton gap

For frequencies inside the polariton gap,

$$0 < \Delta^2 < 1, \tag{63}$$

we have the series of expansions

$$\left(\frac{ck}{\omega}\right)^2 - 1 = -1 + \frac{(\Delta^4 + \kappa^2)^2}{\Delta^4(\Delta^2 - 1)(\Delta^2 + \kappa^2)}\varepsilon^2 + \ldots = -1 + \tilde{\alpha}_2\varepsilon^2 + \ldots, \tag{64}$$

$$\Lambda^2\left[\left(\frac{c}{V}\right)^2 - 1\right] = \frac{(1-\Delta^2)(\Delta^2+\kappa^2)}{\Delta^2} + \frac{\Delta^8 + 5\Delta^4\kappa^2 - 3\kappa^4 + \Delta^2\kappa^2(4\kappa^2 - 3)}{\Delta^4(1-\Delta^2)}\varepsilon^2 + \ldots = \tilde{\gamma}_0 + \tilde{\gamma}_2\varepsilon^2 + \ldots, \tag{65}$$

$$2\Lambda\left(\frac{c^2k}{V\omega} - 1\right) = \frac{2\kappa^2}{\Delta^3}\varepsilon - \frac{4\kappa^2(\Delta^2 + 2\kappa^2)}{\Delta^7}\varepsilon^3 + \ldots = \beta_1\varepsilon - \beta_3\varepsilon^3 + \ldots, \tag{66}$$

where

$$\varepsilon \ll 1 - \Delta^2, \quad \varepsilon \ll \Delta^2. \tag{67}$$

Because $\tilde{\gamma}_0 \neq 0$, the soliton solution is obtained in the first approximation, and therefore $\mathscr{E}$ and u do not have a small factor proportional to a power of ε. The equations of the first approximation are given by

$$-\Delta^2 u + \tilde{\chi}u^3 = \frac{1}{4\pi}\mathscr{E}, \tag{68}$$

$$\frac{1-\Delta^2}{\Delta^2}\ddot{\mathscr{E}} + \mathscr{E} = -4\pi u. \tag{69}$$

If we were able to express u in terms of $\mathscr{E}$ from Eq. (68) and substitute the result in Eq. (69), we would obtain the equation for $\mathscr{E}$ having solitary wave solutions. Unfortunately, this can be done only numerically except in the case where

$$|\tilde{\chi}|u^2 \ll \Delta^2. \tag{70}$$

In this limit, we have

$$u \cong -\frac{1}{4\pi\Delta^2}\mathscr{E} - \frac{\tilde{\chi}}{\Delta^2(4\pi\Delta^2)^3}\mathscr{E}^3 \tag{71}$$

and Eq. (69) takes the form

$$\ddot{\mathscr{E}} = \mathscr{E} + \frac{\tilde{\chi}}{16\pi^2\Delta^6(1-\Delta^2)}\mathscr{E}^3. \tag{72}$$

It has the soliton solution

$$\mathscr{E} = \sqrt{\frac{32\pi^2\Delta^6(1-\Delta^2)(\omega_L^2 - \omega_T^2)}{|\chi|}}\frac{1}{\cosh\left[\frac{1}{\tau}\left(\tau - \frac{x}{V}\right)\right]}, \tag{73}$$

where the pulse velocity is given by

$$\left(\frac{c}{V}\right)^2 = 1 + \frac{(1-\Delta^2)(\Delta^2+\kappa^2)(\omega^2 - \omega_T^2)\tau^2}{\Delta^2}. \tag{74}$$

Using the estimate

$$u \sim \frac{a}{4\pi\Delta^2},$$

we can transform condition (70) into

$$1 - \Delta^2 \ll 1. \tag{75}$$

The frequency must therefore be sufficiently close to the upper limit of the polariton gap.

Solution (73) only applies to sufficiently long pulses

$$\varepsilon^2 \ll 1 - \Delta^2. \tag{76}$$

We note that in this case, the amplitude is independent of the pulse width τ, but its velocity strongly depends on τ. If $\kappa \gg 1$, the ratio of amplitude (73) to amplitude (49) is in magnitude on the order of

$$\frac{1}{\kappa\varepsilon} \sim (\omega_L - \omega_T)\tau \gg 1,$$

and as could be expected, is much greater than the amplitude of soliton solution (62) at the boundary of the gap.

When condition (75) is not satisfied, we must solve Eqs. (68) and (69) numerically. For this, we introduce new variables

$$\mathscr{E} = \frac{E}{\sqrt{|\tilde{\chi}|}}, \quad u = \frac{U}{\sqrt{|\tilde{\chi}|}}, \tag{77}$$

where $\tilde{\chi} = -|\tilde{\chi}|$. Equations (68) and (69) then reduce to

$$\Delta^2 U + U^3 = -\frac{1}{4\pi}E, \quad \frac{1-\Delta^2}{\Delta^2}\ddot{E} + E = -4\pi U. \tag{78}$$

Numerical solution of the first equation in (78) yields the function

$$U = U(E), \tag{79}$$

substitution of which in the second equation in (78) gives the differential equation for E,

$$\frac{1-\Delta^2}{\Delta^2}\frac{d^2E}{d\zeta^2} = -E - 4\pi U(E), \tag{80}$$

or

$$\frac{d^2E}{d\zeta^2} = -\frac{\partial V(E)}{\partial E}, \tag{81}$$

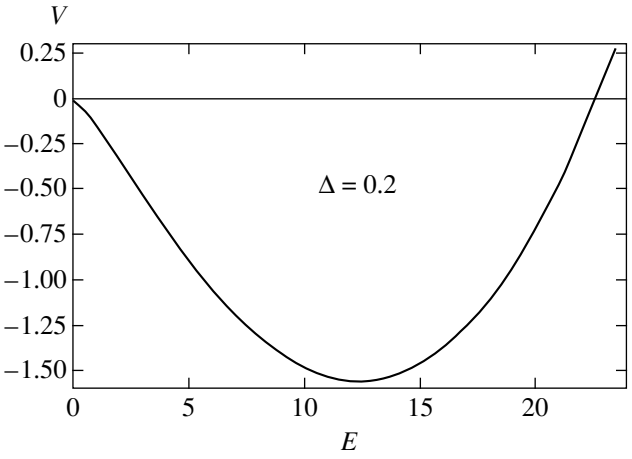

Fig. 3. The potential V as a function of the electric field amplitude for $\Delta = 0.2$.

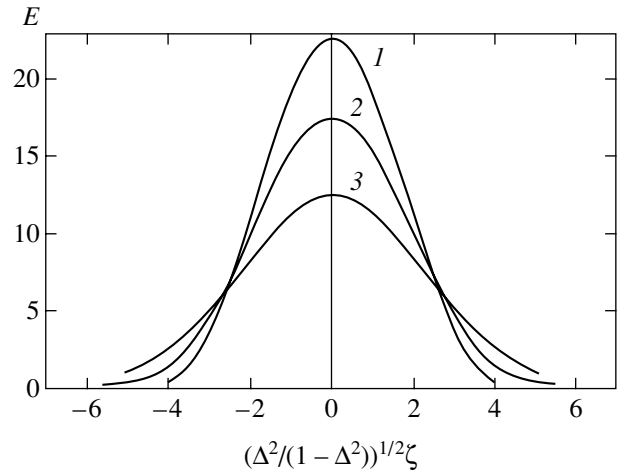

Fig. 4. Profiles of solitary wave solutions for three different values of the carrier wave frequency (see Eq. (20)) inside the polariton gap; $\Delta = 0.2$ (*1*), 0.6 (*2*), 0.8 (*3*).

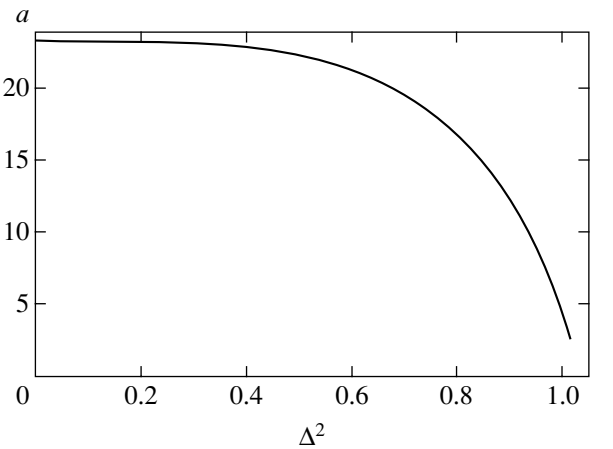

Fig. 5. Dependence of the amplitude of the solitary wave on the carrier wave frequency (see Eq. (20)) inside the polariton gap.

where

$$V(E) = \frac{\Delta^2}{1-\Delta^2}\left(\frac{1}{2}E^2 + 4\pi\int_0^E U(E')dE'\right) \qquad (82)$$

can be considered as a potential in which a particle moves in accordance with Newton equation (81). A typical plot of potential (82) is shown in Fig. 3. The maximum value of E (the soliton amplitude a) is determined by the point $E = a$ where $V(E)$ vanishes. The solution of Eq. (80) with the initial conditions $E(0) = a$ and $E'(0) = 0$ then provides the soliton solution. We have performed these calculations for several values of Δ. The results are shown in Fig. 4, where the dependence of the pulse profile E on the scaled variable $\sqrt{\Delta^2/(1-\Delta^2)}\,\zeta$ is plotted. The dependence of the amplitude on Δ is shown in Fig. 5.

5. CONCLUSIONS

We have studied the nonlinear optical pulse propagation in a frequency region in the vicinity of the polariton gap. The problem is described by a coupled set of Maxwell equations for the electromagnetic field and a material equation for the macroscopic polarization allowing a Kerr-like nonlinearity. To solve this nonlinear system of equations analytically, we used the approach [8] based on series expansion in powers of a small parameter related to the width of the polariton gap and pulse duration. Different bright solitary wave solutions depending on the position of the carrier wave frequency with respect to the polariton gap are found, and their parameters are expressed in terms of material system parameters. Outside the polariton gap, the soliton solution corresponds to the well-known soliton of the NLS equation for the envelope of a wave packet made of plane waves. However, inside the polariton gap, there are no plane wave solutions and the notion of their envelope loses its physical sense. Nonetheless, solitary wave solutions can occur there with sufficiently high values of the electromagnetic field strength such that the local value of the polariton gap diminishes in the center of the polariton gap due to the Kerr nonlinearity. The difference in physical situations outside and inside the polariton gap is reflected in different dependences of the soliton amplitude on the pulse duration τ: the amplitude is independent of τ inside the gap, is proportional to $\tau^{-1/2}$ at the gap boundary, and is proportional to τ^{-1} sufficiently far from the gap.

ACKNOWLEDGMENTS

S. D. thanks Marseilles University for kind hospitality and NATO Linkage Grant PST. CLG. 978177 for partial support.

REFERENCES

1. *Confined Electrons and Photons. New Physics and Applications*, Ed. by E. Burstein and C. Weisbuch (Plenum, New York, 1995).
2. *Optics of Excitons in Confined Systems*, Ed. by A. D'Andrea *et al.* (IOP, Bristol, 1991).
3. *Photoactive Organic Materials. Science and Applications*, Ed. by F. Kajzar, V. M. Agranovich, and C. Y.-C. Lee (Kluwer, Dordrecht, 1996).
4. V. M. Agranovich, A. M. Kamchatnov, H. Benisty, and C. Weisbuch, in *Beam Shaping and Control with Nonlinear Optics*, Ed. by F. Kajzar and P. Reinisch (Plenum, New York, 1998).
5. A. Schenzle and H. Haken, Opt. Commun. **6**, 96 (1972); H. Haken and A. Schenzle, Z. Phys. **258**, 231 (1973).
6. E. Hanamura, J. Phys. Soc. Jpn. **37**, 1553 (1974).
7. M. Inoue, J. Phys. Soc. Jpn. **37**, 1560 (1974).
8. O. Akimoto and K. Ikeda, J. Phys. A: Math. Gen. **10**, 425 (1977); K. Ikeda and O. Akimoto, J. Phys. A: Math. Gen. **12**, 1105 (1979).
9. S. V. Branis, O. Martin, and J. L. Birman, Phys. Rev. A **43**, 1549 (1991).
10. J. Goll and H. Haken, Phys. Rev. A **18**, 2241 (1978).
11. S. A. Moskalenko, P. I. Khadzhi, and A. Kh. Rotaru, *Solitons and Nutation in the Exciton Region of Spectrum* (Shtiintsa, Chisinau, 1980); S. A. Moskalenko, *An Introduction to the Theory of High-Density Excitons* (Shtiintsa, Chisinau, 1983).
12. I. B. Talanina, M. A. Collins, and V. M. Agranovich, Solid State Commun. **88**, 541 (1993).
13. U. Peschel, T. Peschel, and F. Lederer, J. Opt. Soc. Am. **14**, 2994 (1997).
14. V. M. Agranovich and V. L. Ginzburg, *Crystal Optics with Spatial Dispersion, and Excitons*, 2nd ed. (Nauka, Moscow, 1979; Springer, New York, 1984).

Journal of Experimental and Theoretical Physics, Vol. 96, No. 5, 2003, pp. 885–896.
Translated from Zhurnal Éksperimental'noĭ i Teoreticheskoĭ Fiziki, Vol. 123, No. 5, 2003, pp. 1006–1018.

PLASMA, GASES

Ionization Focusing of a Short Intense Laser Pulse and Generation of Wake Plasma Waves

N. E. Andreev, M. V. Chegotov*, and A. A. Pogosova**

Institute of Thermal Physics of Extremal States of the Joint Institute of High Temperatures, Russian Academy of Sciences, Moscow, 127412 Russia

**e-mail: chegotov@ihed.ras.ru*

***e-mail: alla@ihed.ras.ru*

Received August 12, 2002

Abstract—The propagation of a short intense laser pulse is studied in a gas taking into account the ionization of gas atoms by the high-frequency electromagnetic field of the pulse. The conditions are found under which the ionization structures produced by the laser pulse cause the pulse focusing accompanied by a substantial increase in its intensity. It is shown that the leading edge of the pulse is subjected to ionization refraction at the ionization front, the temporal profile of the pulse becoming steeper. This results in the efficient generation of a wake wave at the ionization front, which is amplified during the development of self-modulation instability. The amplitude of the wake plasma wave achieves a substantial value already at small paths of the pulse in matter (smaller than the diffraction length of the pulse). © *2003 MAIK "Nauka/Interperiodica".*

1. INTRODUCTION

One of the promising applications of short intense laser pulses is the laser–plasma acceleration of particles (see, for example, reviews [1, 2]). This method attracts attention due to the compactness of setups, which is caused by record high acceleration of particles.

Initially, a preliminary prepared plasma was used in schemes of laser–plasma acceleration (see, for example, [3, 4]). Note that, to efficiently generate wake plasma waves and then to accelerate electrons, rather strict relations between the parameters of laser radiation and plasma should be fulfilled. The use of an initially neutral gas, which is ionized directly by an intense laser pulse, offers a number of advantages both from the point of view of the plasma production and the necessity of its confinement in a certain configuration, and in relation to the specificity of interaction of radiation with matter. First of all, it is easy to obtain a stable and sufficiently homogeneous concentration of a neutral gas. Upon irradiation of the neutral gas by an intense ionizing pulse, plasma waves are generated efficiently at the ionization front [5]. In this case, comparatively long laser pulses can be used to generate high-amplitude plasma waves in the self-modulation regime of the laser pulse [6–8]. Another mechanism of generation of plasma waves, which can be realized in a neutral gas, is generation due to a steep leading edge of the laser pulse [9]. The advantage of using ionized gases is that, unlike the conditions studied in [9], an increase in the slope of the leading edge of the laser pulse upon ionization occurs self-consistently during the propagation of the laser pulse in the gas due to the so-called ionization refraction [10].

The influence of ionization refraction on the propagation of intense laser pulses is attracting great attention because of a variety of practical applications of short intense laser pulses. Under conditions when the transverse radius r_0 (for definition, see Eq. (18)) of a pulse is small compared to the wavelength λ_p of a plasma wave and the pulse duration τ is on the order of the period λ_p/c of the plasma wave (c is the speed of light), the range of a laser pulse retaining a sufficiently high intensity in a gas being ionized decreases; in this case, the maximum intensity of the pulse proves to be lower than that in vacuum [11]. As the pulse radius ($r_0 \sim \lambda_p$) and duration $\tau \sim \lambda_p/c$ increase, the action of ionization refraction on the main part of the pulse is small if a sufficiently large part of the pulse energy is in the region of ionized matter [12]. For $r_0 \sim \lambda_p$ and $\tau \gg \lambda_p/c$, the range of a laser pulse retaining a sufficiently high intensity in gas proves to be on the order of that in vacuum [i.e., on the order of the vacuum diffraction (Rayleigh) length z_R]. In this case, the main part of the pulse can propagate over distances exceeding z_R with a comparatively low maximum intensity [13]. To obtain a comparatively large propagation depth, the ionization potential of the gas should be sufficiently low, so that the radius of a plasma region would be considerably greater than the pulse radius r_0. When the pulse power P is high (higher than the critical power $P_c \approx 17 n_c/n_e$ GW of relativistic self-focusing, where n_c is the critical density and n_e is the electron density in plasma [1]), the pulse range increases; however, in the presence of relativistic self-focusing, the pulse propagation is unstable [14].

In this paper, we study the generation of wake plasma waves, which accelerate electrons upon irradia-

tion of an initially neutral gas by a laser pulse with a power below the critical power of relativistic self-focusing and a radius that greatly exceeds the wavelength of the plasma wave. In Section 2, by using the kinetic equation for the distribution function of free electrons, we obtained a system of hydrodynamic equations that take into account the creation of free electrons in the field of an intense laser pulse. In addition, the free-electron current in the Maxwell equations for electromagnetic fields in an ionized substance is supplemented with an ionization current, which takes into account the laws of conservation of energy and momentum in the "electromagnetic radiation + substance" system. In Section 3, we performed a harmonic analysis of the system of hydrodynamic equations derived in Section 2. As a result, we obtained the system of equations for slowly varying amplitudes of the laser field, the electron density, and the field of a wake wave. By neglecting ionization effects (preliminarily prepared plasma), this system coincides with the generally accepted system [1, 15], which describes self-consistently the propagation and generation of a wake plasma wave by an intense laser pulse. The influence of ionization effects is taken into account both in the equation for the envelope of the electric field of a laser pulse and in the equation for the electron density and amplitude of the wake plasma wave. In Section 4, we studied the propagation of a comparatively long (at the scale of the plasma-wave period) laser pulse in a gas being ionized by the pulse. The propagation of the pulse in the gas is accompanied by the ionization refraction at nonstationary spatially inhomogeneous plasma structures, which are formed upon ionization of the gas by the pulse. When the peak intensity satisfies the resonance condition with respect to the threshold ionization intensity, the propagation of the pulse in the gas is accompanied by an increase in its maximum intensity. This increase (which we will call ionization focusing) is caused by the development of the ionization modulation of the laser pulse [16]. Such a modulation appears at the leading edge of the laser pulse, unlike ionization modulation [17–20], which is manifested as the instability at the trailing edge of the pulse. The consideration of nonlinearity of the electron motion (relativistic and ponderomotive), which does not qualitatively change the behavior of a laser pulse during its propagation, results in an additional increase in the electromagnetic-field intensity in the region of ionization focusing. The generation of a wake plasma wave is discussed in Section 5. The laser pulse duration was chosen long enough to provide the formation of a high-amplitude plasma wave due to the development of self-modulation instability. The mechanism of excitation of a "seed" plasma wave for such instability changes during the pulse propagation: for a small depth of penetration of the pulse into the material, the pulse shape remains comparatively smooth and the ionization mechanism of generation takes place [5]. As the pulse penetrates more deeply, its leading edge becomes steeper due to ionization refraction and the generation of a seed plasma wave is already determined by the mechanism considered in paper [9] in the case of a short leading edge of the pulse. As a result, two main factors lead to efficient generation of a high-amplitude wake plasma wave: first, ionization refraction causes both a strong increase in the slope of the leading edge of the laser pulse and a substantial increase in its maximum intensity due to ionization focusing; second, a plasma wave generated at the leading edge is enhanced in the most intense part of the pulse due to self-modulation instability, this effect being strongly enhanced due to ionization focusing. The amplitude of the wake plasma wave becomes large at a comparatively small depth of penetration of the laser pulse into gas, which is smaller than the diffraction length z_R of the pulse [21].

2. BASIC EQUATIONS

We will describe the space–time dynamics of ionization and generation of a wake plasma wave in the field of a short high-power laser pulse using hydrodynamic equations. Let us consider ionization in these equations with the help of a standard procedure for obtaining hydrodynamic equations from the kinetic equation for the electron function of distribution $f(\mathbf{r}, \mathbf{p}, t)$ over momenta:

$$\frac{\partial f}{\partial t} + (\mathbf{v}\cdot\nabla) f + e\left(\mathbf{E} + \frac{1}{c}[\mathbf{v}\times\mathbf{B}]\right)\cdot\frac{\partial f}{\partial \mathbf{p}} = \Gamma(\mathbf{r}, t)\delta(\mathbf{p}), \quad (1)$$

where $\mathbf{E}(\mathbf{B})$ is the electric (magnetic) field in substance. The term $\Gamma(\mathbf{r}, t)\delta(\mathbf{p})$ represents a source of electrons produced upon ionization by the intense electromagnetic field. The ionization of an atom (or ion) by the field of a short (the duration τ is shorter or of about 1 ps) intense laser pulse occurs due to tunneling because the Keldysh parameter $\gamma = \omega_0\sqrt{2m_eU}/|e|E$ (ω_0 is the laser radiation frequency, U is the ionization potential of an atom (ion), m_e and e are the electron mass and charge, respectively) [22] proves to be comparatively small ($\gamma \lesssim 1$) [23]. We can assume that a free electron produced upon such ionization has a zero initial velocity [24, 25], which corresponds to the ionization source proportional to $\delta(\mathbf{p})$ in Eq. (1). A similar approach for used to derive hydrodynamic equations for ionized gas from the kinetic equation [26, 27]. Note that the consideration of ionization processes in the kinetic equation with the help of the term of the type $\Gamma(\mathbf{r}, t)\delta(\mathbf{p})$ leads to reasonable energy relations in the description of the propagation of a laser pulse in a material being ionized [16].

Equation (1) neglects recombination processes, as well as all inelastic and elastic collision processes: electron–atomic, electron–ion, and electron–electron, because the characteristic duration of these processes in

a plasma of a moderate density is much longer than the characteristic times involved in the problem under study: the pulse duration and the plasma-wave period (the latter is shorter than or of about the pulse duration, see below).

By integrating (1) over momenta, we obtain the equation for the electron density $n(\mathbf{r}, t) \equiv \int d\mathbf{p}\, f(\mathbf{r}, \mathbf{p}, t)$:

$$\frac{\partial n}{\partial t} + \mathrm{div}(n\mathbf{V}_e) = \Gamma, \tag{2}$$

where

$$\mathbf{V}_e(\mathbf{r}, t) \equiv \frac{1}{n(\mathbf{r}, t)}\int d\mathbf{p}\mathbf{v}\, f(\mathbf{r}, \mathbf{p}, t)$$

is the average velocity of the directed movement of electrons. By multiplying (1) by $\mathbf{p}$ and integrating over $\mathbf{p}$, and also using Eq. (2) for the average momentum

$$\mathbf{P}_e(\mathbf{r}, t) \equiv \frac{1}{n(\mathbf{r}, t)}\int d\mathbf{p}\mathbf{p}\, f(\mathbf{r}, \mathbf{p}, t)$$

we obtain the equation

$$\frac{\partial \mathbf{P}_e}{\partial t} + (\mathbf{V}_e\nabla)\mathbf{P}_e + \frac{\Gamma}{n}\mathbf{P}_e = e\left(\mathbf{E} + \frac{1}{c}[\mathbf{V}_e \times \mathbf{B}]\right). \tag{3}$$

We neglected in Eq. (3) the pressure force $-n^{-1}\partial\Pi_{ij}/\partial r_j$ (summation is performed over doubly repeated subscript, $\Pi_{ij} = \int d\mathbf{p}\,(v_j - V_{e,j})(p_i - P_{e,i})$) compared to ponderomotive forces acting on the electron liquid, which are determined by the right-hand side of Eq. (3) and the second term in its left-hand side. Indeed, under the conditions when collisions between electrons and ions and neutral atoms during the action of a short laser pulse can be neglected, the scatter in the electron energy, which is characterized by the quantity $n^{-1}\Pi_{ij}$, will be determined in a gas being ionized not by inverse-bremsstrahlung absorption but by the nonadiabatic interaction of electrons with the laser-pulse field at the instant of their escape from an atom. The value of $n^{-1}\Pi_{ij}$ is on the order of the so-called residual energy, which is small when the ionization potentials of atoms of the substance are comparatively low [24, 26, 28].

Hydrodynamic equations (2) and (3) contain the source Γ, which represents the rate of creation of free electrons per unit volume. To determine Γ, it is necessary to calculate the rate of extraction from all atomic shells. During the ionization of a substance by a rapidly oscillating laser field, the charge densities both for free electrons (ρ_e) and ions (ρ_i) also become rapidly oscillating functions of time. This circumstance is caused by the dependence of the probability W_m of ionization per unit time of an ion with the charge $m|e|$ to an ion with the charge $(m + 1)|e|$ on the instantaneous value of the laser-pulse field $|\mathbf{E}|$ [29, 30]:

$$W_m(|\mathbf{E}|) = \omega_{at}\frac{\exp(1)}{2\pi}\frac{(m+1)^2}{n_*^4} \times\left[4\exp(1)\frac{(m+1)^3}{n_*^4}\frac{E_{at}}{|\mathbf{E}|}\right]^{2n_*-1}\exp\left(-\frac{2}{3}\frac{(m+1)^3}{n_*^3}\frac{E_{at}}{|\mathbf{E}|}\right), \tag{4}$$

where $n_* = (m + 1)\sqrt{U_\mathrm{H}/U_m}$, U_H is the potential of ionization of a hydrogen atom from the ground state, U_m is potential of ionization of an ion with the charge $m|e|$ to an ion with the charge $(m + 1)|e|$ ($m = 0$ corresponds to a neutral atom), $E_{at} \approx 5.1 \times 10^9$ V/cm is the atomic-field strength, and $\omega_{at} \approx 4.1 \times 10^{16}$ s^{-1} is the atomic frequency. Because of the comparatively short duration of the laser pulse, we will assume that ions are at rest. Under such conditions, the equation for the ion charge density has the form

$$\frac{\partial \rho_i}{\partial t} \equiv |e|\Gamma = |e|\sum_{m=0}^{Z-1} W_m N_m \equiv |e|\sum_{m=0}^{Z-1}\Gamma^{(m)}, \tag{5}$$

where Z is the atomic nucleus charge, N_m is the concentration of ions with the charge $m|e|$, and $\Gamma^{(m)}$ is the rate of ionization of ions with the charge $m|e|$ to ions with the charge $(m + 1)|e|$ per unit volume. Equations for N_m are also spatially local:

$$\frac{\partial N_0}{\partial t} = -\Gamma^{(0)}, \quad \frac{\partial N_m}{\partial t} = -\Gamma^{(m)} + \Gamma^{(m-1)},$$
$$\Gamma^{(m)} \equiv W_m N_m, \quad m = 1, \ldots, Z-1, \tag{6}$$
$$\Gamma^{(0)} \equiv W_0 N_0.$$

We should take ionization processes into account in the Maxwell equations, as in kinetic equation (1). For this purpose, we should consider, along with the current $\mathbf{J}$ of free electrons, the current $\mathbf{J}_\mathrm{ion}$ caused by polarization of the atoms ionized in the laser field [5, 31]. To determine $\mathbf{J}_\mathrm{ion}$, we will take into account the fact that, due to the direct ionization of atoms by the electromagnetic field with the wave vector $\mathbf{k}$ and frequency ω, the energy density $\omega_{\mathbf{k}\omega}$ of laser radiation decreases at a rate of

$$\left(\frac{\partial w_{\mathbf{k}\omega}}{\partial t}\right)_\mathrm{ion} = -\sum_{m=0}^{Z-1} W_m N_m U_m, \tag{7}$$

while the flux density of the laser pulse $\mathbf{S}/c^2$ ($\mathbf{S} = (c/4\pi)[\mathbf{E} \times \mathbf{B}]$ is the Poynting vector) changes at a rate of

$$\left(\frac{\partial}{\partial t}\frac{\mathbf{S}}{c^2}\right)_\mathrm{ion} = -\sum_{m=0}^{Z-1} W_m N_m U_m \frac{\mathbf{k}}{\omega}. \tag{8}$$

Changes in the energy (7) and pulse (8) of laser radiation can be taken into account in the Maxwell equation

$$\mathrm{rot}\mathbf{B} = \frac{4\pi}{c}(\mathbf{J} + \mathbf{J}_{\mathrm{ion}}) + \frac{1}{c}\frac{\partial \mathbf{E}}{\partial t} \quad (9)$$

by introducing, along with the current $\mathbf{J} = en_e\mathbf{V}_e$ of free electrons, the ionization current $\mathbf{J}_{\mathrm{ion}}$, which is defined by the expression

$$\mathbf{J}_{\mathrm{ion}} = \frac{\mathbf{E}}{E^2}\sum_{m=0}^{Z-1} W_m N_m U_m. \quad (10)$$

The ionization current $\mathbf{J}_{\mathrm{ion}}$ in Eq. (9) produces, generally speaking, an additional (along with the usual hydrodynamic free charge density $\rho(\mathbf{r}, t) \equiv en + |e|\sum_{m=1}^{Z} mN_m$) ionization charge density ρ_{ion} in the Maxwell equation

$$\mathrm{div}\mathbf{E} = 4\pi\rho + 4\pi\rho_{\mathrm{ion}}.$$

Indeed, because the rates of the appearance of free electrons and a total charge of ions are identical, the hydrodynamic densities of the free charge $\rho = \rho_i + \rho_e$ and current $\mathbf{J}$ satisfy the law of conservation of free charge

$$\frac{\partial \rho}{\partial t} + \mathrm{div}\mathbf{J} = 0.$$

By applying the div operation to Eq. (9) and using the law of conservation of free charge, we obtain the law of conservation of ionization charge

$$\frac{\partial \rho_{\mathrm{ion}}}{\partial t} + \mathrm{div}\mathbf{J}_{\mathrm{ion}} = 0.$$

It follows, in particular, from this expression that, if $\mathrm{div}\mathbf{J}_{\mathrm{ion}} \neq 0$, then also $\rho_{\mathrm{ion}} \neq 0$. Note that, in the one-dimensional geometry, the ionization current (10) caused by the ionization produced by the transverse field of the laser pulse proves to be also transverse, so that $\mathrm{div}\mathbf{J}_{\mathrm{ion}} = 0$ and $\partial\rho_{\mathrm{ion}}/\partial t = 0$ and $\rho_{\mathrm{ion}} = 0$. The current (10) was introduced for energetic reasons earlier in paper [32] and was used in papers [17, 27, 33, 34]. Expression (8) presented above additionally substantiates ionization current (10), based on the law of conservation of momentum of the "field + material medium" system during the ionization of the material by the radiation field.

3. FORMULATION OF THE PROBLEM

3.1. Derivation of Equations for Slowly Varying Amplitudes

We will describe the evolution of a laser pulse propagating in a gas being ionized using the approximation of slowly varying amplitudes. This approximation can be applied for comparatively rarified gases because the characteristic spatial and temporal variations in the amplitudes of fields and density of free electrons exceed the wavelength and period of laser radiation. In this approximation, we represent the rapidly oscillating electric field $\mathbf{E}$ of laser radiation in the form

$$\mathbf{E} = \frac{m_e\omega_0 c}{2e}\left[\mathbf{a}\exp\left(-i\omega_0 t + \frac{i\omega_0 z}{c}\right) + \text{c.c.}\right], \quad (11)$$

where $\mathbf{a}$ is a slowly varying dimensionless amplitude of the electric field of laser radiation.

We will derive equations for slowly varying envelopes taking into account ionization processes as in [12]. Let us represent the ionization source Γ and the ion and electron densities in the form

$$\Gamma = \Gamma_0 + \frac{1}{2}[\Gamma_2\exp(-2i\omega_0 t) + \text{c.c.}] + \ldots,$$

$$\rho_i = |e|\left\{n_0 + \frac{1}{2}[n_2\exp(-2i\omega_0 t) + \text{c.c.}] + \ldots\right\},$$

$$\rho_e = en = e\left\{n_e + \frac{1}{2}[n_{e2}\exp(-2i\omega_0 t) + \text{c.c.}] + \ldots\right\},$$

where Γ_0, Γ_2, n_0, n_2, n_e, and n_{e2} are the functions of time that are slowly varying at the scale $2\pi/\omega_0$, and n_e and n_{e2} take into account the electron motion in the intense field of a laser wave. The value of the second harmonic Γ_2 substantially depends on the polarization of laser radiation. For circular polarization, $\Gamma_2 = 0$, whereas for linear polarization for comparatively light gases ($Z \leq 10$), $\Gamma_2 \approx 1.56\Gamma_0$ [5].

The equation for a slowly varying amplitude of the laser field in the system of comoving coordinates z, $\xi = z - ct$ in an axial field $|\mathbf{a}|$ has the form (cf. [12, 15]

$$2\omega_0 c\frac{\partial \mathbf{a}}{\partial z} - 2ic^2\frac{\partial^2 \mathbf{a}}{\partial z\partial \xi} - ic^2\Delta_\perp \mathbf{a} + i\omega_p^2\left(\frac{n_e}{n_0} - \frac{1}{4}|\mathbf{a}|^2\right)\mathbf{a} = \frac{\Gamma_2\omega_0}{4n_c}\mathbf{a}^* - \mathbf{a}\frac{2\omega_0}{|\mathbf{a}|^2}\sum_{m=0}^{Z-1}\frac{\Gamma_0^{(m)}}{n_c}\frac{U_m}{m_e c^2}, \quad (12)$$

where

$$\Delta_\perp = \frac{1}{r}\frac{\partial}{\partial r}\left(r\frac{\partial}{\partial r}\right)$$

is the transverse part of the Laplace operator, $\omega_p^2 = 4\pi e^2 n_0/m_e$. The equations for the zero harmonics $\Gamma_0^{(m)}$

of corresponding ionization rates and for the concentrations $n_0^{(m)}$ have the form

$$n_0 = \sum_{m=1}^{Z} m n_0^{(m)}, \quad \Gamma_0^{(m)} = w_m n_0^{(m)},$$
$$\Gamma_0^{(Z)} = 0, \quad c\frac{\partial n_0^{(0)}}{\partial \xi} = \Gamma_0^{(0)},$$
$$c\frac{\partial n_0^{(m+1)}}{\partial \xi} = -\Gamma_0^{(m)} + \Gamma_0^{(m+1)}, \quad (13)$$
$$m = 0, \ldots, Z-1,$$
$$\Gamma_0 = \sum_{m=0}^{Z-1} \Gamma_0^{(m)},$$

where

$$w_m(|\mathbf{a}|) = \omega_{at}\sqrt{3}\left(\frac{\exp(1)}{\pi}\right)^{3/2}\frac{(m+1)^2}{n_*^{4.5}}$$
$$\times\left[4\exp(1)\frac{(m+1)^3}{n_*^4}\frac{a_{at}}{|\mathbf{a}|}\right]^{2n_*-1.5} \quad (14)$$
$$\times\exp\left(-\frac{2}{3}\frac{(m+1)^3}{n_*^3}\frac{a_{at}}{|\mathbf{a}|}\right)$$

is the ionization probability (4) averaged over the laser period $2\pi/\omega_0$, and $a_{at} = eE_{at}/m_e\omega_0 c$.

We will determine the electron concentration in (12) by using the equations for slowly varying quantities $\bar{\mathbf{P}}_e$ and n_e, which can be obtained from Eqs. (2) and (3) by averaging over $|\mathbf{a}| < 1$:

$$\frac{\partial \bar{\mathbf{P}}_e}{\partial t} = e\mathbf{E}_p - m_e c^2 \nabla\left(\frac{1}{2}\frac{\bar{\mathbf{P}}_e^2}{m_e^2 c^2} + \frac{1}{4}|\mathbf{a}|^2\right)$$
$$-\frac{\Gamma_0}{n_e}\bar{\mathbf{P}}_e + \frac{m_e c}{2n_e}\left[\Gamma_0|\mathbf{a}|^2 - \frac{1}{2}\mathrm{Re}(\Gamma_2(\mathbf{a}^*)^2)\right]e_z,$$
$$\frac{\partial(en_e)}{\partial t} = e\Gamma_0 - \mathrm{div}\bar{\mathbf{J}},$$

where the slowly varying plasma fields $\mathbf{E}_p$ and $\mathbf{B}_p$ are described by the Maxwell equations

$$\frac{\partial \mathbf{E}_p}{\partial t} = -4\pi\bar{\mathbf{J}} + c\,\mathrm{rot}\mathbf{B}_p, \quad \frac{\partial \mathbf{B}_p}{\partial t} = -c\,\mathrm{rot}\mathbf{E}_p,$$

in which $\bar{\mathbf{J}}$ is a slow electron current

$$\bar{\mathbf{J}} = \frac{e}{m_e}\bar{\mathbf{P}}_e\left(1 - \frac{1}{2}\frac{\bar{\mathbf{P}}_e^2}{m_e^2 c^2} - \frac{1}{4}|\mathbf{a}|^2\right).$$

As in the absence of ionization effects (a preliminary prepared plasma), these equations can be solved by introducing a scalar dimensionless function ϕ ("potential") for slowly varying amplitudes in the system of co-moving coordinates z, $\xi = z - ct$. This function is related to the slowly varying longitudinal $E_{p,z}$ and transverse $E_{p,r}$ components of the electric field and the azimuthal magnetic field $B_{p,\varphi}$ of a plasma wave by the expressions [15]

$$\frac{\partial \phi}{\partial \xi} = \frac{eE_{p,z}}{m_e c^2}, \quad \frac{\partial \phi}{\partial r} = \frac{eE_{p,r}}{m_e c^2} - \frac{eB_{p,\varphi}}{m_e c^2}.$$

The electron concentration n_e entering Eq. (12) is also expressed in terms of the potential ϕ:

$$\frac{n_e}{n_0} = 1 + \frac{1}{4}|\mathbf{a}|^2 + \frac{1}{k_p^2}(\Delta_\perp - k_p^2)\phi$$
$$+\frac{1}{k_p^2}\int_{+\infty}^{\xi}\left[\phi + \frac{1}{4}|\mathbf{a}|^2 - \mathrm{Re}\left(\mathbf{a}^{*2}\frac{\Gamma_2}{8\Gamma_0}\right)\right]\frac{\partial k_p^2}{\partial \xi}d\xi. \quad (15)$$

The equation for this potential has the form [12]

$$(\Delta_\perp - k_p^2)\frac{\partial^2 \phi}{\partial \xi^2} + k_p^2(\Delta_\perp - k_p^2)\phi$$
$$-\frac{\partial \ln n_0}{\partial r}\frac{\partial^3 \phi}{\partial r \partial \xi^2} = \frac{k_p^2}{4}(\Delta_\perp - k_p^2)|\mathbf{a}|^2 \quad (16)$$
$$-k_p^2\int_{+\infty}^{\xi}\left[\phi + \frac{1}{4}|\mathbf{a}|^2 - \mathrm{Re}\left(\mathbf{a}^{*2}\frac{\Gamma_2}{8\Gamma_0}\right)\right]\frac{\partial k_p^2}{\partial \xi}d\xi,$$

where $k_p^2 = \omega_p^2/c^2$.

Equations (12)–(16) describe the relativistic and ponderomotive self-focusing of the laser pulse and the generation of an electron wake plasma wave by this pulse, as well as the influence of the processes of plasma formation on the propagation of the laser pulse and excitation of the wake field. In the absence of ionization, the right-hand side of Eq. (12) is zero and Eqs. (15) and (16) do not contain integral terms.

The effect of ionization on the generation of a wake plasma wave was studied within the framework of a one-dimensional model in papers [5], where it was shown that ionization causes an increase in the amplitude of the wake wave. The propagation of a comparatively short laser pulse (of duration on the order of the plasma-wave period) in the non-one-dimensional case in a substance being ionized and generation of plasma waves by this pulse were discussed in papers [12]. Note that the terms proportional to U_m in the right-hand part of (12) are caused by the ionization current $\mathbf{J}_{\mathrm{ion}}$ and describe the ionization losses of the laser-pulse energy.

A combined consideration of the mixed derivative $\partial^2\mathbf{a}/\partial\xi\partial z$ in the left-hand side of Eq. (12) and the term proportional to Γ_2 in the right-hand side of Eq. (12) allows us to describe the losses of the laser radiation energy associated with the acquirement of the residual energy by electrons. A combined action of these losses on the space-time profile of the pulse causes an increase in the slope of the ionization front of the pulse [16, 19, 23, 35].

3.2. Initial and Boundary Conditions

The system of equations (12)–(16) was solved numerically. We assume that a gas is neutral initially (with the concentration of neutrals n_{at}) and a laser field is absent:

$$n_0^{(0)}(z, \xi = +\infty, r) = n_{at},$$
$$n_0^{(m)}(z, \xi = +\infty, r) = 0, \quad m = 1, \ldots, Z. \tag{17}$$

We will also assume that an incident laser pulse at the gas boundary ($z = 0$) is described by a Gaussian both over the cross section and in time

$$\mathbf{a}(z = 0, \mathbf{r}, \xi) = \mathbf{a}_0 \exp\left[-\frac{r^2}{r_0^2} - \frac{(\xi - \xi_0)^2}{c^2\tau^2}\right], \tag{18}$$

where $\mathbf{r} = x\mathbf{e}_x + y\mathbf{e}_y$ is the radius vector in the direction perpendicular to the z-axis. The characteristic diffraction length (Rayleigh length) of such a pulse is $z_R = \omega_0 r_0^2/2c$, $\xi_0 = \text{const}$. The laser field $\mathbf{E}$ can have an arbitrary polarization, which is determined by the parameter $1 \geq \eta \geq 0$:

$$\mathbf{a}_0 = a_0 \frac{\mathbf{e}_x + i\eta\mathbf{e}_y}{\sqrt{1 + \eta^2}}. \tag{19}$$

A constant a_0 in this expression is related to the initial peak intensity of a laser pulse $I_0 = c\langle\mathbf{E}^2(z = 0, \mathbf{r} = 0, \xi = \xi_0)\rangle/4\pi$ by the expression

$$I_0 = n_c m_e c^3 a_0^2/2, \tag{20}$$

where $n_c = m_e\omega_0^2/4\pi e^2$ is the critical electron density for the frequency ω_0. We also assume that the field $\mathbf{E}$ is linearly polarized ($\eta = 0$). Note that boundary conditions (18)–(20) correspond to the laser-pulse focusing on the gas boundary $z = 0$.

4. PROPAGATION OF A LASER PULSE

We solved Eqs. (12)–(16) describing the dynamics of propagation of a laser pulse in a gas ionized by the pulse and the generation of plasma waves under the conditions of a comparatively low power ($P < P_c$), a comparatively high intensity ($\tau \gg \Omega^{-1}$), and a comparatively large radius ($r_0 \gg K^{-1}$) of the laser pulse. Here, $\Omega = \sqrt{4\pi e^2 n_{0,\max}/m_e}$, $|e|n_{0,\max}$ is the maximum density of the ion charge, and $K = \Omega/c$. For such parameters (low power and large radius), the initial peak intensity I_0 of the pulse can be comparatively low, much lower than the relativistic intensity for a chosen wavelength of the laser. Figure 1 shows the dynamics of propagation of the laser pulse in helium being ionized for the concentration of neutral atoms $n_{at} = 0.35 \times 10^{18}$ cm^{-3}, the initial peak intensity of the pulse $I_0 = 8.55 \times 10^{16}$ W/cm^2, the wavelength $\lambda_0 = 0.8$ μm, the radius $r_0 = 146$ μm, the FWHM duration $\tau_{FWHM} = \sqrt{2\ln 2}\tau = 1.25$ ps, and $\xi_0 K = 75$. Note that I_0 is an order of magnitude lower than the relativistic intensity for the chosen wavelength λ_0. For such parameters, the dimensionless quantities are $P/P_c = 0.67$, $\Omega\tau = 50$, $Kr_0 = 23$. The leading edge of the pulse is subjected to a strong ionization refraction even after a shallow penetration of the pulse into gas ($z \approx 0.1z_R$). The ionization refraction causes an increase in the slope of the temporal intensity profile of the laser pulse, which is shown in Fig. 2 for different propagation paths of the pulse corresponding to Fig. 1. Note that, as the pulses penetrates deeper into the gas, its maximum intensity at the axis $r = 0$ substantially increases (see Figs. 1 and 2).

To explain this effect, we consider the behavior of the laser pulse by excluding from Eq. (12) the influence of the nonlinearity of motion of free electrons. In particular, we exclude the relativistic self-focusing and excitation of a wake plasma wave, by retaining only ionization nonlinearity, which is manifested in (12) through the dependence of the electron density ($n_e = n_0$) on the electric field strength $|\mathbf{a}|$. The latter is caused by the dependence of the ionization probability (14) on $|\mathbf{a}|$. Figure 3 shows the dependences of the maximum intensity $I_{\max}$ of the laser pulse on the axis $r = 0$ on the depth z of the laser pulse penetration into helium for the same initial peak intensity of the pulse and the same wavelength as in Figs. 1 and 2 ($I_0 = 8.55 \times 10^{16}$ W/cm^2, $\lambda_0 = 0.8$ μm) but for different values of the concentration of neutral atoms, the initial radius of the pulse and its duration such that the dimensionless parameters

Concentrations of neutral helium atoms, Rayleigh lengths, and pulse durations used in calculations

n_{at}, 10^{18} cm^{-3}	z_R, mm	τ, ps
8.75	3.4	0.212
2.2	13.5	0.425
0.35	84.2	1.062

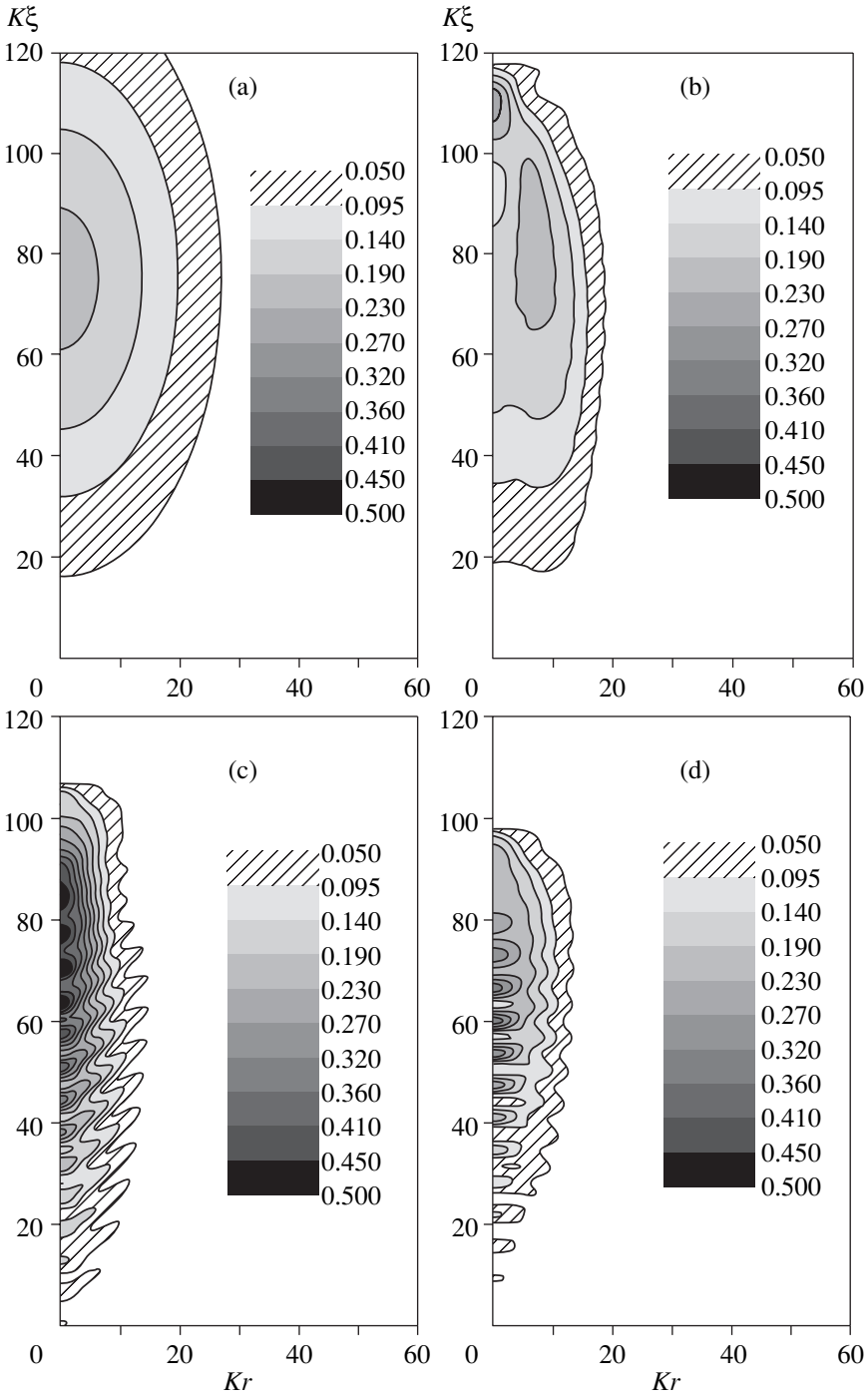

Fig. 1. Distribution of the envelope $|\mathbf{a}|$ of the laser pulse in the Kr–$K\xi$ plane: z = (a) 0, (b) $0.2z_R$, (c) $0.4z_R$, (d) $0.6z_R$.

$\Omega\tau = 50$ and $Kr_0 = 23$ are fixed (see table). The function $I_{max}(z)$ achieves the maximum value for $z_{max} \approx 0.4z_R < z_R$. The dependence of $I_{max}(z)$ for small values of z proves to be oscillating, which corresponds to the development of ionization modulation [16] during the pulse propagation to the matter being ionized.

In the simplest three-dimensional model of ionization modulation [16], the maximum relative deviation ε_{max} of the intensity I on the initial value $I^{(0)}$ in the temporal profile of the laser pulse depends on the penetration depth z as

$$\varepsilon_{max}(z) \equiv \frac{I - I^{(0)}}{I^{(0)}} \approx 0.12\frac{z}{z_R}k_{p,at}^2 r_0^2 \exp\left(-u^{(2)}\frac{z}{z_R}\right), \quad (21)$$

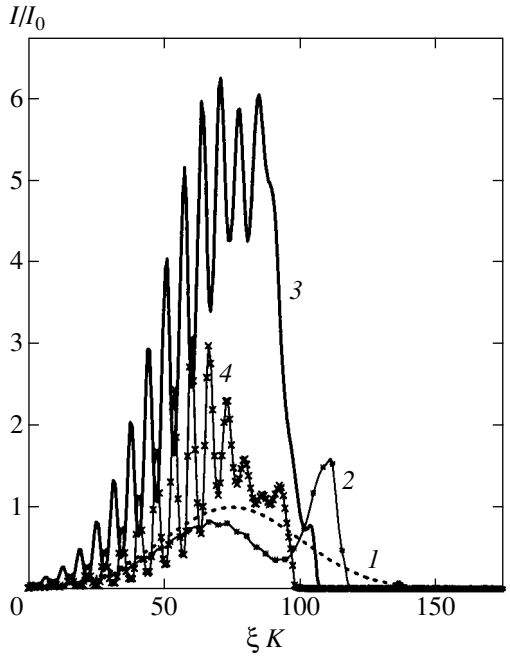

Fig. 2. Temporal profiles of the laser pulse intensity $I(\xi)/I_0$ on the axis $r = 0$ for the different penetration depths of the pulse into helium: (*1*) $z = 0$, (*2*) $0.2z_R$; (*3*) $0.4z_R$, (*4*) $0.6z_R$.

where $u^{(2)} \approx 3.384$, $k_{p,\,at} \approx \sqrt{4\pi e^2 n_{at}/m_e c^2}$. The maximum value ε_{max} of the modulation amplitude is achieved at a distance of $z \approx z_{st} = z_R/u^{(2)} \approx 0.3z_R$ from the boundary where the pulse enters the matter. For the parameters of Fig. 3, a relative increase in the pulse intensity predicted by Eq. (21) is within the limits of the application of (21) and is approximately 3.5. According to Fig. 3, the relative increase is equal approximately to three and is determined, according to (21), by the parameter $k_{p,\,at}r_0$, which is fixed in Fig. 3 when the concentration of neutral atoms and the pulse radius are varied in broad limits. Note that such a great increase in the pulse intensity (which we will call ionization focusing) is possible only for the resonance relationship between the ionization threshold I_m^{th} and the initial peak intensity I_0 [see (20)] of the laser pulse described by the distribution (18) [16]:

$$\frac{I_0}{I_m^{th}} = \exp\left(2\frac{z_{st}}{z_R}u^{(2)}\right) \approx 7.39. \qquad (22)$$

According to the calculations presented in Fig. 3, the maximum ionization threshold for He^+ $I_1^{th} \approx 10^{16}$ W/cm^2 proves to be resonant ($U_1 = 54.4$ eV).

The importance of the fulfillment of resonance condition (22) for the appearance of ionization focusing is demonstrated in Fig. 4, where the results of calculations of $I_{max}(z)$ are presented. The calculations were performed by neglecting the nonlinearity of the free electron motion for the same concentration of neutral atoms $n_{at} = 0.35 \times 10^{18}$ cm^{-3} and the same parameters of laser

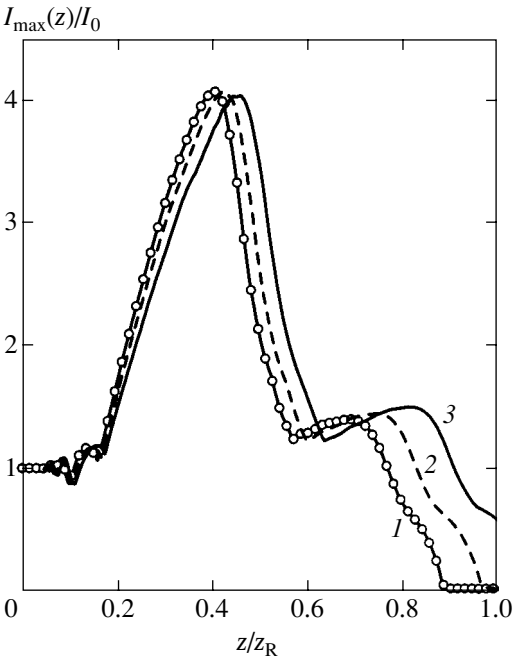

Fig. 3. Dependences of $I_{max}(z)/I_0$ on the penetration depth z/z_R obtained by neglecting the nonlinear motion of free electrons for $Kr_0 = 23$, $\Omega\tau = 50$, and different concentrations of neutral helium atoms: (*1*) 8.75×10^{18}, (*2*) 2.2×10^{18}, and (*3*) 0.35×10^{18} cm^{-3}.

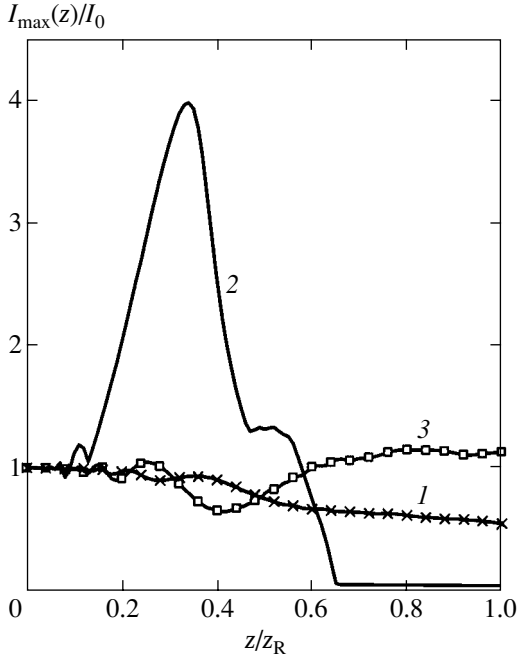

Fig. 4. Dependences $I_{max}(z)/I_0$ obtained by neglecting the nonlinear motion of free electrons for different substances: (*1*) hydrogen (the ionization potential is 13.6 eV); (*2*, *3*) model one-electron atoms with ionization potentials equal to 54.4 eV (singly ionized helium) and 24.58 eV (neutral helium).

radiation as in Figs. 1, 2, and 3 (curves *3*) but for different substances: for hydrogen and model one-electron atoms whose ionization potentials are equal to those of He and He^+. One can easily see that ionization focusing observed in Fig. 3 is distinctly pronounced in Fig. 4 only for atoms with the ionization potential U = 54.5 eV.

In the case of lower ionization potentials, the radius of the plasma structure proves to be substantially greater than the radius r_0. As a result (see Fig. 4), the diffraction spread of the main part of the pulse becomes suppressed upon pulse propagation over a distance exceeding z_R [13]. However, the maximum pulse intensity is comparatively low (when the pulse power is lower than the critical one) and a wake plasma wave is generated less efficiently than upon ionization focusing.

According to (21), at small depths of penetration of the laser pulse into gas, the amplitude of ionization modulation quadratically depends on the parameter $k_{p,at}r_0$, so that, by neglecting the nonlinearity of the free electron motion, the amplitude increases with increasing radius r_0 (the gas density being constant). This is illustrated in Fig. 5, in which the initial peak pulse intensity is $I_0 = 8.55 \times 10^{16}$ W/cm^2, the wavelength λ_0 = 0.8 μm, and the initial concentration of helium atoms is $n_{at} = 0.35 \times 10^{18}$ cm^{-3}. The maximum $I_{max}(z)$ of the function increases with increasing Kr_0, the resonance condition (22) and the maximum intensity observed upon ionization focusing (21) being independent of the laser pulse duration in a broad range, which is illustrated by curves *4* and *5* in Fig. 5 plotted for a pulse duration of τ_{FWHM} = 1.25 ps and 125 fs, respectively.

Returning to the complete system of equations (12)–(16), which takes the nonlinearity of the free electron motion into account, note that the ratio of the power P of laser radiation to the critical power P_c for relativistic self-focusing $P/P_c = |a_0|^2(Kr_0)^2/32$ quadratically depends on Kr_0. For parameters used in Fig. 2, we have P/P_c = 0.67. Because this ratio is close to unity, the intensity of laser radiation additionally increases (due to relativistic self-focusing below the threshold) at the axis compared to the case of only ionization focusing (Fig. 3).

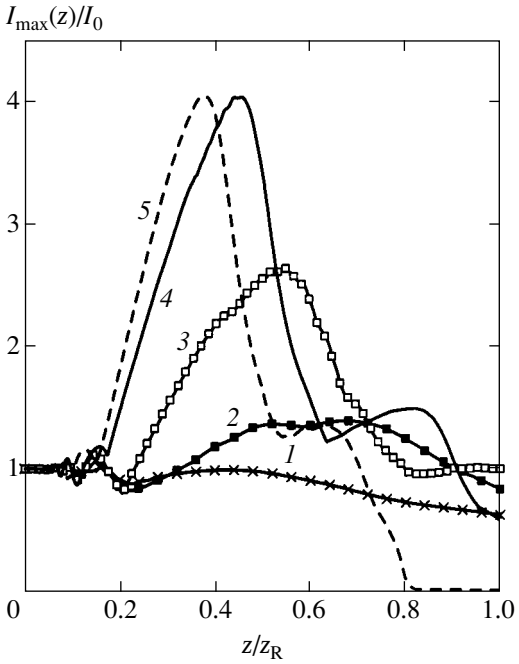

Fig. 5. Dependences $I_{max}(z)/I_0$ obtained by neglecting the nonlinear motion of free electrons for τ_{FWHM} = 1.25 ps (curves *1–4*) and τ_{FWHM} = 0.125 ps (curve *5*) and the dimensionless parameter Kr_0 = 7.1 (*1*), 11.5 (*2*), 17.25 (*3*), 23 (*4*, *5*).

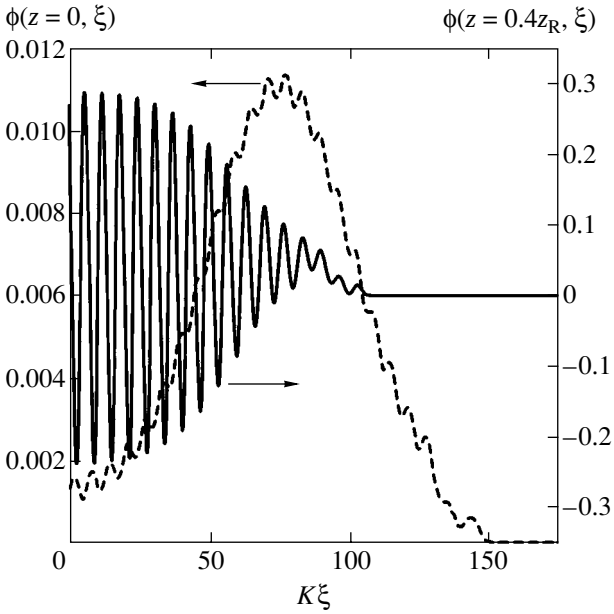

Fig. 6. Dependences of the dimensionless potential $\phi(\xi)$ of the wake wave on the pulse axis r = 0 upon pulse entering into helium (z = 0) (dashed curve) and for $z = 0.4z_R$ (solid curve).

5. GENERATION OF A WAKE PLASMA WAVE

According to [5], in the case of comparatively long pulses ($\tau \gg \Omega^{-1}$), the ionization front is a seed for the efficient generation of a wake plasma wave. The dashed curve in Fig. 6 shows the dependence of the potential $\phi(\xi)$ on the pulse axis r = 0 at the entrance to helium (z = 0). The amplitude of oscillations of the potential ϕ after the pulse propagation is close to that predicted by the theory [5]. Note that for the parameters of gas and laser radiation corresponding to Fig. 6, the amplitude of the wake wave in a preliminary prepared plasma of completely ionized helium proves to be 10^{133} times lower than that shown in Fig. 6.

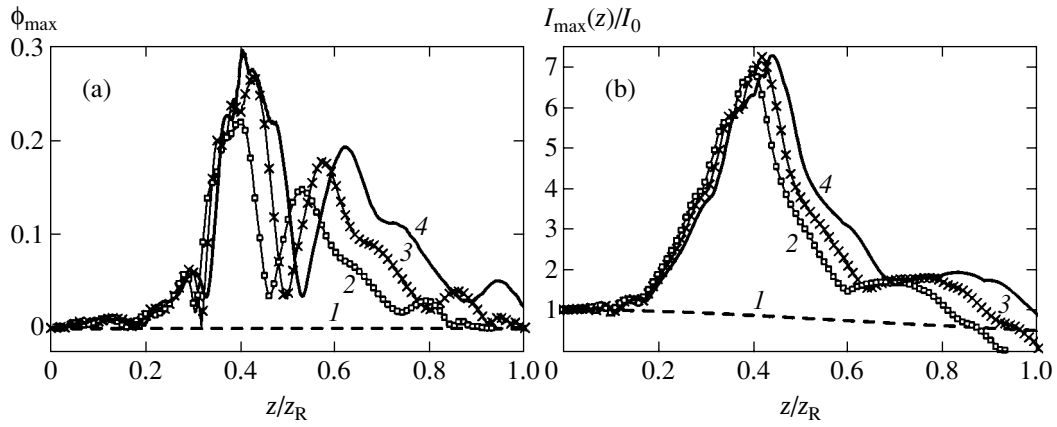

Fig. 7. Dependences of ϕ_{max} (a) and I_{max}/I_0 (b) on z/z_R on the pulse axis for $Kr_0 = 23$ and $\Omega\tau = 50$ and different initial concentrations of helium: (*1*) a preliminary prepared completely ionized plasma for $n_{0,\,max} = 0.7 \times 10^{18}$ cm^{-3}, (*2*) $n_{at} = 8.75 \times 10^{18}$ cm^{-3}, (*3*) $n_{at} = 2.2 \times 10^{18}$ cm^{-3}, (*4*) $n_{at} = 0.35 \times 10^{18}$ cm^{-3}.

As the laser pulse penetrates deeper into the gas, the ionization front on the temporal profile of the pulse shifts to the central, most intense part of the pulse. This is accompanied by an increase in the pulse slope caused by ionization refraction (Figs. 1 and 2), which in turn enhances the generation of a wake plasma wave (see the solid curve in Fig. 6 corresponding to the pulse propagation over the distance $z = 0.4z_R$). As a result, the mechanism of generation of a plasma wave at the leading edge of the pulse changes [21] so that more than 75% of the amplitude of the wake wave is caused by a steep slope of the leading edge of the laser pulse (see the mechanism of generation of a plasma wave [9]), whereas the remaining 25% are produced by the ionization mechanism [5].

The wake plasma wave created in the region of the ionization front is a seed wave for excitation of self-modulation instability [6–8]. Due to the development of the instability, the temporal profile of the laser pulse proves to be modulated with a period equal to the plasma-wave period (see Figs. 1 and 2). In turn, when the laser-pulse duration is long enough, the amplitude of a wake plasma wave after the pulse propagation at the fixed spatial point z substantially increases compared to its seed level in the region of the ionization front (see the solid curve in Fig. 6).

Consider the generation of a plasma wave in the regime of self-modulation of the laser pulse for the same fixed dimensionless parameters of the pulse as in Figs. 1 and 2 ($a_0 = 0.2$, $P/P_c = 0.67$, $\Omega\tau = 50$, $Kr_0 = 23$), but for different values of gas density (see table). Figure 7a demonstrates the increase in the maximum amplitude of the potential of the plasma wave (together with the increase in the amplitude of laser pulse modulation, see Fig. 2) during the penetration of the laser pulse into the helium being ionized. Figure 7b shows the evolution of the maximum of the laser-field intensity with penetration depth z. One can easily see that a great increase in the amplitude of the potential of the plasma wave is caused by the ionization focusing of the laser field (cf. Figs. 7a and 7b).

A comparison of Figs. 7 and 3 shows that ionization focusing is accompanied be relativistic and ponderomotive self-focusing because the consideration of the nonlinearity of the free-electron motion (Fig. 7) results in the additional increase in the intensity of the pulse being focused on the axis $r = 0$. In addition, it follows

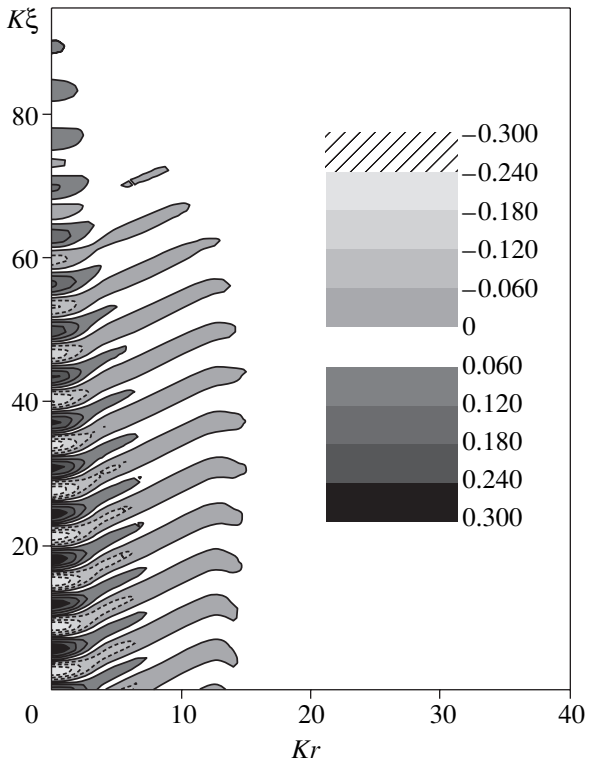

Fig. 8. Distribution of the potential ϕ of the wake wave in the Kr–$K\xi$ plane for $z = 0.4z_R$.

from Fig. 7 that, for the parameter Kr_0 being fixed, the length z/z_R of the region where ϕ_{max} is comparatively large increases with decreasing ratio $n_{0,\,max}/n_c$. A comparison of Figs. 7 and 3 shows that this effect is mainly caused by the influence of ionization processes on the laser-pulse propagation.

The space–time structure of the potential ϕ of the plasma wave for the penetration depth $z = 0.4z_R$ of the laser pulse into helium is shown in Fig. 8. According to Fig. 7, the amplitude of plasma oscillations once the pulse propagated the distance close to $z = 0.4z_R$ proves to be maximum. In this case, the structure of the wake field is regular, with the characteristic transverse scale on the order of the plasma wavelength.

Note that (see Fig. 7), when the penetration depth z is normalized to the Rayleigh depth z_R, the distribution $\phi_{max}(r = 0, z)$ over the penetration depth weakly depends on the initial gas density n_{at}, the dimensionless parameters $\Omega\tau$ and Kr_0 being constant. The constant value of the latter parameter means that the Rayleigh lengths for the three different distributions $\phi_{max}(r = 0, z)$ shown in Fig. 7 are substantially different (see table) and, therefore, the propagation lengths of the laser pulse at which the wake wave is generated are also different.

6. CONCLUSIONS

Taking into account a high efficiency of the generation of a high-amplitude wake wave during the development of the self-modulation instability of an intense laser pulse [6–8], we considered pulses with durations substantially exceeding the period of the plasma wave and lying in the picosecond range (see table). Under such conditions, the generation of a wake wave upon the interaction of an intense laser pulse with a gas ionized by the pulse is mainly determined by spatially inhomogeneous dynamic plasma structures produced during ionization. In particular, a small radius of the plasma structures produced upon ionization of the gas by the leading edge of the laser pulse leads to a rapid diffraction of this part of the pulse. The main part of the pulse is subjected to ionization modulation [16], as well as to the relativistic and ponderomotive self-focusing below the threshold. As a result, the maximum intensity of the pulse increases (almost by an order of magnitude) at a comparatively small penetration depth, and a region with a very steel slope appears in the temporal profile of the pulse. It is these factors that lead to the efficient generation of a seed wake wave at the leading steep edge of the laser pulse and to the subsequent amplification of the wave in the main, most intense part of the pulse. A strong laser field produced due to ionization focusing leads to a strong electric field of the plasma wave and, hence, to a great maximum energy of electrons (on the order of 1 GeV), which can be accelerated by the wake plasma wave.

ACKNOWLEDGMENTS

This work was partially supported by the Russian Foundation for Basic Research (project no. 01-02-16723).

REFERENCES

1. E. Esarey, P. Sprangle, J. Krall, *et al.*, IEEE Trans. Plasma Sci. **24**, 252 (1996).
2. N. E. Andreev and L. M. Gorbunov, Usp. Fiz. Nauk **169**, 1 (1999).
3. L. M. Gorbunov and V. I. Kirsanov, Zh. Éksp. Teor. Fiz. **93**, 509 (1987) [Sov. Phys. JETP **66**, 290 (1987)].
4. P. Sprangle, E. Esarey, A. Ting, *et al.*, Appl. Phys. Lett. **53**, 2146 (1988).
5. N. E. Andreev, M. V. Chegotov, and M. E. Veisman, IEEE Trans. Plasma Sci. **28**, 1098 (2000); N. E. Andreev, M. E. Veĭsman, M. G. Cadjan, and M. V. Chegotov, Fiz. Plazmy (Moscow) **26**, 1010 (2000) [Plasma Phys. Rep. **26**, 947 (2000)].
6. N. E. Andreev, L. M. Gorbunov, V. I. Kirsanov, *et al.*, Pis'ma Zh. Éksp. Teor. Fiz. **55**, 550 (1992) [JETP Lett. **55**, 571 (1992)].
7. T. M. Antonsen and P. Mora, Phys. Rev. Lett. **69**, 2204 (1992).
8. J. Krall, A. Ting, E. Esarey, *et al.*, Phys. Rev. E **48**, 2157 (1993).
9. N. E. Andreev, V. I. Kirsanov, A. S. Sakharov, *et al.*, Phys. Plasmas **3**, 3121 (1996).
10. W. P. Leemans, C. E. Clayton, W. B. Mori, *et al.*, Phys. Rev. A **46**, 1091 (1992).
11. V. Malka, E. De Wispelaere, J. R. Marques, *et al.*, Phys. Plasmas **3**, 1682 (1996).
12. N. E. Andreev, M. V. Chegotov, M. C. Downer, *et al.*, IEEE Trans. Plasma Sci. **28**, 1090 (2000); N. E. Andreev, Y. Nishida, and N. Yugami, Phys. Rev. E **65**, 056407 (2002).
13. V. B. Gildenburg, M. D. Chernobrovtseva, A. V. Kim, *et al.*, in *Proceedings of the International Conference on LASERS'97, New Orleans, LA*, Ed. by J. J. Carroll and T. A. Goldman (1997), p. 853; V. B. Gildenburg, M. D. Chernobrovtseva, A. V. Kim, *et al.*, Laser Part. Beams **17**, 129 (1999).
14. Z. Najmudin, A. E. Dangor, A. Modena, *et al.*, IEEE Trans. Plasma Sci. **28**, 1057 (2000).
15. N. E. Andreev, L. M. Gorbunov, V. I. Kirsanov, *et al.*, Phys. Plasmas **4**, 1145 (1997); N. E. Andreev, L. M. Gorbunov, and A. A. Frolov, Fiz. Plazmy (Moscow) **24**, 888 (1998) [Plasma Phys. Rep. **24**, 825 (1998)].
16. M. V. Chegotov, J. Phys. D **35**, 647 (2002); Kvantovaya Élektron. (Moscow) **32**, 19 (2002).
17. P. Sprangle, E. Esarey, and B. Hafizi, Phys. Rev. Lett. **79**, 1046 (1997).
18. P. Sprangle, E. Esarey, and J. Krall, Phys. Rev. E **56**, 5894 (1997).
19. T. M. Antonsen and Z. Bian, Phys. Rev. Lett. **82**, 3617 (1999).
20. P. Sprangle and B. Hafizi, Phys. Plasmas **6**, 1683 (1999).
21. N. E. Andreev, M. V. Chegotov, and A. A. Pogosova, in *Proceedings of the Workshop on 2nd Generation Laser and Plasma Accelerators, Presqu'ile de Giens, France*

(2001), http://icfa.lbl.gov/icfapanel.html, Newsletter, Special Issue: Giens Workshop Proceedings (2001), Contributed Papers.

22. L. V. Keldysh, Zh. Éksp. Teor. Fiz. **47**, 1945 (1964) [Sov. Phys. JETP **20**, 1307 (1964)].
23. M. V. Chegotov, Fiz. Plazmy (Moscow) **26**, 940 (2000) [Plasma Phys. Rep. **26**, 881 (2000)].
24. P. B. Corkum, N. H. Burnett, and F. Brunel, Phys. Rev. Lett. **62**, 1259 (1989).
25. N. B. Delone and V. P. Krainov, J. Opt. Soc. Am. B **8**, 1207 (1991).
26. N. E. Andreev, M. V. Chegotov, M. E. Veĭsman, *et al.*, Pis'ma Zh. Éksp. Teor. Fiz. **68**, 566 (1998) [JETP Lett. **68**, 592 (1998)].
27. P. Mulser, F. Cornolty, and D. Bauer, Phys. Plasmas **5**, 4466 (1998).
28. N. E. Andreev, M. E. Veĭsman, S. P. Goreslavskiĭ, and M. V. Chegotov, Fiz. Plazmy (Moscow) **27**, 296 (2001) [Plasma Phys. Rep. **27**, 278 (2001)].
29. A. M. Perelomov, V. S. Popov, and M. V. Terent'ev, Zh. Éksp. Teor. Fiz. **50**, 1393 (1966) [Sov. Phys. JETP **23**, 924 (1966)].
30. M. V. Ammosov, N. B. Delone, and V. P. Kraĭnov, Zh. Éksp. Teor. Fiz. **91**, 2008 (1986) [Sov. Phys. JETP **64**, 1191 (1986)].
31. E. V. Vanin, M. S. Dauner, A. V. Kim, and A. M. Sergeev, Pis'ma Zh. Éksp. Teor. Fiz. **58**, 964 (1993) [JETP Lett. **58**, 900 (1993)].
32. S. C. Rae and K. Burnett, Phys. Rev. A **46**, 2077 (1992).
33. V. P. Kandidov, O. G. Kosareva, and S. A. Shlenov, Kvantovaya Élektron. (Moscow) **21**, 971 (1994).
34. A. V. Borovskiĭ and A. L. Galkin, Zh. Éksp. Teor. Fiz. **108**, 426 (1995) [JETP **81**, 230 (1995)].
35. M. V. Chegotov, Izv. Ross. Akad. Nauk, Ser. Fiz. **63**, 1088 (1999); Proc. SPIE **3683**, 33 (1999).

Translated by M. Sapozhnikov

Journal of Experimental and Theoretical Physics, Vol. 96, No. 5, 2003, pp. 897–903.
Translated from Zhurnal Éksperimental'noĭ i Teoreticheskoĭ Fiziki, Vol. 123, No. 5, 2003, pp. 1019–1026.

PLASMA, GASES

On the Role of Prepulses during Solid Target Heating by Picosecond Laser Pulses

V. S. Belyaev[a], V. I. Vinogradov[a], A. S. Kurilov[a], A. I. Magunov[b], A. P. Matafonov[a], T. A. Pikuz[b], I. Yu. Skobelev[b,*], and A. Ya. Faenov[b]

[a] *Central Research Institute of Machine Building, Korolev, Moscow oblast, 141070 Russia*
[b] *Center for Spectroscopic Data on Multicharged Ions, VNIIFTRI, Mendeleevo, Moscow oblast, 141570 Russia*
** e-mail: skobelev@orc.ru*

Received October 4, 2002

Abstract—X-ray emission spectra of the plasma created at the surface of magnesium, aluminum, copper, and zinc targets heated by 1-ps laser pulses with a peak power density of up to 10^{16} W/cm^2 were measured. The effect of a picosecond prepulse on the spectra was studied for various power densities and intensity contrasts of the main laser pulse. It is established that the emission spectra of laser plasmas are weakly affected by a change from 10^5 to 10^7 in the main pulse contrast relative to the first prepulse. Variations in the parameters of emission from aluminum and magnesium plasmas were calculated using relative intensities and widths of the resonance lines of H- and He-like ions and their two-electron satellite peaks. *© 2003 MAIK "Nauka/Interperiodica".*

1. INTRODUCTION

In recent years, special attention of researchers has been devoted to the interaction of high-power ultrashort (pico- and femtosecond) laser pulses with solid and gas targets. These investigations provide information on the properties of substances under extremal conditions, on the one hand, and help us to develop new approaches to solving applied problems (such as initiation of nuclear fusion, acceleration of electrons and heavy ions, development of high-intensity X-ray sources for medicine, biology, and lithography, etc.), on the other hand [1–4].

The results of our first experiments with solid targets showed that there is a very important parameter determining the character of interaction between ultrashort laser pulses and substances. This is the laser pulse intensity contrast K defined as the ratio of the main laser pulse power to that of the prepulse:

$$K = P_{\text{pulse}}/P_{\text{prep}}.$$

In particular, it was found that the formation of a superhigh density plasma is possible only using pulses of very high contrast ($K \sim 10^{10}$), whereby the power density of a prepulse is insufficient for the plasma formation and the main pulse energy is absorbed in the solid target proper (see, e.g., [5–9]).

An ultrashort laser pulse is typically preceded by two principal prepulses. The first prepulse has a duration comparable with that of the main pulse and is generated several nanoseconds before this pulse. The second prepulse is situated in the immediate vicinity of the main pulse (being essentially its pedestal) and is several picoseconds to several nanoseconds wide. Both prepulses may influence the parameters of the laser plasma.

We have used high-resolution X-ray spectroscopic techniques to study the plasmas generated by picosecond laser pulses acting upon solid (Mg, Al, Cu, and Zn) targets. The emission spectra of multicharged ions were measured with one-dimensional spatial resolution. Our experiments were aimed primarily at determining the influence of a picosecond prepulse on the emission properties of laser plasmas for the main pulse power contrast varied from 10^5 to 10^7. The parameters of aluminum and magnesium plasmas were determined by modeling relative intensities and widths of the resonance lines of H- and He-like ions and their two-electron satellite peaks in the X-ray emission spectra measured.

2. EXPERIMENTAL

The experiments were performed with a terawatt laser setup of the Neodymium type [10], which generated laser pulses with the following parameters: pulse energy, up to 1 J; laser wavelength, 1.055 μm; pulse duration, 1 ps. The laser radiation was focused on a target to form a spot with a diameter varied from 900 to 100 μm, which corresponded to a laser power density of 10^{14} to 10^{16} W/cm^2.

The laser radiation generated by the Neodymium setup is characterized by the presence of prepulses of two types, with picosecond and nanosecond durations. The former prepulse is related to the multipath charac-

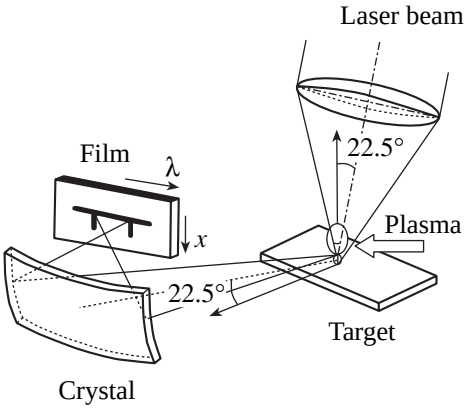

Fig. 1. Schematic diagram of the experimental arrangement.

ter of amplification in the regenerative amplifier and to a finite radiation transmission of the Pockels cell in this amplifier [11]. This prepulse is generated 13 ns before the main pulse and has a duration of 1 ps. The second prepulse results from luminescence amplified in the regenerative amplifier and has a full width at half-maximum (FWHM) equal to 4 ns. Since the energy of the amplified luminescence prepulse, having traveled through the entire amplification tract, does not exceed 0.3 mJ, the intensity contrast of the main laser pulse is $K_{ASE} \sim 10^7$.

Figure 1 shows a schematic diagram of the experimental setup. The laser beam was focused by an optical system onto the flat surface of a solid target (at an incidence angle of 22.5°). The targets represented plates made of Mg, Al, Cu, and Zn. The X-ray emission from laser-generated plasmas was measured using spectrographs of the FSPR type [12–14] based on spherically bent quarts or mica crystals (with a crystal surface curvature radius of R = 150 mm). In all experiments, the emission take-off angle relative to the target surface was 22.5° (Fig. 1). The radiation reflected from the crystal was detected by an X-ray sensitive photographic film of the Kodak-2492 type. The entrance window of a cassette with film was protected from visible and vacuum UV radiation by a two-layer filter representing a 1-μm-thick polypropylene film with aluminum layers deposited on both sides to a total thickness of 0.2 μm.

The X-ray emission spectra of laser plasmas were studied in three overlapping wavelength intervals 0.64–0.74, 0.71–0.78, and 0.75– 0.87 nm. Under the experimental conditions employed, the spectrographs provided a spectral resolution $\lambda/\Delta\lambda$ of not less than 3000 and 5000 in the FSPR-2 and FSPR-1 schemes, respectively. The measurement geometry ensured a one-dimensional spatial resolution in the direction of plasma torch expansion, which allowed the emission spectra of expanding plasma to be measured at various distances from the target surface (as indicated by arrow x in Fig. 1).

Targets made of different materials were studied at various laser pulse power densities and contrasts. The power density was controlled by shifting a target to within Δf = 0–1.8 mm from the focal plane position. The experiments were conducted with two values of the main peak intensity contrast relative to the picosecond prepulse: low ($K = 10^5$) and high ($K = 4 \times 10^7$). The contrast with respect to the amplified luminescence prepulse was the same throughout the experiments ($K_{ASE} \approx 10^7$). We measured the spectra of X-ray emission from multicharged Mg, Al, Cu, and Zn ions. Typical spectra obtained from magnesium and aluminum targets probed by laser pulses of various contrast are presented in Fig. 3.

3. MODELING LASER PLASMA SPECTRUM

The parameters of laser plasmas were determined using X-ray spectral line intensities (integrated with respect to time) at various distances from the target surface. From these data, the laser plasma parameters can be evaluated within the simplest approximation offered by description of the spectrum using a single set of parameters assuming the plasma to be homogeneous in the plane perpendicular to the torch axis (i.e., to the target surface normal). Time evolution of the plasma parameters and spatial inhomogeneity of the plasma can be effectively modeled using several independent sets of parameters with properly selected weights (see, e.g., [15, 16]). Obviously, this would lead to a large number of free parameters upon solving the inverse spectroscopic problem, while not providing more detailed information due to the lack of empirical data. Under these conditions, additional information can be obtained, for example, using the results of hydrodynamic calculations.

In this context, the observed spectrum containing resonance and satellite lines is described by the following expression

$$I(\omega) \propto \omega \sum_{Z,\,n} A^Z_{n1}(\omega, N_e, T_e) N^Z_n(N_e, T_e), \qquad (1)$$

where

$$A^Z_{n1}(\omega, N_e, T_e) = \frac{1 - \exp[-g^Z_n A^Z_{n1} S^Z_{n1}(\omega, N_e, T_e) N^Z_1 L / g^Z_1]}{g^Z_n N^Z_1 / g^Z_1}; \qquad (2)$$

A^Z_{n1} is the probability of the $n \longrightarrow 1$ radiative transition in Z ion; N_e and T_e are the electron density and temperature in the plasma, respectively; N^Z_n and g^Z_n are the population and statistical weight of the nth level of Z ion; and L is the linear dimension of the radiative plasma region. Here, the expression in the numerator of

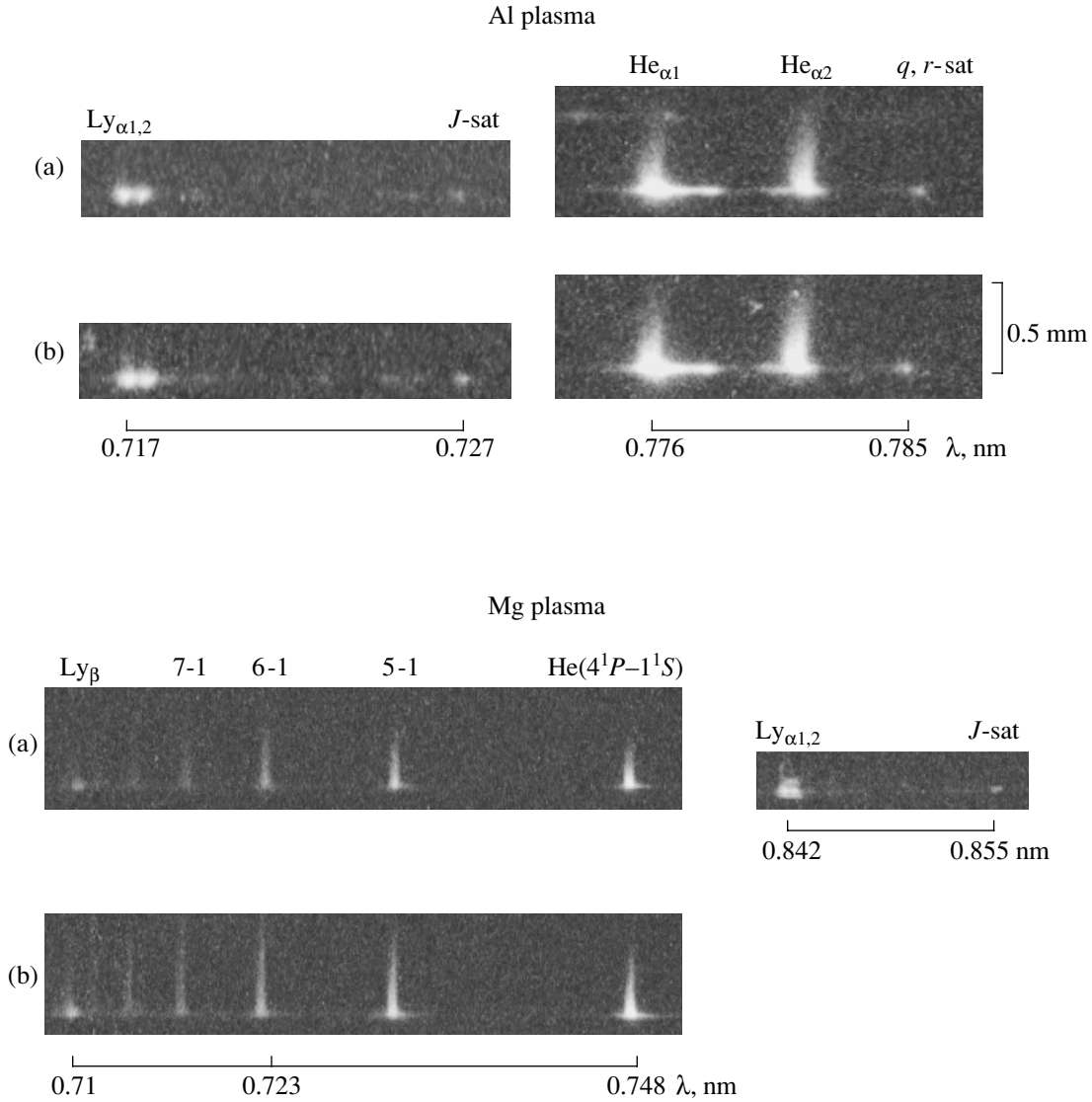

Fig. 2. Typical X-ray emission spectra of magnesium and aluminum plasmas generated at a laser power density of $q_{las} = 10^{16}$ W/cm^2 and different values of the main pulse contrast relative to prepulse: (a) high contrast, $K = 4 \times 10^7$; (b) low contrast, $K = 10^5$.

exponent determines the optical thickness for the corresponding emission line, with the spectral function S^Z_{n1} of an optically thin plasma layer having the form

$$S^Z_{n1}(\omega, N_e, T_e) = \frac{1}{\sqrt{\pi}\gamma^D_{n1}} \sum_{\alpha} b^Z_{n\alpha} \times \int_0^{\infty} V\left(\frac{\omega - \omega^Z_{n1} - \Delta^Z_{n\alpha}\beta}{\gamma^D_{n1}}, \frac{\gamma^Z_{n\alpha 1}}{\gamma^D_{n1}}\right) P_a(Z_i, \beta) d\beta, \quad (3)$$

where

$$b^Z_{n\alpha} = \frac{A^Z_{n\alpha,1}}{g^Z_n A^Z_{n\alpha,1}}$$

is the branching factor for the rate of the radiative transition $n\alpha \longrightarrow 1$ from the αth Stark sublevel; $V(x, y)$ is the Voigt contour possessing the Doppler width $\gamma^D_{n1}(T_i)$ and the collisional width $\gamma^Z_{n\alpha 1}(N_e, T_e)$ [17]; $\Delta^Z_{n\alpha}$ is the linear Stark shift of the αth sublevel in the ion microfield with an average strength of $F_0 = Z_i e/r_0^2$; $r_0 = 0.62 N_i^{-1/3}$ is the average distance between ions; Z_i and N_i are the average ion charge and number density; T_i is the effective ion temperature, taking into account the macroscopic motion of plasma toward the observer; and $P_a(Z_i, \beta)$ is the distribution function of the ion microfield $F = F_0\beta$ taking into account the Debye screening [18], with the parameter $a = r_0/r_D$ determined by the number of ions within a sphere of the Debye screening radius r_D (for $a \ll 1$, P_a converts into the well-

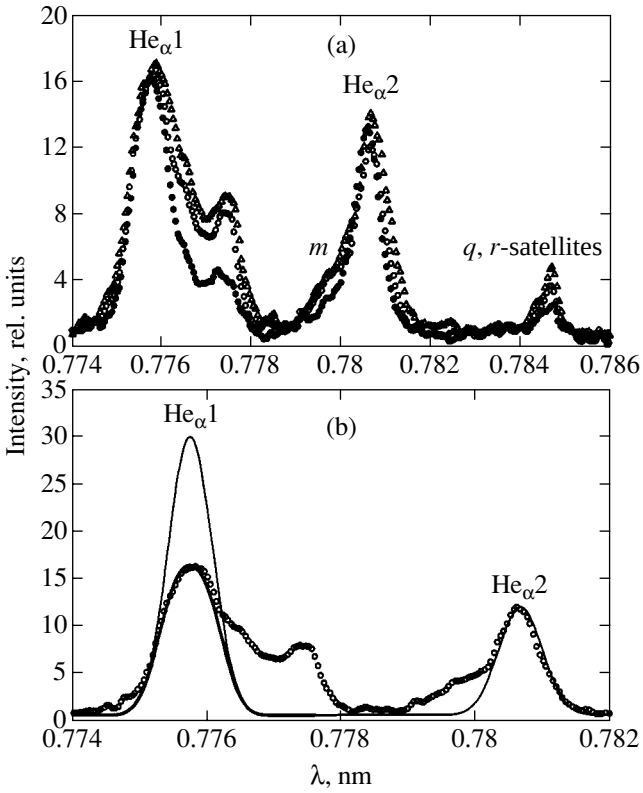

Fig. 3. X-ray emission spectra of aluminum plasma in the region of $He_{\alpha 1,\,2}$ AlXII ion lines and the two-electron satellites: (a) experimental spectra measured at (○) high contrast ($K = 4 \times 10^7$) and (△) low contrast ($K = 10^5$) in the maximum brightness region ($x = 0$), and (●) at high contrast and a distance of $x = 20$ μm from the maximum brightness region; (b) calculated spectra representing Doppler contours for an optically thin plasma (thin solid curve), a thick plasma with optical thickness $\tau = 1.4$ (at the center of the $He_{\alpha 1}$ resonance line) (thick solid line); points show the experimental spectrum for $K = 4 \times 10^7$ and $x = 0$.

known Holtsmark distribution function [19]).

The use of a linear approximation for the Stark shift in Eq. (3) needs justification. For non-hydrogen-like ions, this approximation is valid provided that the Stark splitting is much greater than the electrostatic splitting caused by the interelectron interaction between sublevels with the same principal quantum number n, but smaller that the distance between the adjacent levels n and $n' = n \pm 1$ [20]. For singlet sublevels with $n = 4$ in a He-like magnesium ion studied here, the splitting does not exceed 1 eV (see [21]), whereby the linear approximation is applicable for $N_i > 10^{20}$ cm^{-3}. With increasing n, the electrostatic splitting decreases as n^{-3}, while the Stark shift increases as n^2; for $n = 5$, the limiting ion density is $N_i \approx 2 \times 10^{19}$ cm^{-3}. This value satisfies conditions for which the Stark broadening was calculated, the Stark shift of the ground level being negligibly small. At lower densities, the line width is determined by the Doppler effect.

The populations of levels for Eq. (1) were calculated in a quasistationary approximation for preselected values of the "rough" parameters T_e and N_e [22]. For the spectra containing the lines of ions with different charges, the charge composition was selected using relative intensities of the corresponding lines.

4. RESULTS AND DISCUSSION

The relative intensities of peaks due to the two-electron satellites and resonance lines (Fig. 2) were used to estimate the electron temperature of the plasma. The rates of elementary processes leading to population or decay of the autoionization states were taken from [23]. The calculations were performed using the results of measurements performed for a laser power density of $q = 10^{16}$ W/cm^2 (at a lower intensity, the satellite peaks were not observed).

Given the emission spectra of aluminum plasma, the electron temperature can be determined using relative intensities of the Ly_α line of an H-like AlXIII ion and the corresponding two-electron J-satellite ($2p^2\,{}^1D_2$–$1s2p^1P_1$ transition). This method yields $T_e = 450$ and 400 eV for the region of maximum brightness in the plasma generated by high- and low-contrast laser pulses, respectively. The relative intensities of the q- and r-satellites of a Li-like ion ($1s2s2p[^3P]\ 2P_{3/2}$–$1s^22s^2S_{1/2}$ and $1s2s2p[^3P]^2P_{1/2}$–$1s^22s^2S_{1/2}$ transitions, respectively) and the $He_{\alpha 1}$ resonance line, determined in the region of maximum brightness both with neglect of a finite optical thickness and with a correction for the absorption, yield $T_e = 280$–330 eV. These estimates are somewhat lower than the values obtained from the spectra of an H-like AlXIII ion. The discrepancy can be explained by the fact that the concentrations of H- and He-like aluminum ions and the corresponding intensities reach maximum at different moments of the plasma evolution, the ions with greater ionization potentials naturally dominating at the instants when plasma possesses a higher temperature.

Figure 3a shows the experimental spectra of emission from aluminum plasma in the range of resonance ($He_{\alpha 1}$) and intercombination ($He_{\alpha 2}$) lines of AlXII ion and the corresponding two-electron satellites measured for different laser pulse contrast and various spatial regions of the plasma torch. A comparison of the spectra from two spatial regions spaced by 20 μm reveals a sharp decrease in intensity of the $1s2pnl$–$1s^2nl$ ($n \geq 3$) satellites in the longwave wing of the $He_{\alpha 1}$ line, m-satellite ($1s2p^2\,{}^2S_{1/2}$–$1s^22p^2P_{3/2}$) in the shortwave wing of the $He_{\alpha 2}$ line, and q,r-satellites at a small distance from the target surface. The intensities of resonance and intercombination lines remain almost unchanged. The ratio of widths of the $He_{\alpha 1}$ and $He_{\alpha 2}$ lines shows that it is necessary to take into account the resonance line absorption in an optically dense plasma, since a maxi-

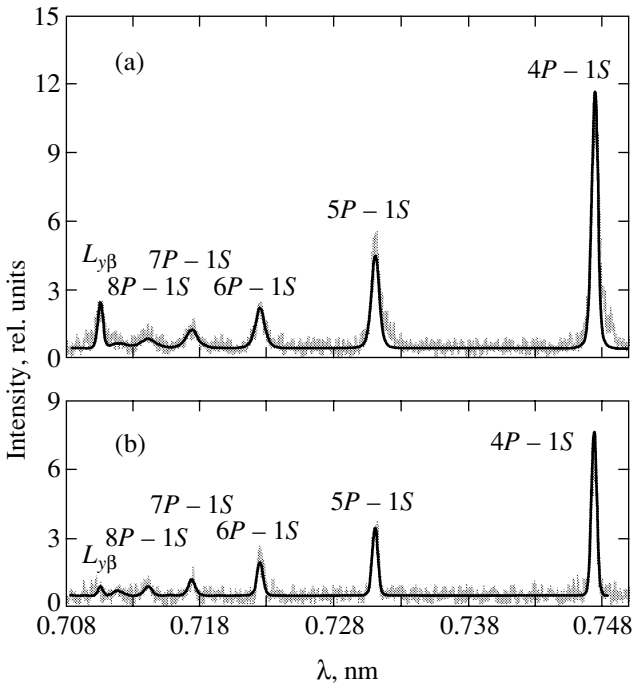

Fig. 4. Experimental (thin curves) and model (calculations by formulas (3) and (7) (thick solid curves) X-ray emission spectra in the region of $1snp$–s^2 (n = 4–9) lines of a He-like MgXI ions generated by high-contrast laser pulses ($K = 4 \times 10^7$) at various distances from the target surface: (a) in the region of maximum brightness (x = 0); calculation for $N_e = 2 \times 10^{20}$ cm^{-3} and T_e = 230 eV; (b) at a distance of x = 80 μm from the region of maximum brightness; calculation for $N_e = 5 \times 10^{19}$ cm^{-3} and T_e = 220 eV.

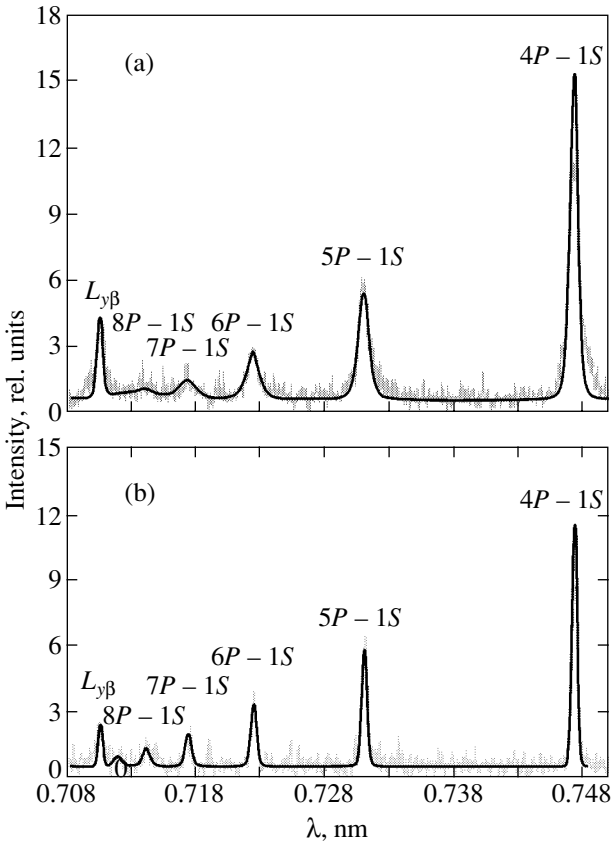

Fig. 5. The same as in Fig. 4, for low-contrast laser pulses ($K = 10^5$): (a) x = 0; calculation for $N_e = 5 \times 10^{20}$ cm^{-3} and T_e = 220 eV; (b) x = 80 μm; calculation for $N_e = 5 \times 10^{19}$ cm^{-3} and T_e = 200 eV.

mum fraction of ions occur in the ground state of a He-like ion.

As can be seen from the results of calculations presented in Fig. 3b, the resonance line intensity for an optically thin plasma would be two times greater than the observed value (for the same line width). An allowance for the optical thickness in expression (2) provides for a perfect fit of the calculated curve to the experimental spectrum (upon subtracting the contribution of satellites with $n \geq 3$). Naturally, the plasma is optically thin for the intercombination line. Here, the measurements at a lower laser pulse contrast yield approximately the same spectrum in the maximum brightness region (Fig. 3a). The optical thickness determined for the radiative plasma region dimensions comparable with the focus spot size yields an electron density of $N_e \approx 10^{20}$ cm^{-3}, which is close to the value calculated using a stationary kinetic model from the relative intensities of the resonance and intercombination lines (with absorption correction).

An analysis of the relative intensities of Ly_α and the J-satellite in the spectrum of magnesium plasma yields the electron temperature $T_e \approx 300$ eV in the maximum brightness region. Similar to the case of an aluminum target, the magnesium plasma with this temperature is optically thin for the Ly_α line of an H-like magnesium ion. By analogy with the aluminum plasma, it can be also expected that the lines of a He-like MgXI ion would yield a lower electron temperature.

Figure 4 and 5 show the results of measurements and calculations of the emission spectra corresponding to transitions from highly excited $1snp\ ^1P$ (n = 4–9) levels of a He-like MgXI ion. The same spectral interval contains the Ly_β line of MgXII ion. The lines with greater n in a dense plasma are broadened, mostly due to the Stark splitting of upper levels in the ion microfield. Therefore, these lines can be used for estimating the electron density. If there is a competition between the channels of recombination population of the upper levels and their excitation from the ground state, the relative intensities of these lines can be also sensitive to the electron temperature. For high-contrast probing pulses, calculations of the line shapes by formulas (1) and (2) yield T_e = 230 eV and $N_e = 2 \times 10^{20}$ cm^{-3} for the region of maximum brightness (Fig. 4a) and T_e = 220 eV and $N_e = 5 \times 10^{19}$ cm^{-3} at a

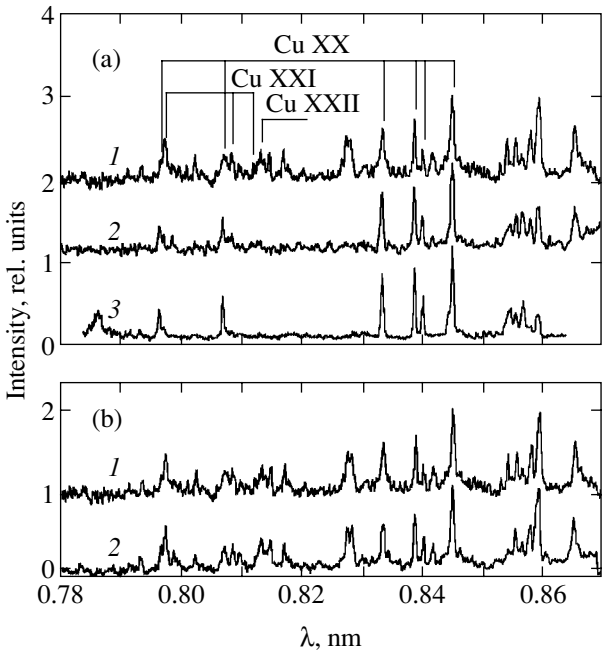

Fig. 6. (a) Experimental X-ray emission spectra of copper plasma measured in the region of 0.78–0.87 nm for laser power densities $q_{las} = 10^{16}$ (*1*) and 10^{14} W/cm^2 (*2*) at a high laser pulse contrast. For the comparison, curve *3* shows the spectra induced by a nanosecond laser pulse with λ_{las} = 1 μm, τ_{las} = 1 ns, and $q_{las} = 10^{14}$ W/cm^2 [25]; (b) the spectra measured at $q_{las} = 10^{16}$ W/cm^2 and high (*1*) and low (*2*) laser pulse contrast.

distance of 80 μm from this region (Fig. 4b). In the latter case, the lines with $n \le 7$ exhibit a Doppler contour with a width corresponding to the effective ion expansion temperature T_i = 1,2 keV, while the electron density corresponds to the Inglis–Teller limit for the line with $n = 9$ [24].

Modeling the results of measurements using low-contrast laser pulses (Fig. 5) leads to a higher electron density ($N_e = 5 \times 10^{20}$ cm^{-3}) and a somewhat lower electron temperature in the region of maximum brightness as compared to the high-contrast case.

The total intensity of lines in the spectrum of a He-like magnesium ion measured using low-contrast laser pulses is 20–30% higher than that for the high-contrast pulses, the difference increasing up to 40–50% for the Ly_β line. This discrepancy can be related to the influence of a preplasma created by the picosecond prepulse in the case of low-contrast laser pulses. At a high contrast, the laser power density in the picosecond prepulse ($q_{prep} < 10^9$ W/cm^2) is insufficient to provide for significant plasma formation. Moreover, even if the plasma were generated, the characteristic hot plasma region with dimensions below 1 mm (see Fig. 2) and a particle velocity on the order of 10^6 cm/s (for $T_i^{eff} \sim 10$ eV) would decay before arrival of the main laser pulse. In this case, the preplasma generated by a nanosecond prepulse would be more significantly manifested (for the same laser power density). During the low-contrast probing, the main pulses are absorbed in the preplasma. Under these conditions, the contribution of hot electrons to the line emission from multicharged ions at a low temperature of thermal electrons increases, similarly to the case of cluster targets ionized by femtosecond pulses [25]. A small effect of the preplasma induced by picosecond prepulses observed in our experiments is most probably explained by the effective decay of this plasma before arrival of the main pulses, which takes place even for a contrast of $K = 10^5$.

Figure 6 presents the emission spectra of copper plasma measured in a wavelength interval of 0.78–0.87 nm. This interval contains the transition $2s2p^64p$–$2s^22p^6$ and $2s^22p^5nd$–$2s^22p^6$ (n = 5, 6) of a Ne-like CuXX ion and the analogous (i.e., 4–5, 5–2, and 6–2) transitions in ions of higher multiplicity: F-like CuXXI and O-like CuXXII [26]. The results of our measurements show evidence of a strong dependence of the emission spectrum on the laser power density (Fig. 6a). For a higher laser power and, hence, a higher plasma temperature, the emission spectrum (especially in the shortwave part) contains a large number of additional lines, including those due to the ions of higher multiplicity (CuXXI and CuXXII). Note that these lines are also present in the spectra of a plasma generated by nanosecond pulses at $q < 10^{14}$ W/cm^2 (Fig. 6a, curve *3*) [27]. For a high laser power density in the picosecond pulse, the emission spectrum of copper plasma in the interval from 0.78 to 0.87 nm is virtually independent of the contrast (Fig. 6b). This conclusion is valid at low laser power densities as well.

Thus, in the laser power density range studied, the emission spectra of copper plasma are independent of the main laser pulse contrast relative to the picosecond prepulse. Analogous conclusions follow from an analysis of the emission spectra of a zinc plasma. These spectra are also characterized by the lack of dependence on the contrast of the laser pulse and exhibit enrichment with the lines of high-multiplicity ions on increasing the laser power. At low laser power densities, the emission spectrum becomes analogous to that of the plasma generated by nanosecond pulses.

5. CONCLUSIONS

We have experimentally studied the plasma formed during the interaction of a picosecond laser pulse with a power density of up to 10^{16} W/cm^2 with solid targets. It is established that a picosecond prepulse produces no significant influence upon the emissive properties and parameters of the laser plasma at a main pulse contrast of 10^5–10^7. The laser plasma parameters determined from the X-ray emission measurements are determined predominantly by the main pulse and, probably, by the second (nanosecond) prepulse related to amplified

luminescence. The action of a nanosecond prepulse can explain the absence of spectral manifestations of a plasma with the density exceeding a critical level. In addition, this prepulse reduces the time-average plasma temperature. It should be noted that identification of the emission spectra of multielectron copper and zinc ions (O- and F-like ions with open *L*-shells) requires additional precise calculations of the corresponding atomic structures. Such calculations, in addition to providing a basis for the interpretation of emission spectra, could be used for the plasma diagnostics.

ACKNOWLEDGMENTS

The work was supported in part by the International Scientific-Technological Center (project no. 2155), INTAS Foundation (grant no. 01-0233), and by the US Civilian Research and Development Foundation for Independent States of the Former Soviet Union (CRDF Award No. RP1-2328-ME-02).

REFERENCES

1. T. Ditmire, T. Donnelly, A. M. Rubenchik, *et al.*, Phys. Rev. A **53**, 3379 (1996).
2. P. Gibbon and E. Forster, Plasma Phys. Controlled Fusion **38**, 769 (1996).
3. T. Ditmire, J. Zweiback, V. P. Yanovsky, *et al.*, Nature **398**, 490 (1999).
4. J. Zweiback, R. A. Smith, T. E. Cowan, *et al.*, Phys. Rev. Lett. **84**, 2634 (2000).
5. A. Ya. Faenov, J. Abdallah, Jr., R. E. H. Clark, *et al.*, Proc. SPIE **3157**, 10 (1997).
6. A. M. Urnov, J. Dubau, A. Ya. Faenov, *et al.*, Pis'ma Zh. Éksp. Teor. Fiz. **67**, 513 (1998) [JETP Lett. **67**, 489 (1998)].
7. A. Ya. Faenov, A. I. Magunov, T. A. Pikuz, *et al.*, Phys. Scr. **80**, 536 (1999).
8. A. Maksimchuk, M. Nantel, G. Ma, *et al.*, J. Quant. Spectrosc. Radiat. Transf. **65**, 367 (2000).
9. F. B. Rosmej, U. N. Funk, M. Gessel, *et al.*, J. Quant. Spectrosc. Radiat. Transf. **65**, 477 (2000).
10. V. S. Belyaev, V. I. Vinogradov, A. S. Kurilov, *et al.*, in *Collection of Scientific Works* (Tsentr. Nauchno–Issled. Inst. Mashinostr., Moscow, 2002), p. 34.
11. V. S. Belyaev, V. I. Vinogradov, A. S. Kurilov, *et al.*, Kvantovaya Élektron. (Moscow) **30**, 229 (2000).
12. T. A. Pikuz, A. Ya. Faenov, S. A. Pikuz, *et al.*, J. X-ray Sci. Technol. **5**, 323 (1995).
13. I. Yu. Skobelev, A. Ya. Faenov, B. A. Bryunetkin, *et al.*, Zh. Éksp. Teor. Fiz. **108**, 1263 (1995) [JETP **81**, 692 (1995)].
14. B. K. F. Young, A. L. Osterheld, D. F. Price, *et al.*, Rev. Sci. Instrum. **69**, 4049 (1998).
15. A. I. Magunov, I. Yu. Skobelev, A. Ya. Faenov, *et al.*, Zh. Éksp. Teor. Fiz. **108**, 1625 (1995) [JETP **81**, 891 (1995)].
16. A. I. Magunov, A. Ya. Faenov, I. Yu. Skobelev, *et al.*, Laser Part. Beams **16**, 61 (1998).
17. H. R. Griem, *Spectral Line Broadening by Plasmas* (Academic, New York, 1974; Mir, Moscow, 1978).
18. R. J. Tighe and C. F. Hooper, Jr., Phys. Rev. A **14**, 1514 (1976).
19. J. Holtsmark, Ann. Phys. (Leipzig) **58**, 577 (1919).
20. H. A. Bethe and E. E. Salpeter, *Quantum Mechanics of One- and Two-Electron Atoms* (Plenum/Rosetta, New York, 1977), p. 245.
21. V. A. Boĭko, V. G. Pal'chikov, I. Yu. Skobelev, and A. Ya. Faenov, *Spectroscopic Constants of Atoms and Ions (Spectra of Atoms with One and Two Electrons): Reference Data* (Izd. Standartov, Moscow, 1988).
22. L. I. Gudzenko and S. I. Yakovlenko, *Plasma Lasers* (Atomizdat, Moscow, 1978).
23. U. I. Safronova, A. M. Urnov, and L. A. Vainshtein, Preprint No. 212, FIAN SSSR (Physical Institute, USSR Academy of Sciences, 1978).
24. D. R. Inglis and E. Teller, Astrophys. J. **90**, 439 (1939).
25. T. Auguste, P. D'Oliveĭa, S. Hulin, *et al.*, Pis'ma Zh. Éksp. Teor. Fiz. **72**, 54 (2000) [JETP Lett. **72**, 38 (2000)].
26. V. A. Boĭko, V. G. Pal'chikov, I. Yu. Skobelev, and A. Ya. Faenov, *X-ray Spectroscopy of Multi-charge Ions* (Énergoatomizdat, Moscow, 1988).
27. K. B. Fournier, A. Ya. Faenov, H.-K. Chung, *et al.*, J. Phys. B (in press).

Translated by P. Pozdeev

Journal of Experimental and Theoretical Physics, Vol. 96, No. 5, 2003, pp. 904–914.
Translated from Zhurnal Éksperimental'noĭ i Teoreticheskoĭ Fiziki, Vol. 123, No. 5, 2003, pp. 1027–1039.

PLASMA, GASES

Ponderomotive Effects in Intense Pumping Wave Action on Electron and Plasma Bunches

N. S. Ginzburg*, A. M. Malkin, and A. S. Sergeev

Institute of Applied Physics, Russian Academy of Sciences, ul. Ul'yanova 46, Nizhni Novgorod, 603600 Russia

**e-mail: ginzburg@appl.sci-nnov.ru*

Received July 19, 2002

Abstract—Ponderomotive effects that arise when an intense plane pumping wave acts on low-concentration electron and plasma bunches are theoretically studied within the framework of a one-dimensional model. Using the Lagrange variables, an electron (plasma) bunch under the action of a pumping field can be represented as a gas comprising macroparticles with ponderomotive and Coulomb interactions. The ponderomotive force at small interparticle distances is attractive, that is, directed oppositely to the Coulomb force; it cannot, however, completely balance the latter. The constructed model is used to study superradiance, which arises when an intense pumping wave acts on an extended electron bunch. Radiation is then scattered in the form of narrow pulses whose amplitude is proportional to the total number of particles in the bunch. In addition, we describe acceleration of a neutral plasma layer, narrow on the wavelength scale, in the field of an intense wave and radiation field-induced partial contraction of an electron bunch with an incompletely compensated charge. *© 2003 MAIK "Nauka/Interperiodica".*

1. INTRODUCTION

In recent years, much attention has been given to theoretical studies of the generation of superradiance pulses by ensembles of classical electrons [1–9]. This process is coherent electromagnetic pulse emission by an extended electron bunch as a result of an increase in electron clustering, which ensures synphase emission from different regions of the bunch at a certain instant of time. Experiments with the generation of ultranarrow subnanosecond superradiance pulses are described in [10–14] for the principal stimulated emission mechanisms, including the cyclotron, Cherenkov, and undulator mechanisms. The experiments were performed in the millimeter wavelength range, where the peak intensity of pulses reached 150 MW. Also note experiments on the generation of pulsed millimeter radiation in a so-called parametric free-electron laser [15] which uses passage of microtron-formed electron bunches short on the wavelength scale through an undulator field. A theoretical analysis of such generators was given in [16]. Of interest as a development of these studies is an analysis of the generation of ultranarrow superradiance pulses in forced Compton scattering of a high-power pumping wave by a counterpropagating electron bunch. At relativistic electron velocities, the frequency of scattered radiation should considerably exceed the pumping wave frequency because of the Doppler effect. This mechanism, in particular, offers a possibility of generating submillimeter radiation pulses.

In this work, we theoretically analyze superradiance that arises in stimulated scattering. The analysis is performed in terms of the one-dimensional model that considers an electron bunch in the form of a plane layer of a finite thickness acted upon by a plane monochromatic pumping wave. The width of the electron bunch is assumed to be large compared with the wavelength of pumping. The action of pumping wave and scattered radiation ponderomotive forces is shown to cause longitudinal electron bunching. As a result, a high-power narrow pulse is coherently emitted in the direction of translational motion of particles at a certain instant of time. The amplitude of the pulse is proportional to the total number of particles in the bunch.

In addition, the model is used to study ponderomotive effects arising when an intense electromagnetic wave acts on electron bunches that are short on the wavelength scale and on neutral plasma bunches. The most important effect for a neutral plasma bunch is the acceleration of the entire bunch caused by radiation field reaction. The acceleration of a plasma bunch is considered using both microscopic and macroscopic (phenomenological) models. Both approaches give coinciding results for the rate of acceleration and, in turn, agree with the results obtained in [17–19] for the theory of radiative acceleration of plasma bunches. An interesting effect for an electron bunch with an incompletely compensated volume charge is its focusing under the action radiation fields. This action prevents bunch expansion caused by volume charge forces. Of the greatest interest is the situation when electrons moving in a periodic magnetic field (undulator field) become involved in oscillatory motion.

1063-7761/03/9605-0904$24.00

2. THE MODEL AND BASIC EQUATIONS

Consider a model of an electron bunch in the form of an initially uniform layer of thickness b which moves in the direction of axis z and is acted upon by a circularly polarized pumping wave. In the frame of reference moving with the bunch, in which the translational velocity of the electrons at the initial time is zero, the pumping wave is given by the vector potential

$$\mathbf{A}_i(z, t) = \mathrm{Re}(\boldsymbol{\xi} A_i \exp(i\omega t + ihz)), \quad (1)$$

where $\boldsymbol{\xi} = \mathbf{x}_0 + i\mathbf{y}_0$; $\mathbf{x}_0$ and $\mathbf{y}_0$ are the transverse unit vectors; and ω and h are the frequency and wave number, which can generally disobey the dispersion law for the propagation of electromagnetic waves in the vacuum. This reservation is made to include the situation when the pumping field is a periodic magnetic field created by an undulator. This field in the moving frame of reference transforms into an electromagnetic wave field with a dispersion law different from that in the vacuum.

In the one-dimensional model, in which a bunch is infinite in the transverse direction, it can be represented as a set of N charged planes, or macroelectrons, with the surface charge density $\sigma = e\rho b/N$, where ρ is the volume layer density. These macroelectrons oscillate in the pumping field and emit (in the moving frame of reference) waves in the $\pm z$ directions whose frequency coincides with the pumping wave frequency, but whose wave vectors $k = \omega/c$ generally differ from the wave vector h of the pumping field. The total combined action on a particle of the pumping field and the fields of the waves scattered by other particles results in the arising of a longitudinal ponderomotive force. This force should shift particles in the longitudinal direction and, eventually, cause layer bunching. In addition, Coulomb repulsion forces act between particles.

Let us find the ponderomotive interaction force between two planes (nth and lth) oscillating in the pumping wave field on the assumption that the scattered wave amplitude is much smaller than the amplitude of the pumping wave. We can then assume that the nth plane only oscillates in the pumping field, and the presence of transverse magnetic field in the radiation scattered by the lth plane results in the arising of a longitudinal Lorentz force, that is, a ponderomotive force, that acts on the nth plane. In response, the nth plane also acts on the lth one. The condition of scattered field smallness will be shown to reduce to the condition of plasma frequency smallness compared with the pumping frequency, that is, to the condition of a low bunch density. In addition, at this stage of constructing the model, we ignore delay; that is, we assume that the average ponderomotive force at a given instant of time depends on the mutual arrangement of the planes at the same instant. The neglect of delay means that the characteristic times of all longitudinal displacements of particles are long compared with the b/c time of radiation propagation along the electron layer.

First, let us find the field of the wave scattered by a plane, or a macroelectron, situated at the point z_n. When motion occurs in a field independent of transverse coordinates, the transverse canonical momentum of the electron is conserved,

$$\mathbf{P} = \mathbf{p}_\perp - \frac{e}{c}\mathbf{A} = \text{const}. \quad (2)$$

Here, $\mathbf{p}_\perp = m\mathbf{v}_\perp$ is the transverse mechanical momentum, $\mathbf{v}_\perp$ is the transverse velocity, m is the mass of the electron, e is its charge, and $\gamma = (1 - v_\perp^2/c^2)^{-1/2}$ is the transverse relativistic mass factor. If we assume that the transverse velocity of electrons is zero at the initial time in the absence of a pumping field, the constant in (2) is zero. Equation (2) then gives $\mathbf{v}_\perp = e\mathbf{A}/m\gamma c$. For the circularly polarized monochromatic wave (1), $\mathbf{v}_\perp = \mathrm{Re}(\boldsymbol{\xi} v_+ \exp(i\omega t))$. Substituting this value into the preceding expression gives the amplitude of oscillations of the nth macroelectron in the form

$$v_+(z_n) = \frac{c\alpha_i \exp(ihz_n)}{\gamma}, \quad z = \sqrt{1 + \alpha_i^2}, \quad (3)$$

where $\alpha_i = eA_i/mc^2$ is the dimensionless field amplitude. Importantly, at high wave intensities, these equations are only valid for a circularly polarized wave. In a linearly polarized field, the energy of the electron depends on time, and the corresponding equations have a much more complex form [20].

At the point z_n, the oscillating plane emits (actually, scatters) plane waves of equal amplitudes in both directions. These plane waves can be written as

$$A_s(z, t) = \mathrm{Re}(\boldsymbol{\xi} A_s(z_n) \exp(i\omega t - ik|z - z_n|)).$$

The amplitude of the A_s vector potential of the scattered wave field can be found from the boundary condition that describes the magnetic field jump on the surface current $\mathbf{j} = \sigma\mathbf{v}$ created by the plane situated in the $z = z_n$ section,

$$\mathbf{H}(z = z_n + 0) - \mathbf{H}(z = z_n - 0) = \frac{4\pi}{c}\mathbf{j}(z = z_n).$$

Expressing the magnetic field through the vector potential gives

$$A_s(z_n) = \frac{2\pi}{ikc}\sigma v_+ = \frac{2\pi}{ik}\sigma\frac{\alpha_i \exp(ihz_n)}{\gamma}. \quad (4)$$

Taking into account relations (2) and (3) for the average ponderomotive force that acts on an electron in a strong field with circular polarization

$$\mathbf{A}(z, t) = \mathrm{Re}(\boldsymbol{\xi} A(z) \exp(i\omega t)),$$

we obtain [21]

$$\frac{dp_z}{dt} = F_{\text{pond}} = -\frac{e^2}{2m\gamma c^2}\frac{\partial}{\partial z}|A(z)|^2, \quad (5)$$

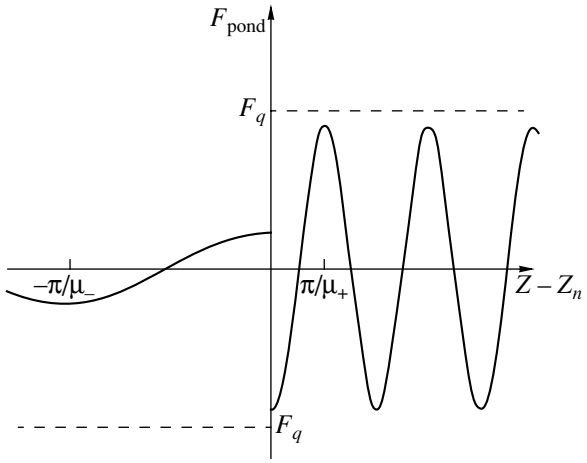

Fig. 1. Longitudinal coordinate dependence of the ponderomotive force with which one macroelectron acts on the others. Dashed lines are Coulomb repulsion forces.

where $\gamma = (1 + |\alpha|^2)^{1/2}$. If the field is a combination of two waves with equal frequencies and different wave vectors,

$$A(z, t) = A_1 \exp(ik_1 z) + A_2 \exp(ik_2 z),$$

(5) gives

$$\frac{dp_z}{dt} = -\frac{e^2}{m\gamma c^2} \times \mathrm{Re}\{i(k_1 - k_2)A_1 A_2^* \exp[i(k_1 - k_2)z]\}. \quad (6)$$

To determine the ponderomotive force that acts in the problem under consideration on the *n*th macroelectron from the *l*th one (it is assumed that $z_n > z_l$), we make the substitutions $k_1 = h$, $A_1 = A_i \exp(ihz_n)$, $k_2 = -k$, and $A_2 = A_s \exp(ihz_l)$. Taking A_i to be real, assuming that $|A_s| \ll |A_i|$, and using (4) and (6), we obtain

$$F_{\text{pond}}(z_n) = 2\pi e\sigma \frac{\alpha_i^2}{1 + \alpha_i^2}(k + h) \times \cos((k + h)(z_n - z_l)). \quad (7a)$$

Similarly, after changing the sign of the wave vector *k*, we obtain the force with which the right (*n*th) electron acts on the left (*l*th) one,

$$F_{\text{pond}}(z_l) = -2\pi e\sigma \frac{\alpha_i^2}{1 + \alpha_i^2}(k - h) \times \cos((k - h)(z_n - z_l)). \quad (7b)$$

Interestingly, the interparticle interaction described by (7) formally does not satisfy the third Newton law. Indeed, part of the longitudinal momentum is carried away by scattered waves. As a result, forces that act between two planes are not equal. The Coulomb forces between these planes are equal and only differ in sign,

$$F_q = (z_n) = -F_q(z_l) = 2\pi\sigma. \quad (8)$$

After the transition to the concentration of electrons $\rho = \sigma N/eb$ and the introduction of the plasma frequency $\omega_p^2 = 4\pi e^2 \rho/m$, the equation for the dimensionless ponderomotive and Coulomb forces takes the form

$$f_{\text{pond}}(Z_l) = -\frac{1}{2}\frac{\omega_p^2}{\omega^2}\frac{B}{N}\frac{\alpha_i^2}{1 + \alpha_i^2}\mu_- \cos(\mu_-(Z_n - Z_l)),$$

$$f_{\text{pond}}(Z_n) = \frac{1}{2}\frac{\omega_p^2}{\omega^2}\frac{B}{N}\frac{\alpha_i^2}{1 + \alpha_i^2}\mu_+ \cos(\mu_+(Z_n - Z_l)),$$

$$f_q(Z_n) = -f_q(Z_l) = \frac{1}{2}\frac{\omega_p^2}{\omega^2}\frac{B}{N}. \quad (9)$$

Here, the following notation is used: $Z = \omega z/c$, $B = \omega b/c$, $\tilde{p} = p/mc$, $\tau = \omega t$, $f = d\tilde{p}/d\tau$, and $\mu_\pm = (h \pm k)/k$. It follows from (9) that the ponderomotive force has alternating signs (see Fig. 1) and, in the near zone (at $|Z_n - Z_l| < \pi/\mu_\pm$), is always directed against the Coulomb force but cannot balance it completely, because, no matter what the amplitude of the pumping wave, the transverse oscillatory velocity of particles is lower than the velocity of light, $\alpha_i/(1 + \alpha_i^2)^{1/2} < 1$. We find that, in the Lagrange variables, an electron (plasma) bunch under the action of a pumping field can be represented as a gas comprising macroparticles that interact by ponderomotive and Coulomb forces determined by (9).

The developed model can be generalized to wave scattering by a plasma layer consisting of light electrons and heavy positively charged ions with mass $M \gg m$. The presence of ions compensates Coulomb repulsion forces and prevents bunch expansion. Heavy ions do not participate in ponderomotive interactions and shift in the longitudinal direction only under the action of Coulomb forces. The dimensionless coordinate of the *l*th ion will be written as Y_l. Under the assumptions made above, the self-consistent system of equations including motions of electrons and ions takes the form

$$\frac{dZ_l}{d\tau} = \frac{\tilde{p}_l}{\gamma},$$

$$\frac{d\tilde{p}_l}{d\tau} = f_q + f_{\text{pond}} = \frac{1}{2}\frac{\omega_p^2}{\omega^2}\frac{B}{N} \times \left[N^-(l) - N^+(l) + \frac{\rho_i}{\rho_e}(N_i^+(l) - N_i^-(l)) + \frac{\alpha_i^2}{1 + \alpha_i^2}\left(\sum_n^{N^+} \mu_+ \cos(\mu_+(Z_n - Z_l))\right.\right. \quad (10)$$

$$-\sum_n^{N^-}\mu_-\cos(\mu_-(Z_n - Z_l))\Bigg)\Bigg],$$

$$\frac{dY_l}{d\tau} = \bar{p}_l,$$

$$\frac{d\bar{p}_l}{d\tau} = -\frac{m}{M}\frac{1}{2}\frac{\omega_p^2}{\omega^2}\frac{B}{N}$$

$$\times\left[N^-(l) - N^+(l) + \frac{\rho_i}{\rho_e}(N_i^+(l) - N_i^-(l))\right].$$

Here, $N^+(l)$ and $N^-(l)$, $N_i^+(l)$, and $N_i^-(l)$ are the numbers of macroelectrons and "macro" ions to the right (+) and to the left (–) of the layer with the coordinate Z_l or Y_l, respectively; ρ_i and ρ_e are the unperturbed concentrations of the ions and electrons; and $\bar{p}_l$ is the dimensionless momentum of the lth ion. In (10), it is taken into account that the forces that act on the given electron from the other electrons are summed additively. Indeed, the scattered field linearly enters into the equation (6) for the ponderomotive force.

If electrons and ions are uniformly distributed in the layer, the initial conditions take the form

$$Z_l(0) = Y_l(0) = \frac{Bl}{N}, \quad \tilde{p}_l = \bar{p}_l = 0. \tag{11}$$

Note that equations similar to (10) describe scattering in the field of a linearly polarized pumping wave,

$$\mathbf{A}(z, t) = \mathrm{Re}(\mathbf{x}_0 A_i \exp(i\omega t + ihz)).$$

However, we must then assume that $\alpha_i \ll 1$; that is, the approximation of a weak nonrelativistic wave should be used. Accordingly, the $\alpha_i^2/(1 + \alpha_i^2)$ factor is replaced by $\alpha_i^2/2$ in the equations for the average ponderomotive force in (10).

Note also that system (10) admits the introduction of the new normalized time $\tilde{\tau} = \omega_p\tau/\omega = \omega_p t$. This means that any solution to these equations is a function of $\omega_p t$ and the characteristic times of all processes are proportional to $1/\omega_p$. Naturally, taking into account delay breaks this similarity. As a first approximation, delay can be included as follows. A wave emitted by the lth electron is considered monochromatic and propagating to the nth electron with the delay $\Delta t = |z_n - z_l|/c$. The right-hand side of equations of motion then contains Z_n and Z_l corresponding to the instants of time spaced Δt rather than to the same instant of time as in (10). The delay can be ignored in considering the Coulomb force, because this force is distance-independent in the one-dimensional model.

The self-consistent system of equations including delay can conveniently be written using the normalized time $\tilde{\tau}$ (the equations of motion of the ions are omitted because their form remains unchanged),

$$\frac{dZ_l(\tilde{\tau})}{d\tilde{\tau}} = \frac{\tilde{p}_l}{\gamma},$$

$$\frac{d\tilde{p}_l}{d\tilde{\tau}} = \frac{1}{2}\frac{B}{N}\Bigg\{N^- - N^+ + \frac{\rho_i}{\rho_e}(N_i^+ - N_i^-)$$

$$+\frac{\alpha_i^2}{1+\alpha_i^2}\Bigg[\sum_n^{N^+}\mu_+\cos(\mu_+(Z_n(\tilde{\tau}-\Delta\tau) - Z_l(\tilde{\tau}))) \tag{12}$$

$$-\sum_n^{N^-}\mu_-\cos(\mu_-(Z_n(\tilde{\tau}-\Delta\tau) - Z_l(\tilde{\tau})))\Bigg]\Bigg\},$$

$$\Delta\tau = \theta|Z_n - Z_l|.$$

Here, $\theta = \omega_p/\omega$ plays the role of the delay parameter. For $\theta \longrightarrow 0$, these equations reduce to system (10) written in new normalizations.

3. SUPERRADIANCE MODE IN SCATTERING OF AN INTENSE PUMPING WAVE BY A MOVING ELECTRON BUNCH

Consider a one-dimensional electron bunch of width b_0 which moves in the +z direction at a relativistic translational velocity V in the vacuum. Let the circularly polarized pumping wave $\mathbf{A}(z, t) = \mathrm{Re}(\boldsymbol{\xi}A_i\exp(i\omega_0 t + ih_0 z))$, where $h_0 = \omega_0/c$, be incident on the bunch, and let this wave propagate in the direction opposite to the translational motion of the particles. In the bunch frame of reference K', the motion of electrons is described by (10) and (11) (delay ignored), into which we must substitute the values recalculated according to the Lorentz transformations

$$\omega = \gamma_\parallel(\omega_0 + h_0 V), \quad h = \gamma_\parallel\left(h_0 + \frac{\omega_0 V}{c^2}\right) = \frac{\omega}{c},$$

$$b = \gamma_\parallel b_0, \quad \omega_p = \frac{\omega_{p0}}{\sqrt{\gamma_\parallel}},$$

where $\gamma_\parallel = (1 - V^2/c^2)^{-1/2}$ is the longitudinal relativistic mass factor and ω_{p0} is the plasma frequency of the bunch in the laboratory frame of reference.

In the problem under consideration, the scattered radiation in the moving frame of reference K' has the same frequency and modulus of the wave vector as the pumping wave. We should therefore set $\mu_- = 0$ and $\mu_+ = 2$ in (10) and (11). Suppose that the static charge of the electron bunch is fully compensated by the ionic background. Next, we ignore longitudinal displacements of ions and assume that the electron layer width is large on the radiation wavelength scale. In this situa-

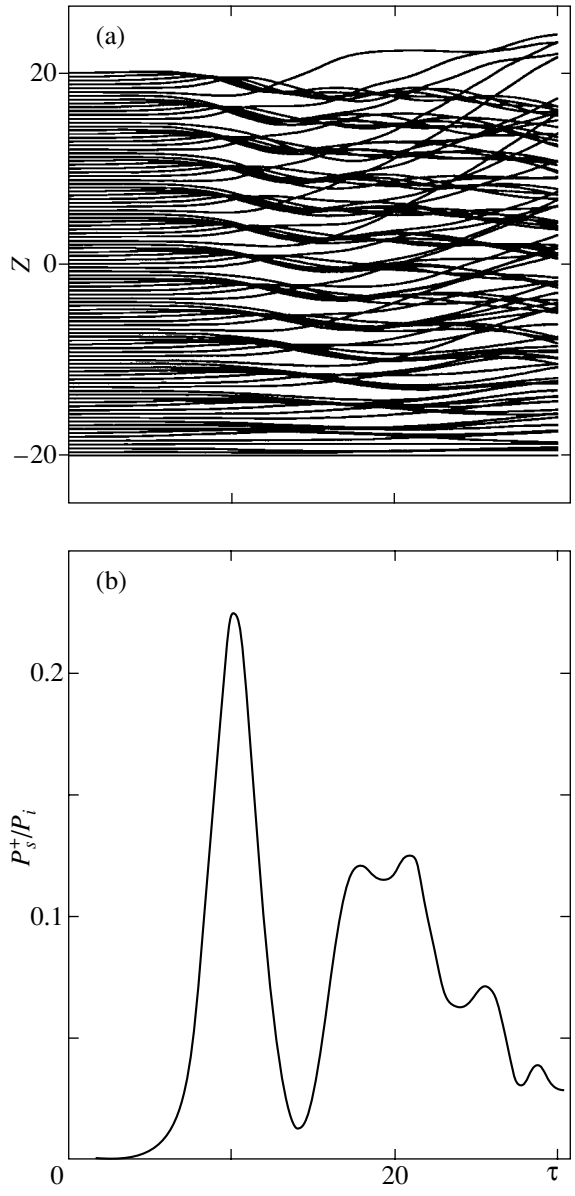

Fig. 2. Time τ dependences of (a) macroelectron coordinates and (b) normalized power P_s^+/P_i of the counterpropagating scattered wave at $\omega_p^2/\omega^2 = 0.08$, $\alpha_i = 0.7$, and $B = 40$.

tion, longitudinal electron shifts are determined by the counterpropagating scattered wave (propagating along the bunch motion direction in the laboratory frame of reference). The interference of this wave with the pumping wave creates a wave of beats whose wavelength equals half the pumping field wavelength. The ponderomotive force in the near zone is then attractive. This behavior of the interaction force should cause instability and layer fragmentation into coherently emitting bunches. The number of such bunches is $B/(2\pi/\mu_+)$, which is the number of ponderomotive force periods along the layer length. This effect at the initial stage ($\tau \sim 15$–20) is shown in Fig. 2, where the time dependences of electron coordinates are plotted. The plots were constructed for $\omega_p^2/\omega^2 = 0.08$, $\alpha_i = 0.7$, and $B = 40$.

Next, consider the anisotropic character of scattering forward and backward by an electron layer of a finite width. The amplitude of the wave codirected with the pumping wave and propagating in the direction opposite to that of the translational motion of the bunch does not depend on time. Indeed, according to (4), at the point Z to the left of the layer, the dimensionless complex amplitude of the wave scattered in the $-z$ direction is

$$\begin{aligned}\alpha_s^-(Z) &= -\frac{i}{2}\frac{\omega_p^2}{\omega^2}\frac{B}{N}\frac{1}{\sqrt{1+\alpha_i^2}}\sum_{l=1}^{N}\alpha_i e^{iZ_l}e^{i(Z-Z_l)} \\ &= -\frac{i}{2}\frac{\omega_p^2 B}{\omega^2}\frac{\alpha_i}{\sqrt{1+\alpha_i^2}}e^{iZ}\end{aligned} \tag{13}$$

(that is, all terms of this sum are equal irrespective of the arrangement of the particles within the layer). The situation with the wave scattered in the $+z$ direction is different. For this wave, the dimensionless complex amplitude at the point Z situated to the right of the layer is given by the equation

$$\begin{aligned}\alpha_s^+ &= \frac{i}{2}\frac{\omega_p^2}{\omega^2}\frac{B}{N}\frac{1}{\sqrt{1+\alpha_i^2}}\sum_{l=1}^{N}\alpha_i e^{iZ_l}e^{-i(Z-Z_l)} \\ &= \frac{i}{2}\frac{\omega_p^2 B}{\omega^2 N}\frac{\alpha_i e^{-iZ}}{\sqrt{1+\alpha_i^2}}\sum_{l=1}^{N}e^{2iZ_l}.\end{aligned} \tag{14}$$

Clearly, the amplitude of the backscattered wave substantially depends on time, and the ratio between the amplitudes of this wave and the wave scattered forward is always smaller than one,

$$\frac{\sum_{l=1}^{N}e^{2iZ_l}}{N} \le 1,$$

because the waves scattered by all electrons in the $-z$ direction are synchronized with the pumping wave and coherent, whereas the waves scattered in the $+z$ direction interfere with each other. It follows that the amplitude of the counterpropagating wave is determined by the factor

$$\left|\sum_{l=1}^{N}e^{2iZ_l}\right|/N.$$

In the continuous layer model, this factor is

$$\left|\int \rho(Z)e^{2iZ}dZ\right|/B.$$

Here, the dimensionless density $\rho(Z)$ is introduced. At the initial time, when $\rho(Z)$ is constant, we have

$$\alpha_s^+ = \frac{2\pi i e^2}{\omega^2}\frac{\alpha_i e^{-iZ}}{\sqrt{1+\alpha_i^2}}\int \rho(Z) e^{2iZ} dZ = \frac{i}{2}\frac{\omega_p^2}{\omega^2}\frac{\alpha_i e^{-iZ}}{\sqrt{1+\alpha_i^2}}\sin(kb). \quad (15)$$

It follows that the amplitude of the counterpropagating field is initially determined by the presence of sharp electron bunch edges. This field is actually a seed field, that is, it initiates the subsequent clustering of particles within the bunch. This clustering makes $\rho(Z)$ a periodic function with the period $2\pi/2k$ (see Fig. 2), and the integral (or the sum) can take on fairly large values. This means that the electrons bunch in a way that ensures a significant increase in the α_s^+ wave amplitude compared with the initial instant of time.

The time dependence of the power ratio between the wave under consideration and the pumping wave,

$$\frac{P_s^+}{P_i} = \frac{|\alpha_s^+|^2}{|\alpha_i|^2} = \frac{1}{1+\alpha_i^2}\left(\frac{1}{2}\frac{\omega_p^2 B}{\omega^2 N}\right)^2 \left|\sum_{l=1}^{N} e^{2iZ_l(\tau)}\right|^2, \quad (16)$$

is shown in Fig. 3 for the moving frame of reference. The plot maxima correspond to the maximum bunching of electrons, which occurs at $\tau \sim 15$ (compare Fig. 2). At an ideal bunching, all planes emit coherently and all terms of the sum in (16) are equal. Accordingly,

$$\frac{P_s^+}{P_i} = \frac{1}{1+\alpha_i^2}\left(\frac{1}{2}\frac{\omega_p^2 B}{\omega^2}\right)^2. \quad (17)$$

The amplitudes of the waves scattered forward and backward are then equal. Simulation shows that, at the parameters specified in Fig. 3, the peak radiation power is approximately 10 times lower than the value given by (17), and the corresponding amplitude of the field is approximately three times smaller than the ideal amplitude. Nevertheless, the analysis made above leads us to conclude that, at a certain instant of time, a fairly high degree of coherence of the emission from the electron layer particles is attained. At long times $\tau > 15$, bunches decay (Fig. 2), which is followed by the formation of secondary bunches. This explains the presence of the next scattered wave amplitude maxima. At still longer times, strong mixing of particles within layers occurs, and the amplitude of scattering in the $+z$ direction decreases virtually to the level given by (15).

It is easy to see that the peak radiation power quadratically depends on the number of particles participating in scattering; this number is proportional to $\omega_p^2 b$. The quadratic dependence of the power on the density of the bunch, that is, on ω_p^2, follows directly from (16)

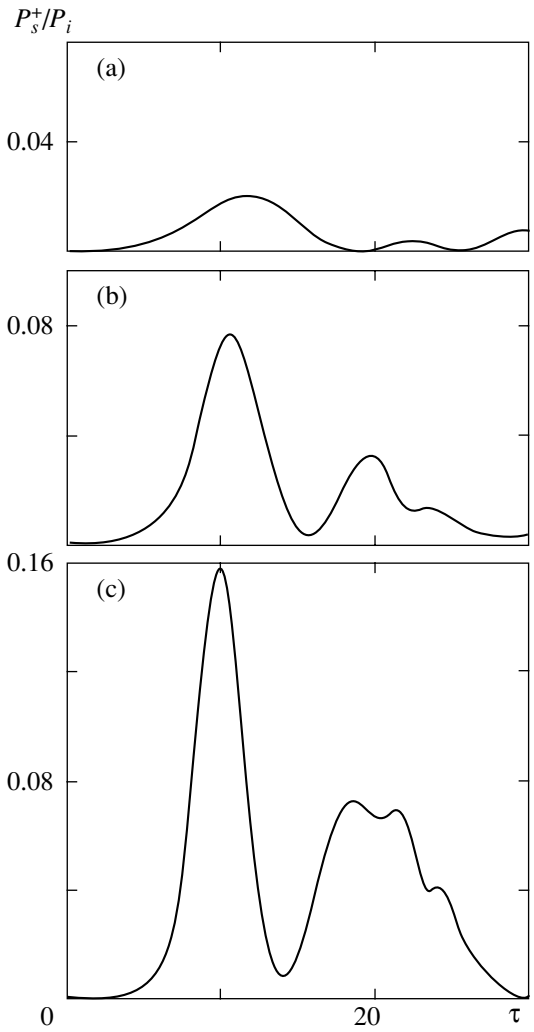

Fig. 3. Time τ dependences of normalized radiation power P_s^+/P_i at various layer widths; $\omega_p^2/\omega^2 = 0.08$, $\alpha_i = 0.7$, and B = (a) 10, (b) 20, and (c) 30.

and from the time similarity of the problem. According to (10) and (11), only the time scales rather than electron coordinates change depending on ω_p^2. It follows that, when ω_p^2 changes, the maximum of the scattered wave amplitude is attained at a somewhat different instant of time, but the maximum

$$\left|\sum_{l=1}^{N} e^{2iZ_l}\right|^2$$

remains unchanged and the coefficient of this value is quadratic in ω_p^2. Numerical simulations (Figs. 3, 4) substantiate the conclusion that the dependence of the peak power on layer width B is also close to quadratic. The time dependences of the emitted power at various b are shown in Fig. 3, and the dependence of the peak

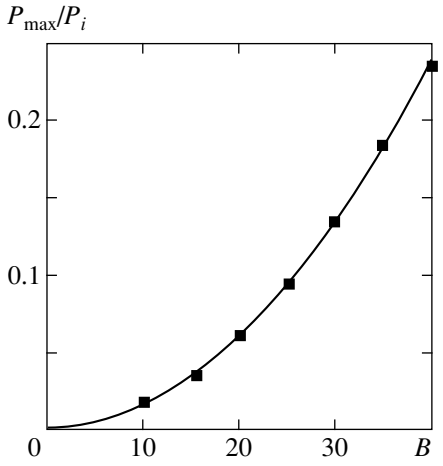

Fig. 4. Dependence of normalized peak superradiance power P_{max}/P_i on layer width B at $\omega_p^2/\omega^2 = 0.08$ and $\alpha_i = 0.7$ (solid line). Symbols are numerical simulation results.

density on the width of the layer, in Fig. 4. The quadratic dependence of the peak power of superradiance pulses on the total number of particles is evidence of the coherent character of radiation.

The width of a superradiance pulse decreases as the total number of particles increases. It also decreases as ω_p increases, which follows from the above-mentioned time similarity of the problem (all characteristic times and, therefore, the pulse width are proportional to $1/\omega_p$). The dependence of the pulse width on layer width b follows from the numerical simulation data (compare Figs. 3a–3c).

The results described above were obtained ignoring delay, that is, on the assumption that the time of radiation propagation along the layer, b/c, was substantially shorter than the characteristic time of bunching of particles t_{bunch} and, accordingly, than the time during which a superradiance pulse was emitted. Let us estimate the t_{bunch} characteristic time as the time of the arising of the main scattered radiation peak. For an ideal bunching, the amplitude of the backscattered wave given by (14) is

$$\alpha_{max}^{+} = \frac{\omega_p^2}{2\omega^2} B\alpha_i (1+\alpha_i^2)^{-1/2}.$$

As follows from (6), the force

$$F_{max} = mc\frac{\omega_p^2 B}{2\omega}\frac{\alpha_i^2}{1+\alpha_i^2}$$

acts on a particle and gives it the acceleration

$$\alpha_{max} = \frac{F_{max}}{m} = \frac{1}{2}\frac{\alpha_i^2}{1+\alpha_i^2}\omega_p^2 b.$$

The time of bunching t_{bunch} can be estimated as the time during which particles cover the distance equal to the wavelength of beats under the action of the force specified above. We have

$$\lambda_{pond} = \frac{\lambda}{2} = \frac{\pi c}{\omega},$$

$$t_{bunch} = \left(\frac{2\lambda_{pond}}{a_{max}}\right)^{1/2} \approx \omega_p^{-1}\sqrt{\frac{4\pi(1+\alpha_i^2)}{\alpha_i^2 B}}.$$

The condition of ignoring delay can then be written as

$$\frac{\omega}{\omega_p}\sqrt{\frac{4\pi(1+\alpha_i^2)}{\alpha_i^2}} \gg B^{3/2}.$$

Taking into account an insignificant delay by (12) does not qualitatively change the character of the process. The dependences of the renormalized radiation power $P_s^+/(\theta^4 P_i)$ on time $\tilde{\tau}$ at various θ parameter values are shown in Fig. 5. Note that, when delay is taken into account, the degree of bunching decreases and, therefore, the peak power lowers. A considerable suppression of the main superradiance pulse occurs at $\theta = 0.1$ if $B = 20$.

Next, consider the principal properties of radiation forward and backward in the laboratory frame of reference. In the moving frame of reference, all processes occur at the same frequency. The frequencies of waves propagating in the opposite directions should then be substantially different in the laboratory frame of reference if the Doppler effect is taken into account. At a translational velocity close to the velocity of light, $V \longrightarrow c$, we have $\omega^+/\omega^- = 4\gamma_\parallel^2$, where $\omega^+ = \gamma_\parallel(\omega + kV)$ and $\omega^- = \gamma_\parallel(\omega - kV) = \omega_0$ are the frequencies of the waves that propagate in the positive and negative directions along z in the laboratory frame of reference.

Taking into account the law of the conservation of the number of quanta, we find that, in the laboratory frame of reference, the power emitted in the direction of the translational motion of an electron bunch substantially exceeds the power emitted in the opposite direction. Indeed, the numbers of emitted quanta P/ω are equal in the two frames of reference; that is,

$$\frac{P_{lab}^+}{P_{lab}^-} = \frac{\omega^+ P^+}{\omega^- P^-} \approx \frac{4\gamma_\parallel P^+}{P^-}.$$

It follows that, in the laboratory frame of reference, the major superradiance energy fraction concentrates in the short-wave component in the case of ultrarelativistic translational motion, $\gamma_\parallel \gg 1$.

In conclusion, consider some numerical estimates. Let the pumping wavelength be 3 cm in the laboratory frame of reference and the power flux density be 1.4 GW/cm^2 ($\alpha_i = 0.7$). We assume that scattering

occurs on a bunch of length $b_0 = 4$ mm with particle energy $E = 2$ MeV ($\gamma_\parallel = 5$) and current density $j \sim 1$ kA/cm^2. Then, in the moving frame of reference, $\omega \sim 6 \times 10^{11}$ s^{-1}, $\omega_p^2/\omega^2 \sim 3 \times 10^{-4}$, and $B = 20$. Accordingly, the frequency of the short-wave superradiance pulse component in the laboratory frame of reference is $\omega^+ \sim 6 \times 10^{12}$ s^{-1} ($\lambda^+ \sim 0.3$ mm). The simulation results shown in Fig. 3 give the pulse width $\Delta t \sim 0.2$ ns and the delay time of the superradiance pulse counted from the instant of time of switching on the pumping field $t \sim 0.1$ ns. The normalized pulse amplitude is $\alpha_s^+ \sim 4 \times 10^{-3}$, which corresponds to the power flux density 0.4 GW/cm^2. We see that the specified mechanism can be used to generate high-power radiation pulses in the range of submillimeter waves.

4. ACCELERATION OF A SHORT PLASMA BUNCH BY RADIATION PRESSURE FORCES

Let a neutral plasma layer with a finite mass of ions, which is thin on the wavelength scale, be at rest at the initial time. Consider its motion as a whole under the action of an intense circularly polarized pumping wave that propagates in the +z direction. We will show that the electromagnetic fields scattered by layer electrons in combination with the field of the incident wave create a ponderomotive force that accelerates layer electrons and thereby, via Coulomb forces, heavy ions too. The acceleration rate calculated with the model described in Section 2 corresponds with the results of a macroscopic analysis.

Clearly, the sum of Coulomb forces within a neutral plasma layer is zero. As concerns ponderomotive forces, it has already been mentioned that they do not obey the third Newton law, and their sum therefore gives a nonzero bunch acceleration. Let us determine the acceleration value. As follows from (10) and (11), accelerating ponderomotive force (7) applied to the electron with the coordinate $Z_n < Z_l$ acts on each pair of electrons with the coordinates $Z_{n,l}$ at $\mu_+ = 2$ and $\mu_- = 0$. As a result the electron with the coordinate Z_n overtakes and outruns the electron with the coordinate Z_l. After this, the accelerating ponderomotive force acts on the second electron of the pair. In this way, periodically exchanging their positions, both electrons get involved in the acceleration process. For estimation purposes, the ponderomotive force acting on a pair of electrons in a layer thin on the scale of the external field wavelength can be considered independent of the distance between particles and, in dimensionless values, equal to

$$f = \frac{\omega_p^2}{\omega^2}\frac{B}{N}\frac{\alpha_i^2}{1+\alpha_i^2}.$$

The number of all possible combinations of pairs of interacting macroelectrons is $N^2/2$. The summed unbalanced force acting on a bunch of N electrons is therefore

$$f_\Sigma = \frac{\omega_p^2 BN}{2\omega^2}\frac{\alpha_i^2}{1+\alpha_i^2}. \quad (18)$$

It follows that the mean force acting on one particle equals half the maximum ponderomotive force value given by (7). Indeed, the electrons being accelerated

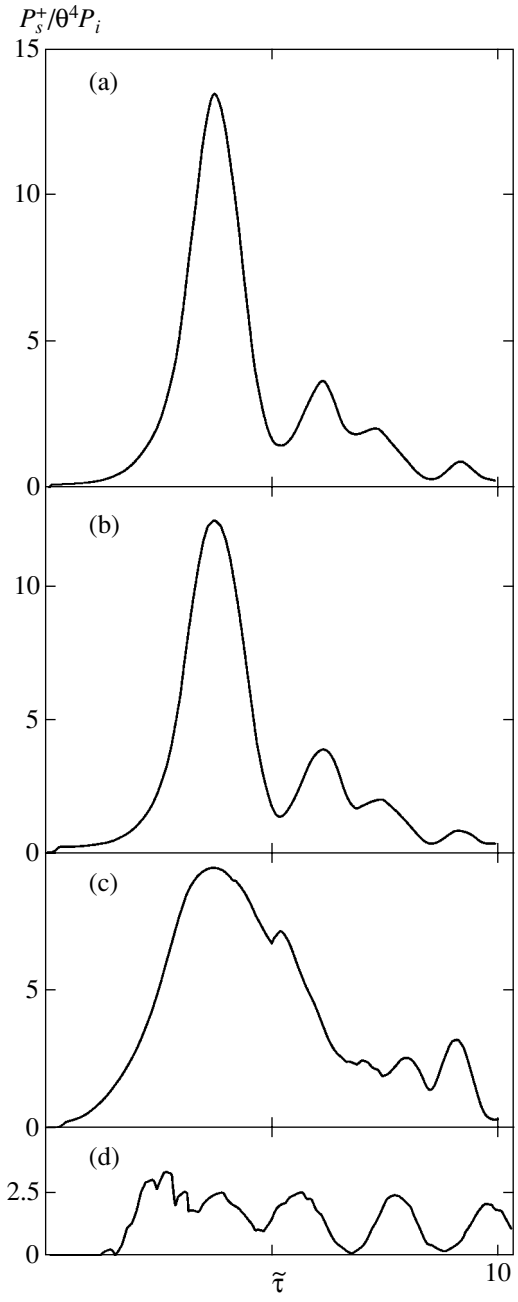

Fig. 5. Time $\tilde{\tau}$ dependences of normalized power $P_s^+/\theta^4 P_i$ taking into account delay; $B = 20$, $\alpha = 0.7$, and $\theta = 0$ (a), 0.005 (b), 0.01 (c), and 0.1 (d).

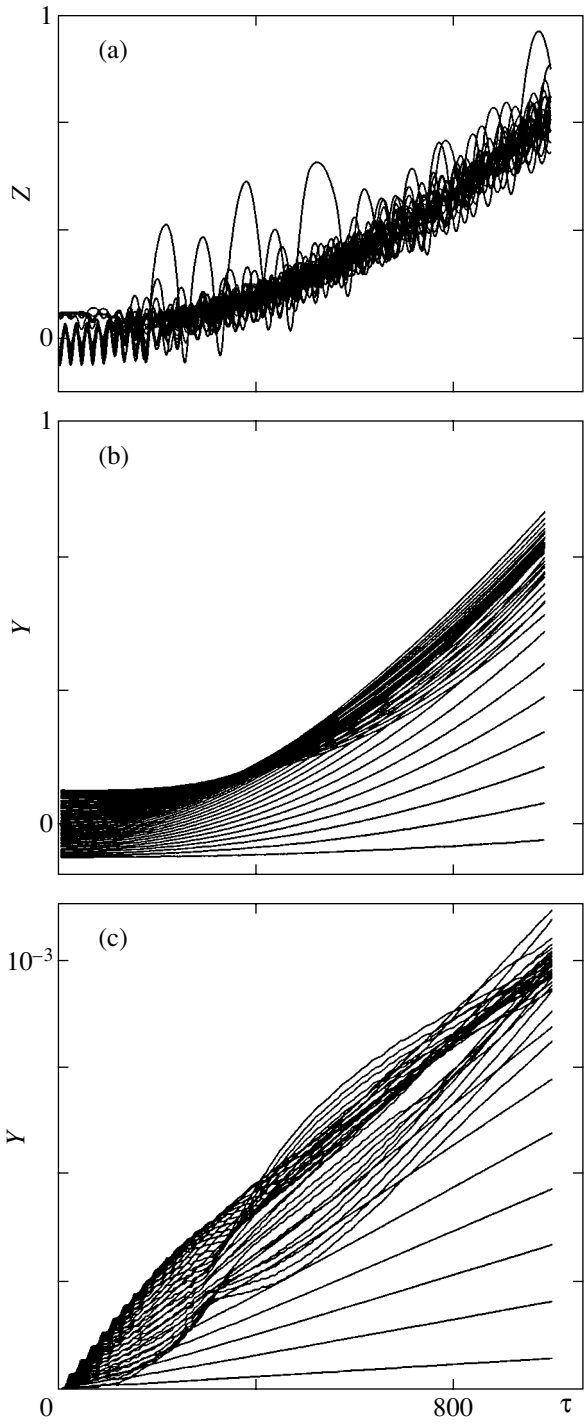

Fig. 6. Time τ dependences of (a) electron coordinates, (b) ion coordinates, and (c) ion velocities during plasma bunch acceleration in an electromagnetic wave field at $\omega_p^2/\omega^2 = 0.08$, $\alpha_i = 0.7$, and $B = 0.1$.

continuously exchange positions, but the total ponderomotive force is independent of the arrangement of the electrons. Through Coulomb interaction, this force acts on ions, whose summed mass for a neutral bunch is $M\rho B$. It follows that the acceleration of the entire bunch is determined by the equation

$$a = \frac{f_\Sigma}{MB\rho} = \frac{m}{M}\frac{\omega_p^2 b}{2}\frac{\alpha_i^2}{1+\alpha_i^2}.$$

In (18), it is expedient to replace the force acting on a bunch by the pressure defined as the force applied to a unit cross section area,

$$p = \frac{m^2\omega_p^4 b^2}{8\pi e^2}\frac{\alpha_i^2}{1+\alpha_i^2} = \frac{\omega_p^4 b^2}{8\pi c^4}\frac{A_i^2}{1+(eA_i/mc^2)^2}. \quad (19)$$

A similar value for the mean rate of acceleration of a plasma bunch under electromagnetic radiation pressure can be obtained in macroscopic electrodynamics. Consider a plane monochromatic wave with amplitude E_0 and frequency ω incident from the vacuum on a layer of thickness b, thin on the wavelength scale, with permittivity ε. The law of the conservation of momentum gives the radiation pressure on this layer expressed through twice the momentum flux of the reflected wave,

$$p = 2\frac{P_R}{c} = \frac{E_0^2}{2\pi}|R|^2, \quad (20)$$

where R is the reflection coefficient of the layer,

$$R = \xi\frac{1-\exp(-2ik\sqrt{\varepsilon}b)}{1-\xi^2\exp(-2ik\sqrt{\varepsilon}b)} \approx \frac{2ik\sqrt{\varepsilon}b}{1/\xi-\xi} = \frac{ikb(\varepsilon-1)}{2}, \quad (21)$$

$$\xi = \frac{\sqrt{\varepsilon}-1}{\sqrt{\varepsilon}+1}.$$

The approximate equality in (21) is written for $\omega\sqrt{\varepsilon}\,b/c \ll 1$. Let ε be the permittivity of the plasma, $\varepsilon = 1 - \omega_p^2/\omega^2$. Equations (20) and (21) for the wave pressure on a layer then give

$$p = \frac{E_0^2}{2\pi}\frac{k^2b^2(\varepsilon-1)^2}{4} = \frac{A_i^2 b^2\omega_p^4}{8\pi c^4}. \quad (22)$$

This equation coincides with the value (19), disregarding the $1 + (eA_i/mc^2)^2$ relativistic factor, which is absent in (22) because the macroscopic approach uses the nonrelativistic equation for the permittivity. The conclusion can be drawn that the pressure (therefore, acceleration rate) obtained macroscopically is in agreement with the acceleration rate determined microscopically.

The mechanism of acceleration described above is illustrated by Fig. 6, where the time dependences of the dimensionless coordinates of the electrons and ions and also dimensionless (measured in c units) ion velocities are plotted for $\omega_p^2/\omega^2 = 0.08$, $\alpha_i = 0.7$, and $B = 0.1$. The figure shows that the mean bunch acceleration is fairly close to the value determined by (18) and (22), and the

internal dynamics of the motion of particles in the bunch has a fairly complex nonlaminar character. In particular, we observe periodic intersections of electron trajectories [this circumstance was mentioned above in deriving (18)]. Interestingly, some ions fall behind the bunch during acceleration, but the bunch nevertheless does not fragment, because excessive Coulomb forces are balanced by ponderomotive interaction, which is attractive in the near zone (see Section 5 for more details).

Let us estimate the acceleration of a bunch of density 4×10^{10} cm^{-3} and length 0.5 mm by an electromagnetic wave with a wavelength of 3 cm and power flux density of 0.4 GW/cm^2 ($\alpha_i = 0.7$). The acceleration of the bunch is $a \approx 4.5 \times 10^{16}$ cm/s^2 at $\omega_p^2/\omega^2 \sim 3$. For instance, the electrons and ions acquire energies of 2.5 keV and 5 MeV, respectively, over a distance of 1 m.

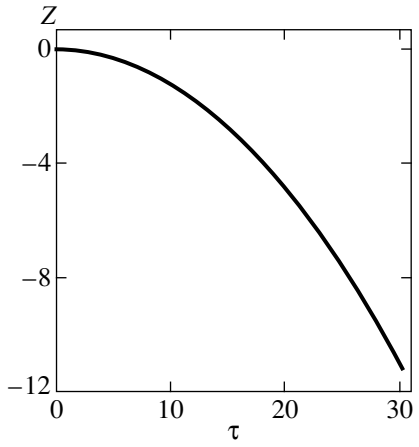

Fig. 7. Time τ dependence of electron coordinates in the process of radiation-field-induced partial contraction of an electron bunch with incompletely compensated charge ($\alpha_i = 1$, $r = 0.5$, $\omega_p^2/\omega^2 = 1$, $B = 0.1$).

5. SELF-FOCUSING OF A SHORT ELECTRON BUNCH MOVING IN AN UNDULATOR FIELD

The superradiance effects considered in Section 3 are also observed when oscillations are imparted to electrons that are involved in translational motion in the field of a planar or helical undulator. As has already been mentioned, in the electron beam frame of reference, this field transforms into the field of a linearly or circularly polarized wave, respectively, with the dispersion law different from the vacuum dispersion law. In the laboratory frame of reference, the static magnetic field of a helical undulator can, ignoring transverse nonuniformity, be described by the vector potential

$$\mathbf{A}_i(z, t) = \mathrm{Re}(\boldsymbol{\xi} A_i \exp(i h_u z)),$$

where $h_u = 2\pi/d$, $|A_i| = H_0/h_u$, d is the undulator period, and H_0 is the magnetic field amplitude. When the electrons move along the undulator axis at velocity V, in the moving frame of reference, the field of the undulator transforms into

$$\mathbf{A}(z, t) = \mathrm{Re}(\boldsymbol{\xi} A_i \exp(i\omega t + i h_i z)),$$

where $h_i = h_u\gamma_\parallel$ and $\omega = h_u V\gamma_\parallel$. It follows that the problem is described by (10) [if delay is taken into account, by (12)], and analysis of the characteristics of this process in both moving and laboratory frames of reference is close to that performed in Section 3. However, note that, for motion in the undulator field, $\mu_- \neq 0$ in (10). For this reason, two waves of beats caused by electromagnetic waves emitted in the z directions participate in electron bunching. Nevertheless, when the translational velocity of the bunch tends to the velocity of light ($V \longrightarrow c$), ponderomotive action related to the beats of the pumping wave and the wave propagating in the $-z$ direction can be ignored compared with the ponderomotive action of the wave propagating in the $+z$ direction. For this reason, for the ultrarelativistic motion of an electron bunch in the undulator field, superradiance is to a considerable extent similar to that described in Section 3. However note that the equation for the frequencies of radiation scattered forward and backward takes the form $\omega^+/\omega^- = 2\gamma_\parallel^2$, where $\omega_- = h_0 c$. Accordingly, the ratio between the powers of the short- and long-wave scattering components is given by

$$\frac{P^+_{\mathrm{lab}}}{P^-_{\mathrm{lab}}} = 2\gamma_\parallel^2 \frac{P^+}{P^-}.$$

Also note that, if a short (on the scale of the radiation wavelength in the moving frame of reference) neutral plasma bunch moves in an undulator field, then, as distinguished from bunch acceleration in the electromagnetic pumping wave field considered in Section 4, the deceleration rather than acceleration of the entire bunch should be observed.

As mentioned in Section 4, electromagnetic pressure forces prevent bunch electrons from expansion caused by Coulomb forces even in the case of partial breaking of plasma bunch neutrality, because the ponderomotive interaction force between the electrons is attractive if the distance between the electrons is fairly small (see Fig. 1). However, this force cannot fully balance Coulomb repulsion forces. The possibility of electron bunch focusing by radiation fields when the bunch moves in an undulator field is, nevertheless, of interest. Focusing proves possible if the Coulomb charge is partially compensated by the metallic walls of the chamber through which the electron bunch moves. Within the framework of the one-dimensional model that we use, such a compensation can be described by introducing reduction $r < 1$ as a coefficient of the Coulomb force in (11). If this is done, Coulomb repulsion is balanced by the ponderomotive force in a fairly strong undulator field with $\alpha_i \sim 1$ already at $r \sim 0.5$. Accordingly, we

observe electron bunch focusing. Figure 7 illustrates the focusing effect for a short electron bunch moving in an undulator field. Naturally, focusing is accompanied by the deceleration of the bunch as a whole because of radiative energy loss.

Note that a more complete analysis of electron bunch focusing by radiation fields requires solving the two-dimensional problem. Such an analysis was performed for a short bunch comprising electrons that rotated in a uniform magnetic field [22]. Direct numerical simulation using the KARAT partial-in-cell code did indeed show that taking into account recoil forces arising in cyclotron emission of electrons substantially increased the lifetime of bunches.

ACKNOWLEDGMENTS

This work was financially supported by the Russian Foundation for Basic Research (project no. 01-02-17029).

REFERENCES

1. R. H. Bonifacio, C. Maroli, and N. Piovella, Opt. Commun. **68**, 369 (1988).
2. R. Bonifacio, N. Piovella, and B. W. J. McNeil, Phys. Rev. A **44**, 3441 (1991).
3. V. V. Zheleznyakov, V. V. Kocharovskiĭ, and Vl. V. Kocharovskiĭ, Izv. Vyssh. Uchebn. Zaved. Radiofiz. **29**, 1095 (1986).
4. N. S. Ginzburg, Pis'ma Zh. Tekh. Fiz. **14**, 440 (1988) [Sov. Tech. Phys. Lett. **14**, 197 (1988)].
5. N. S. Ginzburg and A. S. Sergeev, Pis'ma Zh. Éksp. Teor. Fiz. **54**, 445 (1991) [JETP Lett. **54**, 446 (1991)].
6. N. S. Ginzburg, I. V. Zotova, and A. S. Sergeev, Pis'ma Zh. Éksp. Teor. Fiz. **60**, 501 (1994) [JETP Lett. **60**, 513 (1994)].
7. N. S. Ginzburg and A. S. Sergeev, Zh. Éksp. Teor. Fiz. **99**, 438 (1991) [Sov. Phys. JETP **72**, 243 (1991)].
8. N. Piovella, P. Chaix, G. Shvets, *et al.*, Phys. Rev. E **52**, 5470 (1995).
9. G. R. M. Robb, N. S. Ginzburg, A. D. R. Phelps, *et al.*, Phys. Rev. Lett. **77**, 1492 (1996).
10. N. S. Ginzburg, I. V. Zotova, A. S. Sergeev, *et al.*, Pis'ma Zh. Éksp. Teor. Fiz. **63**, 322 (1996) [JETP Lett. **63**, 331 (1996)].
11. N. S. Ginzburg, A. S. Sergeev, I. V. Zotova, *et al.*, Phys. Rev. Lett. **78**, 2365 (1997).
12. N. S. Ginzburg, A. S. Sergeev, I. V. Zotova, *et al.*, Opt. Commun. **175**, 139 (2000).
13. V. G. Shpak, M. I. Yalandin, N. S. Ginzburg, *et al.*, Dokl. Akad. Nauk **365**, 50 (1999) [Dokl. Phys. **44**, 143 (1999)].
14. N. S. Ginzburg, Yu. V. Novozhilova, A. S. Sergeev, *et al.*, Phys. Rev. E **60**, 3297 (1999).
15. V. I. Alekseev, E. V. Alieva, K. A. Belovintsev, *et al.*, Dokl. Akad. Nauk SSSR **306**, 580 (1989) [Sov. Phys. Dokl. **34**, 452 (1989)].
16. E. G. Bessonov, Kvantovaya Élektron. (Moscow) **8**, 1617 (1986).
17. V. I. Veksler and L. M. Kovrizhnykh, Zh. Éksp. Teor. Fiz. **35**, 1116 (1959) [Sov. Phys. JETP **8**, 781 (1959)].
18. G. A. Askar'yan, At. Énerg. **5**, 1644 (1958).
19. V. V. Yankov, Zh. Éksp. Teor. Fiz. **32**, 326 (1957) [Sov. Phys. JETP **5**, 269 (1957)].
20. L. D. Landau and E. M. Lifshitz, *The Classical Theory of Fields*, 7th ed. (Nauka, Moscow, 1989; Pergamon Press, Oxford, 1975).
21. V. A. Kozlov, A. G. Litvak, and E. V. Suvorov, Zh. Éksp. Teor. Fiz. **76**, 147 (1979) [Sov. Phys. JETP **49**, 75 (1979)].
22. N. S. Ginzburg, Yu. V. Novozhilova, R. M. Rozental', and A. S. Sergeev, Pis'ma Zh. Tekh. Fiz. **26**, 12 (2000) [Tech. Phys. Lett. **26**, 650 (2000)].

Translated by V. Sipachev

Journal of Experimental and Theoretical Physics, Vol. 96, No. 5, 2003, pp. 915–921.
From Zhurnal Éksperimental'noĭ i Teoreticheskoĭ Fiziki, Vol. 123, No. 5, 2003, pp. 1040–1047.

FLUIDS

Temperature Pitch Variations in Planar Cholesteric Layers: The Role of Fluctuations and Surface Anchoring¶

V. A. Belyakov[a,b,*], P. Oswald[b], and E. I. Kats[c,a]

[a]*Landau Institute for Theoretical Physics of Russian Academy of Sciences, Moscow, 117334 Russia*
[b]*Ecole Normale Supérieure de Lyon, Laboratoire de Physique 69364, Lyon, Cedex 07, France*
**e-mail: bel@landau.ac.ru*
[c]*Institut Laue-Langevin 38042, Grenoble, Cedex 9, France*

Received January 13, 2003

Abstract—The influence of thermodynamic fluctuations on temperature pitch variations in planar cholesteric samples with a finite surface anchoring energy is theoretically investigated in the framework of the continuum theory of liquid crystals. It is shown that taking fluctuations into account allows explanation of experimental observations, namely, the absence of a temperature pitch jump hysteresis in sufficiently thick samples and its existence in thin ones. A description of fluctuations, including two phenomenological parameters, is proposed. It allows us to predict temperature points at which the pitch jumps in the sample between two configurations, with the numbers of director half-turns differing by one, as a function of the anchoring energy, Frank elastic modulus, sample thickness, and temperature (or fluctuation energy). It is shown that performing precise measurements of the pitch versus the temperature in well-controlled samples should allow determination of the phenomenological constants and then prediction the influence of fluctuations on pitch jump parameters in samples of an arbitrary thickness and/or surface anchoring energy. The corresponding calculations are performed using the Rapini–Papoular anchoring potential. It is shown that the influence of fluctuations on the pitch variation is only negligible in sufficiently thin layers. It is also noted that the results obtained could be useful for investigating pitch jump dynamics in the future. © *2003 MAIK "Nauka/Interperiodica".*

1. INTRODUCTION

Temperature unwinding of the helical structure of cholesteric liquid crystal layers of a finite thickness and surface anchoring energy has not yet been investigated sufficiently to clarify the physics of this phenomenon or to ensure optimal applications of the corresponding effects. Only cholesteric liquid crystal layers of a finite thickness down to monomolecular layers [7] have been investigated intensively, and they have revealed some interesting phenomena, in particular, related to the molecular anchoring at the layer surfaces. The effects observed in the cholesteric liquid crystal layers and their influence on the optical properties of the layer are of great applied value because precisely the electrooptics of liquid crystal layers forms a basis for numerous efficient applications of liquid crystals in displays and information processing devices.

As has been known since long ago, the temperature evolution of the cholesteric liquid crystal structure [1, 2] in samples with a finite, surface anchoring energy can be continuous at some temperature ranges with jumpwise changes at certain temperature points, with a strong hysteresis occurring when the temperature changes in opposite directions [2, 3]. This problem was recently investigated in [4]. In this theoretical paper, a simple model for temperature variations of the pitch was developed in the framework of the Frank elasticity theory by taking the surface anchoring forces into account.

However, recent experimental investigations [2, 3] show that the simple model in [4], where the pitch jump mechanism is related to the sliding of the director at layer surfaces through the anchoring potential barrier, is not directly applicable. The most probable cause of the discrepancy between theory and experiments is that the theory neglects liquid crystal thermal fluctuations in the layer. It turns out that this assumption can be justified for sufficiently thin layers only. In what follows, we therefore present the same model with thermal fluctuations in the liquid crystal layer additionally taken into account. We show that taking thermal fluctuations into account allows us to explain the tendencies observed in the experiments, to predict some new effects accessible experimentally, and to determine the range of the parameters where the simple model is valid.

In general, our primary aim in this paper is to give a qualitative or semiquantitative interpretation of the available experimental data and to propose a model for pitch variations.

¶This article was submitted by the authors in English.

2. ELASTIC MODEL WITHOUT FLUCTUATIONS

We first summarize the main results of the simple model without thermal fluctuations [4]. We examine the cholesteric liquid crystal helix unwinding as the temperature changes.

We consider a perfect planar layer of cholesteric liquid crystal and assume that the anchoring energies and the alignment directions are identical at both surfaces. The pitch variations due to temperature changes are determined by minimizing the free energy [1]

$$F(T) = 2W_s(\varphi) + \frac{K_{22}d}{2}\left(\frac{2\pi}{p_d(T)} - \frac{2\pi}{p(T)}\right)^2, \qquad (1)$$

where K_{22} is the twist Frank modulus, $W_s(\varphi)$ is the surface anchoring potential, d is the sample thickness, $p(T)$ is the equilibrium pitch at temperature T in a bulk cholesteric sample, $p_d(T)$ is the pitch measured at the same temperature in the layer, and φ is the deviation angle of the director with respect to the alignment direction at the surface. Because the pitch value $p_d(T)$ in the layer is determined by the angle φ and the equilibrium pitch $p(T)$ is determined by the angle $\varphi_0(T)$ that corresponds to a free deviation of the director from the alignment direction at the surface (in the absence of anchoring), free energy (1) can also be expressed as a function of these angles. As a result, the φ variations due to pitch (temperature) changes can be described by the equation [4]

$$\frac{\partial W_s(\varphi)}{\partial \varphi} + \frac{2K_{22}}{d}[\varphi - \varphi_0(T)] = 0. \qquad (2)$$

The pitch jumps occur when the angle φ reaches some critical value φ_c that depends on the shape of the anchoring potential $W_s(\varphi)$. The value of the free rotation angle $\varphi_0(T)$ at the jump point (or in other words, the corresponding value of the pitch in a bulk cholesteric liquid crystal) is related to the surface anchoring potential by

$$\varphi_0(T_j) = \varphi_c + \left(\frac{\partial W_s(\varphi)}{\partial \varphi}\right)_{\varphi = \varphi_c}\frac{1}{2WS_d}, \qquad (3)$$

where T_j is the jump temperature and $S_d = K_{22}/dW$ is a dimensionless parameter (with W being the depth of the surface potential).

Some results of this model, especially related to the hysteresis phenomena, are presented in [4]. In particular, formulas are given for the height of the anchoring barrier B between two director configurations in which the numbers N of director half-turns differ by 1 in the layer thickness.

In this paper, we give some additional results related to this simple model.

First of all, we examine the director deviation angle for the temperature points of special physical interest. All our calculations are performed using the Rapini–Papoular anchoring potential [1, 4, 5]

$$W_s(\varphi) = -(W/2)\cos^2\varphi,$$

for which the critical angle is $\varphi_c = \pi/4$.

Figure 1 shows the director deviation angle φ_e (from the rubbing direction) as a function of the parameter S_d at a temperature corresponding to equal free energies of the configurations with N and $N + 1$ director half-turns in the layer thickness. The corresponding equation determining φ_e follows from (2) and is given by

$$\sin(2\varphi_e) + 4S_d[\varphi_e - \pi/4] = 0. \qquad (4)$$

Figure 2 presents the director deviation angle (from the rubbing direction) as a function of the layer thick-

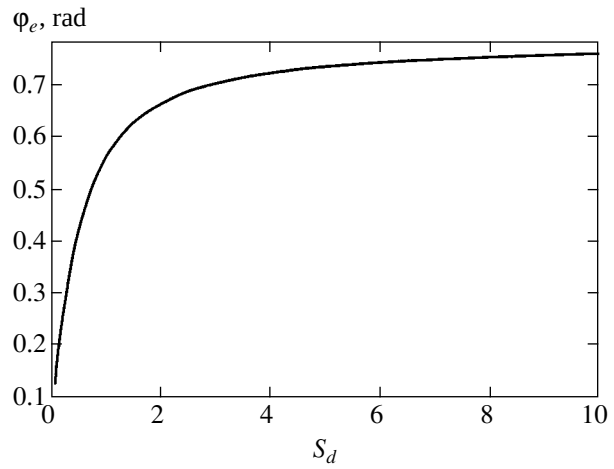

Fig. 1. The calculated director deviation angle (from the rubbing direction) φ_e as a function of the parameter S_d for the temperature corresponding to equal free energies of configurations with N and $N + 1$ director half-turns in the layer thickness.

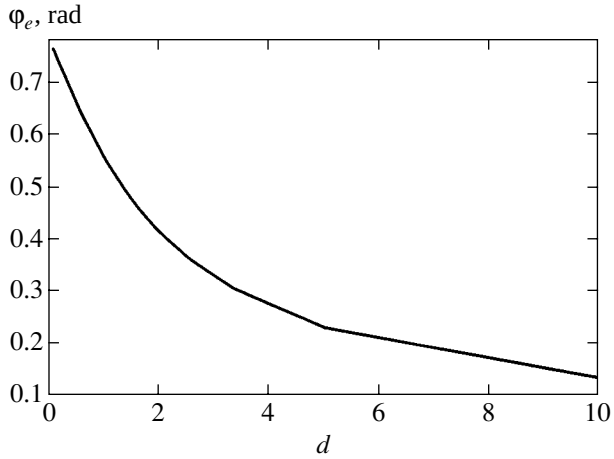

Fig. 2. The calculated director deviation angle φ_e versus the sample thickness normalized by the penetration length K_{22}/W (other conditions are the same as in Fig. 1).

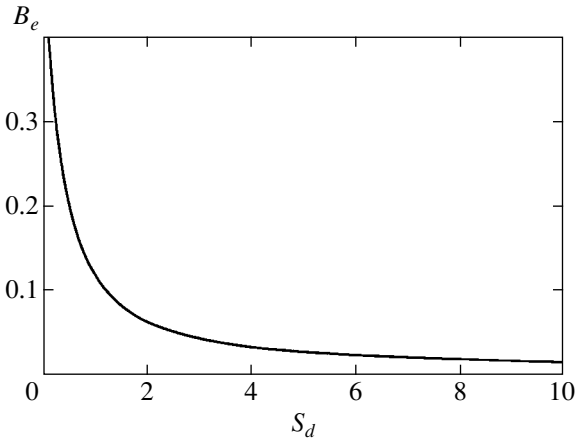

Fig. 3. The calculated height of the barrier B_e between director configurations in the layer differing by 1 in the number of the director half-turns N in the layer thickness as a function of the parameter S_d for the temperature corresponding to equal free energies for N and $N + 1$ configurations.

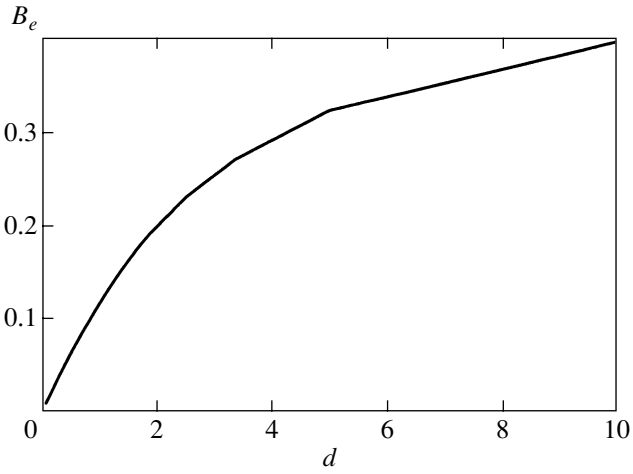

Fig. 4. The calculated height of the barrier B_e versus the sample thickness normalized by the penetration length K_{22}/W (other conditions are the same as in Fig. 1).

ness for the temperature corresponding to equal free energies of the configurations with N and $N + 1$ director half-turns in the layer thickness. We note that in thick samples, the deviation angle φ_e approaches zero, while in thin ones, it becomes larger, reaching $\pi/4$ (which is the value of the critical angle φ_c) at zero thickness.

In Figs. 3 and 4, we show the results of the calculation of the barrier B_e between two director configurations with the numbers N of director half-turns differing by 1 in the layer thickness as a function of the parameter S_d (or the sample thickness) at a temperature corresponding to equal free energies for N and $N + 1$ configurations. We note that the expression for B_e normalized by W can be found from Eq. (14) in [4], which reduces to

$$B_e = \cos^2(2\varphi_e) - \frac{\sin^2(2\varphi_e)}{8S_d} - \frac{1}{2}, \tag{5}$$

where φ_e is the director deviation angle from the rubbing direction at the surface for the free director rotation angle $\varphi_0 = \pi/4$ (see Figs. 1 and 2 for the calculated values of φ_e).

It is useful to note that the limit of B_e at $S_d = 0$, or infinite thickness, is 0. The opposite limit at infinite S_d, or zero thickness, is $W/2$.

Figures 5 and 6 present the energy difference between N and $N + 1$ configurations versus φ and the free rotation angle φ_0 (director deviation angle from the alignment direction) beginning at the point where

$$F(N) = F(N + 1).$$

Calculations have been performed using the formula deduced from Eq. (1),

$$\Delta E = \frac{F(N, \varphi_0) - F(N + 1, \varphi_0 - \pi/2)}{W}$$
$$= \frac{\sin^2[2\varphi(\varphi_0)]}{8S_d} - \cos^2[\varphi(\varphi_0)] \tag{6}$$
$$- \frac{\sin^2[2\varphi(\varphi_0 - \pi/2)]}{8S_d} + \cos^2[\varphi(\varphi_0 - \pi/2)],$$

for $S_d = 1/2\pi$, $1/\pi$, $5/2\pi$, and $5/\pi$, where the argument of φ indicates that φ is a function of φ_0. In what follows, we assume that the value of S_d is larger than $1/2\pi$ in order to ensure that only one director configuration

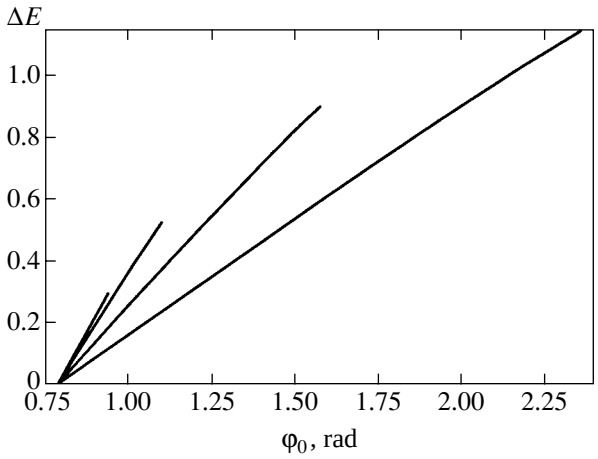

Fig. 5. The calculated difference of the free energy of configurations with N and $N + 1$ director half-turns versus the free rotation angle φ_0; the calculations have been performed (from the bottom to top curves) for $S_d = 1/2\pi$, $1/\pi$, $5/2\pi$, $5/\pi$.

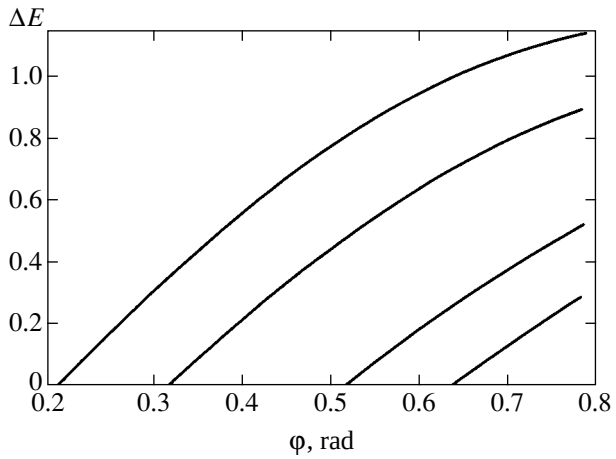

Fig. 6. The calculated difference of the free energy of configurations with N and $N + 1$ director half-turns versus the director deviation angle from their alignment direction φ; the calculations have been performed (from the left- to right-hand-side curves) for $S_d = 1/2\pi, 1/\pi, 5/2\pi, 5/\pi$.

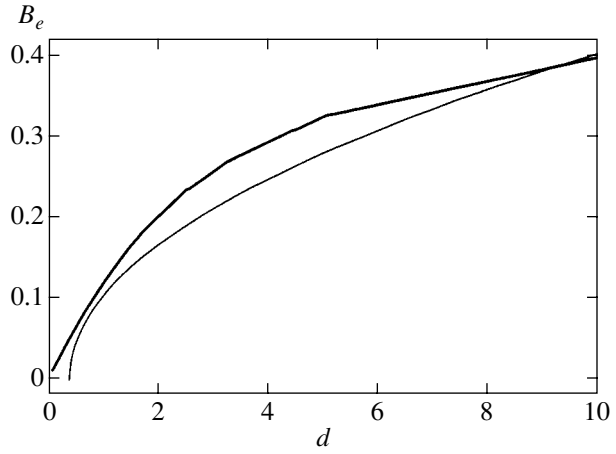

Fig. 7. The thickness d_f at which the hysteresis in the pitch jumps disappears is given at the intersection point between the two curves representing the barrier B_e and the fluctuation energy E_f as a function of the layer thickness normalized by the penetration length K_{22}/W (in the calculations, it was assumed that $d_0 = 0.4$ and $qk_BT/W = 0.13$).

with the number of director half-turns differing from N by 1 can have a free energy below that of the initial configuration. This assumption allows us to disregard pitch jumps with $\Delta N = \pm 2, \pm 3$, etc., which sometimes occur in jumpwise changes of the director field [10].

As mentioned above, this model must be improved by including the effects of liquid crystal thermal fluctuations in the bulk of the layer. The corresponding modification of the model is presented in the next section.

3. THE INFLUENCE OF FLUCTUATIONS ON PITCH CHANGES

The expressions given in the previous section relate thermodynamic equilibrium values of the parameters. However, close to the points where the pitch jumps (transitions between N and $N + 1$ configurations), bulk thermodynamic fluctuations can change the position of the transition points. For example, the hysteresis can decrease and even completely disappear because of fluctuations. In terms of the height of the surface anchoring potential between two configurations related to the transition, this implies that if in the simple model [4] the height of the barrier B must be equal to zero for the transition to occur, in a model taking fluctuations into account the transition can occur at $B \neq 0$, namely, for B differing from 0 by qk_BT, where T is the temperature, k_B is the Boltzmann constant, and q is some phenomenological coefficient to be determined experimentally. This means that the thermodynamic fluctuations of the energy of the liquid crystal allow the system to overcome the barrier, even if the equilibrium energy of the system is below the barrier.

It is now very essential to stress that the anchoring energy is proportional to the area of the layer surface and is independent of the thickness of the layer. In contrast, the bulk fluctuations of the energy, E_f, are proportional to the square root of the volume [6],

$$E_f = \sqrt{\langle \Delta E^2 \rangle} \sim qk_BT\sqrt{V} = qk_BT\sqrt{dS}, \qquad (7)$$

where ΔE is the deviation of the energy from the equilibrium value due to fluctuations, V is the volume of the system, and S and d are the surface area and the layer thickness, respectively. In what follows, we do not attempt at maintaining numerical accuracy, but only indicate the form of answers. Because the height of the anchoring barrier B is independent of d, the ratio $\sqrt{\langle \Delta E^2 \rangle}/W$ grows proportionally to $\sqrt{d}$, such that for some value of the layer thickness d, the fluctuation energy $\sqrt{\langle \Delta E^2 \rangle}$ becomes larger than the height of the surface anchoring potential barrier B.

Because fluctuations are reduced near the solid surfaces, we rewrite Eq. (7) as

$$E_f = \sqrt{\langle \Delta E^2 \rangle} \sim qk_BT\sqrt{(d - d_0)S}, \qquad (8)$$

where d_0 is some effective "surface thickness" in which fluctuations are suppressed. In principle, d_0 could be found from microscopic theory, but we consider it as a new phenomenological parameter.

We note that the coefficient q in Eq. (8) is of dimension $[L]^{-3/2}$. It can of course be made dimensionless by replacing qk_BT in Eq. (8) with $[L]^{-3/2}(qk_BT)$, where L_p is, for instance, the anchoring penetration length K_{22}/W.

To find the sample thickness for which the fluctuation energy becomes equal to the barrier B_e, we calculated the fluctuation energy E_f together with B_e as a function of the layer thickness (Fig. 7). Because the value of B_e given by Eq. (4) is the barrier height at the

temperature point of equal free energies of two configurations differing by 1 in N, the intersection point of the curves for B_e and for $\sqrt{\langle \Delta E^2 \rangle}$ in Fig. 7 gives the thickness d_f for which the hysteresis disappears in the pitch jumps.

This is why the hysteresis in the pitch jump must disappear at layer thicknesses larger than d_f. The jump value of the director deviation angle φ_j then coincides with the director deviation angle φ_e corresponding to the temperature at which the configurations with N and $N + 1$ director half-turns in the layer thickness have equal free energies (see Fig. 2). This statement is confirmed by experimental observations resolving the hysteresis only for sufficiently thin samples [2, 3].

If the sample thickness is less than d_f, hysteresis occurs and the jump value of the deviation angle φ_j does not coincide with the deviation angle φ_e and exceeds it, while remaining smaller than the critical angle φ_c.

The physical reason why the fluctuation energy becomes larger than the surface anchoring barrier at some layer thickness is in the fact that the height of the surface anchoring potential is independent of the layer thickness, whereas the thermal fluctuation energy increases as the layer thickness increases.

The results of the calculations for the jump angle φ_j at thicknesses smaller than d_f and for the behavior of the jump angle φ_j at thicknesses both larger and smaller than d_f are presented in Figs. 8 and 9, respectively.

Figure 8 shows that the jump angle φ_j is substantially reduced by fluctuations, and the hysteresis is therefore also reduced. For layer thicknesses of $d > d_f$, the hysteresis completely disappears and the jump angle φ_j is equal to φ_e. For $d < d_f$, the hysteresis reveals itself, but is less than in the model that does not take thermal fluctuations into account. This is why the jump angle φ_j is less than the critical angle φ_c that determines the jump angle in the model neglecting thermal fluctuations. It is only in sufficiently thin samples that the jump angle φ_j approaches the critical angle φ_c (which is $\pi/4$ for the Rapini anchoring potential), when fluctuations may be neglected.

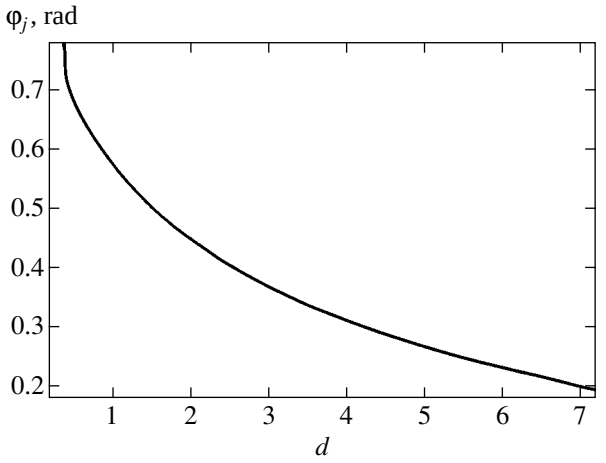

Fig. 8. The calculated jump angle φ_j for thicknesses of $d < d_f$.

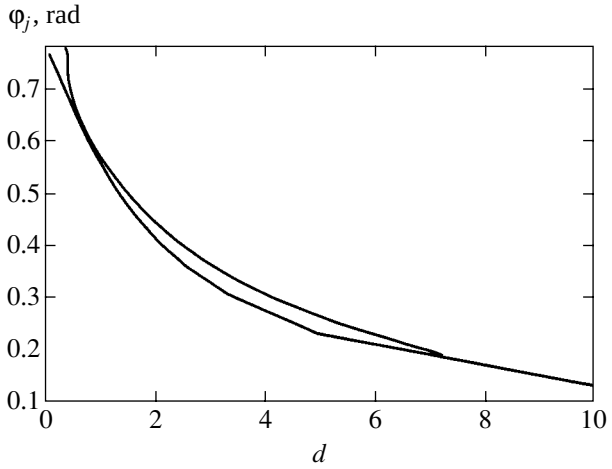

Fig. 9. The calculated jump angle φ_j at thicknesses both larger and smaller than d_f.

4. TRANSITION IN A LIMITED AREA OF THE LAYER

It was tacitly assumed above that the $N \longrightarrow N + 1$ transitions driven by fluctuations occur over the entire surface area of the layer simultaneously. We now examine the role of the surface area S of the layer subjected to transition. The difference between the anchoring barrier and the fluctuation energy can be estimated as

$$E_f - B \sim \sqrt{(d - d_0)S} - bS, \qquad (9)$$

where b is some coefficient. If we assume that the layer thickness d is fixed, the maximum of expression (8) is reached for the surface area:

$$S^* = \frac{d - d_0}{4b^2}.$$

This is the surface area of the sample in which the transition is most favorable.

If the surface area of the sample is larger than S^*, we must analyze the situation where only a part of the layer experiences a fluctuation-induced $N \longrightarrow N + 1$ transition. The question then arises about the energy cost of the defect separating this region from the rest of the layer. The answer can be found using an estimate similar to (9), where we add the line energy of the defect line. The corresponding estimate allows us to determine the minimal surface area $S_{\min}$ of the region of the layer subjected to the $N \longrightarrow N + 1$ transition, which does not

collapse and spontaneously increases in size after nucleation.

It is known [I] that in a wedge Cano–Grandjean structure, regions with N and $N + 1$ half-pitches are separated by linear defects (χ disclination lines). We therefore also assume that the region induced by fluctuations with N +1 director half-turns is separated from the rest by a linear defect of the same type.

Consequently, we must now find the maximum of an expression of the type

$$E_f - B - E_d \sim \sqrt{(d - d_0)S} - bS - t\sqrt{S}, \qquad (10)$$

where the last term represents the energy E_d of the linear defect, proportional to its length and its energy per unit length (which we assume to be independent of the layer thickness, even if we know that it varies as $\ln(d/r_c)$, where r_c is the core radius). Expression (10) passes through a maximum at

$$S = \frac{(\sqrt{d - d_0} - t)^2}{4b^2},$$

where it is assumed that

$$\sqrt{d - d_0} > t$$

(otherwise, the fluctuation energy is insufficient for creating a linear defect). It follows from Eq. (10) that the maximal possible surface area for the fluctuation-induced $N \longrightarrow N + 1$ transition is given by

$$S_{\max} = \frac{(\sqrt{d - d_0} - t)^2}{b^2}. \qquad (11)$$

To ensure further growth of the area with the $N + 1$ configuration after the fluctuation transition, the condition

$$SF(N + 1) + K_{22}\sqrt{S} < SF(N) \qquad (12)$$

must be satisfied, assuming that the energy of the defect is on the order of K_{22} per unit length. This condition gives the minimal surface area of the fluctuation able to grow,

$$S_{\min} = \left[\frac{K_{22}}{F(N) - F(N + 1)}\right]^2, \qquad (13)$$

where the corresponding differences $F(N) - F(N + 1)$ are shown in Figs. 5 and 6 as a function of φ_{0j} (φ_j) for some values of S_d. We note that after the pitch jump to the $N + 1$ configuration, the angle φ differs from the initial angle at the jump point φ_j in the N configuration.

Finally, the condition $S_{\max} > S_{\min}$ must be satisfied for a fluctuation transition to the $N + 1$ configuration to occur in the layer.

We note that expression (12), which gives the energy gain during the $N \longrightarrow N + 1$ transition, may also be useful in describing the dynamics of defects (associated with the pitch jumps); this has not yet been studied in detail, contrary to the case with homeotropic anchoring [8]).

5. DETERMINATION OF THE PHENOMENOLOGICAL CONSTANTS

The phenomenological constants q and d_0 introduced above could in principle be found from the microscopic theory of liquid crystals. But the complexity of liquid crystals and many uncertainties in their parameters do not allow us to expect good accuracy of the corresponding calculations. A more practical way to determine them is therefore to compare the present theory with experimental measurements.

As regards d_0, it has a clear physical meaning and can be estimated quite well. It must be of the order of the penetration length K_{22}/W of the anchoring, i.e., of a micrometer order with $K_{22} = 10^{-6}$ dyn and $W = 10^{-2}$ erg/cm^2 [1]. The parameter q cannot be estimated so easily (it can be found in a nonanalytical form in the framework of the rather sophisticated approach of fluctuations in liquid crystal in restricted geometries [9]).

We now analyze what measurements could be used to extract the information about the phenomenological parameters under discussion. Keeping in mind that the coefficients in expressions (9) and (10) are related to the introduced phenomenological parameters as

$$b = \frac{B_e}{qk_BT}, \quad t = \frac{K_{22}}{qk_BT}, \qquad (14)$$

we can find their values. Indeed, in accordance with Eqs. (8) or (10) and (13), this can be done by first measuring the sample thickness at which the hysteresis in jumps of the pitch disappears and then by measuring the minimal surface area of the region where the $N \longrightarrow N + 1$ transition occurs and does not collapse (i.e., grows) at a later time. We thus obtain two relations that allow us to find the two parameters d_0 and q.

The corresponding measurements would consist of measuring the director deviation angle φ as a function of the temperature for different sample thicknesses d (or strength of the anchoring W). From these measurements, one can extract the jump angle (φ_j and the value of d (or W) at which the temperature hysteresis for jumps disappears. Another measurement could be performed at the temperature of the pitch jump and would consist in measuring the minimal surface area of the region that is subjected to the $N \longrightarrow N + 1$ transition due to the fluctuation and which begins to grow after nucleation.

6. CONCLUSIONS

The results of the previous sections show that the dependence of the temperature-induced pitch jump hysteresis on the sample thickness can be explained by taking thermal fluctuations into account. In addition, our phenomenological theory should allow us to make quantitative predictions, provided the introduced phenomenological constants are determined from experiments. In theory, it should be sufficient to determine d_0 and q in a sample of a given thickness d in order to be able to predict the angle of the pitch jump and the hysteresis value for any other values of d or the anchoring strength W. Unfortunately, the experiments performed up to now do not allow us to determine these phenomenological constants. A specially designed experiment for studying hysteresis phenomena in cholesteric layers would therefore be desirable. We can nevertheless give a rough estimate of q from the experiments described in [2]. In this work, hysteresis was observed for the layer thickness $d = 4.8$ μm and was not observed for $d = 18$ μm. If we assume that hysteresis disappears for $d = 10$ μm and the area of fluctuation S is on the order of 10^4 μm^2, the dimensionless parameter $q = 0.2$ (by taking $L_p = 1$ μm). This value looks quite reasonable, because according to [6], this quantity can be estimated as $\sqrt{C_{ve}/C_v}$, where C_v and C_{ve} are the total specific heat of the substance and the part of specific heat related to liquid crystal elasticity, respectively. It should also be mentioned that the method chosen in [2, 3] for measuring the pitch with the help of spectral optical measurements in the region of the reflection band, which are then fitted to the theoretical curves (see, e.g., [11]), gives a very precise measurement of the pitch. Other methods can also be used for the same purpose. We note that in situations where the Mauguin approximation of the cholesteric optics is valid, measurements of the rotation of the polarization plane of the light crossing the layer should give similar information about the changes of the pitch in the layer.

We finally emphasize that this work could be used as a starting point for studying the dynamics of pitch jumps in cholesteric layers.

Although the accuracy of our results is open to debate and the results are mostly based on assumptions, we believe that the proposed model for specific pitch changes demonstrates the possibility of the scenario considered in our paper, and a reasonable agreement with experimental data shows that we are on the right track.

ACKNOWLEDGMENTS

The authors are grateful for the advice of A. Muratov related to numerical calculations.

One of the authors (E.I.K.) is indebted to INTAS (grant no. 01-0105) for partial support and another author (V.A.B.) gratefully acknowledges the support from the Russian Foundation for Basic Research (project no. 03-02-16173).

REFERENCES

1. P. G. de Gennes and J. Prost, *The Physics of Liquid Crystals*, 2nd ed. (Clarendon Press, Oxford, 1993; Mir, Moscow, 1982); P. Oswald and P. Pieranski, *Les Cristaux Liquides: Concepts et Propriétés Physiques Illustrées par des Expériences* (Gordon and Breach, Paris, 2000).
2. H. Zink and V. A. Belyakov, Mol. Cryst. Liq. Cryst. **265**, 445 (1995); Pis'ma Zh. Éksp. Teor. Fiz. **63**, 50 (1996) [JETP Lett. **63**, 43 (1996)].
3. W. Kuczynski, private communication.
4. V. A. Belyakov and E. I. Kats, Zh. Éksp. Teor. Fiz. **118**, 560 (2000) [JETP **91**, 488 (2000)].
5. L. M. Blinov, E. I. Kats, and A. A. Sonin, Usp. Fiz. Nauk **152**, 449 (1987) [Sov. Phys. Usp. **30**, 604 (1987)].
6. L. D. Landau and E. M. Lifshitz, *Course of Theoretical Physics*, Vol. 5: *Statistical Physics*, 3rd ed. (Nauka, Moscow, 1976; Pergamon Press, Oxford, 1980).
7. P. O. Andreeva, V. K. Dolganov, R. Fouret, *et al.*, Phys. Rev. E **59**, 4143 (1999).
8. P. Oswald, J. Baudry, and S. Pirkl, Phys. Rep. **337**, 67 (2000).
9. A. Yu. Val'kov, V. P. Romanov, and M. V. Romanov, Zh. Éksp. Teor. Fiz. **120**, 398 (2001) [JETP **93**, 344 (2001)].
10. S. P. Palto, Zh. Éksp. Teor. Fiz. **121**, 308 (2002) [JETP **94**, 260 (2002)].
11. V. A. Belyakov, *Diffraction Optics of Complex-Structured Periodic Media* (Nauka, Moscow, 1988; Springer, New York, 1992).

Journal of Experimental and Theoretical Physics, Vol. 96, No. 5, 2003, pp. 922–931.
From Zhurnal Éksperimental'noĭ i Teoreticheskoĭ Fiziki, Vol. 123, No. 5, 2003, pp. 1048–1058.

SOLIDS
Structure

Theoretical Investigation of the Resonant Hyper-Raman Scattering by Optical Phonons¶

L. E. Semenova* and K. A. Prokhorov

Institute of General Physics, Russian Academy of Sciences, Moscow, 119991 Russia
**e-mail: semenov@sci.lebedev.ru*

Received November 1, 2002

Abstract—A theoretical model for the resonant hyper-Raman scattering in semiconductor crystals is presented. The Wannier excitons are considered as intermediate states. The expressions for the resonant hyper-Raman scattering cross section are obtained. The theoretical model developed allows taking into account different mechanisms of the exciton–photon and exciton–phonon interactions. *© 2003 MAIK "Nauka/Interperiodica".*

1. INTRODUCTION

Raman scattering (RS) is a powerful technique in the study of excitations in semiconductors and their interactions. Hyper-Raman scattering (HRS) is a nonlinear optical process where two incident photons are absorbed simultaneously and one photon of scattered light and a phonon are created [1–4]. Because HRS is a three-photon process, it has other selection rules with respect to that of Raman scattering and therefore allows us to obtain information inaccessible to RS methods.

Of special interest is resonant HRS where the energy of two incident photons or a scattered photon is close to that of electronic excitations [2, 5, 6]. In this case, HRS allows us to obtain additional information on electron–photon and electron–lattice interactions and on some parameters of electronic transitions. Resonant HRS by optical phonons was first observed in a CdS crystal where resonant conditions were provided by a temperature variation of the energy gap with a fixed frequency of the exciting radiation [7]. Recently, resonant HRS by optical phonons in cadmium sulfide was studied by means of a frequency tunable optical parametric oscillator using a KTP crystal [8]. Resonant effects in HRS were also reported in $SrTiO_3$ [9, 10], TiO_2 [11, 12], ZnSe [13, 14], and Cu_2O [15]. However, publications devoted to theoretical investigations of resonant HRS in semiconductor crystals have been very scarce up to now. Some mechanisms of HRS were theoretically studied for a CdS crystal [16–19]. In the paper by García-Cristóbal *et al.* [20], the HRS process mediated by a dipole-allowed Fröhlich interaction was analyzed in detail and the HRS efficiency was calculated with the excitonic effects taken into account.

In this paper, a theoretical model for resonant HRS by optical phonons is given for semiconductor crystals. We assume that virtual intermediate states in the scattering process are the Wannier excitons. We consider different mechanisms for the HRS in the framework of the three-band model; i.e., we also take transitions in higher lying conduction bands and from deeper valence bands into account. In Section 2, the basic formulas for the HRS cross section are given. In Section 3, expressions for the HRS tensor are derived using the Green function formalism. Section 4 is devoted to a discussion of different scattering mechanisms and their contributions to the HRS efficiency.

2. BASIC FORMULAS

From a microscopic point of view, the first-order HRS process can be described as follows: two incident photons with wave vector $\mathbf{q}_L$, frequency ω_L, and polarization $\boldsymbol{\varepsilon}_L$ are absorbed simultaneously; a phonon with the wave vector $\mathbf{q}_P$ and frequency ω_P is then created; and a scattered photon ($\mathbf{q}_S$, ω_S, $\boldsymbol{\varepsilon}_S$) is finally emitted. Using time-dependent perturbation theory, the differential cross section for one-phonon HRS can be written as [21]

$$\frac{d\sigma}{d\Omega} = \frac{\omega_S^3 \eta_S^3 \eta_L V}{4\pi^2 \hbar^2 c^4 \omega_L N_L} \sum_{\mathbf{q}_P} \left| \sum_{l_1, l_2, l_3} \frac{\langle f|\hat{H}_{ER}|l_3\rangle\langle l_3|\hat{H}_{EL}|l_2\rangle\langle l_2|\hat{H}_{ER}|l_1\rangle\langle l_1|\hat{H}_{ER}|i\rangle}{(E_{l_3} - \hbar\omega_S)(E_{l_2} - 2\hbar\omega_L)(E_{l_1} - \hbar\omega_L)} \right|^2, \quad (1)$$

¶This article was submitted by the authors in English.

1063-7761/03/9605-0922$24.00 © 2003 MAIK "Nauka/Interperiodica"

where $\hat{H}_{ER}$ and $\hat{H}_{EL}$ are the Hamiltonians of the electron–photon and electron–lattice interactions, V is the crystal volume, $N_L = n_L/V$ is the photon density of incident radiation, η_L (η_S) is the refractive index for the frequency ω_L (ω_S), $|i\rangle$ and $|f\rangle$ are the initial and final states, $|l_j\rangle$ ($j = 1, 2, 3$) are the intermediate virtual states, and E_{l_j} are the corresponding energies of the electronic system. We assume that in the initial and final states, the electronic system of a semiconductor is in the ground state, but the virtual intermediate states are the Wannier excitons.

In the dipole approximation, the matrix element for a transition from the ground state to an excitonic state is given by [22]

$$\langle n_L - 1; \mathbf{K}, \Lambda|\hat{H}_{ER}|i\rangle = \frac{(2\pi)^2 e}{m\eta_L}\sqrt{\frac{\hbar N_L}{\omega_L}}\delta(\mathbf{K} - \mathbf{q}_L)\varepsilon_\alpha^L \Pi_{\Lambda 0}^\alpha, \quad (2)$$

$$\Pi_{\Lambda 0}^\alpha = \{\pi_{cv}^\alpha - M_{cv}^{\alpha'\alpha} p_{\alpha'}\}(\chi_{cv}^\lambda(\mathbf{r}))^*\big|_{r=0}, \quad (3)$$

where $\hat{p}_a = -i\hbar\,\partial/\partial r_\alpha$, e and m are the charge and mass of the electron, π_{cv} is the interband matrix element of the momentum operator, $\chi_{cv}^\lambda(\mathbf{r})$ is the hydrogenic wave function of relative electron–hole motion, $\mathbf{K}$ is the exciton wave vector, $\Lambda = (c, v, \lambda)$ describes an exciton belonging to the valence band v and the conduction band c, and $\lambda = (\zeta, l, m)$ denotes a set of inner quantum numbers of the exciton: the principal quantum number ζ is n for the discrete spectrum or k for the continuous spectrum. In expression (3), the first term in braces describes the allowed dipole transitions to s-excitonic states. The second term corresponds to another type of the dipole transitions (weakly forbidden transitions) that cause an excitation of p-excitons [22, 23]. The parameter $M_{cv}^{\alpha'\alpha}$ is defined by [22]

$$M_{cv}^{\alpha'\alpha} = \frac{1}{m}\sum_n{}'\left[\frac{\pi_{cn}^{\alpha'}\pi_{nv}^{\alpha}}{E_c - E_n} + \frac{\pi_{cn}^{\alpha}\pi_{nv}^{\alpha'}}{E_v - E_n}\right], \quad (4)$$

where the prime on the summation indicates that the terms with vanishing denominators are omitted. The matrix element describing the transitions between excitonic states can be written as [24]

$$\langle n_L - 1; \mathbf{K}', \Lambda'|\hat{H}_{ER}|n_L; \mathbf{K}, \Lambda\rangle = \frac{e}{m\eta_L}\sqrt{\frac{2\pi\hbar N_L}{\omega_L}}\delta(\mathbf{K}' - \mathbf{K} - \mathbf{q}_L)\varepsilon_\beta^L \Pi_{\Lambda'\Lambda}^\beta, \quad (5)$$

$$\Pi_{\Lambda'\Lambda}^\beta = (\pi_{c'c}^\beta \delta_{v'v} - \pi_{v'v}^\beta \delta_{c'c})\langle\chi_{c'v'}^{\lambda'}|\chi_{cv}^\lambda\rangle + \delta_{c'c}\delta_{v'v}(M_{c'c}^{\beta'\beta} - M_{v'v}^{\beta'\beta})\langle\chi_{c'v'}^{\lambda'}|\hat{p}_{\beta'}|\chi_{cv}^\lambda\rangle. \quad (6)$$

In expression (6), the first term corresponds to the transitions between excitonic states belonging to different pairs of bands (interband transitions), whereas the second term describes the intraband dipole transitions between excitonic states.

It is known that there are two types of electron–lattice interactions [25]. This is the deformation potential interaction, which is due to scattering of electrons by perturbations of a periodic potential caused by the displacement of atoms of the lattice. For longitudinal optical (LO) phonons, the deformation potential interaction is supplemented by the Fröhlich interaction due to the electric field associated with these phonons. In the general case, the matrix element of the exciton–lattice interaction can be written as [26]

$$\langle n_P + 1; \mathbf{K}', \Lambda'|\hat{H}_{EL}|n_P; \mathbf{K}, \Lambda\rangle = \frac{\gamma\sqrt{n_P + 1}}{\sqrt{V}}\delta(\mathbf{K}' + \mathbf{q}_P - \mathbf{K})P_{\Lambda'\Lambda}, \quad (7)$$

$$P_{\Lambda'\Lambda} = \langle\chi_{c'v'}^{\lambda'}|\hat{P}|\chi_{cv}^\lambda\rangle = \langle\chi_{c'v'}^\lambda|\Theta_{c'c}\delta_{vv'}\exp(-i\alpha_e\mathbf{q}_P\cdot\mathbf{r}) - \Theta_{vv'}\delta_{cc'}\exp(i\alpha_h\mathbf{q}_P\cdot\mathbf{r})|\chi_{cv}^\lambda\rangle, \quad (8)$$

where n_P is the phonon number. For the deformation potential interaction in a crystal with two atoms per unit cell,

$$\Theta_{n'n} = \Xi_{n'n} \quad (9)$$

and

$$\gamma = \gamma_D = \sqrt{\frac{\hbar\Omega}{2\omega_P d^2 M^*}}, \quad (10)$$

where Ω is the cell volume, M^* is the reduced mass of atoms in the cell, d is the lattice constant [25, 26], and $\Xi_{n'n}$ is the deformation potential defined by Bir and Pikus [27]. For the Fröhlich interaction, $\Theta_{n'n}$ and γ are given by

$$\Theta_{n'n} = \hat{q}_j r_{n'n}^j(1 - \delta_{n'n}) + iq_P^{-1}\delta_{n'n} \quad (11)$$

and

$$\gamma = \gamma_F = \sqrt{2\pi\hbar\omega_P e^2\left(\frac{1}{\varepsilon_\infty} - \frac{1}{\varepsilon_0}\right)}, \quad (12)$$

where $\hat{\mathbf{q}}$ is the unit vector in the direction of $\mathbf{q}_P$, and ε_∞ and ε_0 are the optical and static dielectric constants,

respectively [26]. The parameter $\alpha_{e(h)}$ is determined by $\alpha_{e(h)} = m^*_{h(e)}/(m^*_e + m^*_h)$, where m^*_e and m^*_h are the effective masses of electrons and holes.

After the substitution of (2), (5), and (7) into expression (1), the HRS cross section becomes

$$\frac{d\sigma}{d\Omega} = \frac{2\pi\hbar e^6 \eta_S \omega_S^2 (n_P + 1)}{m^6 c^4 \eta_L^3 \omega_L^3} \times N_L V \left|\varepsilon_\gamma^S \varepsilon_\beta^L \varepsilon_\alpha^L \beta_{\alpha\beta\gamma}(2\mathbf{q}_L - \mathbf{q}_S)\right|^2, \quad (13)$$

where the HRS tensor $\beta_{\alpha\beta\gamma}(\mathbf{q})$ is given by

$$\beta_{\alpha\beta\gamma}(\mathbf{q}) = \gamma \sum_{\Lambda_1,\Lambda_2,\Lambda_3} \frac{\Pi^\gamma_{0\Lambda_3} P_{\Lambda_3\Lambda_2} \Pi^\beta_{\Lambda_2\Lambda_1} \Pi^\alpha_{\Lambda_1 0}}{[E_{\Lambda_3}(\mathbf{q}_S) - \hbar\omega_S][E_{\Lambda_2}(2\mathbf{q}_L) - 2\hbar\omega_L][E_{\Lambda_1}(\mathbf{q}_L) - \hbar\omega_L]}. \quad (14)$$

Here, the exciton energy is

$$E_\Lambda(\mathbf{q}) = E_{cv} + \frac{\hbar^2 q^2}{2M} + \Delta E_\lambda, \quad (15)$$

where $M = m^*_e + m^*_h$, E_{cv} is the energy gap, and $\Delta E_\lambda = \Delta E_\zeta$ is the energy associated with the relative motion of the electron and the hole (i.e., $\Delta E_n = -R/n^2$ or $\Delta E_k = Rk^2$, where R is the Rydberg constant of an exciton). Because the photon wave vector is small, we assume that $E_\Lambda(\mathbf{q}) = E_\Lambda(0)$ in what follows.

3. THEORETICAL MODEL

3.1. Scattering Mechanisms

We consider the resonant HRS process, i.e., the process where the double frequency of the exciting radiation is close to the energy gap E_{cv}. If only the dipole-allowed transitions are taken into account, the absorption of the incident photon leads to the excitation of an *s*-excitonic state, while another photon induces an intraband transition to a *p*-exciton or an interband transition to an *s*-exciton belonging to the higher lying conduction band or the lower valence band. In case of the resonant HRS, where $2\hbar\omega_L \sim E_{cv}$, the two-photon transition to a *p*-exciton is of interest. It is known that for first-order HRS, the phonon wave vector is small and the scattering process can be considered in the Brillouin zone center. In the approximation of the zero wave vector of the phonon, the intraband Fröhlich interaction reduces to

$$P_{\Lambda'\Lambda} \approx \delta_{c'c}\delta_{vv'} \langle \chi^{\lambda'}_{c'v'} | \hat{\mathbf{q}} \cdot \mathbf{r} | \chi^{\lambda}_{cv} \rangle \quad (16)$$

and therefore leads to transitions between the *s*- and *p*-excitonic states. When $q_P \approx 0$, the corresponding matrix elements of the deformation potential and interband Fröhlich interactions are given by

$$P_{\Lambda'\Lambda} \approx \{\Theta_{c'c}\delta_{vv'} - \Theta_{vv'}\delta_{cc'}\} \langle \chi^{\lambda'}_{c'v'} | \chi^{\lambda}_{cv} \rangle \quad (17)$$

and therefore connect states with the same parity. Thus, in the HRS process considered, the deformation potential or interband Fröhlich interaction leads to the transition to a *p*-exciton, but the intraband Fröhlich coupling causes the transition to an *s*-state. Because the transition from the *p*-excitonic state to the ground state is weakly forbidden, the intraband Fröhlich mechanism plays the leading role in the scattering. The corresponding HRS tensor is therefore given by

$$\beta^{(1)}_{\alpha\beta\gamma}(\mathbf{q}) = \gamma \pi^\gamma_{vc} \pi^\alpha_{cv} [M^{\beta'\beta}_{cc} - M^{\beta'\beta}_{vv}] \sum_{\lambda_3,\lambda_2,\lambda_1} \frac{\chi^{\lambda_3}_{cv}(0) \langle \chi^{\lambda_3}_{cv} | \hat{P} | \chi^{\lambda_2}_{cv} \rangle \langle \chi^{\lambda_2}_{cv} | \hat{p}_{\beta'} | \chi^{\lambda_1}_{cv} \rangle (\chi^{\lambda_1}_{cv}(0))^*}{(E_{cv} + \Delta E_{\lambda_3} - \hbar\omega_S)(E_{cv} + \Delta E_{\lambda_2} - 2\hbar\omega_L)(E_{cv} + \Delta E_{\lambda_1} - \hbar\omega_L)}. \quad (18)$$

If HRS is considered in the framework of the three-band model and the weakly forbidden dipole transitions to the *p*-excitons belonging to the highest valence band v and the lowest conduction band c are taken into account, we can also identify two other scattering mechanisms including two-photon transitions to *s*-excitonic states. The exciton–lattice interaction then causes the transition to a *p*-exciton belonging to the same pair of bands (the intraband Fröhlich coupling) or induces interband transition to another *s*-excitonic state (the deformation potential or interband Fröhlich interaction). The corresponding HRS tensors $\beta^{(2)}_{\alpha\beta\gamma}(\mathbf{q})$ and $\beta^{(3)}_{\alpha\beta\gamma}(\mathbf{q})$ are given by

$$\beta^{(2)}_{\alpha\beta\gamma}(\mathbf{q}) = \gamma \sum_{\lambda_3, \lambda_2} \frac{M^{\gamma'\gamma *}_{cv} \hat{p}_{\gamma'} \chi^{\lambda_3}_{cv}(\mathbf{r})\big|_{r=0} \langle \chi^{\lambda_3}_{cv} | \hat{P} | \chi^{\lambda_2}_{cv} \rangle A_{\alpha\beta}(\lambda_2, \omega_L)}{(E_{cv} + \Delta E_{\lambda_3} - \hbar\omega_S)(E_{cv} + \Delta E_{\lambda_2} - 2\hbar\omega_L)} \tag{19}$$

and

$$\beta^{(3)}_{\alpha\beta\gamma}(\mathbf{q}) = \gamma \sum_{c'', v''} \sum_{\lambda_3, \lambda_2} \frac{\pi^{\gamma}_{v''c''} \chi^{\lambda_3}_{c''v''}(0) \langle \chi^{\lambda_3}_{c''v''} | \hat{P} | \chi^{\lambda_2}_{cv} \rangle A_{\alpha\beta}(\lambda_2, \omega_L)}{(E_{c''v''} + \Delta E_{\lambda_3} - \hbar\omega_S)(E_{cv} + \Delta E_{\lambda_2} - 2\hbar\omega_L)}, \tag{20}$$

where $A_{\alpha\beta}(\lambda_2, \omega_L)$ describes the two-photon transition to the *s*-excitonic state,

$$A_{\alpha\beta}(\lambda_2, \omega) = (M^{\beta'\beta}_{cc} - M^{\beta'\beta}_{vv})(-M^{\alpha'\alpha}_{cv}) \times \sum_{\lambda_1} \frac{\langle \chi^{\lambda_2}_{cv} | \hat{p}_{\beta'} | \chi^{\lambda_1}_{cv} \rangle \hat{p}_{\alpha'} (\chi^{\lambda_1}_{cv}(\mathbf{r}))^* \big|_{r=0}}{E_{cv} + \Delta E_{\lambda_1} - \hbar\omega} + \sum_{c', v'} (\pi^{\beta}_{cc'} \delta_{vv'} - \pi^{\beta}_{v'v} \delta_{cc'}) \pi^{\alpha}_{c'v'} \sum_{\lambda_1} \frac{\langle \chi^{\lambda_2}_{cv} | \chi^{\lambda_1}_{c'v'} \rangle (\chi^{\lambda_1}_{c'v'}(0))^*}{E_{c'v'} + \Delta E_{\lambda_1} - \hbar\omega}. \tag{21}$$

The first term in (21) describes the two-photon excitation of the *s*-exciton in the framework of the two-band model where the absorption of the first photon is accompanied by the weakly forbidden transition to a *p*-excitonic state. The intraband dipole transition to the *s*-excitonic state occurs when the second photon is absorbed. The second term in (21) describes the contribution of the three-band model where the intermediate state is assumed to be an *s*-exciton composed of an electron from some higher lying conduction band *c*' and a hole from the valence band *v*, or an exciton belonging to the conduction band *c* and a deeper valence band *v*'. In this case, the second photon induces the interband transition of the electron or the hole.

3.2. The Green Function Approach

To evaluate the HRS tensors obtained, it is necessary to calculate the matrix elements and the sums over all the intermediate discrete and continuous excitonic states. The problem can be considerably simplified using the Green function method [28]. This approach was earlier used in theoretical investigation of two-photon absorption [24, 29] and first-order resonant RS [26]. We have also applied the Green functions for a theoretical treatment of two-photon resonant RS [30, 31]. In accordance with this method, the sums over intermediate states can be expressed as Whittaker functions $W_{\kappa, \mu}(z)$ [28, 29],

$$\sum_{\lambda} \frac{\chi^{\lambda}_{cv}(\mathbf{r})(\chi^{\lambda}_{cv}(0))^*}{E_{cv} + \Delta E_{\lambda} - \hbar\omega_L} = \frac{\mu\Gamma(1-\kappa_L)}{2\pi\hbar^2 r} W_{\kappa_L, 1/2}\left(\frac{2r}{\kappa_L a}\right) \tag{22}$$

and

$$\frac{\partial}{\partial r'_j} \sum_{\lambda} \frac{\chi^{\lambda}_{cv}(\mathbf{r})(\chi^{\lambda}_{cv}(\mathbf{r}'))^*}{E_{cv} + \Delta E_{\lambda} - \hbar\omega_L}\bigg|_{r'=0} = \frac{\mu\Gamma(2-\kappa_L)}{2\pi\hbar^2 \kappa_L a} \frac{r_j}{r^2} W_{\kappa_L, 3/2}\left(\frac{2r}{\kappa_L a}\right), \tag{23}$$

where $\Gamma(z)$ is the gamma function and a and μ are the Bohr radius and the reduced mass of the exciton. The parameter κ_L is defined as $\kappa_L = \sqrt{R/(E_{cv} - \hbar\omega_L)}$. Hereafter, the respective indices "*L*" and "*S*" correspond to the incident and scattered light. The Whittaker function has the integral representation [32]:

$$W_{\kappa, \mu}(z) = \frac{z^{\mu + 1/2} e^{-z/2}}{\Gamma(1/2 - \kappa + \mu)} \times \int_0^{\infty} e^{-zt} t^{-1/2 - \kappa + \mu} (1+t)^{-1/2 + \kappa + \mu} dt, \quad \mathrm{Re}(\mu - \kappa) > -\frac{1}{2}. \tag{24}$$

Because the frequency of the incident radiation is away from the excitonic resonance for the resonant HRS ($\kappa_L \ll 1$), the Green function approach enables us to reduce the sum over λ_1 to the integral. Further, after the substitution of explicit expressions for the hydrogenic wave function [33] and the **r** integration, the sums over the intermediate states λ_1 can be calculated. Taking the results obtained in [24, 29] into account, we write

$$\sum_{\lambda'} \frac{\langle \chi^{(\zeta 1m)}_{cv} | \hat{p}_j | \chi^{\lambda'}_{cv} \rangle (\chi^{\lambda'}_{cv}(0))^*}{E_{cv} + \Delta E_{\lambda'} - \hbar\omega_L} = (\hat{p}_j \chi^{(\zeta 1m)}_{cv}(\mathbf{r})\big|_{r=0})^* \kappa_L^2 R^{-1} \begin{cases} J_4(n, \kappa_L), & \zeta = n, \\ J_4(i/k, \kappa_L), & \zeta = k \end{cases} \tag{25}$$

and

$$A_{\alpha\beta}(\lambda, \omega_L) = (\chi^{\lambda}_{cv}(0))^* \begin{cases} B_{\alpha\beta}(n, \omega_L), & \zeta = n, \\ B_{\alpha\beta}(i/k, \omega_L), & \zeta = k, \end{cases} \quad (26)$$

where [34]

$$B_{\alpha\beta}(n, \omega_L) = \mu M^{\alpha'\alpha}_{cv}(M^{\beta'\beta}_{cc} - M^{\beta'\beta}_{vv})\delta_{\alpha'\beta'}J_2(n, \kappa_L) + \sum_{c', v'} \frac{(\pi^{\beta}_{cc'}\delta_{vv'} - \pi^{\beta}_{v'v}\delta_{cc'})\pi^{\alpha}_{c'v'}}{E_{c'v'} - \hbar\omega_L} J_1(n, \kappa'_L). \quad (27)$$

Here, κ'_L is defined for $E_{c'v'}$: $\kappa'_L = \sqrt{R'/(E_{c'v'} - \hbar\omega_L)}$. The integrals $J_1(n, \kappa')$, $J_2(n, \kappa)$, and $J_4(n, \kappa)$ are given in [24, 29],

$$J_1(n, \kappa') = 4\int_0^{\infty} dt \left(\frac{1+t}{t}\right)^{\kappa'} \left(\frac{2t+1-\kappa'/nb}{2t+1+\kappa'/nb}\right)^n \times \frac{2t+1-\kappa'/b}{[(2t+1)^2 - (\kappa'/nb)]^2}, \quad (28)$$

$$J_2(n, \kappa) = \frac{16}{3}\kappa\int_0^{\infty} dt t^{1-\kappa}(1+t)^{1+\kappa}\left(\frac{2t+1-\kappa/n}{2t+1+\kappa/n}\right)^n \times \frac{3(2t+1)^2 + 3(\kappa/n)^2 - 2\kappa(2t+1)(1+2n^{-2})}{[(2t+1)^2 - (\kappa/n)^2]^3}, \quad (29)$$

$$J_4(n, \kappa) = 4\int_0^{\infty} dt \left(\frac{t+1}{t}\right)^{\kappa}\left(\frac{2t+1-\kappa/n}{2t+1+\kappa/n}\right)^n \times \frac{2t+1}{[(2t+1)^2 - (\kappa/n)^2]^2}, \quad (30)$$

where $b = a/a'$ (R' and a' are the Rydberg constant and the Bohr radius of the exciton belonging to the pair of bands, c' and v').

When the energy of the scattered photon is below the excitonic resonances ($\kappa_S < 1$), we can also apply the Green functions to calculate the sums over λ_3 in expressions (18) and (20). In works devoted to second-order resonant RS, we calculated the sums over λ_3 similar to the ones in expressions (18) and (20) for the intraband Fröhlich interaction [30, 31]. In the general case, taking the results obtained in [30] into account, we can write

$$\sum_{\lambda_3} \frac{\chi^{\lambda_3}_{c'v'}(0)\langle \chi^{\lambda_3}_{c'v'}|\hat{P}|\chi^{(\zeta lm)}_{cv}\rangle}{E_{c'v'} + \Delta E_{\lambda_3} - \hbar\omega_S} = \frac{Y_{lm}(\vartheta_q, \varphi_q)\kappa'^2_S}{(2l+1)!\sqrt{a}(E_{c'v'} - \hbar\omega_S)} \begin{cases} \frac{2^{l+2}}{n^{l+2}}\sqrt{\frac{(n+l)!}{(n-l-1)!}} J^{(\Theta)}_l(qa, \kappa'_S, n), & \zeta = n, \\ \sqrt{\frac{a^3}{V}} 2^{l+2}k^{l+1}e^{\pi/2k}\left|\Gamma\left(l+1-\frac{i}{k}\right)\right| J^{(\Theta)}_l\left(qa, \kappa'_S, \frac{i}{k}\right), & \zeta = k, \end{cases} \quad (31)$$

where

$$J^{(\Theta)}_l(Q, \kappa', n) = \frac{i^l}{a}\left\{(-1)^l\Theta_{c'c}\delta_{vv'}\frac{I^{(\Theta)}_l(\alpha_e Q, \kappa', n)}{(\alpha_e Q)^{l+1}} - \Theta_{vv'}\delta_{cc'}\frac{I^{(\Theta)}_l(\alpha_h Q, \kappa', n)}{(\alpha_h Q)^{l+1}}\right\}, \quad (32)$$

$Q = qa$, $Y_{lm}(\vartheta_q, \varphi_q)$ is a spherical function of the angular coordinates of the phonon wave vector. The integral $I^{(\Theta)}_l(Q, \kappa', n)$ is given by

$$I^{(\Theta)}_l(\theta, \kappa', n) = \frac{b}{2^{l+2}\kappa'^3}\int_0^{\infty} dt\left(\frac{1+t}{t}\right)^{\kappa'} \sum_{v=0}^{l} \frac{(l+v)!(l+1-v)!}{v!}\left(\frac{\kappa' Q}{b}\right)^{l-v} \times \mathrm{Re}\left\{(-i)^{l-v+1}\left(t + \frac{1}{2} + \frac{\kappa'}{2nb} - i\frac{\kappa' Q}{2b}\right)^{v-l-2} F\left(-n+l+1, l-v-2; 2l+2; \frac{\kappa'/nb}{t+\frac{1}{2}+\frac{\kappa'}{2nb} - i\frac{\kappa' Q}{2b}}\right)\right\}, \quad (33)$$

where $F(a, b; c; z)$ is the hypergeometric function.

To calculate the sum over λ_3 in expression (19), we applied the method previously used by us in [30, 31] and obtained the expression (for the intraband Fröhlich interaction and $\kappa_S < 2$)

$$\sum_{\lambda_3}\hat{p}_\gamma\chi_{cv}^{\lambda_3}(\mathbf{r})\big|_{r=0}\frac{\langle\chi_{cv}^{\lambda_3}|\hat{P}|\chi_{cv}^{(\zeta 00)}\rangle}{E_{cv}+\Delta E_{\lambda_3}-\hbar\omega_S} = \frac{-i\hbar\hat{q}_\gamma}{E_{cv}-\hbar\omega_S} \times\chi_{cv}^{(\zeta 00)}(0)\begin{cases}\mathrm{Jp}(qa,\kappa_S,n), & \zeta = n,\\ \mathrm{Jp}(qa,\kappa_S,i/k), & \zeta = k,\end{cases} \quad (34)$$

where

$$\mathrm{Jp}(Q,\kappa,n) = \frac{1}{Q}\left[\frac{\mathrm{Ip}(\alpha_e Q,\kappa,n)}{(\alpha_e Q)^2}+\frac{\mathrm{Ip}(\alpha_h Q,\kappa,n)}{(\alpha_h Q)^2}\right] \quad (35)$$

and

$$\mathrm{Ip}(Q,\kappa,n) = \frac{1}{\kappa^3}\int_0^\infty dt t^{1-\kappa}(1+t)^{1+\kappa} \times\left\{\mathrm{Im}\left[\frac{\left(t+\frac{1}{2}-\frac{\kappa}{2n}-i\frac{\kappa Q}{2}\right)^{n-1}}{\left(t+\frac{1}{2}+\frac{\kappa}{2n}-i\frac{\kappa Q}{2}\right)^{n+1}}\right]\right. \quad (36)$$

$$\left.-\kappa Q\mathrm{Re}\left[\frac{\left(t+\frac{1}{2}-\frac{\kappa}{2n}-i\frac{\kappa Q}{2}\right)^{n-2}}{\left(t+\frac{1}{2}+\frac{\kappa}{2n}-i\frac{\kappa Q}{2}\right)^{n+2}}\left(t+\frac{1}{2}-\frac{\kappa}{2}-i\frac{\kappa Q}{2}\right)\right]\right\}.$$

Next, after the substitution of the relations obtained for the sums over λ_3 and λ_1 into expressions (18)–(20), we have

$$\beta_{\alpha\beta\gamma}^{(1)}(\mathbf{q}) = i\frac{2\hbar\gamma_F\pi_{vc}^{\gamma}\pi_{cv}^{\alpha}(M_{cc}^{\beta'\beta}-M_{vv}^{\beta'\beta})\hat{q}_j\delta_{j\beta'}}{3\pi R^3a^3} \times\kappa_L^2\kappa_S^4\left\{\sum_{n=2}^\infty\frac{n^2-1}{n^5}\frac{J_1^F(qa,\kappa_S,n)J_4(n,\kappa_L)}{\xi(\omega_L)-n^{-2}-i\gamma_n}\right. \quad (37)$$

$$\left.+\int_0^\infty\frac{dkk(1+k^2)}{1-e^{-2\pi/k}}\frac{J_1^F(qa,\kappa_S,i/k)J_4(i/k,\kappa_L)}{\xi(\omega_L)+k^2-i\gamma_k}\right\},$$

$$\beta_{\alpha\beta\gamma}^{(2)}(\mathbf{q}) = -i\frac{\hbar\gamma_F M_{cv}^{\gamma'\gamma^*}\hat{q}_j\delta_{j\gamma'}}{\pi R^2a^3}\kappa_S^2 \times\left\{\sum_{n=1}^\infty\frac{1}{n^3}\frac{\mathrm{Jp}(qa,\kappa_S,n)}{\xi(\omega_L)-n^{-2}-i\gamma_n}B_{\alpha\beta}(n,\omega_L)\right. \quad (38)$$

$$\left.+\int_0^\infty\frac{dkk}{1-e^{-2\pi/k}}\frac{\mathrm{Jp}(qa,\kappa_S,i/k)}{\xi(\omega_L)+k^2-i\gamma_k}B_{\alpha\beta}\left(\frac{i}{k},\omega_L\right)\right\},$$

and

$$\beta_{\alpha\beta\gamma}^{(3)}(\mathbf{q}) = \frac{2\gamma}{\pi Ra^2}\sum_{c'',v''}\frac{\pi_{v''c''}^{\gamma}\kappa_S''^2}{E_{c''v''}-\hbar\omega_S} \times\left\{\sum_{n=1}^\infty\frac{1}{n^3}\frac{J_0^{(\Theta)}(qa,\kappa_S'',n)}{\xi(\omega_L)-n^{-2}-i\gamma_n}B_{\alpha\beta}(n,\omega_L)\right. \quad (39)$$

$$\left.+\int_0^\infty\frac{dkk}{1-e^{-2\pi/k}}\frac{J_0^{(\Theta)}(qa,\kappa_S'',i/k)}{\xi(\omega_L)+k^2-i\gamma_k}B_{\alpha\beta}\left(\frac{i}{k},\omega_L\right)\right\},$$

where $\xi(\omega) = (E_{cv}-2\hbar\omega)/R$, $\gamma_n = \Gamma_n/R$, Γ_n is an exciton damping, and $J_l^F(Q,\kappa,n)$ is the integral $J_l^{(\Theta)}(Q,\kappa,n)$ defined for the intraband Fröhlich interaction, i.e., for $\Theta_{nn'} = iq^{-1}\delta_{nn'}$.

We note that the expressions obtained for the HRS tensors can be simplified. As mentioned above, in the case of resonant HRS, the energy of the incident photon is far from the resonance ($E_{cv}-\hbar\omega_L \gg R$) and the parameters κ_L and κ_L' are therefore considerably smaller than unity. Further, it is not difficult to show that $J_1(n,\kappa), J_4(n,\kappa) \approx [1-(\kappa/n)^2]^{-1}$ for $\kappa \ll 1$.

We note that expression (37) obtained via the Green function method is applicable for the computation of the resonant HRS cross section only if the scattered frequency is below excitonic resonances, i.e., for $\hbar\omega_S < E_{cv}-R$ ($\kappa_S < 1$). As a result of using the Green functions for the summation over λ_3, expressions (38) and (39) can be used only when $\kappa_S < 2$ and $\kappa_S' < 1$. For higher frequencies of incident radiation, the exciton–lattice matrix elements must be calculated and summation over all the intermediate excitonic states λ_2 and λ_3 must be performed. This approach was used by Garsía-Cristóbal *et al.* [20] to calculate the efficiency of HRS induced by the two-photon excitation of a *p*-exciton followed by the transition to an *s*-exciton due to the Fröhlich interaction. We therefore do not consider this case here. Although the expression obtained using the Green function method has a limited applicability range with respect to the photon energy, this method

considerably simplifies cumbersome computations of the HRS cross section and at the same time enables one to take all the intermediate discrete and continuous excitonic states into account. Moreover, because the phonon wave vector is small, an approximation of the above expressions can be obtained. In [30, 31, 35], it was shown that $J_l^F(Q, \kappa, n)$ weakly depends on Q for $\kappa Q \ll 1$ and in the limit as $Q \longrightarrow 0$ coincides with [8, 16]

$$J_5(n, \kappa) = 4\int_0^\infty dt\left(\frac{t+1}{t}\right)^\kappa\left(\frac{2t+1-\kappa/n}{2t+1+\kappa/n}\right)^n \times \frac{4t+2-\kappa}{[(2t+1)^2-(\kappa/n)^2]^3}. \quad (40)$$

It can also be shown that as $\kappa Q \longrightarrow 0$, $Jp(Q, \kappa, n) \longrightarrow J_3(n, \kappa)$, where [16, 18]

$$J_3(n, \kappa) = \frac{2^5}{3}\int_0^\infty dt t^{1-\kappa}(1+t)^{1+\kappa}\left(\frac{2t+1-\kappa/n}{2t+1+\kappa/n}\right)^n \times \frac{3(2t+1-\kappa)[(2t+1)^2+(\kappa/n)^2-2\kappa(2t+1)]-\kappa^3(1-n^{-2})}{[(2t+1)^2-(\kappa/n)^2]^4}. \quad (41)$$

Expanding $I_0^{(\Theta)}(Q, \kappa, n)$ in a series in Q, we have

$$J_0^{(\Theta)}(Q, \kappa', n) \approx \frac{1}{2\kappa'^2 a}(\Theta_{c'c}\delta_{vv'} - \Theta_{vv'}\delta_{cc'})J_1(n, \kappa') \quad (42)$$

for $Q \ll 1$. Thus, the approximation of the zero wave vector of the phonon allows us to considerably simplify the computations. In addition, the phonon energy is often greater than the exciton Rydberg, $\hbar\omega_p > R$, and the expressions obtained via the Green function approach can therefore be applicable in a sufficiently wide frequency range.

4. DISCUSSION

In the general case, different mechanisms of electron–photon and electron–phonon interactions can be involved in the resonant HRS process. Their contributions depend on the electronic structure and parameters of the crystal, the incident frequency, the selection rules, and the scattering geometry. Specifically, if the one-photon dipole transition is allowed ($\pi_{cv} \neq 0$) and the two-photon transition is forbidden in the semiconductor, the HRS process is described by the tensor $\beta^{(1)}_{\alpha\beta\gamma}(\mathbf{q})$ corresponding to the intraband Fröhlich scattering. Therefore, the LO lines are dominant in the resonant HRS spectra.

For the crystal with the dipole-forbidden transition ($\pi_{cv} = 0$), the resonant HRS process can be caused by the two-photon excitation of an *s*-exciton. This "forbidden" HRS is described by the tensors $\beta^{(2)}_{\alpha\beta\gamma}(\mathbf{q})$ and $\beta^{(3)}_{\alpha\beta\gamma}(\mathbf{q})$, and therefore, both the Fröhlich and deformation potential scattering mechanisms are involved in the resonant HRS process. Consequently, the effect of the deformation potential interaction in the hyper-Raman spectra can be expected in this case. Such a forbidden resonant HRS near the energy gap was experimentally investigated in Ti_2O, which is a centrosymmetric crystal [11, 12]. Because its lowest conduction and top valence bands have the same parity, the interband dipole transition is strictly forbidden in it. In rutile, Watanabe *et al.* [11, 12] observed resonant HRS by transverse optical (TO) phonons along with scattering by LO phonons.

At first sight, the forbidden resonant HRS under consideration is similar to the resonant RS in which the one-photon interband transition is replaced by a two-photon transition. As mentioned above, both the two-band and three-band models contribute to the two-photon excitation of an *s*-exciton. The parameter $M^{\alpha\alpha}_{cv}$ in expression (27) can be written as

$$M^{\alpha\alpha}_{cv} = -\frac{2}{m}\sum_{c', v'}\frac{(\pi^\alpha_{cc'}s_{c'c}\delta_{vv'} - \pi^\alpha_{v'v}s_{vv'}\delta_{cc'})\pi^\alpha_{c'v'}}{E_{c'v'}}, \quad (43)$$

where $s_{nn'} = 1 + E_{cv}/2E_{nn'}$. Taking into account that $M_{cc} - M_{vv} = m/\mu$, it is easy to show that the difference of the two-band and three-band contributions is contained in the expression for $B_{\alpha\alpha}(n, \omega_L)$. In particular, $B_{\alpha\alpha}(n, \omega_L)$ can be approximated by

$$B_{\alpha\alpha}(n, \omega_L) \approx \sum_{c', v'}\frac{(\pi_{cc'}\delta_{vv'} - \pi_{v'v}\delta_{cc'})\pi_{c'v'}}{E_{c'v'}} \times [J_1(n, \kappa'_L) - 2J_2(n, \kappa_L)] \quad (44)$$

for $E_{c'c}, E_{vv} \gg E_{cv}$. Owing to this, the resonance profile of HRS can contain additional features caused by the interference of dissimilar transitions. Their appearance is governed by the semiconductor parameters and the exciton–lattice interaction mechanism.

HRS is of special interest if one-photon and two-photon transitions are allowed in a crystal. In this case, the scattering mechanisms described by $\beta^{(1)}_{\alpha\beta\gamma}(\mathbf{q})$, $\beta^{(2)}_{\alpha\beta\gamma}(\mathbf{q})$, and $\beta^{(3)}_{\alpha\beta\gamma}(\mathbf{q})$ are involved in the hyper-Raman process. It is obvious that the "allowed" HRS mechanism, which is determined by $\beta^{(1)}_{\alpha\beta\gamma}(\mathbf{q})$, gives the main contribution to the HRS intensity because it assumes only the dipole-allowed transitions and is described in the framework of the two-band model, as distinct from $\beta^{(2)}_{\alpha\beta\gamma}(\mathbf{q})$ and $\beta^{(3)}_{\alpha\beta\gamma}(\mathbf{q})$. This conclusion agrees with experimental results because only resonant HRS by LO phonons was reported in CdS and ZnSe crystals [8, 13, 14]. The forbidden scattering mechanisms should not be neglected, however.

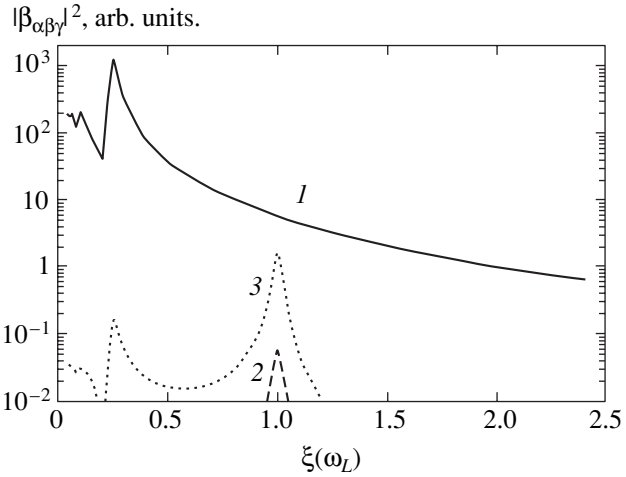

The contributions of three scattering mechanisms, $\left|\beta^{(1)}_{\alpha\beta\gamma}(\mathbf{q})\right|^2$, $\left|\beta^{(2)}_{\alpha\beta\gamma}(\mathbf{q})\right|^2$, and $\left|\beta^{(F)}_{\alpha\beta\gamma}(\mathbf{q})\right|^2$, to HRS as a function of the parameter $\xi(\omega_L) = (E_{cv} - 2\hbar\omega_L)/R$ (curves *1*, *2*, and *3*, respectively).

Because the forbidden resonant HRS is due to the two-photon transition to *s*-excitonic states, the resonant enhancement for this scattering mechanism occurs when the doubled energy of the incident photons, $2\hbar\omega_L$, coincides with the energy level of the 1*s* exciton, E_{1s}. On the other hand, a resonant increase of the allowed HRS occurs for other frequencies of the incident radiation ($2\hbar\omega_L \approx E_{2p}$), i.e., the resonance sets earlier for the forbidden HRS rather than for the allowed scattering. In addition, a new scattering mechanism can be involved in the hyper-Raman process and can contribute to the HRS intensity. It is known that the intensive forbidden LO line was observed in the RS spectra for some semiconductors when the incident frequency was near the excitonic resonance [36, 37]. Its appearance was explained by the forbidden Fröhlich interaction that corresponds to the second term in the expansion of the intraband Fröhlich coupling matrix element,

$$P_{\Lambda'\Lambda} \approx \langle \chi^{\lambda'}_{cv} | \hat{\mathbf{q}} \cdot \mathbf{r} | \chi^{\lambda}_{cv} \rangle + \frac{i}{2q_P} \frac{m_e^* - m_h^*}{m_e^* + m_h^*} \langle \chi^{\lambda'}_{cv} | (\mathbf{q}_P \cdot \mathbf{r})^2 | \chi^{\lambda}_{cv} \rangle, \quad (45)$$

and induces transitions between *s*-excitons. For resonant HRS, a similar scattering mechanism is accompanied by the following sequence of processes: two-photon transition to an *s*-excitonic state, intraband transition between *s*-excitons due to the Fröhlich interaction, and the return of the electronic system to the ground state. The corresponding tensor $\beta^{(F)}_{\alpha\beta\gamma}(\mathbf{q})$ coincides with $\beta^{(3)}_{\alpha\beta\gamma}(\mathbf{q})$ for $\Theta_{n'n} = iq^{-1}\delta_{n'n}$. The estimations performed show that for $2\hbar\omega_L \approx E_{1s}$, the contributions of the allowed and forbidden scattering mechanisms, $\beta^{(1)}_{\alpha\beta\gamma}(\mathbf{q})$ and $\beta^{(F)}_{\alpha\beta\gamma}(\mathbf{q})$, can be comparable, providing there are substantially different effective masses m_h^* and m_e^* and a small magnitude of γ_{1s}. As an example, the figure shows the result of the computation of the hyper-Raman tensors $\left|\beta^{(1)}_{\alpha\beta\gamma}(\mathbf{q})\right|^2$, $\left|\beta^{(2)}_{\alpha\beta\gamma}(\mathbf{q})\right|^2$, and $\left|\beta^{(F)}_{\alpha\beta\gamma}(\mathbf{q})\right|^2$ for $qa = 0.15$, $m_e^*/m_h^* = 0.2$, $|\pi_{cv}| \approx \hbar/d$, $d = 5$ Å, $R = 0.03$ eV, $E_{cv} = 100R$, $\hbar\omega_P = 1.5R$, and $\Gamma = 0.02R$. In the calculation, the virtual transition in the one higher lying conduction band c' ($E_{c'c} = 1.5E_{cv}$) was only taken into account in expression (28). It can be seen from the figure that $\left|\beta^{(F)}_{\alpha\beta\gamma}(\mathbf{q})\right|^2$ sharply increases as the doubled frequency approaches two-photon resonance with the 1*s* excitonic state. When $2\hbar\omega_L \approx E_{1s}$, the contributions of forbidden and allowed HRS are of the same order of magnitude. If the forbidden scattering mechanisms play an appreciable role in the resonant HRS, they can affect the frequency dependence of the HRS intensity. Such a feature was observed in a ZnSe crystal where a small enhancement was found for $2\hbar\omega_L \approx E_{1s}$ along with the increase of the HRS signal as the doubled frequency approaches the resonance with a 2*p* exciton [13]. Interesting peculiarities of HRS in a CdS crystal were also observed [8].

The increase in the HRS intensity by LO phonons (by more than two orders of magnitude) was found in a CdS crystal when the doubled frequency of the exciting radiation approaches excitonic resonances [8]. The signal then decreases, which was explained by attenuation of the scattered light near the fundamental absorption edge. We apply the theoretical model developed here to analyze HRS in CdS. The 90°-scattering geometry with the incident radiation propagating along to optical axis

z of the crystal was used in experiment [8]. In this configuration (ε_L is directed perpendicularly to the *z* axis), the dipole transition to the *s*-exciton state is allowed for the *A*, *B*, and *C* series. All three excitonic series can therefore participate in the allowed HRS. As regards the forbidden mechanisms, the two-photon transition is allowed to the dipole-forbidden *s*-exciton of the Γ_6 symmetry for the *A* series and to the dipole-allowed *s*-exciton for the *B* or *C* series. Therefore, in the configuration used in experiment [8], resonant HRS caused by the two-photon transitions to *s*-excitons and *p*-excitons can contribute to the HRS intensity. We evaluated the HRS cross section as a function of the doubled energy of incident photons for the allowed ($\beta^{(1)}_{\alpha\beta\gamma}(\mathbf{q})$) and forbidden ($\beta^{(2)}_{\alpha\beta\gamma}(\mathbf{q}) + \beta^{(F)}_{\alpha\beta\gamma}(\mathbf{q})$) scattering mechanisms separately. In the calculation, we used the known parameters of CdS ($\hbar\omega_P = 0.038$ eV, $m_e^* = 0.2m$, $m_h^* = 1.34m$ [38]) and took the following values for the *A*, *B*, and *C* excitonic series: $E_{cvA} = 2.579$ eV, $E_{cvB} = 2.596$ eV, $E_{cvC} = 2.66$ eV, $R_A = 0.028$ eV, $R_B = 0.03$ eV, $R_C = 0.026$ eV [39, 40], $f_{1sA} = 0.0014$, $f_{1sB} = 0.001$, and $f_{1sC} = 0.0013$ (here, f_{1s} is the oscillator strength for the transition to the 1*s* exciton state) [41]. We also used the energies of the excitons with $n = 1$ and $n = 2$ ($E_{An=1} = 2.548$ eV, $E_{Bn=1} = 2.56$ eV, and $E_{An=2} = 2.568$ eV [40]) and the damping ($\Gamma_A = 0.004$ eV, $\Gamma_B = 0.005$ eV, and $\Gamma_C = 0.026$ eV [41]) known for the temperature at which the measurements were made ($T = 80$ K) [8]. We considered the higher lying conduction band ($E_{c'v} \approx 6.2$ eV) as the intermediate band [42]. The estimations have shown that the HRS intensity enhancement caused by the allowed HRS is approximately an order of magnitude less than the increase measured in the experiment when the doubled energy of incident photons varies from 2.49 to 2.53 eV. On the other hand, the cross section gain calculated for the forbidden resonant HRS was found to be comparable to the change in the HRS intensity observed. Consequently, it is plausible that the resonant HRS observed was induced by the forbidden scattering mechanisms. Let us consider expression (37), where we can write $M_{cc}^{\beta'\beta} - M_{vv}^{\beta'\beta} = (m/\mu)\delta_{\beta\beta'}$ for CdS. From this fact, it transpires that the scattering mechanism described by $\beta^{(1)}_{\alpha\beta\gamma}(\mathbf{q})$ is effective if the polarization vector of the exciting radiation lies in the plane determined by the photon wave vectors (i.e., $\hat{q}_\beta \neq 0$ in this case). The allowed HRS mechanism is therefore forbidden if the incident radiation is polarized along the *x* axis and the scattering light propagates in the *y* direction. Only the forbidden scattering mechanisms then contribute to the HRS intensity. Also, the appearance of the intensive forbidden 2LO line, which is characteristic of the resonant RS in the HRS spectra near the excitonic resonance, agrees well with our assumption. The strong HRS by LO phonons in CdS for the two-photon resonance with the 2*p* exciton was reported in [13]. However, the measurements were performed in the $x(yy, z + x)y$ geometry, where the scattering described by $\beta^{(1)}_{\alpha\beta\gamma}(\mathbf{q})$ is allowed according to our model. The above discussion shows that additional experimental research into resonant HRS in a CdS crystal is of great interest.

5. CONCLUSIONS

A theoretical model for resonant hyper-Raman scattering in semiconductors was developed. The model includes the Wannier excitons as intermediate states in the scattering process. Different mechanisms of exciton–photon and exciton–lattice interactions were considered and their contributions to the HRS cross section were analyzed for crystals with both allowed and forbidden dipole transitions. Agreement with the experimental results was obtained. It was shown that under the resonant conditions, the forbidden HRS can give a contribution compatible with the one of the allowed HRS mechanisms. The model developed allows one to calculate the cross section for HRS when the doubled energy of incident photons is below or in the range of excitonic resonances.

ACKNOWLEDGMENTS

This work was supported by the Russian Foundation for Basic Research (project no. 01-02-16526).

REFERENCES

1. S. Kielich, Kvant. Élektron. (Moscow) **4**, 2574 (1977) [Sov. J. Quant. Electron. **7**, 1471 (1977)].
2. D. A. Long and L. Stanton, Proc. R. Soc. London, Ser. A **318**, 441 (1970).
3. L. D. Ziegler, J. Raman Spectr. **21**, 769 (1990).
4. V. N. Denisov, B. N. Mavrin, and V. B. Podobedov, Phys. Rep. **151**, 1 (1987).
5. A. V. Baranov, Ya. S. Bobovich, and V. I. Petrov, Usp. Fiz. Nauk **160** (10), 35 (1990) [Sov. Phys. Usp. **33**, 812 (1990)].
6. S. A. Akhmanov and D. N. Klyshko, Pis'ma Zh. Éksp. Teor. Fiz. **2**, 171 (1965) [JETP Lett. **2**, 108 (1965)].
7. Yu. N. Polivanov and R. Sh. Sayakhov, Pis'ma Zh. Éksp. Teor. Fiz. **30**, 617 (1979) [JETP Lett. **30**, 580 (1979)].
8. V. A. Maslov, K. K. Ondriash, Yu. N. Polivanov, *et al.*, Laser Phys. **6**, 132 (1996).
9. K. Watanabe and K. Inoue, J. Phys. Soc. Jpn. **58**, 726 (1989).
10. K. Inoue and K. Watanabe, Phys. Rev. B **39**, 1977 (1989).
11. K. Watanabe and K. Inoue, Phys. Rev. B **41**, 7957 (1990).
12. K. Watanabe, K. Inoue, and F. Minami, Phys. Rev. B **46**, 2024 (1992).
13. K. Inoue, F. Minami, Y. Kato, and K. Yoshida, J. Cryst. Growth **117**, 738 (1992).

14. K. Inoue, K. Yoshida, F. Minami, and Y. Kato, Phys. Rev. B **45**, 8807 (1992).
15. S. Kono, N. Naka, M. Hasuo, *et al.*, Solid State Commun. **97**, 455 (1996).
16. L. E. Semenova and K. A. Prokhorov, Laser Phys. **7**, 263 (1997).
17. L. E. Semenova and K. A. Prokhorov, in *Proceedings of XVI International Conference on Raman Spectroscopy, Cape Town, 1998* (Wiley, Chichester, 1998), p. 120.
18. L. Semenova and K. Prokhorov, Proc. SPIE **3734**, 207 (1999).
19. L. Semenova and K. Prokhorov, Proc. SPIE **4069**, 190 (2000).
20. A. Garsía-Cristóbal, A. Cantarero, C. Trallero-Ginner, and M. Cardona, Phys. Rev. B **58**, 10443 (1998).
21. R. Loudon, *The Quantum Theory of Light* (Clarendon Press, Oxford, 1973; Mir, Moscow, 1976).
22. M. M. Denisov and V. P. Makarov, Phys. Status Solidi B **56**, 9 (1973).
23. R. J. Elliott, Phys. Rev. **124**, 340 (1961).
24. K. Rustagi, F. Pradere, and A. Mysyrowicz, Phys. Rev. B **8**, 2721 (1973).
25. R. Loudon, Proc. R. Soc. London, Ser. A **275**, 218 (1963).
26. R. M. Martin, Phys. Rev. B **4**, 3676 (1971).
27. G. L. Bir and G. E. Pikus, Fiz. Tverd. Tela (Leningrad) **2**, 2287 (1960) [Sov. Phys. Solid State **2**, 2039 (1961)].
28. L. Hostler, J. Math. Phys. **5**, 591 (1964).
29. G. D. Mahan, Phys. Rev. B **170**, 825 (1968).
30. L. E. Semenova and K. A. Prokhorov, Zh. Éksp. Teor. Fiz. **119**, 886 (2001) [JETP **92**, 771 (2001)].
31. L. E. Semenova and K. A. Prokhorov, J. Raman Spectr. **32**, 942 (2001).
32. H. Bateman, *Higher Transcendental Functions* (McGraw-Hill, New York, 1953).
33. L. D. Landau and E. M. Lifshitz, *Course of Theoretical Physics*, Vol. 3: *Quantum Mechanics: Non-Relativistic Theory*, 4th ed. (Nauka, Moscow, 1989; Pergamon, New York, 1977).
34. L. Semenova and K. Prokhorov, Proc. SPIE **4748**, 275 (2002).
35. L. E. Semenova and K. A. Prokhorov, Laser Phys. **12**, 349 (2002).
36. C. Trallero-Giner, A. Cantarero, and M. Cardona, Phys. Rev. B **40**, 4030 (1989).
37. R. M. Martin and L. M. Falicov, in *Light Scattering in Solids*, Ed. by M. Cardona (Springer, Berlin, 1975; Mir, Moscow, 1979), No. 1.
38. *Physical Quantities: A Handbook*, Ed. by I. S. Grigor'ev and E. Z. Meĭlikhov (Énergoizdat, Moscow, 1991).
39. D. C. Reynolds, in *Optical Properties of Solids*, Ed. by S. Nudelman and S. S. Mitra (Plenum, New York, 1969), p. 239.
40. F. Pradere, Thése de doctorat d'état des-sciences physiques (Univ. de Paris Sud, 1973).
41. V. V. Sobolev, *Bands and Excitons for $A^{II}B^{VI}$ Compounds* (Shtiintsa, Kishinev, 1980).
42. M. Cardona and G. Harbeke, Phys. Rev. A **137**, 1467 (1965).

Journal of Experimental and Theoretical Physics, Vol. 96, No. 5, 2003, pp. 932–939.
Translated from Zhurnal Éksperimental'noĭ i Teoreticheskoĭ Fiziki, Vol. 123, No. 5, 2003, pp. 1059–1066.

SOLIDS
Electronic Properties

1/*Q* Expansion for the Energy Spectrum of Quantum Dots

Yu. E. Lozovik[a,*], V. D. Mur[b], and N. B. Narozhnyi[b,]**

[a]*Institute of Spectroscopy, Russian Academy of Sciences, Troitsk, Moscow oblast, 142190 Russia*
**e-mail: lozovik@isan.troitsk.ru*
[b]*Moscow Institute of Engineering Physics, Kashirskoe sh. 31, Moscow, 115409 Russia*
***e-mail: narozhny@theor.mephi.ru*
Received October 3, 2002

Abstract—A new method is proposed for calculating the energy spectrum and the wave functions of *N*-electron quantum dots with an arbitrary confining potential. The method consists in expansion with respect to a dimensionless quantum parameter $1/Q$, which is expressed in terms of the ratio of the characteristic Coulomb energy of electron–electron interaction to the characteristic energy of one-particle transition in a confining potential. Two-electron quantum dots with a parabolic confining potential in an external magnetic field are considered. Strongly correlated states of the system and the spin rearrangement in a strong magnetic field are analyzed. Analytic expressions are obtained for the energy and the wave functions of the system. It is shown that restriction of the analysis only to the first three terms in the quantum-parameter expansion gives an accuracy of one percent when calculating the energy even for values of Q on the order of unity, i.e., for the presently implementable GaAs quantum dots. The expressions for energy obtained are in a good agreement with the experimental data for quantum dots in a perpendicular magnetic field. © *2003 MAIK "Nauka/Interperiodica".*

1. INTRODUCTION

Quantum dots are a promising object for application in opto- and nanoelectronics [1, 2]. Moreover, they are very interesting as a model object for investigating quantum systems consisting of a few or many particles. In contrast to ordinary atoms, where the correlation energy is much less than the Hartree–Fock energy, any regimes, from weakly correlated to strongly correlated and even crystallized electron systems [3], are attainable in quantum dots under variation of their size (the confining potential) and the number of electrons. An analysis of the strong-correlation regime in a system of several electrons may prove to be useful in a more general aspect—when studying short-range ordering and possible phase transitions in an extensive electron system. An analysis of the strong-correlation regime requires the development of new methods that are nonperturbative with respect to the electron–electron interaction. The present work is a step in this direction. A system of several electrons in a quantum dot at zero or sufficiently low temperature is characterized by a single dimensionless quantum parameter Q that is expressed in terms of the ratio of the characteristic Coulomb energy of electron–electron interaction to the characteristic energy of one-particle transition in a confining potential [3]. In the limit of infinite Q, a system of electrons crystallizes, and its energy and equilibrium configuration are determined by the minimum of the total potential energy. The method used in our study consists in expansion with respect to the parameter $1/Q$ and is a variant of the so-called $1/\mathcal{N}$ expansion [4–8], where $\mathcal{N}$ is either the dimension of the space, $\mathcal{N} \equiv D$ [9], or the principal quantum number of a level, $\mathcal{N} \equiv n = n_r + l + 1$ [10, 11], or the number of components of the wave function [12], etc. In the limit of large Q, the analytic expressions for energies and wave functions obtained within the $1/Q$ expansion are asymptotically exact. At the same time, in experimentally studied quantum dots, for example, in GaAs quantum dots [13–15], the parameter Q is on the order of unity. However, it turns out that the $1/Q$ expansion gives a surprisingly good accuracy in a very wide range of Q, including even values of $Q \sim 1$. We will demonstrate this result by calculating two-electron quantum dots. With regard to spin-electronic problems, the rearrangement of the spin states of a system under the variation of Q, i.e., under the variation of the confining potential or of external magnetic field, is of great interest. We study such a rearrangement for the ground state of a system and compare the results obtained with the available experimental data.

In the next section, we describe a method for calculating the spectrum and the wave functions that is based on the expansion with respect to the dimensionless quantum parameter $1/Q$. In Section 3, we consider the case of an axially symmetric confining potential and present analytic formulas for the energy of two- and three-electron quantum dots. In Section 4, we analyze an important case of a parabolic confining potential. By comparing this with the results of exact (numerical) calculation for a two-electron quantum dot, we show that taking into consideration the first three terms in the $1/Q$ expansion provides an accuracy of one percent even for values of $Q \sim 1$. In Section 5, we consider a

quantum dot in a magnetic field, analyze the spin rearrangement, and demonstrate good agreement between the results of calculations and the experimental data.

2. 1/Q EXPANSION FOR AN N-PARTICLE QUANTUM DOT

Consider a system of N particles with pairwise Coulomb repulsion $V_c = \sum_{a<b}^{N} V_{ab}$ that move in an arbitrary confining potential $V_{\text{cf}} = \sum_{a=1}^{N} V_a$, where

$$V_{ab} = \frac{a_0}{r_{ab}}E_0, \quad V_a = \nu\left(\frac{\mathbf{r}_a}{a_0}\right)E_0. \tag{2.1}$$

Here, $E_0 = e^2/\epsilon a_0$ and a_0 are the characteristic Coulomb energy and the characteristic size of the system, respectively; ν is the shape of the confining potential; $\mathbf{r}_a$ is the radius vector of the ath electron; $r_{ab} = |\mathbf{r}_a - \mathbf{r}_b|$; e is the electron charge; and ϵ is the permittivity of the medium. Denoting $\mathbf{x}_a = \mathbf{r}_a/a_0$ and introducing the reduced energy $\varepsilon(N) = E(N)/E_0$, we write the Schrödinger equation as

$$\left\{-\frac{1}{4Q^2}\sum_{a=1}^{N}\Delta_a + \sum_{a=1}^{N}\nu(\mathbf{x}_a) + \frac{1}{2}\sum_{a\neq b}^{N}|\mathbf{x}_a - \mathbf{x}_b|^{-1}\right\}\Psi_N = \varepsilon(N)\Psi_N, \tag{2.2}$$

where

$$Q = \sqrt{\frac{m_* e^2 a_0}{2\epsilon\hbar^2}} = \sqrt{\frac{\mu}{\epsilon}\frac{a_0}{2a_{\text{B}}}} \tag{2.3}$$

is the only dimensionless parameter that determines the dynamics of the system. It is clear from (2.3) that this parameter is expressed via the square root of the ratio of the characteristic Coulomb energy E_0 to the characteristic kinetic energy $\hbar^2/2m_* a_0^2$, where $\mu = m_*/m_{\text{e}}$ is the ratio of the effective mass of a particle to the electron mass and $a_{\text{B}} = \hbar^2/m_{\text{e}}e^2 = 0.529 \times 10^{-8}$ cm is the Bohr radius. The magnitude of Q may vary in a wide interval from values on the order of unity for GaAs quantum dots [13–15] to $Q \gtrsim 10^4$ for ion traps [16, 17]. Therefore, it is natural to apply the $1/Q$ expansion, which is a particular case of the $1/\mathcal{N}$ expansion (see [4–12] and references therein), to calculate the energy spectrum and the wave functions of quantum dots. An attractive feature of this method is that the results can be obtained in analytic form even for systems with nonseparable variables.

By analogy with [10], the application of the $1/Q$-expansion method is as follows. In the classical limit, $Q \longrightarrow \infty$, Eq. (2.2) determines an equilibrium configuration $\{\mathbf{x}_a^{(0)}\}$ and the corresponding energy $\varepsilon^{(0)}$ equal to the minimum of the potential for $\{\mathbf{x}_a\} = \{\mathbf{x}_a^{(0)}\}$. The next approximation corresponds to small oscillations with an amplitude proportional to $Q^{-1/2}$ about the equilibrium. Setting

$$x_{a\alpha} = \left(1 + \frac{\xi_{a\alpha}}{Q^{1/2}}\right)x_{a\alpha}^{(0)}, \quad -\infty < \xi_{a\alpha} < \infty, \tag{2.4}$$

$1 \le a \le N$, $1 \le a \le D$ (D is the dimension of the system), and expanding the wave function and the potential in powers of $Q^{-1/2}$, we successively determine the expansion coefficients of the wave function,

$$\Psi_N = \Psi^{(0)} + \Psi^{(1/2)}/Q^{1/2} + \Psi^{(1)}/Q + \ldots, \tag{2.5}$$

and the corresponding coefficients $\varepsilon^{(k)}$ in the expansion of the reduced energy,

$$\varepsilon(N) = \varepsilon^{(0)} + \varepsilon^{(1)}/Q + \varepsilon^{(2)}/Q^2 + \ldots. \tag{2.6}$$

3. AN AXIALLY SYMMETRIC CONFINING POTENTIAL

To illustrate the method, consider a two-dimensional ($D = 2$) quantum dot with an axially symmetric confining potential. To avoid the difficulties associated with the presence of a zero mode, we single out a joint rotation of the particles. To this end, we consider the states in which the projection M of the total angular momentum onto the symmetry axis is preserved and represent the wave function of the system as

$$\Psi_N = (\rho_1\rho_2\ldots\rho_N)^{-1/2}e^{iM\phi}\chi_M(\{\rho_a, \varphi_{ab}\}), \quad M = 0, \pm1, \pm2, \ldots. \tag{3.1}$$

Here, we use the cylindrical coordinates

$$\mathbf{x}_a = (\rho_a, \varphi_a), \quad \phi = \sum_{a=1}^{N}\frac{\varphi_a}{N}, \quad \varphi_{ab} = \varphi_a - \varphi_b.$$

The energy $\varepsilon^{(0)}$ is determined from the classical equilibrium condition for N interacting electrons in a confining potential that arises when the first term in curly brackets on the left-hand side of Eq. (2.2) is neglected, i.e., in the limit of $Q = \infty$. The coefficient $\varepsilon^{(1)}$ in expansion (2.6), i.e., the first quantum correction in the reduced energy, is nothing more than the energy of normal oscillations about the equilibrium with frequencies ω_i:

$$\varepsilon^{(1)}(n_1, n_2, \ldots) = \sum_{i=1}^{2N-1}\left(n_i + \frac{1}{2}\right)\omega_i, \quad n_i = 0, 1, 2, \ldots \tag{3.2}$$

The next coefficient, $\varepsilon^{(2)}$, can be found by taking into consideration the anharmonic terms proportional to $1/Q^{3/2}$ and $1/Q^2$ in Eq. (2.2) in perturbation theory. In

particular, for the states with the minimal energy for a given M, we have

$$\varepsilon^{(2)}(M) = \frac{1}{2\kappa_N}M^2 - k_N, \tag{3.3}$$

where $\kappa_N = I_N/2Q^2$ and I_N is a "rigid-body" moment of inertia of a system of two particles with masses $2Q^2$. For small values of N, when particles at equilibrium are situated at the vertices of a regular polyhedron at a distance of ρ_0 from the center of the system, $\kappa_N = 2N\rho_0^2$, $N \le 6$. The constant k_N depends on the shape of the confining potential and is expressed in terms of the parameters of the problem in a rather cumbersome way.

In the simplest case of a two-electron quantum dot ($N = 2$), the equilibrium value ρ_0 is determined from the equation

$$v'(\rho_0) = (2\rho_0)^{-2}. \tag{3.4}$$

Here,

$$\begin{aligned} &\varepsilon^{(0)} = 2v(\rho_0) + 1/2\rho_0, \quad \omega_1^2 = 2\rho_0, \\ &\omega_2^2 = 8\rho_0^4 v''(\rho_0), \quad \omega_3^3 = 2\omega_1^2 + \omega_2^2. \end{aligned} \tag{3.5}$$

The expression for k_2 is not simplified even for power-law potentials

$$v(\rho) = \rho^\nu, \quad \nu > 1,$$

when the equilibrium value ρ_0 is expressed analytically:

$$\rho_0 = (4\nu)^{-1/(\nu+1)}, \quad \varepsilon^{(0)} = 2(1+\nu)(4\nu)^{-\nu/(\nu+1)},$$
$$\omega_2^2/\omega_1^2 = \nu - 1.$$

In a physically important case of a parabolic confining potential ($\nu = 2$), we have

$$\begin{aligned} &\rho_0 = 1/2, \quad \varepsilon^{(0)} = 3/2, \quad \omega_1 = \omega_2 = 1, \\ &\omega_3 = \sqrt{3}, \quad \kappa_2 = 1, \quad k_2 = 1/36. \end{aligned} \tag{3.6}$$

Hence, according to (2.6), (3.2), and (3.3), we obtain the following expression for the states of two-electron quantum dots with the minimal energy for a given M:

$$\begin{aligned} \varepsilon_{M,0}(2) &= 1.5 + 1.8660Q^{-1} \\ &+ (0.5M^2 - 0.0278)Q^{-2}. \end{aligned} \tag{3.7}$$

The degeneracy ($\omega_1 = \omega_2$) allows for the full separation of variables in Eq. (2.2); thus, it is this case that admits the comparison of the results of the $1/Q$ expansion with those of exact (numerical) solutions. Below, we will show that the accuracy of approximation (3.7) for $Q \gtrsim 1$ and $m = 0.1$ (see (4.8)) is no worse than two percent.

Similarly, in the case of $\nu = 2$ and $N = 3$, we have

$$\begin{aligned} &\rho_0 = (2\sqrt{3})^{-1/3}, \quad \varepsilon^{(0)} = 3\sqrt{3}/2\rho_0, \\ &\omega_1 = \omega_2 = 1, \quad \omega_3 = \omega_4 = \sqrt{3/2}, \\ &\omega_5 = \sqrt{3}, \quad \kappa_3 = 6\rho_0^2, \quad k_3 = -0.02843; \end{aligned} \tag{3.8}$$

up to terms proportional to Q^{-2}, this yields

$$\begin{aligned} \varepsilon_{M,0}(3) &= 3.9311 + 3.0908Q^{-1} \\ &+ (0.1908M^2 + 0.0284)Q^{-2}. \end{aligned} \tag{3.9}$$

Since the ratio of the Coulomb energy to the oscillator energy for the equilibrium configuration is the same (and equal to 2) for $N = 2$ and $N = 3$, while the relative contribution of the term $\varepsilon^{(0)}$ is greater for $N = 3$ than for $N = 2$, one can expect that the accuracy of formula (3.9) is no worse than that of (3.7).

4. A TWO-DIMENSIONAL TWO-ELECTRON QUANTUM DOT WITH A PARABOLIC CONFINING POTENTIAL

For a parabolic confining potential $V_a = m_*\Omega^2\mathbf{r}_a^2/2$, the characteristic size a_0 and the characteristic energy E_0 of the system are given by

$$\begin{aligned} a_0 &= \left(\frac{2e^2}{\epsilon m_*\Omega^2}\right)^{1/3} = \frac{\epsilon}{\mu}Q^2 2a_B, \\ E_0 &= Q\hbar\Omega = \frac{\mu}{\epsilon^2 Q^2}E_B, \end{aligned} \tag{4.1}$$

and the dimensionless quantum parameter is

$$Q = \frac{1}{\hbar}\left(\frac{m_* e^4}{2\epsilon^2\Omega}\right)^{1/3} = \left(\frac{\mu}{\epsilon^2}\right)^{1/3}\left(\frac{E_B}{\hbar\Omega}\right)^{1/3}, \tag{4.2}$$

where Ω is the steepness of the confining potential and $E_B = m_e e^4/2\hbar^2 = 13.606$ eV is the electron energy in the first Bohr orbit.

In this case, as mentioned above, the motion of the center of masses and the relative motion of particles,

$$\mathbf{R} = \mathbf{x}_1 + \mathbf{x}_2, \quad \mathbf{r} = \mathbf{x}_1 - \mathbf{x}_2, \tag{4.3}$$

are separated in Eq. (2.2): $\Psi_2 = \Psi_F\Psi_{rel}$ and $\varepsilon(2) =$

$\varepsilon_F + \varepsilon_{rel}$, and we have

$$\left\{-\frac{1}{2Q^2}\Delta_{\mathbf{R}} + \frac{1}{2}R^2\right\}\Psi_F = \varepsilon_F\Psi_F, \quad (4.4)$$

$$\left\{-\frac{1}{2Q^2}\Delta_{\mathbf{r}} + \frac{1}{2}r^2 + \frac{1}{r}\right\}\Psi_{rel} = \varepsilon_{rel}\Psi_{rel}. \quad (4.5)$$

The first of these equations determines the Fock–Darwin spectrum and wave functions [18],

$$\varepsilon_F = (|M_F| + 2n_F + 1)/Q = (n_1 + n_2 + 1)/Q, \quad (4.6)$$

where $M_F = 0, \pm1, \pm2, \ldots$; n_F, n_1, $n_2 = 0, 1, 2, \ldots$; and

$$\Psi_F(\mathbf{R}) \equiv \Psi_{M_F n_F} \frac{1}{\sqrt{2\pi R}} e^{iM_F\varphi_F}\chi_{M_F}(R) = \Psi_{n_1}(R_1)\Psi_{n_2}(R_2) \quad (4.7)$$

is the wave function of a circular oscillator, $\mathbf{R} = \{R, \varphi_F\} = \{R_1, R_2\}$ [19]. In this case, $\Psi_{n_i}(R_i)$ are the wave functions of a one-dimensional oscillator of mass Q and frequencies $\omega_i = 1$, $i = 1, 2$.

On the other hand, singling out the angular part from the wave function Ψ_{rel},

$$\Psi_{rel}(\mathbf{r}) \equiv \Psi_m = \frac{1}{\sqrt{2\pi r}} e^{im\varphi}\chi_m(r), \quad \mathbf{r} = (r, \varphi), \quad (4.8)$$

we arrive at the one-dimensional equation

$$\left\{-\frac{1}{2Q^2}\left(\frac{d^2}{dr^2} - \frac{4m^2-1}{4r^2}\right) + \frac{1}{2}r^2 + \frac{1}{r}\right\}\chi_m = \varepsilon_m\chi_m, \quad (4.9)$$

with $\varepsilon_{rel} \equiv \varepsilon_m$. In the classical limit, this equation determines the equilibrium point $r_0 = 1$ and the corresponding energy $\varepsilon^{(0)} = 3/2$, equal to the minimum of the potential at $r = r_0$, which coincides with (3.6) since $r_0 = 2\rho_0$. Setting, according to (2.4),

$$r = 1 + \frac{\xi}{Q^{1/2}}, \quad -\infty < \xi < \infty, \quad (4.10)$$

and restricting the consideration to the first three terms in expansions (2.5) and (2.6), we obtain

$$\left\{-\frac{1}{2}\frac{d^2}{d\xi^2} + \frac{3}{2}\xi^2 - \frac{\xi^3}{Q^{1/2}} + \frac{\xi^4}{Q}\right\}\chi_m(\xi) = \left(\varepsilon^{(1)} + \frac{\varepsilon^{(2)}}{Q} - \frac{4m^2-1}{8Q}\right)\chi_m(\xi), \quad (4.11)$$

i.e., the Schrödinger equation for a one-dimensional anharmonic oscillator. Hence, in the zero approximation in the parameter $Q^{-1/2}$, we derive

$$\varepsilon^{(1)} = \sqrt{3}(n + 1/2), \quad \chi_n^{(0)} = \left(\frac{\sqrt{3}}{\pi}\right)^{1/4}\frac{1}{\sqrt{2^n n!}}\exp\left(-\frac{\sqrt{3}\xi^2}{2}\right)H_n(\xi^{1/4}), \quad (4.12)$$

where $H_n(x)$ is the Hermitian polynomial and $n = 0, 1, 2, \ldots$ is the oscillator quantum number. Taking into consideration anharmonic corrections yields

$$\varepsilon_m = \frac{3}{2} + \frac{\sqrt{3}(n + 1/2)}{Q} + \frac{(n + 1/2)^2 + 6m^2}{12Q^2} - \frac{7}{144Q^2}. \quad (4.13)$$

Summing up (4.6) and (4.13), we obtain the following expression for the total energy $E(2) = \varepsilon(2)E_0$:

$$E_{n_1 n_2 m n} = \hbar\Omega\left\{\frac{3}{2}Q + n_1 + n_2 + 1 + \sqrt{3}\left(n + \frac{1}{2}\right) + \left[\frac{1}{12}\left(n + \frac{1}{2}\right)^2 + \frac{1}{2}m^2 - \frac{7}{144}\right]\frac{1}{Q}\right\}, \quad (4.14)$$

$$n_1, n_2, n = 0, 1, 2, \ldots, \quad m = 0, \pm1, \pm2, \ldots.$$

Expansions (4.13) and (4.14) are asymptotically exact for $Q \longrightarrow \infty$ and fixed quantum numbers n and m. For finite values of Q, the accuracy of these expansions can be determined by comparison with the numerical solution of Eq. (4.9). Such a comparison is demonstrated in Fig. 1. One can see that the first three terms of the $1/Q$ expansion guarantee an accuracy no worse than 1% for $n, m \le 1$ and $Q \ge 1.5$. Note that the approximation (4.12) for the wave function is valid only in the region of its localization, $r \sim r_0$, whereas, as $r \longrightarrow 0$ and $r \longrightarrow \infty$, i.e., in the subbarrier region, one can apply a quasiclassical approximation (see [10, 11] for details). Thus, expression (4.14), which is asymptotically exact in the limit of $Q = \infty$, is extended to the parameter values of $Q \sim 1$. Apparently, this is a general property of various versions of the $1/\mathcal{N}$ expansion.

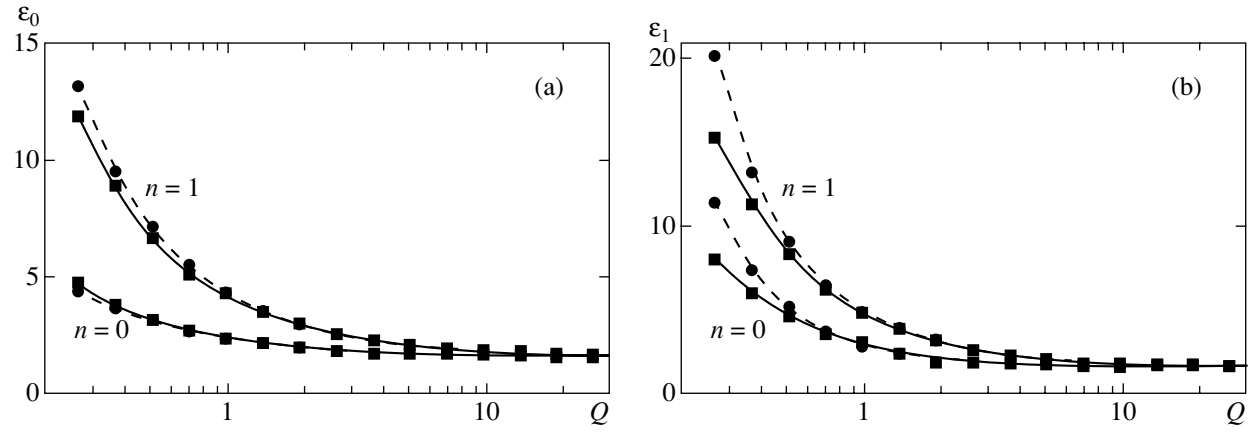

Fig. 1. Reduced energies ε_m versus the quantum parameter Q for states (a) with $m = 0$ and (b) $m = 1$. The solid curves represent the results of exact (numerical) solution of Eq. (4.9), and the dashed curves represent the results of $1/Q$ expansion (4.13). The figures at the curves indicate the value of the radial oscillator quantum number n.

From (3.1) and (4.6)–(4.8), we obtain

$$M = M_\mathrm{F} + m, \quad |M_\mathrm{F}| = n_1 + n_2 - 2n_F. \tag{4.15}$$

Since $n_1 = n_2 = 0$ for the states with the minimal energy for a given projection M, we have $n_\mathrm{F} = 0$ and $M = m$; hence, as expected, spectra (3.7) and (4.14) completely coincide.

5. A TWO-ELECTRON QUANTUM DOT IN A TRANSVERSE MAGNETIC FIELD

The Schrödinger equation for a two-dimensional quantum dot in a transverse magnetic field $\mathscr{H}$ in a symmetric gauge of the vector potential

$$\mathbf{A} = \frac{1}{2}[\mathscr{H}\times\mathbf{r}]$$

with regard to the electron spins is given by

$$\left\{-\frac{\hbar^2}{2m_*}\left(\frac{\partial^2}{\partial\mathbf{r}_1^2}+\frac{\partial^2}{\partial\mathbf{r}_2^2}\right)+\frac{1}{2}m_*\Omega_\mathrm{L}^2(\mathbf{r}_1^2+\mathbf{r}_2^2)\right.$$
$$\left.+\frac{e^2}{\epsilon|\mathbf{r}_1-\mathbf{r}_2|}-\hbar\omega_\mathrm{L}(L_z+\mu g S_z)\right\}\Psi = E\Psi, \tag{5.1}$$

where

$$\Omega_\mathrm{L} = \sqrt{\Omega^2+\omega_L^2}, \tag{5.2}$$

$\omega_\mathrm{L} = e\mathscr{H}/2m_*c = \omega_\mathrm{B}\mathscr{H}/\mu\mathscr{H}_a$ is the Larmor frequency, $\hbar L_z$ and $\hbar S_z$ are the operators of the projections of total angular and spin momenta of electrons, and g is the effective Landé factor. Here, $\mathscr{H}_a = cm_\mathrm{e}^2e^3/\hbar^3 = 2.3506\times 10^5$ T is the atomic magnetic field and $\omega_\mathrm{B} = m_\mathrm{e}e^4/2\hbar^3 = 2.067\times 10^{16}\ \mathrm{s}^{-1}$.

Setting

$$\Psi^{(S)}_{MM_\mathrm{F}\Sigma} = \frac{1}{2\pi\sqrt{Rr}}\exp[i(M_\mathrm{F}\varphi_\mathrm{F}+m\varphi)]$$
$$\times\chi_{M_\mathrm{F}}(R)\chi_m(r)\chi^{(S)}, \quad m = M - M_\mathrm{F}, \tag{5.3}$$

where χ_{M_F} and χ_m are defined in (4.7) and (4.8) and $\chi^{(S)}$ is a two-electron spin function, we have

$$E^{(S)}_{MM_\mathrm{F}\Sigma}(2;\mathscr{H}) = \varepsilon^{(S)}_{MM_\mathrm{F}}(\mathscr{H})E_0 - (M+\mu g\Sigma)\hbar\omega_\mathrm{L},$$
$$\varepsilon^{(S)}_{MM_\mathrm{F}}(\mathscr{H}) = \varepsilon_\mathrm{F}+\varepsilon_\mathrm{rel}. \tag{5.4}$$

Here, M and Σ are the projections of the total angular and spin momenta onto the direction of the magnetic field, and ε_F and ε_rel are determined from Eqs. (4.4) and (4.5), in which Q is replaced by Q_L, where

$$Q_\mathrm{L} = \frac{1}{\hbar}\left(\frac{m_*e^4}{2\epsilon^2\Omega_\mathrm{L}}\right)^{1/3}. \tag{5.5}$$

For antiparallel spins, when $S = 0$ (a singlet), the quantum number m takes only even values according to the Pauli principle, whereas, for parallel spins, $S = 1$ (a triplet), m takes only odd values.

In the limit of weak fields, when $\omega_L \ll \Omega$, the energy $E^{(S)}_{MM_F\Sigma}$ differs from $\varepsilon(2)E_0$ only by a Zeeman shift that is linear in $\hbar\omega_L$. In a strong magnetic field, when $\omega_\mathrm{L} \gg \Omega$, the parameters a_0 and Q are determined by the magnitude of the magnetic field:

$$a_0(\mathscr{H}) = 2a_\mathrm{B}\left(\frac{\mu}{\epsilon}\right)^{1/3}\left(\frac{a_\mathscr{H}}{a_\mathrm{B}}\right)^{4/3},$$

$$Q(\mathscr{H}) = \left(\frac{\mu}{\epsilon}\right)^{2/3}\left(\frac{a_\mathscr{H}}{a_\mathrm{B}}\right)^{2/3},$$

where $a_{\mathcal{H}} \equiv a_B\sqrt{\mathcal{H}_a/\mathcal{H}}$ is the "magnetic" length. When $a_{\mathcal{H}} \gg a_B$, i.e., when the external magnetic field is much weaker than the atomic magnetic field, we obtain the following expression from (5.4) and (4.14) in approximation (2.6):

$$E^{(S)}_{MM_F\Sigma}(2;\mathcal{H}) = \hbar\Omega_L\left\{\frac{3}{2}Q_L + |M_F| + 2n_F + 1 + \sqrt{3}\left(n+\frac{1}{2}\right) + \left[\frac{1}{12}\left(n+\frac{1}{2}\right)^2 + \frac{1}{2}(M-M_F)^2 - \frac{7}{144}\right]\frac{1}{Q_L}\right\} - \hbar\omega_L(M+\mu g\Sigma), \quad (5.6)$$

n_F, $n = 0, 1, 2, \ldots$, $M_F = 0, \pm1, \pm2, \ldots$

In the experiments carried out in [14], the authors measured the ground-state energies $E_{gr}(N)$ of N-electron two-dimensional quantum dots in GaAs heterostructures ($\mu = 0.67$, $\epsilon = 12.5$, and $g = 0.44$) in a perpendicular magnetic field $0 \le \mathcal{H} \le 16$ T by the method of one-electron tunneling spectroscopy. According to [20], for low-lying levels in real two-dimensional quantum dots, a good approximation is given by the oscillator model, i.e., a parabolic confining potential

$$V_a(N) = \frac{1}{2}m_*\Omega^2(N)\mathbf{r}_a^2$$

in Eqs. (2.1) and (2.2). It is convenient to compare such an approximation for the confining potential with the experimental data of [14] by considering the reduced energy as a function of the magnetic field:

$$\varepsilon^{(S)}_M(N;\mathcal{H}) = \frac{E^{(S)}_{M\Sigma}(N;\mathcal{H}) + (M+\mu g\Sigma)\hbar\omega_L}{Q_L(N)\hbar\Omega_L(N)}, \quad (5.7)$$

where S is a quantum number that characterizes the symmetry of the wave function and coincides with the total spin for $N = 2$. Note that the sign of the paramagnetic term in the expression for energy is chosen such that, for the states with the minimal energy for given M and Σ, these quantum numbers cannot be negative (see, for example, (5.4)). In contrast to $E^{(S)}_{M\Sigma}(N;\mathcal{H})$, in the case of a parabolic confining potential, the reduced energy is a universal function of the single parameter $Q_L(N)$. This parameter is determined from Eq. (5.5), in which the effective steepness $\Omega_L(N)$ of the confining potential may depend, as was mentioned in [21], on the number of electrons in a quantum dot.

The results of a similar analysis for $N = 2$ are shown in Fig. 2. The experimental points are borrowed from Fig. 3a of [14] and are recalculated by formula (5.7). Here, as the ground-state energy

$$E_{gr}(1) = \hbar\Omega_L(1) - \frac{1}{2}\mu g\hbar\omega_L, \quad (5.8)$$

of a one-electron quantum dot, we took the value $\hbar\Omega(1) = 3.6$ meV indicated in [14]. For the steepness of the confining potential of a two-electron quantum dot,

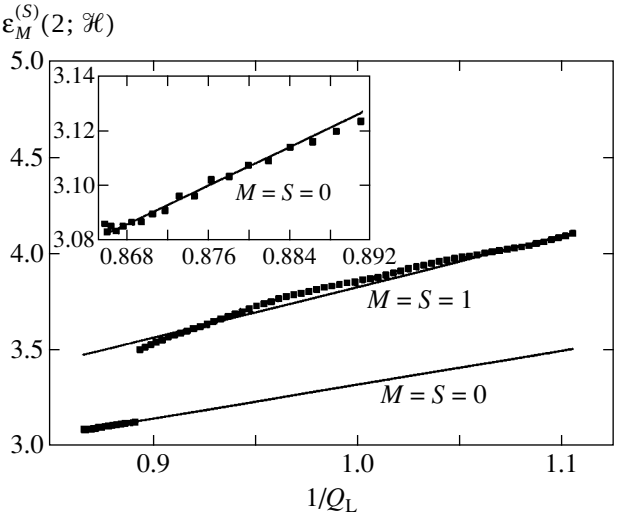

Fig. 2. Reduced energy $\varepsilon^{(S)}_M(2;\mathcal{H})$ versus the quantum parameter $1/Q_L$ for the value of the steepness of the confining potential of $\hbar\Omega = 3.8$ meV. The solid curves represent the results of calculation by Eq. (4.9) with Q replaced by Q_L. Experimental dots are recalculated by Eqs. (5.7) and (5.8) from the data of [14, Fig. 3a]. The inset presents the enlarged fragment in the interval of $0.86 < 1/Q_L < 0.89$ ($0 < \mathcal{H} < 2$ T).

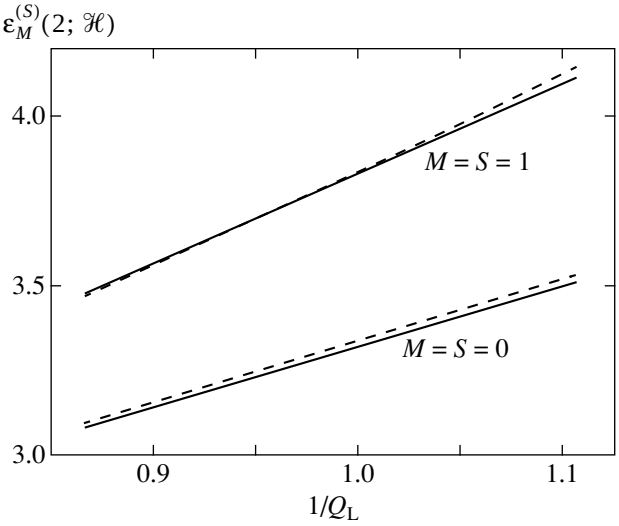

Fig. 3. Reduced energy $\varepsilon^{(S)}_M(2;\mathcal{H})$ for $\hbar\Omega = 3.8$ meV in the range of magnetic fields of $0 < \mathcal{H} < 8$ T. The solid curves represent the results of exact calculation, and the dashed curves represent the contribution of the first three terms of the $1/Q$ expansion.

we obtained a value of $\hbar\Omega \equiv \hbar\Omega(2) = 3.8$ meV. The jump of experimental points from the curve $\varepsilon_0^{(0)}(2; \mathcal{H})$ to the curve $\varepsilon_1^{(1)}(2; \mathcal{H})$ corresponds to a singlet–triplet crossing [14, 22].

In the general case, the position of the crossing, i.e., the value $\mathcal{H}_{cr}$ of the magnetic field for which one compares the energies of levels with different symmetries [22], is determined from the equation

$$E_{M_1\Sigma_1}^{(S_1)}(N; \mathcal{H}_{cr}) = E_{M_2\Sigma_2}^{(S_2)}(N; \mathcal{H}_{cr}). \quad (5.9)$$

For a two-electron quantum dot within the $1/Q$ expansion, this yields

$$\mathcal{H}_{cr}^{(1/Q)} = \gamma\mu\frac{\hbar\Omega}{E_B}\mathcal{H}_a,$$
$$\frac{\gamma}{(1+\gamma^2)^{2/3}} = \frac{M_2^2 - M_1^2}{2(\Delta M + \mu g\Delta\Sigma)Q}. \quad (5.10)$$

Here, $\gamma = \hbar\omega_{cr}/\hbar\Omega$, $\hbar\omega_{cr} = \mu^{-1}(\mathcal{H}_{cr}/\mathcal{H}_a)E_B$, $\Delta M = M_2 - M_1 > 0$, and $\Delta\Sigma = \Sigma_2 - \Sigma_1$. Hence, we obtain $\mathcal{H}_{s-t}^{(1/Q)} = 2.13$ T for the singlet–triplet ($\Delta M = \Delta\Sigma = 1$) crossing $\mathcal{H}_{s-t}$ for $\hbar\Omega = 3.8$ meV. An exact calculation yields a value of $\mathcal{H}_{s-t}^{exact} = 2.25$ T, while the experimental result is $\mathcal{H}_{s-t}^{exp} = 2.0$ T [14].

According to (5.10), for the maximal value $\mathcal{H}_m$ of the magnetic field, which corresponds to the crossing at a given steepness of the confining potential $\hbar\Omega$, we have

$$\mathcal{H}_m^{(1/Q)} = \sqrt{3}\mu\mathcal{H}_a\hbar\Omega/E_B. \quad (5.11)$$

Since this equality yields the estimate $\mathcal{H}_m^{(1/Q)} \approx 7.6$ T, there is no singlet–triplet crossing for the magnetic field values of $0 < \mathcal{H} < 8$ T. An exact calculation by Eq. (5.1) confirms this conclusion (see Fig. 2 in the present paper, as well as Fig. 3 in [15]).

As regards the characteristic ripples in Fig. 3a of [14] in the interval of $2 < \mathcal{H} < 8$ T, which may imitate additional crossings, they may be attributed to the oscillations of conductivity as a function of the magnetic field [14], i.e., to the Shubnikov–de Haas effect [23]. In Fig. 2 in the present paper, these oscillations manifest themselves in the behavior of experimental points in the interval $0.9 < 1/Q_L < 1.1$, which corresponds precisely to the above-mentioned interval of magnetic fields $\mathcal{H}$.

The values of $\mathcal{H}_{s-t}^{(1/Q)}$ and $\mathcal{H}_{s-t}^{exact}$ given above show that the error of the $1/Q$ expansion in the determination of the crossing is about 5%. This error is associated with the error in calculating the energy $\varepsilon_M^{(S)}(2; \mathcal{H})$ in the range of values of the parameter Q_L under consideration and can be judged from Fig. 3, which shows that the first three terms of the $1/Q$ expansion provide an accuracy of calculation no worse than three percent.

6. CONCLUSION

We have developed a nonperturbative method for calculating multielectron quantum dots that is based on the expansion in the dimensionless quantum parameter $1/Q$ expressed through the ratio of the characteristic Coulomb energy of electron–electron interaction to the characteristic energy of electrons in a given confining potential. This method gives analytic expressions for the spectrum and the wave functions of the system. These expressions are asymptotically exact in the limit of large Q. However, taking into consideration only the first three terms in the expansion in $1/Q$ provides an accuracy of about one percent even for $Q \sim 1$. We have considered a spin rearrangement of a two-electron quantum dot in a strong magnetic field and have demonstrated good agreement between the results of calculations and the experimental data obtained by the method of one-electron tunneling spectroscopy.

In conclusion, we stress that the advantage of the $1/Q$ expansion over other variants of the $1/\mathcal{N}$ expansion lies in the fact that Q is a control parameter whose variation changes neither the dimension of the system, nor its symmetry, nor the shape of the effective potential energy (in contrast, for example, to the $1/D$ or $1/n$ expansions). Therefore, the method of $1/Q$ expansion gives a good accuracy when calculating the characteristics of quantum dots in the regions of both weak and strong electron correlations.

According to the aforesaid, one can hope that the method of $1/Q$ expansion can be successfully applied to quantum dots or clusters with a large number of particles and an arbitrary shape of the confining potential and the form of the interparticle interaction.

ACKNOWLEDGMENTS

We are grateful to A.N. Petrosyan and M.S. Fofanov for assistance in carrying out numerical experiments.

This work was supported in part by the Russian Foundation for Basic Research (project nos. 00-02-16354 and 01-02-16850) and by the Ministry of Education of the Russian Federation (project no. 1501).

REFERENCES

1. R. C. Ashoori, Nature **379**, 413 (1996).
2. T. Chakraborty, *Quantum Dots* (Elsevier, Amsterdam, 1999).
3. Yu. E. Lozovik and V. A. Mandelshtam, Phys. Lett. A **165**, 469 (1992); Yu. E. Lozovik, Usp. Fiz. Nauk **153**, 356 (1987) [Sov. Phys. Usp. **30**, 912 (1987)]; A. V. Filinov, M. Bonitz, and Yu. E. Lozovik, Phys. Rev. Lett. **86**, 3851 (2001).

4. E. Witten, in *Recent Development in Gauge Theories* (Plenum, New York, 1980).
5. L. G. Jaffe, Rev. Mod. Phys. **54**, 407 (1982).
6. A. Chatterjee, Phys. Rep. **186**, 249 (1990).
7. *Dimensional Scaling in Chemical Physics*, Ed. by D. R. Herschbach, J. Avery, and O. Goscinsky (Kluwer, Dordrecht, 1993).
8. *New Methods in Quantum Theory*, Ed. by C. A. Tsipis, V. S. Popov, D. R. Herschbach, and J. S. Avery (Kluwer, Dordrecht, 1995).
9. A. A. Belov, A. Gonsales, and Yu. E. Lozovik, Phys. Lett. A **142**, 389 (1990); A. A. Belov and Yu. E. Lozovik, Zh. Éksp. Teor. Fiz. **94** (12), 38 (1988) [Sov. Phys. JETP **67**, 2413 (1988)]; Teor. Mat. Fiz. **81**, 405 (1989); A. A. Belov, Yu. E. Lozovik, and V. A. Mandel'shtam, Zh. Éksp. Teor. Fiz. **98**, 25 (1990) [Sov. Phys. JETP **71**, 12 (1990)].
10. V. S. Popov, V. M. Vaĭnberg, and V. D. Mur, Pis'ma Zh. Éksp. Teor. Fiz. **41**, 439 (1985) [JETP Lett. **41**, 539 (1985)]; Yad. Fiz. **44**, 1103 (1986) [Sov. J. Nucl. Phys. **44**, 714 (1986)]; V. S. Popov, B. M. Karnakov, and V. D. Mur, Phys. Lett. A **224**, 15 (1996).
11. B. M. Karnakov, V. D. Mur, and V. S. Popov, Yad. Fiz. **64**, 729 (2001) [Phys. At. Nucl. **64**, 670 (2001)].
12. S. M. Apenko, D. A. Kirzhnits, and Yu. E. Lozovik, Phys. Lett. A **92**, 107 (1982).
13. R. S. Ashoori, H. L. Stormer, J. S. Weiner, *et al.*, Phys. Rev. Lett. **71**, 613 (1993).
14. T. Schmidt, M. Tewordt, R. H. Blick, *et al.*, Phys. Rev. B **51**, 5570 (1995).
15. L. P. Kowenhoven, T. H. Oosterkamp, M. W. S. Danoesastro, *et al.*, Science **278**, 1788 (1997).
16. H. Dehmelt, Usp. Fiz. Nauk **160** (12), 129 (1990).
17. R. Blumel, J. M. Chen, E. Peik, *et al.*, Nature **334**, 309 (1988); S. L. Gilbert, J. J. Bollinger, and D. J. Wineland, Phys. Rev. Lett. **60**, 2022 (1988); Th. Sauter, H. Gilhaus, I. Siemers, *et al.*, Z. Phys. D **10**, 153 (1988); J. Hoffnagle, R. G. DeVoe, L. Reyna, and R. G. Brewer, Phys. Rev. Lett. **61**, 255 (1988); V. Gomer, H. Strauss, and D. Meschede, Appl. Phys. B **60**, 89 (1995).
18. V. Fock, Z. Phys. **47**, 446 (1928); C. G. Darwin, Proc. Cambr. Philos. Soc. **27**, 86 (1930).
19. S. Flugge, *Practical Quantum Mechanics* (Springer, Berlin, 1971; Mir, Moscow, 1974), Vol. 1.
20. N. A. Bruce and P. A. Maksym, Phys. Rev. B **61**, 4718 (2000).
21. P. Hawrylak, Phys. Rev. Lett. **71**, 3347 (1993).
22. M. Wagner, U. Merkt, and A. V. Chaplik, Phys. Rev. B **45**, 1951 (1992).
23. E. M. Lifshitz and L. P. Pitaevskiĭ, *Physical Kinetics* (Nauka, Moscow, 1979; Pergamon Press, Oxford, 1981).

Translated by I. Nikitin

Journal of Experimental and Theoretical Physics, Vol. 96, No. 5, 2003, pp. 940–944.
Translated from Zhurnal Éksperimental'noĭ i Teoreticheskoĭ Fiziki, Vol. 123, No. 5, 2003, pp. 1067–1072.

SOLIDS
Electronic Properties

Detection of Photoconductivity in Hyperfine Metal Films in the Visible and Infrared Spectral Regions

A. P. Boltaev*, N. A. Penin, A. O. Pogosov, and F. A. Pudonin**
Lebedev Institute of Physics, Russian Academy of Sciences, Moscow, 119991 Russia
**e-mail: boltaev@sci.lebedev.ru*
***e-mail: pudonin@sci.lebedev.ru*
Received October 17, 2002

Abstract—Photoelectric phenomena in island metal films are investigated. The electrical conductivity and photoconductivity are measured in island films of Ti, W, FeNi, and others grown by the method of radio-frequency sputtering in argon. The photoconductivity effect is observed in metal films whose resistivity varies with temperature by the activation law of $\rho \propto \exp(T_0/T)^{0.5}$. This law is interpreted within the model of variable range hopping conductivity in the region of a Coulomb quasi-gap. The photoconductivity in metal films is detected in the visible and near-infrared spectral regions. The mechanisms of photoconductivity in an island metal film are discussed. © *2003 MAIK "Nauka/Interperiodica".*

1. INTRODUCTION

Investigations of the structure and physical properties of hyperfine metal films less than 2–3 nm thick began in the late 1950s, when the methods of thermal evaporation were used to produce the first metal films [1]. The new stage in the investigation of such structures is defined by interest in systems of reduced dimension (quantum wells, dots, wires) and by progress made in the development of the technology of preparing various nanostructures and of the methods of their investigation. Interest in thin island metal films is associated both with the detection of radiation in such structures in an external electric field [2] and with the development and investigation of new classes of materials such as nanocomposites [3]: thin island films represent a particular case of such new materials. The flow of current in such disordered systems is defined by the electron tunneling from some localized states to other states, leading to the activation dependence of the electric resistance,

$$R(T) = R_0 \exp(T_0/T)^n,$$

where T is the temperature and R_0, T_0, and n are quantities determined by the parameters of the disordered system, the electron interaction, and the system dimension, respectively. According to Mott [4], $n = 1/(d + 1)$, where d is the system dimension, although, as was demonstrated by Efros and Shklovskii [5], $n = 1/2$ for any dimension. Dependences of the resistance, corresponding both to the Mott law and to the Efros–Shklovskii law, were experimentally revealed in thin disordered films of various materials. However, a number of researchers found that $n = 0.75$, which is at variance with the existing theoretical concepts [6]. The reasons for the emergence of such a dependence have not yet been clarified. For example, the quantity R_0 in the general case may be other than constant and depend on the temperature, $R_0 = bT^m$, where b and m are constants, and the hops from island to island may be correlated. Therefore, no unified viewpoint exists at present with respect to the mechanism of electric current flow in thin island metal films. Photoconductivity in metallic island films has not been studied. We have investigated the conductivity and the photoconductivity (revealed for the first time) of thin films of Ti, W, FeNi, and Co. Tunnel microscopy was used to investigate the surface morphology of the structures under study.

2. EXPERIMENTAL PROCEDURE AND RESULTS OF MEASUREMENT

Thin films of Ti, W, FeNi, and others were grown by the method of radio-frequency (rf) sputtering in argon. The initial vacuum in the sputtering system was at least 10^{-6} mbar, with an argon pressure of 7×10^{-4} mbar. The rate of deposition of the materials used was determined prior to sputtering; for all metals being grown, this rate was in the range from 0.4 to 0.5 Å/s. In view of the invariability of the deposition rate throughout the process, the sputtering was monitored over time. KEF-4.5 silicon and glass ceramic were used as substrates. The substrate temperature during the film deposition did not exceed 80°C. All films of one metal were grown under the same process conditions. After sputtering, each metal structure was coated with a thin layer of dielectric (Al_2O_3, d = 8 Å) or semiconductor (ZnTe, SiC, d = 8 Å). The metal film thickness was varied from 5 to 100 Å; in so doing, the majority of prepared samples were in the range of small thickness (5–15 Å).

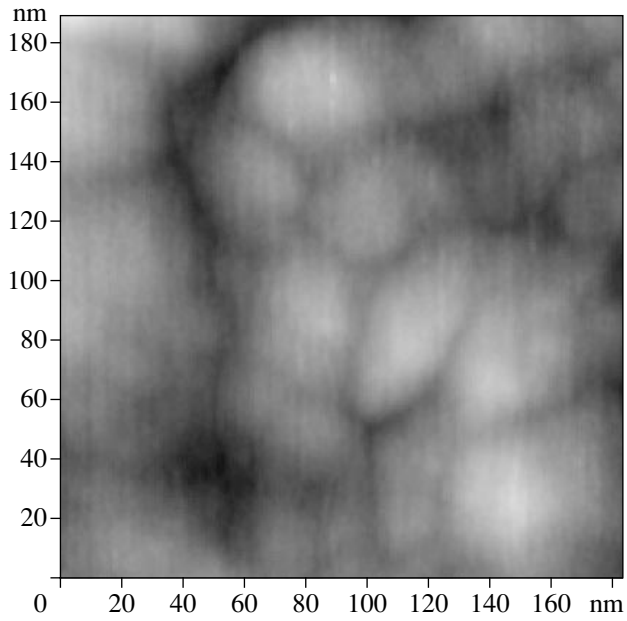

Fig. 1. An image of the surface of a 6.3 Å thick tungsten film deposited on a dielectric substrate.

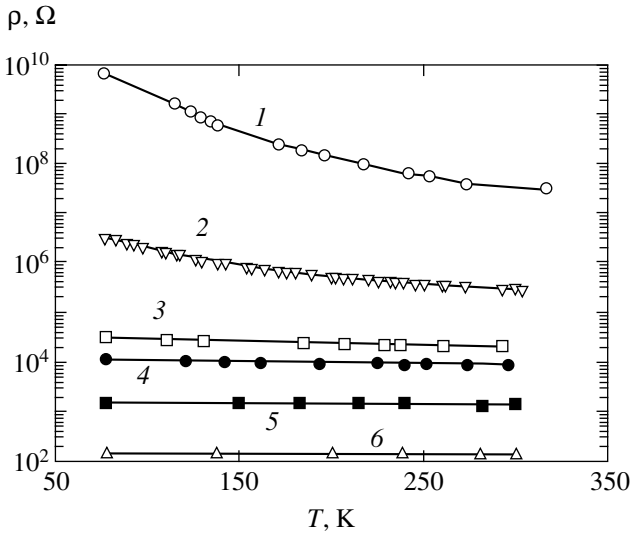

Fig. 2. The temperature dependence of the surface resistivity of tungsten film for six structures of different thickness of metal film (6.3 (*1*), 7.9 (*2*), 9.8 (*3*), 11 (*4*), 19 (*5*), and 100 Å (*6*)).

Mesostructures 0.5–1.5 mm wide and 2–3.5 mm long were prepared for measuring the conductivity and photoconductivity of structures obtained. Ohmic contacts were provided by applying indium onto the metal film surface. The film resistivity was measured under constant voltage in the linear region of the current–voltage characteristics of the sample in the temperature range from 77 to 300 K. The photoconductivity was measured at room and nitrogen temperatures in the wavelength range of incident radiation from 0.5 to 2 μm. The structures were illuminated using an MDR-2 monochromator, with a ribbon filament lamp as the radiation source. The light was modulated at a frequency of $f = 2 \times 10^{-2}$ Hz (period $T = 50$ s).

In studying the photoelectric properties of metal films, we investigated the topography of structures by atomic-force microscopy and measured the surface resistivity of metal films as a function of temperature and the photoconductivity spectrum of metal films applied onto the dielectric substrate.

Figure 1 is a typical image of the surface of a 6.3 Å thick tungsten film applied onto a dielectric substrate. One can see that the film exhibits an island pattern with an island size of about 150 Å; in this way, the islands are spaced on the average about 15 Å apart. Investigation of samples with a film of a different composition but the same thickness produces similar images which differ only by island size. When the film thickness is increased, the islands gradually merge together and, with a metal film thickness on the order of 20 Å, the film becomes continuous.

The temperature dependence of the surface resistivity of a tungsten film on a dielectric substrate is given in Fig. 2 for six structures of different thickness of metal film (d = 6.3, 7.9, 9.8, 11, 19, and 100 Å). Figure 3 gives the surface resistivity as a function of the film thickness at a temperature of 77 K. The dependences of the surface resistivity of Ti- and FeNi-based films differ little from the dependences of the resistivity of tungsten given in Figs. 2 and 3. One can see in Figs. 2 and 3 that a three-fold variation of the thickness of tungsten film on a dielectric substrate (from 6 to 20 Å) causes its resistivity to change by seven orders of magnitude. The film resistivity decreases with increasing temperature. With the metal film thickness ranging from 19 to 100 Å, the film resistivity does not depend on temperature in the temperature range of our measurements.

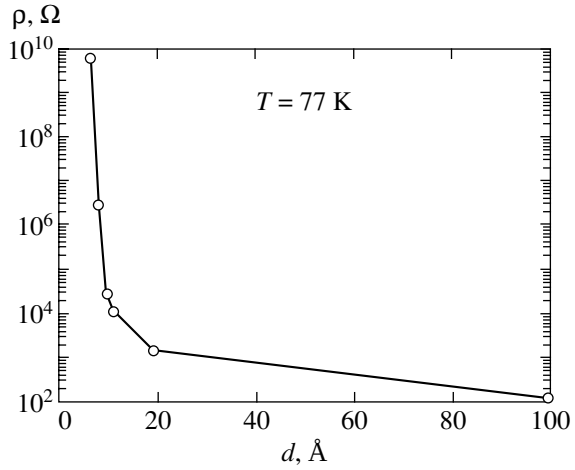

Fig. 3. The surface resistivity as a function of the film thickness at a temperature of 77 K.

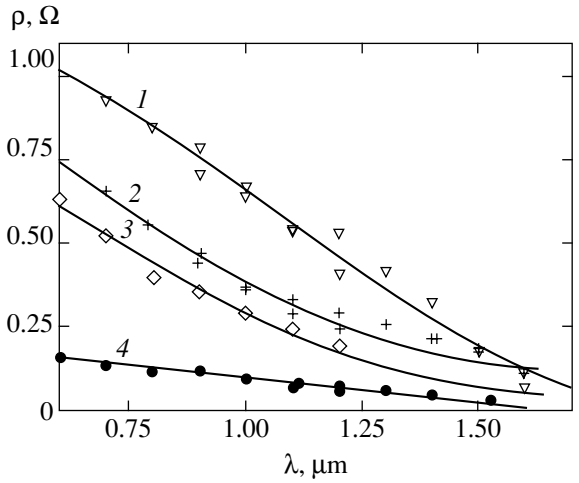

Fig. 4. Spectra of relative photoconductivity of tungsten films of different thickness (6.5 (*1*), 8 (*2*), 9.5 (*3*), and 11 Å (*4*)).

We also performed measurements of the time in which the current through the sample responds to the step of voltage applied to the sample. When a voltage step was applied to the contacts of a sample with a metal film of thickness d = 6.3 Å, the time dependence of the variation of current through the sample exhibited an exponential pattern. This dependence was approximated by the sum of two exponents with different characteristic times ($\tau \sim 10^{-2}$ s and $\tau \sim 10$ s). As the film thickness was increased, the fast component of the time of variation of current upon application to the sample decreased, while the slow component of the time of variation of current remained almost unchanged. Note that the current caused by the fast mechanism was approximately ten times higher than the current associated with the slow mechanism.

Figure 4 gives the spectrum of relative photoconductivity of tungsten film applied onto a dielectric substrate, reduced to the intensity of incident radiation; in this figure, $\delta\sigma$ is the variation of film conductivity reduced to the intensity of light incident on the sample and σ is the film conductivity in the absence of light. The spectrum was measured in the wavelength range from 0.5 to 2 μm at a temperature of 77 K in four samples of different thickness of metal film (d = 6.5, 8, 9.5, and 11 Å). The photoconductivity of the film was measured in the linear region of the curve describing the dependence of film photoconductivity on the light intensity. Figure 5 gives the reduced relative photoconductivity as a function of the metal film thickness on the wavelength of light incident on the sample λ = 0.7 μm. One can see in Figs. 4 and 5 that the relative photoconductivity smoothly decreases with increasing wavelength; when the film thickness is varied, the curve of relative photoconductivity exhibits a maximum at a metal layer thickness of about 9 Å.

Figure 6 gives a reduced variation of photocurrent through the sample upon delivery to the film of a light pulse with a duration of 25 s; in this figure, δI is the variation of current through the sample at the given moment of time under the effect of light and δI_{max} is the maximal variation of current under the effect of light. One can see in Fig. 6 that the rise time and fall time of photocurrent are the same and approximately equal to 10 s.

3. DISCUSSION OF THE RESULTS

An image of the surface of a tungsten film of thickness d = 6.3 Å applied onto a dielectric substrate is given in Fig. 1. This sample was not randomly chosen to demonstrate the structure of the film surface. It is with this thickness of tungsten film applied onto a dielectric substrate that the film begins to conduct the electric current (see Fig. 3). No electric current flow through the film is observed for a smaller film thickness; the film resistivity decreases abruptly with

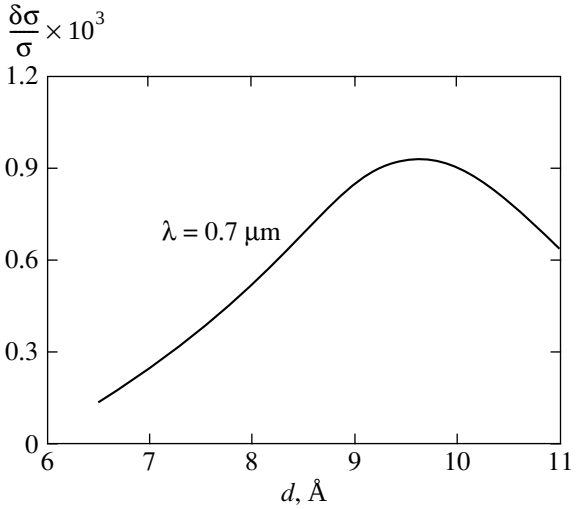

Fig. 5. The relative photoconductivity as a function of the metal film thickness at λ = 0.7 μm.

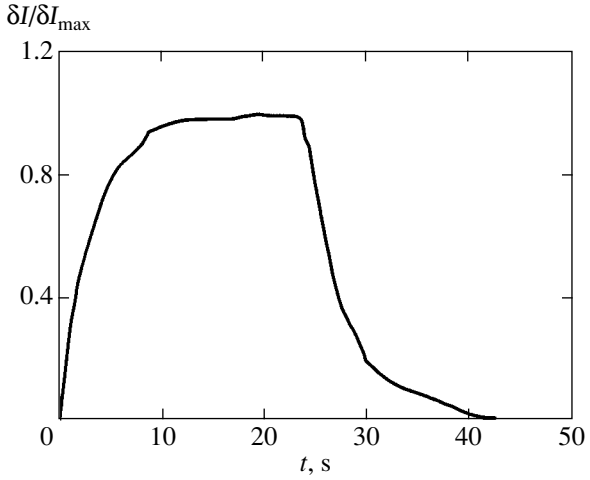

Fig. 6. A variation of photocurrent through the sample upon incidence on the film of a light pulse with a duration of 25 s.

increasing thickness. One can see in Fig. 1 that the film exhibits an island pattern. According to estimates, the average island radius (we assume that the islands are circular in shape) is r = 150–160 Å, the number of islands per unit area is $N = 7 \times 10^{10}$ cm^{-2}, and the fraction of the substrate surface taken up by metal islands is $\Theta_c = N\pi r^2 = 0.47$–$0.57$. Therefore, in metal films with a thickness of 6.3 Å and $\Theta_c = 0.47$–0.57, the percolation threshold of current is observed and an infinite cluster is formed; this agrees well with the percolation threshold of the continual problem of percolation theory for a two-dimensional case ($\Theta_c = 0.5$) [5].

The measured dependences of the surface resistivity of metal films on the sample temperature, given in Figs. 2 and 3, drastically differ from, and exceed by many orders of magnitude, those of massive metal samples. The resistivity of metal films of thickness d = 6.3, 7.9, 9.48 Å varies with temperature by the activation law of $\rho \propto \exp(T_0/T)^{0.5}$ (see Fig. 7). This law is interpreted within the model of variable range hopping conductivity in the region of the Coulomb quasi-gap [5]. Hopping conductivity of two types is possible in metal films. The conductivity of the first type is associated with the electron tunneling from one metal island to another involving phonons. The conductivity of the second type is associated with the transition of electrons on the Fermi level from a metal island to traps which are always present in the protective (semiconductor or dielectric) layer. From the traps, the electrons may tunnel to another metal island. These traps may be located on the surface or within the thin protective layer covering the metal island and separating it from the neighboring metal island. One can distinguish between these two mechanisms of current flow in island metal films by measuring the time of response of the current through the sample to the step of voltage applied to the sample. In the case of electron tunneling directly from one metal island to another, the time of current response to the step of voltage must be shorter compared to the transition of electrons between metal islands through traps. As was demonstrated by the results of measurements given in the previous section, the time of response of the current in the sample to the step of voltage is characterized by two times (short and long), and the current associated with short times is much higher than the current associated with slow processes. It is obvious that the fast component of current variation is defined by hops of electrons directly between metal islands, and the slow component is defined by the intermediate capture of electrons in the traps; consequently, the mechanism of current flow through island metal films is largely defined by hops of electrons between metal islands.

With a metal film thickness exceeding 10 Å, the metal islands increase in size and form a continuous film. However, the film thickness remains much smaller than the mean free path of electrons during their scattering by phonons. In the films, the conduction electrons are scattered from the boundaries and from the defects and nonuniformities of the film; as a result, the mean free path of electrons in the film depends weakly on temperature and, therefore, films with a thickness of up to 100 Å exhibit a weak dependence of their resistivity on temperature.

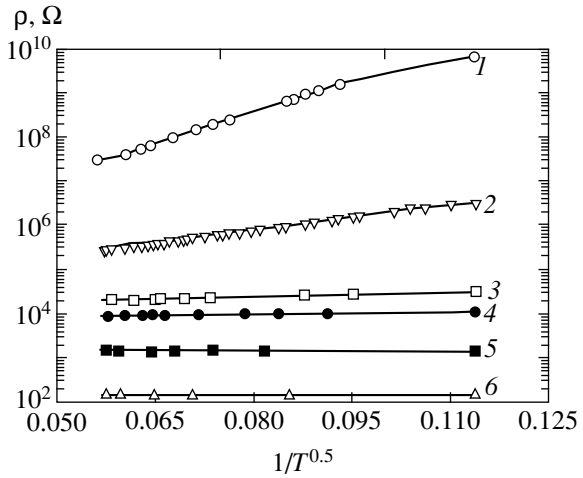

Fig. 7. The logarithmic dependence of the resistivity of a series of metal films as a function of $T^{-0.5}$ (6.3 (*1*), 7.9 (*2*), 9.8 (*3*), 11 (*4*), 19 (*5*), and 100 Å (*6*)).

Under the effect of electromagnetic radiation, the conductivity of metal film varies. As in the case of conductivity, the mechanisms of photoconductivity may be associated with hops of electrons directly from one metal island to another with the absorption of a light quantum, or with the electron transition from a metal island to a trap with the absorption of a light quantum and a subsequent electron transition from the trap to another metal island. The dependence of the photoconductivity on the wavelength of incident radiation and the time characteristic of variation of photoconductivity upon stimulation of the metal film by a radiation pulse are given in Figs. 4, 5, and 6. The special features of the photoconductivity effect in thin metal films are as follows.

(1) The photoconductivity decreases with increasing wavelength of electromagnetic radiation. This regularity is observed in all measured samples (Fig. 4).

(2) The absolute value of photoconductivity of a metal film increases with increasing film thickness. However, the relative magnitude of photoconductivity has a maximum and decreases with increasing film thickness (Fig. 5).

(3) The rise time and the fall time of photocurrent are the same and approximately equal to 10 s.

The foregoing features characterizing the photoconductivity in thin metal films lead to the assumption that the photoelectric phenomena in these films are not directly associated with the electron tunneling from one metal island to another. This conclusion follows from the observation that the time of response of photoconductivity to the radiation pulse exceeds by three orders

of magnitude the time of response of current in the film to the step of voltage.

Obviously, in this case, the photoconductivity is associated with the transition of electrons from metal islands to traps with the absorption of a light quantum. Then, the electrons make a transition from the traps to other metal islands. These traps may be located on the surface of a thin oxide or dielectric layer covering a metal island and separating it from the neighboring metal island, or within the dielectric layer proper. The dielectric layers between metal islands are noncrystalline; such substances are characterized by allowed states in the forbidden band, with the density of the states as a function of energy increasing abruptly from the middle of the forbidden band of the dielectric towards the conduction and valence bands [4]. Under the effect of radiation, the electrons located on traps in the vicinity of the Fermi level or on metal islands are excited to higher states in the forbidden band of the dielectric, where the density of states of the traps is much higher than the density of their states in the vicinity of the Fermi level. Therefore, the probability of the electron capture to the traps increases with the light quantum energy and, consequently, the metal film conductivity must increase with the energy of absorbed light quantum. It is this behavior of the dependence of photoconductivity on the wavelength of incident light that has been observed experimentally (Fig. 4).

One can see in Fig. 5 that the relative photoconductivity of metal film has a maximal value at a film thickness of d = 9–10 Å. This fact is additional evidence for the existence in metal films of hopping conductivity of nonequilibrium electrons over localized states of two types. Figure 5 gives the photoconductivity as a function of metal film thickness, divided by the total conductivity of metal film associated with the electron tunneling both directly between metal islands and via traps. As the film thickness is varied while the film exhibits an island pattern, the number of islands and the number of dielectric interlayers vary proportionally with the variation of the film thickness. On the other hand, an increase in the film thickness leads to an increase in the quantum yield and, consequently, to an increase in the relative photoconductivity. As the film thickness is further increased, the metal islands grow in size to form a continuous film and the conductivity associated with the transition of electrons between metal islands abruptly increases compared to the transition of electrons to traps. This explains the decrease in the relative photoconductivity with increasing film thickness and confirms the existence of two types of hopping conductivity in thin metal films.

4. CONCLUSIONS

We have investigated the photoconductivity and revealed for the first time the photoelectric effect in hyperfine island metal films. The investigations were performed in films of Ti, W, FeNi and others, grown by the method of rf sputtering in argon. It has been demonstrated that these metal films exhibit an island pattern and their resistivity varies with temperature by the activation law of $\rho \propto \exp(T_0/T)^{0.5}$. This law is interpreted within the model of variable range hopping conductivity in the region of the Coulomb quasi-gap; in such a way, it has been demonstrated that electrons may hop directly between metal islands with the participation of phonons or they may hop between metal islands with an intermediate hop to traps in the dielectric layer separating the islands. The photoconductivity in such films was observed in the visible and near-infrared spectral regions. Two models of photoconductivity in island metal films were suggested in order to determine the mechanism of photoconductivity. It has been demonstrated that the photoconductivity in the visible and near-infrared spectral regions is associated with the transition of electrons from metal islands to traps with the absorption of light quanta. Then, the electrons make a transition from traps to other metal islands. These traps may be located on the surface of a thin oxide or dielectric layer covering a metal island and separating it from the neighboring metal island, or within the dielectric layer proper.

ACKNOWLEDGMENTS

We are grateful to N.N. Sibel'din for numerous consultations and valuable advice.

This study was made within the framework of the Russian interdisciplinary scientific and technical program on Physics of Solid-State Nanostructures and was supported by the Russian Foundation for Basic Research.

REFERENCES

1. L. I. Maissel and R. Glang, *Handbook of Thin-Film Technology* (McCraw-Hill, New York, 1970; Sovetskoe Radio, Moscow, 1977), p. 38.
2. R. D. Fedorovich, A. G. Naumovets, and P. M. Tomchuk, J. Phys.: Condens. Matter. **11**, 9955 (1999).
3. V. M. Shalaev, Phys. Rep. **272**, 61 (1996).
4. N. F. Mott and E. A. Davis, *Electronic Processes in Non-Crystalline Materials*, 2nd ed. (Clarendon Press, Oxford, 1979; Mir, Moscow, 1982), Vols. 1 and 2.
5. B. I. Shklovskiĭ and A. L. Éfros, *Electronic Properties of Doped Semiconductors* (Nauka, Moscow, 1979; Springer, New York, 1984).
6. N. Markovic, C. Christiansen, D. E. Grupp, *et al.*, Phys. Rev. B **62**, 2195 (2000).

Translated by H. Bronstein

Journal of Experimental and Theoretical Physics, Vol. 96, No. 5, 2003, pp. 945–952.
Translated from Zhurnal Éksperimental'noĭ i Teoreticheskoĭ Fiziki, Vol. 123, No. 5, 2003, pp. 1073–1081.

SOLIDS
Electronic Properties

Theoretical Prediction of a Surface-Induced Spin-Reorientation Phase Transition in $BaFe_{12}O_{19}$ Nanocrystals

S. N. Zinenko[a], A. A. Murakhovski[a], L. P. Ol'khovik[a], Z. I. Sizova[a], E. V. Shurinova[a], and A. S. Kamzin[b,*]

[a] *Kharkov State University, Kharkov, 61077 Ukraine*

[b] *Ioffe Physicotechnical Institute, Russian Academy of Sciences, ul. Politekhnicheskaya 26, St. Petersburg, 194021 Russia*

**e-mail: kamzin@spb.cityline.ru*

Received August 27, 2002

Abstract—The equation of the magnetization of a hexagonal crystal is derived for the first time for an arbitrary orientation of the external magnetic field relative to the crystallographic *c* axis. In order to clarify the magnetization mechanism for a real ensemble of small particles in the framework of the given problem, surface anisotropy (which is significant for nanosize objects) was taken into account along with crystalline magnetic anisotropy and anisotropy in the particle shape. Model computer experiments prove that the magnetization curves for nanocrystals oriented in a polar angle range of 65–90° exhibit an anomaly in the form of a jump, indicating a first-order spin-reorientation phase transition. This explains a larger steepness of the experimental curve reconstructed taking into account the interaction between particles as compared to the theoretical dependence obtained by Stoner and Wohlfarth [IEEE Trans. Magn. MAG **27** (4), 3469 (1991)]. An analysis of variation of the characteristic anisotropy surface and its cross section with increasing ratio $|K_2|/K_1$ of the crystalline magnetic anisotropy constants upon a transition from a macroscopic to a nanoscopic crystal shows that surface anisotropy leads to a change in the magnetic structure. As a result, an additional easy magnetization direction emerges in the basal plane apart from the easiest magnetization direction (along the *c* axis). The direction of hard magnetization emerges from the basal plane, the angle of its orientation relative to the *c* axis being a function of the ratio $|K_2|/K_1$. *© 2003 MAIK "Nauka/Interperiodica".*

1. INTRODUCTION

In contrast to its macroscopic analog, the magnetization curve for a system of small particles is characterized by a weak variation of magnetization over an extended initial region of fields ($H \le 0.25H_A$, H_A being the anisotropy field), followed by an abrupt increase. Such a shape of the curve was theoretically substantiated for the first time in [1] for an ensemble of randomly oriented monodomain noninteracting particles. The case of uniaxial magnetic anisotropy associated with the shape of the particles was considered. At the same time, it was assumed that the value of the anisotropy field is the same for the entire ensemble. Hysteresis loops were calculated numerically, and the basic magnetization curve was obtained by averaging the descending and ascending branches of the limiting hysteresis loop.

Analysis of the behavior of real ensembles of small particles in a magnetic field [2, 3] indicates the necessity of taking into account, in addition, the surface anisotropy and the interaction between particles.

2. SPECIFIC FEATURES OF A SYSTEM OF NANOPARTICLES OF BARIUM HEXAFERRITE

The form of the field dependence of magnetization, which was described theoretically in [1], was observed for a close-packed ensemble of lamellar nanoparticles (diameter d = 10–100 nm and d/h = 2–5, where h is the particle thickness) of the highly anisotropic ferrimagnet $BaFe_{12}O_{19}$ ($P6_3/mmc$, c = 2.32 nm) at 300 K, i.e., in the range of the magnetically stable state [4]. This object corresponds to the theoretical model in three main features: monodomain nature, uniaxial (here, crystalline magnetic) anisotropy of the material, and random orientation of particles. The main specific feature of the system under investigation is the particle distribution over morphological parameters, leading to anisotropy field distributions with different contributions of the shape anisotropy and especially surface anisotropy.

Analysis of the anisotropy field distributions indicating a decrease in anisotropy fields from 18 to 8 kOe depending on the particle size [2] makes it possible to explain the observed displacement of the magnetization

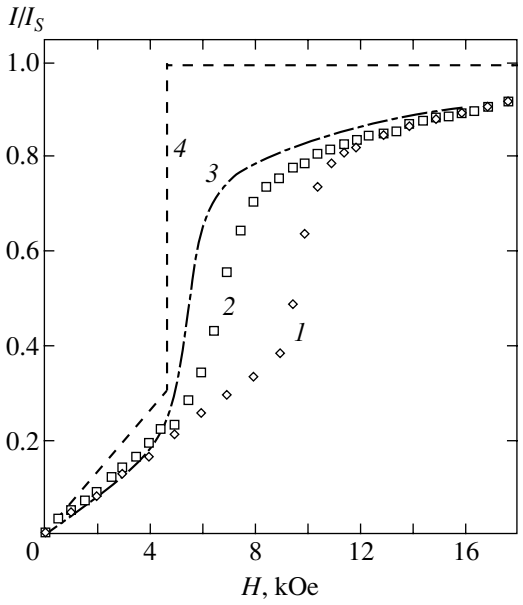

Fig. 1. Main magnetization curve at 300 K: results of calculations with the value of the anisotropy field of barium ferrite (*1*), experimental data for nanocrystalline $BaFe_{12}O_{19}$ powder (*2*), experimental curve reconstructed taking into account the particle interaction (*3*), and theoretical curve as the result of computer simulation for a nanocrystal, $\mathbf{H} \perp \mathbf{c}$ (*4*).

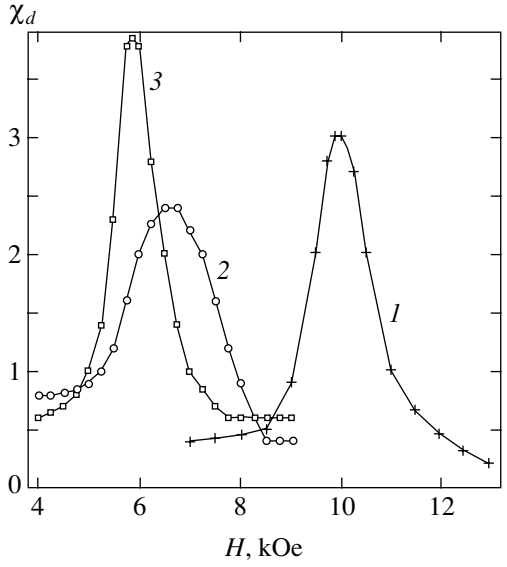

Fig. 2. Field dependence of the differential magnetic susceptibility for cases *1*, *2*, and *3* (see Fig. 1).

jump on the experimental curve relative to the theoretical position towards smaller field values (Fig. 1).

Since the powder sample under investigation is a close-packed ensemble of particles (packing factor $p \approx 0.4$), the effect of particle interaction was manifested in it in spite of strong crystalline magnetic anisotropy of the material. It was shown in [3] that the resultant interaction in the given system is negative and significant precisely in the magnetization jump region, i.e., in fields corresponding to irreversible magnetization processes. It can be seen from Fig. 1 that the shape of the magnetization curve reconstructed by taking into account the correction to the particle interaction has not changed, but its maximal steepness (differential susceptibility) in the jump region (Fig. 2) has increased and exceeded the theoretical value by 40%. This points to the existence of an additional (relative to the theoretical model) mechanism of formation of the magnetization curve, which is typical of the system in question. Here, we put forth the assumption that this mechanism, which is masked by the particle interaction, is associated with the effect of surface anisotropy.

3. ANISOTROPIC PART OF THE FREE ENERGY OF A $BaFe_{12}O_{19}$ NANOCRYSTAL

For a hexagonal crystal, the anisotropic part of the free energy can be written in the form

$$F(\theta, \varphi) = K_1 \sin^2\theta + K_2 \sin^4\theta + (K_3 + K_3' \cos 6\varphi)\sin^6\theta + \ldots, \quad (1)$$

where K_1, K_2, … are the crystalline magnetic anisotropy constants, and θ and φ are the polar and azimuth angles of the magnetization vector, respectively.

The crystalline magnetic anisotropy energy of barium ferrite is described by the first anisotropy constant alone,

$$W(\theta) = K_1 \sin^2\theta, \quad (2)$$

where $K_1 = 3.3 \times 10^6$ erg cm^{-3} at $T = 300$ K. As we pass to a nanocrystal, the contributions from other anisotropy types (surface and shape anisotropy) characteristic of the given object must be taken into account in Eq. (2) along with the main contribution of crystalline magnetic anisotropy.

Surface anisotropy appears as the result of structural distortions in the surface layer with broken stoichiometry [5, 6]. Being crystallographic in nature, surface anisotropy is due to single-ion contributions of magnetically active ions localized in positions with a lower symmetry. It is found that the surface layer thickness determined in [7] for a $BaFe_{12}O_{19}$ macrocrystal along its *c* axis amounts to 2–5 nm and is commensurate with the thickness of nanoparticles under investigation. For this reason, it is expedient to characterize the surface anisotropy in the present case by introducing constant K_S, viz., the energy per unit volume and not per unit area, as is generally expected [8]. The results of calculations show that constant $K_S = -1.8 \times 10^6$ erg cm^{-3} [2]; i.e., its sign is opposite to that of the first magnetocrystalline anisotropy constant and is comparable to its value.

The surface anisotropy constant K_S was taken into account by introducing it into formula (1) for free energy as constant K_2. This is substantiated by the data

obtained from the investigation of the magnetic anisotropy of a hexaferrite macrocrystal of the same structural class with an unsubstituted magnetic matrix (the total number of Fe^{3+} ions and their localization remain unchanged), but with perturbed crystalline structure. For example, substitution of a pair of La^{3+}–Na^{1+} with different valences for Ba^{2+} ions in a unit cell of $BaFe_{12}O_{19}$ ferrite lowers the symmetry in view of their superstructural ordering and changes the degree of local distortions of crystallographic positions responsible for the formation of magnetocrystalline anisotropy. This leads to the emergence of a fourth-order anisotropy constant K_2, which, in contrast to K_1, is negative and has the same order of magnitude [9].

In order to verify the correctness of the assumption that the surface anisotropy constant K_S is equivalent to the magnetocrystalline anisotropy constant K_2, we analyze the diagram of equilibrium magnetization states for a hexagonal ferromagnet [10]). The computer version of the equilibrium state diagram of magnetization [11] for $K_1 > 0$ is shown in Fig. 3. In the equilibrium state, spontaneous magnetization in the crystal is oriented in the direction corresponding to the absolute minimum of the anisotropy energy. The existence of local minimum and maximum in regions II–V indicates the possibility of existence of angular magnetic structures and spin-reorientation phase transitions. The curves on the diagram mark the stability boundaries of phases [10].

If the anisotropy energy of a ferromagnet can be described by Eq. (2) (as in the case of a barium ferrite macrocrystal), the point corresponding to its magnetic state falls in region I; namely, it is at the origin of the equilibrium state diagram for magnetization. In this case, the equilibrium magnetization is oriented parallel to the *c* axis. The basic magnetization curves have no singularities for any orientation of the external magnetic field. If the anisotropy parameters of the crystal correspond to regions I and II on the diagram, where $K_1 > 0$, $K_2 < 0$, and $K_1 \geq |K_2|$, $K_3 = K_3' = 0$, the easiest magnetization direction of the crystal is oriented along the *c* axis. If the crystal magnetization is perpendicular to the *c* axis, a magnetization jump can appear in the critical magnetic field. According to the classification introduced in [10], this is a first-order spin-reorientation phase transition.

Such a case is realized in the barium ferrite nanopowder under investigation with the anisotropy parameters $K_1 > 0$, $K_S = K_2 < 0$, and $|K_2|/K_1 \approx 0.6$. The fact that the experimental samples of barium ferrite nanopowder exhibit this singularity in the behavior of magnetization in a magnetic field justifies the identification of constant K_S with the magnetocrystalline anisotropy constant K_2.

It should be noted that regions I and II of the orientation diagram, where $K_1 > 0$, $K_2 < 0$, and $K_1 \geq |K_2|$, are characterized by the existence of a local minimum of the anisotropy energy in the basal plane in addition to the absolute minimum along the *c* axis. For this reason, sixth-degree invariants (anisotropy constants K_3 and K_3') must be taken into account in the general case in the expression of the anisotropic part of the free energy of the nanocrystal.

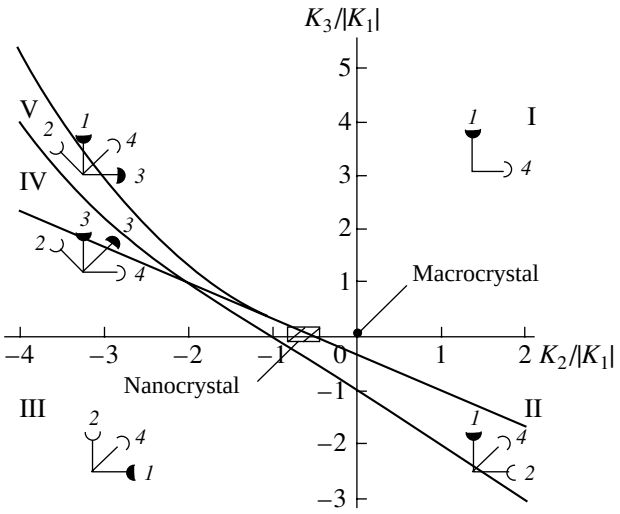

Fig. 3. Equilibrium state diagram for magnetization of a hexagonal crystal for $K_1 > 0$: *1* and *2* are the absolute and local minima, and *3* and *4* are the absolute and local maxima of the anisotropy energy [10].

In order to analyze magnetization processes correctly, we must also take into account the magnetostatic energy of nanoparticles. In the problem under consideration, nanoparticles have a platelet shape and can be treated in the first approximation as oblate ellipsoids of revolution. In this case, the anisotropic part and the magnetostatic energy can be represented in the form

$$W_{\text{dem}} = \frac{I_S^2}{2}(N_b - N_a)\sin^2\theta = K_N \sin^2\theta, \qquad (3)$$

where I_S is the magnetization and N_a and N_b are the demagnetizing factors. The form of expression (3) for the anisotropic part of the magnetostatic energy coincides with expression (2). Consequently, we can combine Eqs. (2) and (3), and constant K_N will be henceforth taken into account as a correction to the first magnetocrystalline anisotropy constant. In the case considered here, $K_N \approx 3 \times 10^5$ erg cm^{-3}, which amounts approximately to 10% of constant K_1. Consequently, the anisotropic part of the free energy of a hexagonal nanocrystal can be written in the form

$$F_A(\theta, \varphi) = (K_1 - K_N)\sin^2\theta + K_2 \sin^4\theta + (K_3 + K_3' \cos 6\varphi)\sin^6\theta + \ldots \qquad (4)$$

This form of representation takes into account the main types of energy responsible for magnetization processes: the magnetocrystalline anisotropy energy, the

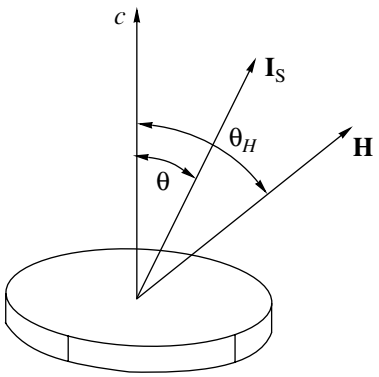

Fig. 4. To the calculation of the magnetization curves of a hexagonal nanocrystal.

surface anisotropy energy, and the magnetostatic energy. In particular, if $K_N \gg K_1$, the Stoner–Wohlfarth model [1] is realized. In order to simplify notation in the subsequent analysis, we will assume that K_1 stands for the difference $K_1 - K_N$.

In order to obtain an analytic description of magnetization processes in ferromagnets, we must also include the Zeeman energy, viz., the energy of interaction of magnetization with the external magnetic field:

$$W_Z = -(\mathbf{I}_S \cdot \mathbf{H}) = -I_S H \cos(\theta_H - \theta), \qquad (5)$$

where θ and θ_H are the angles between the *c* axis of the crystal and the directions of magnetization and external magnetic field, respectively (Fig. 4). Taking into account relations (4) and (5), we can write the free energy of a hexagonal crystal in the form

$$F = F_A(\theta, \varphi) + W_Z = F_A(\theta, \varphi) - I_S H \cos(\theta_H - \theta). \qquad (6)$$

This equation was used for deriving the equation of state or the equation describing the main magnetization curve and for analyzing the dynamics of magnetization processes in hexagonal barium ferrite nanocrystals.

4. EQUATION OF STATE FOR A HEXAGONAL CRYSTAL FOR THE CASE OF ARBITRARY ORIENTATION OF THE EXTERNAL MAGNETIC FIELD RELATIVE TO THE *c* AXIS

The equation describing the main magnetization curve or the equation of state of a hexagonal crystal can be derived by equating to zero the derivatives of free energy (6) with respect to angles θ and φ and by solving the obtained system of equations [10]. In particular cases when the external magnetic field is oriented parallel or perpendicular to the *c* axis, the corresponding equations describing the magnetization curve have the form

$$h = -2m[1 + 2x(1 - m^2) + 3y(1 - m^2)^2] \times (1 + 2x + 3y), \qquad (7)$$

or

$$h = 2m(1 + 2xm^2 + 3ym^4), \qquad (8)$$

where

$$x = \frac{K_2}{|K_1|}, \quad y = \frac{K_3}{|K_1|}, \quad m = \frac{I}{I_S},$$

$$h = \frac{2H}{H_{A1}}, \quad H_{A1} = \frac{K_1}{I_S}.$$

In the general case when $0 \le \theta_H \le 90°$, the equation of state taking into account the second, fourth, and higher order invariants in the free energy expansion for an arbitrary orientation of the magnetic field is a transcendental fifth-degree equation. Its exact solution involves rather complicated calculations.

Let us consider a general approach to solving the given problem and obtain the required results using a numerical method of solution of the state equation for a hexagonal magnetically ordered crystal.

We normalize Eq. (6) in the modulus $|K_1|$ of the first magnetic crystallographic anisotropy constant; considering that $K_1 = H_{A1}I_S/2$, we can write the free energy of the crystal in question in the form

$$f(\theta, h) = w(\theta) - h\cos(\theta_H - \theta), \qquad (9)$$

where

$$w(\theta) = \frac{W(\theta)}{|K_1|}, \quad h = \frac{2H}{H_{A1}}, \quad \cos(\theta_H - \theta) = \frac{I}{I_S}.$$

For the rotational mechanism of magnetization, the magnetization vector $\mathbf{I}_S$ deviates from the easy magnetization direction and rotates in the direction of the field under the action of the torque $\mathbf{M} = \mathbf{I}_S \times \mathbf{H}$ created by the field (Fig. 4). In equilibrium, this torque is compensated by the opposite moment $M_A = -df(\theta, h)/d\theta$ of anisotropy forces tending to rotate magnetization vector in the easy magnetization direction.

If the magnetization of a ferromagnetic nanoparticles occurs as the process of rotation of the magnetization vector towards the direction of the applied magnetic field, the magnetization curve is described by the equation

$$m(h) = \cos[\theta^{\min}(h) - \theta], \qquad (10)$$

where $\theta^{\min}(h)$ is the angle for which the anisotropy energy has a minimum for a given value of *h*.

It should be noted that function *m*(*h*) increases monotonically. Indeed, if $h_1 < h_2$ and $\theta_1^{\min}$, $\theta_2^{\min}$, and

m_1, m_2 are the corresponding angles and the values of cosines, inequalities

$$f(\theta_1^{\min}, h_1) \le f(\theta_2^{\min}, h_1),$$
$$f(\theta_2^{\min}, h_2) \le f(\theta_1^{\min}, h_2) \quad (11)$$

after term-by-term summation give

$$(h_2 - h_1)(m_2 - m_1) \ge 0, \quad (12)$$

whence $m_2 > m_1$.

Further, it should be noted that the anisotropy energy minimum is attained at points $\theta^{\min}$ satisfying the conditions

$$f'(\theta, h) = -w'(\theta) - h\sin(\theta_H - \theta)\big|_{\theta = \theta^{\min}} = 0, \quad (13)$$

so that

$$h = -\frac{w'(\theta)}{\sin(\theta_H - \theta)}\bigg|_{\theta = \theta^{\min}}.$$

Consequently, the parametrically defined curves

$$m = \cos(\theta_H - \theta), \quad h = -\frac{w'(\theta)}{\sin(\theta_H - \theta)}, \quad 0 \le \theta < \theta_H \le \frac{\pi}{2}, \quad (14)$$

can be treated as the "theoretical" magnetization curves. The real magnetization curve $m(h)$ consists of individual "theoretical" branches. A transition from one branch to another occurs jumpwise; this is the jump on the magnetization curve.

The properties of the function $m(h)$ mentioned above suggest the following numerical method for constructing this function, which leads to a certain sequence of points

$$(h_0, m_0), \ldots, (h_k, m_k), \ldots, (h_n, m_n).$$

Let us specify a small step Δm along the m axis. Assuming that the previous point (n_{k-1}, m_{k-1}) has been determined (we take (0,0) as the initial point (h_0, m_0)), we construct the next point (h_k, m_k).

The angle corresponding to the minimum anisotropy energy for $h = h_{k-1}$ is denoted by $\theta_k^{\min}$. Depending on the relation between m_{k-1} and $\cos\theta_k^{\min}$, the choice of point (h_k, m_k) can be made in different ways.

1. If $m_{k-1} = \cos(\theta_k^{\min} - \theta)$, we have

$$m_k = m_{k-1} + \Delta m, \quad h_k = -\frac{w'(\theta_k^{\pm})}{\sin(\theta_k^{\pm} - \theta)}, \quad (15)$$

where $\theta_k^{\pm} = q \pm \arccos m_k$ (the plus or minus sign is determined by the sign of difference $\theta_k^{\min} - \theta$).

2. If $m_{k-1} < \cos(\theta_k^{\min} - \theta)$, we have

$$m_k = \cos(\theta_k^{\min} - \theta), \quad h_k = h_{k-1}. \quad (16)$$

The value of the field $h = h_{k-1} = h_k$ is critical, and the magnetization curve contains the jump $\Delta m = m_k - m_{k-1}$.

Thus, Eq. (14) can be treated as the equation of the main magnetization curve of the hexagonal crystal for an arbitrary orientation of the external magnetic field relative to the c axis. The magnetization process associated with rotation of the spontaneous magnetization vector can be reversible (15) or irreversible (16) with a jump in the critical magnetic field.

5. RESULTS OF MODEL COMPUTER EXPERIMENT

Equations (4), (6), and (14) form the basis of the program Crystal for simulating the dynamics of magnetization processes. In order to obtain magnetization curve, it is sufficient to indicate a point on the plane of the orientation phase diagram and to specify the direction of the external magnetic field. The values of anisotropy constants for the chosen point are introduced automatically in the programs for constructing not only magnetization curves, but also the characteristic anisotropy surface and its cross section.

Figure 5 shows the model of the main magnetization curves for macrocrystalline and nanocrystalline barium ferrite samples for various orientations of the magnetic field relative to the crystallographic c axis. It can be seen from Fig. 5a that the magnetization curve has the form typical of a uniaxial macrocrystal. In the direction of hard magnetization ($\theta_H = 90°$), the magnetization increases linearly and attains saturation in a magnetic field equal to the anisotropy field. The deviation of the external field direction from the basal plane leads to a sharp increase in the technical saturation field (Figs. 5b and 5c); for $\theta_H = 65°$ (Fig. 5c), this field exceeds the anisotropy field by a factor of ~8. For intermediate angles $0 < \theta_H < 90°$, a magnetization component along the c axis simultaneously appears; the value of this component increases as angle θ decreases from 90° to zero. This can be clearly seen from the "starting" points of the magnetization process.

For comparison, Figs. 5d–5f show the models of the main magnetization curves for a barium ferrite nanocrystal. The value $|K_2|/K_1 = 0.60$ corresponds to the experimentally obtained ratio of the surface and magnetocrystalline anisotropy constants.

Let us consider in greater detail the models of the magnetization curves for nanocrystalline samples. For $\theta_H = 90°$, the magnetic field in which a magnetization jump is observed amounts to 0.23 of the anisotropy field of the macrocrystal and 0.34 of the mean value of the anisotropy field on the system of nanocrystals under investigation. The latter value corresponds to the field

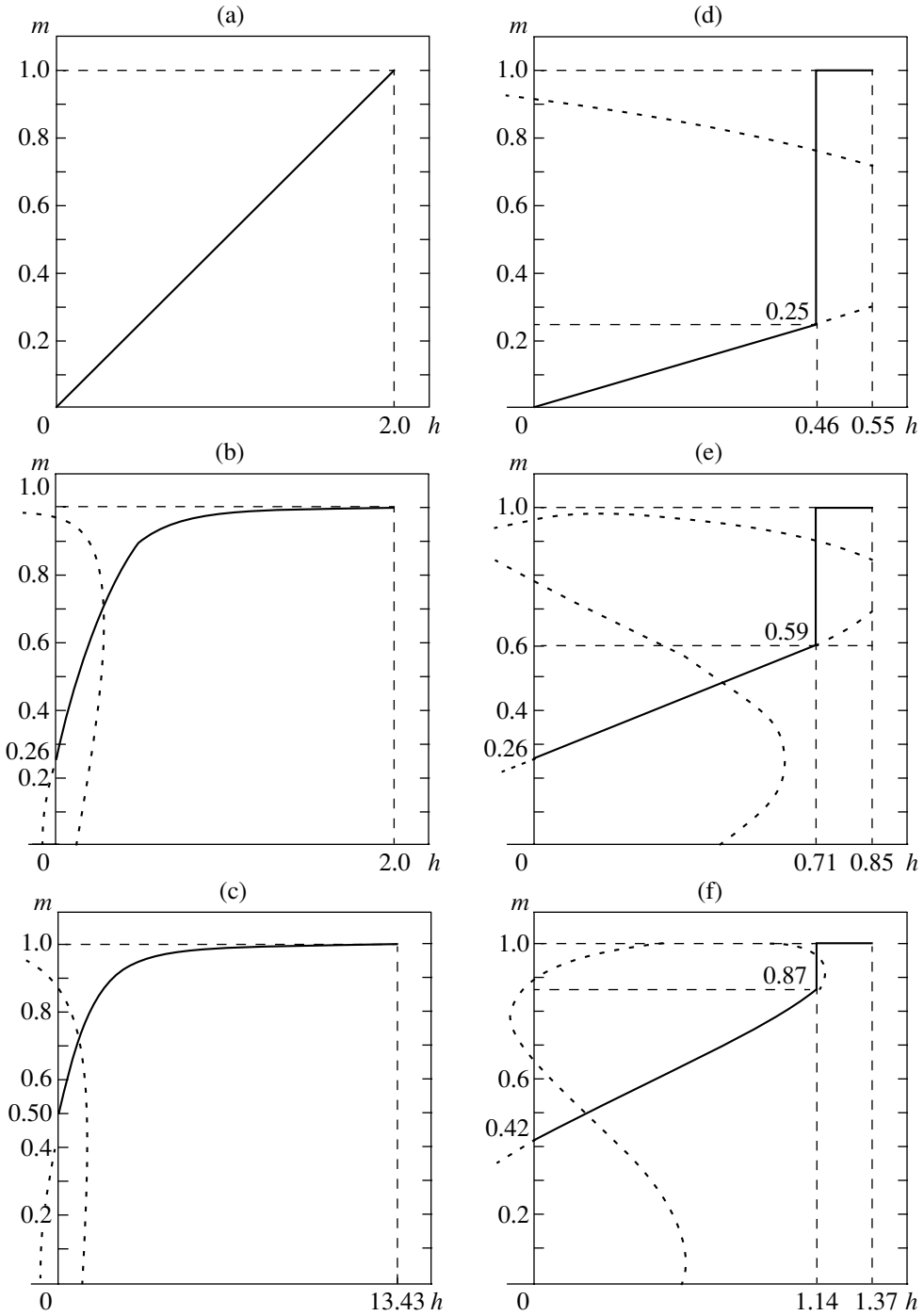

Fig. 5. Computer models of the magnetization curves for a macrocrystal, $|K_2|/K_1 = 0$ (a–c), and for a nanocrystal, $|K_2|/K_1 = 0.6$ (d–f) for different orientations of the external magnetic field relative to the *c* axis: $\theta_H = 90°$ (a, d), 75° (b, e), and 65° (c, f). Short dashes in the figures correspond to solutions to Eqs. (14).

of the jump on the experimentally obtained magnetization curve (curve *3* in Fig. 1). As angle θ_H decreases from 90° to 65°, the field corresponding to the magnetization jump increases to $h = 0.60H_A$. If angle $\theta_H < 65°$, the magnetization jump vanishes and the magnetization curves of the nanocrystalline sample become similar to those for a macrocrystalline sample.

In order to find the factors leading to a spin-reorientation phase transition in barium ferrite nanocrystals, we obtained the characteristic anisotropy surfaces and their cross sections, i.e., vector anisotropy diagrams, which give a visual idea of the spatial distribution of the anisotropy energy. The concept of the characteristic anisotropy surface was introduced in [12] on the basis

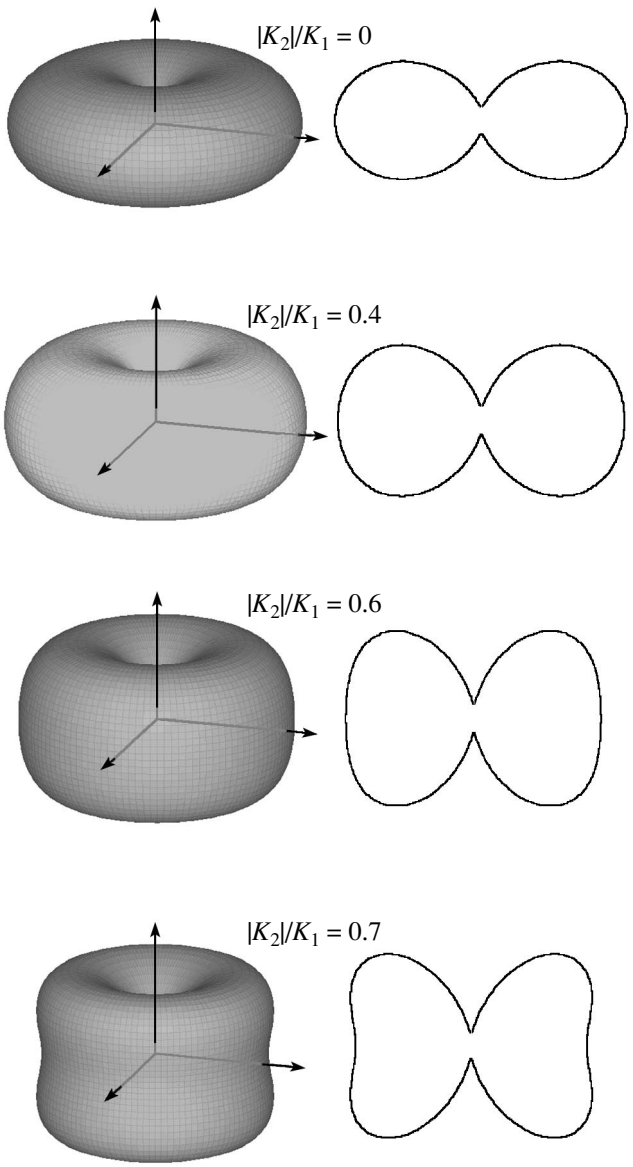

Fig. 6. Evolution of the characteristic surfaces and vector diagrams of anisotropy upon transition from a macrocrystal to a nanocrystal.

of the anisotropic part of free energy in the form of a tensor series [12, 13], which contains symmetric tensors of even (second, fourth, and sixth) ranks in accordance with the crystal symmetry. Equation (1) was derived as a result of transformation of the tensor representation of the anisotropic part of free energy into a trigonometric form [13].

The characteristic surfaces and the vector anisotropy diagrams for $BaFe_{12}O_{19}$ macrocrystal and the nanocrystal are shown in Fig. 6. In all cases considered here, the characteristic surfaces are of toroidal shape. As the ratio of the anisotropy constants increases from zero to 0.9, the shape of the characteristic surface and, accordingly, of the vector diagram, changes. Analysis of these variations in the range of $|K_2|/K_1$ values under investigation makes it possible to study in detail the effect of surface anisotropy on the dynamics of variation of the magnetic structure upon a transition from a macrocrystal to a nanocrystal and, hence, to establish the nature of the spin-reorientation phase transition in question.

For a macrocrystal, we have $|K_2|/K_1 = 0$. In this case, the vector diagram of anisotropy displays an absolute minimum and an absolute maximum of the anisotropy energy lying, respectively, at angles of $\theta = 0$ and $\theta = 90°$ to the *c* axis. These angles correspond to the easiest and hard magnetization directions. As the ratio of the constants increases from 0 to 0.9, the anisotropy energy in the basal plane gradually decreases, and for $|K_2|/K_1 \geq 0.2$, there appears a local energy minimum whose depth increases upon a further increase in the ratio of the constants. The absolute and local minima are separated by an absolute maximum whose position shifts from $\theta = 90°$ to $\theta \approx 60°$ with increasing ratio of constants from 0 to 0.9.

The emergence of the hard magnetization direction from the basal plane indicates a change in the magnetic structure of the crystal: a uniaxial crystal becomes at least biaxial. The easiest magnetization direction coincides with the *c* axis as before, and the new direction of easy magnetization lies in the basal plane. The hard magnetization direction forms with the *c* axis an angle whose value depends on the ratio of the surface and magnetocrystalline anisotropy constants. Consequently, the reason for a spin-reorientation phase transition occurring in a magnetic field in barium ferrite nanocrystals is the change in the magnetic structure caused by the open surface of nanoparticles and the surface anisotropy energy associated with it.

6. CONCLUSIONS

It is proved that the specific auxiliary mechanism of formation of the magnetization curve for a highly anisotropic ferrimagnet upon a transition from a macrocrystal to a system of nanocrystals as compared to the Stoner–Wohlfarth theoretical model [1] is the mechanism associated with surface magnetic anisotropy. This effect, which is masked by particle magnetic interaction in the case of a close-packed system, was revealed by appropriate reconstruction of the magnetization curve.

An equation is derived for the main magnetization curve taking into account the specific features of the object in question, such as the particle morphology and the large contribution from the surface. For this purpose, we have introduced in the expression for the anisotropic part of free energy, in addition to the magnetocrystalline anisotropy constant K_1, the surface anisotropy constant K_S (for K_2) and the particle shape anisotropy constant K_N (as a correction to K_1).

Computer simulation of the magnetization curves shows that for the ratio $|K_2|/K_1 = 0.6$ determined from experiment, the contribution to the magnetization jump comes from particles with the easiest magnetization axis oriented in the angular interval $65° \le \theta_H \le 90°$ relative the external magnetic field, which experience a first-order spin-reorientation phase transition.

Combined analysis of the characteristic anisotropy constants and the vector anisotropy diagrams for a macrocrystal and a nanocrystal leads to the conclusion that the reason for the spin-reorientation phase transition occurring in barium ferrite nanocrystals in a magnetic field is the change in the magnetic structure due to the open surface of nanoparticles and the surface anisotropy energy associated with it.

ACKNOWLEDGMENTS

This study was carried out under the Fundamental Research program (KPKV 2201020) financed by the Ministry of Education and Science of the Ukraine and partly supported by the Russian Foundation for Basic Research (grant nos. 01-02-17889 and 02-02-39006).

REFERENCES

1. E. S. Stoner and E. P. Wohlfarth, IEEE Trans. Magn. **27** (4), 3469 (1991).
2. Z. V. Golubenko, A. S. Kamzin, L. P. Ol'khovik, *et al.*, Fiz. Tverd. Tela (St. Petersburg) **40**, 1894 (1998) [Phys. Solid State **40**, 1718 (1998)].
3. Z. V. Golubenko, A. S. Kamzin, L. P. Ol'khovik, *et al.*, Fiz. Tverd. Tela (St. Petersburg) **44**, 1622 (2002) [Phys. Solid State **44**, 1698 (2002)].
4. L. P. Ol'khovik, Z. I. Sizova, Z. V. Golubenko, and T. G. Kuz'micheva, J. Magn. Magn. Mater. **183**, 181 (1998).
5. V. K. Sankaranarayanan, Q. A. Pankhuzst, D. P. E. Dickson, and C. E. Johnson, J. Magn. Magn. Mater. **125**, 199 (1993).
6. A. S. Kamzin, V. L. Rozenbaum, L. P. Ol'khovik, and E. D. Kovtun, J. Magn. Magn. Mater. **161**, 139 (1996).
7. A. Kamzin, B. Stahl, R. Gellert, *et al.*, Fiz. Tverd. Tela (St. Petersburg) **4**, 5 (2000) [Phys. Solid State **42**, 897 (2000)].
8. L. Neel, C. R. Acad. Sci. **237**, 1468 (1953).
9. Yu. A. Mamaluĭ, L. P. Ol'khovik, and L. F. Checherskaya, Fiz. Tekh. Vys. Davlenii **12**, 17 (1983).
10. G. Asti and F. Bolzoni, J. Magn. Magn. Mater. **20**, 29 (1980).
11. A. A. Murachovski, S. N. Zinenko, and J. Pietrzak, in *Proceedings of the 5th International Conference on Physics of Magnetic Materials, Madralin, Poland, 1990,* Ed. by W. Gorzkowski (World Sci., Singapore, 1990), p. 243.
12. L. A. Shuvalov, A. A. Urusovskaya, I. S. Zheludev, *et al.*, in *Modern Crystallography,* Vol. 4: *Physical Properties of Crystals* (Nauka, Moscow, 1981), p. 495.
13. W. P. Mason, Phys. Rev. **96**, 302 (1954).

Translated by N. Wadhwa

Journal of Experimental and Theoretical Physics, Vol. 96, No. 5, 2003, pp. 953–960.
From Zhurnal Éksperimental'noĭ i Teoreticheskoĭ Fiziki, Vol. 123, No. 5, 2003, pp. 1082–1089.

SOLIDS
Electronic Properties

Time Reversal Symmetry Breaking in Cuprates Induced by the Spiral Spin Order¶

M. Ya. Ovchinnikova

Institute of Chemical Physics, Russian Academy of Sciences, Moscow, 117334 Russia
e-mail: movchin@center.chph.ras.ru

Received November 1, 2002

Abstract—We propose a new interpretation of the spontaneous time reversal symmetry breaking (TRSB) observed recently in a pseudogap state of cuprates (Kaminsky *et al.*). It is shown that the TRSB dichroism in an ARPES signal may be related to the local spin spiral structures in the system. It may be caused by a spin-orbit interaction and by spin polarization of electrons at various sections of the Fermi surface in the spiral state. The angular dependence of the dichroism signal is studied in a schematic KKR approximation. Tests are proposed to check the existence of the local spiral spin structure and to distinguish it from the TRSB state with microcurrents constructed by Varma. © *2003 MAIK "Nauka/Interperiodica".*

The nature of a pseudogap (PS) state of high-T_c cuprates in the underdoped (UD) region remains an intriguing problem [1, 2]. Using the angular-resolved photoemission (ARPES) with circularly polarized light (CPL), Kaminsky *et al.* [3] recently revealed a new property of the pseudogap state of UD $Bi_2Sr_2CaCu_2O_{8-\delta}$ (BSCCO). It was shown that this state displays a spontaneous time reversal symmetry breaking (TRSB). Earlier, Varma [4] predicted the possibility of TRSB in cuprates. They proposed the fascinate ground state with circular microcurrents inside plaquettes of the CuO_2 plane with a definite alignment of the orbital angular momenta associated with these microcurrents. Namely, the up-directed orbital momenta arrange themselves along one diagonal and the down-directed orbital momenta arrange themselves along the other diagonal. The alignment of orbital angular momenta proposed in [4, 5] is not related to any spin alignment.

The aim of the present paper is to discuss an alternative possibility for constructing a state with TRSB. We propose a state in which the TRSB is due to a spiral spin structure. The arguments in favor of this hypothesis are as follows. The electric field of CPL actually interacts only with the orbital motion. Therefore, the TRSB dichroism implies a definite orientation of orbital angular momenta, $\langle L_n \rangle \neq 0$. Such momenta, centered on the atoms, can be induced by aligned spin momenta $\langle S_n \rangle \neq 0$ via the spin–orbit interaction. This implies that a TRSB dichroism D can be observed in the ARPES if the photoemission setup can selectively measure the ejected electrons with a definite spin projection $\sigma = \uparrow$ or $\sigma = \downarrow$. The sign of the TRSB dichroism must then depend on the sign of σ. Because the ARPES is usually nonselective with respect to the final spin projection of the ejected electron, the total TRSB dichroism is expected to be zero if the mean spin polarization of the initial states is zero. However, for the spiral spin structure, the occupancy $n_{k\sigma}$ of the initial one-electron band state $\{k\sigma\}$ with definite k depends on σ. Such a spin polarization of the initial k-state can induce nonzero TRSB effects in the ARPES signal. We therefore calculate a dichroism that might manifest itself in the ARPES for the spiral spin configuration of cuprates.

The spiral spin structure has been discussed as a possible ground state of a doped CuO_2 plane. Calculations in the mean field approximation or in the slave boson technique [6–8] were carried out in such a class of functions. The calculations have shown that the spiral state is lower in energy than the antiferromagnet (AF) state and that the deviation $\Delta Q = |Q - Q_{AF}|$ of the spirality vector Q from $Q_{AF} = (\pi, \pi)$ increases with doping. The spiral or any other periodic spin structures are associated with incommensurate peaks in the spin susceptibility $\chi(q, \omega)$ as $\omega \longrightarrow 0$ [9, 10]. Such peaks have been observed in $La_{1-x}Sr_xCuO_4$ (LSCO) at $q = (\pi \pm \delta, \pi)$, $(\pi, \pi \pm \delta)$ [11]. It has now been proved (see [12] and references therein) that the peaks in LSCO are related to the stripe phases. For BSCCO, a variety of hidden orders (spin and charge stripes, orbital AF order, etc.) have been discussed [13, 14]. The latest tunnel spectroscopy studies of BSCCO reveal structures with a periodicity of four unit cells around a vortex or an antiphase AF stripe structure along CuO bonds [15–17]. However, the TRSB effect is not displayed in the static stripe phase. It may be expected in states with spin or charge currents, such as the spiral spin state. To verify this possibility, we calculate the dichroism of the ARPES signal for the spiral state.

The scheme of the experiment [3] is given in Fig. 1. The right (left) polarized light with a propagation vec-

¶This article was submitted by the author in English.

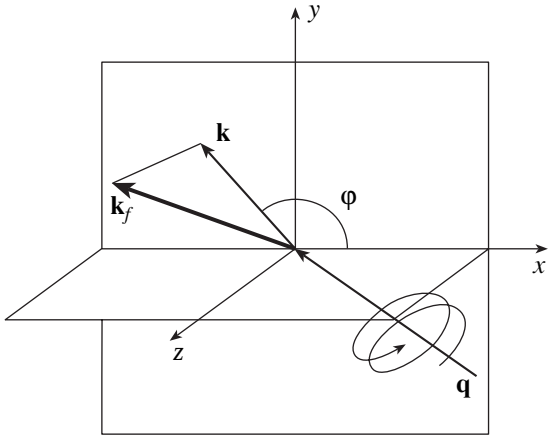

Fig. 1. Setup configuration of the ARPES experiment [3]. The propagation vector $\mathbf{q}_\gamma$ of CPL lies in the mirror plane *xz*; $\mathbf{k}_f$ and $\mathbf{k}$ are the final momentum of the ejected electron and its component in the CuO_2 plane (*xy* plane).

tor $\mathbf{q}_\gamma$ impacts on the crystal surface determined by normal vector $\mathbf{n}$. The *xz* plane is one of the mirror planes of the crystal with the *x* axis along the CuO bonds or along the diagonal direction. The ejected electron has a final momentum of $\mathbf{k}_f$. The ARPES intensity

$$I \propto |M_{if}|^2 \delta(E_i - E_f - \hbar\omega)$$

is determined by the matrix element of the interaction

$$O = (e/2m_e c)(\mathbf{Ap} + \mathbf{pA})$$

with the field

$$M = A_\alpha F_\alpha, \quad F_\alpha = \langle \psi_f | p_\alpha | \psi_i(k) \rangle \qquad (1)$$

between initial and final states. In the dipole approximation, it contains the vector potential $\mathbf{A}$ of the right ($\zeta_R = 1$) or left ($\zeta_L = -1$) CPL with a complex amplitude,

$$\mathbf{A}_{\mathbf{R(L)}} = A_0[\mathbf{e}_x \cos\theta_\gamma + i\zeta_{R(L)}\mathbf{e}_y + \mathbf{e}_z \sin\theta_\gamma]. \qquad (2)$$

For a given configuration of the setup vectors $\mathbf{n}$, $\mathbf{k}_f$, and $\mathbf{q}_\gamma$, the ARPES dichroism signal *D* is determined by the relative difference of intensities for the two light polarizations,

$$D = (M_R - M_L)/(M_R + M_L). \qquad (3)$$

We study the symmetry properties of ARPES matrix elements with respect to reflection in the mirror plane of the crystal, which is perpendicular to the surface in a typical photoemission experiment. Following [3], we first consider a tune reversal invariant initial state $\psi_i(k)$ and let $\mathbf{q}_\gamma$ and $\mathbf{n}$ lie in the mirror plane *m* of the crystal (here, the *xz* plane). The dichroism signal *D* is then nonzero only if $\mathbf{k}_f$ does not lie in the mirror plane *m* and *D* has opposite signs for *k* at different sides of the mirror plane. This dichroism is called geometrical. This large effect has been observed at any doping [3]. However, in UD BSCCO, the residual dichroism ($D \neq 0$) has been observed even for a coplanar configuration of $\mathbf{n}$, $\mathbf{k}_f$, and $\mathbf{q}_\gamma$, in which all three vectors lie in the mirror plane *m*. In what follows, we let q_z and $\mathbf{q}$ denote the normal and 2D intra-layer components of the photon momentum $\mathbf{q}_\gamma$ and, similarly, let k_z and $\mathbf{k}$ denote the respective components of the final electron momentum $\mathbf{k}_f$.

We first consider a large geometrical dichroism and then discuss the possible origin of the observed residual dichroism related to TRSB of the ground state of the UD cuprate. We suggest that the main contributions to the matrix element are given by space regions inside the atomic spheres. This is in accordance with the fact that frequency dependences of the photoemission intensity roughly repeat the dependences of photoemission cross-sections coming from the corresponding atomic components [18].

The formalism for evaluating the optical matrix element for a general lattice within the KKR scheme is given in [19]. Some corrections must be introduced to provide the common asymptotic behavior $\propto e^{ik_f r}$ of the final wave function of the ejected electron outside the sample ($z > 0$). We restrict our consideration to the one-step model (see [20]) describing the coherent part of photoemission. Generalization to a three-step model requires incorporating rescattering and relaxation processes in order to describe the background in the energy distribution function of the ejected electron. We believe that the one-step model is sufficient for a qualitative description of the angular dependence of dichroism. For this, we use the most simplified form of the initial and final states in the process.

The starting point in calculating F_α in (1) is the KKR wave function for a multicomponent lattice [19]. In the Hartree–Fock representation, the one-particle initial state ψ_i with the quasi-momentum $\mathbf{k}$ is a superposition of orbitals belonging to each center,

$$\psi_i(r, k) = \frac{1}{\sqrt{N}} \sum_{n,\beta} B(n_z) e^{ikr} i^l C^i_{L\beta} \psi^i_{L\beta}(r - R_{n\beta}), \qquad (4)$$

where β enumerates all atoms placed at $R_{n\beta}$ in the unit cell $n = (n_x, n_y, n_z)$ and $L = l, m$ are the angular momentum quantum numbers of the orbitals inside each atomic sphere $|r - R_{n\beta}| < a_{n\beta}$. For the upper valence antibonding band of the CuO_2 plane, the main orbitals $\psi^i_{L\beta}$ are the $d_{x^2-y^2}$ orbital of Cu and p_x, p_y orbitals of two oxygen atoms, O_x, O_y. These orbitals constitute a basis set of the Emery model.

Thus, the initial one-electron state is taken as a superposition of the main real orbitals; in the secondary quantization representation, it is given by

$$\psi_i(k, \sigma) = \sum_{n_z} B_i(n_z)[c_d d^\dagger_{k\sigma} + ic_x x^\dagger_{k\sigma} + ic_y y^\dagger_{k\sigma}]. \quad (5)$$

The corresponding site operators $d^\dagger_{k\sigma}$, $x^\dagger_{n,\sigma}$, $y^\dagger_{n,\sigma}$ of the Emery model refer to the real functions $d_{x^2-y^2}(r - R_{n,d})$ and $p_\nu(r - R_{n,\nu})$ with $R_{n,\nu} = R_n + e_\nu a/2, \nu = x, y$. The functions are considered to extend inside the corresponding atomic (muffin-tin) spheres. The real coefficients c_d, c_x, and c_y in (5) are obtained by solving the Emery model. The summands in Eqs. (4) and (5) refer to a layer number n_z. The amplitudes $B(n_z)$ depending on the distance of the layer from the surface phenomenologically describe a coherent or incoherent interlayer transport along z near the surface depending on the phase correlations between different layers. For the standard bulk initial state ψ_i used in [19], $B(n_z) \propto \exp(ik_z n_z)$.

The final state inside the sample is taken in a similar KKR form with the same in-plane momentum k,

$$\psi_f = \frac{1}{\sqrt{N}} \times \sum_{n,\beta} B^f(n_z) e^{ikR_{n\beta}} i^j C_{L\beta} Y^*_L \psi_{L\beta}(r - R_{n\beta}). \quad (6)$$

Here, each function $\psi_{L\beta}$ with the angular momentum quantum numbers $L = (l, m)$ is determined inside atomic spheres around the corresponding center $R_{n,\beta}$. The influence of the surface at $z = 0$ is described by introducing the factors $B^f(n_z)$, by phases $\delta_{l,\beta}$ of complex coefficients

$$C_{L\beta} = |C_{L\beta}| e^{\delta_{l\beta}}, \quad (7)$$

and by explicit angular spherical harmonics $Y_L = Y_{lm}(\hat{k}_f)$ depending on the direction of the final momentum k_f. The phases are specific for centers β in the unit cell and for the angular momentum l. These phases arise from matching final state (6) inside the sample to the common plane wave $\propto e^{ik_f r}$ in the empty space outside it. The phase modulation of contributions in (6) determines the geometrical dichroism of the photoemission.

The origin of spherical harmonics in Eq. (6) and of the phase modulation of coefficients (7) can be illustrated as follows. We first construct the final state $\psi_{f,\beta}(r)$ for the electron photoemission along the direction $\hat{k}_f$ from one center $\{n, \beta\}$ only. According to [21], it must be a function of the continuum with the plane-wave asymptotic form $\propto e^{i\mathbf{k}_f \mathbf{r}}$ and incoming radial waves as $|r - R_{n\beta}| \longrightarrow \infty$. This final state is

$$\psi_f = \exp(ik_f R_{n\beta}) \times \sum_{l,m} i^l e^{i\delta_{l\beta}} Y_{lm}(\hat{r}) Y^*_{lm}(\hat{k}_f) \varphi_l(r_\beta), \quad (8)$$

where $r_\beta = |r - R_{n\beta}|$. The scattering phase $\delta_{l\beta}$ for the orbital momentum l is defined by the asymptotic behavior of the real radial function of continuum,

$$\varphi_{l\beta}(r) \propto \frac{1}{r} \sin\left(kr - \frac{\pi l}{2} + \delta_{l\beta}\right).$$

(According to the KKR approach, we can consider the asymptotic form achieved at the surface of the muffin-tin sphere.)

In a similar manner, the final state ψ_f for the electron ejected from N_s centers of the surface layer must be a function whose asymptotic form at large $z > 0$ is given by the common plane wave $\propto e^{i\mathbf{k}_f \mathbf{r}}$ and incoming spherical waves contributed by different centers.

If $k_f |R_{n\beta} - R_{n'\beta'}| > 1$ and if we neglect the secondary scattering processes, then the final state wave function inside each nonoverlapping muffin-tin sphere surrounding the center $(n\beta)$ of the surface layer must have form (6) with complex coefficients $C_{L'\beta} \propto e^{i\delta_{l\beta}}$. The secondary processes actually synchronize the phases $\delta_{l\beta}$ of all contributions to the final state from different angular harmonics and different centers. The KKR bulk solution for the final state $\psi_f(k_f)$ found in [19] takes into account the phase and amplitude synchronization of all secondary processes, but neglects the necessary additional synchronization and phase modulation coming from the boundary surface where solutions should be matched with the plane wave with momentum k_f.

For a qualitative study of the angular dependence of dichroism and its symmetry, it is sufficient to use the final state in form (6) without specifying the values and phases of $C_{L'\beta}$ in (6). We therefore use Eqs. (5) and (6) for a schematic representation of initial and final states to study the symmetry and possible angular dependence of dichroism manifested in the ARPES. The components F_α of matrix element (1) are expressed as a sum of integrals over the interior of atomic spheres with the centers (β) for the corresponding channels $l \longrightarrow l'$,

$$M_{R(L)} = A_\alpha(\zeta) F^\nu_\alpha(l' \hat{k}). \quad (9)$$

Here, A_α are components of vector potential (2) depending on the right or left polarization of CPL, $\zeta = \zeta_{R(L)} = \pm 1$ and $\hat{k} = \mathbf{k}_f / k_f$. The functions $F^\nu_\alpha(l', \hat{k})$ correspond to real initial orbitals $\nu = d_{x^2-y^2}, p_x, p_y$. To obtain these, we use the selection rules $l' = l \pm 1$ for orbital

The functions $F_\alpha^\gamma(l', \hat{k})$ determining the α-components of the matrix element in Eq. (1). The index "γ" enumerates the contributions from different orbitals of the initial state, from $p_{x(y)}$ orbitals of oxygens $O_{x(y)}$ or $d_{x^2-y^2}$, d_{xy} orbitals of Cu; the final channels *s*, *p*, *d* correspond to the angular momenta $l' = 0, 1, 2$. The respective functions $G_{x(y)}$, L_k, g_x and g_y, P_k are even and odd functions with respect to the mirror plane *zx*

$\psi_{i\beta}$	ψ_f	F_x	F_y	F_z
p_x	*s*	$C_0 g_x$	0	0
p_x	*d*	$C_\mathrm{I} g_x G_x$	$C_\mathrm{I} g_x P_k$	$C_\mathrm{I} g_x L_k$
p_y	*s*	0	$C_0 g_y$	0
p_y	*d*	$C_\mathrm{I} g_y P_k$	$C_\mathrm{I} g_y G_y$	$C_\mathrm{I} g_y L_k$
$d_{x^2-y^2}$	*p*	$C_\mathrm{II}\sin\theta\cos\varphi$	$-C_\mathrm{II}\sin\theta\sin\varphi$	0
d_{xy}	*p*	$C_\mathrm{II}\sin\theta\sin\varphi$	$C_\mathrm{II}\sin\theta\cos\varphi$	0

Note: $G_{x(y)} = \pm\sin^2\theta\cos2\varphi - \cos^2\theta + 1/3$, $g_{x(y)}$ are determined by Eqs. (10), $L_k = \sin 2\theta\cos\varphi$, $P_k = \sin^2\theta\sin2\varphi$.

angular momenta for integrals inside the atomic spheres. For simplicity, we retain only the matrix elements for the transitions $p_{x(y)} \longrightarrow s, d$ and $d_{x^2-y^2} \longrightarrow p$ from the $O_{x(y)}$ and Cu centers of the CuO_2 plane. According to the KKR calculations [19], such transitions give the main contributions. Omitting the transition $d_{x^2-y^2} \longrightarrow f$ at the Cu center does not change the symmetry properties of the calculated dichroism. It leads only to neglect of the small higher harmonics in the angular dependence of the ARPES intensity.

The resulting expressions for the functions $F_\alpha^\nu(l'\hat{k})$ are presented in the table. For the $p \longrightarrow s, d$ transitions in oxygen, they also include the factors

$$g_{x(y)} = s_{x(y)}/\sqrt{s_x^2 + s_y^2}, \quad s_{x(y)} = \pm\sin(k_{x(y)}/2) \qquad (10)$$

that originate from the angular dependence of the real amplitudes $c_{x(y)}$ and c_d of different orbitals in initial band state (5) of the Emery model (with the effective parameters ϵ_d, ϵ_p, t_{pd}, t_{pp}). At $t_{pp} \ll t_{pd}$, the amplitudes in (5) are

$$c_{x(y)} = g_{x(y)}\sin\eta, \quad c_d = \cos\eta,$$
$$\tan2\eta = 2t_{pd}(\cos k_x + \cos k_y)/(\epsilon_d - \epsilon_p). \qquad (11)$$

Extension to large t_{pp} does not change the symmetry of the amplitudes.

The coefficients $C_{0(\mathrm{I,\,II})}(k)$ in the table include (1) the sum over the layers $\sum B_f^*(n_z)B_i(n_z)$ based on the phenomenological or tight-binding dependences $B(n_z)$; (2) the phase factors $\exp(i\delta_l)$ coming from the boundary conditions; (3) the reduced integrals $\langle l'\beta\|p\|l\beta\rangle$ over angular variables after removing the *m* dependence; (4) the radial integrals; and (5) the factors $\sin\eta$ and $\cos\eta$ from amplitudes (11).

The ARPES dichroism signal is then given by

$$D(\varphi) = \mathrm{Im}\{M(\Delta M)^*\}/(|M|^2 + |\Delta M|^2), \qquad (12)$$

where $M = M_R + M_L$, $\Delta M = M_R - M_L$, and the angles θ and φ describe the final momentum $\mathbf{k}_f$. Dependence (12) can be represented as $D(\varphi) \propto \tilde{G}(k)\sin\varphi$, where the function $\tilde{G}(k)$ is even with respect to reflection in the mirror plane *zx*. In accordance with (9), the quantities $M_{R(L)}$ are determined by complex constants C_0, C_I, and C_II, whereas the other angular functions listed in the table are real. It can be shown that the dichroism signal is zero if all the coefficients $C_{L\beta}$ in (7) have the same phases $\delta_{\beta,\,l}$ or their differences are multiples of π. A representation of the final state with correct phases is therefore significant for description of geometrical dichroism.

At $\hat{q}_\gamma = \mathbf{n}$, when the photon impacts normally to the CuO_2 plane, we obtain

$$M = C_\mathrm{II}\sin\theta\cos\varphi + g_x[C_0 - C_\mathrm{I}(\cos^2\theta - \sin^2\theta\cos2\varphi)] + g_y C_\mathrm{I}\sin^2\theta\sin2\varphi, \qquad (13)$$

$$\Delta M = -C_\mathrm{II}\sin\theta\sin\varphi + g_y[C_0 - C_\mathrm{I}(\cos^2\theta + \sin^2\theta\cos2\varphi)] + g_x C_\mathrm{I}\sin^2\theta\sin2\varphi, \qquad (14)$$

where θ and φ are the polar angles of $\mathbf{k}_f$. It follows from (11) and (12) that the dichroism signal is an odd function, $D(-\varphi) = -D(\varphi)$, which vanishes at $\varphi = \pi$ and $\varphi = 0$. This is an expected property of geometrical dichroism.

Manifestations of geometrical dichroism depend on numerous parameters. In Fig. 2, we give examples of the functions $D(\varphi)$ for three angles $\theta_g = 0$, π/6, and π/3 of the photon momentum in the mirror plane *zx* for *k* moving along the boundary $|k_x \pm k_y| = \pi$ and $k_z = |\mathbf{k}\cdot\mathbf{n}|$. We assign arbitrary values to the relative amplitudes, $|C_0/C_\mathrm{I}| = |C_0/C_\mathrm{II}| = 1.0$, and the relative phases $\{\delta_{l'=0}(\mathrm{O}), \delta_{l'=2}(\mathrm{O}), \delta_{l'=1}(\mathrm{Cu})\} = \{0, 3\pi/4, \pi/4\}$ of the coefficients C_0, C_I, C_II in different channels of O and Cu centers. Two setup configurations with *x* along the CuO bond or along the diagonal direction are considered. The function $D(\varphi)$ is an odd function of φ and vanishes at $\varphi = 0, \pi$. The calculated geometrical dichroism disappears for all φ if all phase differences $\delta_l - \delta_{l'} = \pi m$ are multiples of π. This is the case for the Cu- and O-contributions to the matrix element calculated in [19]. There, the standard KKR bulk wave functions were used and the additional phase modulation was neglected. At the normal photon impact ($\theta_\gamma = 0$), the

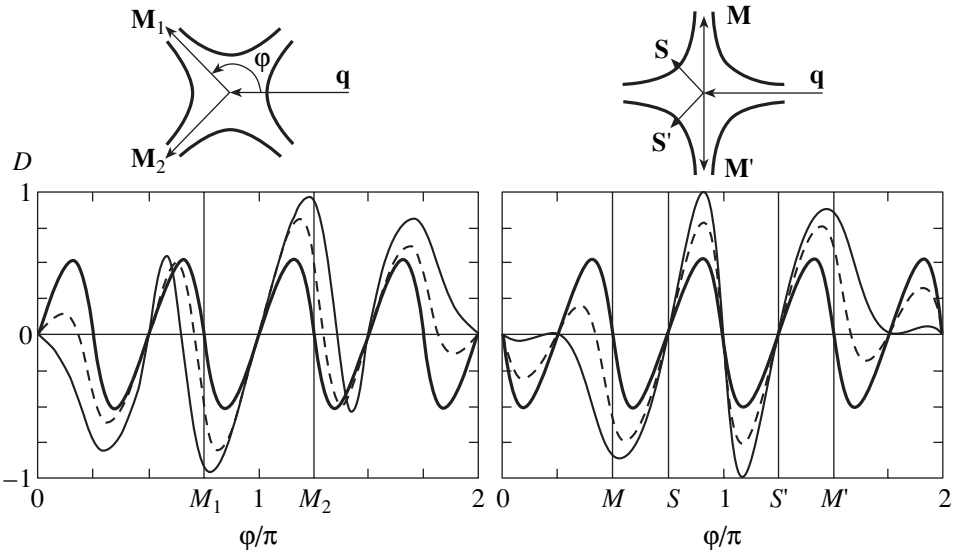

Fig. 2. Dependence of the geometrical dichroism $D(\varphi)$ on the azimuthal angle φ of the vector $\mathbf{k}_f$ for k moving along the nesting lines $|k_x \pm k_y| = \pi$. Solid, dashed, and thin curves correspond to the angles $\theta_\gamma = 0, \pi/6, \pi/3$ of the photon momentum q. Setup configurations with x along the diagonal direction or along the CuO bonds refer to left or right graphs. Arbitrarily taken coefficients (7) are given in text.

dichroism signal is zero on each mirror plane of the tetragonal lattice, i.e., at $\varphi = \pi m/A$.

We now take the spin-orbit interaction on Cu into account,

$$V_{LS} = \lambda \sum_n \mathbf{L}_n \mathbf{S}_n, \tag{15}$$

where λ is the corresponding constant.

The initial band function $\psi^i_{k\sigma}$ then transforms to $\psi^i_{k\sigma} + \delta\psi$ in a manner equivalent to replacement of $d^\dagger_{x^2-y^2,\sigma}$ in (5) by

$$d^\dagger_{x^2-y^2,\sigma} + C_\lambda[2i\xi_\sigma d^\dagger_{xy,\sigma} - \xi_\sigma d^\dagger_{zx,-\sigma} - id^\dagger_{zy,-\sigma}] \tag{16}$$

in Eqs. (5) and (4). Here, $\xi_\sigma = \sigma/|\sigma| = \pm 1$ and $C_l \propto l/2\delta E$, where δE is the energy difference of the d-orbitals of $x^2 - y^2$ and xy, yz, xz symmetries. The additional contribution to $\psi^i_{k\sigma}$ leads to changes $M \longrightarrow M + \delta M$, $\Delta M \longrightarrow \Delta M + \delta\Delta M(\sigma)$ in Eqs. (10), (11), and (12). The TRSB dichroism signal at the normal photon impact ($\theta_\gamma = 0$) is then determined by

$$\sigma\Delta M = \xi_\sigma 4 C_\lambda C_{II} \sin\theta\cos\varphi. \tag{17}$$

As a result, the dichroism signal $D(\varphi, \sigma)$ of photoemission with the final momentum k_f and spin projection σ of the ejected electron is given by

$$Dd(\sigma, k) = A\sin\varphi - \frac{\xi_\sigma \mathrm{Re}(MC^*_{II})}{|M|^2 + |\Delta M|^2} 4C_\lambda \sin\theta\cos\varphi, \tag{18}$$

where M, ΔM, and C_{II} are determined by Eqs. (13), (14), and (7) and by the functions in the table. Only the term that is linear in λ is retained in (18). It is determined only by the admixture of the d_{xy} orbital in Eq. (16). The contributions from d-orbitals of xz, yz symmetries in (16) are of the second order of magnitude in λ. The second term in (18) is an even function of φ and has a nonzero value at $\varphi = 0$ and π when all three vectors $\mathbf{q}_\gamma$, $\mathbf{n}$, and $\mathbf{k}_f$ lie in the mirror plane xz and geometrical dichroism disappears.

Because the sign of $D(\varphi = 0)$ depends on the sign of the spin projection σ of the ejected electron, the overall dichroism $D = \sum_\sigma D(\sigma, \varphi)$ must be zero for the initial paramagnet (PM) state of the system. For the PM state, the dichroism at $\varphi = 0$ and π can therefore be observed only if the ejected electrons with a definite spin projection on $\mathbf{n}$ are selected. For this PM state, the time reversal symmetry is broken just by a measurement of the spin polarization of the photoelectron.

However, there exist TRSB states in which different regions of the k space are characterized by different spin polarizations. For example, for the ground state with a spiral spin structure, the TRSB effect manifests itself in the ARPES by a nonzero overall dichroism upon arrangement of all vectors $\mathbf{q}_\gamma$, $\mathbf{n}$, $\mathbf{k}_f$ in the mirror plane.

We now demonstrate the polarization selectivity of the level occupancies in the k-space for the spiral state of the 2D $t - t' - U$ Hubbard model. Calculations were carried out for the model with $U/t = 6$, $t'/t = 0.1$ at a doping of 0.15 hole per site. The spiral mean-field (MF) solution is characterized by average spins $\langle \mathbf{S}_n \rangle = d(\mathbf{e}_x \cos Qn + \mathbf{e}_y \sin Qn)$ rotating in the xy plane. We

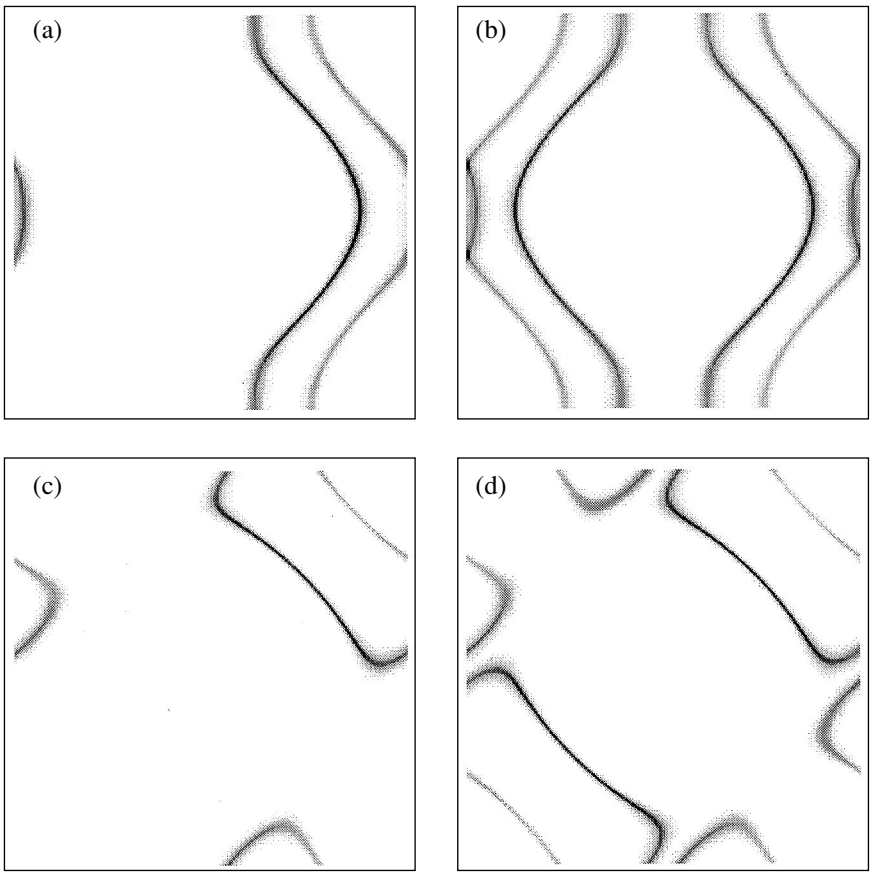

Fig. 3. The images of the spin-selective (plots a, c) and overall (plots b, d) spectral functions $A_\uparrow(k, \omega)$, $A(k, \omega)$ at $\omega = 0$ in the Brillouin zone. The main and shadow Fermi surfaces are shown for the spiral states with the spirality vectors $Q = Q_{\mathrm{I}}$ and $Q = Q_{\mathrm{II}}$ in (19) (plots a, b and c, d, respectively).

study the MF states of two types, with the spirality vectors

$$Q_{\mathrm{I}} = (\pi - \delta Q_x, \pi), \quad Q_{\mathrm{II}} = (\pi - \delta Q, \pi - \delta Q) \quad (19)$$

directed along the CuO bond or along the diagonal. The spectral function $A_\sigma(k, \omega)$ at $\omega = 0$ for a definite spin projection σ on the z axis (perpendicular to the spin rotation plane) is given by

$$A_\sigma(k, \gamma) = \sum_{i,f} |\langle \psi_f | c_{k\sigma} | \psi_i \rangle|^2 f(E_i) \delta_\Gamma(E_i - E_f), \quad (20)$$

where the Fermi function $f(E_i)$ depends on the one-electron levels of the MF solution and $\delta_\Gamma(x)$ is the δ-function broadened with the parameter $\Gamma \sim 0.05t$. In Fig. 3, we show an image of the spin-selective and overall spectral functions $A_{\sigma=\uparrow}(\boldsymbol{k})$ and $A(\mathbf{k}) = \sum_\sigma A_\sigma$ at $\omega = 0$ for two types of spiral states. Dark and light gray lines in Fig. 3 correspond to the main and shadow spin-selective ($\sigma = \uparrow$) sections of the Fermi surfaces. Similar images for $\sigma = \downarrow$ are obtained from those for $\sigma = \uparrow$ by inversion $\mathbf{k} \longrightarrow -\mathbf{k}$. The spin dependence of the level occupancy in the k space is related to the spin currents $J_\uparrow = J_\downarrow \propto Q$ existing in the spiral state.

Thus, the TRSB state with a spiral spin structure certainly has spin-selective sections of the Fermi surface. As a consequence, we can observe the TRSB dichroism of the ARPES signal even at a coplanar arrangement of the setup vectors $\mathbf{q}_\gamma$, $\mathbf{n}$, and $\mathbf{k}_f$ in the mirror plane. Two factors are decisive here. (1) The ARPES signal corresponds to a definite local region of k, that is associated with a definite spin polarization for a given spirality vector Q. (2) In accordance with Eqs. (16) and (17), a definite spin polarization induces the orbital angular momenta on Cu centers and corresponding nonzero dichroism at the coplanar setup configuration via the spin–orbit interaction.

In order to estimate the effect, we use the spin–orbit constant $\lambda \sim 800$ cm^{-1} following from the excitation spectrum of Cu$^{\mathrm{I}}$, Cu$^{\mathrm{II}}$ [22] and the splitting of d-orbitals $\delta E = E_{x^2-y^2} - E_{xy} \sim 1$–$2$ eV in the crystal field. We then have the value $C_\lambda = 0.0025$–0.005 for the amplitude in (16). At the setup configuration with $\theta_\gamma = 0$, $\theta = \theta_k = \pi/4$, $\varphi = \pi$ and 0 and with the same arbitrarily chosen

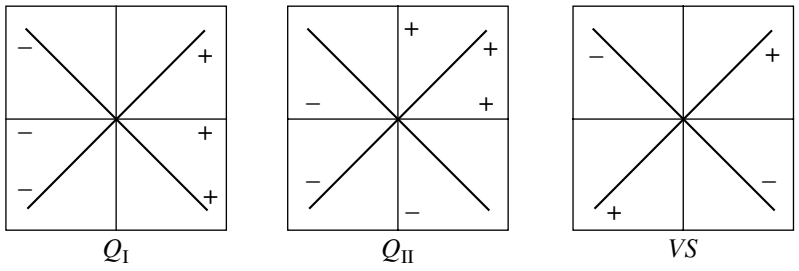

Fig. 4. Relative signs of the TRSB dichroism signal for **k** lying on different mirror planes of the lattice for spiral states with the spirality vectors Q_I and Q_{II} in (19), or for the state proposed by Varma (VS).

coefficients (7) as in Fig. 2 ($|C_I/C_0| = |C_{II}/C_0| = 1$, $\delta_{\beta l} = 0, 3\pi/4, \pi/4$), we obtain for the TRSB dichroism $\max|D| = 0.033–0.066$ at k corresponding $\varphi = 0$ or π lying in the mirror plane. This value is consistent with the TRSB dichroism signal ~3–5% observed in UD cuprates [3].

In conclusion, we have shown that the TRSB dichroism observed in the ARPES spectra of the UD cuprates may be related to a local spiral spin order in the system. This hypothesis differs from the model TRSB state proposed by Varma *et al.* [4, 5], who connect the TRSB with aligned charge circular microcurrents on plaquettes of the CuO_2 plane. Instead, the spiral spin order implies the appearance of local spin currents $\mathbf{J}_\uparrow = -\mathbf{J}_\downarrow$ of a macro scale, about domain size. The existence of different domains with different signs and values of the TRSB dichroism signal has been shown by studying a set of samples of UD BSCCO in [3]. The following test for the new hypothesis may be proposed. The rotation of the sample by 180° around the z axis does change the sign of the TRSB dichroism $D(\varphi = \pi)$ in our hypothesis and does not change the sign in the case of the TRSB state constructed in [4]. In the former case, the rotation changes the signs of the spin currents and of the spin polarization. Relative signs of the TRSB dichroism signal at different mirror planes of cuprate for two types of spiral states (19) and for the state proposed by Varma are illustrated in Fig. 4. These signs can be measured only if the ARPES signal conies from the same domain of a sample before and after its rotation and if the spin currents of the spiral state are pinned during the rotation of the sample. We note that for the ferromagnet alignment of spins in surface layers, the TRSB dichroism has the same signs along all directions in mirror planes of the lattice.

Great sensitivity of the Fermi surface (FS) to the spin structure leads to questions that are important for understanding the pseudogap state of BSCCO: Is the observed FS a composed result coming from several domains with different currents? What is the dynamics of these currents and domains in the UD cuprates? Can the spin fluctuations be frozen near the surface into static domains with a spiral or ferromagnet spin order? We note that the ARPES technique probes only a few surface layers. Observing the TRSB effect with the use of ARPES therefore requires a correlated spiral order only in these few surface layers, whereas the bulk TRSB effect may be destroyed. An additional test for the supposed local spiral order is possible. One can measure the spin polarization $\langle \mathbf{S} \rangle$ of electrons ejected from different sections of the Fermi surface and check the correlations of the direction of $\langle \mathbf{S} \rangle$ with the sign of the TRSB dichroism signal $D(\varphi)$ at $\varphi = \pi$. This program requires a spin-selective detection of photoelectrons. Such detection is now realized in a total "spin–orbit photoemission" measurement [23]. Its application in ARPES might elucidate the nature of TRSB dichroism of photoemission from a UD cuprate.

ACKNOWLEDGMENTS

This work was supported by the Russian Fund for Basic Research (project nos. 00-03-32981 and 00-15-97334). The author is grateful to A. A. Ovchinnikov and V. Ya. Krivnov for useful discussions.

REFERENCES

1. T. Timusk and B. Statt, Rep. Progr. Phys. **62**, 61 (1999).
2. J. C. Campusano, M. R. Norman, and M. Raderia, in *Physics of Conventional and Unconventional Superconductors*, Ed. by K. H. Benneman and J. B. Ketterson; cond-mat/0209476.
3. A. Kaminsky, S. Rosenkranz, H. M. Fretwell, *et al.*, cond-mat/0203133.
4. C. M. Varma, Phys. Rev. B **61**, R3804 (2000).
5. M. E. Simon and C. M. Varma, cond-mat/0201036.
6. B. I. Shramian and E. D. Siggia, Phys. Rev. B **40**, 9162 (1989).
7. R. Fresard and P. Woelfle, J. Phys.: Condens. Matter **4**, 3625 (1992).
8. P. J. M. Denteneer and H. Blaubaer, J. Phys.: Condens. Matter **7**, 115 (1995).
9. A. V. Chubukov and K. A. Musaelyan, Phys. Rev. B **51**, 12605 (1995); J. Phys.: Condens. Matter **7**, L153 (1995).
10. K. Krüger and S. Scheidl, cond-mat/0211593.
11. Ph. Bourges, in *The Gap Symmetry and Fluctuations in High Temperature Superconductors*, Ed. by J. Bok, G. Deutscher, D. Pavuna, and S. A. Wolf (Plenum, New York, 1998).

12. B. Khaykovich, R. J. Birgeneau, F. C. Chou, *et al.*, cond-mat/0209648.
13. S. A. Kivelson, E. Fradkin, J. M. Tranquada, *et al.*, cond-mat/0210683.
14. S. Sachdev, cond-mat/0211005; cond-mat/0203363; A. Polkovnikov, M. Vojta, and S. Sachdev, Phys. Rev. B **65**, 220509 (2002); S. Sachdev and S. C. Zhang, Science B **295**, 452 (2002).
15. B. Lake, G. Aeppli, K. N. Clausen, *et al.*, Science **291**, 1759 (2001).
16. J. E. Hoffman, E. V. Hudson, K. M. Lang, *et al.*, Science **295**, 466 (2002).
17. C. Howald, H. Eisaki, N. Kaneko, and A. Kapitulnik, cond-mat/0201546.
18. Y. Sakisaka, J. Electron Spectrosc. Relat. Phenom. **66**, 387 (1994).
19. M. Lindroos, S. Sahrakorpi, and A. Bansil, cond-mat/0109039; Phys. Rev. B **65**, 054514 (2002).
20. A. Damascelli, Z. X. Shen, and Z. Hussain, cond-mat/0208504.
21. L. D. Landau and E. M. Lifshitz, *Course of Theoretical Physics*, Vol. 3: *Quantum Mechanics: Non-Relativistic Theory*, 4th ed. (Nauka, Moscow, 1989; Pergamon, New York, 1977).
22. *Atomic Energy Levels*, Ed. by R. F. Bacher and S. Goudsmoth (McGraw-Hill, New York, 1932).
23. G. Ghiringhelli, L. H. Tjeng, A. Tanaka, *et al.*, Phys. Rev. B **66**, 75101 (2002).

Journal of Experimental and Theoretical Physics, Vol. 96, No. 5, 2003, pp. 961–965.
Translated from Zhurnal Éksperimental'noĭ i Teoreticheskoĭ Fiziki, Vol. 123, No. 5, 2003, pp. 1090–1095.

SOLIDS
Electronic Properties

Magnetic and Structural Phase Transitions in YMn_2O_5 Ferromagnetoelectric Crystals Induced by a Strong Magnetic Field

Yu. F. Popov, A. M. Kadomtseva*, S. S. Krotov, G. P. Vorob'ev, K. I. Kamilov, M. M. Lukina, and M. M. Tegranchi

Moscow State University, Moscow, Russia
**e-mail: kadomts@plms.phys.msu.su*

Received November 18, 2002

Abstract—Magnetic, magnetoelectric, and magnetoelastic properties of YMn_2O_5 ferromagnetoelectric single-crystals are investigated in strong pulsed magnetic fields of up to 250 kOe and in static magnetic fields of up to 12 kOe. It is found that, in YMn_2O_5 at $T < T_N = 42$ K, a transverse weakly ferromagnetic moment of $\sigma_0 = 0.8$ G cm^3/g exists that is oriented along axis *a* and is attributed to the magnetoelectric interaction. When a magnetic field is directed along axis *b*, which is likely to be the axis of antiferromagnetism, a spin-flop transition is observed that is accompanied by jumps in magnetostriction and electric polarization. When a magnetic field is directed along axis *a*, the temperature of ferroelectric transition shifts from 20 to 25 K at $H \approx 200$ kOe. A theoretical analysis of the experimental results is given within phenomenological theory with regard to the fact that a YMn_2O_5 compound belongs to noncollinear antiferromagnetic crystals even in the exchange approximation.

1. INTRODUCTION

According to the neutron diffraction data [1, 2], RMn_2O_5 rare earth manganates (R is a rare earth ion), which belong to the orthorhombic space group *Pbam*, exhibit an antiferromagnetic ordering of the spins of manganese ions below $T_N = 40$ K; at low temperatures, they also exhibit an ordering of the spins of rare earth ions. In YMn_2O_5 (Y is a nonmagnetic ion), the spins of Mn^{3+} and Mn^{4+} ions lie in the *ab* plane and form a modulated antiferromagnetic structure with a propagation vector $\mathbf{k} = \{1/2, 0, 0.32\}$. According to [3, 4], YMn_2O_5 exhibits a ferroelectric phase transition near $T_c = 20$ K that is accompanied by a spontaneous electric polarization along axis *b* of the crystal. Earlier, investigations of the magnetic and structural phase transitions in RMn_2O_5 compounds have been carried out mainly in weak magnetic fields (see, for example, [5–7]). However, it is beyond doubt that, in strong magnetic fields, new phase transitions occur that are associated with the rearrangement of the magnetic and electric subsystems. In view of this fact, we started the investigation of the anomalies of magnetic, magnetoelectric, and magnetoelastic properties associated with the field-induced phase transitions in strong magnetic fields of up to 250 kOe.

2. EXPERIMENTAL RESULTS

YMn_2O_5 magnetoelectric single-crystals used in the experiments were grown by the method of spontaneous crystallization from a solution or a melt [5]. The magnetic properties of these crystals in static magnetic fields of up to 12 kOe were investigated on a torsion balance magnetometer with a self-balancing potentiometer. Magnetization curves in strong magnetic fields of up to 250 kOe were measured by the induction method. Electric polarization and magnetostriction induced by a strong magnetic field were measured by the method described in [8].

The curves of torques for YMn_2O_5 crystals in the *ac* plane are described by the relation

$$L_{ac}(\varphi) = \frac{\Delta\chi_{ac}}{2}H^2 \sin 2\varphi \pm \sigma_0 H \sin\varphi,$$

where $\Delta\chi_{ac}$ is the difference of magnetic susceptibilities, σ_0 is a spontaneous magnetic moment, H is an external magnetic field, and φ is the angle between the direction of the magnetic field and axis *a* of the crystal.

The curve $L_{ac}(\varphi)$ in Fig. 1 displays characteristic breaks that indicate the presence of a weakly ferromagnetic moment along axis *a* of the YMn_2O_5 crystal. Figure 2 represents the temperature dependence of the weakly ferromagnetic moment, obtained from the rotation curves, that arises below $T_N = 42$ K and slightly increases near $T_c = 25$ K. The specific weakly ferromagnetic moment reaches a value of $\sigma_0 = 0.8$ G cm^3/g, which is substantially greater than the value observed in [3].

The weak ferromagnetism in YMn_2O_5 is likely to be attributed to the tilt of manganese antiferromagnetic

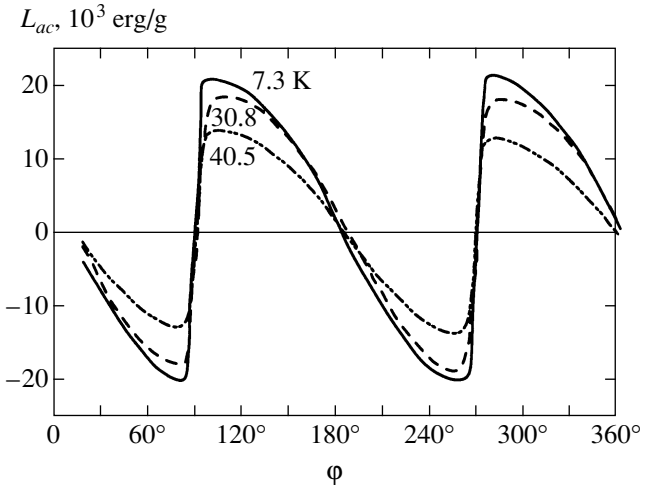

Fig. 1. Torque L as a function of angle φ between the magnetic field direction and axis a in a YMn_2O_5 crystal at different temperatures measured at $H = 11.2$ kOe.

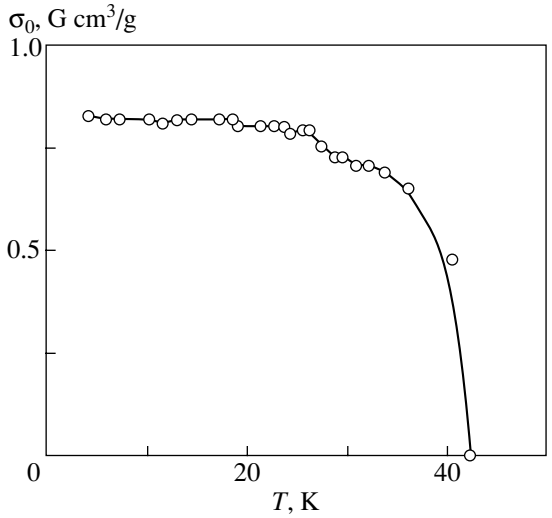

Fig. 2. Temperature dependence of a weakly ferromagnetic moment of YMn_2O_5 along axis a.

sublattices due to the Dzyaloshinskii-type interaction with regard to the magnetoelectric coupling.

We also measured the magnetization curves along axes *a*, *b*, and *c* in the range of temperatures from 10 to 50 K in magnetic fields of up to 250 kOe, which revealed the presence of strong anisotropy (Fig. 3). The maximal magnetization was observed along axis *a*: first, in a field of up to 50 kOe, the magnetization sharply increased to 20 G cm^3/g and then slowly increased with the field. When the field **H** is directed along axis *a*, the growth of magnetization with the field is likely to be attributed to different processes. First of all, the growth of the field may be associated with the increase of the tilt angle of manganese antiferromagnetic sublattices. Moreover, taking into account the complex magnetic structure of YMn_2O_5 [1, 2], one may also assume that the spins of Mn^{3+} and Mn^{4+} ions are reversed by a strong magnetic field and that the modulated spin structure is partially suppressed.

When a magnetic field is applied along axis *b*, which is supposed to be the axis of antiferromagnetism, the magnetization curve exhibits a jog at a sufficiently high magnetic field of about 175 kOe, which is likely to be associated with the reorientation of the weakly ferromagnetic moment from axis *a* to axis *b* of the crystal.

When field **H** is directed along axis *c*, the magnetization almost linearly depends on the field and does not display any anomalies.

The orientation of the magnetic field along various crystallographic directions induces electric polarization; the maximum polarization occurs along axis *b*, which, according to [4], is the axis of spontaneous electric polarization.

When the field is directed along axis *a* of the crystal, the magnetoelectric susceptibility of YMn_2O_5 along axes *a* and *b* changes its sign at a temperature of 25 K (Fig. 4), similar to the situation observed in $EuMn_2O_5$ under spontaneous transition from an incommensurable to a commensurable structure [9, 10]. As is clear from Fig. 4, at a temperature of 25 K, the dependence of electric polarization on the magnetic field exhibits qualitatively different behavior as compared with that at other temperatures. In particular, in a field of about 200 kOe, the electric polarization displays sharp jumps along axes *a* and *b* that are accompanied by a consider-

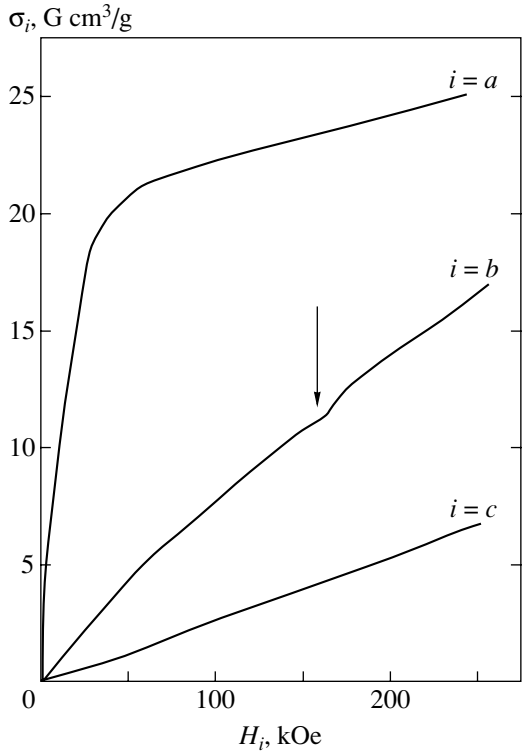

Fig. 3 Magnetization curves of YMn_2O_5 along axes *a*, *b*, and *c* at a temperature of 15 K.

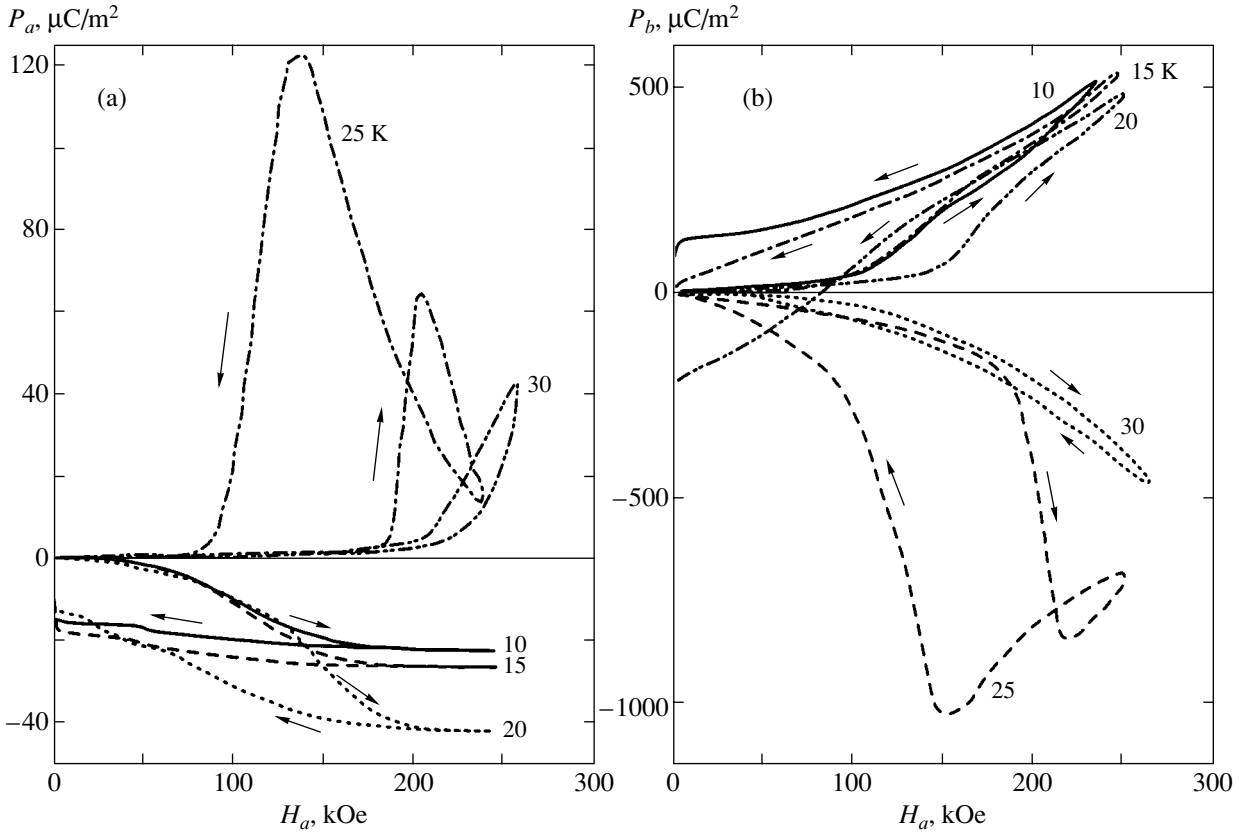

Fig. 4. Electric polarization of YMn_2O_5 along axes (a) *a* and (b) *b* versus the magnetic field applied along axis *a* at different temperatures.

able field hysteresis, which is characteristic of a first-order phase transition. A possible reason for these anomalies of electric polarization at this temperature in a field of H = 200 kOe is field-induced growth of the ferroelectric transition temperature, which, according to [4], occurs at 20 K in the absence of field. The growth, induced by a magnetic field, of the ferroelectric transition temperature has been predicted in [11] by a simple thermodynamic analysis. The jump of the electric polarization could also be stimulated by a field-induced transition from an incommensurable to a commensurable phase.

When measuring magnetostriction $\lambda_a(H_a)$, we found that it exhibits an increase followed by a sharp decrease ($\Delta\lambda = -2 \times 10^{-5}$) in a field interval of $150 < H < 200$ kOe, where the electric polarizations $P_a(H_a)$ and $P_b(H_a)$ display anomalies (Fig. 4). This fact suggests that there exists a correlation between magnetoelectric and magnetoelastic properties.

For **H** parallel to the *b* axis, the longitudinal electric polarization $P_b(H_b)$ along this axis has a relatively low value in the temperature interval $20 < T < 40$ K and quadratically depends on field up to 250 kOe (Fig. 5a). However, at $T \le 20$ K, this dependence qualitatively changes. In this temperature interval, electric polarization in a field of $H \approx H_{cr}$ increases stepwise (Fig. 5a). The threshold field H_{cr} decreases, as temperature increases, from 200 kOe at 10 K to 150 kOe at 20 K. Such a behavior of electric polarization versus field at low temperatures is obviously associated with spontaneous electric polarization, which, as we mentioned above, occurs at $T \le T_c = 20$ K. It is natural to assume that the reorientation of the magnetic moment from axis *a* to axis *b* (rotation through 90°) changes the sign of the electric polarization along axis *b*, similar to the phenomenon observed earlier in boracites [12].

As a rule, the spin reorientation is accompanied by magnetostriction strains. When measuring the longitudinal magnetostriction along axis *b* at low temperatures, we observed sharp anomalies at H_{cr} that correlated with the character of the field dependence of electric polarization.

For the field **H** parallel to the *c* axis, the electric polarization along this axis in magnetic fields of $H < 100$ kOe monotonically depends on field and attains its maximum at 20 K (Fig. 5b). However, in strong magnetic fields of $H > 100$ kOe at 25 K, we observed a sharp multistep jump in electric polarization that was accompanied by a strong field hysteresis and an aftereffect (Fig. 5b). The jump in electric polarization along axis *c* in a strong magnetic field may be attributed to variation of the inhomogeneous interfacial exchange during the

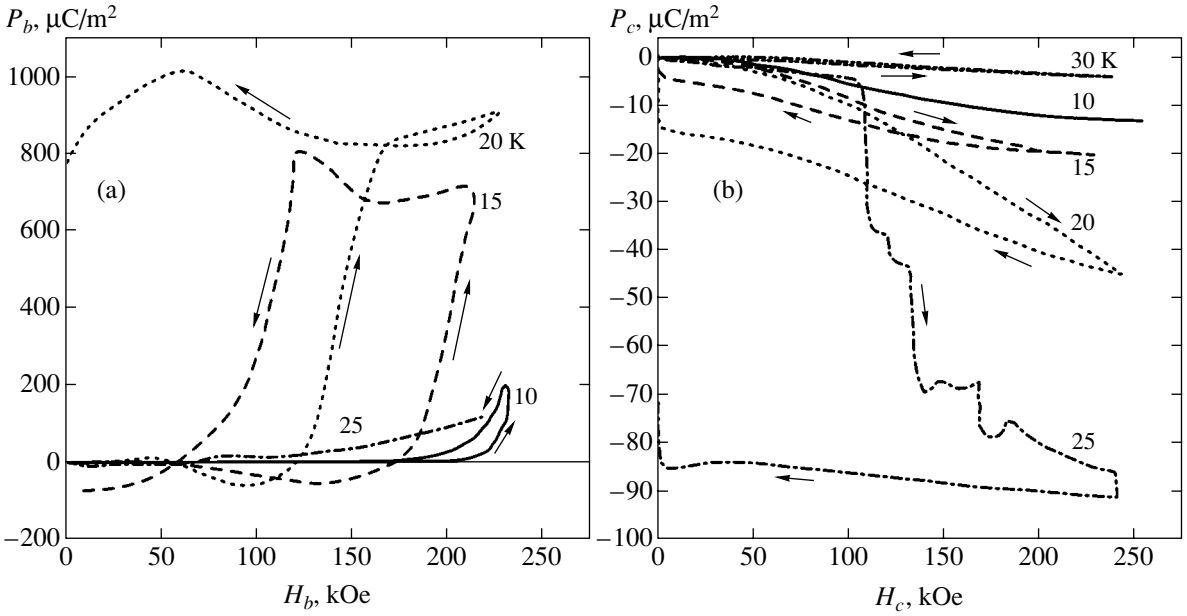

Fig. 5. Isotherms of longitudinal electric polarization of YMn_2O_5 along axes (a) *b* and (b) *c* versus magnetic field.

rearrangement of the magnetic structure under the phase transition from an incommensurable to a commensurable phase.

3. DISCUSSION OF THE RESULTS

Before proceeding to the discussion of experimental results concerning the specific features of antiferromagnetic, electric, and magnetoelectric properties of the YMn_2O_5 system, we recall the basic theoretical data about this system within the phenomenological (symmetry) approach in the spirit of the Landau theory. As is known, the magnetic properties of this system are determined by the behavior of the spins ($\mathbf{S}_1$, $\mathbf{S}_2$, $\mathbf{S}_3$, $\mathbf{S}_4$) of Mn^{3+} ions and the spins ($\mathbf{S}_5$, $\mathbf{S}_6$, $\mathbf{S}_7$, $\mathbf{S}_8$) of Mn^{4+} ions. To describe the variation in the symmetry of the system at the phase transition point on the basis of the experimental data of [1, 2, 10], we will use the results of the representation theory of space groups (in the present case, of the group $Pbam = D_{2h}^9$). Then, as was shown in [13], the antiferromagnetic structure arising at the Neél point T_N is characterized by a two-dimensional magnetic representation with the order parameter constructed on two antiferromagnetic vectors $\mathbf{L}_1$ and $\mathbf{L}_2$, where $\mathbf{L}_1 \perp \mathbf{L}_2$. The invariant form of the thermodynamic potential Φ of the system implies that, at the Neél point, an exchange-noncollinear antiferromagnetic structure (an exchange cross) [14] arises that is modulated due to an inhomogeneous exchange interaction along axis *c*. Among the magnetoelectric contributions to the thermodynamic potential Φ of the system, we distinguish the exchange term

$$\Phi_{\mathrm{ME}}^{\mathrm{ex}} = \alpha P_y (L_1^2 - L_2^2), \qquad (1)$$

which is responsible for the improperly appearing spontaneous electric polarization $P = P_y$ below the Neél point. This is the so-called antiferroelectric transition [15]. We restrict ourselves to the contribution

$$\Phi_{\mathrm{ME}}^{\mathrm{rel}} = P_y[K_1(L_{1x}^2 - L_{2x}^2) + K_2(L_{1y}^2 - L_{2y}^2)] \qquad (2)$$

among appropriate relativistic contributions. One of the most surprising properties of our centrally symmetric system (the point group *mmm* for RMn_2O_5) is a weakly ferromagnetic moment that arises as a result of the phase transition at the point T_N and is accompanied by the variation of the translation symmetry and a spontaneous polarization. Therefore, it is worthwhile to discuss this phenomenon. It is well known that, along with the spontaneous polarization along a certain direction, the structural changes due to phase transitions may give rise to antiferroelectric ordering along other directions [16]. In our system, the spontaneous magnetization (weak ferromagnetism) cannot be described in terms of conventional mechanisms. Therefore, we assume (although there is also indirect evidence [10]) that, in addition to the ferroelectric ordering, there is another structural (for example, antiferroelectric) ordering that is characterized by a two-dimensional (this is essential) representation, which is not magnetic, defined by a pair of quantities P_1 and P_2 that correspond to an antiferroelectric state; this structural ordering is due to the mechanism of the type described in [17].

Then, we take into consideration the following contributions (antiferroelectric proper and the magnetoantiferroelectric) to the energy of the system:

$$\Phi_{\mathrm{MAE}} = \beta(P_1^2 + P_2^2) - \gamma(P_1^2 + P_2^2)(L_1^2 + L_2^2). \qquad (3)$$

In addition to this mechanism, which imposes rather stringent requirements on the magnitude and sign of the interaction parameter γ in (3), we can suggest another explanation for the antiferroelectric ordering. Due to the symmetry properties of the system, one can construct another invariant contribution:

$$\Delta\Phi = \gamma_1(L_1^2 - L_2^2)(P_1^2 - P_2^2), \quad (4)$$

which corresponds to the energy of interaction between the antiferromagnetic (described by the pair $\mathbf{L}_1$ and $\mathbf{L}_2$) and antiferroelectric vectors (described by the pair P_1 and P_2); in this case, the requirements for the parameter γ_1 are much less stringent.

Taking into consideration the variables P_1 and P_2 allows one to obtain another cross contribution, which is the most important magnetoelectric contribution (provided that the representations with the bases (P_1, P_2) and ($\mathbf{L}_1 \cdot \mathbf{M}$), ($\mathbf{L}_2 \cdot \mathbf{M}_2$) are equivalent):

$$\Phi_{\mathrm{MLE}} = \Delta[P_1(\mathbf{L}_1 \cdot \mathbf{M}) + P_2(\mathbf{L}_2 \cdot \mathbf{M})], \quad (5)$$

where $\mathbf{M}$ is the magnetization vector.

The latter contribution gives rise to a specific weak ferromagnetism below the Neél point, which is described by the vector $\mathbf{M}$, related to the antiferromagnetic structure not only by the vectors $\mathbf{L}_1$ and $\mathbf{L}_2$ but also by the ratio of P_1 to P_2.

Then, in particular, under application of a strong magnetic field along axis *b*, the system experiences a magnetic reorientation by an angle of $\pi/2$ (a spin-flop transition). Magnetic field applied along axis *a* (across the effective direction of the axis of antiferromagnetism) does not lead to a spin-flop transition, which agrees with experiment. Formula (2) clarifies that the reorientation of the exchange cross obtained in a strong magnetic field gives rise to a jump in the dependence $P_y(H_y)$ at the transition point, which was also observed experimentally.

Interest in the investigation of magnetoelectric interaction in RMn_2O_5 compounds has also been stimulated by the fact that, according to the classification of [18], these compounds represent antitoroics. In addition, one more structural axial vector $\mathbf{G}$ that is invariant with respect to the time inversion spontaneously arises at the Neél point; this vector is dual to the antisymmetric part of the displacement vector; i.e., it corresponds to the torsional strain in accordance with the noncollinearity of the antiferromagnetic structure; moreover, $\mathbf{G} \propto \mathbf{L}_1 \times \mathbf{L}_2$.

4. CONCLUSIONS

In YMn_2O_5 ferromagnetoelectric single-crystals at $T < T_N = 42$ K, a spontaneous weakly ferromagnetic moment along crystal axis *a* has been observed ($\sigma_0 = 0.8$ G cm^3/g) that is induced by the magnetoelectric interactions. The anomalies of the magnetoelectric and magnetoelastic properties of YMn_2O_5 have been investigated under magnetic and structural phase transitions induced by a magnetic field of $H \le 250$ kOe. A strong magnetic field along axis *a* shifts the temperature of ferroelectric phase transition. A spin-flop transition has been observed in the field $\mathbf{H}$ oriented along the *b* axis that is accompanied by a change in the sign of spontaneous polarization.

Theoretical explanation within the representation theory of space groups has been given for the experimental results listed above. It has been shown that the main role is played by the exchange-symmetry approximation.

ACKNOWLEDGMENTS

This work was supported by the Russian Foundation for Basic Research, project nos. 01-02-16468 and 00-15-96695.

REFERENCES

1. G. Buisson, Phys. Status Solidi A **17**, 191 (1973).
2. C. Wilkinson, F. Sinclair, P. Gardner, *et al.*, J. Phys. C **14**, 1671 (1981).
3. A. Ikeda and K. Kohn, Ferroelectrics **169**, 75 (1995).
4. A. Inomata and K. Kohn, J. Phys.: Condens. Matter **8**, 2673 (1996).
5. V. A. Sanina, L. M. Sapozhnikova, E. I. Golovenchits, and N. V. Morozov, Fiz. Tverd. Tela (Leningrad) **30**, 3015 (1988) [Sov. Phys. Solid State **30**, 1736 (1988)].
6. E. I. Golovenchits, N. V. Morozov, V. A. Sanina, and L. M. Sapozhnikov, Fiz. Tverd. Tela (St. Petersburg) **34**, 108 (1992) [Sov. Phys. Solid State **34**, 56 (1992)].
7. T. Doi and K. Kohn, Phase Transit. **38**, 273 (1992).
8. Yu. F. Popov, A. M. Kadomtseva, D. V. Belov, *et al.*, Pis'ma Zh. Éksp. Teor. Fiz. **69**, 302 (1999) [JETP Lett. **69**, 330 (1999)].
9. Yu. F. Popov, A. M. Kadomtseva, G. P. Vorob'ev, *et al.*, J. Magn. Magn. Mater. **188**, 237 (1998).
10. V. Polyakov, V. Plakhty, M. Bonnet, *et al.*, Physica B (Amsterdam) **297**, 208 (2001).
11. Yu. F. Popov, A. M. Kadomtseva, S. S. Krotov, *et al.*, Ferroelectrics **279**, 165 (2002).
12. L. N. Baturov, N. A. Sokolov, and B. I. Al'shin, Fiz. Tverd. Tela (St. Petersburg) **25**, 1994 (1983) [Sov. Phys. Solid State **25**, 1150 (1983)].
13. A. V. Lesnyak, Candidate's Dissertation in Physics and Mathematics (Moscow State Univ., Moscow, 2002).
14. A. F. Andreev and V. I. Marchenko, Zh. Éksp. Teor. Fiz. **70**, 1522 (1976) [Sov. Phys. JETP **43**, 794 (1976)].
15. E. A. Turov, A. V. Kolchanov, V. V. Men'shin, *et al.*, *Symmetry and Physical Properties of Antiferromagnetics* (Fizmatlit, Moscow, 2001), p. 259.
16. G. A. Smolenskiĭ, V. A. Belov, V. A. Isupov, *et al.*, *The Physics of Ferroelectric Phenomena* (Nauka, Leningrad, 1985).
17. J. Holakovsky, Phys. Status Solidi B **56**, 615 (1973).
18. H. Schmid, Ferroelectrics **252**, 41 (2001).

Translated by I. Nikitin

Journal of Experimental and Theoretical Physics, Vol. 96, No. 5, 2003, pp. 966–974.
Translated from Zhurnal Éksperimental'noĭ i Teoreticheskoĭ Fiziki, Vol. 123, No. 5, 2003, pp. 1096–1105.

SOLIDS
Electronic Properties

Resonant Tunneling of Electrons Interacting with Phonons

V. F. Elesin

Moscow Institute of Engineering Physics (Technical University), Kashirskoe sh. 31, Moscow, 115409 Russia
e-mail: vef@supercon.mephi.ru

Received December 16, 2002

Abstract—The effect of the electron–phonon interaction on resonant tunneling of electrons through a two-barrier nanostructure is investigated in the framework of a consistent quantum-mechanical model. The wave function is determined by solving the Schrödinger equation with correct boundary conditions in the semiclassical approximation in the electron–phonon interaction. The current calculated with the help of the wave function is averaged over the phonon subsystem with the help of the Bloch theorem. The analytic expressions derived for static and varying currents in a resonance tunnel diode taking into account the electron–phonon interaction formally coincide with the Mössbauer effect probability. In the adiabatic limit and for a strong electron–phonon interaction, the static current decreases in proportion to η, while the varying low-frequency current is proportional to η^2. The shape of the resonance curve becomes Gaussian with a width of τ_{ph}^{-1}. The fundamental result is that the properties inherent in coherent tunneling are preserved even in the limit $\eta \ll 1$ (which is often regarded as incoherent). The most striking effect (analogous to the Mössbauer effect) is the conservation of a narrow Lorentzian resonance curve in the limit $\eta \ll 1$, $\omega_{ph} \gg \Gamma$. This means that even for $\eta \ll 1$, the resonance current is due to coherent electrons (experiencing interference), but their fraction decreases in view of the electron–phonon interaction. It is concluded that the application of the rate equations and other approximate methods disregarding interference may lead to incorrect results. The expressions for the high-frequency and nonlinear responses are also derived. The quantum-mechanical regime is found to be less sensitive to the effect of phonons than the classical regime. © *2003 MAIK "Nauka/Interperiodica".*

1. INTRODUCTION

Resonant tunneling is a purely quantum effect closely related to interference of electrons. The interaction with phonons causes an electron phase breakdown, reducing the resonance current. For this reason, the resonance tunnel current, say, in two-barrier nanostructures depends on the relation between the resonant level width Γ and the phase breakdown time τ_{ph}.

If $\Gamma\tau_{ph} \gg 1$, resonant tunneling is coherent. In this case, electrons with resonance energy ε_R pass through a nanostructure with symmetrical barriers without being reflected, thus ensuring maximal current. Reflection from the structure is suppressed by destructive interference.

The situation becomes much more unclear in the opposite limiting case, when $\Gamma\tau_{ph} \ll 1$. Although the theory of the effect of the electron–phonon interaction on resonant tunneling has been considered by many authors, the problems of interpreting experimental results (see, for example, [1]) and of adequate description of coherence breakdown processes have not been solved completely.

In view of the complexity of the competition between interference and phase breakdown processes, approximate methods are often employed. One of the simplest methods is that of consecutive tunneling [1, 2]. In this method, it is assumed that electrons lose their phase completely in the limit $\Gamma\tau_{ph} \ll 1$ and rate equations are used. In another widely used approximate method (see [3, 4]), the nanostructure is divided into uncoupled regions of the instrument and contacts, and the coupling between them is introduced as a perturbation. The corresponding Hamiltonian is written in the strong coupling representation. This method is similar to the tunnel Hamiltonian method (THM) in the theory of superconductivity. For the sake of brevity, we will henceforth use this abbreviation. Owing to the simplifications made, the boundary value problem can be omitted and the formalism of nonequilibrium Green functions, which is well adapted for describing the electron–phonon interaction, can be used (see, for example, [3, 5]).

However, resonant tunneling is very sensitive to boundary conditions. For this and some other reasons, the THM may turn out to be excessively simplified. For example, it is shown in [6] that it is reduced to rate equations.

This study is aimed at an analysis of the effect of the electron–phonon interaction in the framework of a more rigorous approach, which takes into account interference and boundary conditions in succession. It includes the direct application of the wave function,

which is determined from the solution to the Schrödinger equation with correct boundary conditions (see [7, 8]). The electron–phonon interaction is taken into account in the semiclassical approximation. This can be done since the interaction energy $\varphi(x, t)$ and the phonon frequency ω_q are smaller than the resonance energy ε_R. The resonance current calculated with the help of the wave function is averaged over the phonon subsystem using the Bloch theorem [9].

We will derive analytic expressions for static and varying resonance currents of a two-barrier nanostructure, viz., a resonance tunnel diode (RTD), taking into account the interaction with phonons. It will be shown that the static current for adiabatic phonons ($\omega_q \ll \Gamma$) in the limit $\eta = \tau_{ph}\Gamma \ll 1$ decreases in proportion to η, while the varying low-frequency current decreases in proportion to η^2. The line profile becomes Gaussian instead of the initially Lorentzian profile.

The main result is that the resonant properties of the RTD are preserved even in the limit $\eta \ll 1$. The number of electrons experiencing interference decreases, but it is these electrons that contribute to the resonance current.

This effect is manifested most clearly for high-frequency phonons for $\omega_q \gg \Gamma$ and $\eta \ll 1$. In this case, the initial sharp resonance dependence is preserved and the current decreases by a factor equivalent to the Debye–Waller factor [10]. The situation is similar in many respects to the Mössbauer effect [10].

It should be emphasized that the above-mentioned results differ in principle from THM predictions.

2. FORMULATION OF THE PROBLEM AND BASIC EQUATIONS

We will analyze the effect of the electron–phonon interaction on the static and varying resonance currents of an RTD. Resonant tunneling is described in the framework of the model [7] taking correctly into account quantum interference of electrons in the well and open boundary conditions.

Following [7], we consider a quantum well (dot) with two δ-function barriers at points $x = 0$ and $x = a$. A steady electron flow proportional to Q and having an energy ε equal approximately to the resonance level energy ε_R is fed to the well from the left ($x = -\infty$).

The wave function $\Psi(x, t)$ of the system satisfies the Schrödinger equation

$$i\frac{\partial\Psi}{\partial t} = -\frac{\partial^2\Psi}{\partial x^2} + [\alpha\delta(x) + \alpha\delta(x-a) + V(x,t) + \hat{\varphi}(x,t)]\Psi = 0. \quad (1)$$

Here, α are the "intensities" of the emitter and collector barriers;

$$V(x, t) = U(x)\cos(\omega t), \quad (2)$$

$$U(x) = \begin{cases} \nu x\theta(x), & x < a, \\ \nu a, & x \geq a, \end{cases} \qquad \nu = -\frac{eE}{2}, \quad (3)$$

E being the amplitude of the uniform ac field of frequency ω, $\theta(x)$ the step function; e the electron charge; and $\hbar = 2m = 1$.

The energy of interaction between electrons and phonons is chosen for simplicity in the deformation potential approximation [11] and a single phonon frequency (generalization will be made below) in the form

$$\hat{\varphi}(x, t) = \mathscr{E}\frac{\partial\hat{u}(x, t)}{\partial x}, \quad (4)$$

$$\hat{u}(x, t) = (2M\omega_q)^{-1/2}[C_q\exp(iqx - i\omega_q t) + \text{h.c.}]. \quad (5)$$

Here, $\mathscr{E}$ is the deformation potential energy, $\hat{u}(x, t)$ is the displacement of atoms of mass M, and $C_q^\dagger(C_q)$ are the production (destruction) operators for photons with frequency ω_q and wave vector q. It is important to note that the interaction energy $\hat{\varphi}(x, t)$ expressed in terms of the secondary quantization operators is a real function exhibiting a periodic dependence on time.

The boundary conditions to Eq. (1) describe a flow of electrons from $x = -\infty$, their reflection, and departure to the region $x = \infty$ (see [7, 8] for details). The static current $J_0(\varepsilon)$ and the varying current $J_c(x, t)$,

$$J_c(x, t) = J_c(x)\cos(\omega t), \quad (6)$$

which has the same phase as potential $V(x, t)$, can be expressed conventionally in terms of the wave function $\Psi(x, t)$ (see [7]). The currents must be averaged over the phonon subsystem.

3. STATIC CURRENT TAKING INTO ACCOUNT THE ELECTRON–PHONON INTERACTION: ADIABATIC CASE

In the absence of interaction with phonons, the static resonance current of the RTD is given by the familiar relation (see, for example, [7])

$$J_0(\delta) = \frac{\Gamma^2}{\Gamma^2 + \delta^2}, \quad \delta = \varepsilon - \varepsilon_R, \quad (7)$$

where Γ is the width of the resonance level with energy ε_R; we assume that the current density Q of impinging electrons is equal to $2/p$, $p^2 = \varepsilon$.

In resonance ($\varepsilon = \varepsilon_R$), the current attains its maximal value and the coefficient of reflection from the structure is equal to zero. This is due to destructive interference of reflected electrons. We can naturally expect that the interaction with phonons will destroy interference due to phase breakdown. The effect of phonons is deter-

mined by the relation between the phonon frequency ω_q and the level width Γ. If the frequency ω_q is smaller than Γ (adiabatic limit), the electron energy varies slowly in accordance with lattice vibrations. The electron energy variation during tunneling draws out the electrons from resonance and, hence, may strongly affect the tunnel current.

In this section, we consider only adiabatic phonons, which strongly affect the current in the RTD. In addition, following the approach proposed in [12] and using the Bloch theorem [9] for averaging over phonons, we can easily find the static and varying resonance currents in the adiabatic limit.

Proceeding from the above considerations, we can represent the electron energy $\hat{\varepsilon}(t)$ in the adiabatic case in the form

$$\hat{\varepsilon}(t) = \varepsilon + \hat{\varphi}(x, t). \tag{8}$$

Then expression (7) for the resonance static current assumes the form

$$\hat{J}_0(\delta) = \frac{\Gamma}{2}[\hat{f}(\delta, t) + \text{h.c.}], \tag{9}$$

$$\hat{f}(\hat{\delta}, t) = \frac{\Gamma}{\Gamma - i\hat{\delta}}, \quad \hat{\delta} = \delta + \hat{\varphi}(x, t). \tag{10}$$

It should be noted that an equivalent notation is also possible:

$$\hat{J}_0(\delta) = \hat{f}\hat{f}^+. \tag{11}$$

The qualitative derivation given above can be proved using the explicit solution to Eq. (1) in the semiclassical approximation. Using the results obtained in [13], we can easily prove that, when conditions

$$\omega_q \ll \Gamma \ll \varepsilon_R, \quad \varphi \ll \varepsilon_R \tag{12}$$

are satisfied, the tunneling amplitude $\hat{f}(\delta, t)$ is defined by formula (10), but instead of $\hat{\varphi}(x, t)$ we must substitute the following quantity integrated with respect to x:

$$\bar{\hat{\varphi}}(t) = \frac{1}{a}\int_0^a dx\hat{\varphi}(x, t). \tag{13}$$

Expression (9) for current must be averaged over the phonon ensemble at temperature T:

$$\bar{J}_0(\delta) = \langle \bar{J}_0(\delta)\rangle. \tag{14}$$

In order to carry out averaging, it is convenient, following [12], to pass to the Laplace representation of the Lorentzian curve:

$$\bar{J}_0(\delta) = \frac{\Gamma}{2} \times\left\{\int_0^\infty d\tau \exp[-\tau(\Gamma - i\delta)]\langle \exp[-i\tau\bar{\hat{\varphi}}(t)]\rangle + \text{h.c.}\right\}. \tag{15}$$

In accordance with the Bloch theorem [9], the average over the phonon ensemble is given by

$$\langle \exp[-i\tau\bar{\hat{\varphi}}(t)]\rangle = \exp\left[-\left(\frac{\tau}{\tau_{ph}}\right)^2\right], \tag{16}$$

$$\frac{1}{\tau_{\text{ph}}} = \frac{\mathscr{E}\sin qa/2}{a}\sqrt{\frac{2N_q + 1}{M\omega_q}}, \quad N_q = (e^{\omega_q/T} + 1)^{-1}. \tag{17}$$

In this section, we will henceforth assume that $T = 0$ and $N_q = 0$. A generalization to the case when $T \neq 0$ can be easily obtained.

The final expression for the static tunnel current has the form

$$\bar{J}_0(\delta) = \frac{\Gamma}{2}\int_0^\infty d\tau \exp\left[-\left(\frac{\tau}{\tau_{ph}}\right)^2\right][e^{-\tau(\Gamma - i\delta)} + \text{c.c.}]. \tag{18}$$

It should be noted that the term leading to a resonant energy shift due to the electron–phonon interaction in the exponential of Eq. (18) has been omitted. This term will be given below (see Section 7) during an analysis of current for high-frequency phonons.

In the general case, current $\bar{J}_0(\delta)$ can be expressed in terms of tabulated functions. For example, in accordance with [14], we have

$$\bar{J}_0(\delta) = \frac{\sqrt{\pi}\Gamma\tau_{\text{ph}}}{2}\{\exp(z^2)[1 - \phi(z)] + \text{c.c.}\}, \tag{19}$$

where

$$z = \frac{(\Gamma - i\delta)\tau_{\text{ph}}}{2}, \quad \phi(z) = \frac{2}{\sqrt{\pi}}\int_0^z \exp(-t^2)dt. \tag{20}$$

Sometimes it is more convenient to represent $\bar{J}_0(\delta)$ in terms of functions $I_+(\beta)$ [15]:

$$\bar{J}_0(\delta) = \frac{i\Gamma\tau_{\text{ph}}}{\sqrt{\pi}}[I_+(\beta) - I_+^*(\beta)], \tag{21}$$

$$I_+(\beta) = -i\sqrt{2\pi}\int_0^\infty \exp\left(i\beta t - \frac{t^2}{2}\right)dt, \quad \beta = \beta' + i\beta'', \quad \beta'' > 0, \quad \beta = \sqrt{2}iz. \tag{22}$$

Functions $\phi(z)$ and $I_+(\beta)$ tabulated in [16] make it possible to determine $\bar{J}_0(\delta)$ for any Γ, τ_{ph}, and δ.

We will analyze below only the limiting cases that demonstrate the main effects of the electron–phonon interaction on resonant tunneling. First, we determine the resonance value of current from Eq. (19) for $\delta = 0$:

$$\bar{J}_0(\delta = 0) = \frac{\sqrt{\pi}\eta}{2}\exp\left(\frac{\eta^2}{4}\right)\left[1 - \phi\left(\frac{\eta}{2}\right)\right], \quad \eta = \Gamma\tau_{ph}. \tag{23}$$

In the coherent limit ($\eta \gg 1$), we have

$$\bar{J}_0(\delta = 0) \approx 1 - 2/\eta^2; \tag{24}$$

i.e., the current decreases in proportion to $1/\eta^2$. In the opposite limiting case ($\eta \ll 1$), in the first approximation, we obtain from Eq. (23)

$$\bar{J}_0(\delta = 0) \approx \frac{\sqrt{\pi}\eta}{2}. \tag{25}$$

It follows from this relation that the static resonance current decreases by a factor of $1/\eta$ due to the violation of the resonance conditions by the interaction between electrons and adiabatic phonons.

In the limit $\eta \ll 1$, we can find the dependence of current on δ in the entire detuning range. Using representation (22) of function $I_+(\beta)$,

$$I_+(\beta) = \sqrt{2\pi}e^{-\beta^2/2}\left[\int_0^\beta e^{\tau^2/2}d\tau - i\sqrt{\pi/2}\right], \tag{26}$$

and expression (21) for current $\bar{J}_0(\delta)$, we obtain

$$\bar{J}_0(\delta) \approx \frac{\sqrt{\pi}\eta}{2}\exp\left(-\frac{\delta^2\tau_{ph}^2}{4}\right). \tag{27}$$

The inclusion of the interaction of electrons with adiabatic phonons leads to a decrease in the resonance current and to a broadening of the resonant dependence $\bar{J}_0(\delta)$. For $\eta \ll 1$, the shape of the curve becomes Gaussian instead of the initial Lorentzian shape (7).

It should be emphasized, however, that the $\bar{J}_0(\delta)$ dependence preserves its resonance nature with width τ_{ph}^{-1} even for $\eta \ll 1$ (but, naturally, for $\varepsilon_R\tau_{ph} \gg 1$). This means that the current is determined by interfering electrons, although their fraction decreases in proportion to η. Some electrons are reflected and make zero contribution. For this reason, we must assume that the criteria of coherent ($\eta \gg 1$) and incoherent ($\eta \ll 1$) tunneling are quantitative rather than qualitative by nature.

It should be noted that the role of the phase breakdown time is played by the quantity τ_{ph} (see Eq. (17)), which is inversely proportional to the matrix element $\mathscr{E}$ and not to its square $\mathscr{E}^2$, in contrast to relaxation times [11].

Let us compare the expressions for $\bar{J}_0(\delta)$ derived above with the results predicted with the help of the THM [3],

$$\bar{J}_0(\delta) = \frac{\Gamma^2}{[\delta^2 + (\Gamma + \Gamma_{ph})^2]}, \tag{28}$$

where Γ_{ph} is the additional broadening due to the interaction with phonons.

In accordance with relation (28), current $\bar{J}_0(\delta)$ preserves its Lorentzian shape even for $\Gamma_{ph} \gg \Gamma$; for $\delta = 0$, it is given by

$$\bar{J}_0(\delta) = \frac{\Gamma^2}{\Gamma_{ph}^2}. \tag{29}$$

Thus, the predicted decrease is stronger and proportional to the square $(\Gamma/\Gamma_{ph})^2$ as compared to the linear decay of $\Gamma\tau_{ph}$ in relation (25). Thus, relations (28) and (29) differ significantly from (27) and (25).

4. EFFECT OF THE ELECTRON–PHONON INTERACTION ON VARYING CURRENT OF A RESONANCE TUNNEL DIODE: ADIABATIC CASE

The varying linear current in an RTD in the model of coherent resonant tunneling, which consistently takes into account interference and boundary conditions, was found in [7]:

$$J_c(\delta, \omega) = -\frac{e^2Ea\Gamma^2\delta}{2[(\delta - \omega)^2 + \Gamma^2][\Gamma^2 + (\delta + \omega)^2]} \equiv -\frac{e^2Ea}{2}G_c(\delta, \omega). \tag{30}$$

Here, $J_c(\delta, \omega)$ is the reduced current proportional to the amplitude E of the varying electric field and $G_c(\delta, \omega)$ is the linear response. It was shown in [7] that current $J_c(\delta, \omega)$ has peaks at frequency $\omega_m = 0$ if $\delta < \Gamma$ and at frequency $\omega_m^2 = \delta^2 + \Gamma^2$ if $\delta > \Gamma$. The latter peak is due to quasi-resonance transitions between states with energies ε and ε_R ($\varepsilon \approx \varepsilon_R + \omega$) and leads to a new ("quantum") regime of emission of the RTD. The quantum regime can ensure a high-power generation of the RTD at frequencies much higher than width Γ [17]. In the "classical" regime ($\delta < \Gamma$, $\omega_m = 0$), the value of response G_c decreases rapidly (in proportion to $1/\omega^4$) upon an increase in frequency for $\omega \gg \Gamma$.

Let us determine the varying current taking into account the electron–phonon interaction and using the approach developed in the previous section. This can be done most easily by taking into account the fact

that response $G_c(\delta, \omega)$ (30) can be represented in the form [7]

$$G_c(\delta, \omega) = \frac{J_0(\delta + \omega) - J_0(\delta - \omega)}{4\omega}, \quad (31)$$

where $J_0(\delta)$ is the static resonance current (7). Averaging current (31) over the phonon subsystem, we obtain

$$\bar{G}_c(\delta, \omega) = \frac{\bar{J}_0(\delta + \omega) - \bar{J}_0(\delta - \omega)}{4\omega}. \quad (32)$$

Thus, we can express response $G_c(\delta, \omega)$ in terms of the static current $\bar{J}_0(\delta \pm \omega)$ determined above. Let us consider the most interesting limiting cases.

We begin with the low-frequency range $\omega \ll \Gamma$, in which, in accordance with relation (32), response G_c can be expressed in terms of the differential static conduction

$$\bar{G}_c(\delta) \approx \frac{d\bar{J}_0(\delta)}{2d\delta}. \quad (33)$$

In the coherent limit $\eta \gg 1$, we have

$$G_c(\delta) = -\frac{\delta\Gamma^2}{(\delta^2 + \Gamma^2)^2}. \quad (34)$$

The peak of response $G_c(\delta)$ is attained for $\delta_0^2 = \Gamma^2/3$ and is equal to

$$G_c(\delta_0) = -\frac{3\sqrt{3}}{16\Gamma}. \quad (35)$$

If the opposite inequality $\eta \ll 1$ holds, we can easily obtain the following formula from relations (33) and (27):

$$\bar{G}_c(\delta) = -\frac{\sqrt{\pi}\delta\eta\tau_{ph}^2}{8}\exp\left[-\frac{(\delta\tau_{ph})^2}{4}\right]. \quad (36)$$

The maximum of response $\bar{G}_c(\delta)$ is attained for $\delta_0^2 = 2/\tau_{ph}^2$ and is found to be

$$\bar{G}_c(\delta_0) = -\frac{\sqrt{\pi}\eta^2}{4\sqrt{2}\Gamma}\exp\left(-\frac{1}{2}\right). \quad (37)$$

It follows hence that adiabatic phonons suppress low-frequency amplification proportional to η^2. The small parameter η, which appears as additional as compared to static current (25), is associated with violation of resonance by the varying current component. It is appropriate to note here that the tunnel Hamiltonian method (see [3]) predicts the absence of the effect of the electron–phonon interaction on the varying response. This immediately leads to the violation of the well-known relation between the low-frequency response and the derivative of the static current with respect to energy (voltage) (see relation (33)).

Let us now analyze the frequency dependence of response $G_c(\delta, \omega)$ in the limiting case $\eta \ll 1$. Using the results obtained in Section 3, we can easily obtain the following equality from Eq. (32):

$$\bar{G}_c(\delta, \omega) = -\frac{\sqrt{\pi}\eta}{4\omega} \times \sinh\left[\frac{\delta\omega\tau_{ph}^2}{2}\right]\exp\left[-\frac{(\omega^2 + \delta^2)}{4}\tau_{ph}^2\right]. \quad (38)$$

Evaluating the derivative $d\bar{G}_c/d\omega$, we obtain the following equation for extremal values of frequency:

$$\omega\delta = \left(\omega^2 + \frac{2}{\tau_{ph}^2}\right)\tanh\left[\frac{\delta\omega\tau_{ph}^2}{2}\right]. \quad (39)$$

The first solution $\omega_1 = 0$ corresponds to the maximum of $\bar{G}_c$ if $0 < \delta < \sqrt{6}\tau_{ph}^{-1}$ and to its minimum for $\delta > \sqrt{6}\tau_{ph}^{-1}$. This solution describes the classical regime. In this regime, $\bar{G}_c$ decreases rapidly with frequency for $\omega\tau_{ph} \gg 1$:

$$\bar{G}_c \approx \frac{\sqrt{\pi}\eta}{4\omega}\exp\left[-\frac{(\delta - \omega)^2\tau_{ph}^2}{4}\right]. \quad (40)$$

It should be noted that the characteristic frequency starting from which the value of $\bar{G}_c$ decreases sharply is now equal to approximately τ_{ph}^{-1}; i.e., the frequency range of the response expands in the classical regime. In the frequency interval $\Gamma \ll \omega \ll \tau_{ph}^{-1}$, the value of $\bar{G}_c$ exceeds G_c:

$$\frac{\bar{G}_c}{G_c} \approx -\frac{\omega^3\tau_{ph}}{\Gamma^2} \gg 1. \quad (41)$$

The second solution to Eq. (39), $\omega_2 \neq 0$, which corresponds to the maximum value of $\bar{G}_c$ for $\delta > \sqrt{6}\tau_{ph}^{-1}$, describes the quantum regime. Confining our analysis to high frequencies $\tau_{ph}\omega \gg 1$, we obtain from Eq. (39)

$$\omega_2 \approx \delta = \varepsilon - \varepsilon_R. \quad (42)$$

This is the quasi-resonance condition. Response $\bar{G}_c$ at the maximum is given by

$$\bar{G}_c(\omega_2) \approx -\frac{\sqrt{\pi}\eta}{4\omega}. \quad (43)$$

Comparing it with the corresponding value (30) in the coherent limit ($\eta \gg 1$),

$$G_c(\omega_2) \approx -\frac{1}{4\omega}, \quad (44)$$

we see that the decrease is proportional to η. Thus, amplification in the quantum regime is suppressed to

a smaller extent than in the classical regime (see relation (37)). The reason for this effect is that the resonance is violated only in the static channel. In the high-frequency channel, this violation is insignificant since $\omega\tau_{ph} \gg 1$.

Consequently, we have demonstrated that the behavior of the response in the limit $\eta \ll 1$ is qualitatively similar to the response in the coherent regime: two peaks (two regimes) are conserved for the relevant intervals of δ. The only difference is that the Lorentzian curve of width Γ is replaced by a Gaussian curve of width τ_{ph}^{-1}. Thus, we again arrive at the conclusion drawn in Section 3 for static current: the boundary at $\eta = 1$ does not play any qualitative role.

5. EFFECT OF THE ELECTRON–PHONON INTERACTION ON NONLINEAR RESPONSE

In order to construct a theory of RTD generation and a number of other problems, we must know the nonlinear response. In the low-frequency range $\omega \ll \Gamma$, the varying current was found analytically for any varying field amplitudes [12] with the help of an approach similar to that used in Section 3. Let us consider the nonlinear low-frequency current, taking phonons into consideration. For this purpose, combining the results obtained in [12] and in Section 3, we arrive at the following expression for current after averaging over the phonon subsystem:

$$\bar{J}_c(\delta, t) = \left\{\int_0^\infty d\tau \exp\left[-\tau\Gamma - \left(\frac{\tau}{\tau_{ph}}\right)^2\right] \times [\exp\{i\tau(\delta + \bar{\nu}\cos\omega t)\} + \text{c.c}]\right\}, \quad (45)$$

where $\bar{\nu} = eEa/4$. Expanding $\exp(i\bar{\nu}\cos\omega t)$ into a series in Bessel functions $J_n(\bar{\nu}\tau)$ and separating the contribution proportional to the first harmonic $\cos\omega t$, we obtain

$$\bar{J}_c(\delta, \bar{\nu}) \approx -2e\Gamma\int_0^\infty d\tau \sin\delta\tau \times \exp\left[-\Gamma\tau - \left(\frac{\tau}{\tau_{ph}}\right)^2\right] J_1(\bar{\nu}\tau). \quad (46)$$

In the coherent limit ($\eta \gg 1$), the integral can be evaluated exactly and we arrive at the expression which was obtained for the first time in [12]. If $\eta \ll 1$, the integral for any $\bar{\nu}$ cannot be evaluated exactly. For this reason, we confine our analysis to the first nonlinear correction.

Using the expansion of the Bessel function

$$J_1(z) \approx \frac{z}{2} - \frac{z^2}{8}, \quad (47)$$

we obtain the following expression for current:

$$\bar{J}_c(\delta, \bar{\nu}) = -e\Gamma\bar{\nu}\int_0^\infty d\tau \exp\left[-\Gamma\tau - \left(\frac{\tau}{\tau_{ph}}\right)^2\right] \times \sin\delta\tau\left[1 - \left(\frac{\bar{\nu}\tau}{2}\right)^2\frac{1}{8}\right]\tau. \quad (48)$$

In the general case (for any η), $\bar{J}_c(\delta, \bar{\nu})$ can be expressed in terms of special functions [14]. In the limit $\eta \ll 1$ we are interested in, we have

$$\bar{G}_c(\delta, \bar{\nu}) = \bar{G}_c(\delta, \bar{\nu} = 0)[1 - \bar{\nu}^2\tau_{ph}^2(6 - \delta^2\tau_{ph}^2)]. \quad (49)$$

For the sake of comparison, we also write the analogous expansion in the coherent limit $\eta \gg 1$ [12]:

$$G_c(\delta, \bar{\nu}) = G_c(\bar{\nu} = 0)\left[1 - \frac{3\bar{\nu}^2(\Gamma^2 - \delta^2)}{2(\delta^2 + \Gamma^2)^2}\right]. \quad (50)$$

Comparing expressions (49) and (50), we see that the results are qualitatively similar in this case also except for the substitution of τ_{ph}^{-1} for Γ. It is important to note that, like in [12] (see expression (50)), the sign reversal of the nonlinear correction takes place (in this case, for $\delta > \sqrt{6}\tau_{ph}^{-1}$). The sign reversal leads to a nonmonotonic dependence of current on the field and to hard generation regime [12].

Thus, we again arrive at the conclusion on the absence of a qualitative boundary for $\eta = 1$. It is also important to emphasize that the nonlinear correction in Eq. (49) is smaller than in relation (50) by a factor of η^2, facilitating the increase in the RTD generation power (see [17]).

6. RELATION WITH STATISTICAL AVERAGING OVER ADIABATIC PHONONS

We can prove that the proposed method of inclusion of adiabatic phonons is equivalent to statistical averaging over the Gaussian distribution $W(y)$:

$$\bar{J}_0(\delta) = \langle J_0(\delta)\rangle = \int_{-\infty}^{\infty} \frac{dy\Gamma^2 W(y)}{[\Gamma^2 + (\delta - y)^2]}, \quad (51)$$

$$W(y) = \frac{\tau_{ph}}{2\sqrt{\pi}}\exp\left(-\frac{y^2\tau_{ph}^2}{4}\right), \quad \int_{-\infty}^{\infty} W(y)dy = 1. \quad (52)$$

To prove this, we use formula (21) and the fact that function $I_+(\beta)$ can be expressed in terms of the integral [15]

$$I_+(\beta) = \int_{-\infty}^{\infty} dx e^{-x^2/2} \frac{1}{\beta - x}, \quad \mathrm{Im}\beta > 0. \tag{53}$$

Then current $\bar{J}_0(\delta)$ can be represented in the form

$$\bar{J}_0(\delta) = \frac{i\eta}{\sqrt{\pi}} \int_{-\infty}^{\infty} dx e^{-x^2/2} \left[\frac{1}{\beta - x} - \frac{1}{\beta^* - x} \right]$$
$$= \int_{-\infty}^{\infty} \frac{dx e^{-x^2/2}}{2\sqrt{2\pi}[(\delta - x\sqrt{2}\tau_{\mathrm{ph}}^{-1})^2 + \Gamma^2]}.$$

Carrying out the substitution of variables $x = y\tau_{\mathrm{ph}}/\sqrt{2}$, we arrive at relation (51).

7. EFFECT OF THE ELECTRON–PHONON INTERACTION ON RESONANT TUNNELING: GENERAL CASE

We can generalize the results obtained above to the case of phonons of arbitrary frequency by using semiclassical perturbation theory for solving the Schrödinger equation (1). In [13], a semiclassical solution to Eq. (1) was obtained with the varying potential

$$W(x, t) = W(x)\cos\omega t \tag{54}$$

for the wave function in the case when $x \geq a$:

$$\Psi(x = a) = f(a, t)\exp(-i\varepsilon t + ipx), \tag{55}$$

$$f(a, t) \equiv f(t) = \Gamma \exp\left[\frac{i\overline{W}}{\omega} \sin\omega t + it(\Gamma - i\delta) \right]$$
$$\times \int_{-\infty}^{-t} \exp\left[t'(\Gamma - i\delta) - \frac{i\overline{W}}{\omega} \sin\omega t' \right] dt', \tag{56}$$
$$\overline{W} = \frac{1}{a}\int_0^a W(x)dx.$$

Here, we assume that frequency ω and field amplitude $W(x)$ are smaller than energy ε_R. Potential $W(x)$ was assumed to be nonzero in the region of the well.

It was mentioned earlier that the above semiclassical conditions are satisfied by the energy of the electron–phonon interaction and the phonon frequency. Since $\hat{\varphi}(x, t)$, as well as $W(x, t)$, is a real function periodic in time, generalizing relation (56), we must replace $i\frac{\overline{W}}{\omega}\sin\omega t$ in $f(t)$ by

$$\hat{A}(t) = -\{C_q B_q(t) - C_q^+ B_q^*(t)\}, \tag{57}$$

$$B_q(t) = \frac{\mathscr{E}(e^{iaq} - 1)e^{-i\omega_q t}}{a\omega_q\sqrt{2M\omega_q}}. \tag{58}$$

Since the resonance current $\bar{J}_0(\delta)$ must be independent of coordinate x, we can choose the wave function $\Psi(x)$ in the form (55), (56) for any x, including $x = a$.

In this case, the resonance current $\bar{J}_0(\delta)$ can be written in the form

$$\bar{J}_0(\delta) = \langle \hat{f}\hat{f}^+ \rangle = \Gamma^2 \exp(2\Gamma t)\exp(\hat{A}(t))\exp(\hat{A}^+(t))$$
$$\times \int_{-\infty}^{-t} dt_1 \exp(t_1(\Gamma - i\delta)) \int_{-\infty}^{-t} dt_2 \exp(t_2(\Gamma + i\delta)) \tag{59}$$
$$\times \langle \exp(\hat{A}(t_1))\exp(\hat{A}^+(t_2)) \rangle.$$

Considering that

$$\hat{A}^+(t) = -\hat{A}(t), \quad e^{\hat{A}}e^{\hat{B}} = e^{\hat{A}+\hat{B}}e^{\frac{1}{2}[\hat{A}, \hat{B}]}, \tag{60}$$

we obtain, instead of relation (59),

$$\bar{J}_0(\delta) = \Gamma^2 \exp(2\Gamma t) \int_{-\infty}^{-t} dt_1 \exp(t_1(\Gamma - i\delta))$$
$$\times \int_{-\infty}^{-t} dt_2 \exp(t_2(\Gamma + i\delta)) \tag{61}$$
$$\times \langle \exp(\hat{A}(t_1) - \hat{A}(t_2)) \rangle \exp\left(-\frac{1}{2}[\hat{A}(t_1), \hat{A}(t_2)] \right).$$

The commutator equal to

$$[\hat{A}(t_1), \hat{A}(t_2)] = i\Phi_q^2 \sin\omega_q(t_2 - t_1) \tag{62}$$

leads to a shift of the resonance level.

Carrying out averaging over phonons with the help of the Bloch theorem [9], we obtain

$$\langle \exp(\hat{A}(t_1) - \hat{A}(t_2)) \rangle = \exp\left[\frac{1}{2}\langle (\hat{A}(t_1) - \hat{A}(t_2))^2 \rangle \right] \tag{63}$$
$$= \exp\{-\Phi_q^2[(2N_q + 1)(1 - \cos\omega_q(t_1 - t_1))]\},$$

$$\Phi_q^2 = \frac{2\mathscr{E}^2 \sin^2(qa/2)}{\omega_q^2 a^2 M\omega_q}. \tag{64}$$

Substituting relations (62) and (63) into formula (59)

and integrating, we obtain (for $T = 0$ and $N_q = 0$)

$$\bar{J}_0(\delta) = \Gamma\left[\int_0^\infty d\tau \exp[-\tau(\Gamma - i\delta) - g_q(\tau)] + \text{c.c.}\right], \quad (65)$$

$$g_q(\tau) = \Phi_q^2\{(1 - \cos\omega_q\tau) - i\sin\omega_q\tau\}. \quad (66)$$

Let us generalize relations (65) and (66) to the case of N phonon frequencies. In view of commutativity of the phonon production and destruction operators $C_q^\dagger$ and C_q with different values of q, the average of the exponential function over the phonon ensemble is equal to the product of the averages of individual exponential functions corresponding to different types of operators. This means that the interaction with phonons with different values of q is not correlated and they can be treated independently. Consequently, generalizing the derivation carried out above, we again arrive at relation (65), where function $g_q(\tau)$ is replaced by $g(\tau)$:

$$\bar{J}_0(\delta) = \Gamma\left[\int_0^\infty d\tau \exp[-\tau(\Gamma - i\delta) - g(\tau)] + \text{c.c.}\right], \quad (67)$$

$$g(\tau) = \sum_q \frac{\Phi_q^2}{N}[(2N_q + 1)(1 - \cos\omega_q\tau) - i\sin\omega_q\tau].$$

It is interesting to note that expression (67) for the resonance current through an RTD coincides formally with the expression for the probability of the Mössbauer effect [10]. The only difference is that the energy transferred by the nucleus is replaced by the deformation potential of the interaction. It should also be borne in mind that the natural line width Γ is assumed to be very small for emission from nuclei, and the process is determined by only two parameters: frequency ω_q (or Debye frequency) and the energy transferred. In the case of an RTD, all three parameters, viz., Γ, ω_q (or Debye frequency ω_{ph}), and Φ_q, are significant.

Let us first compare the general formula with the results obtained above (see Section 3). For the sake of simplicity, we use formulas (65) and (66) and set $T = 0$ and $N_q = 0$. If frequency ω_q is smaller than Γ, we obtain from relations (65) and (66)

$$\bar{J}_0(\delta) = \frac{\Gamma}{2} \times\left[\int_0^\infty d\tau \exp\left[-\tau(\Gamma - i\delta - i\varepsilon_{ph}) - \left(\frac{\tau}{\tau_{ph}}\right)^2\right] + \text{c.c.}\right], \quad (68)$$

where $\varepsilon_{ph} = \sum_q \Phi_q^2\omega_q$ is the resonance level shift. In all other respects, relation (68) coincides with Eq. (18) for the adiabatic case analyzed above.

In the limit $\omega_{ph} \gg \Gamma$, we use formula (67), when two cases similar to those realized in the Mössbauer effect are possible. If $\Phi_q \gg 1$ (so-called strong coupling), function $\exp(-g(\tau))$ decreases so rapidly that $\cos\omega_q\tau$ and $i\sin\omega_q\tau$ appearing in it can be replaced by the first nonvanishing terms in their series expansions. In this case, we again arrive at the situation that was already considered (i.e., to formula (68)), when the Lorentzian line of width Γ is replaced by a Gaussian line of width τ_{ph}^{-1}. The time of coherence breaking is given by the formula

$$\frac{1}{\tau_{ph}^2} = \sum_q \frac{\mathscr{E}^2\sin^2(qa/2)}{M\omega_q N a^2}(2N_q + 1). \quad (69)$$

In the opposite limit $\Phi < 1$ (weak coupling), the oscillating terms in $\exp(-g(\tau))$ vanish (as $\frac{\sin\omega t}{t}$ for $t \longrightarrow \infty$) and we are left only with the time-independent component. In this case, we obtain the following expression for current:

$$\bar{J}_0(\delta) = \exp\left(-\sum_q \frac{\Phi_q^2}{N}\right)\frac{\Gamma^2}{\Gamma^2 + \delta^2}. \quad (70)$$

Consequently, the initially narrow shape of the resonance curve is preserved, but the current decreases by a factor of $\exp\left(-\sum_q \frac{\Phi_q^2}{N}\right)$. The exponential function in relation (70) is an analog of the Debye–Waller factor and reflects the virtual elastic interaction of electrons with phonons.

It should be noted that, along with inequalities $\Phi < 1$ and $\omega \gg \Gamma$, the condition

$$\Phi\omega_{ph} = \frac{1}{\tau_{ph}} \gg \Gamma, \quad \eta = \Gamma\tau_{ph} \ll 1 \quad (71)$$

can also hold.

Thus, for an RTD with a small width Γ and weak coupling, the initial Lorentzian profile of the line can be conserved completely in the limit $\eta \ll 1$, which is regarded as "incoherent."

If we take into account the contribution from oscillating terms in the exponential in the next approximation, this leads to the emission of high-frequency phonons. The probability of these processes is low for $\Phi < 1$ and $\omega_q \gg 1$.

8. CONCLUSIONS

The results obtained above make it possible to describe the behavior of the static and varying resonance currents taking into account the electron scattering from phonons. Low-frequency adiabatic phonons ($\omega_q < \Gamma$) make a considerable contribution to the variation of the currents. The reason is that lattice vibrations

lead to a slow variation of the electron energy and, hence, to violation of the resonance condition.

Time τ_{ph} is a characteristic parameter. If $\tau_{ph}\Gamma \ll 1$, the Lorentzian line of width Γ is replaced by a Gaussian line of width τ_{ph}^{-1}. In this case, the resonance value of the static current decreases in proportion to $\eta = \Gamma\tau_{ph}$. The varying current in the low-frequency limit decreases more strongly since the resonance is violated twice (in the static and the varying channels).

It cannot be stated, however (as it is often done), that tunneling becomes completely incoherent in the limit $\eta \ll 1$ (but $\varepsilon_R\tau_{ph} \gg 1$). On the contrary, it was proved above that tunneling preserves its resonant nature under these conditions. Coherent electrons (experiencing interference) carry the resonance current, but their fraction decreases in view of increased number of reflected electrons having interacted with phonons.

This point of view is supported by the behavior of the linear and nonlinear varying currents, namely, by the existence of maxima of the reduced current for $\omega = 0$ (classical regime) and $\omega = \delta$ (quantum regime) in the linear response as well as by the conservation of fine features of the nonlinear response (e.g., the sign reversal for $\delta > \sqrt{6}\tau_{ph}^{-1}$).

However, the most striking effect is the conservation of the narrow line of the static resonance current (see relation (70)) in the incoherent limit $\eta \ll 1$, $\omega_q \gg \Gamma$. This effect is similar to the Mössbauer effect.

Thus, it can be concluded that interference plays a fundamental role in resonant tunneling in the limit $\eta \ll 1$. Resonant tunneling is always coherent and exists as long as time τ_{ph} (see relation (69)) exceeds $\hbar/\varepsilon_R$. For this reason, the application of the rate equations as well as the THM for describing tunneling is, strictly speaking, incorrect. This follows, for example, from a comparison of the results obtained above with the corresponding results from [3], where the THM was used. Indeed, according to [3], the varying current remains almost unchanged due to the electron–phonon interaction, while the static current decreases in proportion to η^2 (see relation (28)), which contradicts formulas (25) and (37). In addition, the known relation between the low-frequency current and derivative (33) of the static current is violated. A number of other THM predictions also contradict the exact analytic results (see [7, 8]).

It should be noted that we used the simplest model of tunneling and interaction with phonons. This enabled us to obtain visual analytic expressions and to reveal basic features of the effect of phase breakdown due to phonons on the resonant tunneling. We believe that the results provide a better description of experimental data (naturally, if the specific features of real structures and the electron energy distribution are taken into consideration).

ACKNOWLEDGMENTS

The author is deeply indebted to Yu.V. Kopaev for fruitful discussions.

This study was made in the framework of the Federal special Program (project no. A0133) and supported financially by the Ministry of Industry and Science of the Russian Federation under the program "Physics of Solid Nanostructures" (grant no. 99-1140) and the project "Construction of the Theory of Interaction of Strong Electromagnetic Fields with the Electronic System of RTDs and Lasers."

REFERENCES

1. J. P. Mattia and Mc. Whorter, J. Appl. Phys. **84**, 1140 (1998); K. L. Jensen and F. Buot, J. Appl. Phys. **67**, 7602 (1990); A. Hernandez-Cabrera, P. Aceituno, and H. Cruz, J. Appl. Phys. **78**, 6147 (1995); Nanzhi Zou *et al.*, J. Appl. Phys. **75**, 1829 (1994).
2. S. Luryi, Appl. Phys. Lett. **47**, 490 (1985).
3. M. P. Anatram and S. Datta, Phys. Rev. B **51**, 7632 (1995).
4. C. Caroli, R. Combescot, P. Nozieres, and D. Saint-Tamas, J. Phys. C **4**, 916 (1971).
5. N. S. Wingreen, A. P. Jahno, and Y. Meir, Phys. Rev. B **48**, 8487 (1993).
6. V. V. Afonin and A. M. Rudin, Phys. Rev. B **49**, 10466 (1994).
7. V. F. Elesin, Zh. Éksp. Teor. Fiz. **116**, 704 (1999) [JETP **89**, 377 (1999)].
8. V. F. Elesin, Zh. Éksp. Teor. Fiz. **121**, 925 (2002) [JETP **94**, 794 (2002)].
9. J. Winter, in *Quantum Optics and Electronics (Les Houches Summer School Lectures)*, Ed. by C. DeWitt, A. Blandin, and C. Cohen-Tannoudi (Gordon and Breach, New York, 1964; Mir, Moscow, 1966).
10. C. Kittel, *Quantum Theory of Solids* (Wiley, New York, 1963; Nauka, Moscow, 1967).
11. A. I. Ansel'm, *Introduction to the Theory of Semiconductors* (Fizmatgiz, Moscow, 1962).
12. V. F. Elesin, Phys. Low-Dimens. Semicond. Struct. **1/2**, 55 (1999).
13. D. Sokolovsky, Phys. Rev. B **37**, 4201 (1988).
14. I. S. Gradshteĭn and I. M. Ryzhik, *Tables of Integrals, Series, and Products*, 4th ed. (Fizmatgiz, Moscow, 1962; Academic, New York, 1980).
15. V. P. Silin and A. A. Rukhadze, *Electromagnetic Properties of Plasma and Plasmalike Media* (Fizmatgiz, Moscow, 1961).
16. V. N. Fadeeva and N. M. Terent'ev, *Tables of Values of the Probability Integral* (Gostekhizdat, Moscow, 1954).
17. V. F. Elesin, I. Yu. Kateev, and A. I. Podlivaev, Usp. Fiz. Nauk **170**, 333 (2000) [Phys. Usp. **43**, 291 (2000)]; Fiz. Tekh. Poluprovodn. (St. Petersburg) **34**, 1373 (2000) [Semiconductors **34**, 1321 (2000)].

Translated by N. Wadhwa

Journal of Experimental and Theoretical Physics, Vol. 96, No. 5, 2003, pp. 975–981.
Translated from Zhurnal Éksperimental'noĭ i Teoreticheskoĭ Fiziki, Vol. 123, No. 5, 2003, pp. 1106–1112.

NONLINEAR PHYSICS

Properties of Weakly Collapsing Solutions to the Nonlinear Schrödinger Equation

Yu. N. Ovchinnikov

Max-Planck Institute for Physics of Complex Systems, Dresden, D-01187 Germany
Landau Institute for Theoretical Physics, Russian Academy of Sciences, ul. Kosygina 2, Moscow, 117940 Russia
e-mail: ovc@itp.ac.ru

Received September 6, 2002

Abstract—It is shown that one of the conditions for a weakly collapsing solution with zero energy produces an infinite number of functionals I_N identically vanishing on the regular solutions to the corresponding differential equation. On the parameter plane $\{A, C_1\}$, there are at least two singular lines. Along one of these lines ($A/C_1 = 1/6$), are located weakly collapsing solutions with zero energy. It is assumed that, along the second line ($A/C_1 = \alpha_c$), another family of weakly collapsing solutions with zero energy is located. In the domain of large values of the parameters $\{C_1, \alpha = A/C_1\}$, there exists a domain of an intermediate asymptotic form, where the amplitude of oscillations of the function U grows in a large domain relative to the ξ coordinate. *© 2003 MAIK "Nauka/Interperiodica".*

1. INTRODUCTION

The nonlinear Schrödinger equation arises in investigations of physical processes in various fields of physics [1, 2]. In a d-dimensional space, this equation can be written in the form

$$i\frac{\partial\psi}{\partial t} + \Delta\psi + |\psi|^{2\sigma}\psi = 0, \qquad (1)$$

where ψ is a scalar function of the coordinates, Δ is the Laplace operator, and σ is a numerical parameter characterizing the type of nonlinearity. Under the condition $\sigma d \geq 2$, Eq. (1) has solutions with a singularity on a finite time interval. There are several types of such solutions [1–5]. Here, we continue an investigation of weakly collapsing solutions in the case $d = 3$, $\sigma = 1$ which is most interesting from the physical point of view. The weakly collapsing solutions form a three-parametric set $\{A, C, C_1\}$. One of the parameters (C) is associated with a scale transformation of Eq. (1) [6]. In [6, 7], it was shown that, on the plane (A, C_1), there exists an infinite discrete set of points corresponding to solutions with zero energy. These points are located along the straight line ($A/C_1 = 1/6$), which was found in [6, 7].

Solutions with zero energy exist when two equations, obtained below, are satisfied. In the domain $C_1 \gg 1$, one of these equations can be expanded in the parameter C_1^{-1}, generating a family of functionals I_N. Each functional I_N vanishes on all regular (at zero) solutions to the differential equation that arises in determining the functional I_N. We explicitly write two such solutions. We also show that, for $C_1 \gg 1$, there exists a domain of intermediate asymptotic form with solutions having a deep minimum in the number density of "particles." The number of particles in an exact weakly collapsing solution is always infinite. This necessitates the truncation of the solution at a finite distance. In this connection, the solutions with a deep minimum in the number density of particles are promising. One should expect their appearance in numerical calculations and real experiments [3].

2. WEAKLY COLLAPSING SOLUTIONS

Equation (1) has weakly collapsing solutions of the form

$$\psi = \lambda^{\nu}\varphi(\rho\lambda)\exp(i\chi(\rho, t)), \qquad (2)$$

where $\lambda = \lambda(t)$ and $\rho = |\mathbf{r}|$.

The energy and particle number conservation laws lead to the following equations for phase χ and parameters λ and ν [3]:

$$\nu\sigma = 1, \quad \chi(\rho, t) = \chi_0(t) + \tilde{\chi}(\rho\lambda),$$
$$\lambda = \frac{C}{\sqrt{t_0 - t}}, \quad \chi_0(t) = -\frac{C_1}{2}\ln(t_0 - t); \qquad (3)$$

here, C and C_1 are constants. It was shown in [3, 8] that both functions φ and $\tilde{\chi}$ can be expressed via a single function Z:

$$\varphi = \frac{\sqrt{Z'}}{y^{(d-1)/2}}, \quad \tilde{\chi}' = -\frac{yZ' + (2/\sigma - d)Z}{4C^2Z'}, \qquad (4)$$

where function Z satisfies the third-order differential

equation

$$Z''' - \frac{(Z'')^2}{2Z'} - \frac{(d-1)(d-3)}{2y^2}Z' - \frac{1}{C^2}\left[C_1 Z' - \frac{y(yZ' + (2/\sigma - d)Z)}{4C^2}\right] - \frac{(yZ' + (2/\sigma - d)Z)^2}{8C^4 Z'} + \frac{2(Z')^{\sigma+1}}{y^{(d-1)\sigma}} = 0. \quad (5)$$

In the case under consideration $\{\sigma = 1, d = 3\}$, Eq. (5) takes the form

$$Z''' - \frac{(Z'')^2}{2Z'} + \frac{2(Z')^2}{y^2} - \frac{C_1}{C^2}Z' + \frac{1}{8C^4}\left(y^2 Z' - \frac{Z^2}{Z'}\right) = 0. \quad (6)$$

Parameter C is related to the scale invariance of Eq. (6) and, in what follows, we assume it to be equal to unity, $C = 1$. There exists a one-parametric family of solutions to Eq. (6), which satisfy the physical boundary conditions at zero:

$$Z = Ay^3 + Ay^5\left(\frac{C_1}{10} - \frac{3A}{5}\right) + \ldots \quad (7)$$

In the asymptotic domain $y \longrightarrow \infty$, the general solution to Eq. (6) is [7, 9]

$$Z = By + \frac{B_1}{y}\left(1 + \frac{16C_1}{9y^2} + \ldots\right) - \frac{4}{y^2}(1 + \ldots) \times \left[d_1 \cos\left(\frac{y^2}{4} - 2C_1 \ln y\right) + d_2 \sin\left(\frac{y^2}{4} - 2C_1 \ln y\right)\right]. \quad (8)$$

Coefficient B_1 in formula (8) is connected with the coefficients $\{B, d_{1,2}\}$ via the simple relation [7]

$$B_1 = -2BC_1 - \frac{d_1^2 + d_2^2}{B}. \quad (9)$$

Parameters $d_{1,2}$ are functions of the quantities $\{A, C_1\}$. The weakly collapsing solution has zero energy if both coefficients $d_{1,2}$ are equal to zero:

$$d_1 = d_2 = 0. \quad (10)$$

3. WEAKLY COLLAPSING SOLUTIONS WITH ZERO ENERGY

In [6, 7], it was shown that, for large values of parameter $C_1 \gg 1$, there exist lines on the plane $\{A, C_1\}$, along which the amplitudes of the oscillatory terms are exponentially small in parameter C_1. The points corresponding to weakly collapsing solutions with zero energy are located on these lines. To obtain functional I (see below), we use the method applied in [7]. Multiplying both sides of Eq. (5) by Z' and differentiating with respect to y, we obtain the equation

$$Z'''' - 2C_1 Z'' + \frac{y}{4}(Z' + yZ'') - \frac{1}{4}Z = \frac{4}{y^3}(Z')^2 - \frac{6}{y^2}Z'Z''. \quad (11)$$

Linearized equation (11), i.e., the equation

$$Z'''' - 2C_1 Z'' + \frac{y}{4}(Z' + yZ'') - \frac{1}{4}Z = 0 \quad (12)$$

has four linearly independent solutions Z_{1-4}. One of these solutions (Z_1) is

$$Z_1 = y. \quad (13)$$

In the principal approximations (in parameter C_1^{-1}), solutions Z_{2-4} are presented in [7] for the entire domain $y > 0$. We also need the subsequent terms (in parameter C_1^{-1}) in these solutions. We define the functions P_{K4} [7] as

$$P_{14} = -\det\begin{pmatrix} Z_2 & Z_3 & Z_4 \\ Z_2' & Z_3' & Z_4' \\ Z_2'' & Z_3'' & Z_4'' \end{pmatrix},$$

$$P_{23} = \det\begin{pmatrix} y & Z_3 & Z_4 \\ 1 & Z_3' & Z_4' \\ 0 & Z_3'' & Z_4'' \end{pmatrix},$$

$$P_{34} = -\det\begin{pmatrix} y & Z_2 & Z_4 \\ 1 & Z_2' & Z_4' \\ 0 & Z_2'' & Z_4'' \end{pmatrix}, \quad (14)$$

$$P_{44} = \det\begin{pmatrix} y & Z_2 & Z_3 \\ 1 & Z_2' & Z_3' \\ 0 & Z_2'' & Z_3'' \end{pmatrix}.$$

The Wronskian W is independent of y and is equal to

$$W = -\det\begin{pmatrix} Z_2 & Z_3 & Z_4 \\ Z_2'' & Z_3'' & Z_4'' \\ Z_2''' & Z_3''' & Z_4''' \end{pmatrix}_{y=0}. \quad (15)$$

The general solution to Eq. (11) satisfying the boundary conditions at zero can be written with the help of functions P_{K4} in the form

$$Z = A_1(Z_4 - Z_3 - y\gamma) + D_1 y + D_2 Z_2 + D_3 Z_3 + D_4 Z_4, \tag{16}$$

where functions D_K can be expressed in terms of integrals of the derivatives of Z, namely,

$$D_K = \frac{1}{W}\int_0^y dy_1 P_{K4}\left(\frac{4(Z')^2}{y_1^3} - \frac{6Z'Z''}{y_1^2}\right). \tag{17}$$

Coefficients A_1 and γ are constants, and the value of γ is determined by the relation

$$\gamma = \frac{\partial}{\partial y}(Z_4 - Z_3)_{y=0}. \tag{18}$$

Formulas (14)–(18) are exact and can be used in any order in parameter C_1^{-1}. A weakly collapsing solution is a solution with zero energy if the following two conditions hold:

$$A_1 + D_4(\infty) = 0, \quad D_2(\infty) = 0. \tag{19}$$

The first equation in (19) is of particular interest to us, because, as will be shown below, the significant values of y_1 in expression (17) for the function $D_4(\infty)$ are small (on the order of $C_1^{-1/2}$).

In the domain of small values of y ($y \le C_1^{-1/2}$), we find the values of functions Z_2, Z_3, and Z_4 from Eq. (12):

$$Z_2 = 1 - \frac{y^2}{16C_1} + \ldots,$$

$$Z_3 = \frac{1}{8C_1}\exp(-\sqrt{2C_1}y)$$

$$\times\left[1 + \frac{5y}{8(2C_1)^{3/2}} + \frac{y^2}{8C_1} + \frac{y^3}{24\sqrt{2C_1}} + \ldots\right], \tag{20}$$

$$Z_4 = \frac{1}{8C_1}\exp(\sqrt{2C_1}y)$$

$$\times\left[1 - \frac{5y}{8(2C_1)^{3/2}} + \frac{y^3}{8C_1} - \frac{y^3}{24\sqrt{2C_1}} + \ldots\right].$$

Substituting expressions (20) into formulas (14) and (15), we obtain the values of Wronskian W and functions P_{K4} up to the terms C_1^{-2}, inclusively:

$$W = -\frac{\sqrt{2C_1}}{8}\left(1 - \frac{9}{32C_1^2}\right),$$

$$P_{14} = \frac{1}{8\sqrt{2C_1}}\left(1 - \frac{9}{32C_1^2}\right),$$

$$P_{24} = -\frac{y}{8\sqrt{2C_1}}\left(1 - \frac{5}{32C_1^2}\right), \tag{21}$$

$$(P_{44} + P_{34}) = \frac{\sqrt{2C_1}}{2}\left(1 - \frac{5}{32C_1^2}\right),$$

$$(P_{44} - P_{34}) = -\frac{1}{2}\left(1 - \frac{1}{8C_1^2}\right).$$

Using expression (7) for function Z for small values of y, we obtain

$$\frac{4(Z')^2}{y^3} - \frac{6Z'Z''}{y^2} = -72A^2 y. \tag{22}$$

Formulas (17), (21), and (22) allow one to find functions D_K in the domain of small values of y:

$$D_1 = \frac{18A^2}{C_1}y^2, \quad D_2 = -\frac{12A^2y^3}{C_1}\left(1 + \frac{1}{8C_1^2}\right),$$

$$D_4 + D_3 = 96A^2y^3\left(1 + \frac{1}{8C_1^2}\right), \tag{23}$$

$$D_4 - D_3 = -\frac{144A^2y^2}{\sqrt{2C_1}}\left(1 + \frac{5}{32C_1^2}\right).$$

Substituting the values of functions D_k into Eq. (16) and using Eqs. (7) and (19), we find the value of coefficient A_1:

$$A_1 = \frac{12A}{\sqrt{2C_1}}\left(1 + \frac{5}{32C_1^2} + O(C_1^{-4})\right). \tag{24}$$

As a result, the first equation in (19) takes the form

$$I = 0, \tag{25}$$

where functional I is defined by the expression

$$I = -6A + \int_0^\infty dy e^{-\sqrt{2C_1}y}\frac{(Z')^2}{y^2}\left\{\left(\frac{2}{y} + 3\sqrt{2C_1}\right)\right.$$
$$\left. + \left(-\frac{1}{8(2C_1)^{3/2}} - \frac{y}{16C_1} + \frac{y^2}{12\sqrt{2C_1}} + \frac{y^3}{8}\right)\right\}. \tag{26}$$

4. FUNCTIONAL I_0 OF ZEROTH-ORDER APPROXIMATION

Consider functional I_0

$$I_0 = -6A + \int_0^\infty dy e^{-\sqrt{2C_1}y}\frac{(Z_0')^2}{y^2}\left\{\frac{2}{y} + 3\sqrt{2C_1}\right\}, \quad (27)$$

where Z_0 is a solution to the equation

$$Z_0''' - \frac{(Z_0'')^2}{2Z_0'} - C_1 Z_0' + \frac{2}{y^2}(Z_0')^2 = 0, \quad (28)$$

such that

$$Z_0 = Ay^3 \text{ at } y \longrightarrow 0. \quad (29)$$

We show that $I_0 \equiv 0$ on any solution to Eq. (28) with boundary condition (29). We set

$$\tilde{\phi} = Z_0' \quad (30)$$

and rewrite Eq. (28) in the form

$$\frac{\partial}{\partial y}\left(\frac{(\tilde{\phi})^2}{\phi}\right) + \frac{2}{y^2}\frac{\partial\tilde{\phi}^2}{\partial y} - 2C_1\frac{\partial\tilde{\phi}}{\partial y} = 0. \quad (31)$$

Using the identity

$$\int_y^\infty \frac{dy_1}{y_1^3}e^{-\sqrt{2C_1}y} = \frac{e^{-\sqrt{2C_1}y}}{2y^2} - \sqrt{2C_1}\frac{e^{-\sqrt{2C_1}y}}{2y} + C_1\int_y^\infty \frac{dy_1}{y_1}e^{-\sqrt{2C_1}y}, \quad (32)$$

we reduce expression (27) for functional I_0 to the form

$$I_0 = -6A + 2\sqrt{2C_1}\int_0^\infty \frac{dy}{y^2}\tilde{\phi}^2 e^{-\sqrt{2C_1}y} - \int_0^\infty \tilde{\phi}^2 d\left(\frac{e^{-\sqrt{2C_1}y}}{y^2}\right). \quad (33)$$

Integrating by parts the last term in Eq. (33) and using Eq. (31), we obtain

$$I_0 = C_1\int_0^\infty dy e^{-\sqrt{2C_1}y}\tilde{\phi}' + \sqrt{2C_1}\int_0^\infty dy e^{-\sqrt{2C_1}y}\left(2\frac{\tilde{\phi}^2}{y^2} - \frac{1}{2}\frac{(\tilde{\phi}')^2}{\tilde{\phi}}\right). \quad (34)$$

The integrand in the last term of formula (34) can be expressed via the derivatives of function $\tilde{\phi}$ with the help of Eq. (28). Using this equation, we obtain

$$I_0 = \int_0^\infty dy e^{-\sqrt{2C_1}y} \times (C_1\tilde{\phi}' + C_1\sqrt{2C_1}\tilde{\phi} - \sqrt{2C_1}\tilde{\phi}'') = 0. \quad (35)$$

5. FUNCTIONAL I WITH ALLOWANCE OF THE FIRST-ORDER TERMS

To obtain functional I_1, it is necessary to retain the terms small in parameter C_1^{-2} in expression (26) for functional I. For this purpose, we represent function Z in the form

$$Z = Z_0 + Z_1, \quad (36)$$

where Z_0 is a solution to Eq. (28) and the first-order correction Z_1 satisfies the equation

$$Z_1''' + \frac{(Z_0'')^2}{2(Z_0')^2}Z_1' - \frac{Z_0''Z_1''}{Z_0'} - C_1 Z_1' + \frac{4}{y^2}Z_0'Z_1' = \frac{Z_0^2}{8Z_0'} - \frac{y^2 Z_0'}{8}. \quad (37)$$

Taking into account formulas (27) and (35), we reduce expression (26) for functional I to the form

$$I = I_0 + I_1,$$

$$I_1 = \int_0^\infty \frac{dy}{y^2}e^{-\sqrt{2C_1}y}\left\{2Z_0'Z_1'\left(\frac{2}{y} + 3\sqrt{2C_1}\right) + (Z_0')^2\left(-\frac{1}{8(2C_1)^{3/2}} - \frac{y}{16C_1} + \frac{y^2}{12\sqrt{2C_1}} + \frac{y^3}{8}\right)\right\}. \quad (38)$$

We pass to the new variables

$$y = \frac{x}{\sqrt{2C_1}}, \quad Z_0(y) = \tilde{Z}_0(x)/\sqrt{2C_1}, \quad Z_1 = \tilde{Z}_1(x)/(2C_1)^{5/2} \quad (39)$$

and set

$$\phi(x) = \frac{\partial\tilde{Z}_0(x)}{\partial} = \tilde{Z}_0'. \quad (40)$$

Functions $\phi(x)$ and $\tilde{Z}_1(x)$ satisfy the equations

$$\begin{aligned}\phi'' - \frac{1}{2}\frac{(\phi')^2}{\phi} - \frac{1}{2}\phi + \frac{2}{x^2}\phi^2 &= 0,\\ \tilde{Z}_1''' + \frac{1}{2}\frac{(\phi')^2}{\phi^2}\tilde{Z}_1' - \frac{\phi'\tilde{Z}_1''}{\phi}&\\ -\frac{1}{2}\tilde{Z}_1' + \frac{4}{x^2}\phi\tilde{Z}_1' &= \frac{\tilde{Z}_0^2}{8\phi} - \frac{x^2\phi}{8}.\end{aligned} \tag{41}$$

In the new variables, functional I_1 (38) is defined as

$$\begin{aligned}I_1 = \frac{1}{C_1}\int_0^\infty \frac{dx}{x^2}e^{-x}\Big\{\tilde{Z}_0\tilde{Z}_1'\Big(\frac{2}{x}+3\Big)&\\ + \frac{(\tilde{Z}_0')^2}{16}\Big(-1-x+\frac{2x^2}{3}+x^3\Big)\Big\}.&\end{aligned} \tag{42}$$

For small values of x, function $\tilde{Z}_0$ is equal to

$$\tilde{Z}_0 = \Big(\frac{A}{C_1}\Big)\frac{x^3}{2} \tag{43}$$

and, hence, depends only on one parameter,

$$\alpha = \frac{A}{C_1}. \tag{44}$$

Function $\tilde{Z}_1$ also depends only on parameter α. As a result, functional C_1I_1 on function $\tilde{Z}_0 + \tilde{Z}_1$ is a function only of parameter α:

$$C_1I_1 = F(\alpha). \tag{45}$$

For all regular solutions to Eq. (41), the condition $I_1 = 0$ holds. We investigate the solution to Eq. (41) in different domains relative to the parameter α.

6. FUNCTIONS $\tilde{Z}_0$ AND $\tilde{Z}_1$ IN THE NEIGHBORHOOD $|\alpha - 1/6| \ll 1$

Equations (41) can be simplified considerably with the help of the substitution

$$\phi = U^2, \quad \tilde{Z}_1' = UG. \tag{46}$$

As a result, system of equations (41) is reduced to the form

$$\begin{aligned}U'' - \frac{U}{4} + \frac{1}{x^2}U^3 &= 0,\\ G'' + \Big(-\frac{1}{4} + \frac{3U^2}{x^2}\Big)G &= \frac{\tilde{Z}_0^2}{8U^3} - \frac{x^2U}{8}.\end{aligned} \tag{47}$$

In the domain of small values of x, functions $\tilde{Z}_0$, U, and G are equal to

$$\begin{aligned}\tilde{Z}_0 &= \frac{\alpha x^3}{2}\Big[1 + \frac{x^2}{20}(1-6\alpha) + \ldots\Big],\\ U &= \sqrt{\frac{3\alpha}{2}}x\Big[1 + \frac{x^2}{24}(1-6\alpha)\\ &\quad + \frac{x^4}{480}(1-6\alpha)\Big(\frac{1}{4} - \frac{9\alpha}{2}\Big) + \ldots\Big],\\ G &= -\sqrt{\frac{2\alpha}{3}}\frac{x^5}{120}\Big[1 - x^2\Big(\frac{\alpha}{4} - \frac{5}{168}\Big) + \ldots\Big].\end{aligned} \tag{48}$$

We set

$$\alpha = \frac{1}{6} + \alpha_1, \quad |\alpha_1| \ll \frac{1}{6}. \tag{49}$$

In the domain $|\alpha_1| \ll 1/6$, Eqs. (41) imply that

$$U = \frac{x}{2} + \alpha_1U_1 + \alpha_1^2U_2, \tag{50}$$

$$\begin{aligned}\tilde{Z}_0 &= \frac{x^3}{12}\\ &\quad + \int_0^x dx_1[\alpha_1x_1U_1(x_1) + \alpha_1^2(U_1^2(x_1) + x_1U_2(x_1))]\\ &= \frac{x^3}{12} + \alpha_1\tilde{Z}_0^{(1)} + \alpha_1^2\tilde{Z}_0^{(2)},\\ G &= G_0 + \alpha_1G_1 + \alpha_1^2G_2,\end{aligned}$$

where

$$\begin{aligned}U_1 &= \frac{3\sqrt{2}}{2}\sin\Big(\frac{x}{\sqrt{2}}\Big),\\ G_0 &= -\frac{x^3}{9} + \frac{4}{3}x - \frac{4\sqrt{2}}{3}\sin\Big(\frac{x}{\sqrt{2}}\Big).\end{aligned}$$

Functions U_2 and $G_{1,2}$ satisfy the equations

$$U_2'' + \frac{1}{2}U_2 = -\frac{3}{2x}U_1^2, \tag{51}$$

$$\begin{aligned}G_1'' + \frac{1}{2}G_1 = \frac{1}{\sqrt{2}}\Big\{-\frac{x}{\sqrt{2}}\cos\Big(\frac{x}{\sqrt{2}}\Big)&\\ + \sin\Big(\frac{x}{\sqrt{2}}\Big)\Big[-11 + \frac{x^2}{2} + \frac{12\sqrt{2}}{x}\sin\Big(\frac{x}{\sqrt{2}}\Big)\Big]\Big\},&\end{aligned}$$

$$G_2'' + \frac{1}{2}G_2 = -\frac{3}{x}G_1U_1 - 3G_0\left(\frac{U_1^2}{x^2} + \frac{U_2}{x}\right)$$

$$-\frac{x^2}{6}U_2 + \frac{1}{6}\tilde{Z}_0^{(2)} - \frac{\tilde{Z}_0^{(1)}U_1}{x} + \frac{x}{6}U_1^2 + \frac{1}{x^3}(\tilde{Z}_0^1)^2.$$

The direct computation of the integral in formula (42) with the help of formulas (47)–(51) confirms the above statement that functional I_1 vanishes for all regular solutions to Eqs. (41).

With the growth of parameter α in the domain $\alpha > \alpha_c$, function $U(x)$ has first-order zeros. Solution U_c for $\alpha = \alpha_c$ exponentially decreases as $x \longrightarrow \infty$ and is a separatrix. Numerical computation leads to the following value of α_c:

$$\alpha_c = 3.1355. \tag{52}$$

Our conjecture is that the straight line

$$A = \alpha_c C_1 \tag{53}$$

is singular and the points corresponding to solutions with zero energy also lie along this line. We shall check this conjecture below.

7. DOMAIN OF LARGE VALUES OF $\alpha \gg 1$

We find a solution to the first equation in (47) in the domain where the values of parameter $\alpha \gg 1$. We set

$$\sqrt{\alpha}x = \xi, \quad U(x) = \tilde{U}(\xi). \tag{54}$$

In the principal approximation in parameter α^{-1}, the first equation in (47) takes the form

$$\frac{\partial^2\tilde{U}}{\partial\xi^2} + \frac{1}{\xi^2}\tilde{U}^3 = 0. \tag{55}$$

Equation (55) is a particular case of the Emden–Fowler equation [10–12]. For small values of ξ, function $\tilde{U}$ can be expanded into a Taylor series:

$$\tilde{U} = \sqrt{\frac{3}{2}}\xi\left[1 - \frac{1}{4}\xi^2 + \frac{9}{160}\xi^4 - \frac{57}{4480}\xi^6 + \ldots\right]. \tag{56}$$

In the domain of large values of ξ, we seek a solution to Eq. (55) in the form

$$\tilde{U} = \xi^\nu\phi_1(\xi^\nu) + \phi_2(\xi^\nu) + \ldots, \tag{57}$$

where $\phi_{1,2}$ are functions bounded on the real axis and ν is a free parameter. Substituting expression (57) for $\tilde{U}$ into formula (55), we obtain equations for functions $\phi_{1,2}$:

$$\frac{\partial^2\phi_1}{\partial\tilde{y}^2} + \frac{1}{\nu^2}\phi_1^3 = 0,$$
$$\frac{\partial^2\phi_2}{\partial\tilde{y}^2} + \frac{3}{\nu^2}\phi_1^2\phi_2 + (3\nu^2 - \nu)\frac{\partial\phi_1}{\partial y} = 0, \tag{58}$$

where

$$\tilde{y} = \xi^\nu. \tag{59}$$

The solvability condition for the second equation in (58) determines the value of parameter ν:

$$\nu = 1/3. \tag{60}$$

The general solution to the first equation in (58) is

$$\phi_1 = 2^{1/4}\sqrt{\frac{E}{3}}\,\mathrm{sn}\left(\frac{\sqrt{3E}}{2^{1/4}}(\xi^{1/3} + \xi_0), i\right), \tag{61}$$

where E and ξ_0 are free parameters whose values are determined by the boundary conditions (solution (56) to Eq. (55)). Function $\mathrm{sn}(x, k)$ is an elliptic Jacobi function [13]. The function $\mathrm{sn}(x, i)$ can be represented in the form

$$\mathrm{sn}(x, i) = \frac{2\pi}{K}\sum_{N=1}^{\infty}\frac{(-1)^{N+1}e^{-\pi(N-1/2)}}{1 + e^{-\pi(2N-1)}} \times \sin\left((2N-1)\frac{\pi x}{2K}\right), \tag{62}$$

where K is the complete elliptic integral

$$K = \frac{\pi}{2\sqrt{2}}F\left(\frac{1}{2}, \frac{1}{2}, 1, \frac{1}{2}\right) = 1.3110287. \tag{63}$$

In formula (63), F is a hypergeometric function. The quantity K can also be represented in the form

$$K^2 = \pi^2\sum_{N=1}^{\infty}(2N-1)(-1)^{N+1}\frac{e^{-\pi(N-1/2)}}{1 + e^{-\pi(2N-1)}}, \tag{64}$$

which follows from formula (62).

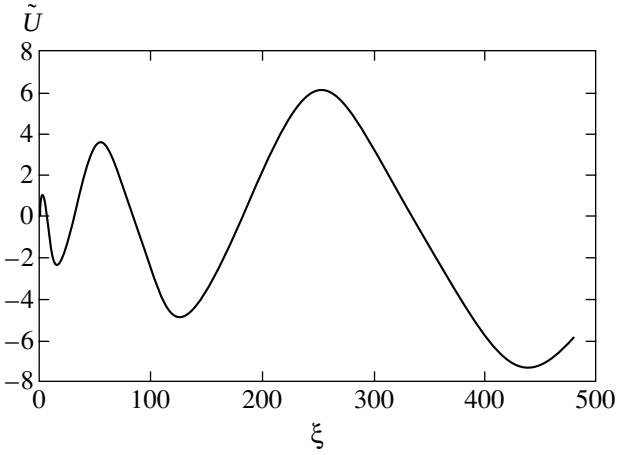

The plot of $\tilde{U}(\xi)$ function.

In the case considered, quantities K and K' are connected via the relation

$$K' = (1 - i)K, \quad (65)$$

which implies formula (64).

Numerical computation (the location of zeros of function $\tilde{U}$) determines the values of parameters E and ξ_0:

$$E = 1.324, \quad \xi_0 = 1.314. \quad (66)$$

Function $\tilde{U}(\xi)$ is presented in the figure. It can be seen that, in the domain of large values of parameters C_1 and α, there exists a large domain in which the intermediate asymptotic form defined by formulas (54), (57), and (61) is realized. A typical feature of the intermediate asymptotic form is that the growth of the amplitude of oscillation of function $\tilde{U}$ is proportional to $\xi^{1/3}$ in the domain

$$1 < \xi < \alpha^{3/4}. \quad (67)$$

The upper bound in formula (67) is connected with the range of applicability of Eq. (55).

8. CONCLUSIONS

Weakly collapsing solutions to Eq. (1) form a three-parametric family of solutions $\{A, C, C_1\}$. One of these parameters (C) corresponds to the scale transformation and can be set equal to unity while investigating the solutions. On plane $\{A, C_1\}$, there exists a discrete set of points corresponding to weakly collapsing solutions with zero energy. An infinite family of such solutions located near the straight line $A = C_1/6$ was found in [6, 7]. We have shown that there exists another singular line on plane $\{A, C_1\}$. This line is defined by the equation

$$A = \alpha_c C_1, \quad \alpha_c \approx 3.1355. \quad (68)$$

We make the conjecture that another family of weakly collapsing solutions with zero energy is located near this line. The study of the condition for the existence of solutions with zero energy shows that there exists an infinite set of functionals I_N such that $I_N \equiv 0$ for the solutions to the corresponding differential equation. Each of these solutions is associated with Eq. (6). A method for constructing functionals I_N and the differential equations associated with it is given.

We have also shown that, for large values of parameters $\{C_1, \alpha = A/C_1\}$, there exists a domain of intermediate asymptotic form. A typical feature of this domain is the growth of the oscillation amplitude $\tilde{U}(\xi)$ in proportion to $\xi^{1/3}$.

ACKNOWLEDGMENTS

The work was financially supported by the CRDF (USA) (grant no. RP-2251) and the Russian Foundation for Basic Research and Ministry of Science of the Russian Federation.

REFERENCES

1. V. E. Zakharov, Zh. Éksp. Teor. Fiz. **62**, 1746 (1972) [Sov. Phys. JETP **35**, 908 (1972)].
2. V. E. Zakharov and V. S. Synakh, Zh. Éksp. Teor. Fiz. **68**, 940 (1975) [Sov. Phys. JETP **41**, 464 (1976)].
3. Yu. N. Ovchinnikov and I. M. Sigal, Zh. Éksp. Teor. Fiz. **116**, 67 (1999) [JETP **89**, 35 (1999)].
4. V. I. Talanov, Pis'ma Zh. Éksp. Teor. Fiz. **11**, 303 (1970) [JETP Lett. **11**, 199 (1970)].
5. G. M. Fraĭman, Zh. Éksp. Teor. Fiz. **88**, 390 (1985) [Sov. Phys. JETP **61**, 228 (1985)].
6. Yu. N. Ovchinnikov and V. L. Vereshchagin, Zh. Éksp. Teor. Fiz. **120**, 1509 (2001) [JETP **93**, 1307 (2001)].
7. Yu. N. Ovchinnikov and V. L. Vereshchagin, Pis'ma Zh. Éksp. Teor. Fiz. **74**, 76 (2001) [JETP Lett. **74**, 72 (2001)].
8. Yu. N. Ovchinnikov, Pis'ma Zh. Éksp. Teor. Fiz. **69**, 387 (1999) [JETP Lett. **69**, 418 (1999)].
9. C. Sulen and P.-L. Sulen, *The Nonlinear Schrödinger Equation: Self-Focusing and Wave Collapse* (Springer, New York, 1999).
10. E. Kamke, *Gewöhnliche Differentialgleichungen* (Academie, Leipzig, 1959; Fizmatgiz, Moscow, 1961).
11. R. Bellman, *Stability Theory of Differential Equations* (McGraw-Hill, New York, 1953; Inostrannaya Literatura, Moscow, 1954).
12. G. Sansone, *Equazioni Differenziali nel Campo Reale* (Bolonia, 1954; Inostrannaya Literatura, Moscow, 1954), Vol. II.
13. I. S. Gradshteĭn and I. M. Ryzhik, *Tables of Integrals, Series, and Products*, 4th ed. (Fizmatgiz, Moscow, 1962; Academic, New York, 1980).

Translated by E. Pankratiev

Journal of Experimental and Theoretical Physics, Vol. 96, No. 5, 2003, pp. 982–984.
Translated from Zhurnal Éksperimental'noĭ i Teoreticheskoĭ Fiziki, Vol. 123, No. 5, 2003, pp. 1113–1116.

MISCELLANEOUS

Extremal Unraveling of a Quantum Operation

L. V. Il'ichev

Institute of Automatics and Electrometry, Siberian Division, Russian Academy of Sciences, Universitetskii pr. 1, Novosibirsk, 630090 Russia

e-mail: leonid@iae.nsk.su

Received December 10, 2002

Abstract—The problem of unraveling a quantum operation, i.e., a procedure of retargeting the environment for obtaining some information from a quantum system, which preserves the operation itself, is considered. An unraveling during which a minimal amount of information enters the environment is found. This unraveling is independent of the number of accomplished events. © *2003 MAIK "Nauka/Interperiodica".*

1. INTRODUCTION

The concept of an operation [1] is a key one in the quantum theory of information. It is the most general map (which is, of course, consistent with the laws of quantum mechanics),

$$\mathscr{E} : \hat{\varrho}_{\text{in}} \longmapsto \hat{\varrho}_{\text{out}} = \mathscr{E}(\hat{\varrho}_{\text{in}}), \tag{1}$$

which transforms the input state $\hat{\varrho}_{\text{in}}$ of a quantum system into an output state $\hat{\varrho}_{\text{out}}$ that might belong to another system. It is conventional to consider the arrow in expression (1) as a channel of transmission of (quantum) information. The physical properties of the channel determine the form of operation $\mathscr{E}$.

There are three conditions that must be satisfied by a quantum operation: (1) for any input state $\hat{\varrho}$, we have $\mathrm{Tr}\mathscr{E}(\hat{\varrho}) \le 1$ (in essence, this quantity is the probability of channel operation); (2) map $\mathscr{E}$ is linear; and (3) $\mathscr{E}$ possesses a so-called complete positivity. The latter condition guarantees the positivity of the output state of the system even in the case when $\mathscr{E}$ acts on a subsystem.

There exists an operator-sum representation of $\mathscr{E}$ [1]. Namely, for any quantum operation $\mathscr{E}$, there exists a set $\{\hat{E}_\alpha\}_{\alpha \in A}$ of operators acting from the space of input states $\mathscr{H}_{\text{in}}$ into the state of output spaces $\mathscr{H}_{\text{out}}$ so that

$$\mathscr{E}(\hat{\varrho}) = \sum_{\alpha \in A} \hat{E}_\alpha \hat{\varrho} \hat{E}_\alpha^\dagger. \tag{2}$$

For the sake of simplicity and definiteness, we confine our analysis to the case of a finite set $\{\hat{E}_\alpha\}_{\alpha=1}^N$. We also assume that the condition of the so-called completeness of the operation

$$\sum_\alpha \hat{E}_\alpha^\dagger \hat{E}_\alpha = 1 \tag{3}$$

holds. Physically, this means that the operation necessarily occurs; i.e., the channel will operate. However, expression (2) shows that the channel operation can be of N types. Here, the probability $P(\alpha)$ of the αth type of operation for an input state $\hat{\varrho}$ is $\mathrm{Tr}(\hat{E}_\alpha^\dagger \hat{E}_\alpha \hat{\varrho})$ and the output state is $\hat{E}_\alpha \hat{\varrho} \hat{E}_\alpha^\dagger / P(\alpha)$. Expression (2) is the result averaged over distribution $\{P(\alpha)\}_{\alpha=1}^N$. Every type of channel operation is an event, e.g., the click of a certain detector (with number α).

From the form of Eq. (2), one can easily guess the transformation of the set $\{\hat{E}_\alpha\}_{\alpha=1}^N$ that preserves operation $\mathscr{E}$,

$$\hat{E}_\alpha \longmapsto \hat{E}_\alpha(U) \stackrel{\text{def}}{=} \sum_\beta U_{\alpha\beta} \hat{E}_\beta, \tag{4}$$

where U is a unitary matrix from $SU(N)$. This fact is well known. If the click of detector α is caused by the absorption of a photon of type α, transformation (4) can be physically realized with the help of a system of beam splitters so that the probability amplitude of a click of detector α includes the alternatives in which this click is caused by photons of type $\beta \ne \alpha$. In a certain sense, this justifies that the aggregate of events corresponding to set $\{\hat{E}_\alpha(U)\}_{\alpha=1}^N$ can be called superpositional with respect to the initial aggregate corresponding to set $\{\hat{E}_\alpha\}_{\alpha=1}^N$. Following Carmichael, we refer to a concrete set $\{\hat{E}_\alpha\}_{\alpha=1}^N$ realizing expansion (2) as the unraveling of the quantum operation $\mathscr{E}$.

2. BASIC RELATIONS

Here, we search for an extremal (in the sense defined below) unraveling. Now, the probability of

occurrence of an event α is

$$P(\alpha; U) = \mathrm{Tr}(\hat{E}_\alpha(U)\hat{\rho}\hat{E}_\alpha^\dagger(U)) = \sum_{\beta,\beta'} M_{\beta\beta'}U_{\alpha\beta'}\bar{U}_{\alpha\beta}, \quad (5)$$

where

$$M_{\beta\beta'} = \mathrm{Tr}(\hat{E}_\beta^\dagger\hat{E}_{\beta'}\hat{\rho}) \quad (6)$$

is the unit trace matrix corresponding to a positive definite Hermitian quadratic form.

When an event occurs (i.e., an operation is executed), the amount of information

$$S_1(U) = -\sum_\alpha P(\alpha; U)\ln P(\alpha; U) \quad (7)$$

is written in the environment. It was shown in [2] that $S_1(U)$ is also the average amount of information required for describing the output state after the occurrence of a specific event. Our problem is to find the unraveling, i.e., matrix $U(1)$ (the number in the parentheses corresponds to the number of events that occurred) for which $S_1(U)$ has an extremum. At the same time, we will show that the extremum found is a minimum. The problem of the search for a "minimal" unraveling of a quantum operation as applied to some problems of quantum optics was formulated in [3], where a solution was found for the case of a pure initial state. In those papers, the criterion for the minimal unraveling was formulated in another way; however, it is equivalent to our criterion and is a particular case of the general solution given below.

To find the extremum, we apply the method of indeterminate Lagrangian multipliers by fixing the unitarity condition $UU^* = 1$. The matrix of the Lagrangian multipliers so far being indeterminate, the condition

$$\frac{\partial}{\partial\bar{U}_{\alpha\beta}}\left(S_1(U) + \sum_{\alpha_1,\alpha_2,\beta'}\lambda_{\alpha_1\alpha_2}\bar{U}_{\alpha_1\beta'}U_{\alpha_2\beta'}\right)\Bigg|_{U=U(1)} = 0 \quad (8)$$

should be satisfied. This implies that

$$[\ln P(\alpha, U(1)) + 1]\sum_{\beta'} M_{\beta\beta'}U_{\alpha\beta'}(1) = \sum_{\alpha'}\lambda_{\alpha\alpha'}U_{\alpha'\beta}(1). \quad (9)$$

Note that, since matrix U is unitary, we can always make the substitution

$$\lambda_{\alpha\alpha'} \longrightarrow \delta_{\alpha\alpha'}\lambda_{\alpha\alpha} \quad (10)$$

without changing the variable quantity in Eq. (8). If we carry out this substitution in Eq. (9), it is immediately transformed into the following condition for $U(1)$:

$$\sum_{\beta'} M_{\beta\beta'}U_{\alpha\beta'}(1) = \mu_\alpha U_{\alpha\beta}(1); \quad (11)$$

i.e., the rows of matrix $U(1)$ are the eigenvectors of matrix M. Simultaneously, quantities $\lambda_{\alpha\alpha}$ are specified. The result can also be written in the following form:

$$M_{\beta\beta'} = \sum_{\alpha'}\mu_{\alpha'}U_{\alpha'\beta}(1)\bar{U}_{\alpha'\beta'}(1). \quad (12)$$

It is natural to consider the problem on extremal unraveling of a quantum operation as applicable also to histories, i.e., series of events obtained by repeatedly applying an operation to the same quantum system. For the sake of simplicity, assume that the system does not evolve during the time intervals between applications of the operation. The expression for the probability of realization of history $\{\alpha_1, \ldots, \alpha_n\}$ is the obvious generalization of relation (5):

$$P(\alpha_1, \ldots, \alpha_n; U) = \mathrm{Tr}(\hat{E}_{\alpha_n}(U)\ldots\hat{E}_{\alpha_1}(U)\hat{\rho}\hat{E}_{\alpha_1}^\dagger(U)\ldots\hat{E}_{\alpha_n}^\dagger(U)) = \sum_{\substack{\beta_1,\ldots,\beta_n \\ \beta_1',\ldots,\beta_n'}} M_{\beta_1\ldots\beta_n,\beta_n'\ldots\beta_1'}U_{\alpha_1\beta_1'}\ldots U_{\alpha_n\beta_n'}\bar{U}_{\alpha_1\beta_1}\ldots\bar{U}_{\alpha_n\beta_n}, \quad (13)$$

where

$$M_{\beta_1\ldots\beta_n,\beta_n'\ldots\beta_1'} = \mathrm{Tr}(\hat{E}_{\beta_1}^\dagger\ldots\hat{E}_{\beta_n}^\dagger\hat{E}_{\beta_n'}\ldots\hat{E}_{\beta_1'}\hat{\rho}). \quad (14)$$

Arguments similar to the ones applied in the case of a one-event history imply the following conditions imposed on the matrix $U(n)$ of extremal unraveling in the case of n events. For any i $(1 \le i \le n)$, we have the equality

$$\sum_{\substack{\beta_1,\ldots,\not{\beta}_i,\ldots,\beta_n \\ \beta_1',\ldots,\beta_n'}} \bar{U}_{\alpha_1\beta_1}(n)\ldots\bar{\not{U}}_{\alpha_i\beta_i}(n)\ldots\bar{U}_{\alpha_n\beta_n}(n) \times M_{\beta_1\ldots\beta_n,\beta_n'\ldots\beta_1'}U_{\alpha_1\beta_1'}(n)\ldots U_{\alpha_n\beta_n'}(n) = \mu_{\alpha_1\ldots\alpha_n}U_{\alpha_i\beta_i}(n). \quad (15)$$

Here, crossing out denotes that the corresponding symbol is absent. Setting $i = 1$ in this expression, summing it over $\alpha_2, \ldots, \alpha_n$, and taking into account that, by virtue of (3),

$$\sum_{\beta_n} M_{\beta_1\ldots\beta_{n-1}\beta_n,\beta_n\beta_{n-1}'\ldots\beta_1'} = M_{\beta_1\ldots\beta_{n-1},\beta_{n-1}'\ldots\beta_1'},$$

etc., we obtain the important result

$$U_{\alpha\beta}(n) = U_{\alpha\beta}(1) \quad (16)$$

for any n and

$$\mu_{\alpha_1 \ldots \alpha_{n-1}} = \sum_{\alpha_n} \mu_{\alpha_1 \ldots \alpha_n}. \quad (17)$$

As a generalization of Eq. (12), we have

$$M_{\beta_1 \ldots \beta_n, \beta_n \ldots \beta_1'} = \sum_{\alpha_1', \ldots, \alpha_n'} \mu_{\alpha_1' \ldots \alpha_n'} U_{\alpha_1' \beta_1}(1) \ldots U_{\alpha_n' \beta_n}(1) \times \bar{U}_{\alpha_1' \beta_1'}(1) \ldots \bar{U}_{\alpha_n' \beta_n'}(1). \quad (18)$$

Now, we prove that the extremum found is a minimum. For this purpose, consider the term bilinear in dU and dU^* in the expansion of the difference

$$\delta S_n(U(1)) = S_n(U(1) + dU) - S_n(U(1)). \quad (19)$$

First, note that the unitarity condition implies that

$$\sum_{\beta} (U_{\alpha\beta}(1) d\bar{U}_{\alpha'\beta} + dU_{\alpha\beta} \bar{U}_{\alpha'\beta}(1) + dU_{\alpha\beta} d\bar{U}_{\alpha'\beta}) = 0 \quad \forall \alpha, \alpha'. \quad (20)$$

With the help of this relation, the probability variation bilinear in dU and dU^* can be represented in the form

$$\delta P(\alpha_1, \ldots, \alpha_n; U(1)) = \sum_{i=1}^{n} \sum_{\alpha_i'} (\mu_{\alpha_1 \ldots \alpha_i' \ldots \alpha_n} - \mu_{\alpha_1 \ldots \alpha_n}) K_{\alpha_i' \alpha_i}. \quad (21)$$

Here,

$$K_{\alpha'\alpha} = \sum_{\beta, \beta'} \bar{U}_{\alpha'\beta'}(1) U_{\alpha'\beta}(1) dU_{\alpha\beta'} d\bar{U}_{\alpha\beta}. \quad (22)$$

One can easily see that, by virtue of (20), $K_{\alpha_i' \alpha_i} = K_{\alpha_i \alpha_i'}$. Moreover, it is obvious that $K_{\alpha_i' \alpha_i} \geq 0$ $\forall \alpha, \alpha'$. Using expression (21), we can represent the entropy variation $\delta S_n(U(1))$ in the form

$$\delta S_n(U(1)) = -\sum_{i=1}^{n} \sum_{\substack{\alpha_1, \ldots, \alpha_n \\ \alpha_i'}} \ln \mu_{\alpha_1 \ldots \alpha_n} (\mu_{\alpha_1 \ldots \alpha_i' \ldots \alpha_n} - \mu_{\alpha_1 \ldots \alpha_n}) K_{\alpha_i' \alpha_i}. \quad (23)$$

Permuting $\alpha_i \longleftrightarrow \alpha_i'$ in each ith term of this series and taking the half-sum of the initial and resultant expressions, we come to the following result:

$$\delta S_n(U(1)) = \frac{1}{2} \times \sum_{i=1}^{n} \sum_{\substack{\alpha_1, \ldots, \alpha_n \\ \alpha_i'}} \ln \frac{\mu_{\alpha_1 \ldots \alpha_i' \ldots \alpha_n}}{\mu_{\alpha_1 \ldots \alpha_n}} (\mu_{\alpha_1 \ldots \alpha_i' \ldots \alpha_n} - \mu_{\alpha_1 \ldots \alpha_n}) K_{\alpha_i' \alpha_i}. \quad (24)$$

Obviously, it is positive.

3. CONCLUSION

Thus, we have proved the following theorem.

The matrix of the unitary transformation of extremal unraveling of a quantum operation for histories with an arbitrary number of events is composed of the eigenvectors of matrix $M_{\beta\beta'}$ (6). In this case, a minimal amount of information possible for a history of this length is transmitted into the environment.

Note that the unraveling principle is also applicable to the quantum control equation in the Lindblad form [4]. Here, the role of set $\{\hat{E}\}_{\alpha \in A}$ is played by a set of the Lindblad operators (the criterion of operation (2) is not necessarily satisfied). The matrix of the minimal unraveling for a single event is defined in the same way. However, in this case, it is not universal and is specific for each number of events.

REFERENCES

1. K. Kraus, *States, Effects, and Operations: Fundamental Notions of Quantum Theory* (Springer, Berlin, 1983).
2. C. M. Caves, Phys. Rev. E **47**, 4010 (1993).
3. J. K. Breslin, G. J. Milburn, and H. M. Wiseman, Phys. Rev. Lett. **74**, 4827 (1995); J. K. Breslin and G. J. Milburn, J. Mod. Opt. **44**, 2469 (1997).
4. G. Lindblad, Commun. Math. Phys. **48**, 119 (1976).

Translated by E. Pankratiev